博士論文

Whole architecture of the Cretaceous Northern Kyushu batholith, SW Japan: Reflections on magmatic and growth processes in small-scale plutonic bodies

（西南日本，白亜紀北部九州バソリスの全貌 −小規模岩体のマグマ過程および成長過程の反映−）

2022 年 3 月

江島 圭祐

山口大学大学院創成科学研究科

Table of contents

1 Introduction ---------- **1**

1–1 Introduction ---------- *1*

1–2 Acknowledgements ---------- *2*

2 Ushikiri-yama area ---------- **4**

2–1 Introduction ---------- *4*

2–2 Geological overview ---------- *7*

2–3 Petrography of the Ushikiri-yama granodiorite body ---------- *11*

2–3–1 Ushikiri-yama granodiorite (Ushikiri-yama Gd) ---------- 11

2–3–2 Porphyritic fine-grained tonalite (Pr Fine To) ---------- 12

2–3–3 Porphyritic fine-grained diorite (Pr Fine Di) ---------- 12

2–3–4 Porphyritic fine-grained granite (Pr Fine Gr) ---------- 13

2–4 Geochemistry and geochronology ---------- *16*

2–4–1 Mineral chemistry ---------- 16

2–4–2 Major and trace elements of whole-rock chemistry ---------- 19

2–4–3 K–Ar geochronology ---------- 21

2–4–4 Sr and Nd isotopes ---------- 22

2–5 Discussions ---------- *26*

2–5–1 Intrusive relationships of the Ushikiri-yama granodiorite and dikes --- 27

2–5–2 Genetic relationships of the south body of Ushikiri-yama granodiorite and related dikes ---------- 28

2–5–2–1 Petrogenesis of Pr Fine Gr ---------- 28

2–5–2–2 Petrogenesis of Pr Fine To ---------- 31

2–5–3 Geochemical characteristics of Pr Fine Di ---------- 32

2–5–4 Petrological evolution of the Ushikiri-yama body ---------- 35
2–5–5 Characteristics of the igneous activity in Cretaceous Northern Kyushu batholith ---------- 41

3 Shaku-dake area ---------- 42

3–1 Introduction ---------- 42

3–2 Geological overview ---------- 45

3–3 Petrography of the Shaku-dake diorite body ---------- 47

3–3–1 Occurrence and petrography of the Group-1 ---------- 47
3–3–1–1 Two-pyroxene diorite (TPD) ---------- 47
3–3–1–2 Dolerite (Do) ---------- 47
3–3–1–3 Porphyritic fine-grained tonalite (PFT) ---------- 48
3–3–1–4 Clinopyroxene granodiorite (CG) ---------- 48
3–3–2 Occurrence and petrography of the Group-2 ---------- 49
3–3–2–1 Hornblende–Biotite granodiorite (HBG) ---------- 49
3–3–2–2 Fine-grained biotite granite (FBG) ---------- 50

3–4 Geochemistry ---------- 54

3–4–1 Mineral chemistry ---------- 55
3–4–2 Major and trace elements of whole-rock ---------- 59
3–4–3 Sr and Nd isotopes ---------- 61

3–5 Discussions ---------- 63

3–5–1 Petrogenesis of the Shaku-dake body ---------- 63
3–5–1–1 Geochemical characteristics of Do and TPD ---------- 63
3–5–1–2 Petrogenetic relationships among the intrusive rocks of the Shaku-dake body ---------- 67
3–5–1–3 Petrological evolution model of the Shaku-dake body ---------- 76
3–5–2 Vertical and horizontal variations in Shaku-dake body (TPD body) ---------- 78

3–5–3 Shaku-dake body (TPD body) growth model and magma plumbing system ---------- 81
3–5–3–1 TPD magma plumbing system ---------- 81
3–5–3–2 TPD growth and lithofacies change model ---------- 85

4 Northern part of Shaku-dake area ---------- 88

4–1 Introduction ---------- 88

4–2 Geological overview ---------- 92

4–3 Petrography of the analyzed samples ---------- 95
4–3–1 Porphyritic fine-grained tonalite (PFT) ---------- 95
4–3–2 Clinopyroxene quartz diorite (CQD) ---------- 96

4–4 Geochemistry ---------- 101
4–4–1 Major and trace elements of whole-rock chemistry ---------- 101
4–4–2 Mineral chemistry ---------- 103

4–5 Discussions ---------- 108
4–5–1 Compositional change processes of the PFT ---------- 108
4–5–2 Compositional change processes of the CQD ---------- 114

4–6 Igneous activity model of the PFT and CQD ---------- 119

5 Kita-taku area ---------- 122

5–1 Introduction ---------- 122

5–2 Geological overview ---------- 125

5–3 Petrography of the Kita-taku mafic complex and related intrusive rocks -- 128
5–3–1 Occurrence and petrography of the Cumulate group (Type 1 to 4) --- 128
5–3–1–1 Ol gabbronorite–Ol bearing Pxs hornblendite (Type 1) ---------- 128
5–3–1–2 Ol gabbronorite (Type 2) ---------- 129
5–3–1–3 Cumulus Cpx gabbro (Type 3) ---------- 130

5–3–1–4 Cumulus Hb gabbro (Type 4) ---------- 130
5–3–2 Occurrence and petrography of the Gabbro group (Type 5 to 7) ------ 131
5–3–2–1 Foliated Hb gabbro (Type 5) ---------- 131
5–3–2–2 Mixed Hb gabbro (Type 6) ---------- 131
5–3–2–3 Pegmatitic Hb gabbro (Type 7) ---------- 132
5–3–3 Occurrence and petrography of the related rocks (granite, PFD, trondhjemite) ---------- 132
5–3–3–1 Ms-Bt granite (Fukae Gr) ---------- 132
5–3–3–2 Trondhjemite (Tdh) ---------- 133
5–3–3–3 Porphyritic fine-grained diorite (PFD) ---------- 133
5–4 Geochronology and geochemistry ---------- 142
5–4–1 Zircon U–Pb dating ---------- 143
5–4–2 Major and trace elements of whole-rock ---------- 147
5–4–3 Mineral chemistry ---------- 149
5–4–4 Trace element composition of clinopyroxene ---------- 157
5–4–5 Sr and Nd isotopes ---------- 160
5–5 Discussions ---------- 161
5–5–1 Activity period of the Kita-taku mafic complex and related igneous rocks ---------- 161
5–5–2 Crystallization of the Kita-taku mafic complex ---------- 162
5–5–3 Characteristics of the parent magma for Kita-taku mafic complex --- 167
5–5–4 Growth and formation processes of the Kita-taku mafic complex ---- 171
6 Northern Kyushu batholith ---------- 175
6–1 Heat source of the large-scale Cretaceous igneous activity in northern Kyushu ---------- 175
6–2 Evidence of partial melting and formation of felsic magma in Northern

Kyushu batholith at Cretaceous period ---------- *179*

6–3 Anatomy of the Cretaceous igneous activity in northern Kyushu ---------- *184*

6–4 Geological development of northern Kyushu to the eastern edge of Eurasia – felsic magma generation and tectonic model---------- *189*

6–5 Summary ---------- *192*

References ---------- 195

Appendix ---------- 226

Figure 1–1. (a) and (b) Distribution of Cretaceous igneous rocks in the northern Kyushu districts. (c) Index map of the northern Kyushu with Cretaceous igneous rocks. Red dotted squares indicate that study areas. HMA: high-Mg andesite, HMD: high-Mg diorite, Gr: granite, Gd: granodiorite, and To: tonalite. 3

Figure 2–1. Distribution of Cretaceous igneous rocks in the northern Kyushu districts. (a) Index map of the northern Kyushu districts with Cretaceous igneous rocks (Karakida, 1985; Owada et al., 1999). (b) Simplified geological map around the study area. Gr: granite, Gd: granodiorite, and To: tonalite. 6

Figure 2–2. (a) Geological map of the study area (Eshima et al., 2019). The white circle indicates sampling sites of the K–Ar dating samples from Ushikiri-yama Gd (north and south bodies: Table 2–2) . (b) Mutual relationships between igneous and metamorphic rocks in the study area. Arrows indicate intrusive relationships, (c) Bird's-eye view of the study area (dip angle 25°). (d) Cross-sections of the study area along lines A–B'–A' and B–B'–B". Abbreviations are shown in the text. 9

Figure 2–3. Field occurrences of the Ushikiri-yama granodiorite (Gd) and related rocks. (a) Xenolith of pelitic hornfels (pelitic metamorphic rocks) within the Ushikiri-yama Gd (south body). (b) Preferred orientation of hornblende and plagioclase crystals indicating flow direction within Ushikiri-yama Gd. (c) Porphyritic fine-grained tonalite (Pr Fine To) dike intruding the Ushikiri-yama Gd (south body). (d) Porphyritic fine-grained diorite (Pr Fine Di) intruding the Ushikiri-yama Gd (south body). (e) Porphyritic fine-grained granite (Pr Fine Gr) dike cutting the Ushikiri-yama Gd (south body). (f) Boundary between the Ushikiri-yama Gd (south body) and Pr Fine To. 10

Figure 2–4. Photomicrographs of the Ushikiri-yama granodiorite (Gd) and related rocks. (a) Ushikiri-yama Gd (south body). (b) Ushikiri-yama Gd (north body). (c) Fine-grained facies (granodiorite) in the central part of the Ushikiri-yama body (between the north and south bodies: Star mark point in Figure 2–2). This sample shows a granoblastic texture, and was collected near the north body. (d) Porphyritic fine-grained tonalite (Pr Fine To). (e) Porphyritic fine-grained diorite (Pr Fine Di). (f) Porphyritic fine-grained granite (Pr fine Gr). Qz: quartz, Pl: plagioclase, Kfs: K-feldspar, Bt: biotite, Hb: hornblende, Mag: magnetite, and Ilm: ilmenite. 14

Figure 2–5. Igneous textures in the Ushikiri-yama granodiorite (a, b, c) and porphyritic fine-grained tonalite (d, e, f). (a) Euhedral epidote crystal. (b) Dusty zoned plagioclase crystal. (c) Sponge cellular plagioclase. (d) Ocellar quartz. (e) Acicular apatite crystals within plagioclase. (f) Chemically zoned hornblende crystal. 15

Figure 2–6. Modal compositions of the Ushikiri-yama granodiorite and porphyritic fine-grained granite on the Qz–Kfs–Pl diagram. Classification boundaries are after Streckeisen (1976). The modal values are listed in Appendix 2–1. Abbreviations are shown in the text. 16

Figure 2–7. The *Ep* contents histogram of the epidote in the Ushikiri-yama granodiorite. References from (a) Yada and Owada (2003), (b) Sial et al. (1999), (c) Zen and Hammarstrom (1984), (d) Barth (1990) and Brandon et al. (1996), and (e) Muraoka et al. (2020). 18

Figure 2–8. Major and trace element variation diagrams relative to SiO_2 (wt%) for the intrusive rocks from the Mt. Ushikiri-yama area. Shoshonite, high-K, medium-K, and low-K fields are after Peccerillo and Taylor (1976). . 20

Figure 2–9. (a) FeO*/MgO–SiO_2 (wt%) diagram (after Miyashiro, 1974). HMA field (red field) is quoted from Kamei et al. (2004). (b) MgO–Fe_2O_3 (wt%) diagram. The blue and red arrows show the trends of the magma mixing and the fractional crystallization, respectively. 21

Figure 2–10. Conceptual diagram of the changes in elemental ratios that occur during the evolution of the Earth's interior. 23

Figure 2–11. Isotopic compositions of the Ushikiri-yama granodiorite and related rocks. (a) 1000/Sr–SrI (105 Ma). (b) SiO_2 (wt%)–SrI (105 Ma) and NdI (105 Ma). (c, d, and e) εSrI (105 Ma)– εNdI (105 Ma) diagrams. (c) Blue and red lines are mixing line between the Pr Fine Di and Ushikiri-yama granodiorite south body. The two Pr Fine To samples are plotted in the proximity of these lines. (d) The three dashed lines (Red, green, and blue) show assimilation line between the Pr Fine Di and pelitic metamorphic rocks, indicating uniform minor assimilation of pelitic host rocks within the Pr Fine Di. One of the Pr Fine To samples are plotted near the green dashed line, indicating that this sample was produced by the assimilation of pelitic rocks into the Pr Fine Di magma. (e) Comparison with data from granodioritic (blue field) and granitic (red field) rocks from Northern Kyushu granitoids batholith. 25

Figure 2–12. Whole-rock SiO_2 (wt%)–modal value (vol%) for the Ushikiri-yama granodiorite south body (Ushi Gd South) and Pr Fine Gr. Stage-1 (red

arrows) represents a variation trend from SiO_2-poor to SiO_2-rich Ushikiri-yama granodiorite south body, and Stage-2 (dashed yellow arrows) indicates a shift from SiO_2-rich Ushikiri-yama granodiorite south body to Pr Fine Gr. The modal values are listed in Appendix 2–1. Modal analysis was performed using the Excel spreadsheet (VBA) developed by Shimura and Kojima (2015). 29

Figure 2–13. Results of fractional crystallization modeling for the Ushikiri-yama granodiorite south body to Pr Fine Gr are shown in the spider diagrams. Normalized values of C1 chondrite are after Sun and McDonough (1989). The Rayleigh fractionation model using partition coefficients are listed in Appendix 3–3..... 30

Figure 2–14. Discrimination diagrams and C1 chondrite-normalized REE patterns for the Pr Fine Di. Cretaceous high-Mg diorites from central and northern Kyushu, and Neogene high-Mg andesites from the central Kyushu and the Setouchi area are shown (modified after Kamei et al., 2004). (a) MgO/(MgO + FeO*)–TiO_2 (wt%) diagram. (b) Y (ppm)–Sr/Y diagram. (c) Yb_N–$(La/Yb)_N$ diagram. The data for comparison were obtained from the following sources; andesite from the Kanmon Group, Yamaguchi (Imaoka and Murakami, 1979; Imaoka et al., 1993), diorite from northern Kyushu (Murakami, 1994; Kamei et al., 2004). The Neogene HMA rocks in Kyushu also geochemically possess the Sanukitic HMA (Shiraki et al., 1991; Nagao et al., 1992; Kakubuchi et al., 1995; Shiraki et al., 1995). 34

Figure 2–15. Horizontal variation in modal compositions. (a)–(f) Qz, Pl, Kfs, Hb, Bt, felsic minerals (Qz + Pl +Kfs), and mafic minerals (Hb + Bt) of the Ushikiri-yama granodiorite. White circles indicate sampling sites. These maps were created using Graph-R. The modal values are listed in Appendix 2–1. 37

Figure 2–16. Intrusive (emplacement) processes model of the Ushikiri-yama

body. 39
Figure 2–17. Schematic model showing magma processes of the Ushikiri-yama granodiorite and related rocks. Abbreviations are shown in text. 40

Figure 3–1. Distribution of Cretaceous igneous rocks in the northern Kyushu districts. (a) Index map of the northern Kyushu with Cretaceous igneous rocks. (b) Simplified geological map of the study area (Karakida, 1985). Gr: granite, Gd: granodiorite, and To: tonalite. 44
Figure 3–2. (a) Geological map of the study area (Eshima et al., 2020). The dotted square in the northern part of map indicates outcrop sites in Figures 3–21d and e. (b) Bird's-eye view of the study area (dip angle 45°). Circles with sample numbers from Sp-1 to Sp-6 are sampling sites for EPMA analyses (Figs 4–6, 7 and 8). (c) Cross-sections of the study area along lines A–B and A–C (SW–NE and NW–SE directions). (d) Mutual relationships between igneous and sedimentary rocks in the study area. Ls: limestone. Arrows indicate intrusive relationships, whereas dotted arrows show coeval relationships. 46
Figure 3–3. Field occurrences of the intrusive rocks. (a) TPD including the Wakino sub-group as xenoliths. (b) Limestone xenoliths in TPD. (c) CG and Do show the intrusive relationship each other. (d) The Do including the Wakino sub-group as xenoliths. (e) The limestone xenoliths included in the Do. (f) The composite dike consisting of the Do and PFT. Abbreviations are shown in the text. 51
Figure 3–4. Field occurrences of the intrusive rocks. (a) The PFT including the Wakino sub-group as xenoliths. (b) The CG intruding the TPD. (c) The network veins derived from the FBG intrudes the CG. (d) The CG capturing the Wakino sub-group as xenoliths. (e) The HBG intruding the TPD. (f) The FBG and Do show the intrusive relationship each other. Abbreviations

are shown in the text. 52
Figure 3–5. Photomicrographs of the intrusive rocks. (a) TPD. (b) Microxenolith of shale probably derived from the Wakino sub-group in the TPD. (c) Do. (d) PFT. (e) CG. (f) HBG. (g) FBG. Qz: quartz, Kfs: K-feldspar, Pl: plagioclase, Bt: biotite, Hb: hornblende, Cpx: clinopyroxene, Opx: orthopyroxene, Ilm: ilmenite, and Mag: magnetite. Abbreviations are shown in the text. 53
Figure 3–6. Mineral compositions of plagioclase in the TPD. (a) *Or–Ab–An* triangular plot of the TPD. (b) BSE map of the TPD (Sp-2 and Sp-6). ... 56
Figure 3–7. Mineral compositions of clinopyroxene in the TPD. (a) and (b) BSE and element mapping (Mg, Ca, and Fe) of the TPD (Sp-1 and Sp-2). (c) Pyroxene trapezoid plot (Morimoto et al., 1988; Deer et al., 2013) of the TPD. 57
Figure 3–8. Mineral compositions of orthopyroxene in the TPD. (a) and (b) BSE map of the TPD (Sp-2 and Sp-5). (c) Pyroxene trapezoid plot (Morimoto et al., 1988; Deer et al., 2013) of the TPD. 58
Figure 3–9. (a)–(f) Major and trace element variation diagrams relative to SiO_2 (wt%) for the intrusive rocks from the Mt. Shaku-dake area. Shoshonite, high-K, medium-K, and low-K fields are after Peccerillo and Taylor (1976). (g) MgO–Fe_2O_3 (wt%) diagram. The blue and red arrows show the trends of the Group-1 and the Group-2, respectively. (h) FeO*/MgO–SiO_2 (wt%) diagram (after Miyashiro, 1974). HMA field is quoted from Kamei et al. (2004). 60
Figure 3–10. Sr and Nd isotopic compositions of the intrusive rocks from the Mt. Shaku-dake area. (a) εSrI (103 Ma)–εNdI (103 Ma) diagram. (b) SiO_2 (wt%)–SrI (103 Ma) and –NdI (103 Ma) diagram. Arrows indicate the AFC trends and the FC trend, respectively. 62
Figure 3–11. (a) Mg#–Si (a.p.f.u. O=6) diagram for clinopyroxenes of the TPD

and Do. Compositional fields are defined by Kamei et al. (2004). (b) TiO_2–MnO*10–P_2O_5*10 triangle diagram for the Do (after Mullen, 1983). (c) Y/15–La/10–Nb/8 triangle diagram for the Do (after Cabanis and Leocolle, 1989). Mg# is 100 × Mg/(Mg + total Fe). 64

Figure 3–12. Discrimination diagrams for the TPD. Cretaceous high-Mg diorites from central and northern Kyushu, and Neogene high-Mg andesites from the central Kyushu and the Setouchi area are shown in these figures (modified after Kamei et al. (2004)). (a) MgO/(MgO + FeO*)–TiO_2 (wt%) diagram. (b) Y (ppm)–Sr/Y diagram. (c) Yb_N–$(La/Yb)_N$ diagram. The data for comparison were obtained from the following sources; andesite from the Kanmon Group, Yamaguchi (Imaoka and Murakami, 1979; Imaoka et al., 1993), diorite from northern Kyushu (Murakami, 1994; Kamei et al., 2004; Eshima et al., 2019). The Neogene HMA rocks in Kyushu also geochemically possess the Sanukitic HMA (Shiraki et al., 1991; Nagao et al., 1992; Kakubuchi et al., 1995; Shiraki et al., 1995). 66

Figure 3–13. Rb–Y (ppm) and Cr–Ni (ppm) diagrams of the Group-1 (Do to PFT and TPD to CG). Fractionated vectors were calculated by the Rayleigh fractionation model using partition coefficient after Arth (1976) and Rollinson (1993). The Rayleigh fractionation model using partition coefficients are listed in Appendix 3–4. 68

Figure 3–14. Whole-rock SiO_2 (wt%)–modal value (vol%) for the TPD and CG. The modal values are listed in Appendix 3–5. Modal analysis was performed using the Excel spreadsheet (VBA) developed by Shimura and Kojima (2015). 69

Figure 3–15. Results of fractional crystallization modeling for the Group-1 (Do to PFT and TPD to CG) are shown in the spider diagrams. Normalized values of C1 chondrite are after Sun and McDonough (1989). The Rayleigh fractionation model using partition coefficients are listed in Appendix 3–4.

.....70
Figure 3–16. Sr (ppm)–SrI (103 Ma) and Nd (ppm)–NdI (103 Ma) diagrams showing assimilation and fractional crystallization (AFC) with the Wakino sub-group and the limestone as contaminants. The AFC model adapts the equations of DePaolo (1981). 'r' stands for the values of assimilation/crystallization rates. 72
Figure 3–17. (a) Rb–Y (ppm) and Sr–Y (ppm) diagrams of the Group-2 (HBG and FBG). Fractionated vectors were calculated by the Rayleigh fractionation model using partition coefficient after Arth (1976) and Rollinson (1993). (b) Results of fractional crystallization modeling for the Group-2 (HBG to FBG) are shown in the spider diagrams. Normalized values of C1 chondrite are after Sun and McDonough (1989). The Rayleigh fractionation model using partition coefficients are listed in Appendix 3–4. Detailed explanations are described in the text. 74
Figure 3–18. The petrological evolution model of the Shaku-dake plutonic body. Various magmatic processes such as AFC and FC are also shown. Waki: wakino sub-group, and Ls: limestone. 77
Figure 3–19. Modal compositions (Qz, Pl, Kfs, Opx, Cpx, Opx, and Bt) and whole-rock compositions (SiO_2, Fe_2O_3, MgO, Cr, and Ni) versus altitude of sampling sites for the TPD. 79
Figure 3–20. Horizontal variation in modal compositions. (a)–(d) Qz, Pl, Kfs, Opx, Cpx, and Opx and whole-rock chemical compositions. (e)–(i) SiO_2, Fe_2O_3, MgO, Cr, and Ni of the TPD. Dots indicate sampling sites. Horizontal variation maps were created using Graph-R. The modal values are listed in Appendix 3–5.....80
Figure 3–21. Field occurrences of intrusive rocks. (a) to (c) Layered structures in the TPD. (d) The TPD intruding into the Wakino sub-group as a sill. (e) Occurrence of the TPD dike. The vertical TPD dike deflects to the sill..83

Figure 3–22. Photomicrographs of studied samples. (a) The boundary between the micro-sheet (left) and the TPD (right). (b) Dusty zoned plagioclase in both TPD and HBG. Kfs: K-feldspar, and Pl: plagioclase. 84
Figure 3–23. Schematic model for the formation of layered structures. (a) Dike deflecting into sill (Hutchinson, 1996; Gudmundsson, 2011). (b) Analog experiments showing the growth of the sill (Kavanagh et al., 2006). (c) Formation of micro-sheet (Miller et al., 2011). RS: rigid sponge, and CM: crystal mush. 84
Figure 3–24. Illustration for growth and lithofacies changes model of the Shaku-dake (TPD) body. 87

Figure 4–1. (a) Simplified geological map of the Northern Kyushu batholith (Karakida, 1985; Owada and Kamei, 2010). (b) Simplified geological map of the Shimonoseki to Tagawa region (Kubo et al., 1993; Nakae et al., 1998). Gr: granite, Gd: granodiorite, To: tonalite, *KTTL*: Kokura–Tagawa tectonic line, and *MITL*: Matsuyama-Imari tectonic line. 91
Figure 4–2. (a) Geological map of the study area. (b) SW–NE cross-section along A–B, W–E cross-section along B–C, and NW–SE cross-section along C–D. (c) A–B–C–D cross-section and bird's eye view of the geological map. (d) Mutual relationships between intrusive rocks and the Wakino sub-group. The solid arrows indicate intrusive relationships. 93
Figure 4–3. Field occurrences of the intrusive rocks. (a) The boundary between the porphyritic fine-grained tonalite and the Wakino sub-group. (b) Peperitic texture in the porphyritic fine-grained and Wakino sub-group boundary. (c) Calcite and quartz veins developed in the porphyritic fine-grained and Wakino sub-group boundary. (d) Calcite, quartz, and prehnite veins in the porphyritic fine-grained tonalite. (e) The clinopyroxene quartz diorite showing a sharp intrusive relationship with the porphyritic fine-

grained tonalite and Wakino sub-group. (f) The preferred orientation of plagioclase and clinopyroxene crystals indicating the flow direction in the clinopyroxene quartz diorite. The dotted arrows indicate flow direction. 94

Figure 4–4. Topographic map showing the sampling localities. These samples are used for the discussion of this chapter 4. 97

Figure 4–5. Photomicrographs of the porphyritic fine-grained tonalite and clinopyroxene quartz diorite. (a) Unaltered sample of the porphyritic fine-grained tonalite. (b) Hydrothermal veins developed in the porphyritic fine-grained tonalite. (c) Secondary minerals (Ep, Prh, and Pmp) in the porphyritic fine-grained tonalite. (d) High-SiO_2 content (Whole-rock (WR): 58.5–60.9 wt%) clinopyroxene quartz diorite. These clinopyroxene quartz diorites generally developed plagioclase crystals with dusty zoning (upper right). Qz: quartz, Pl: plagioclase, Bt: biotite, Hb: hornblende, Cpx: clinopyroxene, Opx: orthopyroxene, Ilm: ilmenite, Ep: epidote, Cal: calcite, Prh: prehnite, and Pmp: pumpellyite. 98

Figure 4–6. Photomicrographs of the clinopyroxene quartz diorite. (a) Low-SiO_2 content (WR: 55.7–57.7 wt%) clinopyroxene quartz diorite. These clinopyroxene quartz diorites generally show weak cumulated texture. (b) Dusty zoned plagioclase crystal in the High-SiO_2 content (WR: 58.5–60.9 wt%) clinopyroxene quartz diorite. This crystal encloses euhedral clinopyroxene and biotite. (c) Autolith in the clinopyroxene quartz diorite (WR: 57.8 wt%). (d) Autolith is divided into the outer edge, which shows granoblastic texture, and the inner part, which has high crystallinity. Qz: quartz, Pl: plagioclase, Bt: biotite, Hb: hornblende, Cpx: clinopyroxene, Opx: orthopyroxene, Ilm: ilmenite, Ep: epidote, Cal: calcite, Prh: prehnite, and Pmp: pumpellyite. 99

Figure 4–7. Modal compositions of the porphyritic fine-grained tonalite and clinopyroxene quartz diorite shown in a Qz–Kfs–Pl diagram. Classification

boundaries are modeled after Streckeisen (1976). The modal compositions of the PFT and CQD are listed in Appendix 4–1..... 100

Figure 4–8. Major and trace element variation diagrams relative to SiO_2 (wt%) (SiO_2– Fe_2O_3, CaO, Na_2O, Ba, Cr, and Sr) for the porphyritic fine-grained tonalite and clinopyroxene quartz diorite. The major and trace element compositions of the PFT and CQD are listed in Appendix 4–2. PFT: porphyritic fine-grained tonalite, and CQD: clinopyroxene quartz diorite. 102

Figure 4–9. Variation in the relative abundance of the dusty zoned plagioclase with the whole-rock SiO_2 contents of the host clinopyroxene quartz diorite. The number of the dusty zoned plagioclase and normal zoned plagioclase in the clinopyroxene quartz diorite is listed in Appendix 4–1..... 104

Figure 4–10. Mineral compositions of plagioclase in the clinopyroxene quartz diorite. (a, b) BSE map of the plagioclase in the clinopyroxene quartz diorite, consisting of the core, mantle, dusty zone, and rim (Samples with whole-rock SiO_2 content of 60.9 and 55.7 wt%). (c) *Or–Ab–An* triangular plot of the clinopyroxene quartz diorite. (d) CaO–Na_2O (wt%) diagram of the clinopyroxene quartz diorite. The samples were those with whole-rock SiO_2 content of 60.9 wt%, 58.5 wt%, 57.9 wt%, and 55.7 wt %. 105

Figure 4–11. Relationship between LOI value (wt%) and lithofacies. 110

Figure 4–12. LOI–Na_2O (wt%) and –Sr (ppm) diagrams of the porphyritic fine-grained tonalite. 110

Figure 4–13. Gains and losses diagram using the model of Humphris and Thompson (1978b) with LOI content of 0.9 to 1.5 (Low-LOI group), 0.9 to 2.7 (Low- to Medium-LOI group), and 0.9 to 5.7 (Low- to High-LOI group). 112

Figure 4–14. Contour maps for the whole-rock composition (SiO_2, Al_2O_3, CaO, Na_2O, and K_2O) and LOI of porphyritic fine-grained tonalite distributed

western part of this study area. Dots indicate sampling sites. Horizontal variation maps were created using Graph-R (S-NEXT Co., Ltd.). 113

Figure 4–15. (a) Sr–Y (ppm) and Cr–Ni (ppm) diagrams of the High- and Low-SiO_2 group for the clinopyroxene quartz diorite. Fractionated and accumulated vectors were calculated by the Rayleigh model using partition coefficient after Arth (1976) and Rollinson (1993). (b) Results of fractional crystallization and accumulation modeling for High- and Low-SiO_2 group. Normalized values of C1 chondrite are after Sun and McDonough (1989). The partition coefficients used in the Rayleigh fractionation modeling are listed in Appendix 4–3. 118

Figure 4–16. SiO_2–FeO (wt%) and FeO+MgO–CaO (wt%) diagrams of the clinopyroxene quartz diorite. The green fields indicate the compositional ranges resulting from the mixing between the high-SiO_2 group samples and the calculated cumulate rocks. The black arrows indicate the mineral composition of the fractionated minerals. 119

Figure 4–17. Illustration for magmatic activity models of the northern part of Shaku-dake area. 121

Figure 5–1. (a) Simplified geological map of the Northern Kyushu batholith (Karakida, 1985; Owada and Kamei, 2010). (b) Simplified geological map of the Kita-taku region (Akagi, 1935). Gr: granite, Gd: granodiorite, To: tonalite, Gb: gabbro, and Amp: amphibolite. 124

Figure 5–2. Geological map of the study area. Tdh: trondhjemite, Ap: aplite, PFD: porphyritic fine-grained diorite, Gr: granite, Gb: gabbro, Amp: amphibolite, Serp: serpentinite, cum:cumulate, Ms: muscovite, Bt: biotite, and Hb: hornblende. 126

Figure 5–3. (a) Intrusive relationships between igneous and sedimentary rocks in the study area. (b) Bird's-eye view of the study area (N30E, dip angle

25°). (c) Cross-sections of the study area along lines A–B in Figure 5–2. Abbreviations are show in caption of Figure 5–2. 127

Figure 5–4. Field occurrences of the Kita-taku mafic complex. (a) Ol Gbn–Ol ber Pxs Hbd (Type 1) characteristics oikocrystic hornblende. (b) Peg Hb Gb (Type 7) intrudes into Ol Gbn–Ol ber Pxs Hbd (Type 1). (c) Ol Gbn–Ol ber Pxs Hbd (Type 1) including the Ol Gbn (Type 2) block1. (d) Ol Gbn–Ol ber Pxs Hbd (Type 1) including the Ol Gbn (Type 2) block2. (e) Cm Cpx Gb (Type 3) including Amp and Ol Gbn (Type 2). (f) Cm Cpx Gb (Type 3) including Ol Gbn–Ol ber Pxs Hbd (Type 1). (g) Cm Hb Gb (Type 4) shows layered structure formed by columnar Hb and Pl. (h) Slab sample of the Cm Hb Gb (Type 4). Abbreviations are show in the text. 135

Figure 5–5. Field occurrences of the Kita-taku mafic complex, continued to Figure 5–4 and related rocks. (a) Fo Hb Gb (Type 5) intrudes into Ol Gbn–Ol ber Pxs Hbd (Type 1), and this boundary is unclear (b) Fo Hb Gb (Type 5) including Ol Gbn–Ol ber Pxs Hbd (Type 1) xenolith. (c) Mingling texture between Mx Hb Gb (Type 6) and Cm Cpx Gb (Type 3). (d) Tdh dike intrudes into Ol Gbn–Ol ber Pxs Hbd (Type 1), and this boundary is clear. (e) Composite dike with Tdh and PFD. (f) Mingling texture between Ms-Bt Gr and Cm Cpx Gb (Type 3). (g) Ocellar Qz in the Cm Cpx Gb (Type 3). Abbreviations are show in the text. 137

Figure 5–6. Photomicrographs of the Kita-taku mafic complex. (a) Ol Gbn–Ol ber Pxs Hbd Ol Gbn–Ol ber Pxs Hbd (Type 1). (b) Ol Gbn (Type 2). (c) Cm Cpx Gb (Type 3). (d) Cm Hb Gb (Type 4). (e) Fo Hb Gb (Type 5). (f) Mx Hb Gb (Type 6). (g) Peg Hb Gb (Type 7). Pl: plagioclase, Bt: biotite, Hb: hornblende, Cpx: clinopyroxene, Opx: orthopyroxene, Ol: olivine, Ilm: ilmenite, Cm: cumulus mineral, and Ic: Intercumulus mineral. Abbreviations are shown in the text. 139

Figure 5–7. Photomicrographs of the related rocks. (a) Ms-Bt Gr. (b) Ms-Bt Tdh.

(c) PFD. Qz: quartz, Kfs: K-feldspar, Pl: plagioclase, Bt: biotite, Hb: hornblende, and Ms: muscovite. Abbreviations are shown in the text... 140

Figure 5–8. Modal compositions of the Kita-taku mafic complex and related rocks shown in (a) plagioclase (Pl)–orthopyroxene (Opx)–clinopyroxene (Cpx) diagram, (b) plagioclase (Pl)–pyroxenes (Pxs)–hornblende (Hb) diagram, (c) plagioclase (Pl)–pyroxenes (Pxs)–olivine (Ol) diagram, and (d) QAP (quartz (Qz)–K-feldspar or alkali feldspar (Kfs or Afs)–plagioclase (Pl)) diagram. Classification boundaries are modeled after Streckeisen (1976). Point-counting application was used for Microsoft Excel VBA (Visual Basic for Applications) made by Shimura and Kojima (2015), and 3000–1500 points were counted from an area of 3 cm × 4 cm per sample. The measurement data are listed in the Appendix 5–1. 141

Figure 5–9. Zircon U–Pb dating. (a) Concordia plot. (b) $^{206}Pb/^{238}U$ grain age probability density curve and histogram. (c) Weighted mean plot. These diagrams were created using Isoplot R by Vermeesch (2018). The selected CL images, stereomicroscope whole images and reflected microscope whole images of the measured zircon grains are shown in Table 5–3, Appendix 5–2, 5–3, and the measured data are listed in Appendix 5–4. 145

Figure 5–10. Cathodoluminescence images of selected zircon grains and ^{238}U–^{206}Pb ages. Blacky areas show positions of analyses. (a) Fo Hb Gb. (b) Tdh dike. 146

Figure 5–11. Major and trace element variation diagrams relative to FeO*/MgO for the Kita-taku mafic complex. Abbreviations are shown in the text. The results of major and trace element analyses are listed in Appendix 5–5. 148

Figure 5–12. Major and trace element variation diagrams relative to *An* content of plagioclase for the Kita-taku mafic complex. 150

Figure 5–13. Major and trace element variation diagrams relative to *Mg#* content

of olivine for the Kita-taku mafic complex. 151
Figure 5–14. Major and trace element variation diagrams relative to *Mg#* content of clinopyroxene for the Kita-taku mafic complex. 152
Figure 5–15. Major and trace element variation diagrams relative to *Mg#* content of orthopyroxene for the Kita-taku mafic complex. 153
Figure 5–16. Pyroxene trapezoid plot (Morimoto et al., 1988; Deer et al., 2013) of the Kita-taku mafic complex. 154
Figure 5–17. Major and trace element variation diagrams relative to *Mg#* content of amphibole for the Kita-taku mafic complex. 155
Figure 5–18. Chemical classification diagrams for the spinel group minerals of the Type 1 from Kita-taku mafic complex. (a) Spinel prism for the multi-component system: spinel–hercynite–chromite–magnesiochromite–magnesioferrite–magnetite (after Deer et al., 2013). The letter "(b)" indicated in the triangle-front face and the letter "(c)" in the lateral-bottom face of the prism, represent the diagrams in the (b) and (c) respectively. (b) Triangular classification diagram (Cr^{3+}–Fe^{3+}–Al^{3+}: after Gargiulo et al., 2013): $Y(Cr^{3+}) = Cr/(Cr+Fe^{3+}+Al)$; $Y(Fe^{3+}) = Fe^{3+}/(Cr+Fe^{3+}+Al)$; $Y(Al^{3+}) = Al/(Cr+Fe^{3+}+Al)$. (c) Binary classification diagram considering the Mg^{2+}–Fe^{2+} exchange in the structural site "X". Field-contours in both diagrams are considering Stevens (1944), Haggerty (1991), and Deer et al. (2013). 156
Figure 5–19. Trace element composition of clinopyroxene in the Kita-taku mafic complex plotting against Zr. 158
Figure 5–20. Primitive mantle- and C1 chondrite-normalized trace element diagrams for clinopyroxene from Kita-taku mafic complex. The normalizing values are from Sun and McDonough (1989). 159
Figure 5–21. Sr and Nd isotopic compositions of the Kita-taku mafic complex and related rocks. εSrI (106 Ma)–εNdI (106 Ma) diagram. The results of Sr

and Nd isotopic analyses are listed in Appendix 5–10. 160
Figure 5–22. *An* content of plagioclase and *Mg#* of mafic minerals for the Kita-taku mafic complex. Type 7 is divided into 2 types, which bearing Cpx and Opx. 163
Figure 5–23. Plagioclase *An* vs. olivine *Mg#* and olivine *Mg#** plot of the Kita-taku mafic complex. The *Mg#* of orthopyroxene was converted to *Mg#* of olivine (Ol *Mg#**) using Fe/Mg exchange coefficient (Beattie, 1993). Fields of various gabbro are from Barnes (1986). 165
Figure 5–24. Phase diagram of plagioclase. (a) Dry (anhydrous) condition (Bowen, 1913), (b) Wet (hydrous) condition (Yoder et al., 1957). (c) Crystallized temperature vs. Water pressure diagram from Yoder and Tilley. (1962). 167
Figure 5–25. spinel *Cr#*–olivine *Mg#* relationships in Ol Gbn–Ol ber Pxs Hbd (Type 1) from the Kita-taku mafic complex. Fields of peridotites from SW Japan, NE Japan and abyssal peridotites are drawn from the data of Arai and Ishimaru (2008), Olivine–Spinel Mantle Array (OSMA) are from Arai (1987). Dashed red line is differentiation trend of the Kita-taku mafic complex..... 168
Figure 5–26. N-MORB- and C1 chondrite-normalized trace element diagrams for equilibrium clinopyroxene from Kita-taku mafic complex. The normalizing values are from Sun and McDonough (1989). Cpx/melt partition coefficients and compared data sources listed in Appendix 5–12. HMA: high-Mg andesite, BABB: back arc basin basalt, OIB: ocean island basalt; ArcTH: arc tholeiite, CC: continental crust, Ave. OB: average oceanic basalt, Ave. CB: average continental basalt, Ave. OA: average oceanic andesite, and Ave. CA: average continental andesite. 170
Figure 5–27. Characteristics occurrences of the Kita-taku mafic complex. (a) Close up to geological map shows occurrence point of the Figures. 5–27b,

c, d, and e. (b) The lithofacies are continuously changing (c→d→e). (c) Cm Hb Gb (Type 3). (d) Mx Hb Gb (Type 6). (e) Cm Hb Gb (Type 4). (f) Fo Hb Gb (Type 5) injects into the accumulating magma and rolls up each cumulate. (g and h) The Peg Hb Gb (Type 7) intrudes into the Fo Hb Gb (Type 5) along the fractures. 172

Figure 5–28. Growth and formation processes of the Kita-taku mafic complex. ICM: intercumulus melt. 174

Figure 6–1. Field occurrences of the migmatite. (a) Trondhjemite (Tdh) dike intrudes into migmatite. (b) Close-up to (a). Abbreviations are show in the text. 176

Figure 6–2. Cathodoluminescence (CL) image and concordia diagram of the zircon grain 006 in the Tdh. 176

Figure 6–3. Partial melting degree vs. temperature diagram. These line of change in partial melting degree are from published experimental results. Data sources: Vielzeuf and Holloway (1988); Rutter and Wyllie (1988); Patiño Douce and Johnston (1991); Skjerlie and Johnston (1993); Wolf and Wyllie (1994); Montel and Vielzeuf (1997); Lopez and Castro (2001). 177

Figure 6–4. (a) Multiple-element diagram for the result of batch melting calculation. (b) Added the composition of trondhjemite. The partition coefficients used in batch melting calculation listed in Appendix 6–1.. 178

Figure 6–5. Geological map of Cretaceous volcanic, plutonic, metamorphic rocks and related rocks in northern Kyushu. Geological map and sample localities of the igneous, metamorphic, and migmatitic rocks used for zircon U–Pb dating. Data sources: Tsutsumi et al., 2003, Tsutsumi et al., 2011, Adachi et al., 2012, Tiepolo et al., 2012, Miyazaki et al., 2013, Miyazaki et al., 2017, Miyazaki et al., 2018, Tsutsumi and Horie, 2019, Yuhara et al., 2019a, 2019b, 2020, 2021, and Mori et al., 2021. SSG:

Shimonoseki sub-group, WSG: Wakino sub-group, HRGd: Hirao granodiorite, MSGr: Masaki granite, ASGd: Asakura granodiorite, OCGd: Ochiai granodiorite, HKGd: Haki granodiorite, TMGd: Tamana granodiorite, KTGb: Kita-taku mafic complex, ITGd: Itoshima granodiorite, MGGr: Mogi granite, and SKGd: Shikanoshima granodiorite. 181

Figure 6–6. Age spectrum (KDE plot: Varmeesh, 2012) of zircon grains from nine plutonic bodies and two volcanic rocks from northern Kyushu with metamorphic zircon and migmatitic zircon ages of 105.1 ± 5.3 Ma (1: Miyazaki et al., 2017), 105 ± 2 Ma (2: Adachi et al., 2012), 105.9 ± 0.5 Ma (3: This study), 119.6 ± 2.1 Ma (4: Tanaka, unpublish data), 113.7 ± 1.6 Ma (5: Miyazaki et al., 2013), and 126.6 ± 1.1 Ma (6: Mori et al., 2021) . Age component calculated using *Mixture Models (auto)* of *DensityPlotter* (Varmeesh, 2012) are also shown. Upper C: upper Cretaceous and Lower C: lower Cretaceous. 182

Figure 6–7. Age spectrum (KDE plot: Varmeesh, 2012) of zircon grains from 10 metamorphic rocks from northern Kyushu with inherited zircon ages of 261.3 ± 8.5 Ma from Tdh in Kita-taku mafic complex. Age component calculated using *Mixture Models (auto)* of *DensityPlotter* (Varmeesh, 2012) are also shown. C: Cretaceous, J: Jurassic, T: Triassic, P: Permian, Car: Carboniferous, D: Devonian, S: Silurian, O: Ordovician, Cam: Cambrian, and Pre: Precambrian. 183

Figure 6–8. Simplified geological map of the Northern Kyushu batholith and related high-Mg diorites (Imaoka and Murakami, 1979; Karakida, 1985; Imaoka et al., 1993; Murakami, 1994; Kamei et al., 2004; Eshima et al., 2019; Eshima et al., 2020; Eshima, 2021a, b). HMA: high-Mg andesite, HMD: high-Mg diorite, Gr: granite, and To: tonalite. 185

Figure 6–9. N-MORB- and C1 chondrite-normalized multi-element and rare

earth element (REE) diagrams for high-Mg diorite from Northern Kyushu batholith. The normalizing values are from Sun and McDonough (1989). 187

Figure 6–10. (a) Multiple-element diagram for the result of geochemical modeling, the parent magma (HMA) mixing with the trondhjemite magma (batch melting of the amphibolite) in the Kita-taku area. (b)–(d) Multiple-element diagram comparing (a) and related rocks from Mt, Ushikiri-yama, Mt. Shaku-dake, and northern part of Mt. Shaku-dake. 188

Figure 6–11. Schematic magmatic processes and growth model in Northern Kyushu batholith. 189

Figure 6–12. Schematic model of slab rollback modified from Mori et al. (2021). 193

Figure 6–13. Crustal evolution model of Northern Kyushu batholith at cretaceous period. 194

Table 2–1. Representative mineral compositions of the Ushikiri-yama granodiorite. 17

Table 2–2. K–Ar age data foe the Ushikiri-yama Gd and Pr Fine Gr. 22

Table 2–3. Results of Sr-Nd isotope analyses of the Ushikiri-yama body and cited data. 24

Table 2–4. Result of the mass balance calculations. 31

Table 3–1. Result of Sr–Nd isotope analyses of the Shaku-dake body and cited data. 54

Table 3–2. Results of mass balance calculation using the major elements for whole-rocks and minerals of the TPD–CG, Do–PFT and HBG–FBG. 75

Table 4–1. Representative chemical analyses for porphyritic fine-grained

tonalite. 106
Table 4–2. Representative chemical analyses for clinopyroxene quartz diorite. 107
Table 4–3. Results of mass balance calculation using the major elements for whole-rocks and minerals of the clinopyroxene quartz diorite and porphyritic fine-grained tonalite. 117

Table 5–1 Summary of textural observations for Kita-taku mafic complex. . 128
Table 5–2. The measurement conditions of the zircon U–Pb dating. 142

Appendix 2–1. Modal value of the Ushikiri-yama granodiorite and Pr Fine Gr. 226
Appendix 2–2. Major (wt%) and trace element (ppm) concentrations of the Ushikiri-yama body 232
Appendix 2–3. Rayleigh fractionation model using partition coefficients. ... 236

Appendix 3–1. Clinopyroxene compositions of TPD and Do. 237
Appendix 3–2. Major (wt%) and trace element (ppm) concentrations of the Shaku-dake body. 238
Appendix 3–3. Representative chemical analyses for each mineral of the TPD. 247
Appendix 3–4. Rayleigh fractionation model using partition coefficients. ... 249
Appendix 3–5. Modal value of the TPD and CG. 250

Appendix 4–1. Modal compositions of the porphyritic fine-grained tonalite and clinopyroxene quartz diorite. 254
Appendix 4–2. Major (wt%) and trace element (ppm) concentrations of the porphyritic fine-grained tonalite and clinopyroxene quartz diorite. 256

Appendix 4–3. Partition coefficients used in the Rayleigh fractionation modeling. 263

Appendix 5–1. Modal compositions of the Kita-taku mafic complex and related rocks. 264

Appendix 5–2. Stereomicroscope whole images of the measured zircon grains. 268

Appendix 5–3. Reflected microscope whole images of the measured zircon grains. 270

Appendix 5–4. U–Pb isotopic data of the zircon grains from 21021408A and 20110807C. 272

Appendix 5–5. Major (wt%) and trace element (ppm) concentrations of the Kita-taku mafic complex and related rocks. 274

Appendix 5–6. Trace element and rare earth element (REE) concentrations of the Kita-taku mafic complex and related rocks determined by LA-ICP-MS. 282

Appendix 5–7. Primitive mantle- and C1 chondrite-normalized trace element diagrams of the Kita-taku mafic complex and related rocks. The normalizing values are from Sun and McDonough (1989). 284

Appendix 5–8. Representative chemical analysis for the Kita-taku mafic complex. 286

Appendix 5–9. Trace element and rare earth element (REE) concentrations of the clinopyroxene from Kita-taku mafic complex determined by LA-ICP-MS at GSJ-lab. 288

Appendix 5–10. Results of Sr-Nd isotope analyses of the Kita-taku mafic complex and related rocks. 293

Appendix 5–11. Results of geothermometer and geobarometer of the Kita-taku mafic complex. 294

Appendix 5–12. Cpx/melt partition coefficients and compared data sources in the Figure 5–24. 295

Appendix 6–1. Partition coefficients used in the batch melting calculation. . 296

1 Introduction

1–1 Introduction

The "arc suite" of Japanese island is located in a subduction zone, and granitoids cover about 30% of the island arc. Large-scale granitic bodies with an area of more than 100 km^2, called batholiths, are exposed in many regions. About 80% of the granitoids exposed on the surface are in the geochronological range of 50–130 Ma age (mainly Paleogene to Cretaceous). The Cretaceous to Paleogene batholiths in Japan are of great importance for the understanding of magma formation and crustal growth processes in the Japanese island. In addition, studies of continental magmatic arcs in the Cordilleras of North and South America, which are representative of the world, have recognized patterns of cyclic magma changes. The episodicity is characterized by periods of high magma addition rate (MAR), called flare-ups, separated by periods of low MAR, called lulls (Ducea, 2001; DeCelles et al., 2009; de Silva et al., 2015; Paterson and Ducea, 2015; Kirsch et al., 2016; Chapman et al., 2021). Numerous models have been proposed for the non-stationary magmatic activity of subduction zones, but their role in driving magmatic rhythms at continental margins remains controversial.

The Cretaceous Northern Kyushu batholith studied here is classified into 17 bodies based on previous studies, and consists of granitic bodies and small amounts of related mafic bodies (Fig. 1–1). Previous studies on the Northern Kyushu batholith have examined the magma formation process of the batholith by examining the intrusive relations and chemical compositions. Although the batholith generally consists of several small-scale bodies, the magmatic processes of these small-scale bodies have not been focused yet. In order to understand the magma formation process at the batholith scale, it is important to precisely age dating and analyze the magma formation process of the constituent small-scale bodies. The study of magma compositional changes and crustal growth processes in the batholith provides a

comprehensive view of batholith-scale igneous activity. In addition, the study of the batholith, which occupies about 30% of the Japanese island arc, will contribute to the understanding of the igneous activity occurring in the subduction zone and the formation process of the middle to lower crust in the magmatic arc.

In this study, I firstly examine the formation process of magma and the growth process of small-scale bodies (Mt. Ushikiri-yama, Mt. Shaku-dake, and northern part of Mt. Shaku-dake in the eastern part) including high-Mg diorites (HMDs), and the maturation process of each body as the smallest unit of the Cretaceous Northern Kyushu batholith. Then, I combine the information on the lower sequence of the crust obtained from the Kita-taku mafic complex in the western part to examine the series of magmatic processes from mafic to felsic rocks (Fig. 1–1). Finally, petrological constraints supported by own eyes (field survey) that are stronger than thought experiments are presented for the problem of magma formation processes including plate motions in subduction zones.

1–2 Acknowledgements

I wish to thank Profs. Masaaki Owada, Atsushi Kamei, Teruyoshi Imaoka and Toshiaki Shimura for their useful advice and discussion, and Prof. Mariko Nagashima and Mr. Youji Morifuku for helping with EPMA analysis. I also thanks to Prof. Kiichiro Kawamura and Dr. Ryosuke Saito for critical reading of this thesis. Thanks also go to Dr. Toru Yamasaki provided many helpful comments and helping with LA-ICP-Mass analysis. This work was supported by JSPS Grant-in-Aid for Scientific Research 15H0348 and Research Fellowship 21J13600.

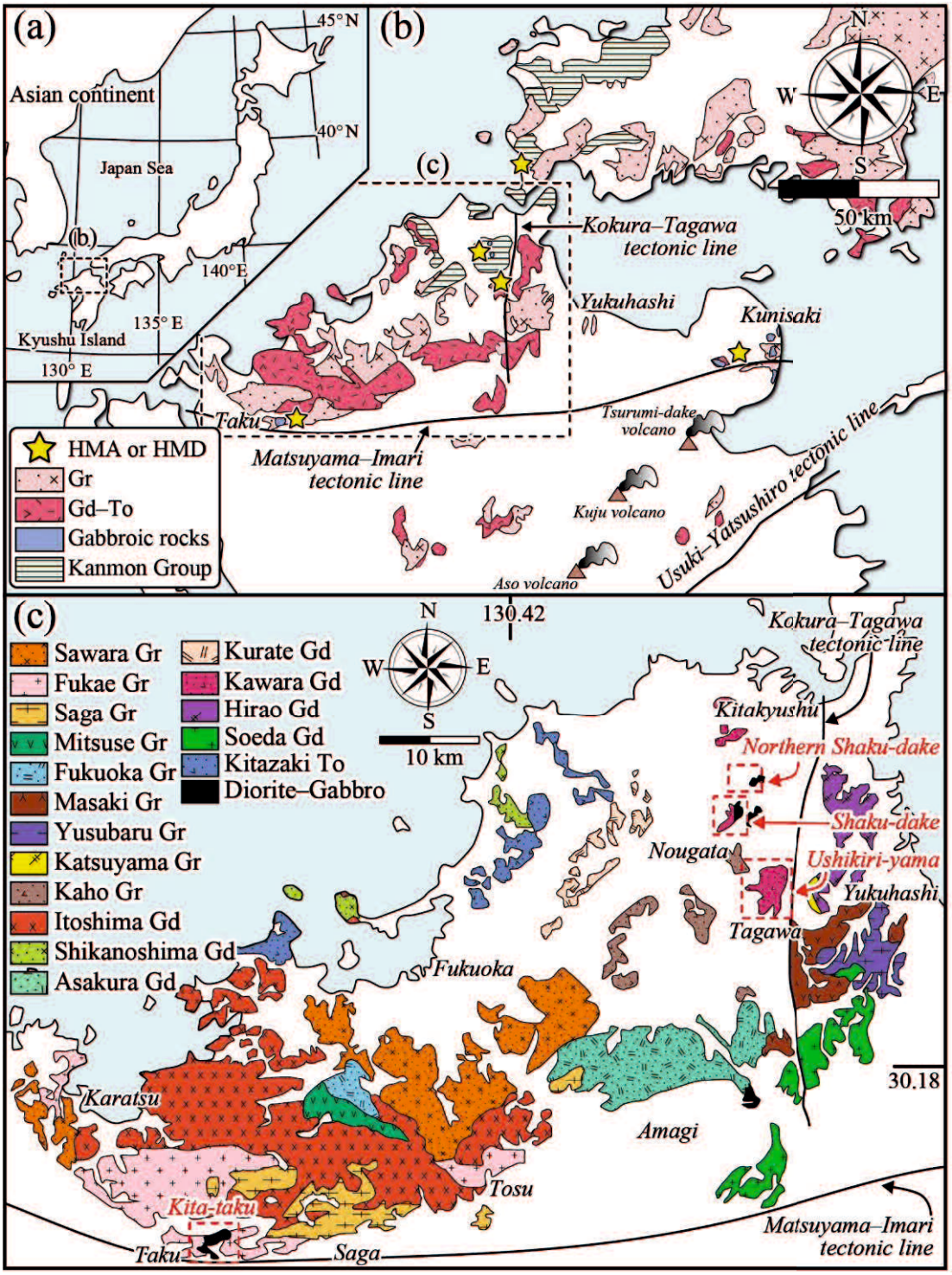

Figure 1–1. (a) and (b) Distribution of Cretaceous igneous rocks in the northern Kyushu districts. (c) Index map of the northern Kyushu with Cretaceous igneous rocks. Red dotted squares indicate that study areas. HMA: high-Mg andesite, HMD: high-Mg diorite, Gr: granite, Gd: granodiorite, and To: tonalite.

2 Ushikiri-yama area

2–1 Introduction

The Cretaceous granitoids are widely distributed in northern Kyushu, the northern side of Matsuyama-Imari tectonic line, and they were formed by the subduction of the oceanic plate along the East Asian active continental margin. The Cretaceous granitoids in northern Kyushu are divided into the eastern ilmenite-series and the western magnetite-series, where both series are bounded by the Kokura-Tagawa tectonic line (Ishihara et al., 1979: Fig. 2–1). Izawa et al. (1990) and Izawa et al. (1994) called the high-Sr granitoids for the magnetite-series granitoids because they have a significantly higher Sr content rather than the ilmenite-series granitoids.

The Ushikiri-yama granodiorite is situated in the west side of the Kokura-Tagawa tectonic line. The granodiorite is one of the stock-type plutons among the Kawara granodiorites described by Karakida (1985) (Fig. 2–1). It has been described by Matsushita (1940), Murakami (1985) and Sasaki and Murakami (1986), and is known to be a magnetite-series granodiorite and meta-aluminous granitoids because of including hornblende as mafic minerals (Eshima et al., 2019). The Ushikiri-yama granodiorite does not consist of only one lithology, but is accompanied by mafic to felsic dikes in addition to the main granodiorite body (Matsushita, 1940; Sasaki and Murakami, 1986; Eshima et al., 2019). A skarn zone with a width from several tens of centimeters to several tens of meters is formed along the contact zones of the host crystalline limestone reported by Katayama (1906) and Sasaki and Murakami (1986). In particular, many contacts alternation deposits around San'no-take on the southeastern side of the body exploited copper, lead, and bismuth until 1960's. Sasaki and Murakami (1986) divided the Ushikiri-yama granodiorite into the north and south bodies, and concluded that the south body was the early intrusion, because the dikes and veins intruding the south body were captured by the north body. The biotite K–Ar age of 113 ± 3 Ma has been reported from the south body (Murakami, 1994). This

age corresponds to the oldest age of the batholithic Cretaceous granitoids in northern Kyushu (Owada and Kamei, 2010).

The Ushikiri-yama granodiorite is an isolated granodiorite body that is not in contact with the other Cretaceous granitoid bodies in northern Kyushu (Fig. 2–1). This means that the Ushikiri-yama granodiorite is free from any alterations with the surrounding later intrusive rocks and/or bodies (e.g., Nishida et al., 2005). The Ushikiri-yama granodiorite is, therefore, a suitable body for the investigation of magmatic processes such as differentiation and crystallization, magma mixing and/or mingling, assimilation of crustal materials, and depth and mechanism during its emplacement.

In this chapter 2, I discuss the relationships between the granodiorite and the dikes, the emplacement pressure-temperature (*P*-*T*) conditions, and the chemical characteristics of the granodiorite in comparison with the other granitic bodies in northern Kyushu. The petrogenesis, petrography, modal composition, mineral and whole-rock chemical compositions, K–Ar ages, and Sr and Nd isotopic compositions of the Ushikiri-yama granodiorite are presented, and the magmatic processes of the Ushikiri-yama granodiorite and the genetic relationship with dikes is discussed based on these data. Finally, the petrological signature of Cretaceous igneous activity widely distributed in northern Kyushu are examined.

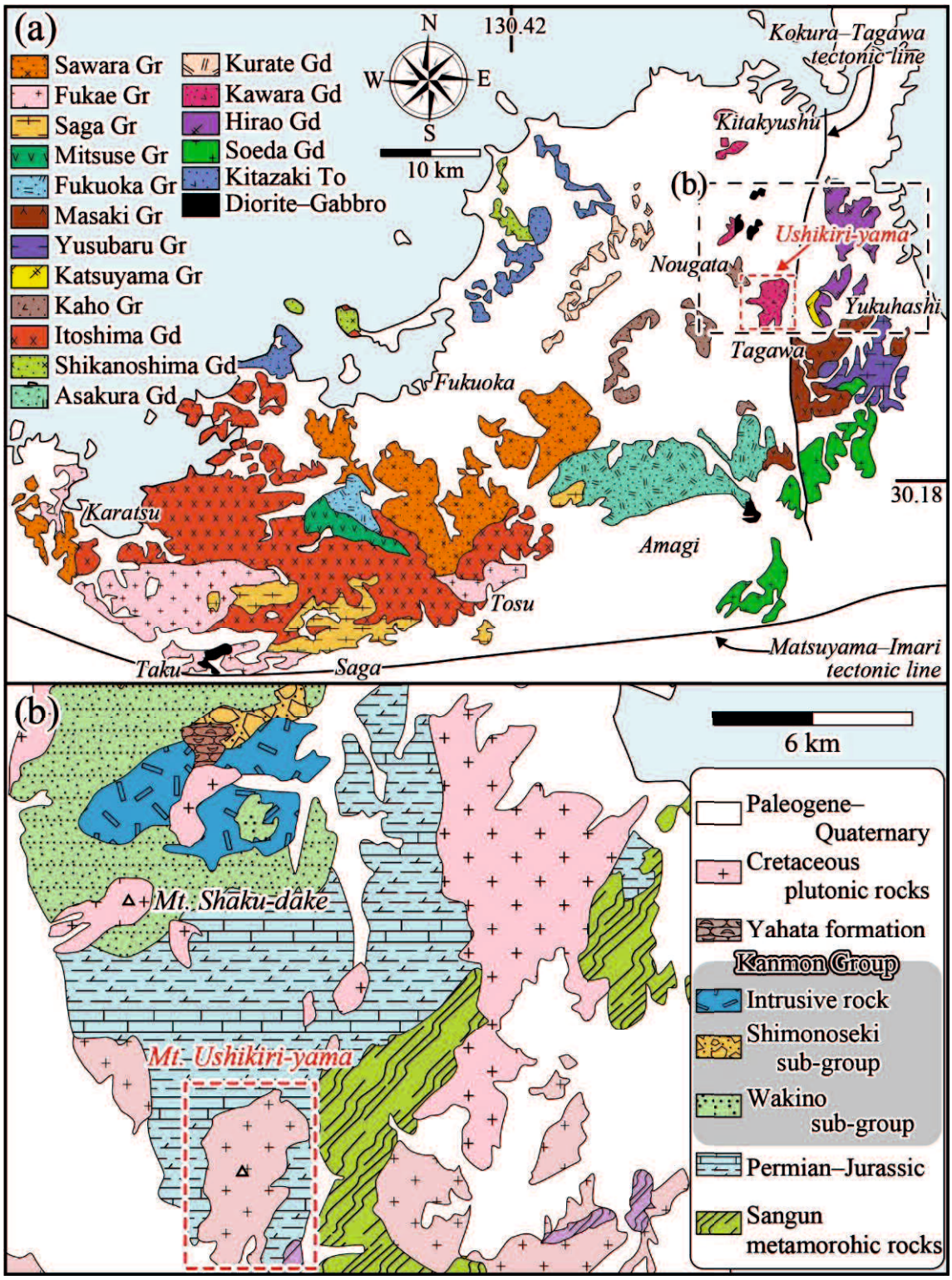

Figure 2–1. Distribution of Cretaceous igneous rocks in the northern Kyushu districts. (a) Index map of the northern Kyushu districts with Cretaceous igneous rocks (Karakida, 1985; Owada et al., 1999). (b) Simplified geological map around the study area. Gr: granite, Gd: granodiorite, and To: tonalite.

2–2 Geological overview

The geology of the Ushikiri-yama area consists of metamorphic rocks, the Ushikiri-yama granodiorite and small-scaled dikes (Fig. 2–2). The metamorphic rocks are of crystalline limestone in southern part and pelitic metamorphic rocks in northern part. In the central part of the Ushikiri-yama granodiorite, the pelitic metamorphic rocks occur as a roof-pendant and they would overhang the granodiorite from east to west sides (Fig. 2–2). The strike and dip of the boundary between the crystalline limestone and the pelitic metamorphic rocks are N70–80° E and 30–45° S, respectively, and the crystalline limestone structurally lies on the pelitic metamorphic rocks. The pelitic metamorphic rocks are of mainly two-mica hornfels locally showing weak foliations with N30°E to E–W strike and 55–85° north or south dipping. Considering constituent rock types, these metamorphic rocks are originated from the Aida Formation or Tsunemori Group of the Permian accretionary complex as protoliths (Miyahisa and Mouri, 1959).

The Ushikiri-yama granodiorite that occurs essentially as plutonic complex including the granodiorite, mafic magmatic enclaves (MME), and felsic and mafic dikes. It is a stock-like body about 6 km north to south by 3 km east to west usually cutting the metamorphic structures. Based on the field occurrence, the granodiorite is divided into the north body and the south body separated by the fine-grained facies. The fine-grained facies develop between the north and south bodies and in the contact zone along the host rocks (crystalline limestone and pelitic metamorphic rock) (Fig. 2–2). The boundary positions between the north and south bodies in the fine-grained facies cannot be determined precisely because of the gradual change in grain size, but the majority of the fine-grained facies are thought to be derived from the south body because of the following lithological character. The south body, including the fine-grained facies, ubiquitously traps the pelitic metamorphic xenoliths, but the north body rarely contains such metamorphic xenoliths (Fig. 2–3a). Flow structure developed along the outline of both bodies is due to alignments of plagioclase, biotite,

and hornblende (Fig. 2–3b). Relationship between the MMEs and mafic dikes described below is unclear.

The three types of dikes mainly intrude the south body including porphyritic fine-grained tonalite (Pr Fine To), porphyritic fine-grained diorite (Pr Fine Di), and porphyritic fine-grained granite (Pr Fine Gr). The dikes generally show less than 5 m wide and 300 m long (Figs. 2–3c, d, and e). The Pr Fine To dikes are 2–5 m wide, extend in the N–S to N20˚E orientation, and intruded the south body and pelitic metamorphic rocks almost vertically dipping. The straddling hornblende crystal observed in the boundary of the south body (Fig. 2–3f). In addition, Sasaki and Murakami (1986) reported that porphyritic granodiorite (called by Pr Fine To in this study) intrudes the south body and is intruded by the north body. The Pr Fine Di is a few tens of centimeters to a few meters wide that intrudes the south body in the N–S to N20˚E orientation and intrudes almost vertically dipping. The Pr Fine Gr is also a vertical dike with 1.0–5.0 m wide and a N–S orientation. It is slightly felsic compositions rather than the Ushikiri-yama granodiorite and mainly intrudes the south body (Fig. 2–3e). These three types of dikes and the Ushikiri-yama granodiorite do not have a chilled margins at any boundaries.

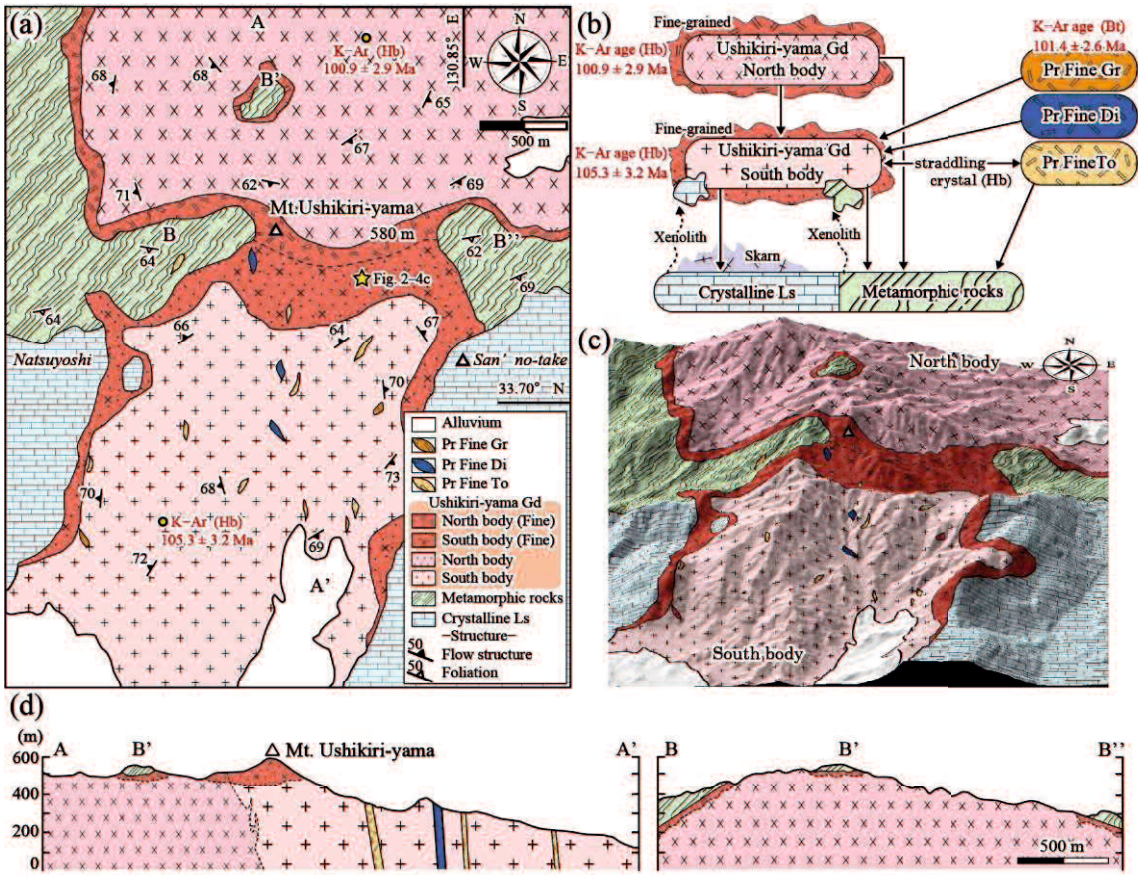

Figure 2–2. (a) Geological map of the study area (Eshima et al., 2019). The white circle indicates sampling sites of the K–Ar dating samples from Ushikiri-yama Gd (north and south bodies: Table 2–2) . (b) Mutual relationships between igneous and metamorphic rocks in the study area. Arrows indicate intrusive relationships, (c) Bird's-eye view of the study area (dip angle 25°). (d) Cross-sections of the study area along lines A–B'–A' and B–B'–B''. Abbreviations are shown in the text.

Figure 2–3. Field occurrences of the Ushikiri-yama granodiorite (Gd) and related rocks. (a) Xenolith of pelitic hornfels (pelitic metamorphic rocks) within the Ushikiri-yama Gd (south body). (b) Preferred orientation of hornblende and plagioclase crystals indicating flow direction within Ushikiri-yama Gd. (c) Porphyritic fine-grained tonalite (Pr Fine To) dike intruding the Ushikiri-yama Gd (south body). (d) Porphyritic fine-grained diorite (Pr Fine Di) intruding the Ushikiri-yama Gd (south body). (e) Porphyritic fine-grained granite (Pr Fine Gr) dike cutting the Ushikiri-yama Gd (south body). (f) Boundary between the Ushikiri-yama Gd (south body) and Pr Fine To.

2–3 Petrography of the Ushikiri-yama granodiorite body

The petrography and representative modal compositions of the Ushikiri-yama granodiorite and related dikes (Pr Fine To, Pr Fine Di, and Pr Fine Gr) are described. Representative photomicrographs of each lithology are shown in Figures 2–4 and 2–5. The QAP diagram is shown in Figure 2–6. Both north and south bodies of the Ushikiri-yama granodiorite are almost plotted within the granodiorite field, whereas Pr Fine Gr shows granite in composition (Fig. 2–6). The modal values are listed in Appendix 2–1.

2–3–1 Ushikiri-yama granodiorite (Ushikiri-yama Gd)

The Ushikiri-yama granodiorite is a hornblende–biotite granodiorite (Hb–Bt Gd) with a very small amount of euhedral epidote (Figs. 2–4a, b, 2–5a, and 2–6). The petrography of the south and north bodies is most alike in both bodies, except for the absence of euhedral epidote in the northern body. The fine-grained facies in both bodies are less than 0.5 mm, but epidote is absent.

The Ushikiri-yama granodiorite shows a hypautomorphic granular texture and is mainly composed of plagioclase, biotite, hornblende, quartz, and K-feldspar. Zircon, titanite, magnetite, allanite, and apatite are present as accessory minerals (Figs. 2–4a, b, and c). The south body includes epidote as an accessory mineral and is characterized by existence of elongated columnar hornblendes (Figs. 2–4a, b, and c). Among the fine-grained facies dividing the north and south bodies, the fine-grained facies near the north body shows a granoblastic structure with rounded quartz grains (Figs. 2–4c).

Euhedral–subhedral plagioclase crystals are 1.0–5.0 mm in long and possess the albite twins and zoned textures. Myrmekite, intergrowth of quartz in plagioclase, is sometimes observed at contact of K-feldspar crystals. Plagioclase with dusty zone and sponge-cellar plagioclase are often observed (Figs. 2–5b and c). Biotite shows euhedral–subhedral crystals that are 0.1–0.3 mm in long, but is often

porphyritic and attains 1.0–3.5 mm. In the fine-grained facies of the Ushikiri-yama granodiorite, the grain size of biotite is smaller (0.1–0.3 mm) than in the main facies described above. Hornblende shows euhedral–subhedral crystals that are 1.0–5.0 mm in long with columnar shapes. Its coarse-grained crystals can attain up to 10–20 mm. The foliated twins of hornblende are well developed and may contain biotite, plagioclase, and quartz crystals. When hornblende contains biotite, the optical orientation of the hornblende and biotite is the same. Quartz and K-feldspar occur as interstitial minerals of the early-crystallized minerals.

2–3–2 Porphyritic fine-grained tonalite (Pr Fine To)

The Pr Fine To shows a porphyritic texture and is mainly composed of dusty zoned plagioclase, biotite, and chemically zoned hornblende as phenocrysts (Figs. 2–4d and 2–5f). The matrix generally shows microgranular texture, but some of that shows micrographic texture and is mainly composed of quartz, K-feldspar, apatite, titanite, and ilmenite. In addition, acicular apatite and ocellar quartz are characteristically present (Figs. 2–5d and e).

Euhedral–subhedral plagioclase phenocrysts are 1.0–5.0 mm in long and ubiquitously developed dusty zone. Plagioclase in matrix part shows strip-shaped of about 0.1 mm in long without zoned textures. Subhedral–euhedral biotite and hornblende phenocrysts are 0.5–1.0 mm and 1.0–4.0 mm in long, respectively. Quartz and K-feldspar occur as interstitial minerals of the early-crystallized minerals. The Pr Fine To also includes rounded quartz with 0.5–1.5 mm in long as ocellar structure (Fig. 2–5d: Hibbard, 1995). Such hornblendes are characterized by vertical growth from the surface of the anhedral quartz crystal (Fig. 2–5d).

2–3–3 Porphyritic fine-grained diorite (Pr Fine Di)

The Pr Fine Di shows a porphyritic texture and is mainly composed of plagioclase and hornblende as a phenocryst (Figs. 2–4e). The matrix generally shows intersertal

texture.

Euhedral–subhedral plagioclase phenocrysts are 2.0–4.0 mm in long and generally developed dusty zone. Subhedral–euhedral hornblende phenocrysts are 1.0–3.5 mm in long. In contrast to the Ushikiri-yama granodiorite and Pr Fine To, most of them have a rhombic shape. The plagioclase and hornblende in matrix part show strip or columnar shape of about 0.1–0.3 mm in long.

2–3–4 Porphyritic fine-grained granite (Pr Fine Gr)

The Pr Fine Gr shows a porphyritic texture and is mainly composed of plagioclase, biotite, quartz, and K-feldspar as a phenocryst (Figs. 2–4f). The matrix generally shows microgranular texture.

Euhedral–subhedral plagioclase are 1.5–2.5 mm in long and developed chemically zoned. Euhedral–subhedral biotite phenocrysts are 0.7–1.5 mm in long. Anhedral quartz and K-feldspar crystals are 0.3–1.0 mm in diameter, and occur as interstitial minerals of the early-crystallized minerals.

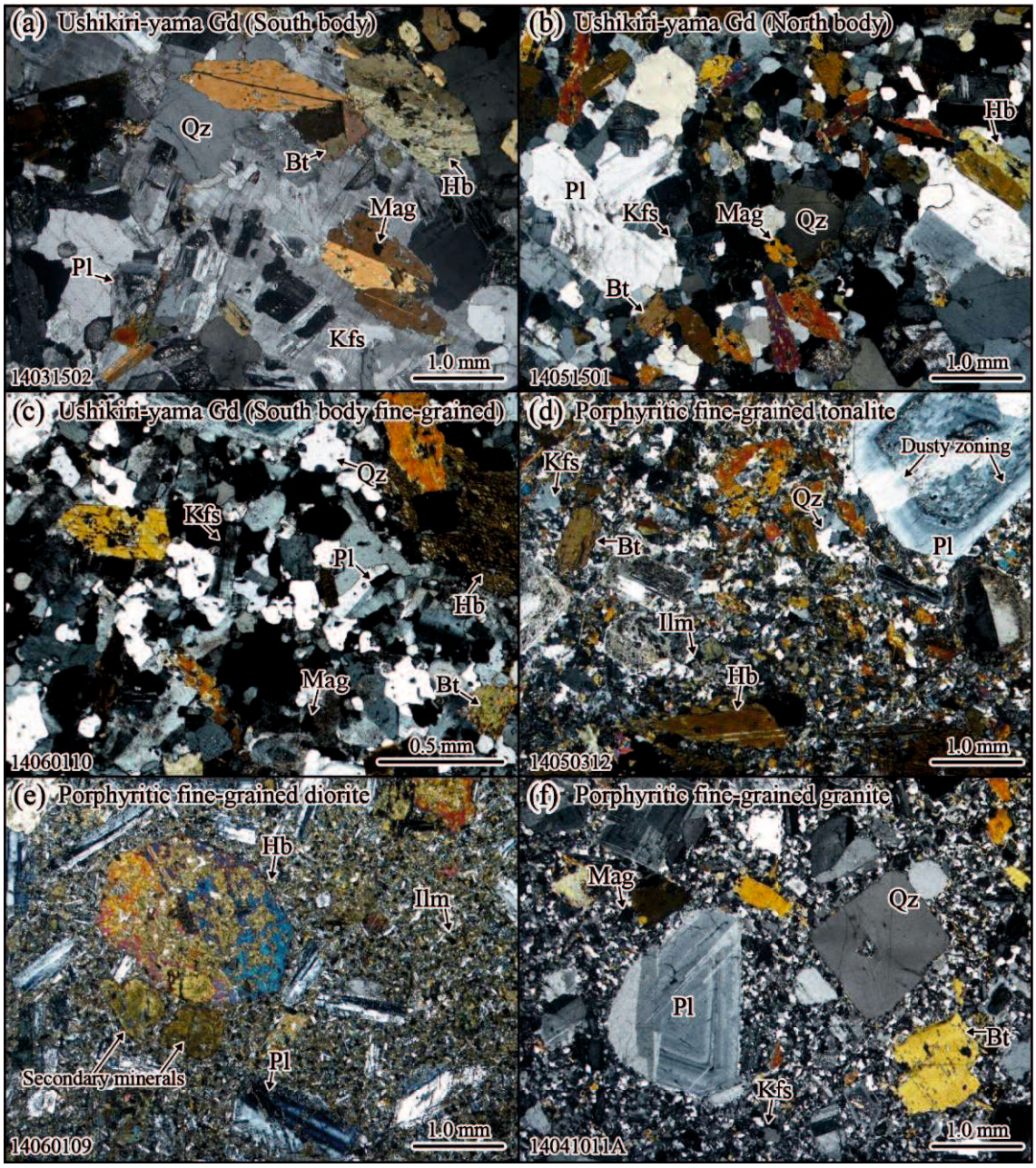

Figure 2–4. Photomicrographs of the Ushikiri-yama granodiorite (Gd) and related rocks. (a) Ushikiri-yama Gd (south body). (b) Ushikiri-yama Gd (north body). (c) Fine-grained facies (granodiorite) in the central part of the Ushikiri-yama body (between the north and south bodies: Star mark point in Figure 2–2). This sample shows a granoblastic texture, and was collected near the north body. (d) Porphyritic fine-grained tonalite (Pr Fine To). (e) Porphyritic fine-grained diorite (Pr Fine Di). (f) Porphyritic fine-grained granite (Pr fine Gr). Qz: quartz, Pl: plagioclase, Kfs: K-feldspar, Bt: biotite, Hb: hornblende, Mag: magnetite, and Ilm: ilmenite.

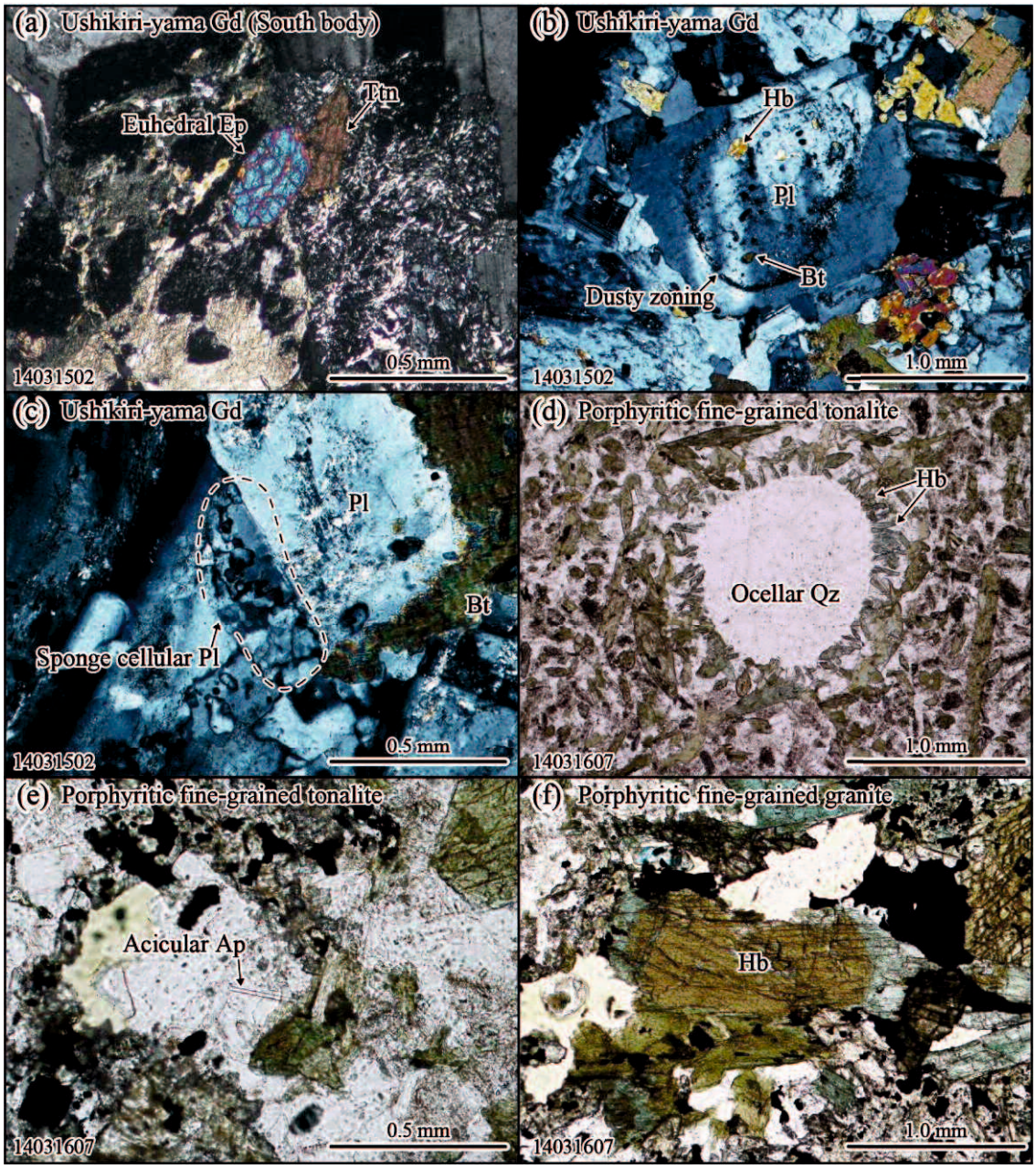

Figure 2–5. Igneous textures in the Ushikiri-yama granodiorite (a, b, c) and porphyritic fine-grained tonalite (d, e, f). (a) Euhedral epidote crystal. (b) Dusty zoned plagioclase crystal. (c) Sponge cellular plagioclase. (d) Ocellar quartz. (e) Acicular apatite crystals within plagioclase. (f) Chemically zoned hornblende crystal.

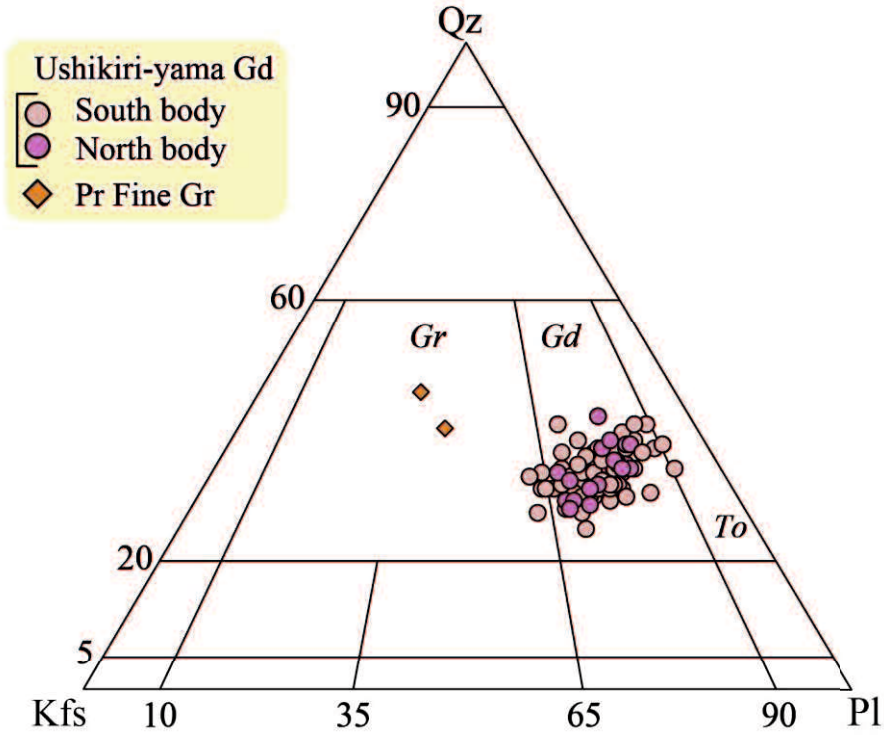

Figure 2–6. Modal compositions of the Ushikiri-yama granodiorite and porphyritic fine-grained granite on the Qz–Kfs–Pl diagram. Classification boundaries are after Streckeisen (1976). The modal values are listed in Appendix 2–1. Abbreviations are shown in the text.

2–4 Geochemistry and geochronology

2–4–1 Mineral chemistry

Mineral compositions were determined using JEOL JXA-8230 electron probe micro-analyzer (EPMA) at the Center for Instrumental Analyses, Yamaguchi University. Operating conditions for chemical analyses were an accelerating voltage of 15 kV, a specimen current of 20 nA, and a beam diameter of 1–5 μm. Wavelength-dispersion spectra were collected with LiF, PET, and TAP crystals to identify interfering elements and located the best wavelengths for background measurements. The ZAF method was used for data correction. Under the conditions described, analytical errors are ±2% for major elements as estimated from the reproducibility observed in multiple measurements. The representative mineral compositions of plagioclase, biotite, hornblende, and epidote in the Ushikiri-yama granodiorite (south body, fine-

grained facies in the south body, and north body) are shown in Table 2–1. The south body and fine-grained facies in the south body are treated as the common body.

Table 2–1. Representative mineral compositions of the Ushikiri-yama granodiorite.

Mineral	Plagioclase					Hornblende			Biotite				Epidote				
type	Ushi-S	Ushi-S	Ushi-N	Ushi-N	Ushi-SF	Ushi-S	Ushi-N	Ushi-SF	Ushi-S	Ushi-N	Ushi-SF		Ushi-S	Ushi-S	Ushi-S	Ushi-S	Ushi-S
SiO_2	56.57	57.86	57.60	59.35	56.05	46.88	43.99	47.49	36.19	35.60	35.82	SiO_2	36.42	36.50	37.05	36.38	36.52
TiO_2	0.02	0.00	0.04	0.05	0.02	1.11	1.49	1.07	3.16	3.91	4.22	TiO_2	0.23	0.09	0.14	0.19	0.09
Al_2O_3	27.24	26.68	26.74	26.04	27.59	6.22	9.08	6.04	14.86	14.37	14.47	Al_2O_3	23.33	23.37	23.19	23.80	22.90
FeO*	0.23	0.19	0.11	0.03	0.10	14.34	15.29	13.84	18.72	19.98	18.17	Fe_2O_3**	11.62	11.70	11.96	11.16	11.48
MnO	0.01	0	0	0	0	0.51	0.53	0.55	0.44	0.45	0.30	MnO	0.20	0.14	0.14	0.35	0.22
MgO	0	0	0	0	0	13.39	11.56	13.36	11.41	10.51	11.80	MgO	0.02	0.01	0.01	0.02	0.02
CaO	8.91	7.84	8.33	6.96	8.95	11.72	11.38	11.67	0	0	0	CaO	22.83	22.74	22.72	22.13	21.94
Na_2O	6.16	7.06	6.58	7.50	6.34	0.98	1.38	0.66	0.09	0.07	0.06	Na_2O	0.02	0.02	0.03	0.01	0.00
K_2O	0.21	0.11	0.18	0.14	0.31	0.63	0.86	0.54	10.37	10.25	10.31	K_2O	0	0	0	0	0
Total	99.35	99.75	99.57	100.07	99.36	95.76	95.56	95.23	95.24	95.14	95.16	Total	94.67	94.58	95.23	94.05	93.17
O	8	8	8	8	8	23	23	23	22	22	22	O	12.5	12.5	12.5	12.5	12.5
Si	2.554	2.595	2.588	2.643	2.534	7.061	6.708	7.149	5.560	5.521	5.501	Si	2.990	2.998	3.021	2.996	3.037
Ti	0.001	0.000	0.001	0.002	0.001	0.125	0.171	0.121	0.365	0.456	0.487	Ti	0.014	0.005	0.008	0.012	0.005
Al	1.450	1.411	1.416	1.367	1.470	1.104	1.633	1.071	2.692	2.627	2.620	Al	2.258	2.263	2.229	2.311	2.244
Fe^{2+}	0.009	0.007	0.004	0.001	0.004	1.806	1.950	1.743	2.406	2.591	2.334	Fe^{3+}	0.718	0.723	0.734	0.691	0.718
Mn	0.001	0	0	0	0	0.065	0.069	0.070	0.057	0.059	0.039	Mn	0.014	0.010	0.009	0.025	0.015
Mg	0	0	0	0	0	3.006	2.627	2.997	2.612	2.429	2.700	Mg	0.002	0.001	0.002	0.002	0.003
Ca	0.431	0.377	0.401	0.332	0.433	1.891	1.860	1.882	0	0	0	Ca	2.009	2.002	1.985	1.953	1.954
Na	0.539	0.614	0.574	0.647	0.556	0.287	0.409	0.193	0.026	0.021	0.018	Na	0.003	0.003	0.004	0.002	0
K	0.012	0.007	0.010	0.008	0.018	0.120	0.168	0.104	2.033	2.027	2.021	K	0	0	0	0	0
Total	4.996	5.010	4.994	5.000	5.016	15.465	15.594	15.331	15.750	15.732	15.721		8.009	8.005	7.992	7.992	7.977
An	43.87	37.78	40.72	33.65	43.02	X_{Mg} 0.63	0.57	0.63	0.52	0.48	0.54	*Ep*	24.13	24.21	24.77	23.03	24.24

Ushi-S: Ushikiri-yama granodiorite south body, Ushi-N: Ushikiri-yama granodiorite north body, Ushi-SF: Ushikiri-yama granodiorite fine-grained facies in the south body. *Total Fe reported as Fe^{2+}. **Total Fe reported as Fe^{3+}.

Plagioclase shows normal zonation and dusty zonation. The anorthite component [$An = 100 \times \{Ca/(Ca + Na)\}$] of the measured samples (normal zoned plagioclase) ranged from 22 to 46% in the core. Within the same crystal, the *An* content is decreasing from the core to the rim. The X_{Mg} content [$X_{Mg} = \{Mg/(Mg + Fe)\}$] of the hornblende and biotite are 0.59 to 0.64 and 0.48 to 0.54, respectively. The Al_2O_3 in the hornblende is higher in the north body than in the south body (Table 2–1). The epidote content [$Ep = 100 \times \{Fe^{3+}/(Fe^{3+} + Al^{3+})\}$] of the euhedral epidote is 23 to 25%. This *Ep* content is similar to that of the Hirao granodiorite and Itoshima granodiorite from Northern Kyushu batholith reported by Muraoka et al. (2020) and Yada and Owada (2003), and magmatic epidote in granites from the Cordilleras, USA reported by Sial et al. (1999), Zen and Hammarstrom (1984), Barth (1990), and Brandon et al. (1996) (Fig. 2–7). On the other hand, the anhedral epidote has a *Ep* content range of 29 to 32%, which is different from that of the euhedral epidote; suggesting that the anhedral epidote is probably formed by altered products (Fig. 2–

7). If the euhedral epidote is magmatic in origin, the pressure at which they crystallized is 6 to 8 kbar (Zen and Hammarstrom, 1984; Schmidt and Poli, 2004). In addition, the hornblende geobarometer (Schmidt, 1992) and hornblende-plagioclase geothermometer (Holland and Blundy, 1994) were used in combination to examined the emplacement *P-T* condition of the Ushikiri-yama granodiorite. The emplacement *P-T* conditions of 4.0 ± 0.6 kbar, 710 ± 40 °C (south body) and 4.3 ± 0.6 kbar, 740 ± 40 °C (north body) were estimated. The emplacement *P-T* conditions of both bodies agree within the calculated error.

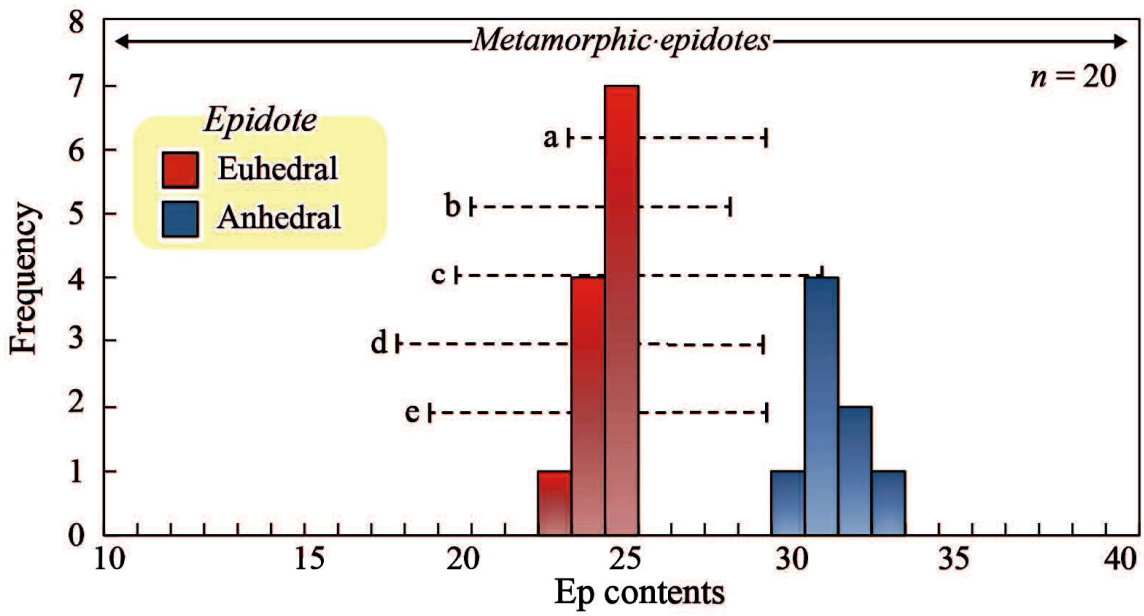

Figure 2–7. The *Ep* contents histogram of the epidote in the Ushikiri-yama granodiorite. References from (a) Yada and Owada (2003), (b) Sial et al. (1999), (c) Zen and Hammarstrom (1984), (d) Barth (1990) and Brandon et al. (1996), and (e) Muraoka et al. (2020).

2–4–2 Major and trace elements of whole-rock chemistry

Geochemical analysis, for determining major and trace elements, was performed via X-ray fluorescence (XRF) spectrometry (Rigaku ZSX Primus-Ⅱ) at the Center for Instrumental Analyses, Yamaguchi University. All analyses were made on glass beads using an alkali flux comprising of lithium tetraborate. The analytical procedure described by Fukami and Owada (2017) and Eshima and Owada (2018) was followed. Trace elements including rare earth elements (REEs) were determined with inductively coupled plasma mass spectrometry (ICP-MS) at Activation Laboratory Ltd., Canada. Samples are fused with sodium peroxide and undergo an acid dissolution. Samples are then analyzed by Agilent 7900 ICP-MS. Calibration is performed using five synthetic calibration standards (μg/ml here after referred to as ppm).

The SiO_2 content of the Ushikiri-yama granodiorite south body, north body, Pr Fine To, Pr Fine Di, and Pr Fine Gr is higher in the order of Pr Fine Di < Pr Fine To < Ushikiri-yama granodiorite south body < north body < Pr Fine Gr, and all of which are of high-K series (Fig. 2–8: Peccerillo and Taylor, 1976). The MgO, Cr and Ni contents in the north body are higher than those in the south body. The SiO_2 content of Pr Fine Di ranges from 53.7 to 53.9 wt%, and Pr Fine Di is characterized by high MgO, Cr, and Ni contents (~ 8.1 wt%, ~ 425 ppm, and ~ 199 ppm) and high *Mg*# [*Mg*# = 100 ×{MgO/(FeO*+MgO)}:mole] (~ 67.0). It is similar to high-Mg andesite compositions discussed in the later section (Fig. 2–8 and Appendix 2–1). The Pr Fine To is plotted on the trend between the Pr Fine Di and Ushikiri-yama granodiorite south body on the variation diagrams of the major and trace elements (Fig. 2–8). On the other hand, the Pr Fine Gr is plotted as an extension of the compositional trend of the south body (Fig. 2–8).

The Ushikiri-yama granodiorite and dikes are classified as calc-alkaline rocks by the FeO*/MgO–SiO_2 (wt%) diagram (Miyashiro, 1974: Fig. 2–9a). In the

MgO(wt%)–Fe_2O_3(wt%) diagram, two trends are formed, the south body to Pr Fine Gr, and the south body to Pr Fine Di trends, respectively. In this Figure 2–9b, the Pr Fine To plots on the trend between the south body and Pr Fine Di (Fig. 2–9b).

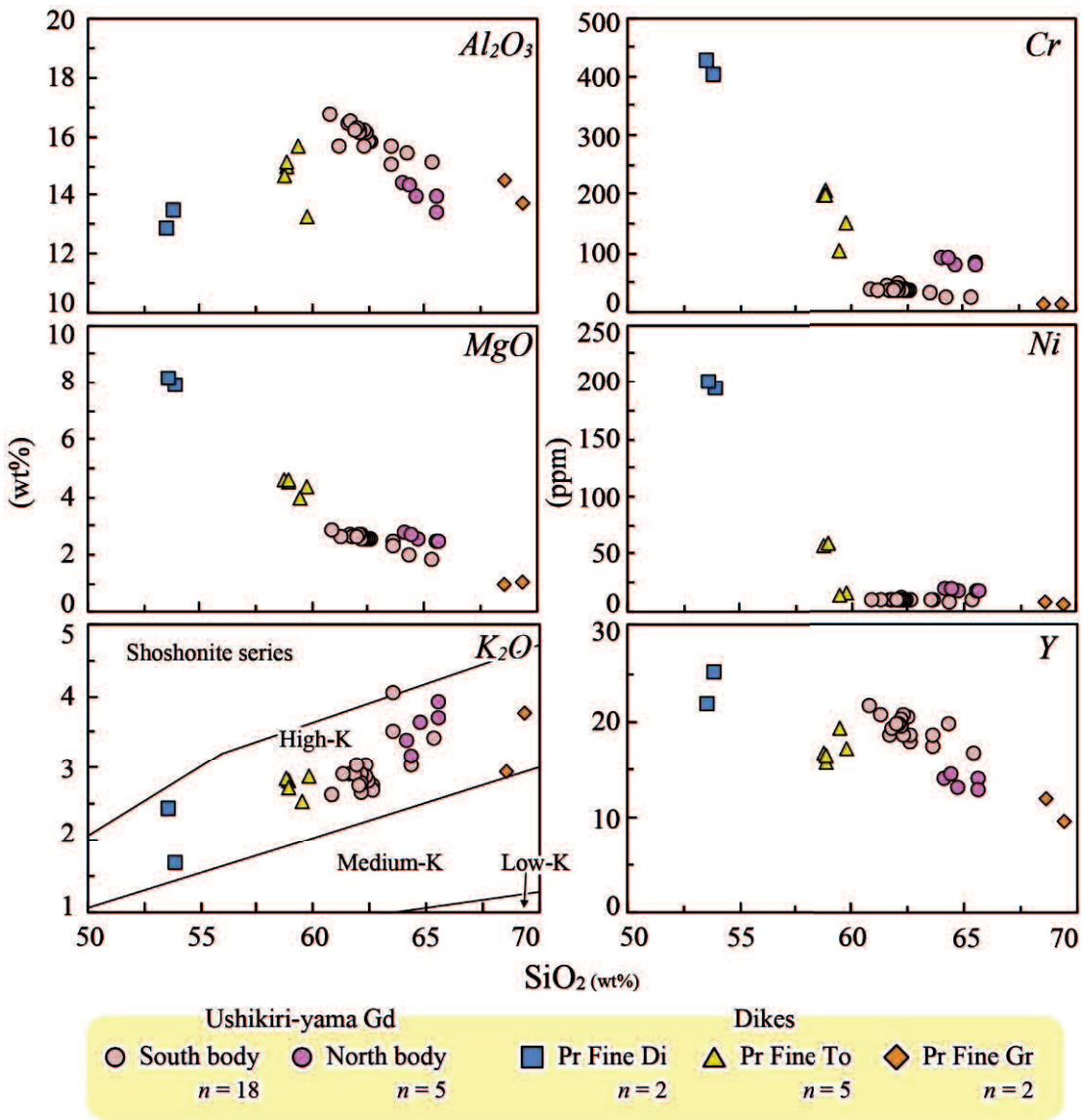

Figure 2–8. Major and trace element variation diagrams relative to SiO_2 (wt%) for the intrusive rocks from the Mt. Ushikiri-yama area. Shoshonite, high-K, medium-K, and low-K fields are after Peccerillo and Taylor (1976).

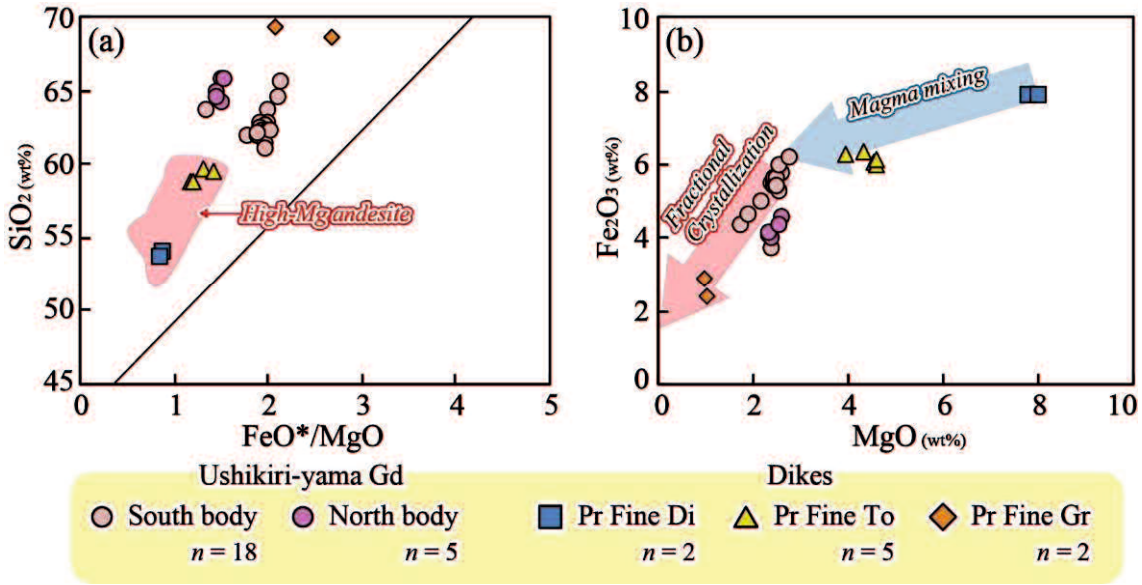

Figure 2–9. (a) FeO*/MgO–SiO_2 (wt%) diagram (after Miyashiro, 1974). HMA field (red field) is quoted from Kamei et al. (2004). (b) MgO–Fe_2O_3 (wt%) diagram. The blue and red arrows show the trends of the magma mixing and the fractional crystallization, respectively.

2–4–3 K–Ar geochronology

Biotite and hornblende from the north and south bodies of Ushikiri-yama granodiorite, and biotite from the Pr Fine Gr were separated on the technical procedure after Imaoka et al. (1997). The K–Ar ages were determined by Geochron EX. The results are shown in Table 2–2. In order to estimate the amount of radiogenic $^{40}Ar^*$ in the K–Ar method, it is usually assumed that the only *Ar* contained in the sample is the *air Ar* other than the radiogenic $^{40}Ar^*$ produced by the decay at ^{40}K. Furthermore, it is known that $^{40}Ar/^{36}Ar$ of *air Ar* is 295.5, therefore, $^{40}Ar^*$ is calculated from the equation of $(^{40}Ar^*) = (^{40}Ar)$-295.5 (^{36}Ar). The hornblende K–Ar ages of the south and north body are 105.3 ± 3.2 Ma and 100.9 ± 2.9 Ma, respectively, corresponding to the Albian, early Cretaceous. The biotite age of the both bodies (south and north) and Pr Fine Gr are 94.7 ± 2.9 Ma, 103.8 ± 3.2, Ma and 101.4 ± 2.6 Ma, respectively. The biotite K–Ar age of the north body is alike within the analytical error but the calculated age is slightly older than that of the hornblende K–Ar age. The hornblende

K–Ar age is generally measured to be older due to the closure temperature (Dodson and McClelland-Brown, 1985). The reason for geochronological inconsistency may be the presence of excess ^{40}Ar or isotopic fractionation of *air* ^{40}Ar, causing the $^{40}Ar/^{36}Ar$ of air being different from 295.5. Therefore, the biotite K–Ar age of the north body is not used for discussion in this study.

Table 2–2. K–Ar age data foe the Ushikiri-yama Gd and Pr Fine Gr.

Sample	Mesh size	K (wt%)	^{40}Ar rad (nl/g)	^{40}Ar air (%)	Age (Ma)	Error 1σ
South body (Bt)	#150	7.49	27.968	6.3	94.7	2.9
South body (Hb)	#150	0.62	2.573	22.4	105.3	3.2
North body (Bt)	#150	6.80	27.699	2.5	103.8	3.2
North body (Hb)	#150	0.55	2.168	14.8	100.9	2.9
Pr Fine Gr (Bt)	#150	6.96	27.678	10.8	101.4	2.6

Abbreviations are shown in text.

2–4–4 Sr and Nd isotopes

In the case of radiogenic isotopes such as ^{87}Sr and ^{143}Nd decayed from ^{87}Rb and ^{147}Sm as the parent isotopes, isotopic ratios divided in stable isotopes in the common system such as $^{87}Sr/^{86}Sr$ and $^{143}Nd/^{144}Nd$ changes with age. In other words, such isotope ratios are a function of "age". In addition, initial isotope ratios are useful information as tracer of magmatic processes. Therefore, it is a major advantage in elucidating the evolution of rocks, the earth, and planets using the age of the isotope ratios (Figure. 2–10).

The Sr and Nd isotopic analyses were performed using the following procedures. Sr and Nd from the powdered whole-rock samples were extracted at the Yoshida Research and Education Building of Yamaguchi University following the methods of Kagami et al. (1987). Isotopic analyses were conducted via thermo-ionization mass spectrometry (TIMS, Finnigan MAT-262) at the Department of Earth and Environment Sciences, Shimane University. The detailed analytical procedure is

described in Iizumi (1996). Measured $^{87}Sr/^{86}Sr$ and $^{143}Nd/^{144}Nd$ ratios were corrected to $^{86}Sr/^{88}Sr$ = 8.357209 and $^{146}Nd/^{144}Nd$ = 0.7219, respectively. The $^{87}Sr/^{86}Sr$ and $^{143}Nd/^{144}Nd$ ratios were normalized relative to reference values of 0.710242 (NIST SRM 987; Kagami et al., 1989) and 0.511858 (JNdi-1; Tanaka et al., 2000), respectively. The initial Sr and Nd isotope ratios were calculated using the decay constants $\lambda^{87}Rb = 1.42 \times 10^{-11}$/year (Steiger and Jäger, 1977) and $\lambda^{147}Sm = 6.54 \times 10^{-12}$/year (Lugmair and Marti, 1978). The epsilon values (ε) were calculated using the method of DePaolo and Wasserburg (1976a, 1976b). The detailed isotopic analytical procedures are reported in Miyazaki and Shuto (1998). Considering the result of hornblende K-Ar ages in this study, the Sr and Nd isotopic ratios of all samples were corrected to 105 Ma obtained from the south body because the south body exemplifies magmatic activity and the earliest activity in this area. The initial Sr and Nd isotopic ratios termed as SrI and NdI, respectively. The initial Sr and Nd isotopic ratios termed as SrI and NdI, respectively. The results of Sr and Nd isotopic analyses are listed in Table 2–3.

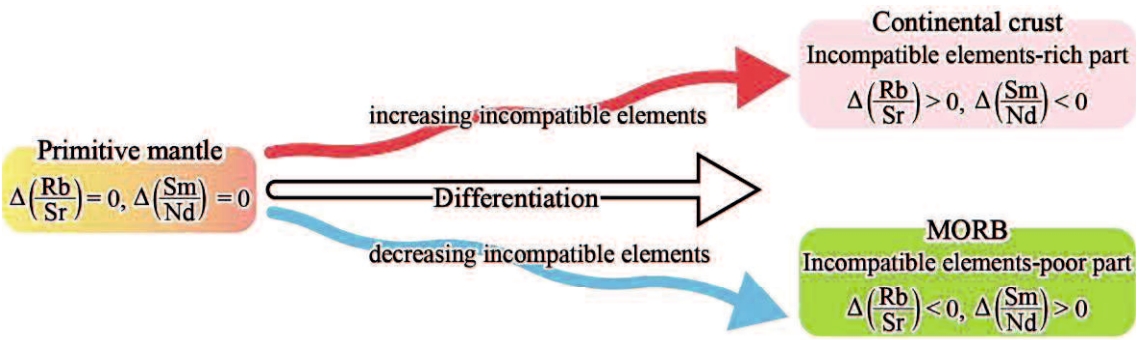

Figure 2–10. Conceptual diagram of the changes in elemental ratios that occur during the evolution of the Earth's interior.

The south body of Ushikiri-yama granodiorite and fine-grained facies in the south body has more fertile Sr and Nd isotopic compositions than those of the north

body (Figs. 2–11a and b). In this thesis, the south body including fine-grained facies are shown in the same symbol in Figure 2–11. The Pr Fine Gr shows the most fertile composition among the dikes (SrI: 0.7055, 0.70529, NdI: 0.51246, 0.51249) and the Pr Fine Di is the most depleted one (SrI: 0.70450, 0.70391, NdI: 0.51263, 0.51262). The isotopic composition of Pr Fine To varies in comparison with the intrusive host rock. Pr Fine To that intrudes the south body and the pelitic metamorphic rocks are SrI: 0.70480, NdI: 0.51259 and SrI: 0.70523, NdI: 0.51242, respectively. In other words, Pr Fine To intruding only the south body shows a more depleted composition. In comparison with the Northern Kyushu batholith, the Sr–Nd isotopic compositions of the south and north bodies are similar to those of the Fukuoka and Sawara granites and the Itoshima granodiorite, respectively (Fig. 2–11e).

Table 2–3. Results of Sr-Nd isotope analyses of the Ushikiri-yama body and cited data.

Type	No	Rb (ppm)	Sr (ppm)	$^{87}Rb/^{86}Sr$	$^{87}Sr/^{86}Sr$	$SrI^{(105Ma)}$	εSr	Sm (ppm)	Nd (ppm)	$^{147}Sm/^{144}Nd$	$^{143}Nd/^{144}Nd$	$NdI^{(105Ma)}$	εNd	2σ(Sr)	2σ(Nd)
Ushikiri-yama area															
Ushi-S	14071810	81	400	0.585795	0.706161	0.705287	12.92	4.0	19.8	0.120606	0.512611	0.512528	0.49	1	13
Ushi-S	16112001	94	365	0.745015	0.706373	0.705261	12.56	3.7	17.7	0.126375	0.512552	0.512465	-0.73	1	14
Ushi-N	16112003	116	382	0.878446	0.706148	0.704837	6.54	3.1	18.2	0.103307	0.512637	0.512567	1.24	1	14
Ushi-N	14042313	131	350	1.082774	0.706484	0.704868	6.98	2.9	14.9	0.118072	0.512633	0.512552	0.95	1	14
Ushi-N	14060114	137	366	1.082856	0.706408	0.704793	5.91	2.9	14.4	0.122592	0.512656	0.512571	1.34	1	14
Ushi-SF	14052107	79	334	0.684252	0.706513	0.705492	15.84	3.9	18.9	0.124749	0.512560	0.512475	-0.55	1	14
Pr Fine To	14031606	124	465	0.771402	0.705949	0.704798	5.99	3.9	19.8	0.118165	0.512666	0.512585	1.59	1	14
Pr Fine To	14040304	110	459	0.693274	0.706262	0.705228	12.08	4.0	18.1	0.132265	0.512511	0.512420	-1.61	1	14
Pr Fine Gr	14050415	120	283	1.226782	0.707382	0.705551	16.68	1.7	9.6	0.108090	0.512538	0.512464	-0.76	1	14
Pr Fine Gr	4041011	88	320	0.795549	0.706473	0.705286	12.91	3.0	15.8	0.114023	0.512569	0.512491	-0.24	1	14
Pr Fine Di	14050412	70	405	0.499948	0.705243	0.704497	1.70	5.2	25.5	0.124234	0.512710	0.512625	2.37	1	14
Pr Fine Di	14060109	103	377	0.790262	0.705086	0.703907	-6.66	5.1	25.1	0.122360	0.512707	0.512623	2.35	1	14
Owada et al., 1999															
Sawara	–	90	421	0.618356	0.705164	0.704241	-1.92	2.8	16.3	0.102367	0.512620	0.512550	0.91	-	-
Itoshima	–	80	420	0.550956	0.705105	0.704283	-1.33	4.3	18.6	0.140414	0.512625	0.512529	0.50	-	-
Fukae	–	53	394	0.389088	0.704924	0.704344	-0.47	3.2	9.8	0.194722	0.512650	0.512516	0.26	-	-
Fukae	–	87	396	0.635445	0.704590	0.703641	-10.44	3.7	22.6	0.098174	0.512616	0.512549	0.89	-	-
Fukuoka	–	93	371	0.725101	0.705427	0.704345	-0.44	1.7	7.8	0.131760	0.512515	0.512424	-1.53	-	-
Fukuoka	–	94	425	0.639753	0.705048	0.704093	-4.02	2.0	9.6	0.125947	0.512522	0.512435	-1.32	-	-
Fukuoka	–	109	325	0.970114	0.705193	0.703745	-8.96	1.4	7.2	0.117060	0.512439	0.512359	-2.82	-	-
Fukuoka	–	149	158	2.727811	0.705323	0.701253	-44.35	1.7	8.9	0.118724	0.512445	0.512363	-2.72	-	-
Mituse	–	96	341	0.814408	0.706265	0.705050	9.56	1.9	10.4	0.110442	0.512371	0.512295	-4.05	-	-
Mituse	–	148	113	3.788645	0.705688	0.700035	-61.64	1.7	7.5	0.137029	0.512465	0.512371	-2.58	-	-
Mituse	–	103	254	1.173097	0.706390	0.704640	3.74	1.5	7.4	0.122538	0.512350	0.512266	-4.63	-	-
Mituse	–	64	455	0.406900	0.706119	0.705512	16.12	2.3	14.5	0.095890	0.512369	0.512303	-3.90	-	-
Saga	–	41	424	0.279702	0.705154	0.704737	5.11	2.3	18.4	0.075569	0.512568	0.512516	0.26	-	-
Saga	–	86	92	2.703740	0.704598	0.700564	-54.13	1.8	9.1	0.120515	0.512616	0.512533	0.59	-	-
Kagami et al., 2006 Kawano et al., 2006															
Gneiss	HA-24R	126	132	2.763874	0.715600	0.711476	100.79	9.1	46.5	0.118619	0.512399	0.512318	-3.62	-	-
Gneiss	HA45	115	123	2.707258	0.715960	0.711920	107.10	3.3	15.7	0.127069	0.512500	0.512413	-1.76	-	-
Gneiss	IM57	174	151	3.336382	0.715170	0.710192	82.56	1.7	6.8	0.151579	0.512435	0.512331	-3.36	-	-

Error values are 5 and 4 decimal places for Sr and Nd, respectively.

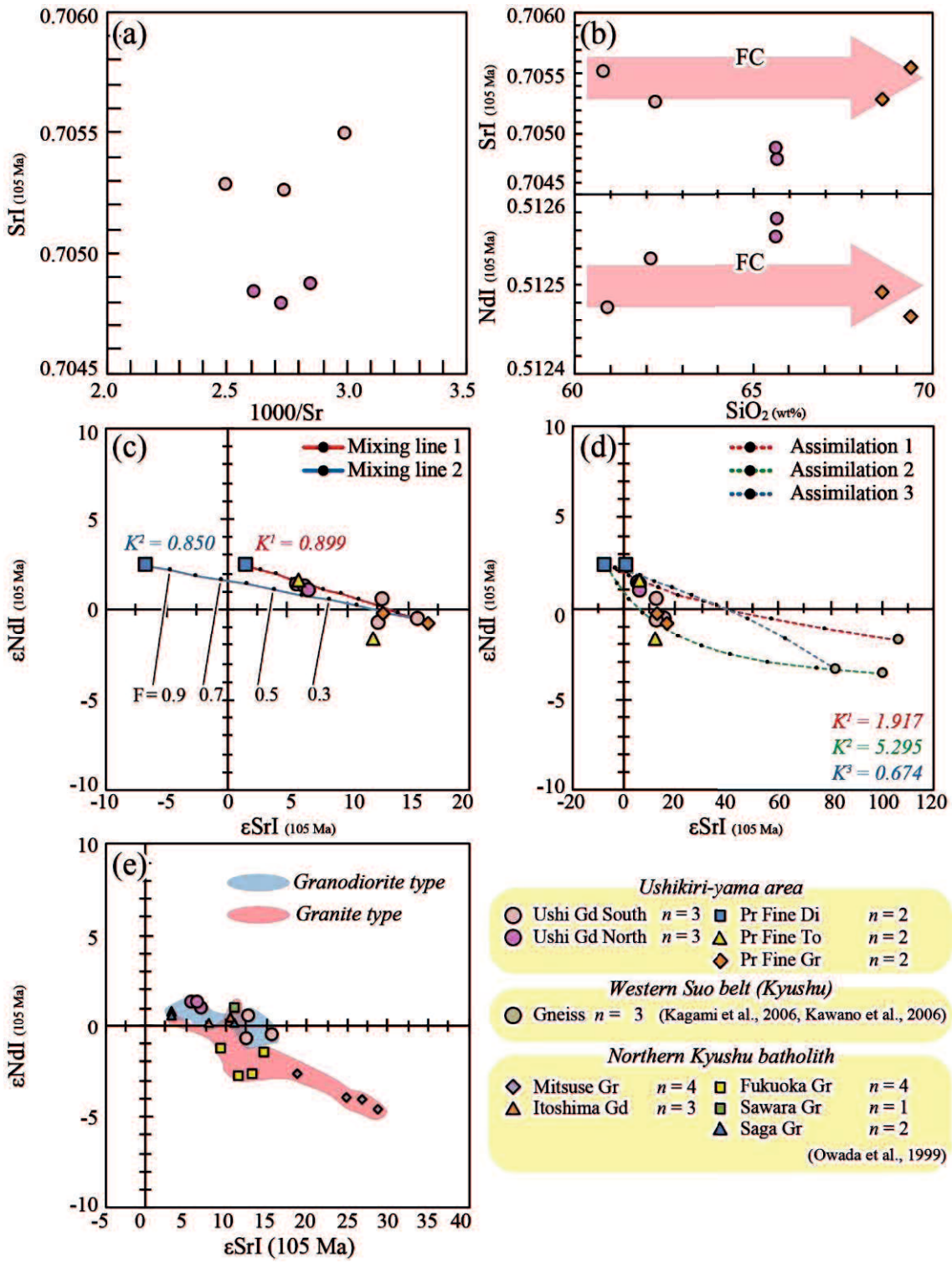

Figure 2–11. Isotopic compositions of the Ushikiri-yama granodiorite and related rocks. (a) 1000/Sr–SrI (105 Ma). (b) SiO_2 (wt%)–SrI (105 Ma) and NdI (105 Ma). (c, d, and e) εSrI (105 Ma)– εNdI (105 Ma) diagrams. (c) Blue and red lines are mixing line between the Pr Fine Di and Ushikiri-yama granodiorite south body. The two Pr Fine To samples are plotted

in the proximity of these lines. (d) The three dashed lines (Red, green, and blue) show assimilation line between the Pr Fine Di and pelitic metamorphic rocks, indicating uniform minor assimilation of pelitic host rocks within the Pr Fine Di. One of the Pr Fine To samples are plotted near the green dashed line, indicating that this sample was produced by the assimilation of pelitic rocks into the Pr Fine Di magma. (e) Comparison with data from granodioritic (blue field) and granitic (red field) rocks from Northern Kyushu granitoids batholith.

2–5 Discussions

The south body of the Ushikiri-yama granodiorite is associated with at least three types of intrusive dikes (Pr Fine Di, Pr Fine To, and Pr Fine Gr). The presence of the straddling crystal (Fig. 2–3f) at the boundary between the Pr Fine To and the south body of Ushikiri-yama granodiorite is strong evidence of coeval intrusive rocks (Yoshikura and Atsuta, 2000). Similarly, Pr Fine Di and Pr Fine Gr do not have a distinct child margin at the boundary with the Ushikiri-yama granodiorite south body (Figs. 2–3d and e). The biotite K–Ar age (101.4 ± 2.6 Ma) of the Pr Fine Gr shows the range of hornblende K–Ar age (100–105 Ma) of the Ushikiri-yama granodiorite (Table 2–2). Although Pr Fine Di lacks evidence for the intrusive age, it shows similar occurrence to the Pr Fine Gr, Pr Fine Di was active at the same time as the south body. Thus, the three types of dikes are coeval intrusive rocks intruded at the same time as the formation of the south body, or formed successively after the formation of the south body.

In this section 2–5, after explaining the relationship between the south and north bodies of the Ushikiri-yama granodiorite, I describe the genetic relationship between the Ushikiri-yama granodiorite and the dikes. Then, geochemical characteristics of Pr Fine Di studied to clarify magmatic processes in the Ushikiri-yama granodiorite and dikes are described. Finally, based on the results of chapter 2, the igneous characteristics of Cretaceous deep-seated rocks widely distributed in

northern Kyushu are described.

2–5–1 Intrusive relationships of the Ushikiri-yama granodiorite and dikes

Sasaki and Murakami (1986) classified the Ushikiri-yama granodiorite into north and south bodies, and revealed the possibility of intrusive order that the north body intruded into the south body because the dikes intruding the south body are captured in the north body as xenoliths. In addition, this study shows petrographical features and hornblende K–Ar dating, indicating the intrusive order of the south and north bodies. The results are shown as follows. (1) In the fine-grained facies separated by the south and north bodies. The granoblastic texture, caused by the thermal effect of the later intrusive rock, is only observed on the south body near the contact of the north body (Fig. 2–4c). The fine-grained facies would be mainly originated from the south body (Fig. 2–2a). Therefore, the south body firstly intruded and emplaced forming the fine-grained facies around the marginal part of body, and underwent the thermal effect from the north body. (2) The south body is intruded by the dikes with north–south striking and almost vertically dipping. In the north body, Sasaki and Murakami (1986) and this study cannot recognize any dikes. Thus, these dikes may intrude prior to the emplacement of the south body. Since the closure temperatures of the hornblende and biotite in the K–Ar systems are 510 ± 25 ˚C and 300 ± 50 ˚C, respectively, assuming a general magma cooling rate of 30 ˚C/million years, the hornblende K–Ar age is closer to the solidus temperature of granitic magmas rather than that of biotite (Dodson and McClelland-Brown, 1985). The hornblende K–Ar age of the south body is 105.3 ± 3.2 Ma that is older than the north body, 100.9 ± 2.9 Ma (Table 2–3).

2–5–2 Genetic relationships of the south body of Ushikiri-yama granodiorite and related dikes

2–5–2–1 Petrogenesis of Pr Fine Gr

Pr Fine Gr is distributed only in the south body of Ushikiri-yama granodiorite (Fig. 2–2). The variation diagram of the major and trace elements (Fig. 2–8) and the MgO wt%–Fe_2O_3 wt% diagram (Fig. 2–9b) show that the south body and Pr Fine Gr make compositional trends. Although the compositional gap (SiO_2 = 65.4 to 68.5 wt%) is observed, Pr Fine Gr is plotted within the compositional range of the south body in εSrI (105 Ma)–εNdI (105 Ma) diagram (Fig. 2–11c). Considering the field occurrence and petrography, Pr Fine Gr possesses little evidence for the magma mixing or mingling (Fig. 2–4f). It suggests that, Pr Fine Gr may have been formed by fractional crystallization of the south body magma (Fig. 2–9b).

According to the whole-rock SiO_2 (wt%)–modal value (vol%) diagram (Fig. 2–12), the modal value of quartz and K-feldspar increase and plagioclase, hornblende, and biotite decrease with differentiation of the south body and Pr Fine Gr. To verify such differentiation process, two-stage process was set and performed by geochemical modeling. Compositional range of Stage-1 changes within the south body. The lowest SiO_2 granodiorite and the most differentiated granodiorite correspond to the parent and daughter magmas, respectively. In Stage-2, the most differentiation granodiorite and Pr Fine Gr were defined as the parent and daughter magmas. Geochemical modeling was examined by the mass balance calculation and Rayleigh fractionation model using mineral chemistry and major–trace elements in whole-rock chemistry. The partition coefficients for each fractionated mineral were obtained from Philpotts and Schnetzler (1970), Nagasawa and Schnetzler (1971), Gill (1981), Nash and Crecraft (1985), Ewart and Griffin (1994), Klein et al. (1997), and Nielsen and Beard (2000). The results of the mass balance calculations and partition coefficients are listed in Table 2–4 and Appendix 2–3. According to pattern diagram

of the model melt and Pr Fine Gr, the values and patterns are consistent with each other. Therefore, the composition of Pr Fine Gr can be reproduced by fractionated hornblende, plagioclase and biotite from the south body magma (Fig. 2–13).

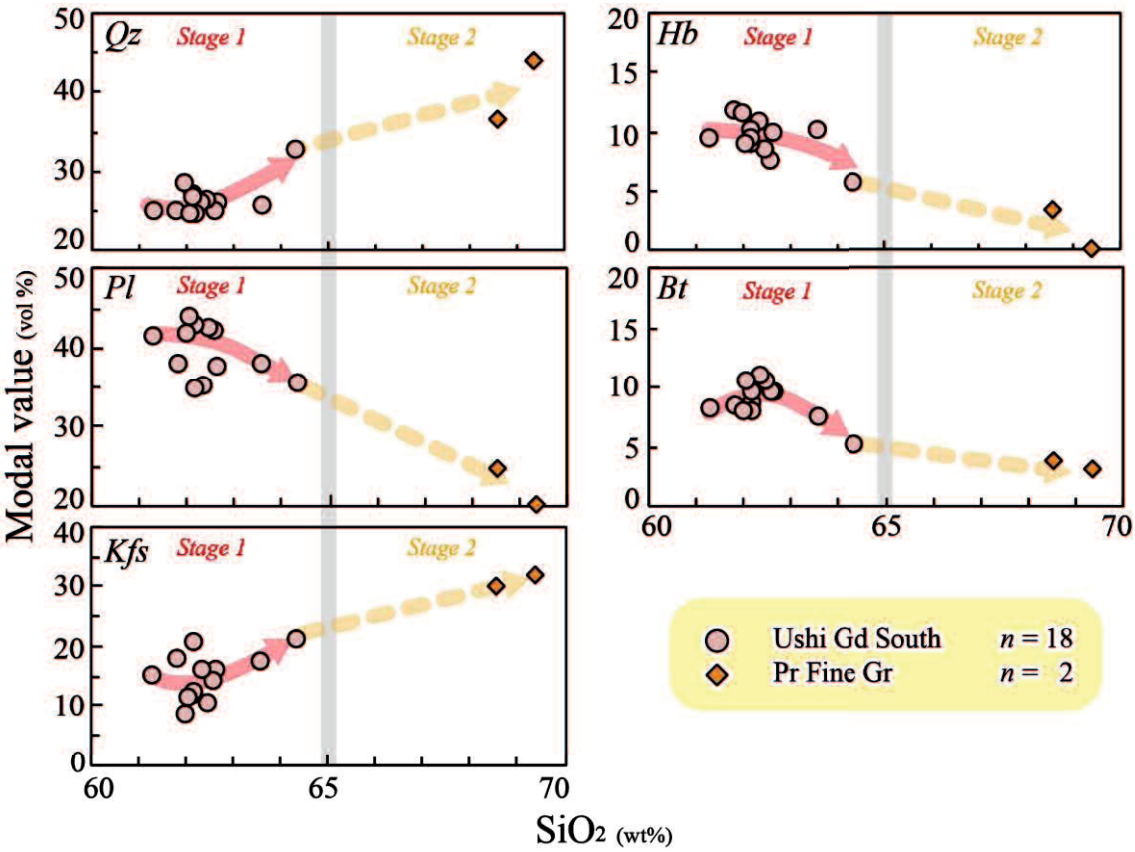

Figure 2–12. Whole-rock SiO_2 (wt%)–modal value (vol%) for the Ushikiri-yama granodiorite south body (Ushi Gd South) and Pr Fine Gr. Stage-1 (red arrows) represents a variation trend from SiO_2-poor to SiO_2-rich Ushikiri-yama granodiorite south body, and Stage-2 (dashed yellow arrows) indicates a shift from SiO_2-rich Ushikiri-yama granodiorite south body to Pr Fine Gr. The modal values are listed in Appendix 2–1. Modal analysis was performed using the Excel spreadsheet (VBA) developed by Shimura and Kojima (2015).

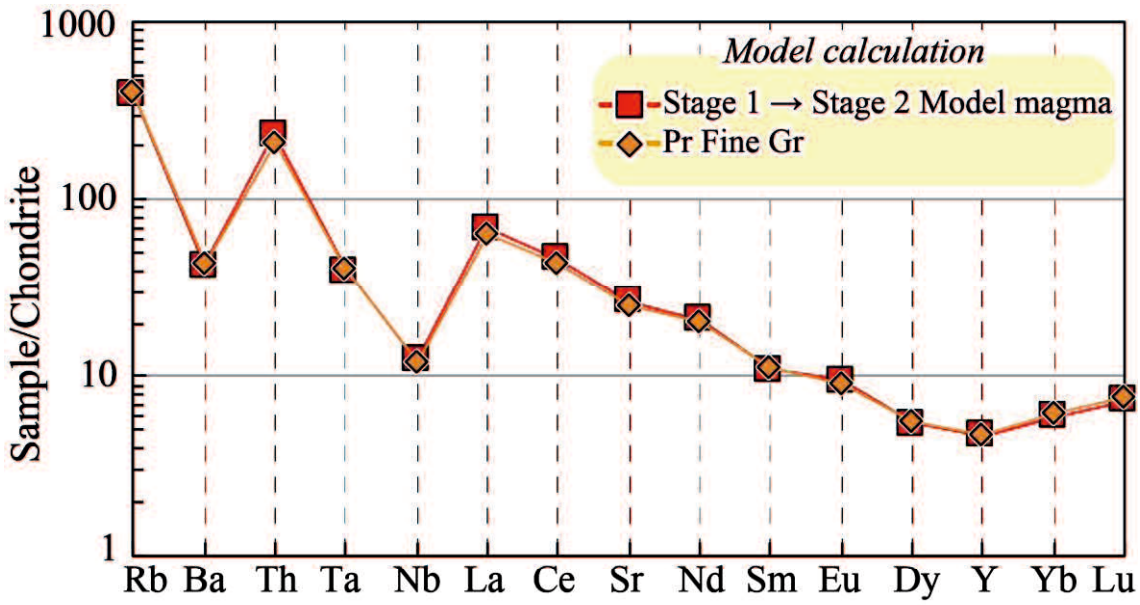

Figure 2–13. Results of fractional crystallization modeling for the Ushikiri-yama granodiorite south body to Pr Fine Gr are shown in the spider diagrams. Normalized values of C1 chondrite are after Sun and McDonough (1989). The Rayleigh fractionation model using partition coefficients are listed in Appendix 3–3.

Table 2–4. Result of the mass balance calculations.

Stage-1	Initial magma	Final magma	Subtracted phases			
			Plagioclase	Hornblende	Biotite	Magnetite
Sample No.	14052107	14060114	14052107	14052107	14052107	Average (n=28)
SiO_2 (wt%)	60.91	65.66	55.91	47.39	35.52	0.00
TiO_2	0.73	0.45	0.01	0.91	4.13	0.10
Al_2O_3	16.36	14.95	27.65	5.81	14.43	0.10
FeO*	5.52	3.66	0.10	12.82	18.03	91.40
MnO	0.11	0.06	0.02	0.51	0.32	0.10
MgO	2.78	2.36	0.00	13.76	11.19	0.00
CaO	4.65	3.7	9.21	11.58	0.00	0.00
NaO	2.96	3.3	6.05	0.86	0.08	0.00
K_2O	2.60	3.66	0.19	0.54	10.19	0.00
P_2O_5	0.21	0.12	0.00	0.00	0.00	0.00
Calculated result (%)		75.25	16.48	4.66	1.81	1.81
Degree of crystallization, 24.97%						
Fractionated proportions (%)			66.58	18.81	7.32	7.29
Sum of squares, 0.632						
Stage-2	Initial magma	Final magma	Subtracted phases			
			Plagioclase	Hornblende	Biotite	Magnetite
Sample No.	14060114	14050415	14060114	14060114	14060114	Average (n=28)
SiO_2 (wt%)	65.66	69.37	56.40	47.59	36.06	0.00
TiO_2	0.45	0.29	0.01	0.92	3.68	0.10
Al_2O_3	14.95	14.88	27.45	6.21	14.72	0.10
FeO*	3.66	2.12	0.13	12.83	18.11	91.40
MnO	0.06	0.03	0.01	0.45	0.31	0.10
MgO	2.36	1.02	0.01	14.22	11.83	0.00
CaO	3.7	2.95	8.93	11.61	0.00	0.00
NaO	3.3	3.36	6.27	1.03	0.07	0.00
K_2O	3.66	3.78	0.21	0.55	10.09	0.00
P_2O_5	0.12	0.07	0.00	0.00	0.00	0.00
Calculated result (%)		83.11	5.57	6.60	4.52	0.20
Degree of crystallization, 16.98%						
Fractionated proportions (%)			32.97	39.08	26.77	1.18
Sum of squares, 0.013						

2–5–2–2 Petrogenesis of Pr Fine To

Pr Fine To contains plagioclase with dusty zones (Fig. 2–4d), acicular apatite (Fig. 2–5e), and ocellar quartz surrounded by fine-grained hornblende (Fig. 2–5d). These textures are similar to the magma mixing reported by Hibbard (1995). The variation diagram of the major and trace elements (Fig. 2–8) shows that Pr Fine To is intermediate in composition between the south body of Ushikiri-yama granodiorite and Pr Fine Di (Fig. 2–8). In the MgO (wt%)–Fe_2O_3 (wt%) diagram (Fig. 2–9b), Pr Fine To is plotted on a line connecting the south body and Pr Fine Di, of which the connecting line is oblique with fractional crystallization trend between the south body and Pr Fine Gr (Fig. 2–9b). In the εSrI (105 Ma)–εNdI (105 Ma) diagram, Pr Fine To

is plotted between the south body and Pr Fine Di (Fig. 2–11c Red line: Mixing line 1). Considering the descriptive and chemical characteristics, Pr Fine To is most likely caused by the mixing of the south body and Pr Fine Di. On the other hand, Pr Fine To intruding the pelitic metamorphic rocks is plotted on the lower NdI side than the two mixing lines (Red and blue lines: Mixing lines 1 and 2) shown in Figure 2–11c, but extend into near the mixing line (Green dashed line: Assimilation 2) between Pr Fine Di and the pelitic metamorphic rock (Fig. 2–11d). In other words, Pr Fine To magma may have been formed by assimilation of pelitic metamorphic rocks in the intrusion site after magma mixing.

2–5–3 Geochemical characteristics of Pr Fine Di

The SiO_2 content of Pr Fine Di is 53.7 and 53.9 wt%, and it has high MgO (7.9 and 8.1 wt%), Cr (399 and 425 ppm) and Ni (193 and 199 ppm) contents (Fig. 2–8 and Appendix 2–2). In the FeO*/MgO–SiO_2 (wt%) diagram in Figure 2–9a, the samples are plotted in the high-Mg andesite (HMA) field. On the other hand, the isotopic ratios of the measured samples are different, and the high-SrI (105 Ma) Pr Fine Di plots on the mixing line (Red and blue lines: Assimilation 1 and 3) between the lower-SrI (105 Ma) Pr Fine Di and pelitic metamorphic rocks (Fig. 2–11d). The assimilation ratio of the pelitic metamorphic rocks is very small, less than a few percent (Fig. 2–11d). Therefore, it is possible that the composition of the high-SrI (105 Ma) Pr Fine Di was influenced by the Sr isotopic composition of the pelitic metamorphic rocks, but the small amount of assimilation is insufficiently affected with the composition of the major elements. Based on the above petrography and geochemical features, in this section 2–5–3, I examine the geochemical characteristics of Pr Fine Di based on the major and trace elements.

The geochemical character of Pr Fine Di in the Ushikiri-yama area, is examined by comparison with the previously reported Cretaceous high-Mg andesite/diorite in northern Kyushu and western Yamaguchi Prefecture; andesite

from the Kanmon Group in western Yamaguchi Prefecture (Imaoka and Murakami, 1979; Imaoka et al., 1993), diorite from the Kita-taku area in western part of northern Kyushu (Kamei et al., 2004), and diorite from the Kunisaki area in eastern part of northern Kyushu (Murakami, 1994; Kamei et al., 2004). In the MgO/(MgO+FeO*)–TiO_2 (wt%) diagram, the andesite from the Kanmon Group, the diorite from the Kita-taku and Kunisaki areas, and Pr Fine Di from Mt. Ushikiri-yama area are plotted in the Sanukitic HMA, Bajaitic HMA, and Adakitic HMA fields (Fig. 2–14a). In the Y (ppm)–Sr/Y diagram (Fig. 2–14b) and the Yb_N–$(La/Yb)_N$ diagram (Fig. 2–14c), all rocks from the four regions including the Mt. Ushikiri-yama are plotted in the Sanukitic HMA field. The rare-earth elements (REEs) content of Pr Fine Di and the Kunisaki and Kita-taku diorites decrease with such described order, and they are similar REE patterns showing enrichment of light REEs (La to Eu) and depletion of heavy REEs (Gd to Lu) (Fig. 2–14d). From the geochemical character described above, Pr Fine Di from Mt. Ushikiri-yama area, as well as the Cretaceous high-Mg andesitic rocks scattered in northern Kyushu, could be derived from the magmatic activity resembling the Sanukitic HMA.

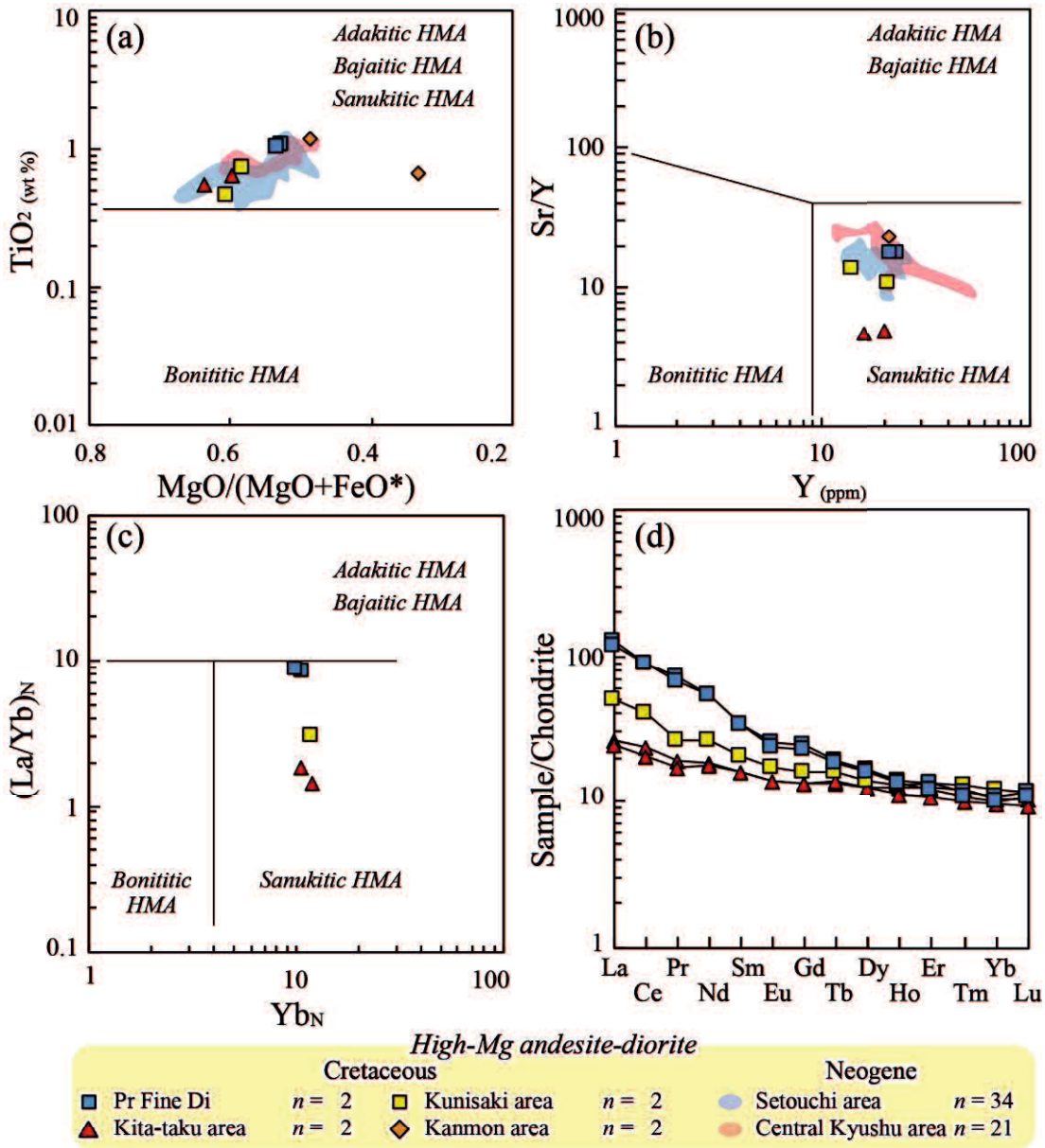

Figure 2–14. Discrimination diagrams and C1 chondrite-normalized REE patterns for the Pr Fine Di. Cretaceous high-Mg diorites from central and northern Kyushu, and Neogene high-Mg andesites from the central Kyushu and the Setouchi area are shown (modified after Kamei et al., 2004). (a) MgO/(MgO + FeO*)–TiO_2 (wt%) diagram. (b) Y (ppm)–Sr/Y diagram. (c) Yb_N–$(La/Yb)_N$ diagram. The data for comparison were obtained from the following sources; andesite from the Kanmon Group, Yamaguchi (Imaoka and Murakami, 1979; Imaoka et al., 1993), diorite from northern Kyushu (Murakami, 1994; Kamei et al., 2004). The Neogene HMA rocks in Kyushu also geochemically possess the Sanukitic HMA (Shiraki et al., 1991; Nagao et al., 1992; Kakubuchi et al., 1995; Shiraki et al., 1995).

2–5–4 Petrological evolution of the Ushikiri-yama body

To reveal the genetic relationship between the Ushikiri-yama granodiorite, north body and south body, is important for the modeling of igneous activity and intrusive (emplacement) processes in this region. The following lines are important observations regarding the relationship between the north and south bodies. (1) The lithofacies of the north and south bodies is the almost same (Fig. 2–2). The south body captures the pelitic metamorphic rocks as a xenolith (Fig. 2–3a). (2) The mineral assemblage of the north and south bodies is similar to each other although the inferred magmatic epidote is only recognized in the south body (Figs. 2–4a and b). (3) The hornblendes of the north body tend to be enriched in Al_2O_3 contents rather than those of the south body (Table 2–1). (4) The whole-rock compositions of the north and south bodies are similar, but the north body is characterized by high MgO, Ni and Cr contents, while the south body is more differentiated with a larger variation in SiO_2 contents (Fig. 2–8). (5) The south body has higher SrI (105 Ma) and lower NdI (105 Ma) values than the north body. In the epsilon diagram, the south body are plotted with a more enriched composition than the north body, and the Sr–Nd values of the south body tend to change to those of the pelitic metamorphic rocks (Fig. 2–11). (6) The hornblende K–Ar ages of the south and north bodies are 105.3 ± 3.2 Ma and 100.9 ± 2.9 Ma, respectively.

The above remarkable features suggest that the south body has advanced isotopic characteristics with assimilation of pelitic metamorphic rocks rather than those of the north body. The horizontal variation in the Ushikiri-yama granodiorite was examined via the modal composition (vol%) of quartz, plagioclase, K-feldspar, hornblende, biotite, sum of felsic minerals (Qz + Kfs + Pl), and sum of mafic minerals (Hb + Bt) (Fig. 2–15). These variation maps were created using Graph-R (S-NEXT Co., Ltd.) by calculating the longitude, latitude, modal composition data of each sample. The modal compositions of quartz, K-feldspar, hornblende, and biotite independently show the systematic behavior within each body; e.g., the sum of felsic

(Qz + Kfs + Pl) and mafic (Hb + Bt) values show correlation in each body (Fig. 2–15). That is to say, the field occurrences and hornblende K–Ar ages suggest that the south body was intruded prior to the north body. The early intruded south body was assimilated with the wall rocks during magma ascending. After that the north body ascended using the same path (vent) with little assimilation due to after vent cleaning by the ascending magma. Harris et al. (1999) showed that the effect of assimilation of crustal materials (contaminant) decreases with the progression of igneous activity in the alkali intrusive body of Namibia, based on O, Sr, and Nd isotope ratios. They proposed a vent cleaning model, in which the walls of magma feeders and reservoirs are covered by early ascending magma, so that later magma did not come into the chance of contact with the host rock (Harris et al., 1999).

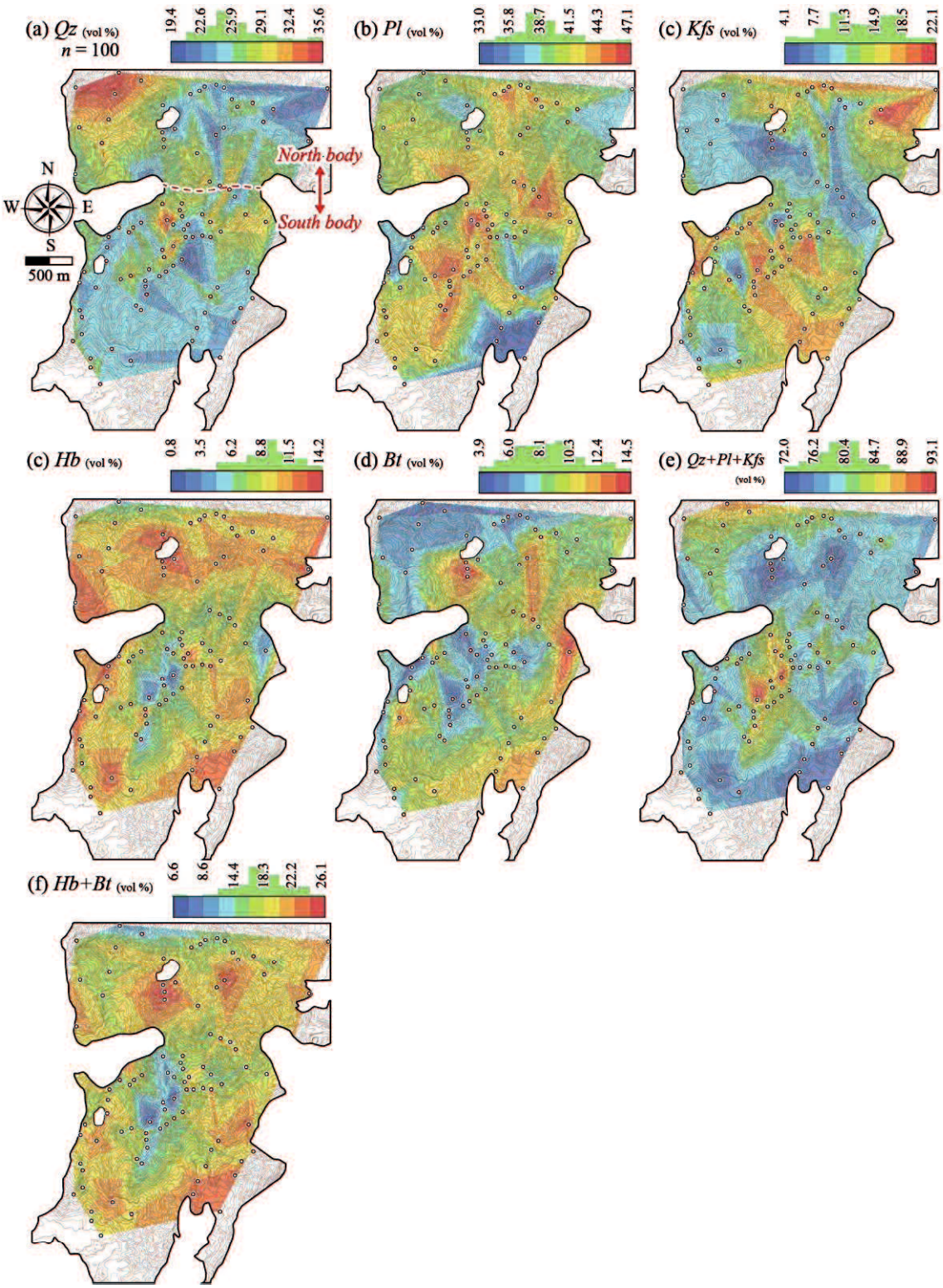

Figure 2–15. Horizontal variation in modal compositions. (a)–(f) Qz, Pl, Kfs, Hb, Bt, felsic minerals (Qz + Pl +Kfs), and mafic minerals (Hb + Bt) of the Ushikiri-yama granodiorite. White circles indicate sampling sites. These maps were created using Graph-R. The modal

values are listed in Appendix 2–1.

Based on the intrusive relationships, chemical characteristics of the two bodies and various dikes, and their genetic relationships, the intrusive (emplacement) model of the Ushikiri-yama body is shown in Figure 2–16. In addition, the magmatic processes of the Ushikiri-yama body including the dikes are shown in Figure 2–17. The granodioritic magma that formed the south body ascended while assimilating the pelitic metamorphic rocks with the activating of igneous activity. The magma was once growing horizontally at the pressure condition under the stable of magmatic epidote (≥ 6–8 kbar: Zen and Hammarstrom, 1984; Schmidt and Poli, 2004). At the same time, Pr Fine Di magma differentiated from the Sanukitic HMA magma also ascended and reacted with the south body magma. As a result, Pr Fine To magma with an intermediate composition between the above two magmas was formed. In addition, the south body magma underwent fractional crystallization to form Pr Fine Gr magma with higher SiO_2 content. Because the Pr Fine Gr is porphyritic texture and there is a compositional gap (SiO_2 = 65.4 to 68.5 wt%) between the south body and Pr Fine Gr, crystal-poor melt lenses already fractionated plagioclase, hornblende, and biotite may have squeezed out from the crystal mash and formed Pr Fine Gr magma. Such mechanism was reported by Bachmann and Bergantz (2004) and Imaoka et al. (2014b) as the model of squeezed differentiated melt from a crystal mash. Finally, the north body magma ascended the intrusive path (vent) formed by the south body magma with little chance to react with the pelitic metamorphic rocks and emplaced on the northern side of the south body (Figs. 2–16 and 2–17). The emplacement *P-T* conditions of the south and north bodies are similar, 4.0 ± 0.6 kbar, 710 ± 40 °C (south body) and 4.3 ± 0.6 kbar, 740 ± 40 °C (north body), respectively, and the emplacement depth is lower than the stability field of the magmatic epidote. Sial et al. (2008) pointed out that if epidote is contained in a magma body solidified at low pressure, the magma rises fast enough so that epidote remains undecomposed.

Based on this suggestion, it is possible that the ascent rate of magma was faster the south body magma than the north body magma.

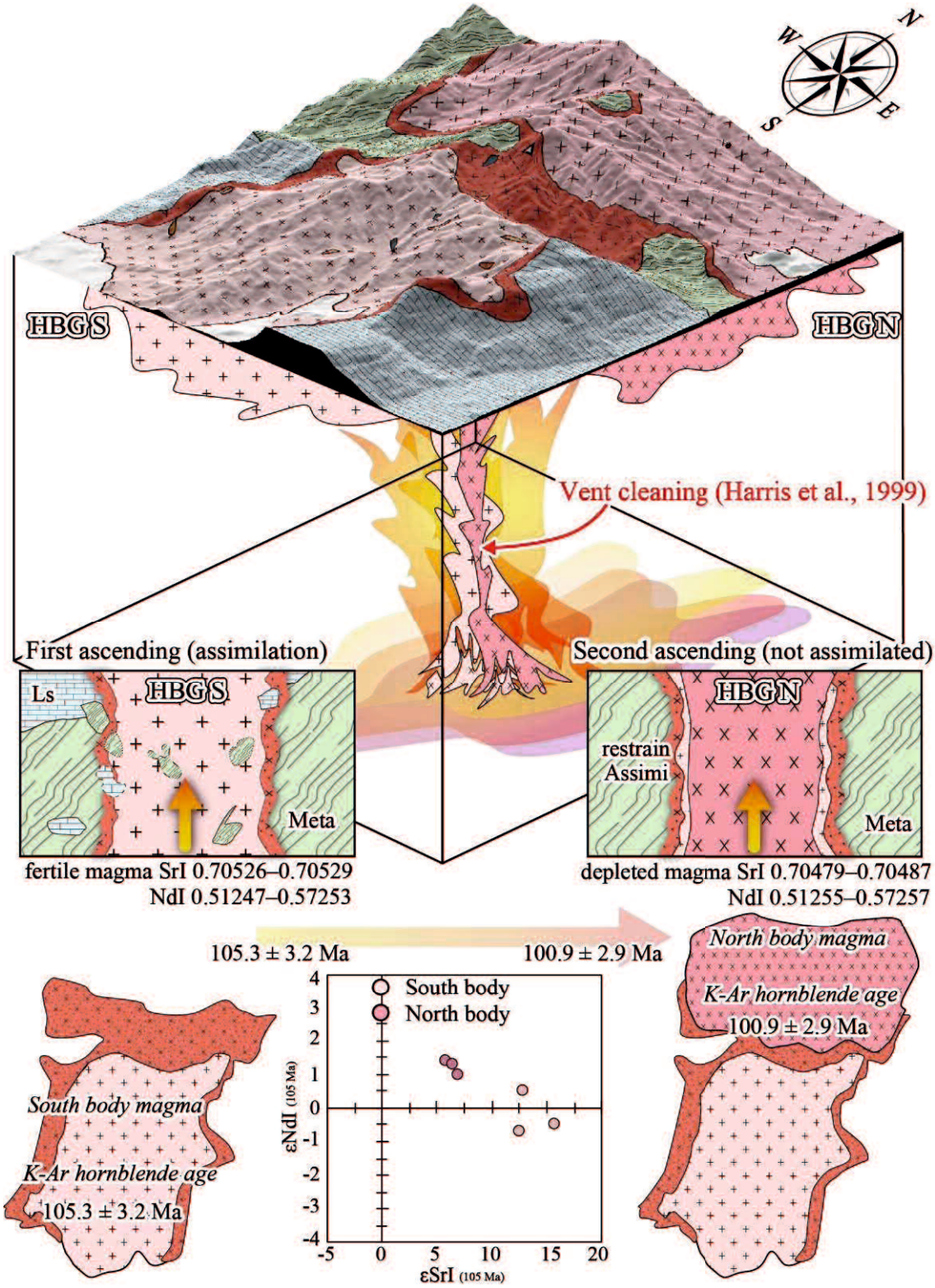

Figure 2–16. Intrusive (emplacement) processes model of the Ushikiri-yama body.

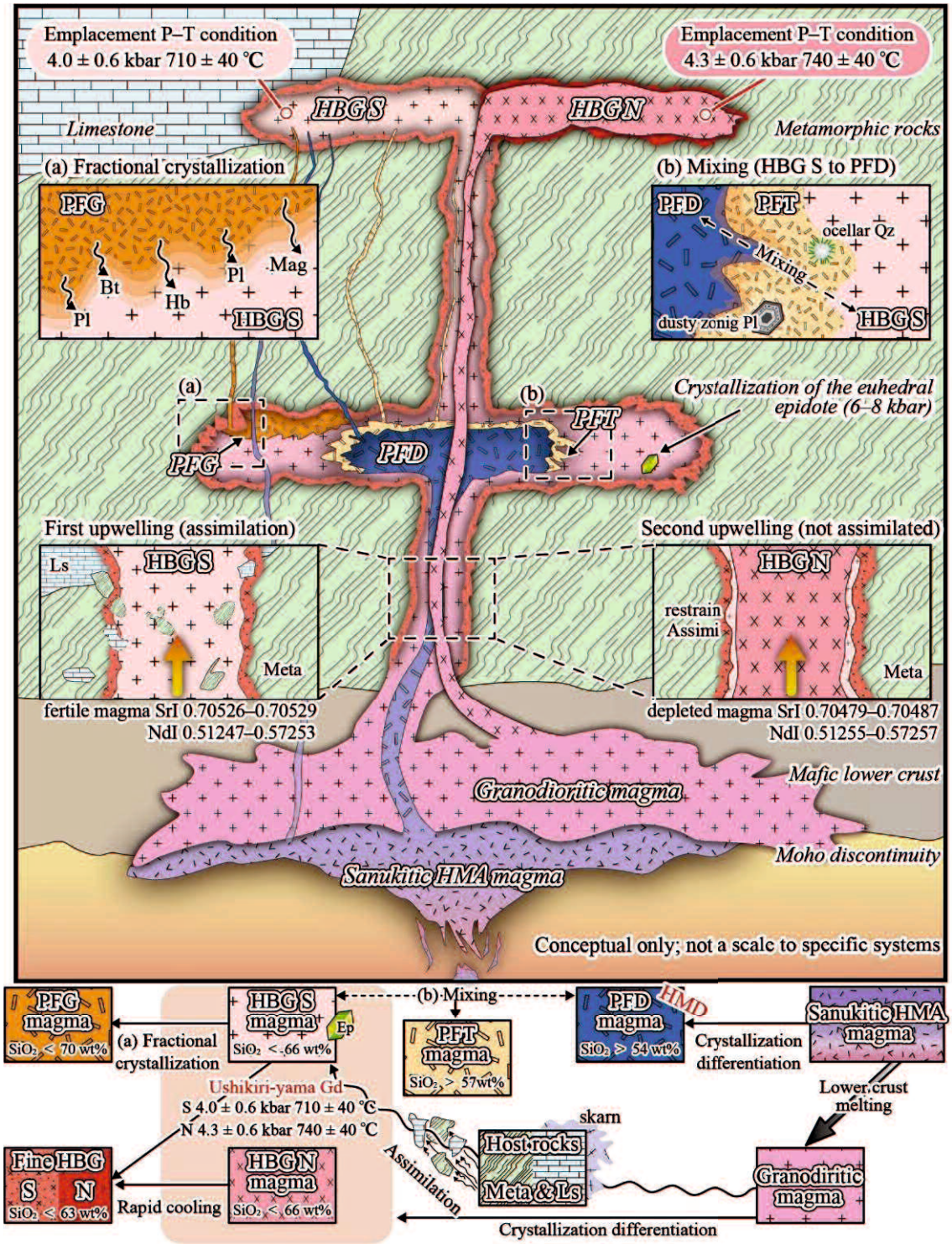

Figure 2–17. Schematic model showing magma processes of the Ushikiri-yama granodiorite and related rocks. Abbreviations are shown in text.

2–5–5 Characteristics of the igneous activity in Cretaceous Northern Kyushu batholith

The intrusive rocks constituting the Cretaceous Northern Kyushu batholith can be broadly divided into granodiorite and granite, the latter generally intruding the former (Karakida, 1985; Yada and Owada 2003; Owada and Kamei, 2010). The granodiorites are accompanied by fine-grained gabbroic to dioritic rocks that are thought to have been intruded as coeval intrusive rocks (Yuhara and Uto, 2007; Owada and Kamei, 2010; Yuhara and Masaki, 2013).

The Ushikiri-yama granodiorite body that is isolated body far from other rocks, but shows the similar Sr–Nd isotopic composition as the Cretaceous granodiorite of northern Kyushu (Fig. 2–11e). In addition, the Ushikiri-yama granodiorite body is accompanied by dikes that are thought to have been active at the same time, and these dikes are ubiquitously distributed throughout northern Kyushu. From the combination of these lithofacies and chemical features, the Ushikiri-yama granodiorite can be regarded as an activity that reflects the characteristics of Cretaceous igneous activity in northern Kyushu. In Central and Northern Kyushu, HMA-derived rocks occur sporadically over a wide area from Taku City, Saga Prefecture to Kunisaki Peninsula, Oita Prefecture (Kita-taku, Shikanoshima, and Kunisaki), and are closely associated with granodiorite in spatiotemporal setting (Fig. 2–1; Murakami, 1994; Kamei et al, 2004; Yuhara and Uto, 2007; Tiepolo et al., 2012). The Cretaceous igneous activity in northern Kyushu is inferred to have been driven by the melting of the lower crust and intrusive of large-scale granitic magmas. The heat source for the crustal melting is thought to be of the mafic magmas derived from wedge mantle, probably representing the Sanukitic HMA magma (Fig. 2–17).

3 Shaku-dake area

3–1 Introduction

The granitoids cover approximately 30% surface area of the Japanese island (Takagi, 2004). Intense magma activities of the granitoids occurred during the Cretaceous (50–130 Ma; Takagi, 2004). The Cretaceous granitoid batholith is exposed over an area of about 100 km from east to west and 50 km from north to south in northern Kyushu (Figs. 1–1 and 3–1), showing zircon U–Pb ages of 116–102 Ma (Adachi et al., 2012; Tiepolo et al., 2012; Miyazaki et al., 2018; Yuhara et al., 2019a, b; Yuhara et al., 2020). Small mafic bodies occur sporadically in the batholith. Some of these mafic bodies represent high-Mg diorite (HMD) compositions derived from high-Mg andesite (HMA) magma, and their petrogenesis has been discussed by several researchers (Murakami, 1994; Kamei et al., 2004; Yuhara and Uto, 2007; Tiepolo et al., 2012; Eshima and Owada, 2018; Eshima et al., 2019, 2020; Eshima, 2021a, b). The coexistence of both mafic and felsic rocks has been reported from volcanic-plutonic sites of the active continental margin in the Cretaceous granitoid batholith of southwest Japan and the Cordillera Mountains in the North America (Tainosho et al., 1985; Tepper et al., 1993). In addition, the mantle derived mafic magma is strongly involved in the origin of granitic magma as a parent magma and a heat source of crustal melting (Reid et al., 1983; Le Bel et al., 1985). Therefore, clarification of the behavior of the HMA-derived magma in the crust play an important role in examining the genetic relationship with granitoids. Furthermore, plutonic rocks are often called “fossils of magma reservoirs” as they preserve magmatic or emplacement processes and the time scale of plutonic activity (e.g., Wiebe, 1994; Wiebe and Collins, 1998). Investigation of internal structures may help to clarify the lithological and chemical variation in plutonic rocks as well as their growth process, which is crucial for understanding the relationship between volcanic and plutonic activity (Lipman, 2007; Macdonald et al., 2014). These studies will contribute to the

understanding of crustal growth and evolution (Bachl et al., 2001; Menand, 2008; Annen, 2011; Menand et al., 2011).

The HMA magma is rich in Mg and has a high Mg/Fe ratio compared with ordinary andesite magma. Based on the melting experiments (Tatsumi, 1981, 1982; Hirose, 1997), the HMA magma is at equilibrium with Mg-rich mantle olivine and pyroxenes, suggesting that the HMA may be formed by the solidification of primary magma from the mantle. Based on this background, many geochemical discrimination diagrams for HMA have been proposed using mineral and whole-rock chemical compositions and isotopic compositions (e.g., Tatsumi and Hanyu, 2003; Kamei et al., 2004). However, detailed studies on magmatic processes, lithofacies variation and internal structure with HMA composition such as differentiation, mixing, and assimilation, and on the relationships among other magmas are scarce. By clarifying this chapter 3, I focus on the characteristics of the large-scale magmatic activity of the Cretaceous period.

In this chapter 3, the magmatic process, lithofacies variations and the growth process of a newly finding HMA-derived rock, the Shaku-dake body (a high-Mg diorite body), are discussed as a member of the Cretaceous granitoids batholith of northern Kyushu.

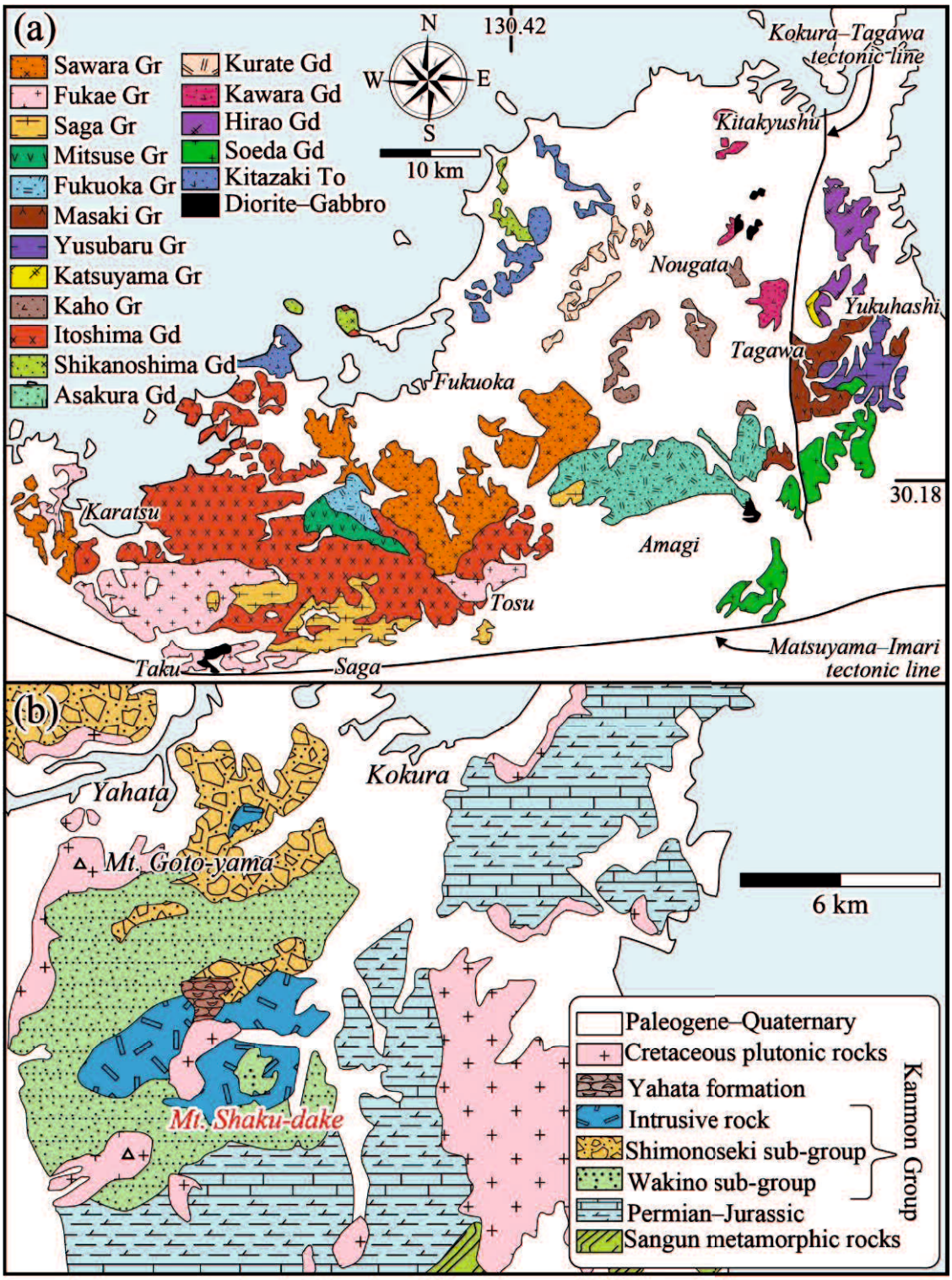

Figure 3–1. Distribution of Cretaceous igneous rocks in the northern Kyushu districts. (a) Index map of the northern Kyushu with Cretaceous igneous rocks. (b) Simplified geological map of the study area (Karakida, 1985). Gr: granite, Gd: granodiorite, and To: tonalite.

3–2 Geological overview

The Mt. Shaku-dake area located in the northeastern part of Kyushu, southwest Japan, is underlain by the Wakino sub-group of the Kanmon group and the Shaku-dake body, a member of the Kawara-dake suite, that intrudes the Wakino sub-group (Fig. 3–2). The Wakino sub-group is composed of Cretaceous shallow marine deposits with well-stratified sequences of lower basal conglomerate, the middle coarse sandstone, and the upper sandstone/shale alternation (Nakae et al., 1998). The basal conglomerate locally includes limestone blocks as large gravels (10–60 cm). The limestone is derived from the Permian accretionary complex (Nakae et al., 1998). The bedding structures of the Wakino sub-group generally show E–W to N 70°E in strikes and 10–40°N or S in dips (Fig. 3–2). The Shaku-dake body consists mainly of two-pyroxene diorite (TPD) and hornblende-biotite granodiorite (HBG) as stocks with several kinds of dikes. Both TPD and HBG are ellipsoidal in shape on the west of Mt. Shaku-dake (Fig. 3–2) and caused contact metamorphism to the surrounding rocks of Wakino sub-group in the range of several hundred meters.

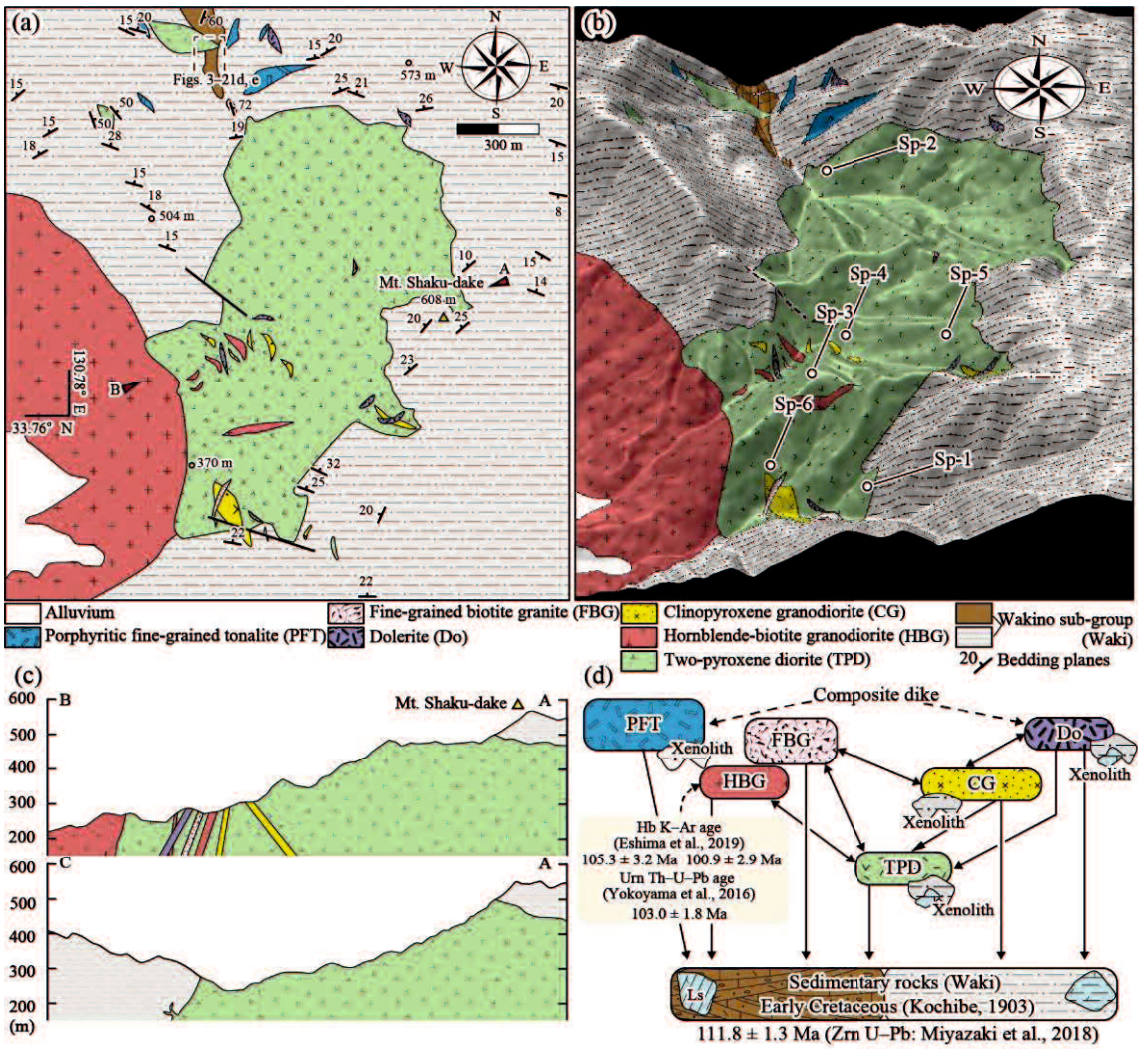

Figure 3–2. (a) Geological map of the study area (Eshima et al., 2020). The dotted square in the northern part of map indicates outcrop sites in Figures 3–21d and e. (b) Bird's-eye view of the study area (dip angle 45°). Circles with sample numbers from Sp-1 to Sp-6 are sampling sites for EPMA analyses (Figs 4–6, 7 and 8). (c) Cross-sections of the study area along lines A–B and A–C (SW–NE and NW–SE directions). (d) Mutual relationships between igneous and sedimentary rocks in the study area. Ls: limestone. Arrows indicate intrusive relationships, whereas dotted arrows show coeval relationships.

3–3 Petrography of the Shaku-dake diorite body

The Shaku-dake body can be divided into two groups, Group-1 and Group-2, in terms of the presence of xenoliths. The Group-1 locally involves xenoliths at the margin of the bodies and contains ilmenite as an opaque mineral. On the other hand, the Group-2 rarely involves xenoliths and bears magnetite. TPD, Do (dolerite), PFT (porphyritic fine-grained tonalite), and CG (clinopyroxene granodiorite) belong to the Group-1, whereas HBG (hornblende–biotite granodiorite) and FBG (fine-grained biotite granite) are classified in the Group-2.

3–3–1 Occurrence and petrography of the Group-1

3–3–1–1 Two-pyroxene diorite (TPD)

The TPD occurs as a stock with an area of 1.9 × 1.5 km (Fig. 3–2). It is dark gray in color. Xenoliths of sandstone, shale, and limestone, probably derived from the Wakino sub-group, are rarely included in the TPD (Figs. 3–3a and b).

The TPD shows a hypautomorphic granular texture and is mainly composed of plagioclase, orthopyroxene, clinopyroxene, and biotite with trace amounts of quartz and K-feldspar. Zircon, titanite, ilmenite, and apatite are observed as accessory minerals (Fig. 3–5a). Plagioclase shows subhedral–euhedral crystals with 0.5–1.5 mm in long and possesses the albite twins and chemically zoned. Orthopyroxene and clinopyroxene are also subhedral–euhedral in shape with a size of 0.5–1.5 mm in long and are locally surrounded by hornblende and biotite. Quartz and K-feldspar occur as interstitial minerals of the early-crystallized minerals. The sandstone/shale micro-xenoliths can be identified under the microscope (Fig. 3–5b).

3–3–1–2 Dolerite (Do)

The Do dikes with less than 100 m in length and 0.4–3.0 m in width intrude the Wakino sub-group, TPD, and CG (Fig. 3–3c). It rarely includes the sandstone/shale and the limestone (Figs. 3–3d and e). The grain sizes are fine-grain, and

clinopyroxene and orthopyroxene are visible as phenocrysts.

The Do shows fine-grained porphyritic texture under the microscope (Fig. 3–5c). Phenocrystic minerals are of plagioclase, orthopyroxene, clinopyroxene, and biotite. Clinopyroxene attains up to 2.5 mm in long. Plagioclase shows dusty zoning. Ilmenite occurring in the groundmass is partly rimmed by very fine plagioclase, orthopyroxene, and clinopyroxene (Fig. 3–5c). Mafic minerals generally show 0.2–1.2 mm in long.

3–3–1–3 Porphyritic fine-grained tonalite (PFT)

The PFT intrudes only into the Wakino sub-group and may form a composite dike with the Do (Fig. 3–3f). It shows pale gray color, fine-grained, and a porphyritic texture. The boundaries between the PFT and the Wakino sub-group are generally clear; however, they show wavy features in some locations (Fig. 3–3f). The PFT sometimes involve the sandstone/shale and the limestone as xenoliths (Fig. 3–4a).

The PFT shows porphyritic texture and mainly composed of plagioclase, hornblende, biotite, and quartz as phenocrysts with 0.5–1.5 mm in long. Some of hornblende locally shows very large crystals, attaining up to 15 mm. The groundmass contains fine-grained plagioclase, quartz with a small amount of K-feldspar and ilmenite, and titanite, ilmenite, and apatite are present as accessory minerals (Fig. 3–5d).

3–3–1–4 Clinopyroxene granodiorite (CG)

The CG occurs as dikes with 1.0–10 m in width and shows massive and fine- to medium-grained with gray in color. It intrudes the TPD, FBG, Do, and the Wakino sub-group and extends the network veins along the intrusive boundary with the TPD and FBG (Figs. 3–4b and c) The CG locally involves the sandstone/shale as xenoliths (Fig. 3–4d)

The CG is hypautomorphic granular texture and mainly composed of

plagioclase, clinopyroxene, biotite, quartz, and K-feldspar. Ilmenite, titanite, zircon, and apatite are present as accessory minerals (Fig. 3–5e). Plagioclase shows subhedral–euhedral crystals with 0.4–1.6 mm in size and possesses a zoned texture. Clinopyroxene is of 0.3–1.8 mm in size and is rimmed by hornblende. Biotite shows a subhedral–euhedral crystals (0.3–1.6 mm) and often includes ilmenite. Quartz occurs as interstitial crystals (0.3–1.0 mm) and shows a wavy extension. K-feldspar shows a perthite texture with a particle size of 0.4–0.7 mm and also appears as interstitial crystals.

3–3–2 Occurrence and petrography of the Group-2

3–3–2–1 Hornblende–Biotite granodiorite (HBG)

The HBG occurs as a stock with an area of 1.5 × 0.5 km in the western part of TPD and intrudes into the TPD and the Wakino sub-group (Fig. 3–2). It is gray to light gray in color with grain size ranging from fine- to medium-grained but ubiquitously includes euhedral hornblende of 0.5–1.5 cm in long as phenocrysts. Mafic magmatic enclaves (MMEs) with diameter of 10–30 cm are observed. The alignment of the MMEs and constituent minerals such as euhedral hornblende and plagioclase weakly form a flow structure. The small dikes or veins derived from the HBG intrude on the TPD in some locations (Fig. 3–4e).

The HBG shows a hypautomorphic granular texture and is mainly composed of plagioclase, biotite, hornblende, quartz, and K-feldspar. Titanite, allanite, apatite, zircon, and magnetite are present as accessory minerals (Fig. 3–5f). Plagioclase shows subhedral–euhedral crystals with 1.0–4.5 mm in long and remarkable development of twins and zoned structure. Myrmekite is sometimes observed between plagioclase and K-feldspar. Biotite shows subhedral–euhedral crystals, generally 0.1–0.5 mm in long, but it often occurs as a phenocryst, attaining up to 1.0–2.0 mm in long. Hornblende is observed as a phenocryst with a particle size of 1.0–4.5 mm, attaining up to 15 mm. Quartz and K-feldspar occur as interstitial

crystals of 0.1–3.0 mm in area and bear plagioclase, biotite, and hornblende as poikilitic inclusions. Quartz shows a wavy extinction and K-feldspar includes rounded quartz.

3–3–2–2 Fine-grained biotite granite (FBG)

The FBG intrudes into the TPD, CG, and Wakino Sub-group and is intruded by the back veins from TPD (Fig. 3–4f).

The FBG shows a hypautomorphic granular texture and is mainly composed of plagioclase, biotite, quartz, and K-feldspar. Magnetite, titanite, and zircon are observed as accessory minerals (Fig. 3–5g). Plagioclase shows subhedral–euhedral crystals with 1.0–2.7 mm in long. Biotite (0.4–1.2 mm) shows subhedral–anhedral crystals and often forms clots. Quartz and K-feldspar occur as interstitial crystals with 0.2–1.8 mm in long and the former show a wavy extension.

Figure 3–3. Field occurrences of the intrusive rocks. (a) TPD including the Wakino sub-group as xenoliths. (b) Limestone xenoliths in TPD. (c) CG and Do show the intrusive relationship each other. (d) The Do including the Wakino sub-group as xenoliths. (e) The limestone xenoliths included in the Do. (f) The composite dike consisting of the Do and PFT. Abbreviations are shown in the text.

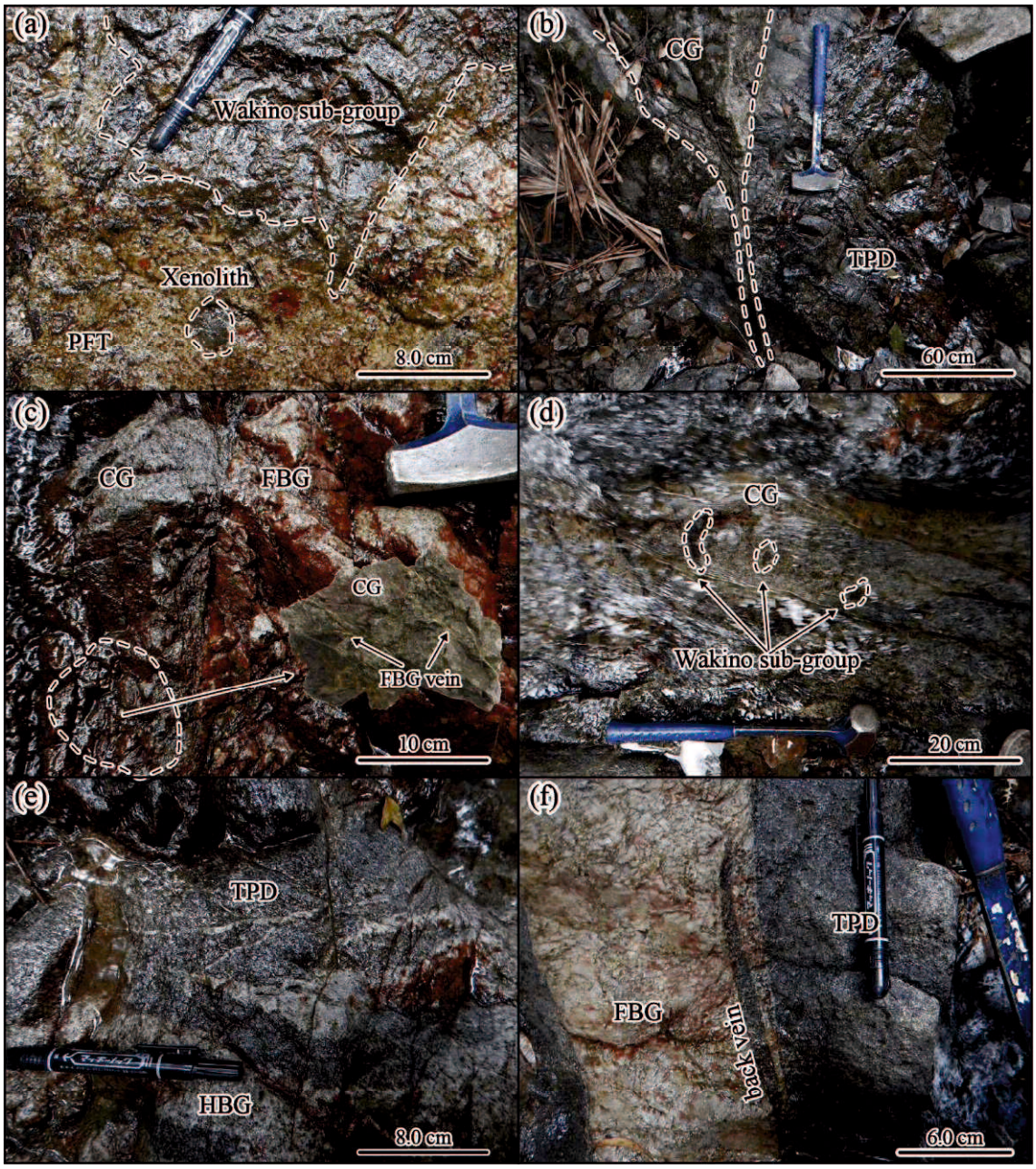

Figure 3–4. Field occurrences of the intrusive rocks. (a) The PFT including the Wakino sub-group as xenoliths. (b) The CG intruding the TPD. (c) The network veins derived from the FBG intrudes the CG. (d) The CG capturing the Wakino sub-group as xenoliths. (e) The HBG intruding the TPD. (f) The FBG and Do show the intrusive relationship each other. Abbreviations are shown in the text.

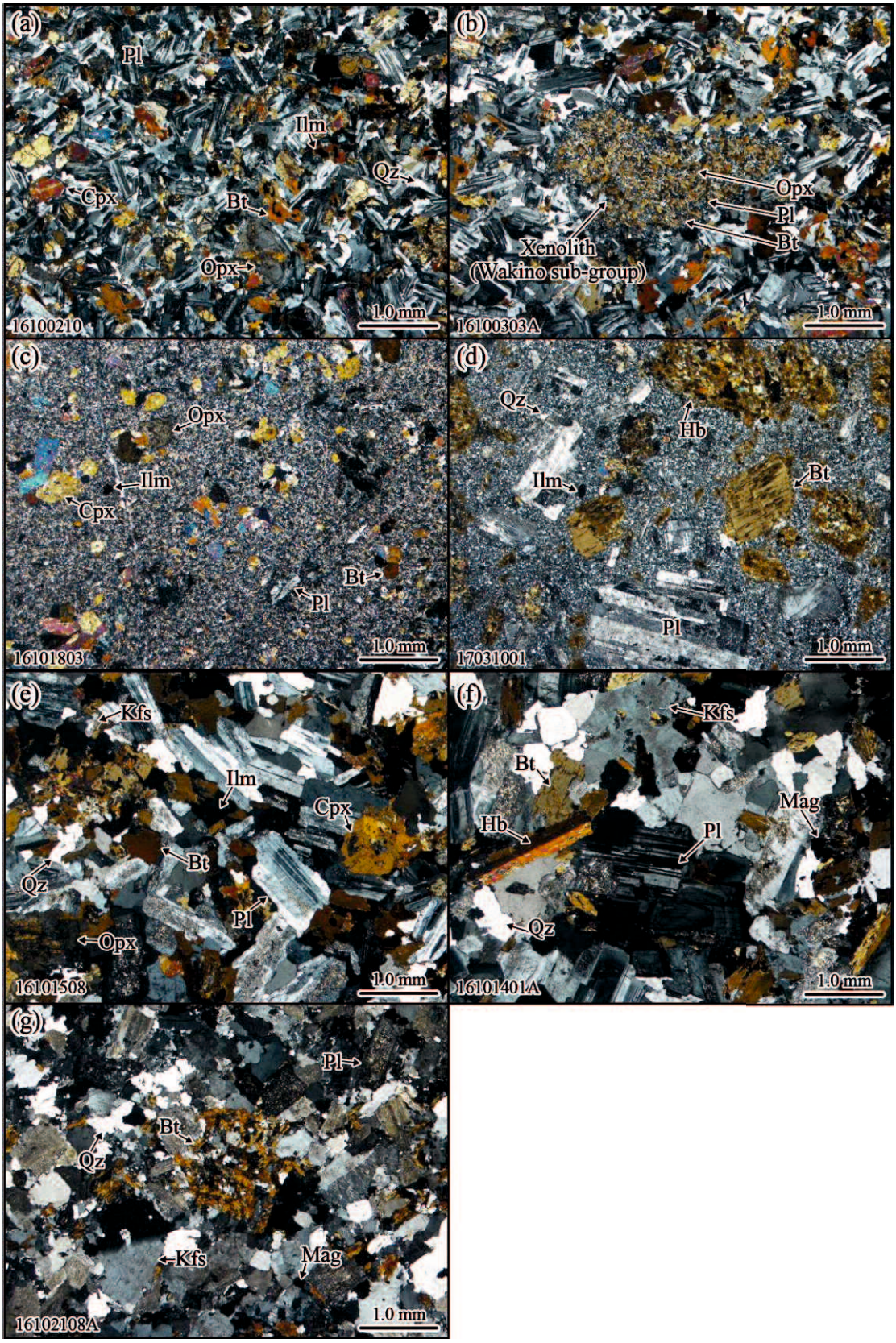

Figure 3–5. Photomicrographs of the intrusive rocks. (a) TPD. (b) Microxenolith of shale probably derived from the Wakino sub-group in the TPD. (c) Do. (d) PFT. (e) CG. (f) HBG.

(g) FBG. Qz: quartz, Kfs: K-feldspar, Pl: plagioclase, Bt: biotite, Hb: hornblende, Cpx: clinopyroxene, Opx: orthopyroxene, Ilm: ilmenite, and Mag: magnetite. Abbreviations are shown in the text.

3–4 Geochemistry

The analytical instruments, methods and procedures used in this chapter were the same as those described in chapter 2 (section 2–4).

The clinopyroxene compositions of the TPD and the Do listed in Appendix 3–1. The results of major and trace element analyses and Sr and Nd isotopic analyses are listed in Appendix 3–2 and Table 3–1.

Table 3–1. Result of Sr–Nd isotope analyses of the Shaku-dake body and cited data.

Type	Rb (ppm)	Sr (ppm)	$^{87}Rb/^{86}Sr$	$^{87}Sr/^{86}Sr$	$SrI^{(103Ma)}$	εSr	Sm (ppm)	Nd (ppm)	$^{147}Sm/^{144}Nd$	$^{143}Nd/^{144}Nd$	$NdI^{(103Ma)}$	εNd	2σ (Sr)	2σ (Nd)
Shaku-dake														
TPD	87	362	0.6952	0.705360	0.704343	-0.51	4.3	21.0	0.1238	0.512656	0.512572	1.30	1	12
TPD	121	362	0.9669	0.705936	0.704521	2.02	4.8	25.5	0.1138	0.512680	0.512603	1.90	1	14
TPD	91	362	0.7272	0.705532	0.704468	1.26	3.9	20.0	0.1179	0.512676	0.512596	1.77	1	13
TPD	189	286	1.9119	0.707415	0.704616	3.37	5.4	27.7	0.1179	0.512646	0.512566	1.19	1	14
TPD	88	369	0.6898	0.705614	0.704604	3.20	4.2	20.8	0.1221	0.512690	0.512608	1.99	1	14
TPD	89	377	0.6829	0.705460	0.704460	1.16	5.0	23.3	0.1297	0.512738	0.512651	2.83	1	12
TPD	79	346	0.6605	0.705693	0.704726	4.93	4.4	20.7	0.1285	0.512680	0.512593	1.71	1	13
Do	50	253	0.5717	0.705642	0.704805	6.05	2.2	8.5	0.1565	0.512726	0.512620	2.24	1	12
Do	61	562	0.3139	0.704893	0.704434	0.78	3.1	11.7	0.1602	0.512688	0.512580	1.46	1	14
Do	51	454	0.3249	0.705663	0.705188	11.48	5.2	26.2	0.1200	0.512681	0.512600	1.85	1	14
CG	131	377	1.0052	0.706194	0.704722	4.88	5.4	27.0	0.1209	0.512639	0.512557	1.01	1	13
CG	164	319	1.4873	0.706903	0.704726	4.93	4.1	23.6	0.1050	0.512640	0.512569	1.24	1	13
PFT	84	431	0.5638	0.706125	0.705299	13.07	3.8	19.2	0.1197	0.512561	0.512481	-0.49	1	13
PFT	95	511	0.5378	0.706469	0.705682	18.50	3.8	19.1	0.1203	0.512576	0.512495	-0.21	1	13
FBG	141	161	2.5340	0.708462	0.704753	5.32	1.3	8.3	0.0947	0.512607	0.512543	0.73	1	13
HBG	122	326	1.0826	0.706312	0.704728	4.95	3.3	16.8	0.1188	0.512641	0.512561	1.07	1	13
HBG	128	310	1.1945	0.706333	0.704585	2.92	3.0	15.9	0.1141	0.512640	0.512563	1.13	1	13
Waki	16	288	0.1607	0.706021	0.705786	19.97	3.5	15.2	0.1392	0.512656	0.512562	1.11	1	12
Waki	69	480	0.4160	0.710052	0.709443	71.90	4.7	23.9	0.1189	0.512126	0.512046	-8.97	1	14
Nishioka et al., 1991														
Limestone	–	479	–	0.706800	–	–	–	–	–	–	–	–	–	–
Limestone	–	430	–	0.707100	–	–	–	–	–	–	–	–	–	–
Limestone	–	491	–	0.706800	–	–	–	–	–	–	–	–	–	–
Limestone	–	230	–	0.707700	–	–	–	–	–	–	–	–	–	–

Error values are 5 and 4 decimal places for Sr and Nd, respectively.

3–4–1 Mineral chemistry

The mineral compositions of plagioclase, clinopyroxene, and orthopyroxene of the TPD and clinopyroxene of the Do were analyzed. The sampling sites and sample numbers (Sp-1 to Sp-6) of the TPD are shown in Figure 3–2b. The results of the representative analyses are shown in Appendix 3–3, and all data of the TPD are plotted in Figures 3–6, 7, and 8. Plagioclase shows normal zoned with oscillatory features (Fig. 3–6). The anorthite component [$An = 100 \times \{Ca/(Ca + Na)\}$] of the measured samples varied from 30 to 74% in the core and 25 to 52% in the rim (Fig. 3–6). The Sp-1 with 54.5 wt% in the whole-rock SiO_2 content includes the highest anorthitic plagioclase (An_{74}) in the TPD with a wide range of *An* contents, 49 to 74% in the core, and 28 to 47% in the rim (Fig. 3–6). The *An* content of the core and rim do not overlap (Fig. 3–6). The plagioclase in Sp-2 with 55.4 wt% in the whole-rock SiO_2 contents also shows a difference in *An* content between the core and rim (Fig. 3–6). Both TPD samples are located at the wall of the TPD body (Fig. 3–2b). On the other hand, plagioclase grains in Sp-3 to Sp-6 have partially overlaps between core and rim compositions, and these samples are located inside the TPD body (Fig. 3–2b). The highest *An* content of each sample consistently decreases with increasing whole-rock SiO_2 although some grains included in the Sp-5 (whole-rock SiO_2: 58.0 wt%) has slightly high-*An* core (Fig. 3–6).

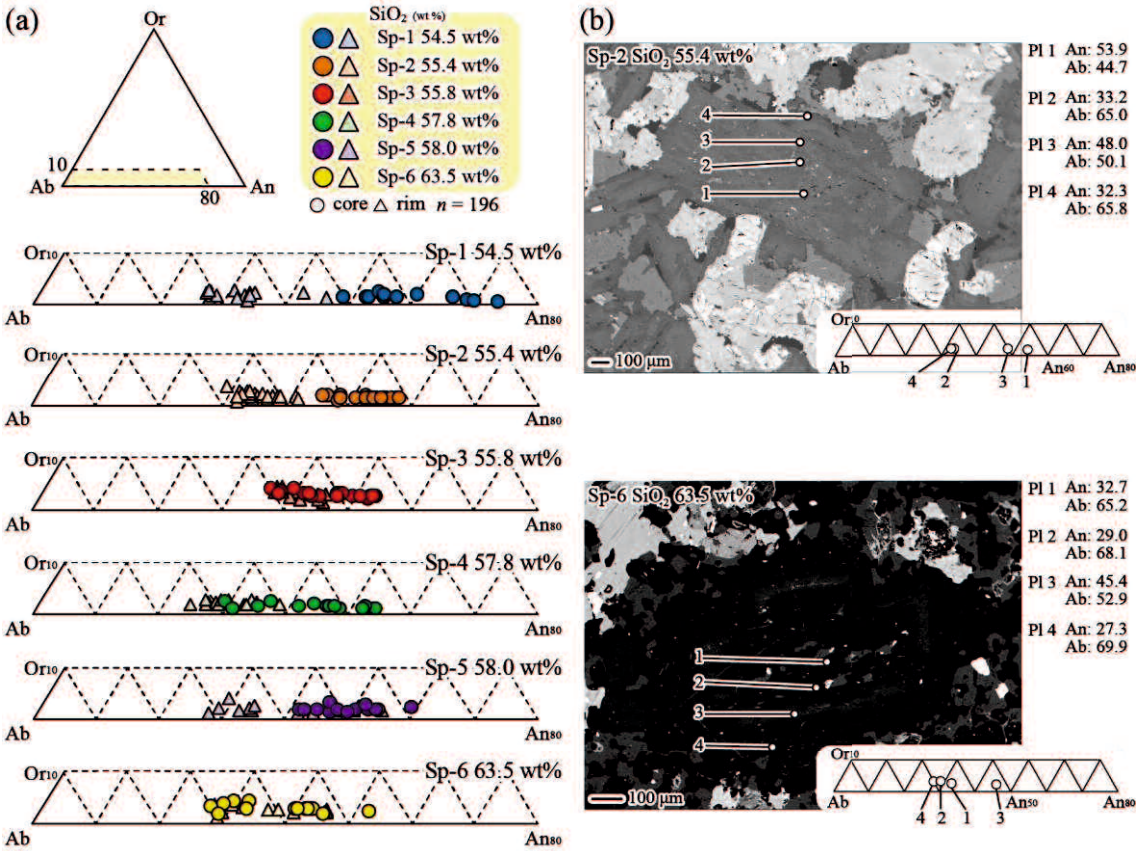

Figure 3–6. Mineral compositions of plagioclase in the TPD. (a) *Or–Ab–An* triangular plot of the TPD. (b) BSE map of the TPD (Sp-2 and Sp-6).

Clinopyroxene generally shows normal zonation, but some grains exhibit reverse one in the marginal areas, then return to normal zonation at the outermost rim (Fig. 3–7a). An exsolution texture with orthopyroxene lamellae appears in the Sp-3 (Fig. 3–7b) located in the central part of the TPD body (Fig. 3–2b). Based on a pyroxene trapezoid proposed by Morimoto et al. (1988) and Deer et al. (2013), clinopyroxene compositions are range from diopside and augite, and clinopyroxene core shows high Mg and Ca values rather than the rim (Fig. 3–7 c). The clinopyroxene rim included in Sp-5 possesses the lowest Ca values (Fig. 3–7c).

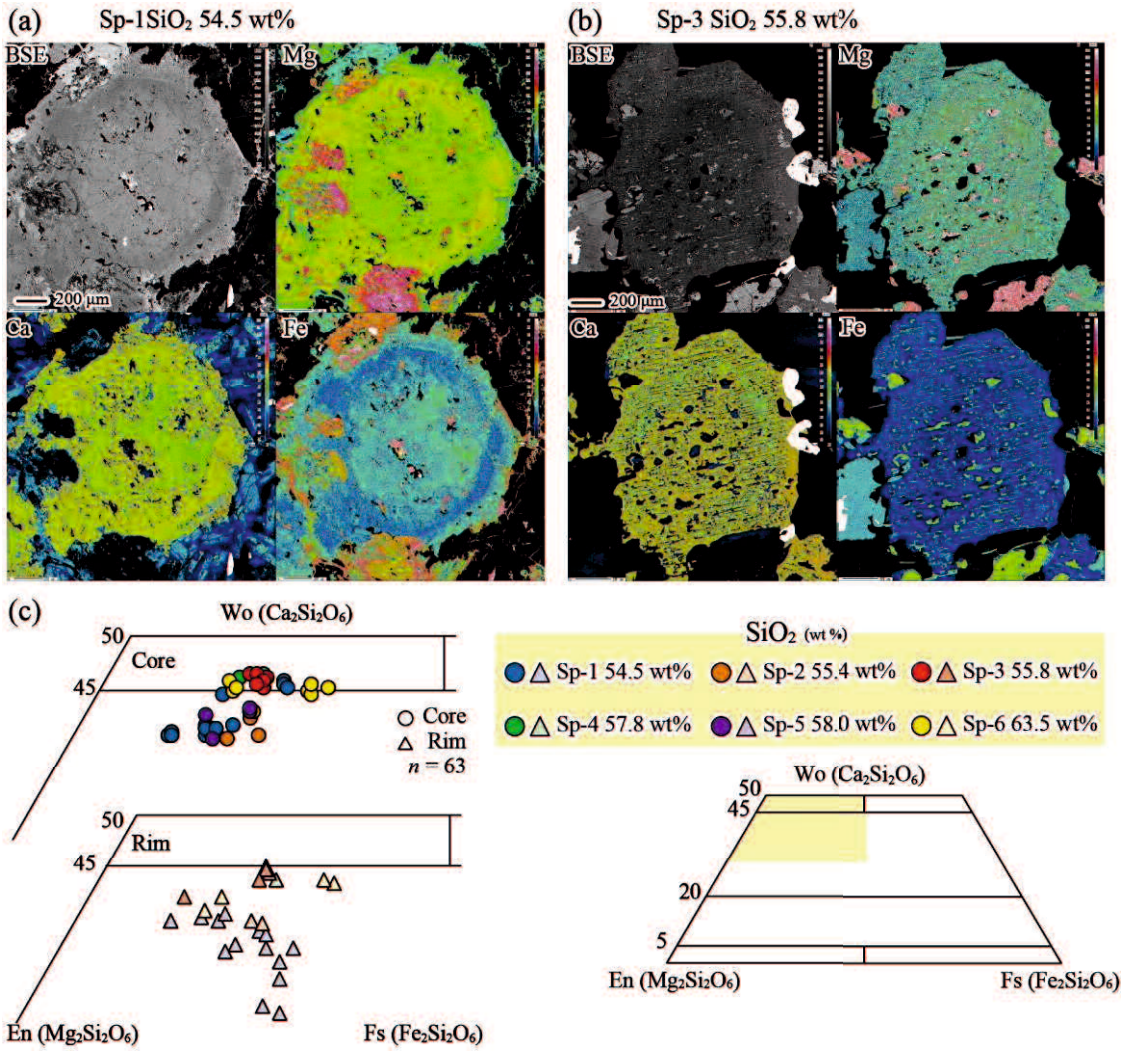

Figure 3–7. Mineral compositions of clinopyroxene in the TPD. (a) and (b) BSE and element mapping (Mg, Ca, and Fe) of the TPD (Sp-1 and Sp-2). (c) Pyroxene trapezoid plot (Morimoto et al., 1988; Deer et al., 2013) of the TPD.

Orthopyroxene essentially shows normal zonation, and *En* [*En* = 100 × Mg/(Mg + Fe + Ca)] content ranges from 55 to 81% (Fig. 3–8). The *En* values tend to decrease with increasing whole-rock SiO_2, except for Sp-5 (Fig. 3–8). The Ca contents of the orthopyroxene lamellae in Sp-3 are slightly higher than those of the orthopyroxene grains (Fig. 3–8).

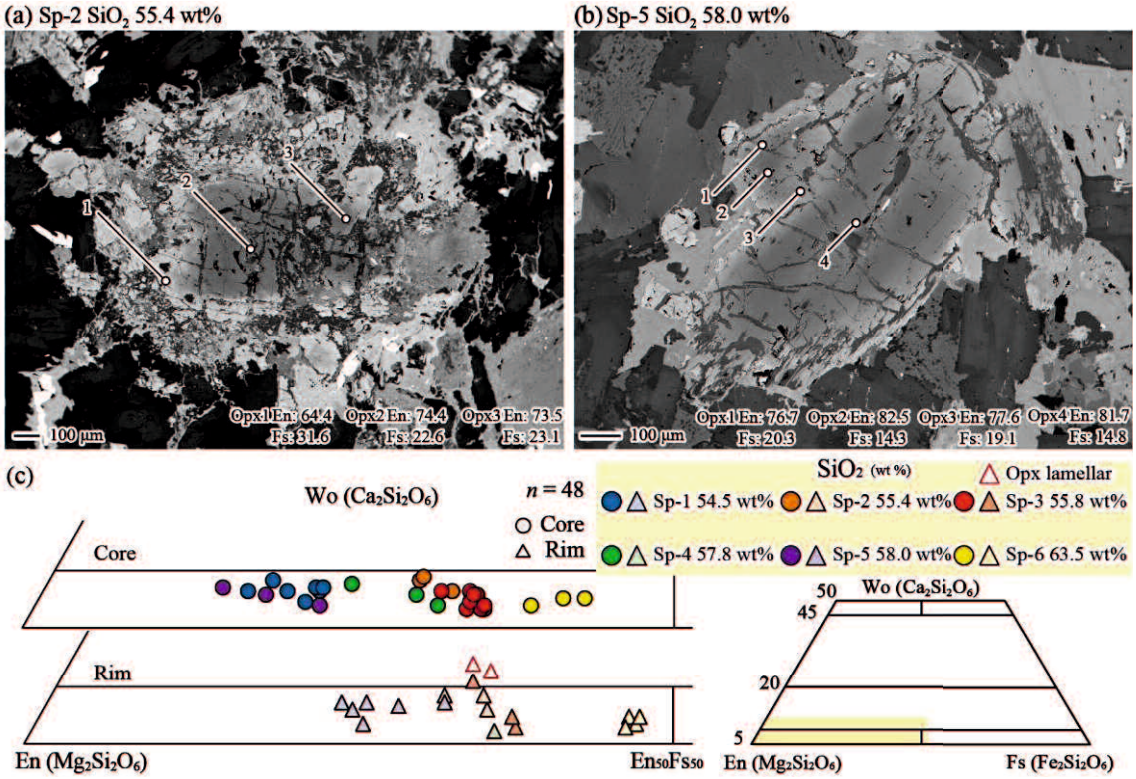

Figure 3–8. Mineral compositions of orthopyroxene in the TPD. (a) and (b) BSE map of the TPD (Sp-2 and Sp-5). (c) Pyroxene trapezoid plot (Morimoto et al., 1988; Deer et al., 2013) of the TPD.

3–4–2 Major and trace elements of whole-rock

The variation diagrams of SiO_2 vs. major and trace elements for the TPD, HBG, CG, FBG, Do, and PFT are shown in Figure 3–9. The chemical compositions of these six intrusive rocks belong to a high-K series (Peccerillo and Taylor, 1976).

The SiO_2 contents of TPD range from 52.0 to 63.5 wt%, and Al_2O_3 and K_2O increase with increasing SiO_2. Some of TPD possess very high MgO contents (~ 7.4 wt%) and low FeO*/MgO ratios (~ 0.98). Cr and Ni decreases with increasing SiO_2, and some samples show very high concentrations of these elements (Cr, ~ 369 ppm; Ni, ~148 ppm). The SiO_2 contents of HBG range from 66.5 to 67.7 wt%, and Al_2O_3, K_2O, and Y increase with increasing SiO_2. MgO, Cr, and Ni decrease with increasing SiO_2. The SiO_2 contents of CG range from 60.5 to 65.2 wt%, and Al_2O_3, MgO, Cr, and Ni decrease with increasing SiO_2. K_2O and Y increase with increasing SiO_2. The SiO_2 contents of FBG range from 72.4 to 74.9 wt%, and the K_2O slightly increases with increasing SiO_2. The SiO_2 contents of Do range from 49.8 to 62.2 wt%, and Al_2O_3, K_2O, and Y increase with increasing SiO_2. MgO, Cr and Ni show very high contents (MgO, ~ 10.8 wt%; Cr, ~825 ppm; Ni, ~191 ppm) and low FeO*/MgO ratios (~ 0.80). Although the SiO_2 contents of Do widely vary, it is described as the Do due to similarity of its occurrence and texture. The SiO_2 contents of PFT range from 61.9 to 63.6 wt%, and Al_2O_3 and K_2O increase with increasing SiO_2. MgO, Cr, Ni, and Y decrease with increasing SiO_2. In the FeO*/MgO–SiO_2 (wt%) diagram, the part of TPD and Do samples are plotted within the field of high-Mg andesite composition (Fig. 3–9h: Kamei et al., 2004). Two trends can be observed in the MgO–Fe_2O_3 (wt%) diagram: The Group-1 and Group-2 trends (Fig. 3–9g).

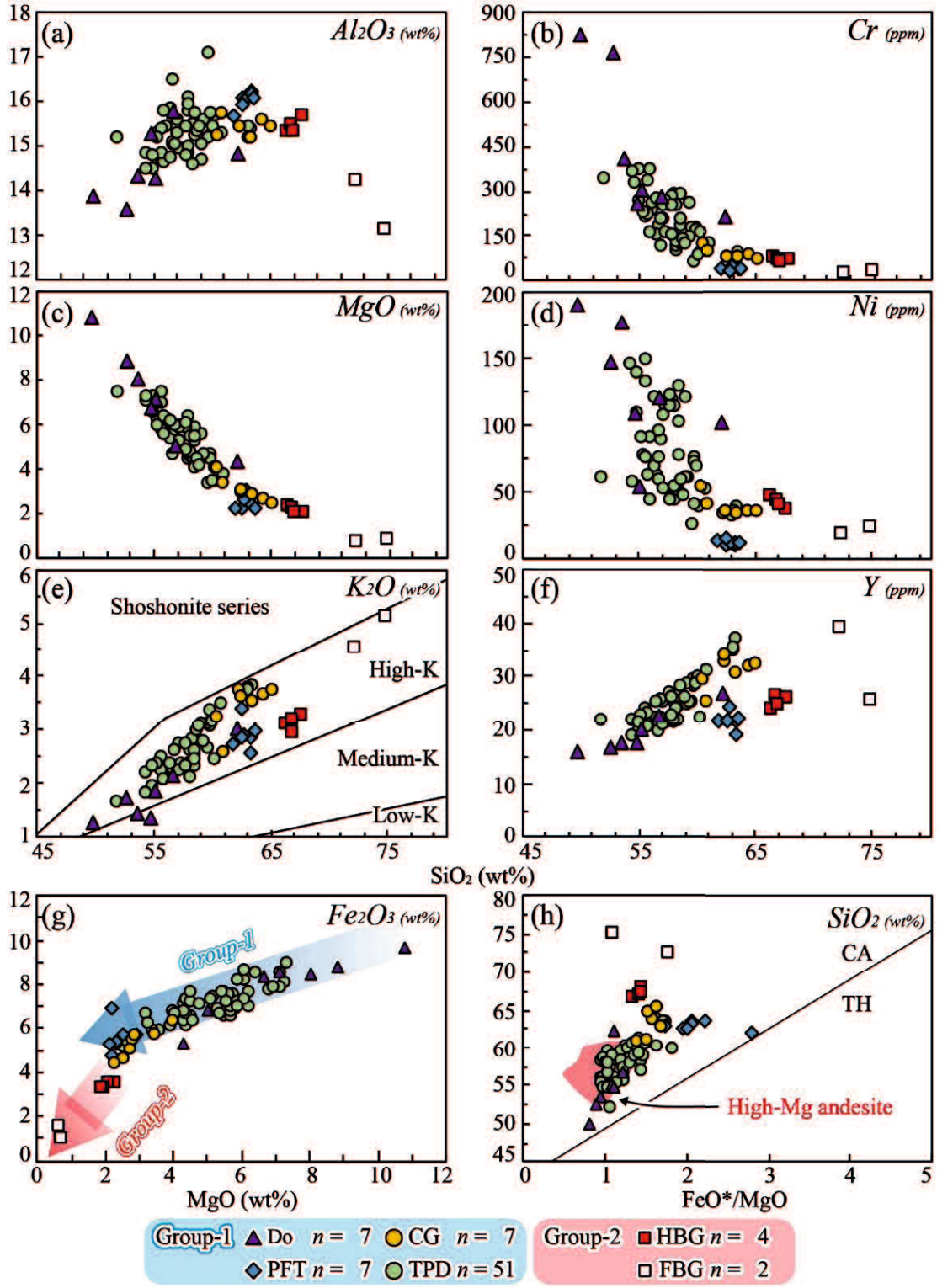

Figure 3–9. (a)–(f) Major and trace element variation diagrams relative to SiO_2 (wt%) for the intrusive rocks from the Mt. Shaku-dake area. Shoshonite, high-K, medium-K, and low-K fields are after Peccerillo and Taylor (1976). (g) MgO–Fe_2O_3 (wt%) diagram. The blue and red arrows show the trends of the Group-1 and the Group-2, respectively. (h)

FeO*/MgO–SiO_2 (wt%) diagram (after Miyashiro, 1974). HMA field is quoted from Kamei et al. (2004).

3–4–3 Sr and Nd isotopes

The initial Sr and Nd isotopic ratios termed as SrI and NdI, respectively. Considering the results of recently published age data from the Kawara-dake suite that involves the HBG (described in chapter 2: Ushikiri-yama granodiorite body), the Sr and Nd isotopic ratios were corrected to 103 Ma because the average hornblende K–Ar age is ~ 103 Ma (105.3 ± 3.2 Ma and 100.9 ± 2.9 Ma: Eshima et al., 2019), furthermore, uraninite Th–U–Pb chemical age from the Kawara-dake suite shows 103.0 ± 1.8 Ma (Yokoyama et al. 2016). Figure 3–10 shows the εSrI–εNdI diagram for the studied samples. The Group-1 (Do, PFT, TPD, and CG) is plotted within the wide area in the epsilon diagram (εSrI = -0.51 –+18.50 and εNdI = -0.49 –+2.83), whereas the Group-2 (HBG and FBG) has the limited values (εSrI = +2.92 –+5.32 and εNdI =+0.73 –+1.13) (Fig. 3–10).

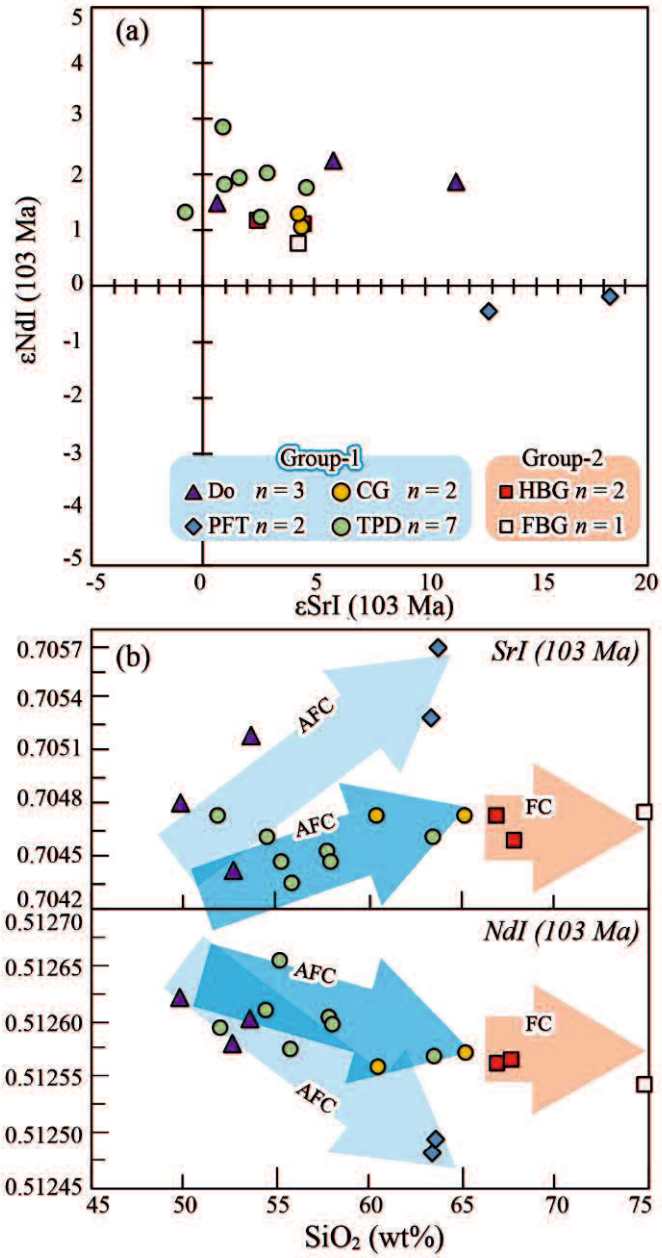

Figure 3–10. Sr and Nd isotopic compositions of the intrusive rocks from the Mt. Shakudake area. (a) εSrI (103 Ma)–εNdI (103 Ma) diagram. (b) SiO_2 (wt%)–SrI (103 Ma) and –NdI (103 Ma) diagram. Arrows indicate the AFC trends and the FC trend, respectively.

3–5 Discussions

3–5–1 Petrogenesis of the Shaku-dake body

The Shaku-dake body is composed of six types of intrusive rocks (TPD, Do, CG, PFT, HBG, and FBG). Most of intrusive rocks such as TPD and HBG, TPD and FBG, CG and FBG, CG and Do show intrusive-intrusive relationship (Figs. 3–3c, 3–4c, e, and f). In addition, the PFT dike forms a composite dike with the Do (Fig. 3–3f). I therefore conclude that the six intrusive rocks from the Shaku-dake body contemporaneously intrude each other.

The Shaku-dake body is divided into two groups, the Group-1 and Group-2, and they show different trends in the variation diagrams including those of SrI and NdI values (Figs. 3–9 and 3–10a). The Group-1 rocks show two trends in the SiO_2 wt% –SrI and –NdI diagrams (Fig. 3–10a), while the Group-2 rocks show monotonous trends in some variation diagrams (Figs. 3–9 and 3–10b).

3–5–1–1 Geochemical characteristics of Do and TPD

The SiO_2 contents of TPD and Do range between 63.5 to 52.0 and 62.2 to 49.8 wt%, respectively. Some samples show relatively primitive compositions; *Mg*# [*Mg*# = 100×Mg/(Mg + Fe)] = 64.5 to 68.9, FeO*/MgO = 0.80 to 0.98, Cr = 288 to 825 ppm, and Ni = 119 to 190 ppm (Fig. 3–9). In the FeO*/MgO–SiO_2 (wt%) diagram (Fig. 3–9h), some TPD samples are plotted in the compositional field of high-Mg andesite (HMA). Moreover, the clinopyroxenes compositions of TPD are similar to those of HMD (Fig. 3–11a: Kamei et al., 2004). In contrast, the SiO_2 contents of Do belong to basalt, and the clinopyroxene compositions of Do show those of the fields in the Sub-alkaline gabbro and Sub-alkaline andesite-basalt (Fig. 3–11a). The SrI and NdI values of TPD and Do are different in the epsilon diagram (Fig. 3–10a); the Do possesses enriched SrI values rather than those of the TPD, but the NdI values of Do (εNdI = +1.46 – +2.24) range within the field of TPD (εNdI = +1.30 – +2.83). This suggests that the TPD is hardly produced via fractionation and assimilation of crustal

materials with basaltic magma as opposed to the Do. Considering the mineral and whole-rock geochemistry including Sr and Nd isotopic compositions, it can be concluded that the TPD was originally derived from a HMA magma, whereas the parent magma of Do was basaltic.

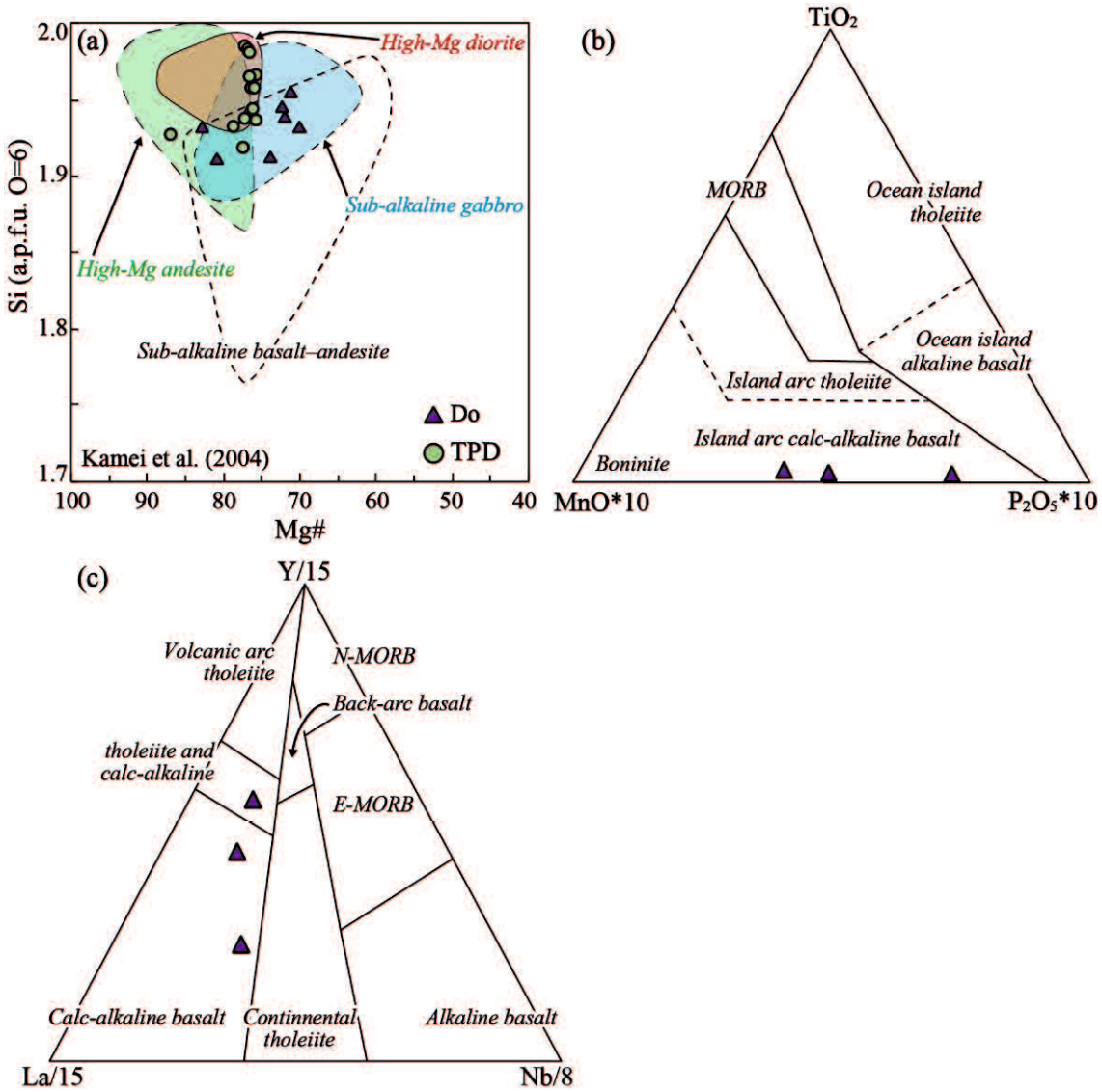

Figure 3–11. (a) Mg#–Si (a.p.f.u. O=6) diagram for clinopyroxenes of the TPD and Do. Compositional fields are defined by Kamei et al. (2004). (b) TiO_2–MnO*10–P_2O_5*10 triangle diagram for the Do (after Mullen, 1983). (c) Y/15–La/10–Nb/8 triangle diagram for the Do (after Cabanis and Leocolle, 1989). Mg# is 100 × Mg/(Mg + total Fe).

The HMA magma is geochemically divided into several types (Kay, 1978; Shiraki et al., 1980; Jenner, 1981; Tatsumi and Ishizaka, 1982a; Tatsumi and Ishizaka, 1982b; Rogers et al., 1985; Saunders et al., 1987; Crawford et al., 1989; Stern and Hanson, 1991; Yogodzinski et al., 1995; Shimoda et al., 1998). Kamei et al. (2004) classified each HMA magma depending on various elements (Fig. 3–12). Figure 3–12 indicate that the TPD shows geochemical signatures similar to those of the Sanukitic HMA but do not resemble the Bajaitic and Boninitic HMA. In addition, the previously reported Cretaceous and Neogene HMA rocks from Southwest Japan are also classified into the Sanukitic HMA (Fig. 3–12; e.g., Murakami, 1994; Kamei et al., 2004; Eshima et al., 2019). On the other hand, the Do is plotted within the composition range of island arc calc-alkaline basalts and tholeiite in some discrimination diagrams (Figs. 3–11b and c). These results suggest that the magma activities of TPD and Do in the Shaku-dake body have similar characteristics to those of the sanukitoid and basalt from the Setouchi volcanic rocks during the Miocene in the Setouchi region, Japan (Tatsumi, 1982).

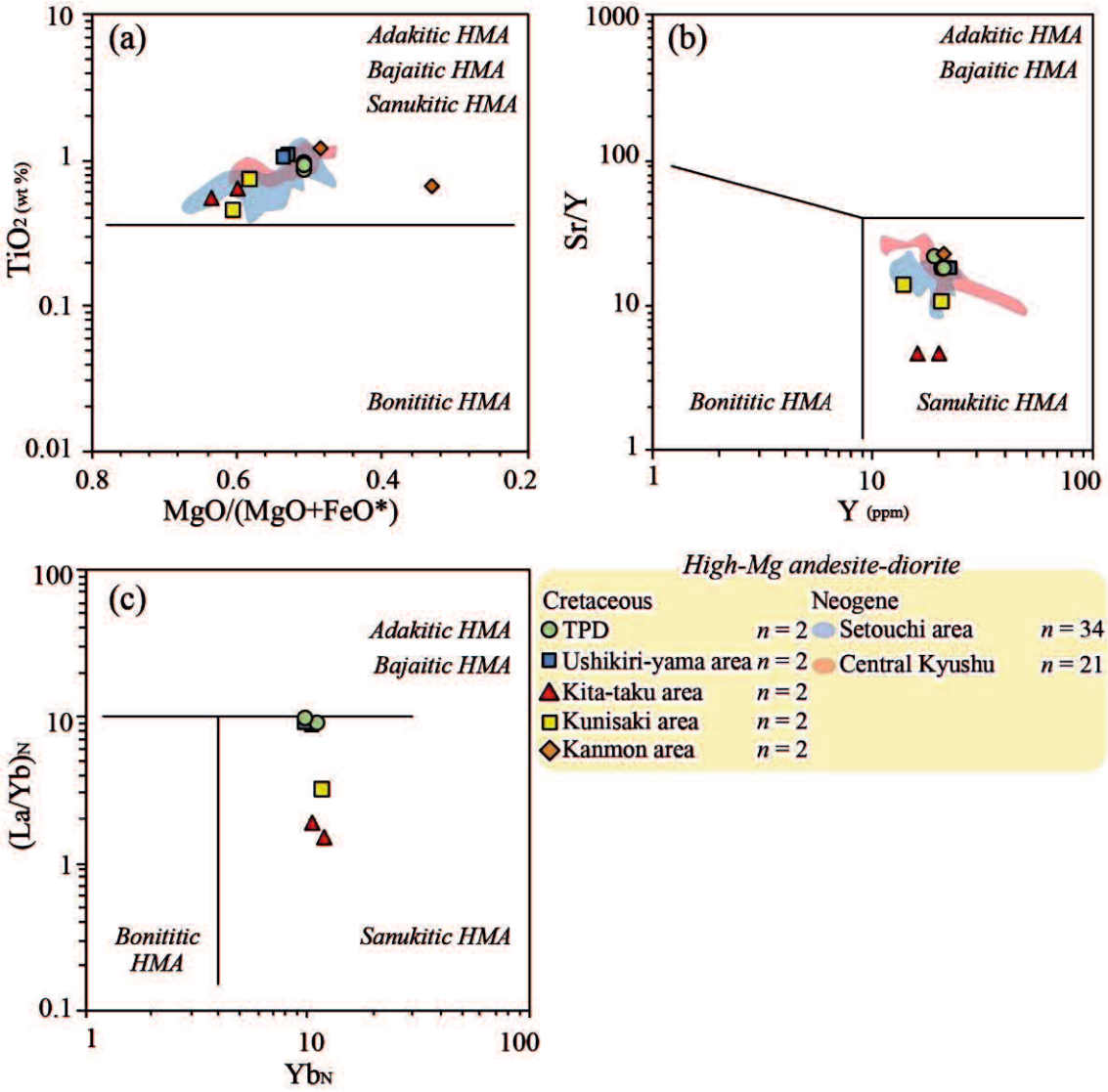

Figure 3–12. Discrimination diagrams for the TPD. Cretaceous high-Mg diorites from central and northern Kyushu, and Neogene high-Mg andesites from the central Kyushu and the Setouchi area are shown in these figures (modified after Kamei et al. (2004)). (a) MgO/(MgO + FeO*)–TiO_2 (wt%) diagram. (b) Y (ppm)–Sr/Y diagram. (c) Yb_N–$(La/Yb)_N$ diagram. The data for comparison were obtained from the following sources; andesite from the Kanmon Group, Yamaguchi (Imaoka and Murakami, 1979; Imaoka et al., 1993), diorite from northern Kyushu (Murakami, 1994; Kamei et al., 2004; Eshima et al., 2019). The Neogene HMA rocks in Kyushu also geochemically possess the Sanukitic HMA (Shiraki et al., 1991; Nagao et al., 1992; Kakubuchi et al., 1995; Shiraki et al., 1995).

3–5–1–2 Petrogenetic relationships among the intrusive rocks of the Shaku-dake body

3–5–1–2–1 Group-1 (Do, TPD, CG, and PFT)

The Group-1 is influenced by assimilation and fractional crystallization because of its field occurrence involving xenoliths and regularly changing Sr–Nd isotopic compositions with SiO_2 contents (Figs. 3–3a, b, d, e, 3–4g, d, and 3–10). Furthermore, the SiO_2 (wt%)–SrI (103 Ma) and –NdI (103 Ma) diagrams show that the TPD–CG and the Do–PFT form different trends, hereafter referred to as the TPD–CG subgroup and the Do–PFT subgroup (Fig. 3–10b). These results suggest that the TPD–CG and the Do–PFT subgroups probably experienced different magma processes.

To verify the above hypothesis, I firstly examined the fractionation effects for each subgroup. Figure 3–13 shows the Rb–Y(ppm) and Cr–Ni (ppm) diagrams, and samples that deviate from the main trend in Figure 3–13d show cumulate texture. In addition, the SiO_2 (wt%)–modal composition for each mineral in the TPD and the CG is shown in Figure 3–14. According to Figures 3–13 and 3–14, the candidates of fractional minerals for the TPD–CG and Do–PFT subgroups would be pyroxenes and plagioclase. I performed mass balance calculation to verify the fractional minerals using the mineral compositions of the candidate minerals (Opx, Cpx, Pl, and Ilm). Then, based on the results of mass balance calculation results, the trace element compositions (Rb, Ba, Th, Ta, Nb, La, Ce, Sr, Nd, Sm, Eu, Dy, Y, Yb, and Lu) were estimated using the Rayleigh fractionation model. The partition coefficients are listed in Appendix 3–4. The calculated compositions are shown in the spider diagram (Fig. 3–15) normalized to the primitive mantle (Sun and McDonough, 1989). These results suggest that simple Rayleigh fractionation model without assimilation process cannot reproduce trace element compositions of the PFT and CG (Fig. 3–15).

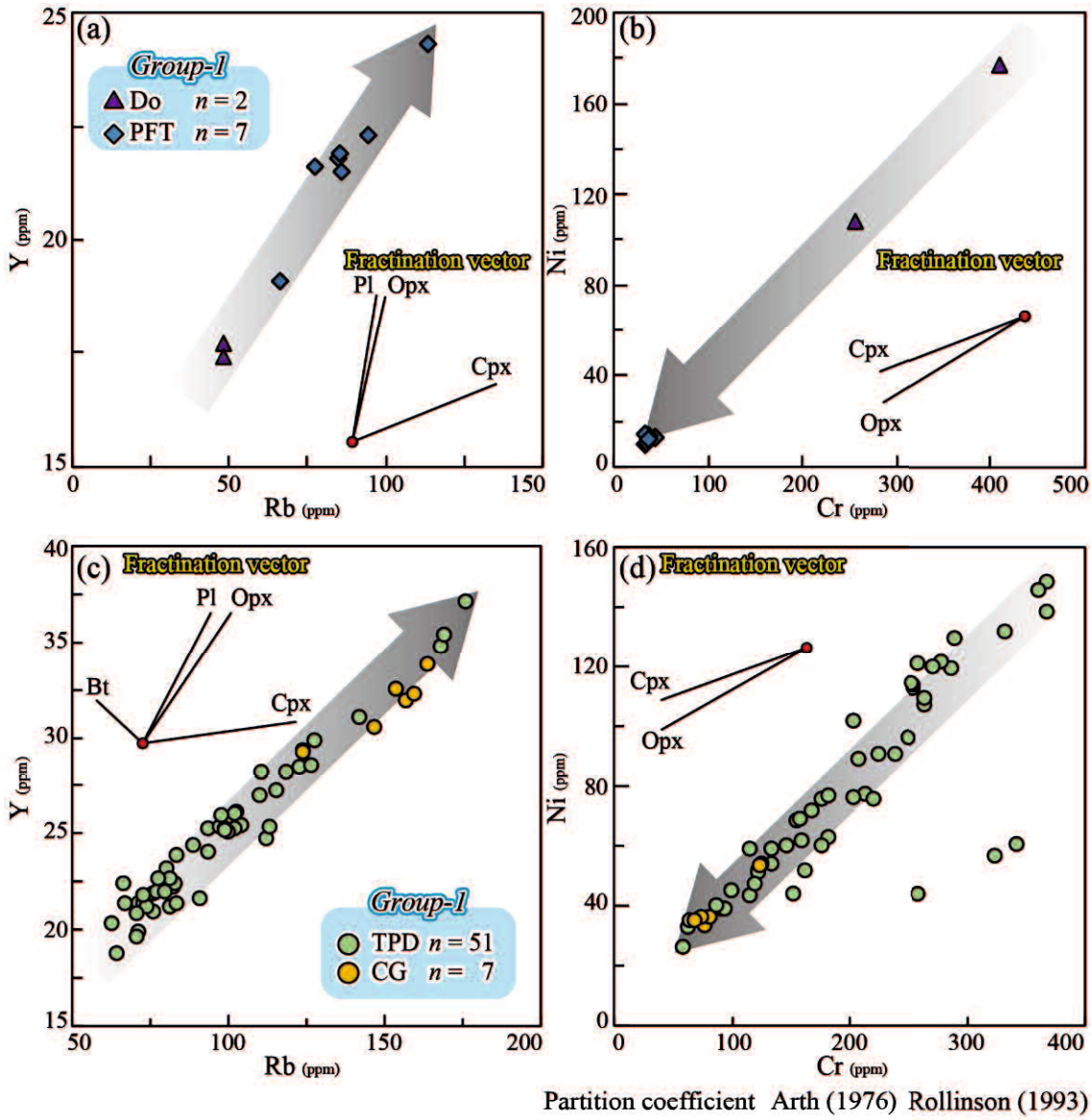

Figure 3–13. Rb–Y (ppm) and Cr–Ni (ppm) diagrams of the Group-1 (Do to PFT and TPD to CG). Fractionated vectors were calculated by the Rayleigh fractionation model using partition coefficient after Arth (1976) and Rollinson (1993). The Rayleigh fractionation model using partition coefficients are listed in Appendix 3–4.

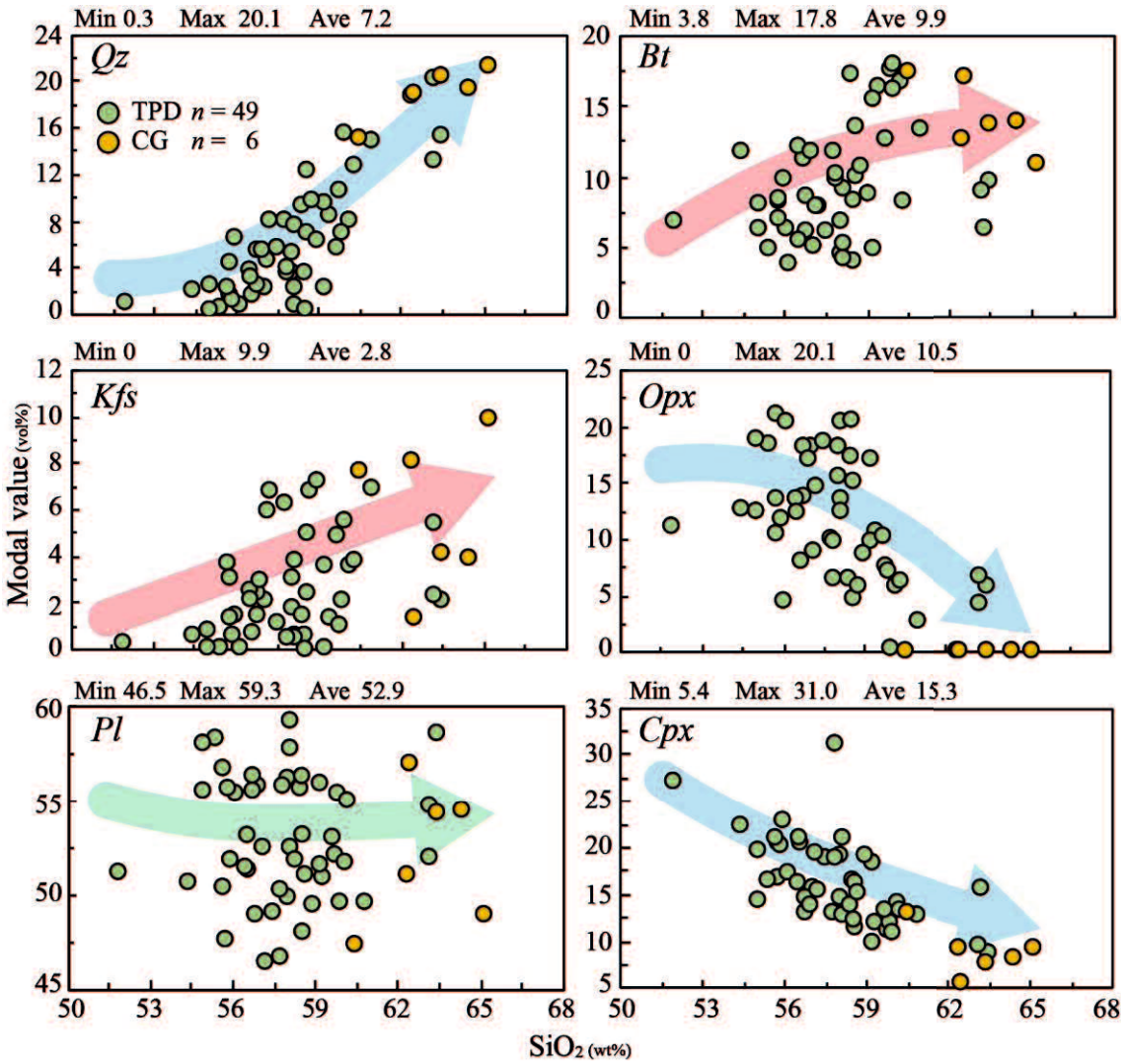

Figure 3–14. Whole-rock SiO_2 (wt%)–modal value (vol%) for the TPD and CG. The modal values are listed in Appendix 3–5. Modal analysis was performed using the Excel spreadsheet (VBA) developed by Shimura and Kojima (2015).

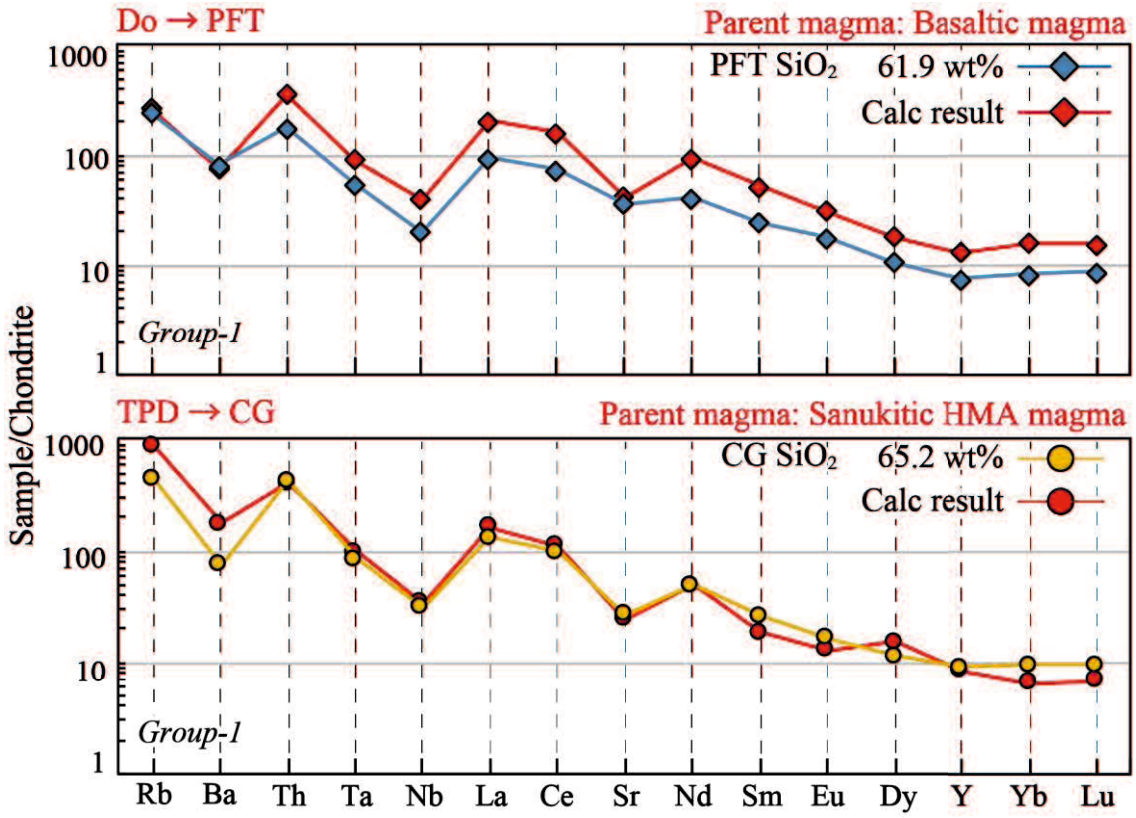

Figure 3–15. Results of fractional crystallization modeling for the Group-1 (Do to PFT and TPD to CG) are shown in the spider diagrams. Normalized values of C1 chondrite are after Sun and McDonough (1989). The Rayleigh fractionation model using partition coefficients are listed in Appendix 3–4.

In order to evaluate the importance of AFC processes with the Wakino sub-group (sandstone/shale) and limestone for the evolution of the Shaku-dake body, I performed AFC calculations utilizing the equation (15b) in DePaolo (1981). For these calculations, the initial TPD and Do magmas were assumed to have SrI (103 Ma) and NdI (103 Ma) ratios of 0.7043 and 0.51265, 0.7044 and 0.51262, respectively, and Sr = 390 ppm, Nd = 19 ppm, and Sr = 562 ppm, Nd = 8.5 ppm, based on data for the least differentiated samples. The Wakino sub-group as assimilated material was assumed to have SrI (103 Ma) and NdI (103 Ma) values of 0.7094 and 0.51205, respectively, and Sr = 480 ppm, Nd = 24 ppm. The limestone as another assimilated material was estimated to have SrI values of 0.7077 and Sr = 479 ppm, respectively,

that has the highest Sr values from the quoted data of Nishioka et al. (1991) to make the assimilation effect easily distinguishable. I addressed the assimilation process using Sr–Nd isotopic compositions for both subgroups. As previously mentioned, the rocks from each subgroup include different types of xenoliths. The TPD–CG and Do–PFT subgroups mainly involve the Wakino sub-group (sandstone/shale) and limestone as xenoliths (Figs. 3–3a, b, d, e, 3–4a, and d), respectively. Therefore, I examined assimilation and fractional crystallization (AFC) modeling using different contaminants. The AFC processes can duplicate the chemical variations for the TPD–CG and the Do–PFT subgroups (Fig. 3–16). According to the results of AFC calculation, the geochemical variations of the Group-1 are attributed by the differences of 'r' value that is assimilation/fractionation rate from 0.01 to 0.5 (Fig. 3–16).

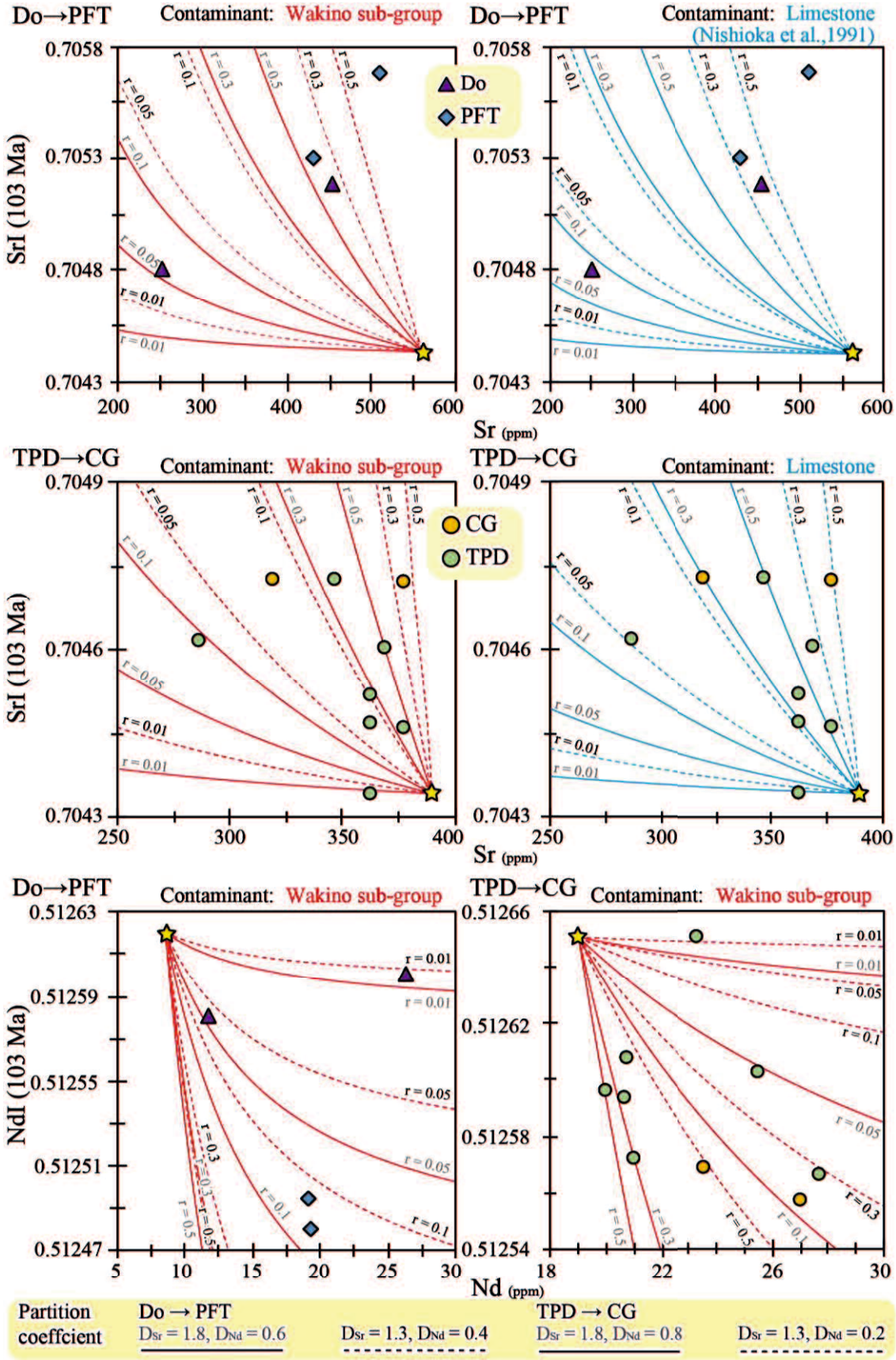

Figure 3–16. Sr (ppm)–SrI (103 Ma) and Nd (ppm)–NdI (103 Ma) diagrams showing

assimilation and fractional crystallization (AFC) with the Wakino sub-group and the limestone as contaminants. The AFC model adapts the equations of DePaolo (1981). 'r' stands for the values of assimilation/crystallization rates.

3–5–1–2–2 Group-2 (HBG and FBG)

The Group-2 (HBG and FBG) shows a clear trend that is different from that of the Group-1 in the MgO–Fe_2O_3 (wt%) diagram (Fig. 3–9). The HBG and FBG are plotted within the same compositional range in the εSrI–εNdI diagram (Fig. 3–10a). In addition, the SiO_2 (wt%)–SrI and –NdI diagrams show fractional crystallization trends where the SrI (103 Ma) and NdI (103 Ma) values do not change with increasing SiO_2 contents (Fig. 3–10b). These data suggest that the FBG is formed by fractional crystallization from the HBG magma. The fractionated minerals are estimated by the Rb–Y (ppm) and Sr–Y (ppm) diagrams (Fig. 3–17a), and the proportion of fractionated minerals are obtained by the mass balance calculation using major elements (Table 3–2). The fractional crystallization model is adopted for the equation of Rayleigh fractionation model, and the results are shown in the spider diagram (Fig. 3–17b). In conclusion, the chemical variations in the Group-2 can be explained by fractional crystallization with the fractionated minerals of plagioclase, hornblende, and magnetite (Fig. 3–17).

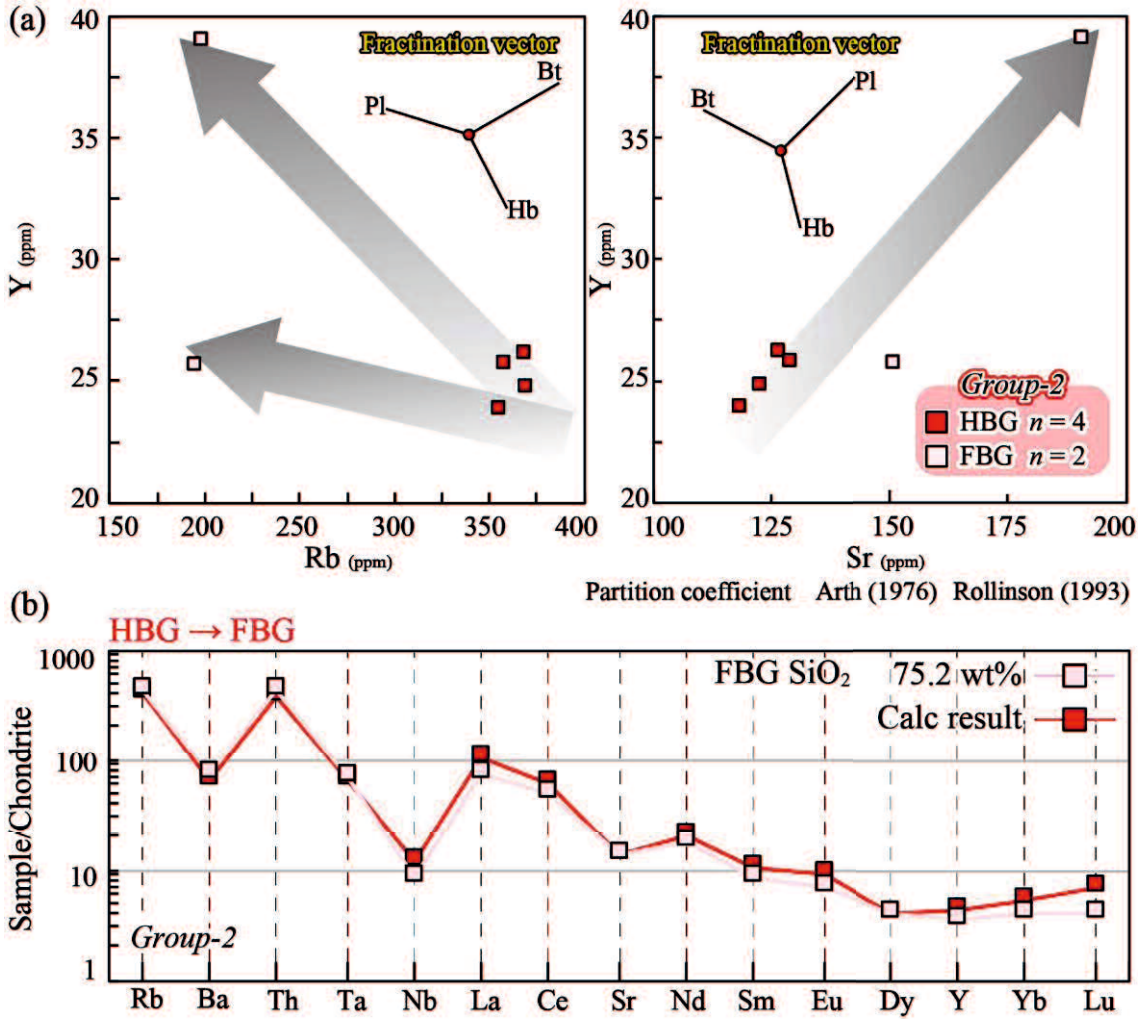

Figure 3–17. (a) Rb–Y (ppm) and Sr–Y (ppm) diagrams of the Group-2 (HBG and FBG). Fractionated vectors were calculated by the Rayleigh fractionation model using partition coefficient after Arth (1976) and Rollinson (1993). (b) Results of fractional crystallization modeling for the Group-2 (HBG to FBG) are shown in the spider diagrams. Normalized values of C1 chondrite are after Sun and McDonough (1989). The Rayleigh fractionation model using partition coefficients are listed in Appendix 3–4. Detailed explanations are described in the text.

Table 3–2. Results of mass balance calculation using the major elements for whole-rocks and minerals of the TPD–CG, Do–PFT and HBG–FBG.

TPD–CG	Initial magma	Final magma	Subtracted phases			
			Plagioclase	Clinopyroxene	Orthopyroxene	Ilmenite
Sample No.	16102103	16110611	16102103	16102103	16102103	16102103
SiO_2 (wt%)	63.5	65.18	58.66	51.64	50.73	0.04
TiO_2	0.83	0.64	0.03	0.31	0.17	49.80
Al_2O_3	15.41	15.42	25.60	1.70	0.84	0.02
FeO*	5.2	4.3	0.18	8.82	26.22	46.28
MnO	0.08	0.08	0.01	0.26	0.75	1.66
MgO	2.81	2.36	0.01	14.19	18.43	0.08
CaO	4.52	3.84	7.49	20.97	0.99	0.30
NaO	3.15	3.52	7.21	0.36	0.02	0.01
K_2O	3.81	3.73	0.39	0.01	0.00	0.03
P_2O_5	0.27	0.21	0.00	0.00	0.00	0.00
Calculated result (%)		88.01	6.07	2.71	2.25	0.97
Degree of crystallization, 11.99%						
Fractionated proportions (%)			50.60	22.57	18.73	8.10
Sum of squares, 0.113						

Do–PFT	Initial magma	Final magma	Subtracted phases			
			Plagioclase	Clinopyroxene	Orthopyroxene	Ilmenite
Sample No.	17031006	17031009	17031006	17031006	17031006	17031006
SiO_2 (wt%)	53.66	61.87	51.92	51.60	53.68	0.00
TiO_2	1.03	0.63	0.08	0.46	0.27	51.90
Al_2O_3	14.34	15.69	29.23	2.50	1.76	0.02
FeO*	8.42	6.92	0.61	7.21	13.27	42.60
MnO	0.13	0.12	0.04	0.20	0.29	3.60
MgO	8.03	2.23	0.13	16.28	27.71	0.13
CaO	7.78	5.67	12.62	19.67	1.58	0.28
NaO	2.85	3.11	4.14	0.31	0.02	0.00
K_2O	1.41	2.73	0.23	0.01	0.00	0.00
P_2O_5	0.38	0.17	0.03	0.00	0.00	0.02
Calculated result (%)		62.23	21.70	11.30	3.44	0.36
Degree of crystallization, 37.77%						
Fractionated proportions (%)			57.44	22.92	9.12	3.52
Sum of squares, 0.297						

HBG–FBG	Initial magma	Final magma	Subtracted phases		
			Plagioclase	Hornblende	Magnetite
Sample No.	16101403	16102108A	16101403	16101403	16101403
SiO_2 (wt%)	66.88	72.36	59.97	48.50	0.02
TiO_2	0.48	0.25	0.02	0.92	0.05
Al_2O_3	15.51	14.23	24.60	4.87	0.04
FeO*	3.44	1.43	0.18	13.66	89.63
MnO	0.07	0.03	0.01	0.49	0.07
MgO	2.14	0.72	0.00	14.21	0.00
CaO	3.55	1.05	6.31	10.52	0.00
NaO	3.88	4.08	7.72	1.13	0.01
K_2O	2.94	4.52	0.27	0.42	0.00
P_2O_5	0.14	0.09	0.01	0.01	0.01
Calculated result (%)		65.92	21.57	11.79	0.72
Degree of crystallization, 13.62%					
Fractionated proportions (%)			63.28	34.59	2.12
Sum of squares, 0.570					

Abbreviation are shown in the text.

3–5–1–3 Petrological evolution model of the Shaku-dake body

In this section, I discuss the magmatic process of the Shaku-dake body utilizing the observations, modeling, and interpretations. The important considerations are listed as follows. (1) The intrusive rocks from the Shaku-dake body can be classified into two groups, the Group-1 (Do, TPD, CG, and PFT) and the Group-2 (HBG and FBG). The Group-1 is further subdivided into the TPD–CG and Do–PFT subgroups. Parental magmas for the TPD–CG and Do–PFT subgroups are interpreted as the Sanukitic HMA and the Island arc calc-alkaline basalt, respectively (Fig. 3–11). (2) The Group-1 is influenced by the assimilation and fractional crystallization during the ascent and emplacement of magma, whereas the Group-2 changes its whole-rock composition through fractional crystallization (Figs. 3–16 and 3–17).

The petrological evolution model of the Shaku-dake body is shown in Figure 3–18. These parental magmas are assimilated by the sandstone/shale and limestone during upward movement of the crust to form the Group-1 rocks. On the other hand, the Group-2 magma is only affected by fractional crystallization during cooling without assimilation. The Cretaceous magma activities in the northern Kyushu were led by the highly thermal structure of the wedge mantle at that time. It is consistent with the ideas proposed by Iwamori (2000), Imaoka et al. (2014a), Iida et al. (2015), and Kim et al. (2016), of which the highly thermal structure of the wedge mantle was the major heat source of the voluminous igneous activities during the Cretaceous in southwest Japan and the Korean Peninsula. In this case, partial melting may take place in the lower crust, giving rise to granitic melt. I will discuss such scenario in chapter 6.

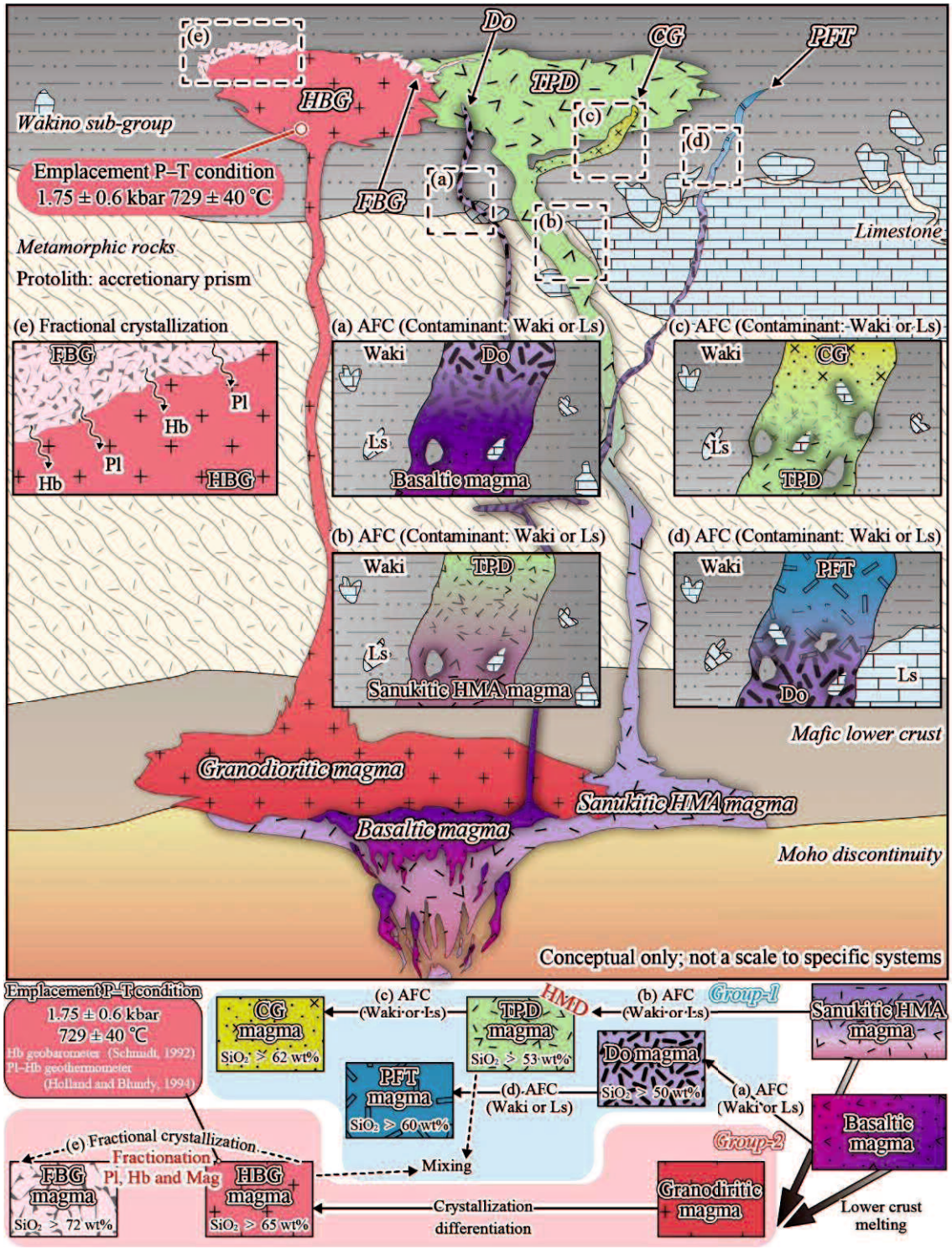

Figure 3–18. The petrological evolution model of the Shaku-dake plutonic body. Various magmatic processes such as AFC and FC are also shown. Waki: wakino sub-group, and Ls: limestone.

3–5–2 Vertical and horizontal variations in Shaku-dake body (TPD body)

According to the relationships between SiO_2 (wt%) and TPD modal composition shown in the section 3–5–1–2–1 (Fig. 3–14), the modal compositions of orthopyroxene and clinopyroxene decreased with increasing SiO_2 content, but those of quartz, K-feldspar, and biotite tended to increase with increasing SiO_2 content. The plagioclase modal composition was dispersed regardless of the SiO_2 contents.

The TPD crops out on the western slope of Mt. Shaku-dake at 200–550 m above sea level (Fig. 3–2). Figure 3–19 shows the vertical variations of modal compositions for each mineral and selected major and trace element compositions according to the altitudes of the sampling sites. The modal compositions of quartz, K-feldspar, and biotite tend to be low at an altitude of 450–550 m, whereas it varies widely at an altitude of 200–400 m. Furthermore, some samples had the highest modal values of these minerals at an altitude of 350 m (Fig. 3–19). Although the modal compositions of clinopyroxene and orthopyroxene vary widely below the altitude of 370 m, the lowest values of modal compositions are present at an altitude of 300–450 m (Fig. 3–19). Moreover, the modal compositions of plagioclase are sporadically varied regardless of altitude. The vertical variation in the whole-rock SiO_2, Fe_2O_3, MgO, Cr, and Ni content vary widely below an altitude of 400 m (Fig. 3–19). The compositional patterns of MgO, Cr, and Ni with altitude roughly resemble those of the modal variations of clinopyroxene and orthopyroxene.

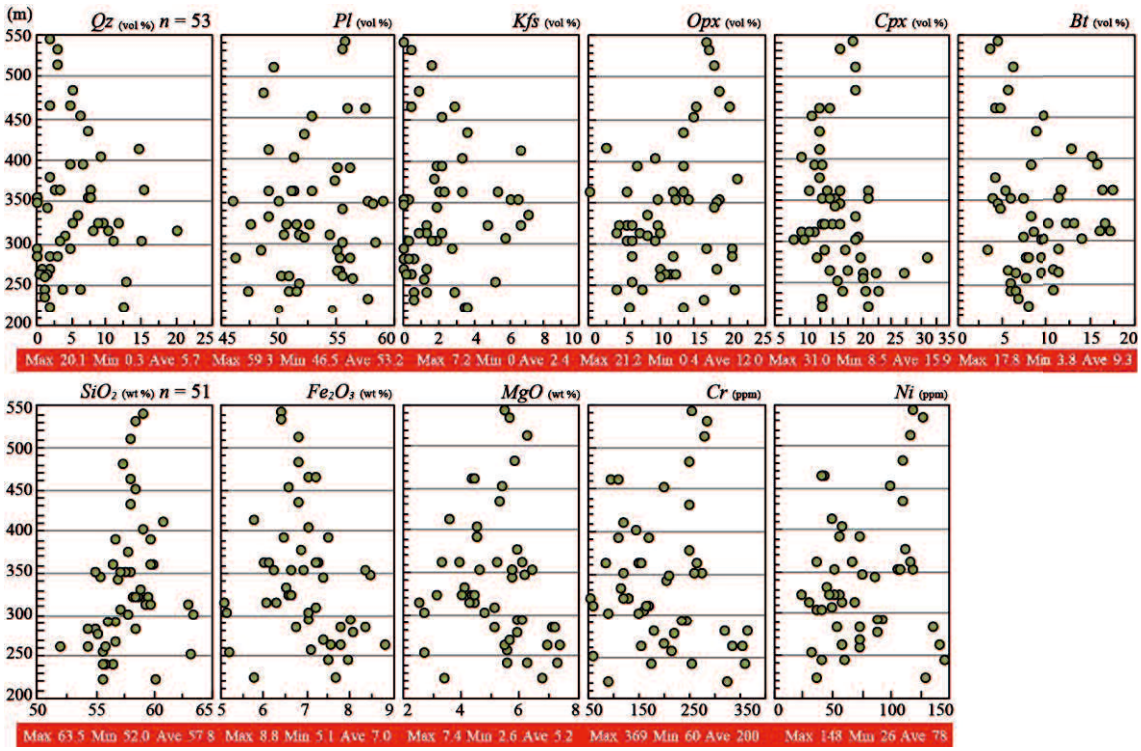

Figure 3–19. Modal compositions (Qz, Pl, Kfs, Opx, Cpx, Opx, and Bt) and whole-rock compositions (SiO_2, Fe_2O_3, MgO, Cr, and Ni) versus altitude of sampling sites for the TPD.

Horizontal variation in the TPD was examined via the modal composition of quartz, plagioclase, clinopyroxene, and orthopyroxene, and the whole-rock compositions of SiO_2, Fe_2O_3, MgO, Cr, and Ni (Fig. 3–20). These horizontal variation maps were created using Graph-R (S-NEXT Co., Ltd.) by calculating the longitude, latitude, modal, and whole-rock composition data of each sample. The modal compositions of quartz and SiO_2 content showed higher values from the central part to the southern part of the TPD body, which corresponds to an altitude of 300–450 m (Fig. 3–20). On the other hand, the higher modal compositions of plagioclase were mainly concentrated in the northern part of the TPD body, but some are found in the southernmost area. The modal compositions of clinopyroxene and orthopyroxene seem to be higher at the marginal parts of the TPD body (Fig. 3–20). In addition, Fe_2O_3, MgO, Cr, and Ni contents tended to concentrate at the marginal part of the body, similar to the modal values of pyroxenes (Fig. 3–20).

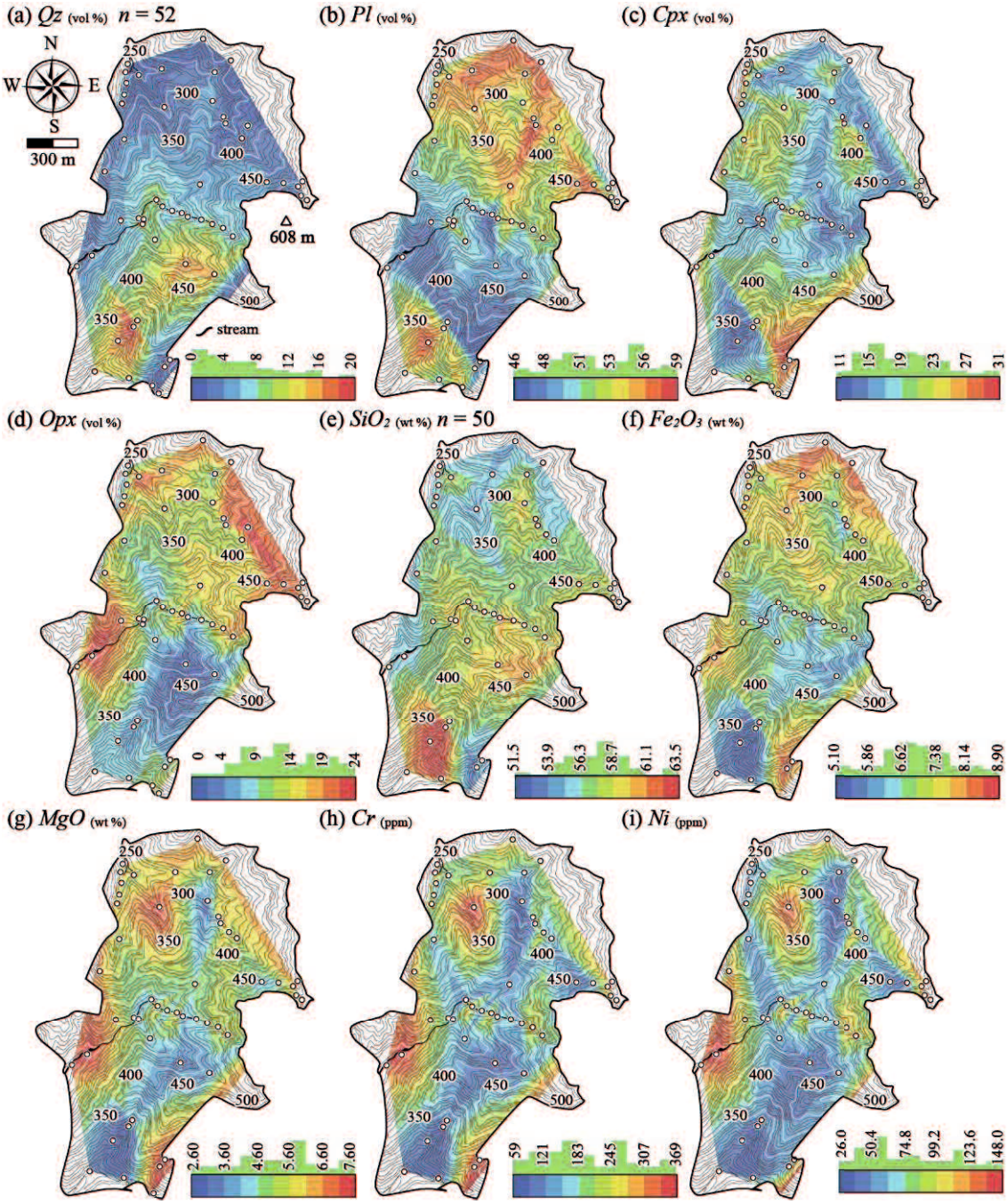

Figure 3–20. Horizontal variation in modal compositions. (a)–(d) Qz, Pl, Kfs, Opx, Cpx, and Opx and whole-rock chemical compositions. (e)–(i) SiO_2, Fe_2O_3, MgO, Cr, and Ni of the TPD. Dots indicate sampling sites. Horizontal variation maps were created using Graph-R. The modal values are listed in Appendix 3–5.

3–5–3 Shaku-dake body (TPD body) growth model and magma plumbing system

3–5–3–1 TPD magma plumbing system

The TPD body mainly crops out on the western slope of Mt. Shaku-dake and intrudes the Wakino sub-group (Fig. 3–2). The TPD locally developed layered structures along its wall (Figs. 3–21a, b, and c). The layered structure consists of mafic and felsic to intermediate sheets with different grain sizes and modal compositions (Figs. 3–21a and b). The mafic layer locally appears as a micro-sheet with a thickness of several centimeters (Fig. 3–21c). The layered structure can easily be identified by the naked eye, but it possesses diffuse boundaries (Figs. 3–21a, b, and c). Rarely, the mafic micro-sheet shows continuous layers (Fig. 3–21c). The mafic micro-sheet mainly consists of orthopyroxene, clinopyroxene, and plagioclase, which is similar to the host TPD but with a finer grain size (Figs. 3–21c and 3–22a). The boundary between the mafic micro-sheet and TPD is also diffuse and indistinct under the microscope (Figs. 3–21c and 3–22a). In addition, the TPD locally intruded the Wakino sub-group as sills (Fig. 3–21d). The sills were transformed from vertical dikes and conformably intruded into the bedding plane between the pelitic and tuffaceous layers of the Wakino sub-group (Figs. 3–21d and e).

According to the models proposed by Hutchinson (1996) and Gudmundsson (2011), when a vertical magmatic intrusion intersects a sub horizontal discontinuity, such as a contact between the pelitic and tuffaceous layers in the case of a TPD body, the intrusion may stop propagation and penetrate into the bedding plane (Fig. 3–23a). The TPD dike in Figure 3–23a shows the deflection in one direction (single-shape type). As shown in Figures 3–21d and e, the TPD sill likely intruded into the magma reservoir because of the direction of the sill, which faced towards the TPD body (Fig. 3–2). Kavanagh et al. (2006) tested the hypotheses regarding sill emplacement using analog experiments by injecting fluid into solid gelatin. The sill formation was found to require varying rigidity between the two layers under hydrostatic conditions (Fig. 3–23b). In the case of the sill, as shown in Figures 3–21d and e, the upper and lower

layers were the fine and dense pelitic layer and light non-welded tuffaceous layer, respectively, suggesting that the rigidity between the two layers varied. Moreover, the sill extended to the main TPD body (Fig. 3–2: northern TPD dike), and the layered structures developed in the TPD body wall. The TPD body therefore formed via the following magma plumbing system: The feeder dike caused by the deflection from the vertical dike could supply andesitic magma (high-Mg andesite to high-Mg diorite) to the TPD body.

The TPD body included layered structures at the body wall, suggesting several magma pulses (Fig. 3–21). The boundary between the mafic micro-sheet and host TPD was diffuse (Fig. 3–22a), and the mafic micro-sheet injected additional magma into the magma reservoir prior to the solidification of the TPD. Hildreth (2004) defined the degree of consolidation in the magma reservoir based on the rheology or crystal content, for example, bands of rigid sponge (60–100% crystal), mush (45–60% crystal), crystal-rich magma (15–45% crystal), and crystal-poor magma (<15% crystal). This suggests that magma with different crystal fractions has different rigidity. Moreover, partially consolidated magma generally has several zones with different melt fractions and strengths (Miller et al., 2011). Considering the magmatic injection model of Hildreth (2004), the occurrence of layered structures in the TPD (Fig. 3–21) serves as proof of replenished magma trapped in the crystal mush layer sandwiched by rigid sponge layers (Fig. 3–23c). In this case, the crystal mush layer likely behaved as a high-melt fraction zone rather than a rigid sponge (Hildreth, 2004).

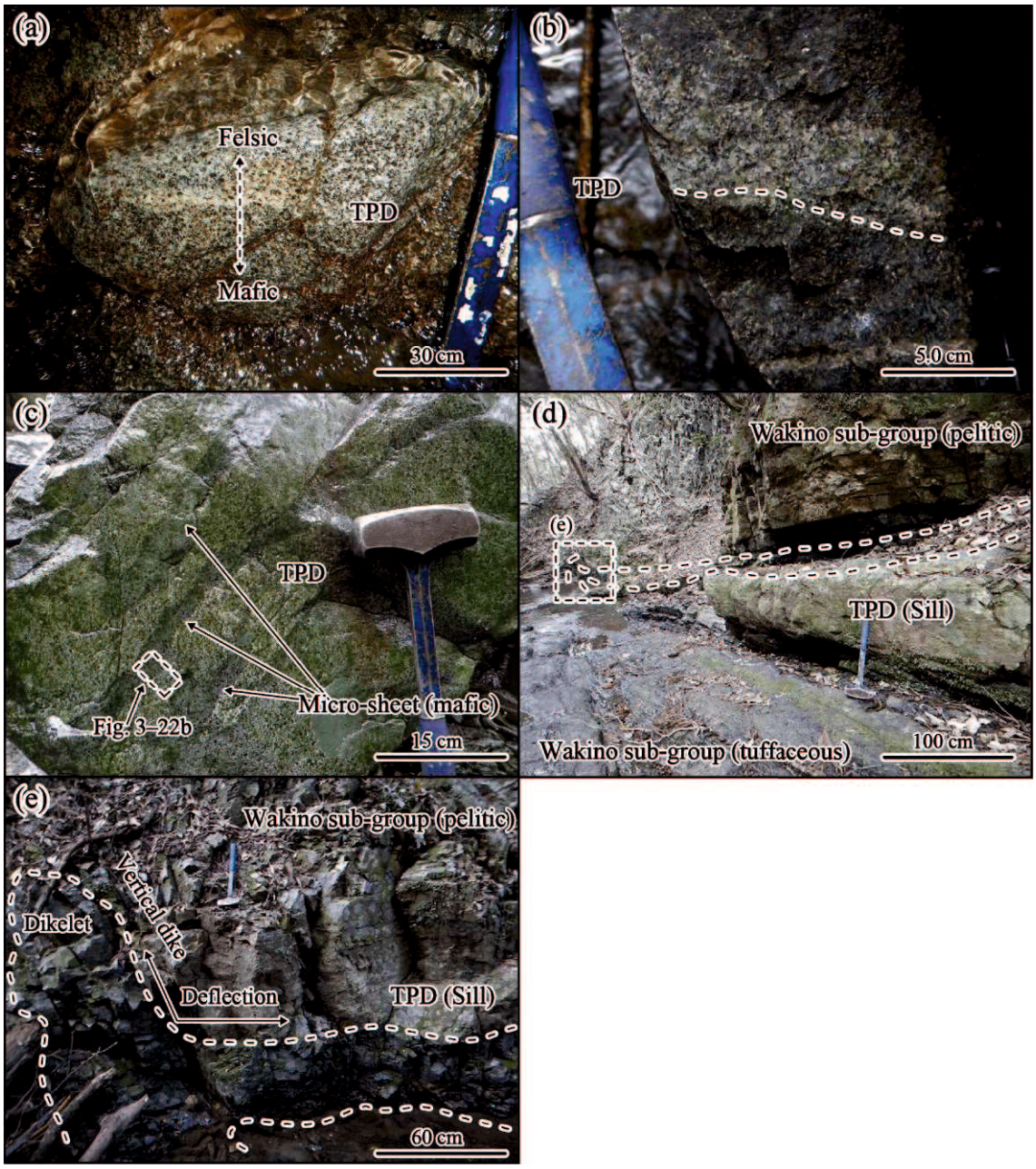

Figure 3–21. Field occurrences of intrusive rocks. (a) to (c) Layered structures in the TPD. (d) The TPD intruding into the Wakino sub-group as a sill. (e) Occurrence of the TPD dike. The vertical TPD dike deflects to the sill.

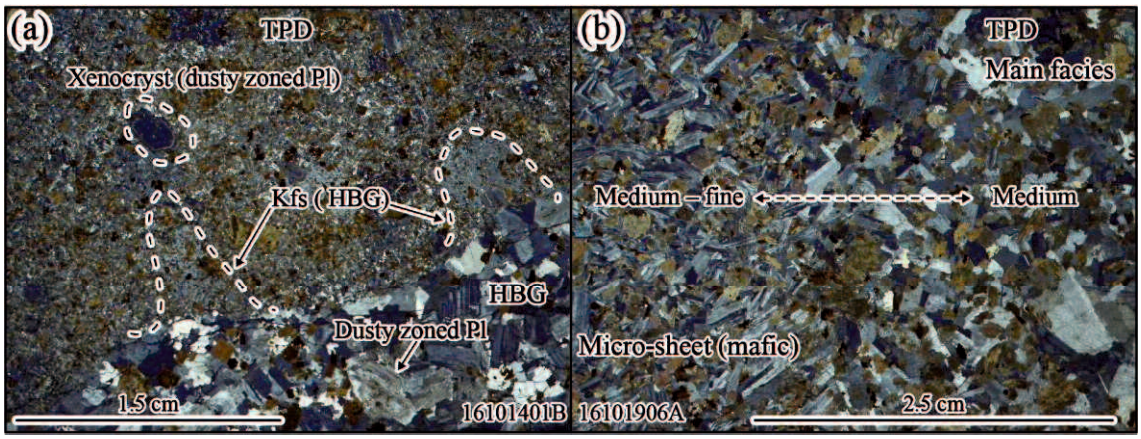

Figure 3–22. Photomicrographs of studied samples. (a) The boundary between the micro-sheet (left) and the TPD (right). (b) Dusty zoned plagioclase in both TPD and HBG. Kfs: K-feldspar, and Pl: plagioclase.

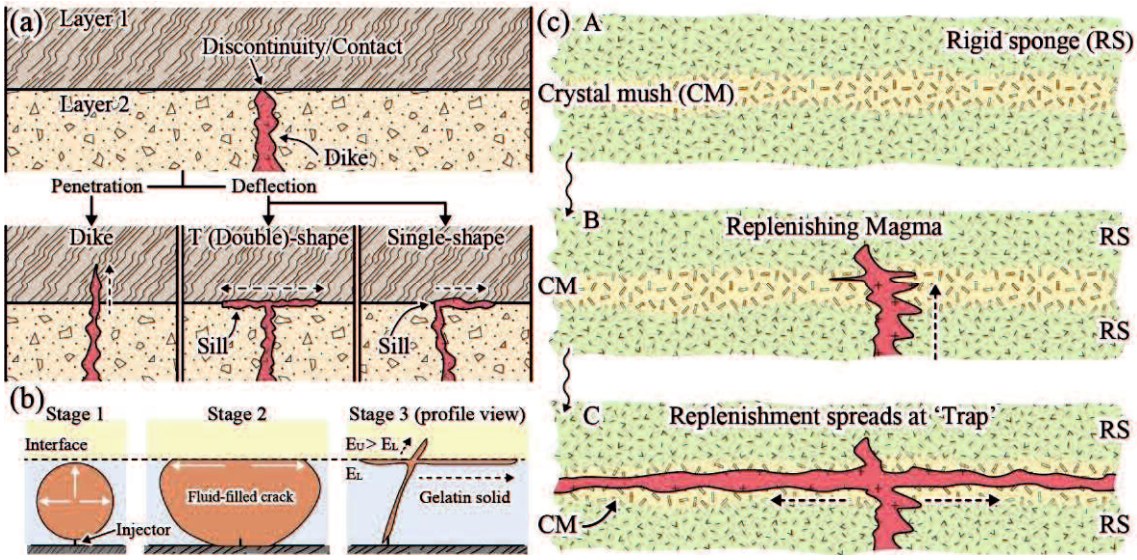

Figure 3–23. Schematic model for the formation of layered structures. (a) Dike deflecting into sill (Hutchinson, 1996; Gudmundsson, 2011). (b) Analog experiments showing the growth of the sill (Kavanagh et al., 2006). (c) Formation of micro-sheet (Miller et al., 2011). RS: rigid sponge, and CM: crystal mush.

3–5–3–2 TPD growth and lithofacies change model

The presence of feeder dikes and layered structures in the TPD body wall is important for the body's growth and maturation. A simplified growth model of the TPD body can be inferred from the features described above and is summarized in Figure 3–24 by adapting the sheet-on-sheet model proposed by Menand (2008) and Miller et al. (2011). Several injection sites of the TPD magma likely existed during the TPD formation because the feeder dikes and layered structures are scattered around the wall of the TPD body (Fig. 3–21). Therefore, the TPD body would have been formed by piled-up sills. In addition, the horizontal variation of the TPD possesses some anomalous spots in the marginal area of the body (Fig. 3–20). The distribution of the feeder dikes and layered structure is identical to that of the anomalous spots (Figs. 3–2 and 3–20), suggesting the existence of multiple magma injection sites. The mingling textures, such as dusty plagioclase, were probably derived from the HBG and were observed in the vicinity of the HBG dike (Fig. 3–22a).

According to Figure 3–19, the vertical variation in the TPD body seems to be irregular of which the differentiated facies rich in modal quartz and K-feldspar are at altitudes of 300–450 m; however, the mafic facies rich in the modal pyroxenes and MgO, Cr, and Ni contents are also present at the same altitude. Furthermore, plagioclase possesses a wide compositional range (Fig. 3–6), and some clinopyroxenes show reverse zoning (Fig. 3–7). Field observations, petrography, and geochemical features suggest that the TPD body was formed by multiple magma injections with variable composition from several sites.

Although the TPD interior gradually changed its lithofacies, the layered structures were confirmed only in the wall of the TPD body (Figs. 3–3, 3–19, and 3–20). Because of the significant temperature difference between the host rock and the TPD magma, the replenishing magma froze immediately after intruding into the reservoir wall. On the other hand, the exsolution texture of clinopyroxene that appears in the center of the TPD body, suggest slow cooling (Figs. 3–2 and 3–7). In

addition, the *An* content of plagioclase in Sp-3 to Sp-6 inside the TPD body partially overlaps between the core and rim (Fig. 3–6), suggesting that multiple magma injections may have slightly altered the composition of the existing magma reservoir and homogenized it. Overall, multiple injections of magma prolonged the supra-solidus state. The sheet-on-sheet structure appearing as layered structures were therefore left only in the TPD wall, and the interior of the TPD tended to be homogenous. This interpretation is consistent with the inference that the plutons were emplaced incrementally as proposed in the sheet-on-sheet model (Glazner et al., 2004; Miller et al., 2011). These plutons commonly show little or no field evidence of internal structures (Glazner et al., 2004; Miller et al., 2011).

The aforementioned models are regarded as the most important plutonic and crustal-scale building units, in accordance with the theoretical models (Gudmundsson, 1990; Annen and Sparks, 2002; Michaud and Jaupart, 2006; Menand, 2008), indicating that the plutonic rocks of the entire crustal growth are formed via the fusion of individual intrusive igneous layers (sheets) as well as on the extensive evidence of geological, geophysical, and geochronological data (de Saint-Blanquat et al., 2006; Pasquarè and Tibaldi, 2007; Morgan et al., 2008; Horsman et al., 2010). The growth model of the small pluton in this study may be helpful in revealing the formation processes of voluminous magmatism in the Northern Kyushu batholith.

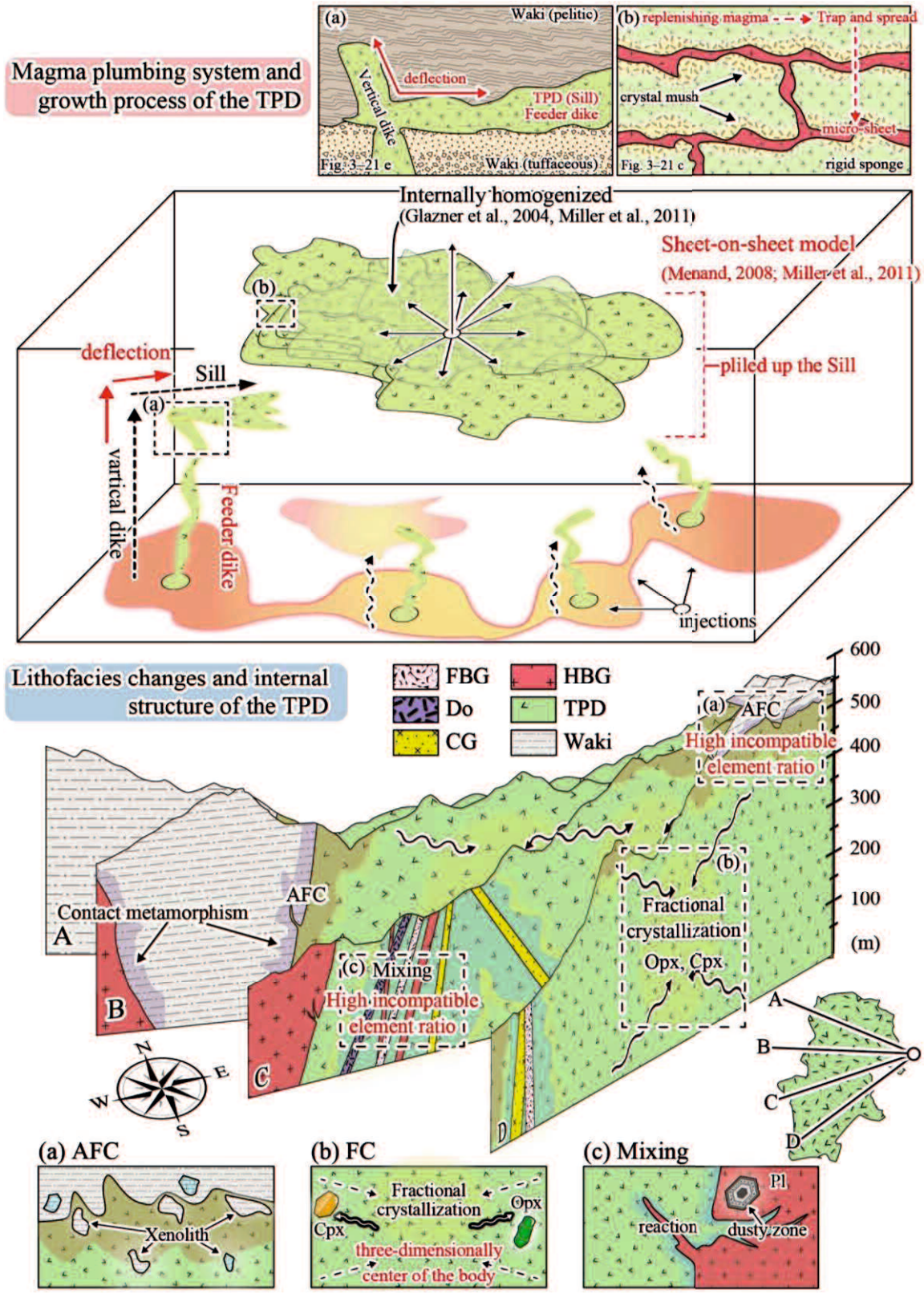

Figure 3–24. Illustration for growth and lithofacies changes model of the Shaku-dake (TPD) body.

4 Northern part of Shaku-dake area

4–1 Introduction

Granitoids occupy approximately 30% surface area of the Japanese island, intruded into the continental crust mostly between 50 and 130 Ma (Takagi, 2004). Thus, the Cretaceous was vigorously active period of granitic magmatism in geological history of Japan. The Cretaceous granite batholiths are widely distributed in northern Kyushu over an area of about 100 km from east to west and about 50 km from north to south, and divided into 17 bodies (Fig. 1–1 and 4–1: Karakida, 1985; Owada et al., 1999; Owada and Kamei, 2010). The magmatic processes of the Northern Kyushu batholiths have been investigated from the intrusive relationships, chemical compositions, and radiometric ages of each intrusive body (Karakida, 1985; Murakami, 1985; Izawa et al., 1990, 1994; Owada et al., 1999). The petrography, petrogenesis, and magmatic processes of the small-scale intrusive bodies that are the components of the batholiths, however, have not been investigated, and the whole picture of batholith activity has not been elucidated. In recent years, field surveys, geochemical analyses, and zircon U–Pb age dating of small-scale intrusive bodies in the Northern Kyushu batholiths have been carried out on the small-scaled plutonic bodies (Eshima and Owada, 2018; Eshima et al., 2019; Yuhara et al., 2019a, b; Eshima et al., 2020; Muraoka et al., 2020; Eshima, 2021a, b). Yuhara et al. (2019a) reclassified the granitic bodies in terms of zircon U–Pb ages and geochemical features. Eshima and Owada (2018), Eshima et al. (2019, 2020), and Eshima (2021a, b) investigated the characteristics of the magmatic processes and growth model of the small-scaled plutons. Moreover, Muraoka et al. (2020) revealed the genetic relationships between the ilmenite-series and magnetite-series granitoids that intruded into the eastern and western sides of the Kokura–Tagawa Tectonic Line, respectively. Therefore, the detailed investigation for the small-scaled intrusive bodies is now available. Such specific data of the small-scale intrusive bodies are

considered to be important for examining the igneous activity and growth process of batholiths in the world wide (Glazner et al., 2004; Menand, 2008; de Saint-Blanquat et al., 2006; Menand et al., 2011; Eshima et al., 2020; Eshima, 2021a).

The igneous rocks in the northern part of the Mt. Shaku-dake are exposed as a stock on Tashiro-cho, Yahatahigashi-ku, to Hata, Yahatanishi-ku in Kitakyushu City with the area of 5 km (east-west) and 3 km (north-south). It intrudes the Cretaceous Wakino sub-group that has been formed as a shallow-marine deposit because of the abundance of shell and fish fossils (Ota, 1959). The stock mainly consists of porphyry (porphyritic fine-grained tonalite: PFT), associated with the following intrusive rocks; two-pyroxene diorite (TPD), clinopyroxene quartz diorite (CQD), and small-scale dikes including porphyritic fine-grained diorite (PFD) and clinopyroxene andesite (CA). These rocks intrude the PFT. The PFT, CQD, and TPD have been so far reported only on their distribution, characteristics of the photomicrographs, and the hornblende K–Ar age of PFT (Kubo et al., 1993; Nakae et al., 1998; Owada et al., 1999). The TPD reported by Kubo et al. (1993) used to be exposed in the eastern side of stock, but now there are no outcrops in this area, where it is the construction area changing into the substations and residential areas. The small-scaled dikes, PFD and CA, were found in this study, but the timing of their activity has not been clarified. Based on the above observations, this chapter 4 focuses on PFT and CQD.

The PFT shows a porphyritic texture and exposed over a wide area of about 5 km from east to west and about 3 km from north to south, despite the fact that it is shallow intrusive body intruded the Wakino sub-group (shallow-marine sediment). The hornblende K–Ar age of 109.5 ± 2.4 Ma (Owada et al., 1999) is slightly older than the zircon U–Pb age of 107 to 100 Ma reported for the intrusive bodies among the Northern Kyushu batholith but is similar to zircon U–Pb age of the volcanic rocks (dacite: 108 Ma) of the Kanmon Group (Adachi et al., 2012; Tiepolo et al., 2012; Miyazaki et al., 2018; Yuhara et al., 2019a, b). This age overlaps with the

depositional age of the Wakino sub-group (Kochibe, 1903; Nakae et al., 1998; Miyazaki et al., 2018). The intrusive order of the PFT (porphyry, shallow intrusive body) followed by CQD (pluton) is similar to the formation sequence of volcanic-plutonic activity (Lipman, 2007; Macdonald et al., 2014). Considering the error range of the radiogenic ages, it is likely that the activity of the PFT magma was the precursor of the Northern Kyushu batholith. In other words, the magma activities of PFT and CQD are considered to preserve important information for understanding the process of magma supply and the genetic relationship between the small-scaled bodies of precursor and the batholith.

In this chapter 4, occurrence, petrography, modal composition, and mineral and whole-rock compositions of the PFT and CQD from the northern part of the Mt. Shaku-dake area are described, and the factors responsible for the compositional change from PFT (porphyry, shallow intrusive body) to CQD (pluton) are discussed.

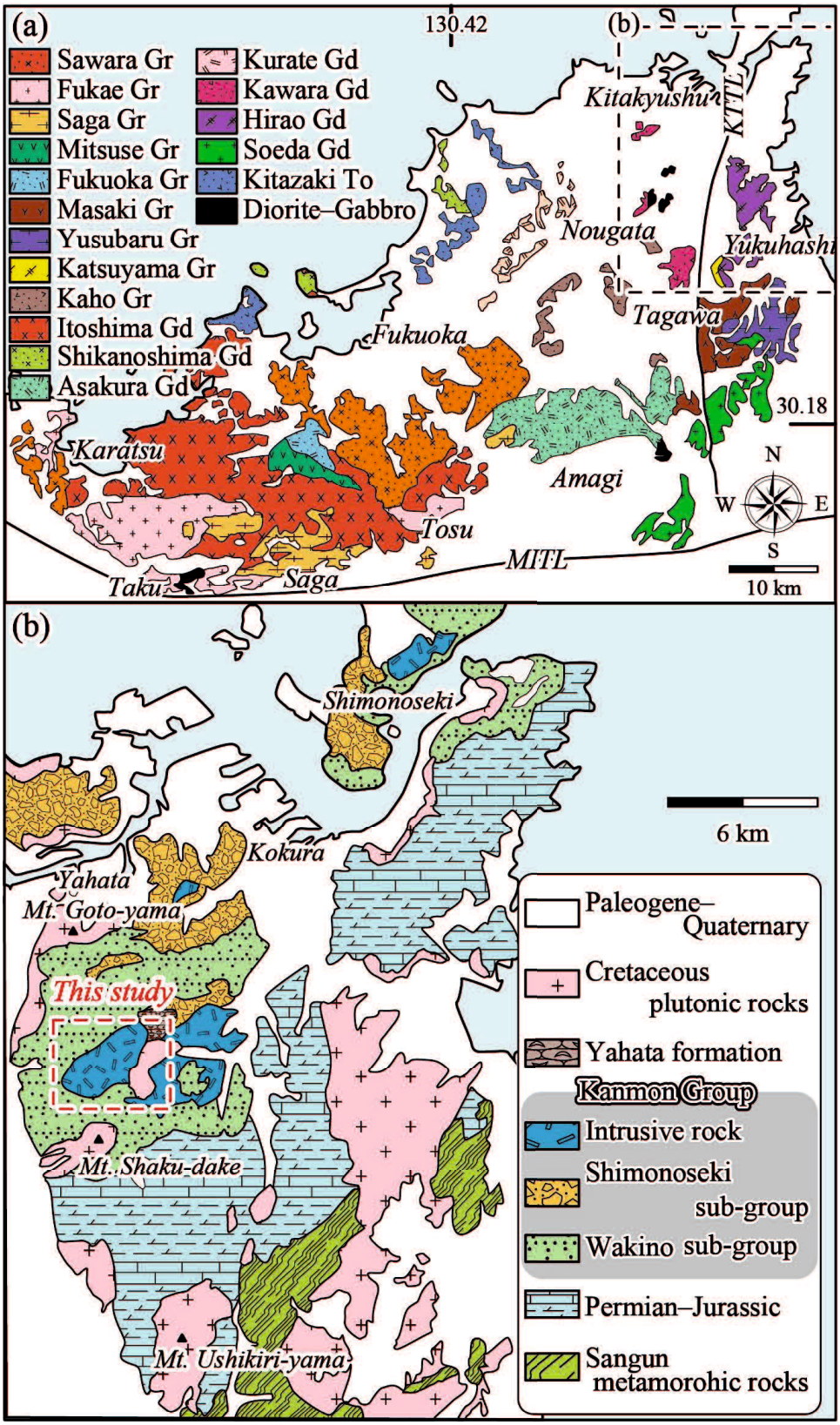

Figure 4–1. (a) Simplified geological map of the Northern Kyushu batholith (Karakida, 1985; Owada and Kamei, 2010). (b) Simplified geological map of the Shimonoseki to

Tagawa region (Kubo et al., 1993; Nakae et al., 1998). Gr: granite, Gd: granodiorite, To: tonalite, *KTTL*: Kokura–Tagawa tectonic line, and *MITL*: Matsuyama-Imari tectonic line.

4–2 Geological overview

The geology of the northern part of the Shaku-dake area consists of the Wakino sub-group that is a lower sequence of the Cretaceous Kanmon group, PFT, CQD, TPD, and small-scale dikes (Fig. 4–2). The bedding planes of the host rock, the Wakino sub-group, predominantly show N70°W–N60°E strike and 10–40° dipping with north or south. The structural sequences of the Wakino sub-group show the lower basal conglomerate, followed by coarse-grained sandstone in the middle part and the alternation of sandstone (tuffaceous) and shale in the upper part (Nakae et al., 1998). The PFT occurs as an oval shape with northeast-southwest direction, and provides the thermal effect to the host Wakino sub-group. The boundary between the PFT and the Wakino sub-group is unclear, at which the veins and droplets derived from PFT magma sporadically occur within the clastic sediments of the Wakino sub-group (Fig. 4–3a). Such features correspond to peperite, and calcite veins are often developed within the peperitic structures (Fig. 4–3b, c). In addition, the PFT is intruded by various kinds of veins consisting of calcite, quartz, prehnite, and pumpellyite (Fig. 4–3d), and the periphery of the veins are pale in color, indicating the influence of hydrothermal alteration. On the other hand, the CQD intrudes the PFT and the Wakino sub-group with sharp and clear contacts (Fig. 4–3e). The CQD generally develops a weak flow structure due to the arrangement of plagioclase and clinopyroxene (Fig. 4–3f). In the area of the TPD, there are almost no exposure because of the construction of residential areas and substations. Therefore, the distribution of TPD follows the geological map of Kubo et al. (1993) (Fig. 4–2). The TPD occurring as boulders resembles its lithofacies to that of the Shaku-dake diorite (Fig. 4–2: Eshima and Owada, 2018; Eshima et al., 2020; Eshima, 2021a) in terms of mineral assemblages and microstructures. The small-scaled dikes are of two

lithofacies, PFD and CA both of which are 1–10 m wide and of N40°W–N52°W or N32°E–N45°E strike, and intrude the PFT or Wakino sub-group with steeply dipping (dip 72–86°) (Fig. 4–2). The intrusive age of the dikes is unknown.

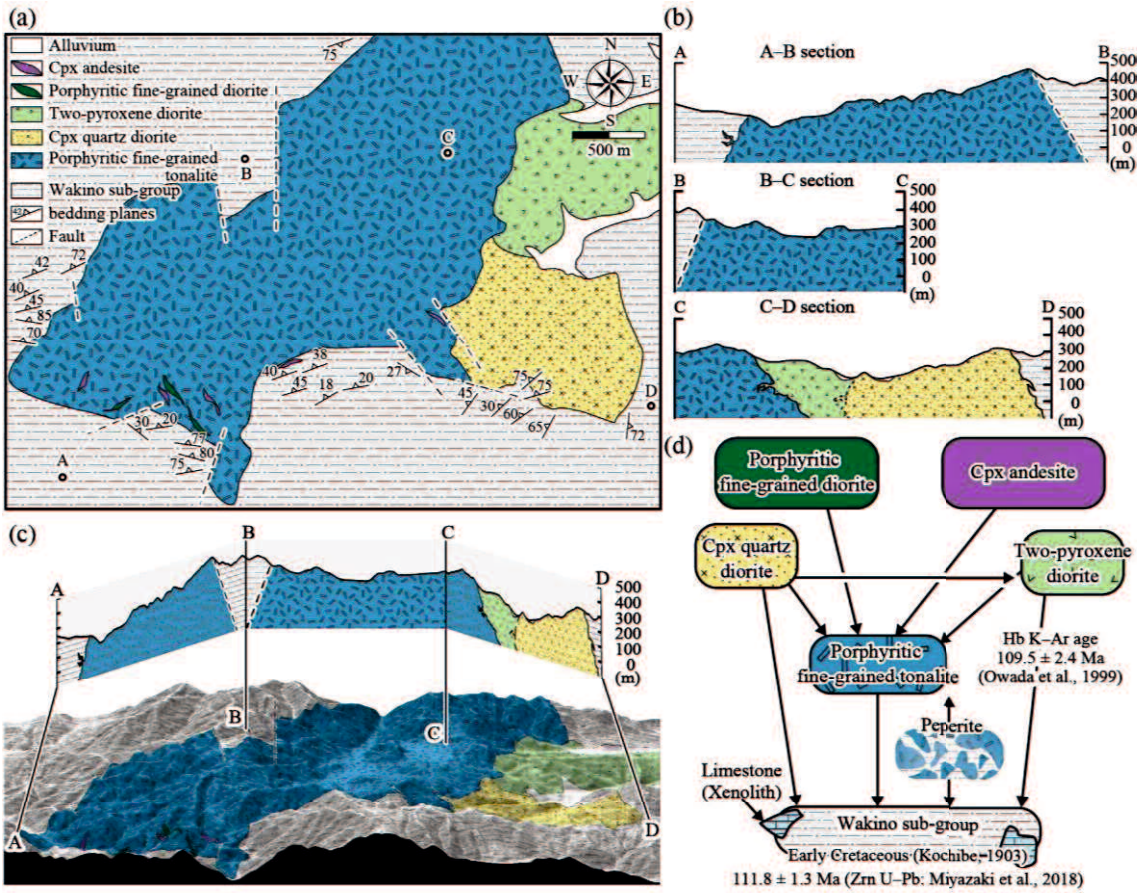

Figure 4–2. (a) Geological map of the study area. (b) SW–NE cross-section along A–B, W–E cross-section along B–C, and NW–SE cross-section along C–D. (c) A–B–C–D cross-section and bird's eye view of the geological map. (d) Mutual relationships between intrusive rocks and the Wakino sub-group. The solid arrows indicate intrusive relationships.

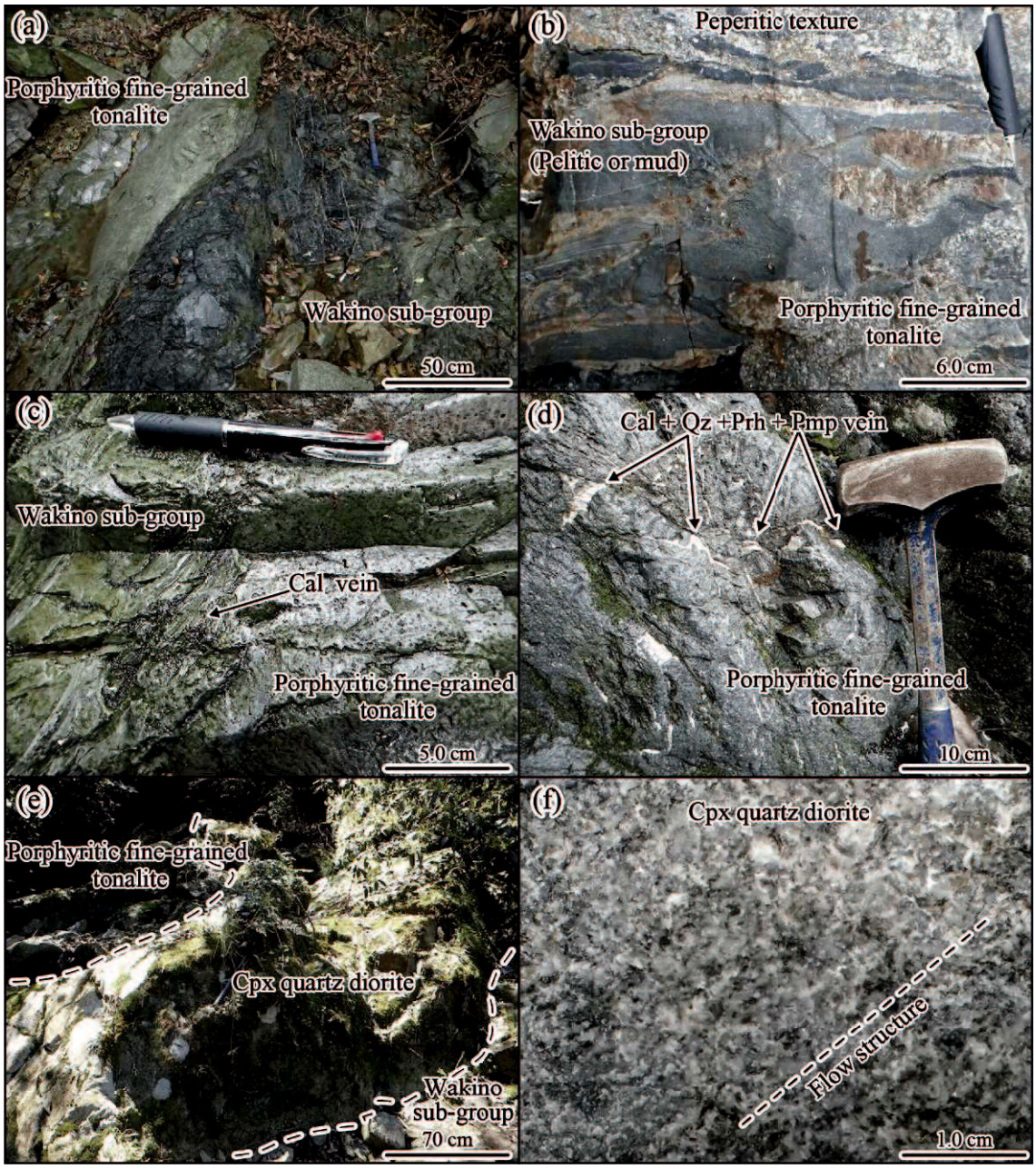

Figure 4–3. Field occurrences of the intrusive rocks. (a) The boundary between the porphyritic fine-grained tonalite and the Wakino sub-group. (b) Peperitic texture in the porphyritic fine-grained and Wakino sub-group boundary. (c) Calcite and quartz veins developed in the porphyritic fine-grained and Wakino sub-group boundary. (d) Calcite, quartz, and prehnite veins in the porphyritic fine-grained tonalite. (e) The clinopyroxene quartz diorite showing a sharp intrusive relationship with the porphyritic fine-grained tonalite and Wakino sub-group. (f) The preferred orientation of plagioclase and clinopyroxene crystals indicating the flow direction in the clinopyroxene quartz diorite.

The dotted arrows indicate flow direction.

4–3 Petrography of the analyzed samples

In this section (4–3), descriptive features and representative modal compositions of PFT and CQD are described. Sample locations, representative photomicrographs and Qz–Afs (Kfs) –Pl (QAP) diagrams for each rock are shown in Figures 4–4, 4–5 and 4–6, respectively.

Modal analysis was performed on 22 PFT samples and 16 CQD samples, and the modal change of magmatic process is examined, excepting high altered rocks. In the case of PFT samples, quartz and plagioclase occur in both phenocrysts and the matrix; thereby, I did not distinguish between phenocryst and matrix. The CQD shows medium-grained and relatively homogeneous. Point-counting application was used for Microsoft Excel VBA (Visual Basic for Applications) made by Shimura and Kojima (2015), and 2000 points were counted from an area of 3 cm × 4 cm per sample. The measurement data are listed in Appendix 4–1.

4–3–1 Porphyritic fine-grained tonalite (PFT)

The PFT shows a porphyritic texture and is mainly composed of plagioclase, biotite, hornblende, and quartz as a phenocryst (Fig. 4–5a). The matrix generally shows microgranular texture, some of which shows micrographic texture and is mainly composed of quartz, K-feldspar, apatite, titanite, and ilmenite. The sample via hydrothermal alteration have well-developed veins of calcite, quartz, epidote, prehnite, and pumpellyite (Figs. 4–5b and c).

Plagioclase phenocryst shows euhedral–subhedral crystals with 0.5–2.5 mm in long having compositional zonation. Hornblende phenocryst shows subhedral–euhedral columnar crystals with 0.7–3.0 mm in long and particularly coarse-grained crystals up to 5.0 mm. Biotite phenocryst shows euhedral–subhedral tabular crystals with 0.5–1.5 mm in long and rarely with a bladed shape. Quartz

phenocryst shows anhedral crystal with 0.5–1.0 mm in diameter and generally with rounded corners and a resorption shape. The QAP diagram of the PFT, which is plotted in the quartz diorite to tonalite composition range and is characterized by trace amounts of K-feldspar (Fig. 4–7).

4–3–2 Clinopyroxene quartz diorite (CQD)

The CQD is hypautomorphic granular texture and is mainly composed of plagioclase, clinopyroxene, biotite, and quartz. Orthopyroxene, ilmenite, titanite, apatite, and zircon occur as accessory minerals (Figs. 4–5d, 4–6a, b, c, and d). The CQD shows a variety of textures, such as accumulated structures of relatively large (1.5–2.0 mm) and euhedral columnar plagioclase with mafic minerals such as clinopyroxene, orthopyroxene, and biotite, and well-developed dusty zoned plagioclase (Figs. 4–6a, b, c, and d). The CQD showing accumulated texture frequently contains dusty zoned plagioclase and patchy mafic enclaves (MME) with less than 5 cm in diameter. In addition, the CQD contains autolith with homogeneous mineral assemblage under the microscope. The autolith is distinguished by outer rims with granoblastic texture and inner cores with hypautomorphic granular texture similar to the host COD (Figs. 4–6c and d).

Subhedral–euhedral plagioclase crystals are 0.5–2.0 mm in long. In some CQDs, the crystals are aligned in the long axis direction. Relatively differentiated CQDs often contain dusty zoned plagioclase. In the dusty zone, fine-grained crystals of clinopyroxene and biotite are contained in the inner part of dusty ring (Fig. 4–6b). Clinopyroxene shows subhedral–euhedral crystals with 0.3–1.7 mm in long and the rim of the crystals is often accompanied by fine-grained (0.1–0.3 mm) biotite (Figs. 4–5d and 4–6a). Subhedral–euhedral orthopyroxene crystals in accumulated CQDs. Biotite shows subhedral–euhedral crystals with 0.5–1.5 mm in long and rarely appears as a bladed shape. Quartz and K-feldspar occur as interstitial crystals with 0.2–1.0 mm in area and the former show a wavy extension. The CQD is plotted within

the field of diorite to quartz diorite in the QAP diagram (Fig. 4–7).

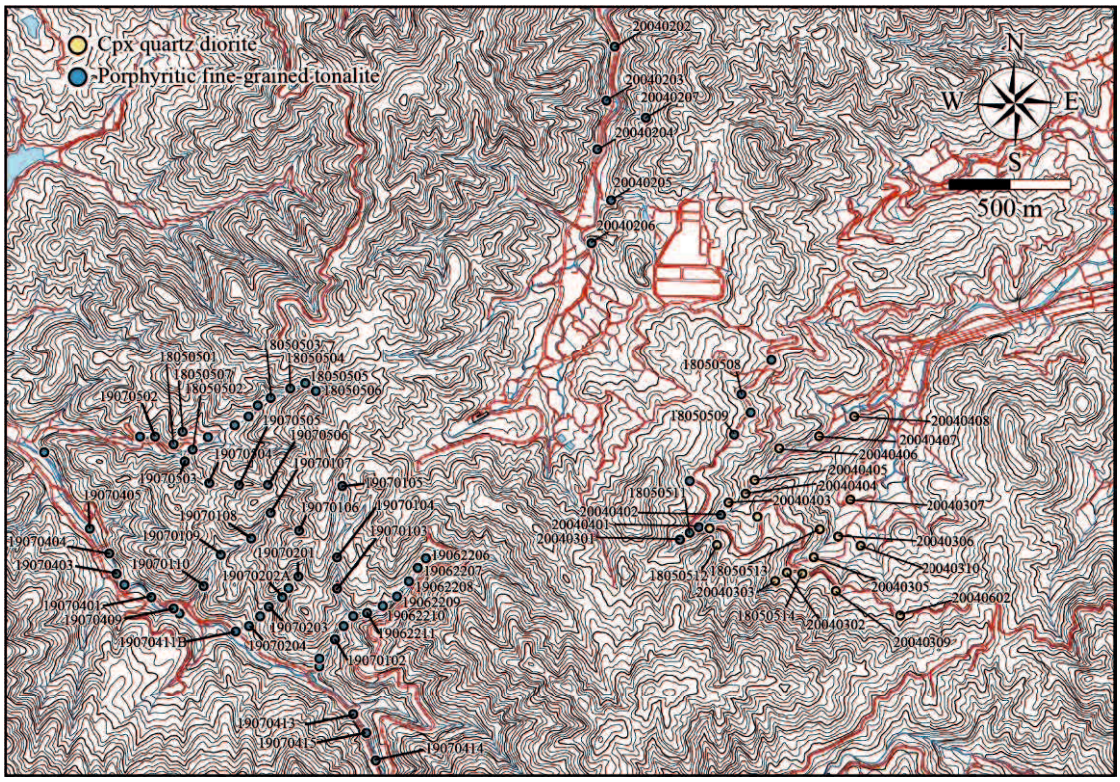

Figure 4–4. Topographic map showing the sampling localities. These samples are used for the discussion of this chapter 4.

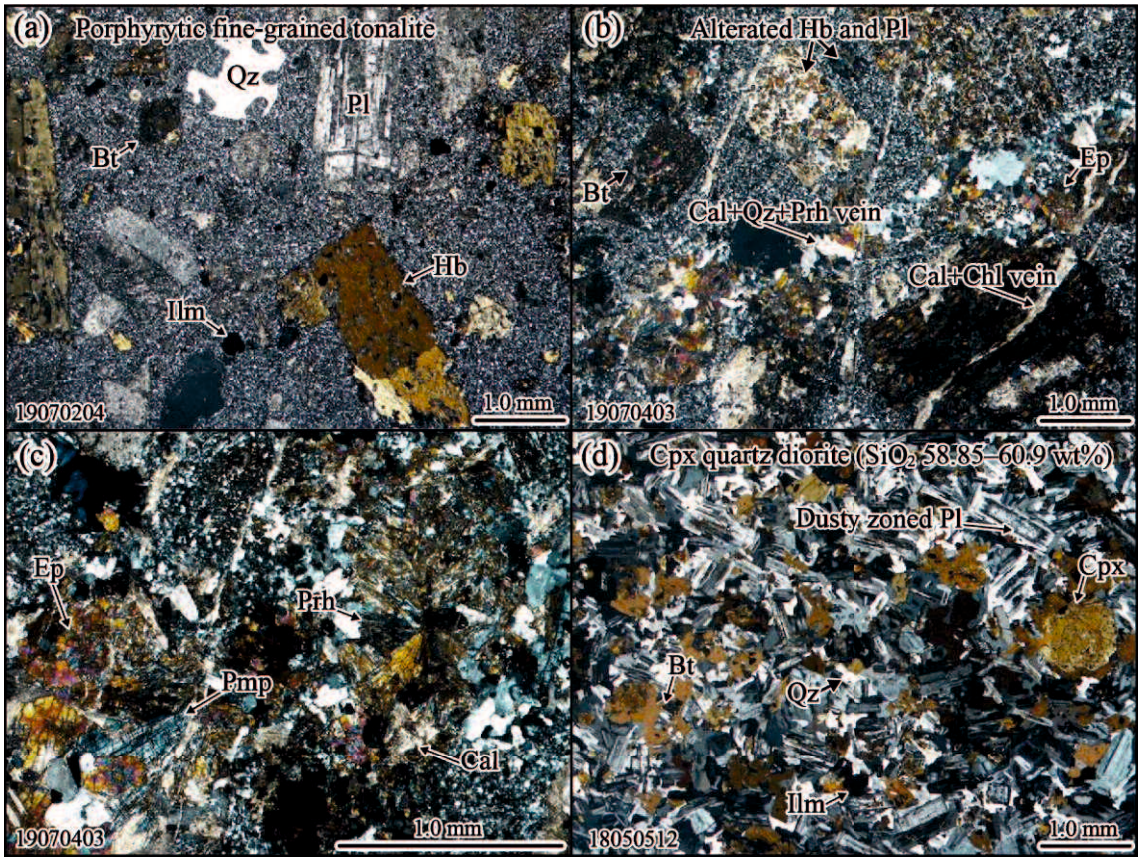

Figure 4–5. Photomicrographs of the porphyritic fine-grained tonalite and clinopyroxene quartz diorite. (a) Unaltered sample of the porphyritic fine-grained tonalite. (b) Hydrothermal veins developed in the porphyritic fine-grained tonalite. (c) Secondary minerals (Ep, Prh, and Pmp) in the porphyritic fine-grained tonalite. (d) High-SiO_2 content (Whole-rock (WR): 58.5–60.9 wt%) clinopyroxene quartz diorite. These clinopyroxene quartz diorites generally developed plagioclase crystals with dusty zoning (upper right). Qz: quartz, Pl: plagioclase, Bt: biotite, Hb: hornblende, Cpx: clinopyroxene, Opx: orthopyroxene, Ilm: ilmenite, Ep: epidote, Cal: calcite, Prh: prehnite, and Pmp: pumpellyite.

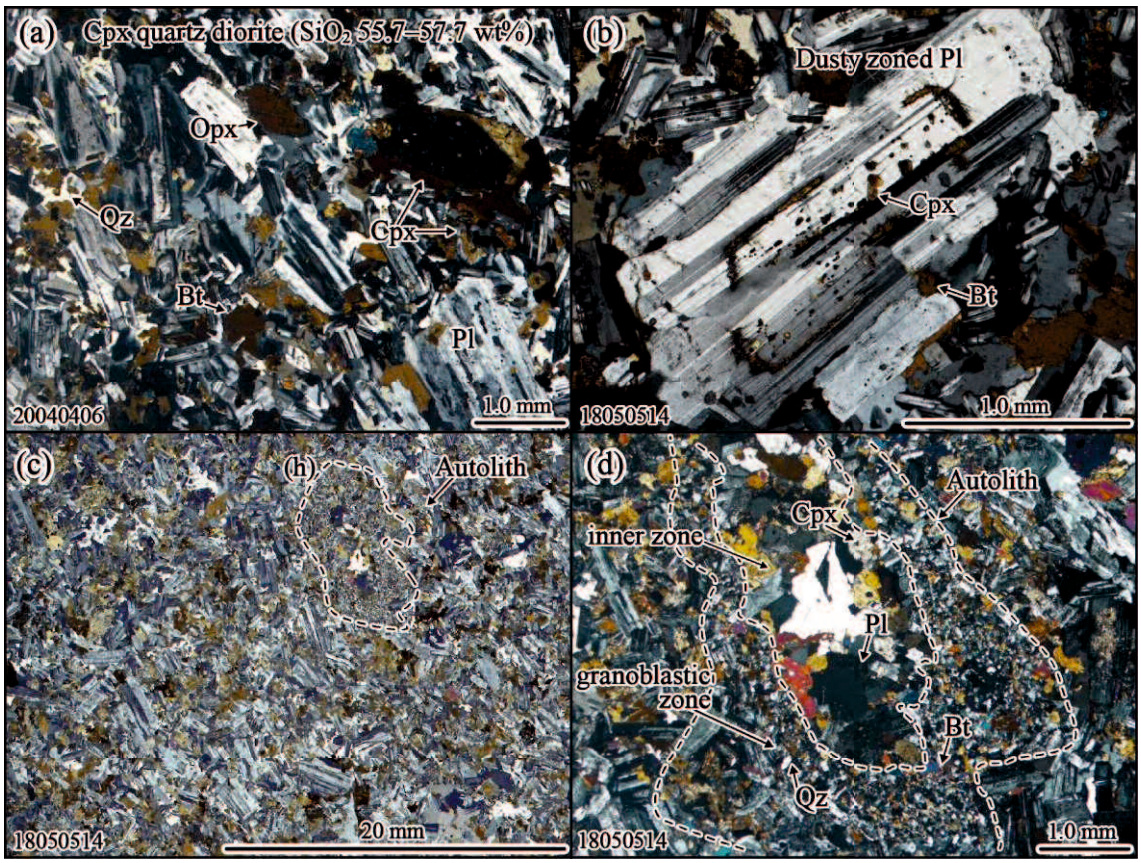

Figure 4–6. Photomicrographs of the clinopyroxene quartz diorite. (a) Low-SiO_2 content (WR: 55.7–57.7 wt%) clinopyroxene quartz diorite. These clinopyroxene quartz diorites generally show weak cumulated texture. (b) Dusty zoned plagioclase crystal in the High-SiO_2 content (WR: 58.5–60.9 wt%) clinopyroxene quartz diorite. This crystal encloses euhedral clinopyroxene and biotite. (c) Autolith in the clinopyroxene quartz diorite (WR: 57.8 wt%). (d) Autolith is divided into the outer edge, which shows granoblastic texture, and the inner part, which has high crystallinity. Qz: quartz, Pl: plagioclase, Bt: biotite, Hb: hornblende, Cpx: clinopyroxene, Opx: orthopyroxene, Ilm: ilmenite, Ep: epidote, Cal: calcite, Prh: prehnite, and Pmp: pumpellyite.

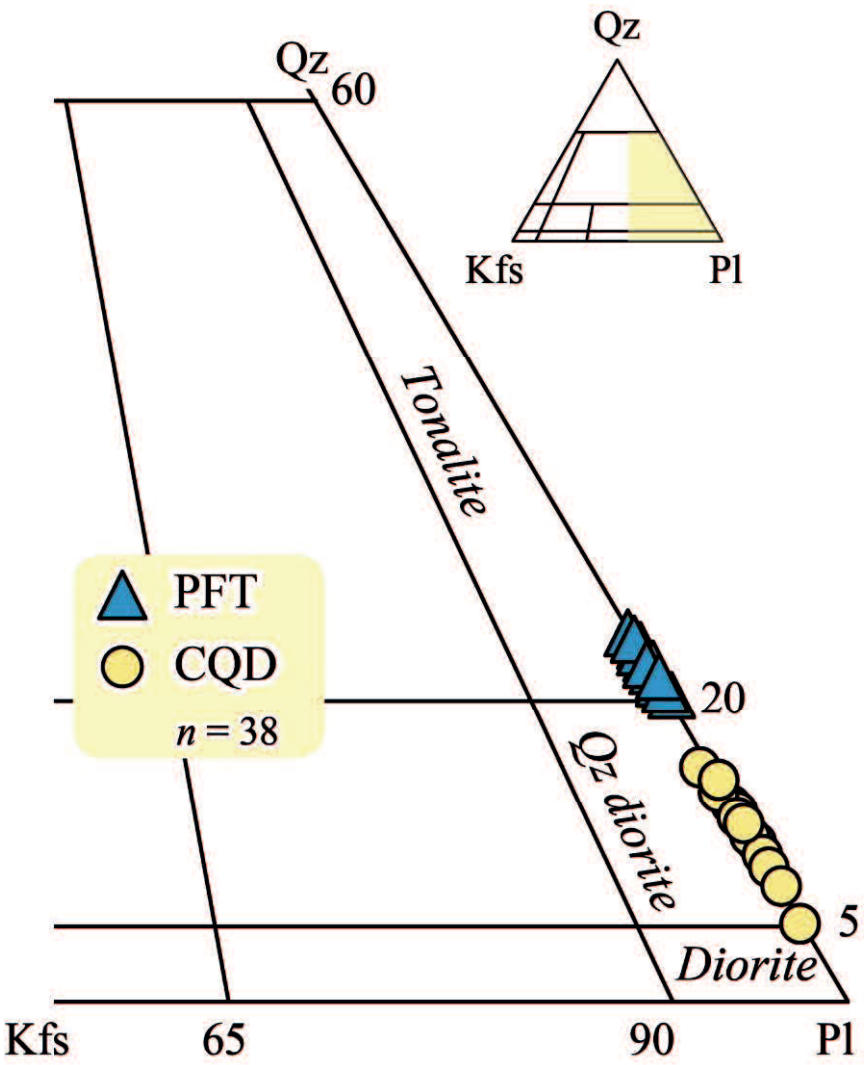

Figure 4–7. Modal compositions of the porphyritic fine-grained tonalite and clinopyroxene quartz diorite shown in a Qz–Kfs–Pl diagram. Classification boundaries are modeled after Streckeisen (1976). The modal compositions of the PFT and CQD are listed in Appendix 4–1.

4–4 Geochemistry

The analytical instruments, methods and procedures used in this chapter were the same as those described in chapter 2 (section 2–4).

4–4–1 Major and trace elements of whole-rock chemistry

The major and trace element compositions of PFT (48 samples) and CQD (16 samples) distributed in this area were measured. The samples were selected based on thin-section observation, which confirm the presence or absence of alteration minerals. The PFT bears the samples with presence or absence of altered minerals, while the CQD samples are less affected by weathering and alteration.

The variation of SiO_2 content in the PFT is limited (63.2–65.1 wt%), but the LOI values widely vary 0.9 to 5.8 wt% (Fig. 4–8 and Appendix 4–2). The alkali metals and alkaline earth metals such as CaO, Na_2O, Ba, and Sr extremely have diverse compositions and show a longitudinally elongated distribution on the variation diagram (Fig. 4–8), while the SiO_2 content is constant (Fig. 4–8: CaO: 3.1–5.1 wt%, Na_2O: 2.0–4.8 wt%, Ba: 398–709 ppm, Sr: 281–669 ppm). In contrast, there are little systematic change with SiO_2 content in some other elements.

The SiO_2 content of the CQD shows a range from 55.7 to 60.9 wt%, which is larger than that of the PFT (Fig. 4–8). Fe_2O_3, CaO and Cr decrease with increasing SiO_2, while Na_2O and Ba increase. The Sr contents is constant. The compositional range of Ba and Cr possesses a wide range in each sample with SiO_2 content less than 58.5 wt% (Fig. 4–8).

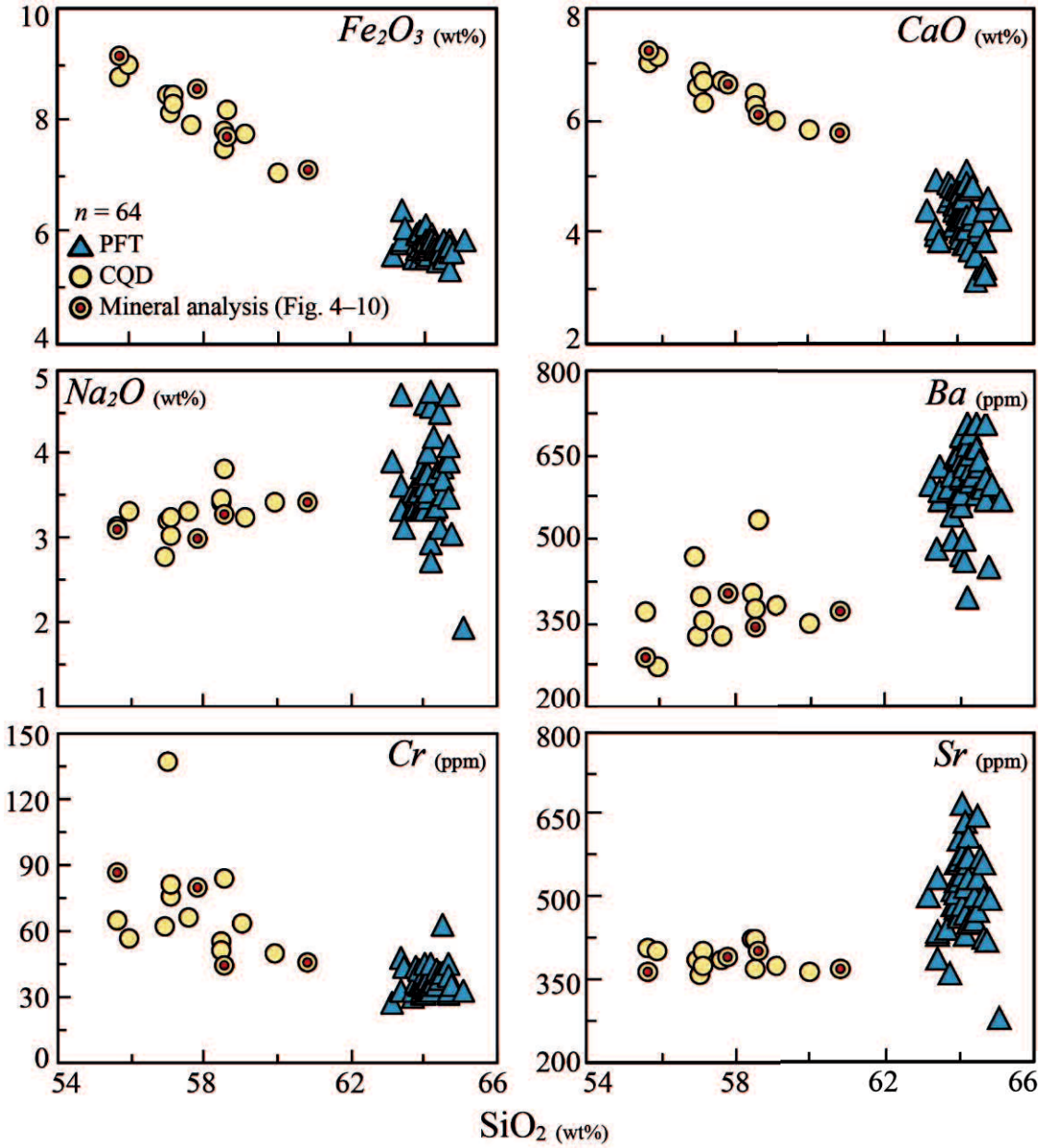

Figure 4–8. Major and trace element variation diagrams relative to SiO_2 (wt%) (SiO_2–Fe_2O_3, CaO, Na_2O, Ba, Cr, and Sr) for the porphyritic fine-grained tonalite and clinopyroxene quartz diorite. The major and trace element compositions of the PFT and CQD are listed in Appendix 4–2. PFT: porphyritic fine-grained tonalite, and CQD: clinopyroxene quartz diorite.

4–4–2 Mineral chemistry

The mineral compositions of plagioclase, hornblende, biotite, and ilmenite of the PFT and plagioclase, biotite and clinopyroxene of the CQD were analyzed (Table 4–1 and 4–2).

In the case of PFT samples, I selected unaltered and altered samples, and the altered samples were measured only in the core part of each mineral because of avoiding the effect of altered minerals in rim parts. Plagioclase in the unaltered PFTs generally shows normal zoning, and anorthite component [An = 100 × {Ca/(Ca + Na) }] decreases from core to rim (Table 4–1: An 33.7–46.5%). The X_{Fe} values [X_{Fe} = {Fe/(Fe + Mg)}] of hornblende and biotite are in the composition range of 0.42–0.45 and 0.48–0.53, respectively (Table 4–2). On the other hand, the compositions of plagioclase, hornblende, and biotite remaining in the PFTs are undistinguished from those of unaltered rocks, with plagioclase (core: An 43.9–46.6%), hornblende (X_{Fe}: 0.41–0.42) and biotite (X_{Fe}: 0.44–0.48).

The differences in the microstructure of the CQDs are related to the whole-rock SiO_2 content and the abundance of plagioclase with dusty zone [(dusty zoned Pl/normal Pl) × 100: modal values], and the presence of dusty zoned plagioclase appears in the samples having more than 58.5 wt% in SiO_2 and such samples rarely show accumulated texture (Fig. 4–9 and Appendix 4–1). On the other hand, samples with whole-rock SiO_2 content of less than 58.5 wt% show a weak accumulated texture with a decrease in whole-rock SiO_2 content and a lower abundance of dusty zoned plagioclase. Based on these observations, the samples were divided into two groups: the low-SiO_2 group (SiO_2 55.7–57.9 wt%), which shows weak accumulated texture and low abundance of dusty zoned plagioclase, and the high-SiO_2 group (SiO_2 58.5–60.9 wt%), which shows high abundance of dusty zoned plagioclase and rarely shows accumulated texture. Chemical analyses were made at 7–12 points from core to rim for each mineral. Samples with whole-rock SiO_2 contents of 60.9, 58.5, and 57.9 wt% possess the dusty zoned plagioclase, and samples with whole-rock SiO_2 content of

55.7 wt% include only normal zoned plagioclase. The *An* content of plagioclase in the CQD are 33.2–60.0% in the core, 25.4–49.8% in the rim, and 45.7–66.4% near the dusty zone in the plagioclase (Fig. 4–10); indicating normal zoning. Some of these minerals show an oscillatory zoning. In addition, the average *An* content of the core parts decreases with increasing whole-rock SiO_2 content (Fig. 4–10 and Table 4–2). The X_{Fe} values of biotite ranges from 0.43 to 0.56 (Table 4–2). The *Mg#* [*Mg#* = {100 × (Mg/(Mg + Fe)}] value of clinopyroxene show a range from 54.5 to 72.1, with crystals in low whole-rock SiO_2 samples and fine-grained crystals including in plagioclase having relatively high Mg#.

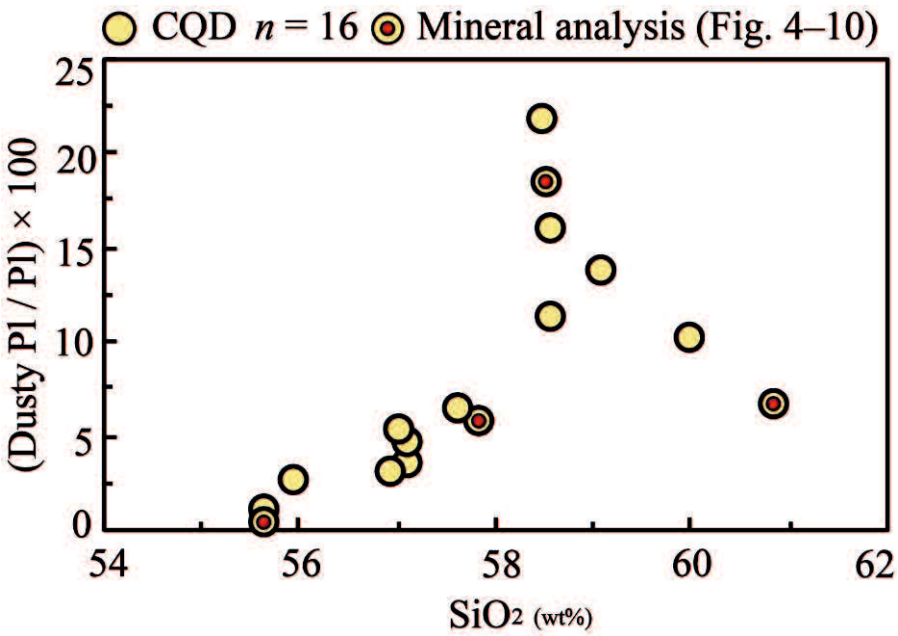

Figure 4–9. Variation in the relative abundance of the dusty zoned plagioclase with the whole-rock SiO_2 contents of the host clinopyroxene quartz diorite. The number of the dusty zoned plagioclase and normal zoned plagioclase in the clinopyroxene quartz diorite is listed in Appendix 4–1.

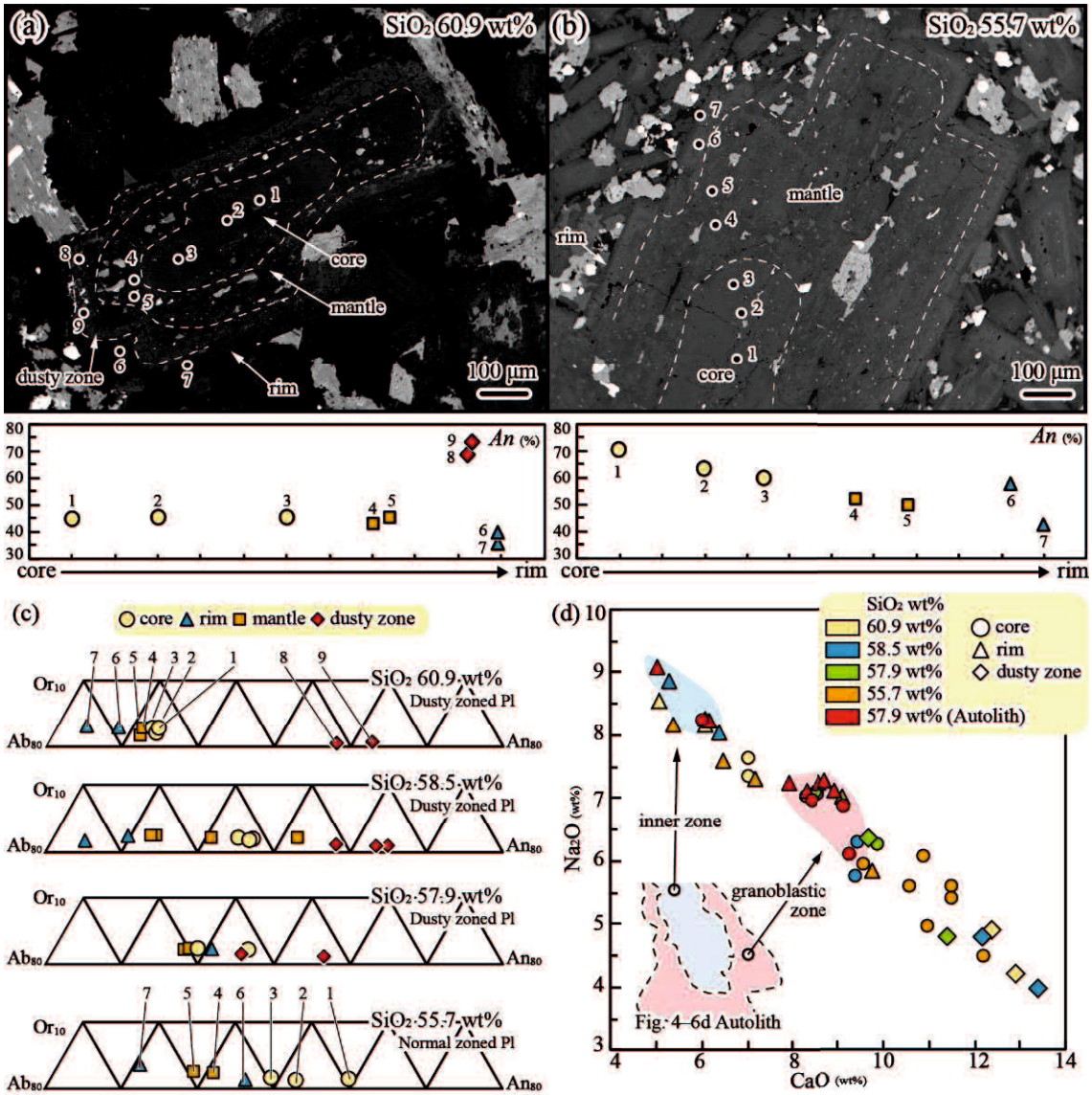

Figure 4–10. Mineral compositions of plagioclase in the clinopyroxene quartz diorite. (a, b) BSE map of the plagioclase in the clinopyroxene quartz diorite, consisting of the core, mantle, dusty zone, and rim (Samples with whole-rock SiO_2 content of 60.9 and 55.7 wt%). (c) *Or–Ab–An* triangular plot of the clinopyroxene quartz diorite. (d) CaO–Na_2O (wt%) diagram of the clinopyroxene quartz diorite. The samples were those with whole-rock SiO_2 content of 60.9 wt%, 58.5 wt%, 57.9 wt%, and 55.7 wt %.

Table 4–1. Representative chemical analyses for porphyritic fine-grained tonalite.

Mineral	Plagioclase				
	unaltered			altered	
Position	rim	core	core	core	core
SiO_2	59.32	57.83	57.05	55.66	56.86
TiO_2	0.02	0	0.03	0.03	0.00
Al_2O_3	25.02	26.35	26.91	27.27	26.67
FeO*	0.87	0.11	0.24	0.20	0.12
MnO	0.04	0.05	0	0.02	0
MgO	0.91	0	0	0	0
CaO	6.43	8.45	8.97	9.66	8.78
Na_2O	6.75	6.58	6.07	6.03	6.09
K_2O	0.35	0.11	0.15	0.15	0.18
Total	99.74	99.48	99.44	99.02	98.75
O	8	8	8	8	8
Si	2.655	2.601	2.571	2.529	2.578
Ti	0.001	0	0.001	0.001	0
Al	1.320	1.397	1.429	1.460	1.425
Fe	0.032	0.004	0.009	0.008	0.005
Mn	0.001	0.002	0	0.001	0
Mg	0.061	0	0	0	0
Ca	0.308	0.407	0.433	0.470	0.426
Na	0.586	0.573	0.531	0.531	0.535
K	0.020	0.006	0.009	0.009	0.011
Total	4.987	4.991	4.983	5.009	4.982
An	33.71	41.25	44.52	46.58	43.86
Ab	64.09	58.10	54.58	52.58	55.04
Or	2.19	0.64	0.90	0.85	1.09

Mineral	Hornblende				
	unaltered			altered	
Position	core	core	core	core	core
SiO_2	43.74	43.30	43.44	43.22	44.06
TiO_2	1.33	1.39	1.69	1.48	1.36
Al_2O_3	8.88	9.37	9.31	9.17	8.80
FeO*	16.36	15.72	15.42	15.02	15.06
MnO	0.47	0.42	0.51	0.37	0.44
MgO	11.40	11.51	11.86	12.02	12.49
CaO	11.20	11.13	10.99	11.13	11.35
Na_2O	1.19	1.39	1.48	1.36	1.23
K_2O	0.87	0.94	0.99	1.00	0.81
Total	95.76	95.43	95.96	95.18	95.91
O	23	23	23	23	23
Si	6.707	6.648	6.628	6.645	6.703
Ti	0.153	0.160	0.194	0.171	0.156
Al	1.606	1.696	1.674	1.662	1.578
Fe	2.099	2.019	1.968	1.931	1.916
Mn	0.061	0.055	0.065	0.048	0.056
Mg	2.605	2.633	2.697	2.754	2.831
Ca	1.840	1.831	1.796	1.833	1.850
Na	0.353	0.413	0.438	0.406	0.363
K	0.171	0.183	0.192	0.197	0.156
Total	15.597	15.641	15.655	15.651	15.611
X_{Mg}	0.55	0.57	0.58	0.59	0.60
X_{Fe}	0.45	0.43	0.42	0.41	0.40

Mineral	Biotite				
	unaltered			altered	
position	core	core	core	core	core
SiO_2	34.80	33.58	35.27	35.62	35.34
TiO_2	3.38	7.18	3.67	4.67	4.20
Al_2O_3	14.69	13.46	14.56	14.61	14.11
FeO*	20.58	20.29	19.04	16.61	18.70
MnO	0.30	0.66	0.34	0.30	0.33
MgO	10.16	10.28	11.58	11.98	11.30
CaO	0	0	0.00	1.44	0.00
Na_2O	0.02	0.12	0.07	0.07	0.13
K_2O	10.36	9.47	10.17	9.29	10.12
Total	95.16	96.00	95.80	95.56	95.26
O	22	22	22	22	22
Si	5.472	5.248	5.470	5.455	5.502
Ti	0.399	0.843	0.428	0.538	0.492
Al	2.721	2.480	2.661	2.637	2.589
Fe	2.706	2.653	2.469	2.127	2.434
Mn	0.040	0.087	0.045	0.039	0.044
Mg	2.381	2.394	2.677	2.734	2.622
Ca	0	0	0.001	0.237	0
Na	0.006	0.036	0.022	0.021	0.038
K	2.079	1.888	2.011	1.815	2.011
Total	15.808	15.631	15.787	15.606	15.735
X_{Mg}	0.47	0.47	0.52	0.56	0.52
X_{Fe}	0.53	0.53	0.48	0.44	0.48

Mineral	Ilmenite (unaltered sample)			
SiO_2	0.06	0.85	0.43	1.82
TiO_2	50.98	51.51	51.58	49.86
Al_2O_3	0.02	0.02	0.02	0.03
Cr_2O_3	0.00	0	0	0.02
FeO*	39.91	41.29	41.24	42.10
MnO	5.89	5.25	5.44	4.46
MgO	0.10	0.11	0.14	0.01
CaO	0.56	1.23	0.81	0.20
Na_2O	0.02	0	0.02	0.02
K_2O	0.08	0.03	0.03	0.00
Total	98.36	100.29	99.71	99.30
O	6	6	6	6
Si	0.003	0.043	0.022	0.092
Ti	1.983	1.942	1.961	1.908
Al	0.001	0.001	0.001	0.002
Cr	0.000	0	0	0.001
Fe	1.726	1.731	1.744	1.791
Mn	0.258	0.223	0.233	0.192
Mg	0.008	0.009	0.011	0.001
Ca	0.031	0.066	0.044	0.011
Na	0.002	0	0.001	0.002
K	0.006	0.002	0.002	0.000
Total	4.017	4.016	4.018	4.000

*Total Fe reported Fe^{2+}.

Table 4–2. Representative chemical analyses for clinopyroxene quartz diorite.

Mineral	Plagioclase										
WR SiO_2 wt%	55.7 wt%		57.9 wt%			58.5 wt%			60.9 wt%		
Position	core	rim	core	rim	D zone	core	rim	dusty zone	core	rim	D zone
SiO_2	55.07	55.38	55.37	55.58	55.63	55.32	55.35	54.56	56.81	58.03	53.52
TiO_2	0.06	0	0.07	0.08	0.04	0.03	0.02	0.02	0.02	0.03	0.04
Al_2O_3	27.64	27.56	27.07	27.55	27.92	28.38	28.18	28.02	24.73	26.65	28.64
FeO*	0.21	0.21	0.30	0.31	0.31	0.23	0.31	0.17	0.15	0.12	0.30
MnO	0	0	0	0.01	0.02	0	0.01	0	0	0	0
MgO	0	0	0.01	0.01	0.02	0	0	0	0	0.01	0
CaO	12.19	9.74	9.87	9.07	11.39	9.36	7.17	12.11	8.86	6.04	12.34
Na_2O	4.47	5.84	6.24	7.03	4.82	5.76	7.64	4.79	9.34	8.14	4.90
K_2O	0.24	0.26	0.37	0.42	0.21	0.31	0.36	0.21	0.44	0.52	0.10
Total	99.87	99.00	99.30	100.07	100.37	99.43	99.06	99.91	100.40	99.57	99.85
O	8	8	8	8	8	8	8	8	8	8	8
Si	2.492	2.518	2.519	2.511	2.500	2.501	2.514	2.471	2.577	2.607	2.432
Ti	0.002	0	0.003	0.003	0.001	0.001	0.001	0.001	0.001	0.001	0.001
Al	1.474	1.477	1.452	1.467	1.479	1.513	1.508	1.496	1.322	1.411	1.534
Fe	0.008	0.008	0.011	0.012	0.012	0.009	0.012	0.006	0.006	0.005	0.011
Mn	0	0	0	0	0.001	0	0	0	0	0	0
Mg	0	0	0	0	0.001	0.002	0	0	0	0.001	0
Ca	0.591	0.474	0.481	0.439	0.549	0.454	0.349	0.588	0.431	0.291	0.601
Na	0.392	0.514	0.551	0.616	0.420	0.505	0.673	0.421	0.821	0.709	0.432
K	0.014	0.015	0.021	0.024	0.012	0.018	0.021	0.012	0.025	0.030	0.006
Total	4.972	5.008	5.038	5.072	4.975	5.002	5.078	4.996	5.184	5.056	5.018
An	59.31	47.26	45.69	40.69	55.98	46.48	33.45	57.61	33.73	28.24	57.85
Ab	39.32	51.26	52.29	57.09	42.82	51.69	64.55	41.23	64.29	68.87	41.57
Or	1.37	1.49	2.02	2.22	1.20	1.83	2.00	1.16	1.98	2.89	0.58

Mineral	Plagioclase			
WR SiO_2 wt%	57.9 wt% Autolith			
Type	inner zone		granoblastic zone	
Position	core	rim	core	rim
SiO_2	57.09	57.10	55.89	55.12
TiO_2	0.01	0	0.05	0.02
Al_2O_3	27.41	27.63	27.38	27.61
FeO*	0.29	0.22	0.21	0.25
MnO	0	0	0	0
MgO	0.01	0	0	0
CaO	6.14	5.01	9.27	8.93
Na_2O	8.23	9.09	6.09	6.97
K_2O	0.61	0.67	0.28	0.31
Total	99.79	99.72	99.17	99.21
O	8	8	8	8
Si	2.568	2.568	2.534	2.508
Ti	0	0	0.002	0.001
Al	1.453	1.465	1.463	1.481
Fe	0.011	0.008	0.008	0.009
Mn	0	0	0	0
Mg	0	0	0	0
Ca	0.296	0.241	0.450	0.436
Na	0.718	0.793	0.535	0.615
K	0.035	0.039	0.016	0.018
Total	5.082	5.115	5.008	5.067
An	28.22	22.49	44.95	40.76
Ab	68.45	73.92	53.41	57.55
Or	3.33	3.59	1.64	1.69

Mineral	Clinopyroxene	
Position	core	rim
SiO_2	52.95	53.21
TiO_2	0.20	0.38
Al_2O_3	0.75	0.80
FeO*	9.41	26.06
MnO	0.28	0.80
MgO	13.57	17.51
CaO	21.28	1.14
Na_2O	0.46	0.06
K_2O	0	0
Total	98.89	99.96
O	6	6
Si	1.997	2.018
Ti	0.006	0.011
Al	0.033	0.036
Fe	0.297	0.826
Mn	0.009	0.026
Mg	0.762	0.989
Ca	0.860	0.046
Na	0.034	0.004
K	0	0
Total	3.997	3.956
Wo	44.80	2.50
En	39.73	53.13
Fs	15.47	44.37
Mg#	71.97	54.49

Mineral	Biotite	
Position	core	rim
SiO_2	36.94	38.12
TiO_2	5.12	4.46
Al_2O_3	12.07	11.73
Cr_2O_3	0.08	0.03
FeO*	20.94	17.04
MnO	0.17	0.09
MgO	9.27	12.76
CaO	0.04	0.03
Na_2O	0.13	0.07
K_2O	11.28	10.59
Total	96.02	94.92
O	22	22
Si	5.730	5.827
Ti	0.597	0.513
Al	2.206	2.113
Cr	0.009	0.003
Fe	2.717	2.178
Mn	0.023	0.012
Mg	2.143	2.908
Ca	0.006	0.005
Na	0.038	0.020
K	2.232	2.065
Total	15.700	15.645
X_{Mg}	0.44	0.57
X_{Fe}	0.56	0.43

WR: whole-rock. D zone: dusty zone. *Total Fe reported Fe2+.

4–5 Discussions

4–5–1 Compositional change processes of the PFT

The PFT shows a peperitic texture at the boundary with the Wakino Sub-group as a host rock. Altered minerals such as chlorite, epidote, calcite, prehnite, and pumpellyite occur in PFT (Figs. 4–3b, 3c, 3d, 4–5b, and 4–5c). This assemblage of altered minerals suggests that the hydrothermal alteration proceeds under the neutral alteration zone at about 200–300°C (Inoue et al., 1995). The whole-rock SiO_2 content has a relatively limited compositional range from 63.2 to 65.1 wt%, whereas the alkali metals and alkaline earth metals (CaO, Na_2O, Ba, and Sr) have a wide range of variation (Fig. 4–8: CaO: 3.1–5.1 wt%, Na_2O: 2.0–4.8 wt%, Ba: 398–709 ppm, Sr: 281–669 ppm) , and the LOI values widely vary 0.9 to 5.8 wt%.

The change in LOI value is related to the content of alteration minerals on the thin section (Fig. 4–11). In addition, based on the results of whole-rock chemical composition analysis, the LOI value does not include the effect of iron valence because the range of change in Fe_2O_3 content is smaller than that of alkali metals and alkaline earth metals (Fig. 4–8). Therefore, the LOI indicates the degree of alteration of PFT. The LOI values reflect the degree of alteration in the texture and color of the lithofacies. The PFT itself, however, is tough even in samples with high LOI values, and no significant mineralization is observed under the microscope. To verify the effect of fractional crystallization, mass balance calculations were conducted to estimate the fractional minerals using the least-squares method for the samples with SiO_2 contents from 63.8 to 65.1 wt%. The calculated results show a large value of sum of squared residuals more than 3.8 (Table 4–3), suggesting that there is little validity of the fractional crystallization process during magmatic cooling. In other words, the PFTs are affected by compositional changes due to external compositional influences such as hydrothermal fluids. In particular, alkali metals and alkaline earth metals (CaO, Na_2O, Ba, and Sr) show compositional changes without any correlation with SiO_2 content (Fig. 4–8), therefore, these compositional change patterns of alkali

metals and alkaline earth metals are likely to be affected by hydrothermal alteration (Ishikawa et al., 1976; Large et al., 2001; Mizuta and Ishiyama, 2009). Based on the above data, the PFTs were classified into the Low-LOI group (0.9 < LOI < 1.5 wt%), Medium-LOI group (1.5 < LOI < 3.0 wt%) and High-LOI group (3.0 < LOI < 5.8 wt%) by the LOI values, which is strongly related to the degree of alteration of PFTs. Examining the process of compositional change of alkaline earth metals represented by Na_2O and Sr, which show remarkable compositional change. As Na_2O and Sr show remarkable compositional changes, I examine to reveal the process of compositional change of alkaline earth metals as exemplified by Na_2O and Sr. As a result, the Na_2O content tends to increase with LOI values from 0.9 to 5.0 wt% and decrease rapidly toward 5.8 wt%, and the Sr content tends to decrease with increasing LOI values (Fig. 4–12). The variation of Na_2O and Sr contents depends on each group (low-, medium-, and high-); the high-LOI group widely shows the Na_2O and Sr variations, and the medium-LOI group possesses the moderate their variations, while those of the low-LOI group are the smallest (Fig. 4–12).

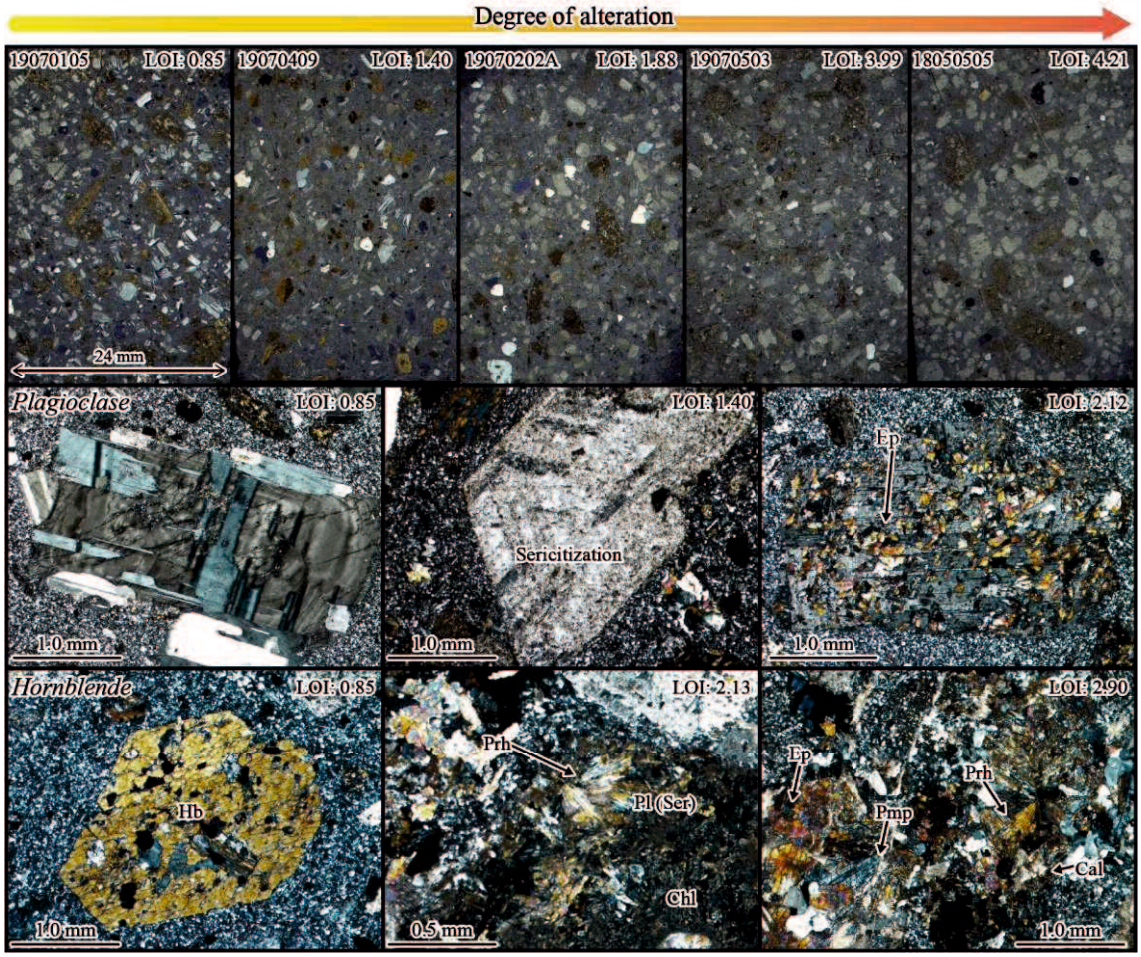

Figure 4–11. Relationship between LOI value (wt%) and lithofacies.

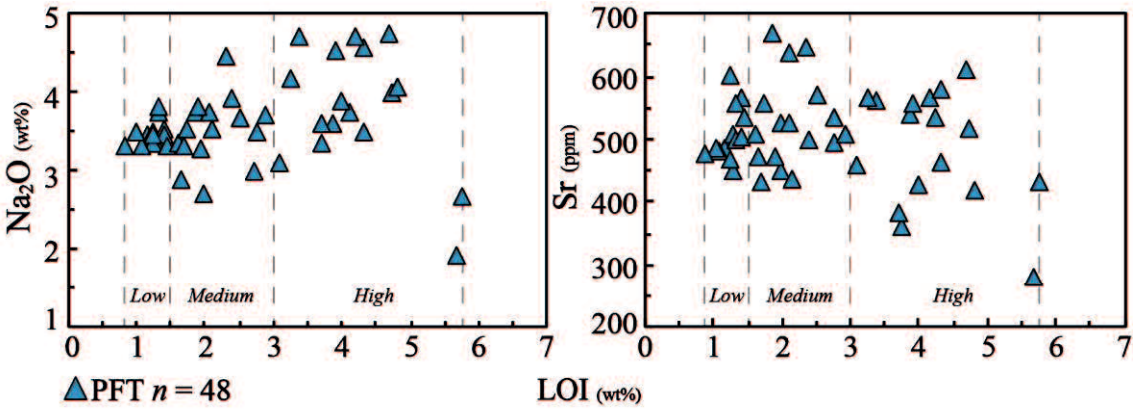

Figure 4–12. LOI–Na_2O (wt%) and –Sr (ppm) diagrams of the porphyritic fine-grained tonalite.

Then, the gains and losses of the major elements during the alteration was investigated to evaluate the effect of hydrothermal process. The PFT with an LOI of 0.9 wt% was used as the representative sample of free from alteration, and the examined gains and losses samples for the medium-LOI group (LOI value: 2.7 wt%) and the high-LOI group (LOI value: 5.7 wt%) are selected in this section. For the calculation of the gains and losses, I adopted the isovolumic gains and losses calculation (Humphris and Thompson, 1978a, b), which is a modified version of the equation of Gresens (1967). The isovolumic gains and losses calculation reported by Humphris and Thompson (1978a, b) assumes that aluminum (Al_2O_3) is immobile element, but it has been reported that not only aluminum but also titanium (TiO_2) and zirconium (Zr) are mobile in strongly acidic hydrothermally altered rocks and pyrophyllite deposits (Hida et al., 1996). Therefore, I calculated the isovolumic gains and losses assuming that the heavy rare-earth element Yb, which is considered to be immobile by Hida et al. (1996). The results are shown in Figure 4–13. The gains and losses of the samples of the low-, medium-, and high-LOI groups clearly show the effect of hydrothermal alteration, such as the addition of SiO_2, Al_2O_3 and K_2O, and the dissolution of CaO and Na_2O (Fig. 4–13). The high-LOI group is of the largest mass-balance change (Fig. 4–13). Based on the isovolumic gains and losses diagram, Figure 4–14 shows diagram of a contour map of the whole-rock compositions in the western part of PFT using highly mobilized elements during the hydrothermal alteration. The contour map was created using Graph-R, and the kriging method was used for interpolation. The contour map shows the gains and losses patterns for selected elements, and these patterns are similar to each other (Fig. 4–14). Therefore, the map indicates that the influence of hydrothermal activity occurs highly in the interior rather than in the exterior of the PFT body (Fig. 4–14). This suggests that the hydrothermal activity did not come from the outside, but rather from the inside of the magma reservoir, which would have been continuously active since the end of the magma activity.

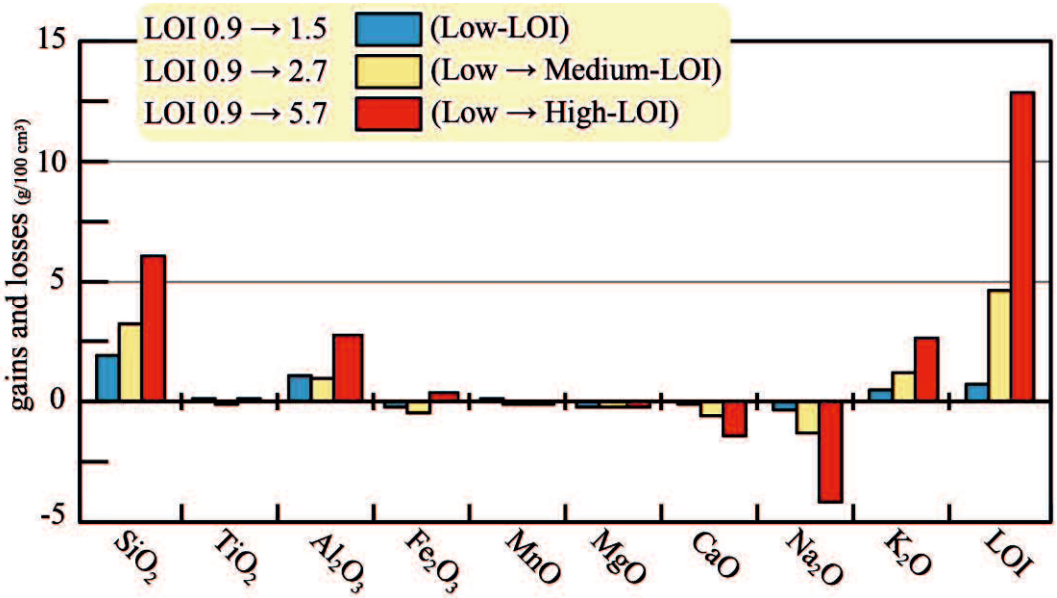

Figure 4–13. Gains and losses diagram using the model of Humphris and Thompson (1978b) with LOI content of 0.9 to 1.5 (Low-LOI group), 0.9 to 2.7 (Low- to Medium-LOI group), and 0.9 to 5.7 (Low- to High-LOI group).

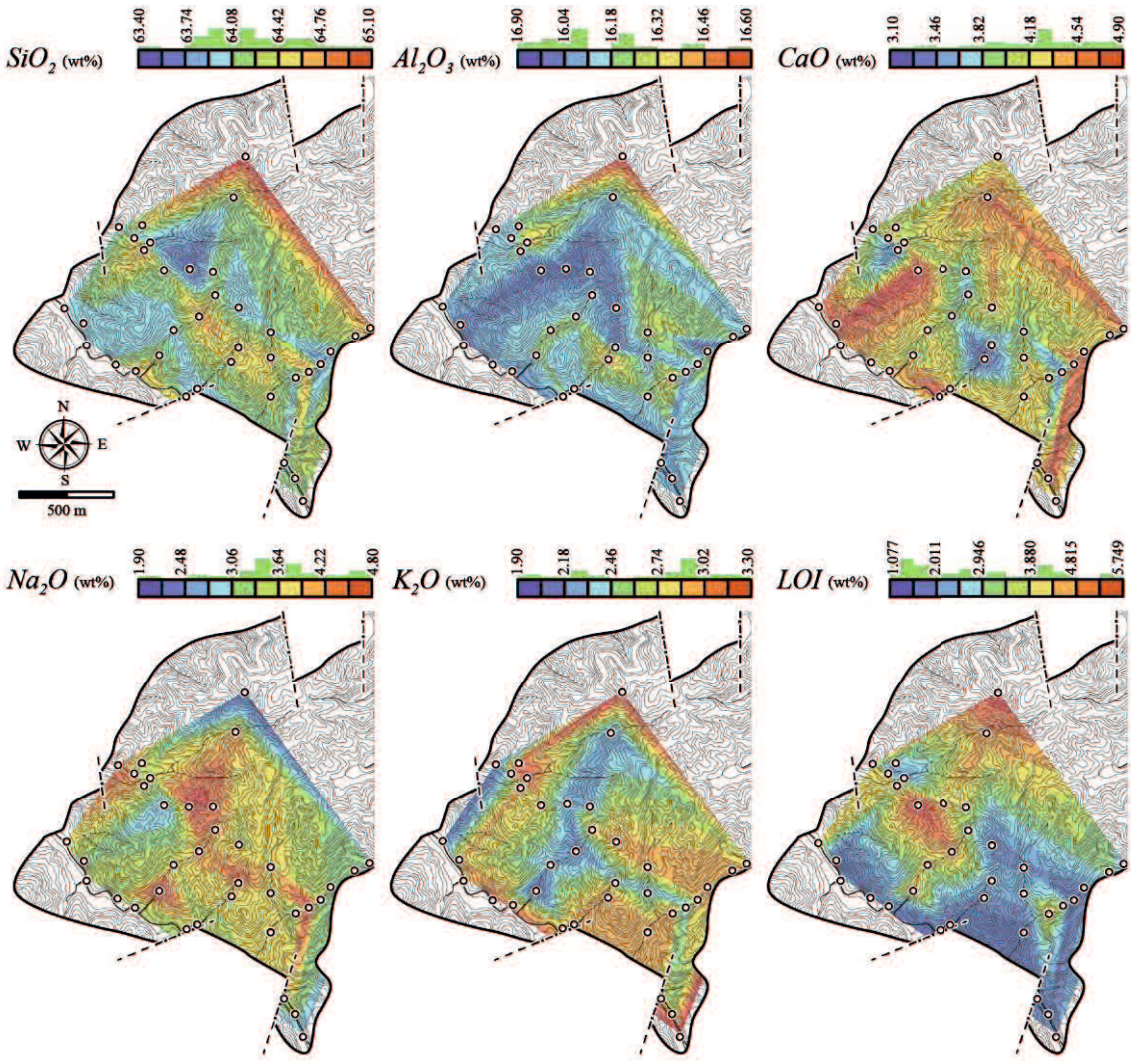

Figure 4–14. Contour maps for the whole-rock composition (SiO_2, Al_2O_3, CaO, Na_2O, and K_2O) and LOI of porphyritic fine-grained tonalite distributed western part of this study area. Dots indicate sampling sites. Horizontal variation maps were created using Graph-R (S-NEXT Co., Ltd.).

4–5–2 Compositional change processes of the CQD

The CQD intrudes the Wakino sub-group and PFT, with a clear boundary, and shows a flow structure mainly alignments of elongated plagioclase and clinopyroxene (Figs. 4–5a and b). Under the microscope, the CQDs can be roughly divided into two types; 1) samples containing dusty zoned plagioclase, and 2) samples showing weak accumulation texture, and some samples in the former capturing an autolith with homogeneous mineral assemblage (Figs. 4–5a, 6a, b, c, and d). The dusty zoned plagioclase was probably formed by magma mixing. Tsuchiyama (1985) determined the formation of dusty zoned plagioclase by the melting experiment in the *Di–An–Ab* (diopside–anorthite–albite) system, and confirmed that dusty zones are formed when plagioclase crystals coexist with a liquid that has a higher liquidus temperature rather than the equilibrium conditions with specific compositions. In the CQD sample, the aggregation of small melt inclusions formed the dusty zone. According to the results of melting experiment, such melt inclusions would be derived from partially molten products of a plagioclase that reacted with the high-temperature magma during magma mixing. As shown in Figure 4–10, the *An* content of plagioclase core decreases continuously from 60.0 to 32.2% with increasing whole-rock SiO_2 content. On the other hand, the composition near the dusty zone of plagioclase in the High-SiO_2 group (SiO_2 58.5–60.9 wt%) is *An* 57.6–64.4 % (Figs. 4–10a and c). This composition is similar to the *An* composition (49.8–60.0 %) of the plagioclase core in the low-SiO_2 group (SiO_2 55.7 wt%) (Figs. 4–10b and c). In addition, the whole-rock sample with SiO_2 = 57.9 wt% contains an autolith with fine-grained granoblastic texture at the outer rim. The granoblastic outer rim would be recrystallized by the thermal effect during incorporation into the low-SiO_2 group (Figs. 4–6c and d). The *An* content of plagioclase in the outer rim is similar to those of plagioclase in the autolith-capturing sample (SiO_2 57.9 wt%), and the inner plagioclase is similar to those of plagioclase in the higher-SiO_2 group (SiO_2 60.9–58.5 wt%) (Figs. 4–6c, d, and 4–10). This suggests that autolith is derived from the high-SiO_2 group and

captured by the low-SiO_2 group. The dusty zoned plagioclase suggests that the inner part of dusty zoned plagioclase once has crystallized from the high-SiO_2 magma, after that such plagioclase was captured by the low-SiO_2 magma to form the dusty zone. Because CQDs show a flow structure, the behavior of the crystals and autoliths in the CQD convective magma reservoir would have been controlled under the partially non-equilibrium conditions resulting from different processes; direction of magma flow and cooling rates. As a result of these processes described above, fractional crystallization, accumulation, and mixing of differentiated magma and parent magma are assumed to have occurred in a single magma reservoir.

To verify such hypothesis, geochemical modeling of fractional crystallization, accumulation, and magma mixing was examined. Firstly, the process of fractional crystallization and accumulation was investigated. Figure 4–15a shows a variation diagram of trace element compositions with the calculated fractionation and accumulation vectors (Fig. 4–15a). The inferred parental magma adopted the compositions of sample with SiO_2 = 57.7 wt% containing little dusty zoned plagioclase and rarely shows accumulation texture. The partitioning coefficients reported by Rollinson (1993) and Arth (1976) were used for calculation of fractionation and accumulation vectors utilizing the equation of Rayleigh fractionation and accumulation model. Figure 4–15a indicates that the compositional change is influenced by the fractionation of plagioclase, clinopyroxene and biotite in the high-SiO_2 group, and is efficient of the accumulation of mainly plagioclase, clinopyroxene and orthopyroxene in the low-SiO_2 group (Fig. 4–15a). The chemical compositions of these minerals and whole-rock samples were used for the calculation of fractionated phases by mass balance calculation (Tsune, 2005), and the differentiation and accumulation processes of magma were investigated by the Rayleigh models for some trace elements to create spider diagrams (Fig. 4–15b). The result of the mass balance calculations is shown in Table 4–3, and the partition coefficients of the elements used in the Rayleigh model and the equations used in the

model calculations are listed in the Appendix 4–3. As a result, the melt compositions of most differentiated sample (High-SiO_2 group) and accumulated sample (Low-SiO_2 group) in CQD could be reproduced from the same starting material (SiO_2 57.7 wt%) (Fig. 4–15b). In contrast, there is obscurity trend in Figure 4–15a using trace elements due to controlled by mineral amounts and effect of magma mixing. Figure 4–16 shows the inferred magmatic processes plotting the data of high- and low-SiO_2 group with an inferred starting composition (white star) and a calculated cumulate composition (red star). The measured samples including high- and low-SiO_2 groups are almost plotted within the elongated green field that connects the calculated cumulate (red star) to the highest SiO_2 sample through the inferred starting composition (with star). If the CQD is aligned in the green field the compositional change of CQD was produced by the process of unmixing between the differentiated melt and the accumulated phase (Fig. 4–16). As a result, most of the compositions fall into the expected field (green field), indicating a mixture of differentiated melt and segregated accumulated phases. Some samples of the low-SiO_2 group are plotted out of the green field but plotted on the vectors towards the specific minerals, indicating accumulation of such minerals in each sample. In other words, the CQD experienced unmixing (mixing with differentiated melt and accumulation phase) with accumulation and fractionation in a closed system of magma reservoirs, and the compositional change of the CQD is considered to have progressed. In addition, plagioclase with dusty zone and the autoliths with different plagioclase compositions in the outer and inner parts are present in the CQDs. It is assumed that these textures were formed as a result of mixing or trapping of some of the crystals and melts while flowing through the magma reservoir in a crystal mash condition.

Table 4–3. Results of mass balance calculation using the major elements for whole-rocks and minerals of the clinopyroxene quartz diorite and porphyritic fine-grained tonalite.

CQD	nitial magma	Final magma	Subtracted phases			
			Pl n=30	Cpx n=18	Bt n=2	Ilm n=5
Sample No.	20040602	18050512	18050514	18050514	18050514	18050514
			WR SiO_2 57.9	WR SiO_2 57.9	WR SiO_2 57.9	WR SiO_2 57.9
SiO_2 (wt%)	57.65	60.89	55.51	51.93	36.92	0.03
TiO_2	1.04	0.87	0.04	0.48	5.16	50.68
Al_2O_3	16.83	16.79	27.50	2.81	12.00	0.01
FeO*	7.09	6.38	0.33	15.82	20.74	45.70
MnO	0.12	0.11	0.01	0.49	0.19	2.29
MgO	3.54	2.98	0.02	12.78	9.40	0.08
CaO	6.71	5.76	8.96	14.89	0.03	0.08
NaO	3.29	3.4	6.70	0.64	0.14	0.01
K_2O	1.83	2.13	0.40	0.22	11.35	0
P_2O_5	0.21	0.19	0	0	0	0
Calculated result (%)		73.49	14.27	8.64	3.08	0.52
Degree of crystallization, 26.51%						
Fractionated proportions (%)			53.82	32.59	11.62	1.97
Sum of squares, 0.626						

CQD (+Opx)	nitial magma	Final magma	Subtracted phases					
			Pl n=30	Cpx n=18	Opx n=21	Bt n=2	Ilm n=5	
Sample No.	20040602	18050512	18050514	18050514	20040405	18050514	18050514	Calc cum
			WR SiO_2 57.9	WR SiO_2 57.9	WR SiO_2 55.7	WR SiO_2 57.9	WR SiO_2 57.9	
SiO_2 (wt%)	57.65	60.89	55.51	51.93	53.43	36.92	0.03	51.75
TiO_2	1.04	0.87	0.04	0.48	0.32	5.16	50.68	1.39
Al_2O_3	16.83	16.79	27.50	2.81	0.95	12.00	0.01	16.58
FeO*	7.09	6.38	0.33	15.82	24.18	20.74	45.70	9.93
MnO	0.12	0.11	0.01	0.49	0.59	0.19	2.29	0.22
MgO	3.54	2.98	0.02	12.78	18.95	9.40	0.08	6.32
CaO	6.71	5.76	8.96	14.89	1.45	0.03	0.08	8.17
NaO	3.29	3.4	6.70	0.64	0.03	0.14	0.01	3.47
K_2O	1.83	2.13	0.40	0.22	0	11.35	0	1.37
P_2O_5	0.21	0.19	0	0	0	0	0	0.08
Calculated result (%)		72.33	15.37	7.90	1.30	2.53	0.57	
Degree of crystallization, 27.67%								
Fractionated proportions (%)			55.54	28.55	4.71	9.12	2.07	
Sum of squares, 0.396								

PFT	nitial magma	Final magma	Subtracted phases		
(Low-SiO_2→High-SiO_2)			Pl n=12	Bt n=31	Ilm n=6
Sample No.	20040402	18050505	20040402	20040402	20040402
			WR SiO_2 63.8	WR SiO_2 63.8	WR SiO_2 63.8
SiO_2 (wt%)	63.8	65.09	57.83	33.58	0.85
TiO_2	0.64	0.66	0.00	7.18	51.51
Al_2O_3	15.78	16.56	26.35	13.46	0.02
FeO*	5.82	5.87	0.11	20.29	41.29
MnO	0.13	0.09	0.05	0.66	5.25
MgO	2.41	2.26	0.00	10.28	0.11
CaO	4.84	4.22	8.45	0.00	1.23
NaO	3.53	1.95	6.58	0.12	0.00
K_2O	2.4	3.32	0.11	9.47	0.03
P_2O_5	0.18	0.19	0.00	0.00	0.00
Calculated result (%)		95.20	5.06	1.25	-1.50
Degree of crystallization, 4.80%					
Fractionated proportions (%)			105.29	26.00	-31.29
Sum of squares, 3.868					

WR: whole-rock, CQD: clinopyroxene quartz diorite, PFT: porphyritic fine-grained tonalite.

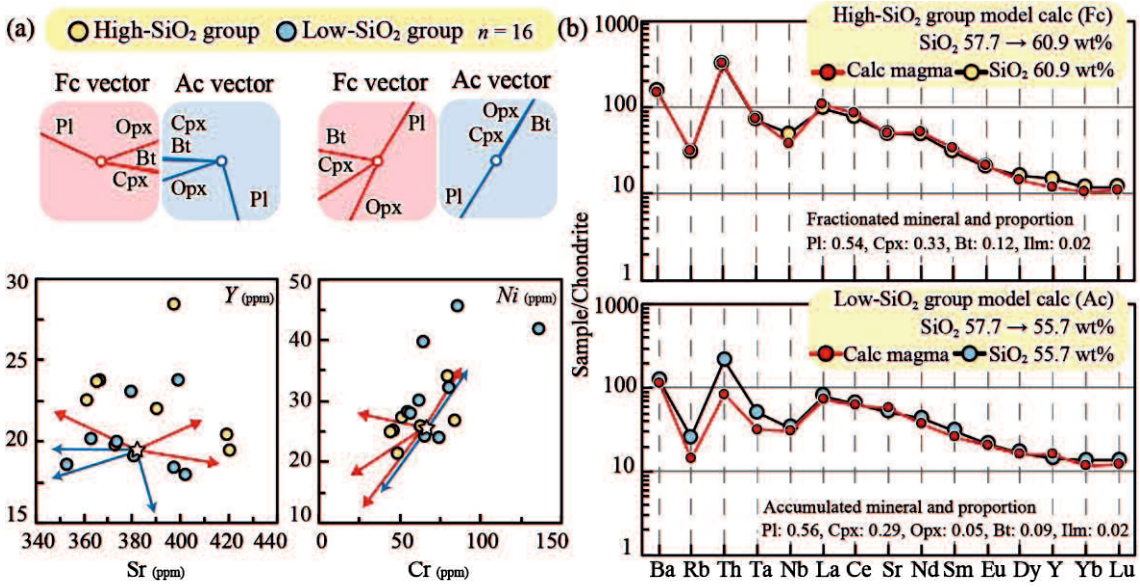

Figure 4–15. (a) Sr–Y (ppm) and Cr–Ni (ppm) diagrams of the High- and Low-SiO_2 group for the clinopyroxene quartz diorite. Fractionated and accumulated vectors were calculated by the Rayleigh model using partition coefficient after Arth (1976) and Rollinson (1993). (b) Results of fractional crystallization and accumulation modeling for High- and Low-SiO_2 group. Normalized values of C1 chondrite are after Sun and McDonough (1989). The partition coefficients used in the Rayleigh fractionation modeling are listed in Appendix 4–3.

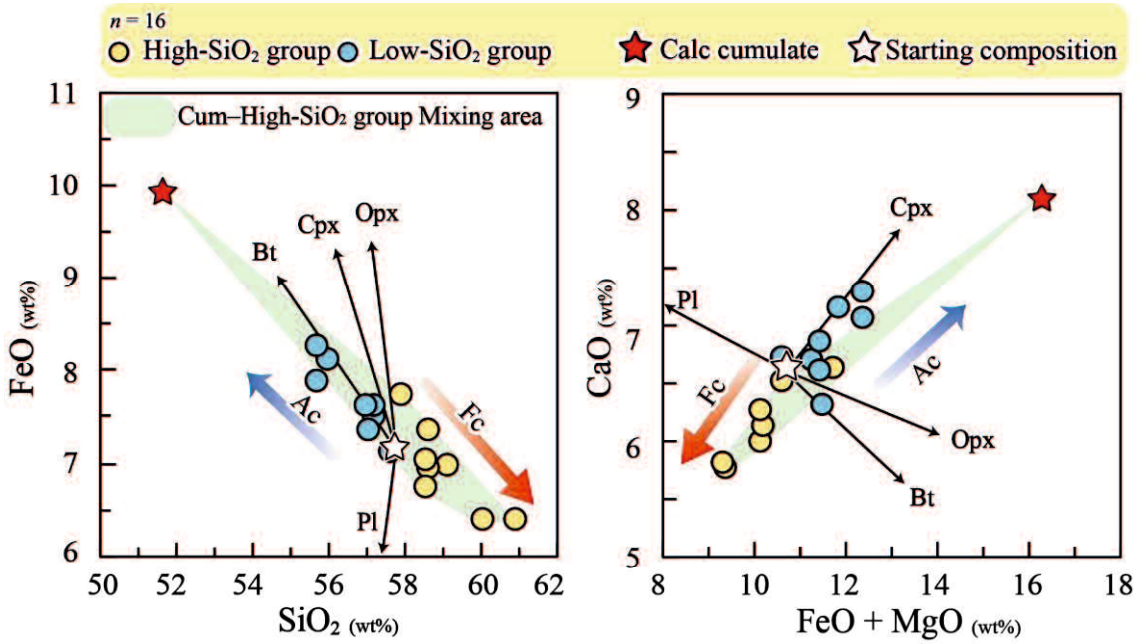

Figure 4–16. SiO_2–FeO (wt%) and FeO+MgO–CaO (wt%) diagrams of the clinopyroxene quartz diorite. The green fields indicate the compositional ranges resulting from the mixing between the high-SiO_2 group samples and the calculated cumulate rocks. The black arrows indicate the mineral composition of the fractionated minerals.

4–6 Igneous activity model of the PFT and CQD

(1)The PFT intrudes into the Wakino sub-group of the host rock as an elliptical body extending in a northeast-southwest direction. At the boundary with the host rock, a peperitic texture and calcite veins are developed. The PFT is injected by veins composed of calcite, quartz, prehnite and pumpellyite, and the contact area is pale in color, indicating the influence of hydrothermal alteration. On the other hand, the CQD intrudes the PFT and the Wakino sub-group with a sharp boundary, and generally develops a weak flow structure with an arrangement of plagioclase and clinopyroxene. The CQD is divided into two lithofacies, showing weak accumulated rocks and containing dusty zoned plagioclase (Fig. 4–17).

(2)The compositional variation of the PFTs is relatively narrow (63.2–65.1 wt%

whole-rock SiO_2 content), whereas the variation of alkali metals and alkaline earth metals (CaO, Na_2O, Ba and Sr) widely changes (CaO: 3.1–5.1 wt%, Na_2O: 2.0–4.8 wt%, Ba: 398–709 ppm, Sr: 281–669 ppm), and LOI values vary widely from 0.9 to 5.8 wt%. The results of isovolumic gains and losses calculations showed that the LOI values increased with the addition of SiO_2, Al_2O_3, and K_2O, and with the dissolution of CaO and Na_2O. The contour map of these elements and LOI values shows that the influence of hydrothermal activity on the gains and losses is strong in the interior of the PFT body rather than in the exterior. This suggests that the hydrothermal fluids were not transported from the outside, but rather came from the inside of the magma reservoir. The hydrothermal activities would, therefore, be continuously acted since the end of the magma cooling (Fig. 4–17).

(3)The compositional change of the CQD is thought to proceed through unmixing (mixing of differentiated melt and accumulation phase), essentially occurring with accumulation and fractional crystallization in a closed system magma reservoir, in terms of the accumulated texture, the abundance of plagioclase with dusty zones, the abundance of autolith, and model calculations. It is also inferred that such magmatic processes occur in the closed magma reservoir under the phenomenon of the convective crystal mash (Fig. 4–17).

(4) The Cretaceous igneous activity in northern Kyushu started from a shallow intrusive porphyritic body (and/or volcanic rocks) such as PFT, transitioned to hydrothermal activity with alteration, then to large-scale igneous activity, Northern Kyushu batholiths scale via stock-like plutonic activity.

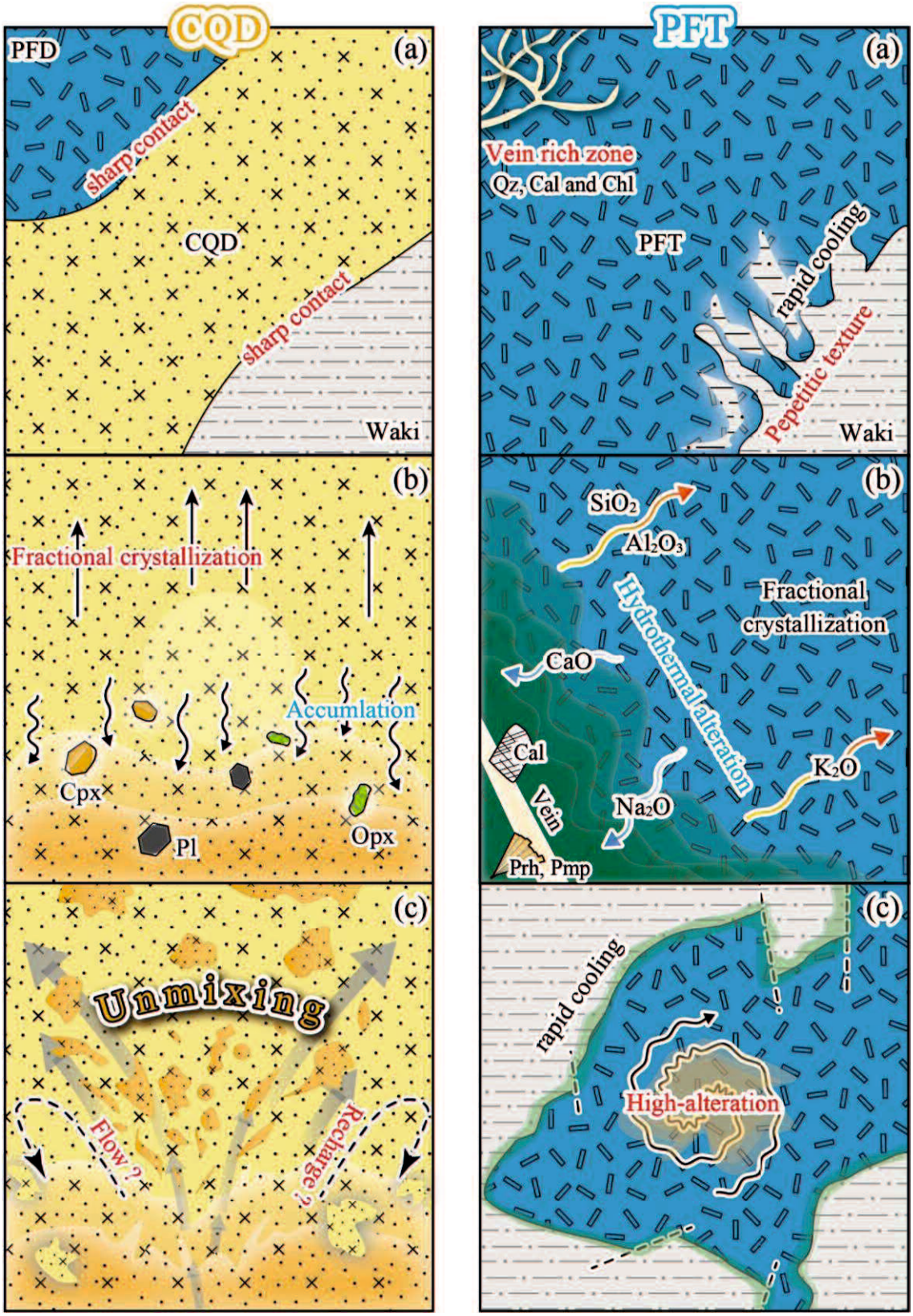

Figure 4–17. Illustration for magmatic activity models of the northern part of Shaku-dake area.

5 Kita-taku area

5–1 Introduction

The Cretaceous granitoid batholith is exposed over an area of about 100 km from east to west and 50 km from north to south in northern Kyushu (Figs. 1–1), showing zircon U–Pb ages of 116–102 Ma (Adachi et al., 2012; Tiepolo et al., 2012; Miyazaki et al., 2018; Yuhara et al., 2019a, b; Yuhara et al., 2020). Detailed description of some bodies of the Cretaceous batholith in the northern Kyushu is reported in the previous chapters, chapters 2, 3, and 4.

Throughout Earth's history, mantle-derived mafic magma has played an important role as a heat-supplying carrier from the mantle to the crust (e.g., Maclennan et al., 2004). The mantle-derived mafic magma intrudes the crust to transfer heat and materials from the mantle to the crust. Such primitive mafic magmas retain in their chemical composition and/or properties of the mantle that strongly constrains the magma-forming field and mechanism of magma generation from the physical-chemical conditions at the time of their origin.

The Cretaceous Northern Kyushu batholith is also scattered with small-scale mafic bodies that are considered to be parts of mafic magmatic activity (e.g., Karakida, 1985; Owada and Kamei, 2010). However, due to the small size and poor exposure of these mafic bodies, there have been few studies on the characteristics of these mafic bodies, such as crystallization, magmatic and growth processes. In recent years, the mafic bodies associated with the Northern Kyushu batholith have been studied in detail, and more data specific to small-scale bodies such as magma characteristics and growth processes have been obtained (Tiepolo et al., 2012; Eshima and Owada, 2018; Eshima et al., 2019; Eshima et al., 2020; Muraoka et al., 2020; Eshima, 2021a, b). The mafic bodies associated with the Northern Kyushu batholith show a number of mixing texture (e.g., MME) (Yada and Owada, 2003; Yuhara and Uto, 2007; Yuhara and Masaki, 2013; Eshima et al., 2019, 2020). In

addition, zircon U-Pb geochronological studies have supported the coeval activity of mafic and felsic magmas (Nakajima et al., 2004; Nakajima et al., 2021). This suggests that such mafic magmatic activity occurred at the same time as the large-scale igneous activity during the formation of the Northern Kyushu batholith. On the other hand, the petrological features of the mafic rocks have been not well understood yet. The mafic rocks showing mixing texture certainly reflect some kind of liquid composition, and their whole-rock chemical compositions are generally differentiated. Therefore, it is difficult to assess the degree of contamination by the surrounding granitic magma and to directly examine the characteristics of the source mantle. In order to understand the characteristics and origin of the mafic magmas in the Northern Kyushu batholith, it is necessary to examine compositions of primitive liquid inferred from volcanic rocks or cumulates. Such primitive liquid can estimate the coexisting mantle properties.

The mafic rocks mainly gabbro in the Kita-taku area, Saga Prefecture, have been studied by Akagi (1935) and Oshima (1961), but have not been the subject of much investigation since these studies. In recent years, Kamei et al. (2004) proposed a discrimination diagram using chemical compositions of whole-rock and clinopyroxene (Cpx) dividing a series of high-Mg andesite (HMA), and adopted it into the gabbro from the Kita-taku area. However, detailed geological and petrological data including photomicrographs, modal composition, whole-rock chemical composition, and mineral chemical composition have not been reported. In chapter 5, the geological information and essential petrological data and discuss the parent magma and crystallization process of the gabbro from the Kita-taku area.

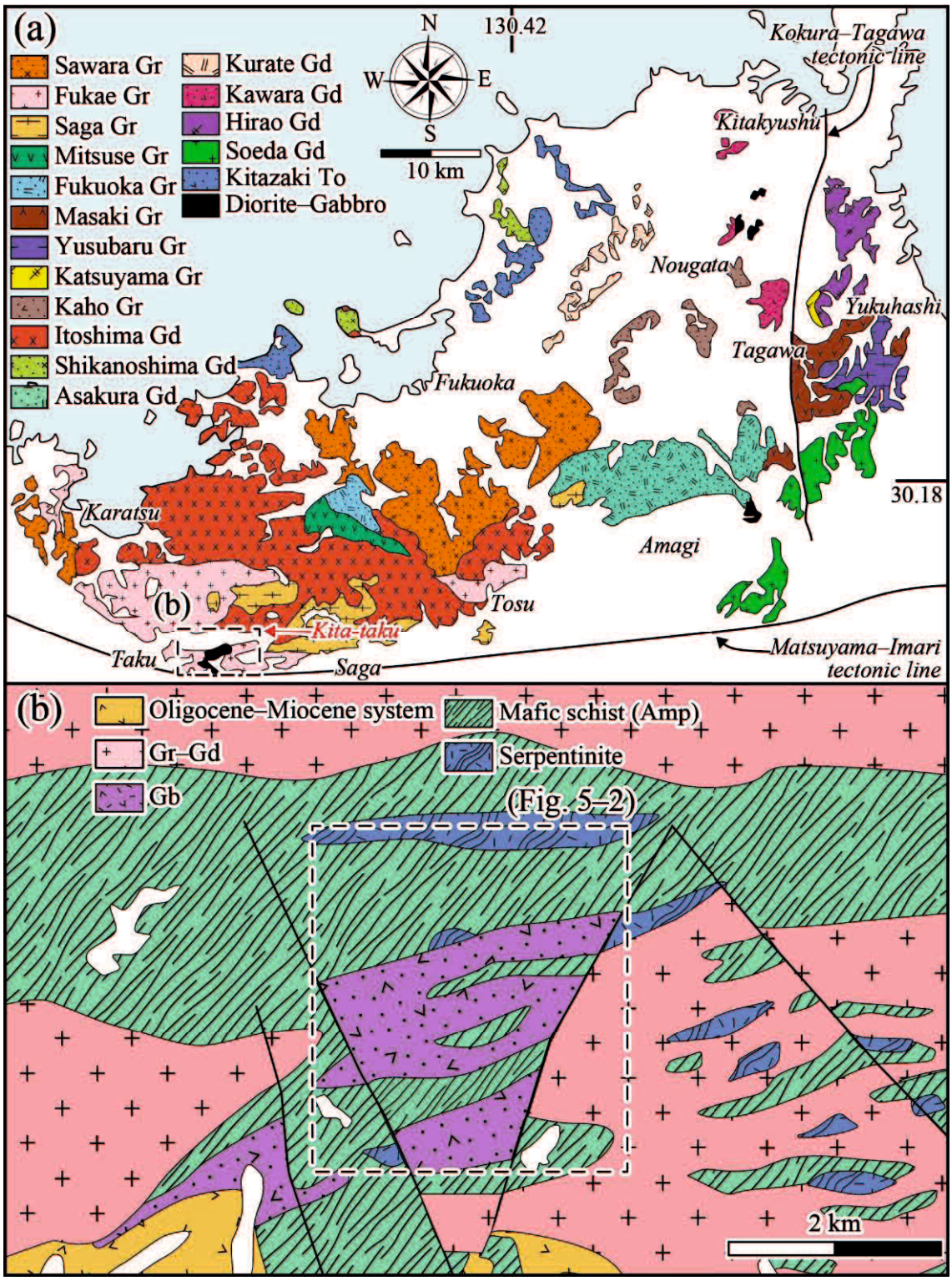

Figure 5–1. (a) Simplified geological map of the Northern Kyushu batholith (Karakida, 1985; Owada and Kamei, 2010). (b) Simplified geological map of the Kita-taku region (Akagi, 1935). Gr: granite, Gd: granodiorite, To: tonalite, Gb: gabbro, and Amp: amphibolite.

5–2 Geological overview

The geology of the Kita-taku area is composed of amphibolite and serpentinite as host rocks, and the gabbro, granite and small-scale dikes as intrusive rocks (Figs. 5–1, 5–2, and 5–3). The amphibolite and serpentinite are also observed as lens-like xenoblocks in the gabbro. The serpentinite generally occurs as lenses and thin layers within the amphibolite; however, it thrusts over the amphibolite with almost flat boundary in the northern part of the Kita-taku area (Fig. 5–3). The gabbro is divided into Cumulate group and Gabbroic group, and the Cumulate group is subdivided into olivine (Ol) gabbronorite–Ol bearing pyroxenes (Pxs: Cpx and Opx) hornblendite (Type 1: (spinel: Spl) Ol-Cpx-Opx orthocumulate), Ol gabbronorite (Type 2: Ol-Cpx-Pl adcumulate.), Cumulus clinopyroxene (Cpx) gabbro (Type 3: Cpx-Pl-(Hb) orthocumulate), and Cumulus hornblende (Hb) gabbro (Type 4: Pl-Hb layered adcumulate), while the Gabbro group is divided into Foliated Hb gabbro (Type 5), Mixed Hb gabbro (Type 6), and Pegmatitic Hb gabbro (Type 7) (Table 5–1). The distribution of the Cumulate group (except for Type 4) is complicated and each type encompasses the other. On the other hand, the Gabbro group is exposed as a narrow band coexisting with the Cumulate group (Figs. 5–2 and 5–3). As described above, the gabbro in this study area is composed of various kinds of rocks, and is tentatively called as the Kita-taku mafic complex. The granitoids are distributed in the western part of this study area and intrude of the Kita-taku mafic complex. The granitoids would be of the Fukae granite according to the geological map of Kubo et al. (1993), and characteristically contain muscovite as a primary phase. The small-scale dikes are porphyritic fine-grained diorite (PFD) and trondhjemite (Tdh), which sometimes occur as composite dikes. Among these rocks, the granite has been reported to have the biotite K–Ar age of 91–95 Ma (Kawano and Ueda, 1966; Kita-hata village History codification committee, 2008) and the Rb–Sr whole-rock and mineral age of 86.7 ± 2.2 Ma (Owada et al., 1999). In addition, newly determined zircon U-Pb ages of the foliated Hb gabbro (Type 5) that is coeval with the Cumulus group and the

trondhjemite give ages of 105.8 ± 0.5 Ma and 105.9 ± 0.5 Ma, respectively. These ages are similar to those of early to late Cretaceous igneous activity in northern Kyushu.

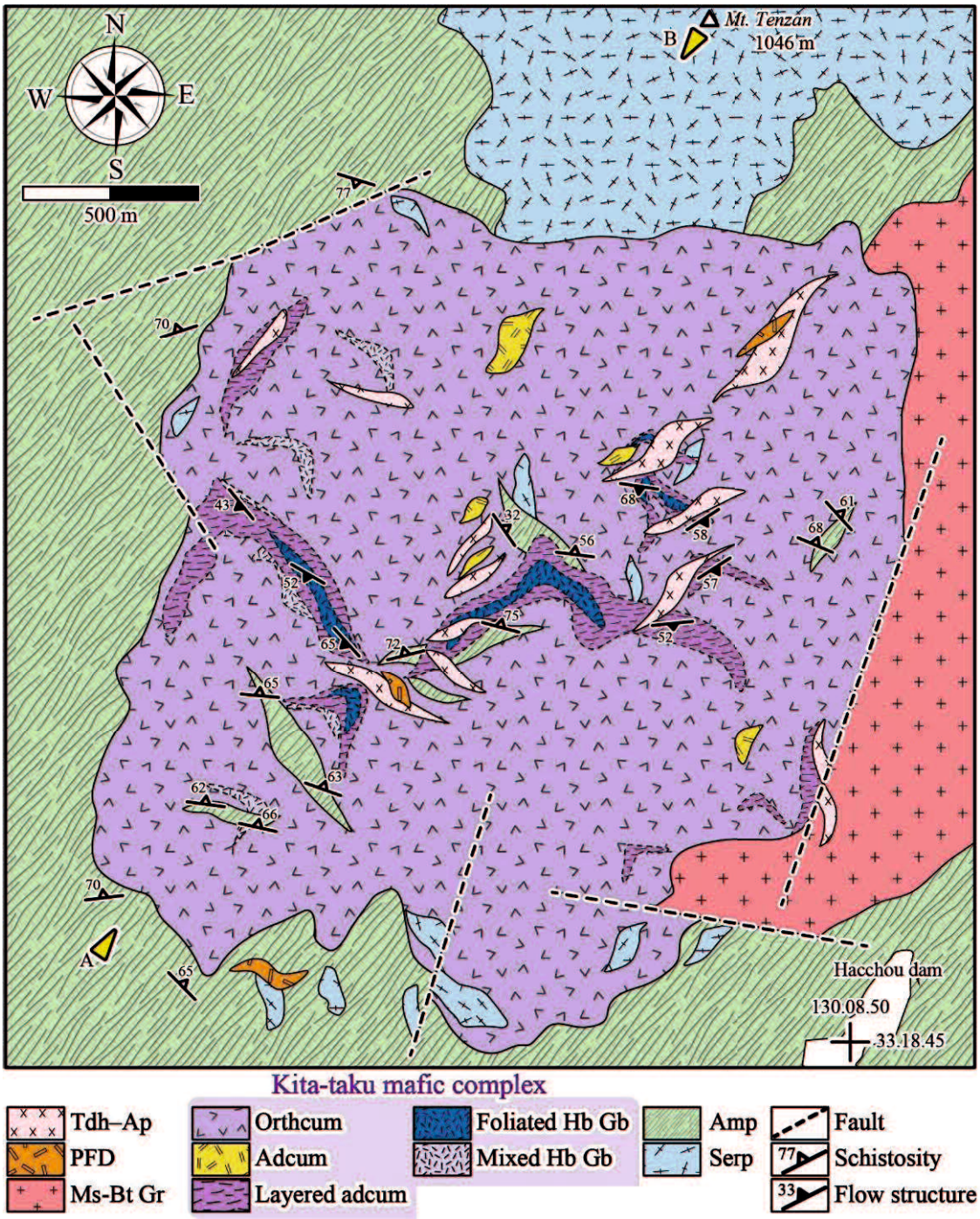

Figure 5–2. Geological map of the study area. Tdh: trondhjemite, Ap: aplite, PFD: porphyritic fine-grained diorite, Gr: granite, Gb: gabbro, Amp: amphibolite, Serp: serpentinite, cum:cumulate, Ms: muscovite, Bt: biotite, and Hb: hornblende.

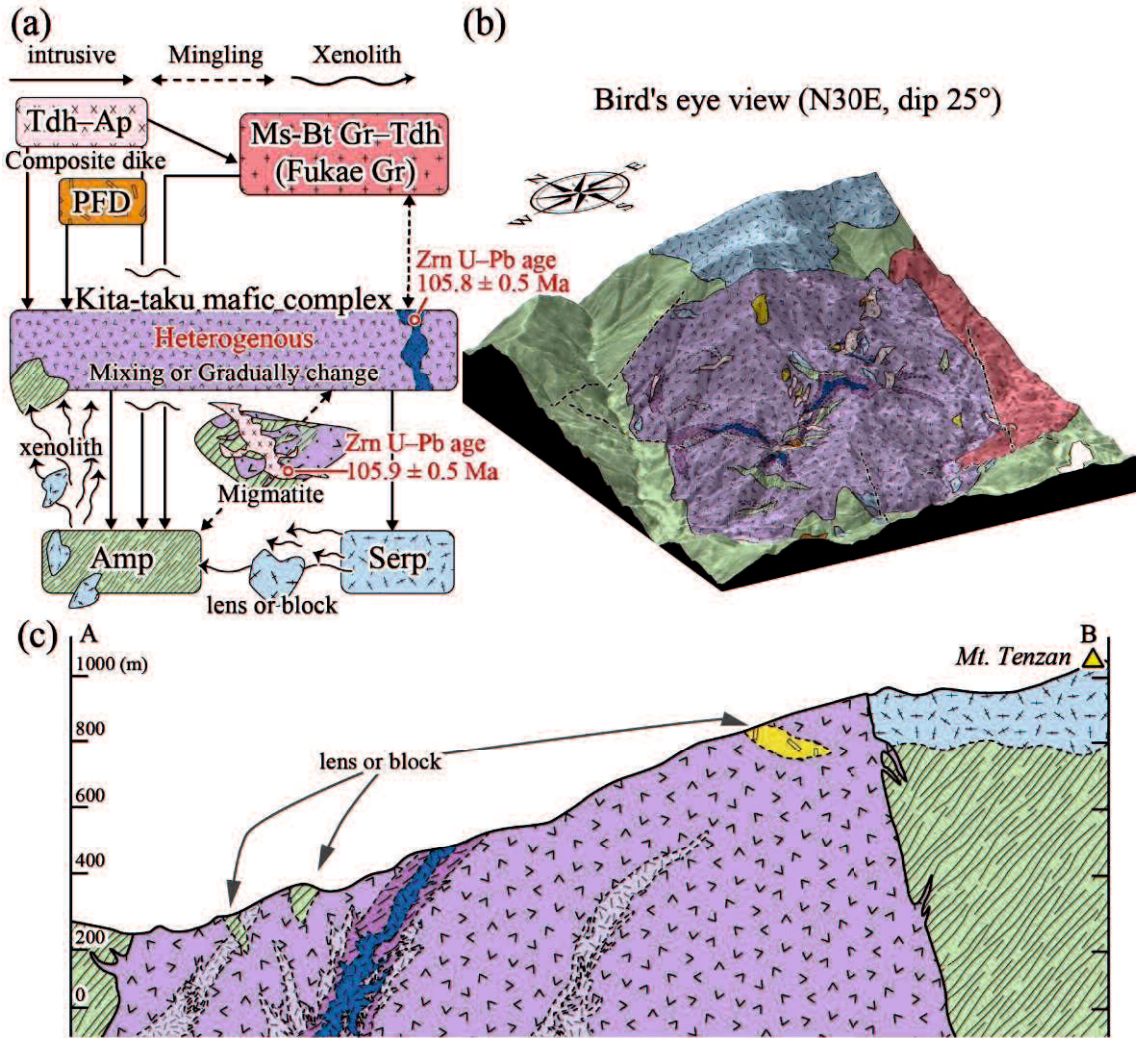

Figure 5–3. (a) Intrusive relationships between igneous and sedimentary rocks in the study area. (b) Bird's-eye view of the study area (N30E, dip angle 25°). (c) Cross-sections of the study area along lines A–B in Figure 5–2. Abbreviations are show in caption of Figure 5–2.

Table 5–1 Summary of textural observations for Kita-taku mafic complex.

Lithofacies	Cm. assem.	Type#	Characteristics	CrSpl	Ol	Cpx	Opx	Pl	Hb	Bt	Other
Cumulate group											
Ol Gbn–Ol ber Pxs Hbd	(Spl) Ol-Cpx-Opx	1	Orthocumulate	Tr	○	○	○	△	△		
Ol Gbn	Ol-Cpx-Pl	2	Adcumulate		○	○	△	○	△		
Cm Cpx Gb	Cpx-Pl-(Hb)	3	Orthocumulate			○		○	◎		
Cm Hb Gb	Pl-Hb	4	Adcumulate, Layered			□		○	○		Fe-Ti Ox
Gabbro group	Min. assem.										
Fo Hb Gb	Pl-Hb	5	Foliated, Fine-grained					○	○	○	Fe-Ti Ox
Mx Hb Gb	Pl-Hb	6	Mixing texture, dusty Pl			□		○	○		Fe-Ti Ox
Peg Hb Gb	Pl-Hb, Pxs	7	Pegmatitic. Pxs bearing			○	○	○	○		Fe-Ti Ox

Gbn: gabbronorite, Hbd: hornblendite, Gb: gabbro, Cm: cumulus, Fo: foliated, Mx: mixing, Peg: pegmatitic, CrSpl: chromian spinel, Ol: olivine, Cpx: clinopyroxene, Opx: orthopyroxene, Pl: palagioclase, Hb: hornblende, Bt: biotite, Ox: oxide, and Tr: trace. ○ cumulus mineral △ intercumulus mineral □ pseudomorph

5–3 Petrography of the Kita-taku mafic complex and related intrusive rocks

The Kita-taku mafic complex is divided into two groups, the Cumulate group and the Gabbro group, based on the presence or absence of cumulus texture. The Cumulate group can be subdivided into Type 1 to 4 based on the type of cumulus minerals and texture, while the Gabbro group can be subdivided into Type 5 to 7 based on the texture (Table 5–1). In this section, I describe the petrographic characteristics of each type, and the accompanying granite, trondhjemite dike, and PFD dike.

5–3–1 Occurrence and petrography of the Cumulate group (Type 1 to 4)

As described above section, the occurrence of Cumulate group is complex in the field, but shows inclusion relationship with each other (Figs. 5–2, 5–4, and 5–5). It is various combinations of each type, and the boundary between them is indistinct (Figs. 5–4c, d, e, and f). In addition, the Gabbro group and the granite are coeval intrusive rocks in terms of the field occurrence (Figs. 5–5a, b, f, and g).

5–3–1–1 Ol gabbronorite–Ol bearing Pxs hornblendite (Type 1)

Type 1 is a dominant type in the Kita-taku mafic complex and characterized by oikocrystic hornblende (Fig. 5–4a). It appears in Type 5 as a xenolith and is intruded

by Type 7 (Figs. 5–4b, 5–5a, and b).

Type 1 shows an orthocumulate texture and is mainly composed of olivine, clinopyroxene, and orthopyroxene as the cumulus minerals with hornblende and plagioclase as the intercumulus minerals (Fig. 5–6a). Type 1 contains trace amounts of chromian spinel, hematite and ilmenite as accessory minerals. Olivine shows subhedral–euhedral crystals with 0.5–1.7 mm in long and the cracks are developed. Orthopyroxene and clinopyroxene are also subhedral–euhedral crystals with a size of 0.5–3.0 mm and are generally included by oikocrystic hornblende. Hornblende and plagioclase occur as intercumulus minerals (Fig. 5–6a). Chadacrystic chromian spinel crystals are 0.05–0.2 mm in long and generally occurs in olivine. Type 1 is plotted within the field of gabbronorite to Pxs hornblendite in the trinity diagrams (Figs. 5–8a, b, and c).

5–3–1–2 Ol gabbronorite (Type 2)

Type 2 occurs generally as blocks and is included in all of the Cumulate group (Figs. 5–4c, d, and e). The lithology is the most felsic among the Cumulate group (Fig. 5–6b).

Type 2 shows an adcumulate texture and is mainly composed of olivine, clinopyroxene, and plagioclase as the cumulus minerals with trace amounts of orthopyroxene, hornblende, hematite, and ilmenite as accessory minerals (Fig. 5–6b). Olivine shows subhedral–euhedral crystals with 0.5–2.0 mm in long and possesses the reaction rim as a film-like orthopyroxene and hornblende. Clinopyroxene shows subhedral–euhedral crystals that are 0.5–1.2 mm and are generally surrounded by film-like hornblende. Subhedral–euhedral plagioclase crystals are 0.5–1.8 mm in long. Symplectite is formed between olivine and plagioclase. Hornblende and orthopyroxene occur as the reaction rim of the cumulus minerals (Fig. 5–6b). Type 2 is plotted within the field of gabbro to Ol gabbronorite in the trinity diagrams (Figs. 5–8a, b, and c).

5–3–1–3 Cumulus Cpx gabbro (Type 3)

Type 3 is an intercumulus hornblende-rich rock and the most dominant type in this study area (Figs. 5–4e and f). In addition, Type 3 possesses a mixing texture and ocellar quartz at the boundary of the granite (Figs. 5–5f and g).

Type 3 shows an orthocumulate texture and is mainly composed of clinopyroxene, plagioclase, and hornblende as the intercumulus and oikocrystic mineral (Fig. 5–6c). Type 3 contains trace amounts of ilmenite and titanite as accessory minerals. Clinopyroxene shows subhedral–euhedral crystals with 0.3–1.0 mm in long and are generally included by oikocrystic hornblende. Subhedral–euhedral columnar plagioclase crystals are 0.3–1.5 mm in long. Cumulus hornblende shows subhedral–euhedral crystals with 0.3–1.0 mm in long, while oikocrystic hornblende appears in Type 3 with more than 2.0 mm in long (Fig. 5–6c). Type 3 is plotted within the field of Hb gabbro to gabbronorite in the trinity diagrams (Figs. 5–8a, b, and c).

5–3–1–4 Cumulus Hb gabbro (Type 4)

Type 4 is generally distributed around Types 5 and 6, and shows a layered structure (Figs. 5–4g and h). The layered structure is formed by an orientation of columnar hornblende and plagioclase (Fig. 5–6d).

Type 4 shows an adcumulate and layered textures and is mainly composed of plagioclase and hornblende as the cumulus mineral with trace amounts of quartz, ilmenite, titanite, and rutile as accessory minerals (Fig. 5–6d). Subhedral–euhedral plagioclase crystals are 0.6–1.6 mm in long. Hornblende shows subhedral–euhedral columnar crystals with 0.7–3.0 mm in long and is generally includes titanite. Quartz occurs as interstitial minerals of the cumulus minerals (Fig. 5–6d). Type 4 is plotted within the field of Hb gabbro in the trinity diagrams (Figs. 5–8a, b, and c).

5–3–2 Occurrence and petrography of the Gabbro group (Type 5 to 7)

5–3–2–1 Foliated Hb gabbro (Type 5)

Type 5 generally occurs as dikes and intrudes the Cumulate group (Figs. 5–5a and b) and is characterized by the occurrence around Types 4 and 6 (Fig. 5–2). Type 5 locally includes Type 2 as a xenolith with unclear boundaries. In addition, Type 5 diffuse into MME like Type 1 resembling back-veining dike (Figs. 5–5a and b).

Type 5 shows a hypautomorphic granular texture and foliated texture and is mainly composed of plagioclase, hornblende, biotite, and quartz with trace amounts of ilmenite, titanite, and rutile as accessory minerals (Fig. 5–6e). Subhedral–euhedral plagioclase crystals are 0.1–1.5 mm in long. Hornblende shows subhedral–euhedral columnar crystals with 0.2–0.8 mm in long and is generally includes titanite. Subhedral–euhedral biotite crystals are 0.2–0.5 mm in long and is generally occurs around hornblende. Quartz occurs as an interstitial mineral of the early-crystallized minerals (Fig. 5–6e). Type 5 is plotted within the field of Hb gabbro in the trinity diagrams (Figs. 5–8a, b, and c).

5–3–2–2 Mixed Hb gabbro (Type 6)

Type 6 is generally occurring association with Types 4 and 5. It is characterized by the presence of a mixing texture that can be seen by the naked eye with another Cumulus group (Fig. 5–5c).

Type 6 shows a hypautomorphic granular texture and is mainly composed of plagioclase and hornblende with trace amounts of quartz, clinopyroxene, ilmenite, titanite as accessory minerals (Fig. 5–6f). Plagioclase shows subhedral–euhedral crystals with 0.5–1.8 mm in long and developed dusty zone. Subhedral–euhedral hornblende crystals are 0.6–1.6 mm in long and is generally includes titanite. Clinopyroxene shows pseudomorph crystals with 0.2–0.7 mm in long and is generally occurs around hornblende. Quartz occurs as an interstitial mineral of the early-crystallized minerals (Fig. 5–6f). Type 6 is plotted within the field of Hb gabbro in

the trinity diagrams (Figs. 5–8a, b, and c).

5–3–2–3 Pegmatitic Hb gabbro (Type 7)

Type 7 intrudes into the Cumulate group along brittle fractures (Fig. 5–4b). Hornblende megacrysts attains to 30 mm in long can be seen by the naked eye, and if they contain a large amount of plagioclase, they have a whitish color.

Type 7 shows a pegmatitic texture and is mainly composed of plagioclase and hornblende with trace amounts of quartz, clinopyroxene, orthopyroxene, ilmenite, titanite as accessory minerals (Fig. 5–6g). Subhedral–euhedral plagioclase crystals are 0.5–3.0 mm in long with chemically zoned. Hornblende shows subhedral–euhedral megacrysts with 10–30 mm in long and is generally includes titanite, clinopyroxene, and orthopyroxene. Orthopyroxene and clinopyroxene are also subhedral–euhedral crystals with a size of 0.5–3.0 mm and are generally included by oikocrystic hornblende megacryst. Quartz occurs as an interstitial mineral of the early-crystallized minerals (Fig. 5–6g). Type 7 is plotted within the field of Hb gabbro in the trinity diagrams (Figs. 5–8a, b, and c).

5–3–3 Occurrence and petrography of the related rocks (granite, PFD, trondhjemite)

5–3–3–1 Ms-Bt granite (Fukae Gr)

The Ms-Bt granite occurs as dikes intruding into the Cumulate group (Type 3), and mixing and mingling textures are recognized between them (Figs. 5–5f and g).

The Ms-Bt granite shows a hypautomorphic granular texture and is mainly composed of plagioclase, biotite, and muscovite with trace amounts of K-feldspar, titanite, and magnetite as accessory minerals (Fig. 5–7a). Subhedral–euhedral plagioclase crystals are 0.5–3.0 mm in long and developed chemical zoning. Biotite shows subhedral–euhedral crystals with 0.5–2.0 mm in long and is generally includes titanite and magnetite. Muscovite shows subhedral–euhedral crystals with 0.2–0.6 mm in long and is generally occurs around biotite. Quartz occurs as an interstitial

mineral of the early-crystallized minerals (Fig. 5–7a). The Ms-Bt granite is plotted within the field of granite to granodiorite in the trinity diagram (Fig. 5–8d).

5–3–3–2 Trondhjemite (Tdh)

The Tdh intrudes the Cumulate group, Gabbro group and amphibolite with clear boundary (Fig. 5–5d). Some of the Tdh dikes constitute composite dike with PFD (Fig. 5–5e).

The Tdh shows a hypautomorphic granular texture and is mainly composed of plagioclase, biotite, muscovite, and quartz with trace amounts of K-feldspar, titanite, and magnetite as accessory minerals (Fig. 5–7b). Plagioclase shows subhedral–euhedral crystals with 0.5–2.0 mm in long and developed chemically zoned. Subhedral–euhedral Biotite crystals are 0.1–0.4 mm in long and is generally formed clot. Muscovite shows subhedral–euhedral crystals with 0.1–0.3 mm in long and is generally including plagioclase. Quartz and K-feldspar occurs as an interstitial mineral of the early-crystallized minerals and the former show a wavy extension (Fig. 5–7b). The Tdh is plotted within the field of granodiorite to tonalite in the trinity diagram (Fig. 5–8d).

5–3–3–3 Porphyritic fine-grained diorite (PFD)

The PFD intrudes the Cumulate group, Gabbro group and amphibolite with clear boundary. Some of the PFD dikes constitute composite dike with Tdh dikes (Fig. 5–5e).

The PFD shows a porphyritic texture and mainly composed of plagioclase, hornblende, and biotite as phenocrysts with 0.3–2.5 mm in long (Fig. 5–7c). Subhedral–euhedral plagioclase crystals are 0.5–2.5 mm in long and developed dusty zone. Hornblende and biotite are also subhedral–euhedral crystals with a size of 0.3–1.0 mm and generally shows columnar and bladed shape, respectively. The groundmass contains fine-grained plagioclase, quartz, with a small amount of K-

feldspar and ilmenite, and titanite, ilmenite, and apatite are observed as accessory minerals (Fig. 5–7c). The PFD is plotted within the field of Qz diorite to diorite in the trinity diagram (Fig. 5–8d).

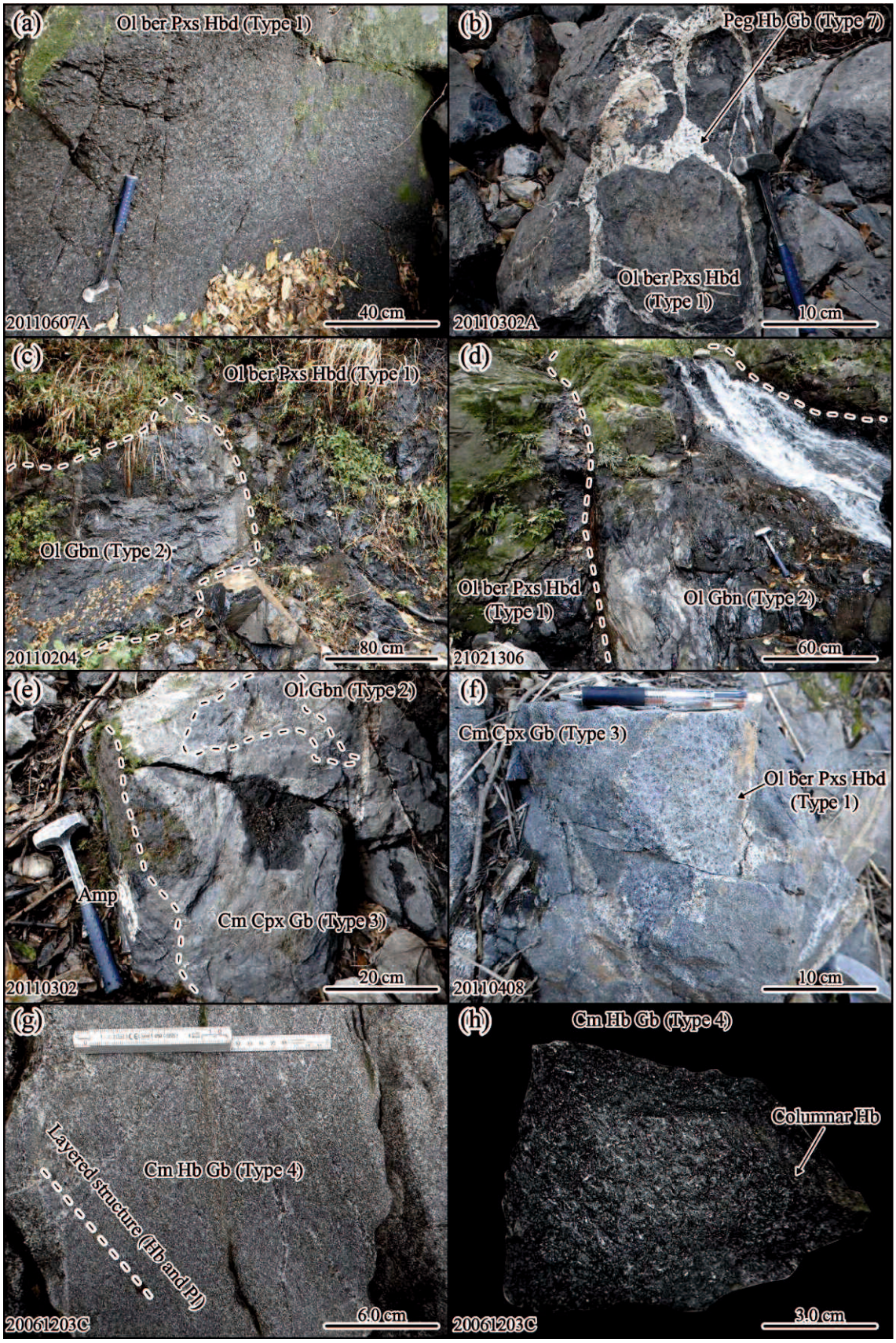

Figure 5–4. Field occurrences of the Kita-taku mafic complex. (a) Ol Gbn–Ol ber Pxs Hbd

(Type 1) characteristics oikocrystic hornblende. (b) Peg Hb Gb (Type 7) intrudes into Ol Gbn–Ol ber Pxs Hbd (Type 1). (c) Ol Gbn–Ol ber Pxs Hbd (Type 1) including the Ol Gbn (Type 2) block1. (d) Ol Gbn–Ol ber Pxs Hbd (Type 1) including the Ol Gbn (Type 2) block2. (e) Cm Cpx Gb (Type 3) including Amp and Ol Gbn (Type 2). (f) Cm Cpx Gb (Type 3) including Ol Gbn–Ol ber Pxs Hbd (Type 1). (g) Cm Hb Gb (Type 4) shows layered structure formed by columnar Hb and Pl. (h) Slab sample of the Cm Hb Gb (Type 4). Abbreviations are show in the text.

Figure 5–5. Field occurrences of the Kita-taku mafic complex, continued to Figure 5–4

and related rocks. (a) Fo Hb Gb (Type 5) intrudes into Ol Gbn–Ol ber Pxs Hbd (Type 1), and this boundary is unclear (b) Fo Hb Gb (Type 5) including Ol Gbn–Ol ber Pxs Hbd (Type 1) xenolith. (c) Mingling texture between Mx Hb Gb (Type 6) and Cm Cpx Gb (Type 3). (d) Tdh dike intrudes into Ol Gbn–Ol ber Pxs Hbd (Type 1), and this boundary is clear. (e) Composite dike with Tdh and PFD. (f) Mingling texture between Ms-Bt Gr and Cm Cpx Gb (Type 3). (g) Ocellar Qz in the Cm Cpx Gb (Type 3). Abbreviations are show in the text.

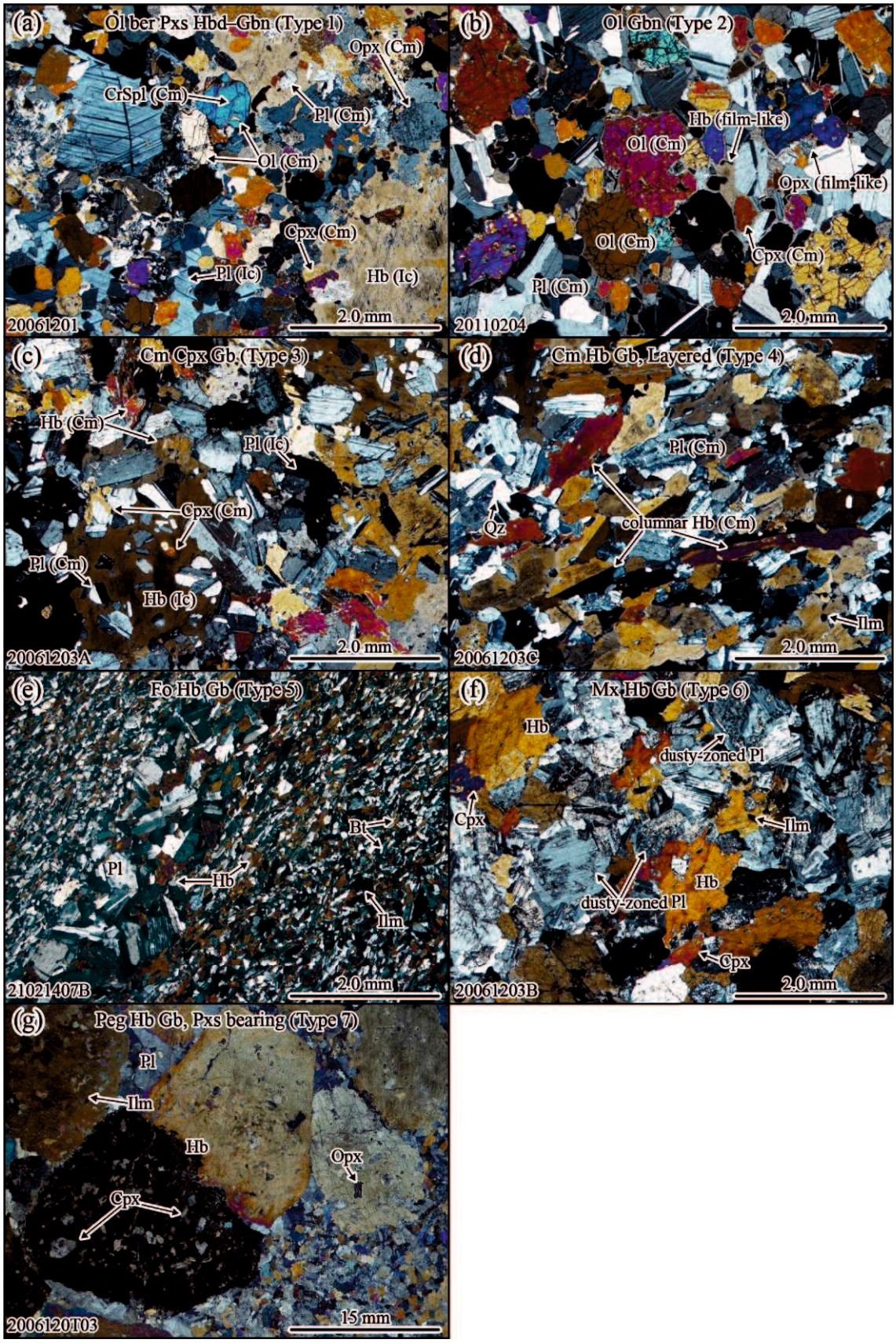

Figure 5–6. Photomicrographs of the Kita-taku mafic complex. (a) Ol Gbn–Ol ber Pxs Hbd

Ol Gbn–Ol ber Pxs Hbd (Type 1). (b) Ol Gbn (Type 2). (c) Cm Cpx Gb (Type 3). (d) Cm Hb Gb (Type 4). (e) Fo Hb Gb (Type 5). (f) Mx Hb Gb (Type 6). (g) Peg Hb Gb (Type 7). Pl: plagioclase, Bt: biotite, Hb: hornblende, Cpx: clinopyroxene, Opx: orthopyroxene, Ol: olivine, Ilm: ilmenite, Cm: cumulus mineral, and Ic: Intercumulus mineral. Abbreviations are shown in the text.

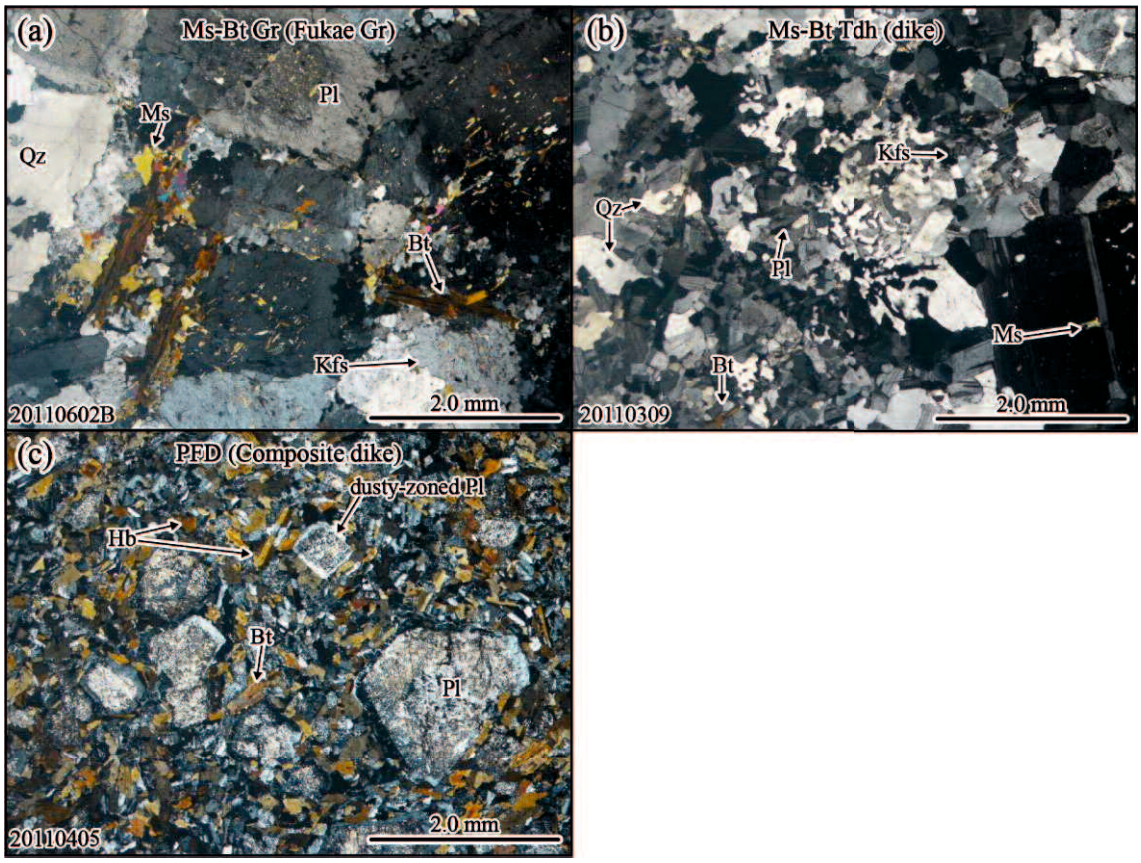

Figure 5–7. Photomicrographs of the related rocks. (a) Ms-Bt Gr. (b) Ms-Bt Tdh. (c) PFD. Qz: quartz, Kfs: K-feldspar, Pl: plagioclase, Bt: biotite, Hb: hornblende, and Ms: muscovite. Abbreviations are shown in the text.

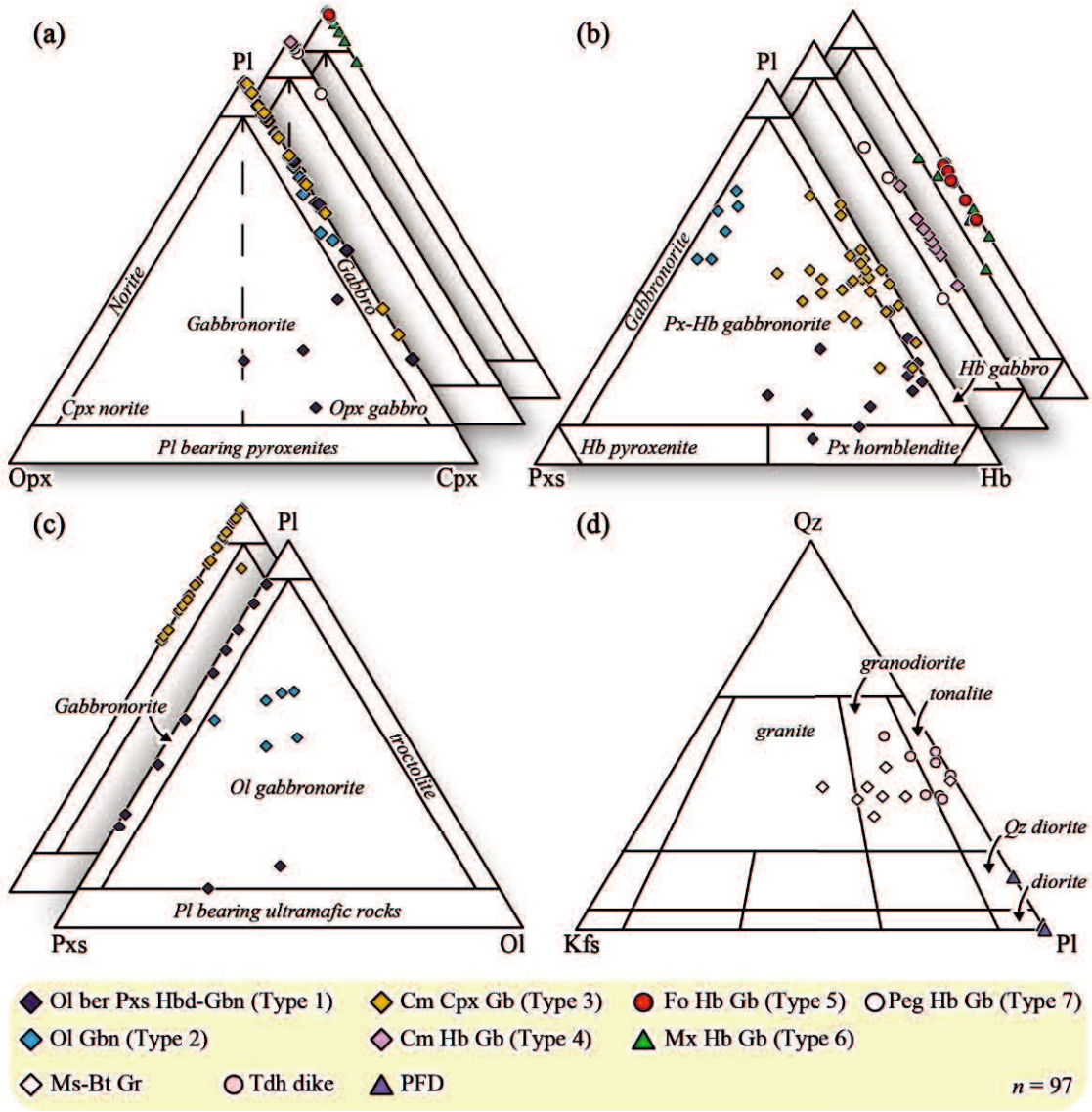

Figure 5–8. Modal compositions of the Kita-taku mafic complex and related rocks shown in (a) plagioclase (Pl)–orthopyroxene (Opx)–clinopyroxene (Cpx) diagram, (b) plagioclase (Pl)–pyroxenes (Pxs)–hornblende (Hb) diagram, (c) plagioclase (Pl)–pyroxenes (Pxs)–olivine (Ol) diagram, and (d) QAP (quartz (Qz)–K-feldspar or alkali feldspar (Kfs or Afs)–plagioclase (Pl)) diagram. Classification boundaries are modeled after Streckeisen (1976). Point-counting application was used for Microsoft Excel VBA (Visual Basic for Applications) made by Shimura and Kojima (2015), and 3000–1500 points were counted from an area of 3 cm × 4 cm per sample. The measurement data are listed in the Appendix 5–1.

5–4 Geochronology and geochemistry

Zircon U–Pb analyses were undertaken at the Kyoto Fission-Track Co., Ltd, Japan. Zircon grains were separated from two samples with weighting 0.2–0.4 kg. The cathodoluminescence (CL) images of zircon grains were taken using JEOL JSM-6360LA scanning electron microscope and Gatan Mini–CL system (Prof. Shimura customized) at the Center for Instrumental Analyses, Yamaguchi University. Photographing conditions for CL images were an accelerating voltage of 5–12 kV, a specimen current of 2.0–4.0 nA, and a working distance of 9 mm. The measurement conditions of the zircon U–Pb dating are shown in Table 5–2.

Table 5–2. The measurement conditions of the zircon U–Pb dating.

LA-ICP-MS system at the Geochemical Research Center, Graduate School of Science, The University of Tokyo		
1	Laser Ablation System	
	Manufacturer	LIGHT CONVERSION
	Product name	CARBIDE
	Laser type	Yb:KGW femtosecond laser
	Pulse rate	290 fs
	Wavelength	257 nm
	Output	30 mW
	Energy Density	3.8 J /cm^2
	Diameter of beam	10 μm
	Laser Irradiation Method	single- spot
	Galvanometer Optical	not used
	Frequency	100 Hz
	Shape of laser beam (area)	circle(10 mm in diameter)
	Shot Count	40
	Irradiation time	0.4 s
	Carrier gas (He)	0.60 L min^{-1}
2	ICP Mass Spectrometer	
	Manufacturer	Nu Instruments
	Product name	New Plasma II
	ICP–Ms type	Multi-collector、dual convergence type
	RF power	1300 W
	Carrier gas (Ar)	0.80 L min^{-1}
	ThO^+/Th Oxide formation rate	< 1%
	Data collection method	Time-resolved analysis
	Data collection time	14 s (10 s gas blank, 4 s ablation signal)
	Measured isotopes	^{202}Hg, ^{204}Pb, ^{206}Pb, ^{207}Pb, ^{208}Pb, ^{232}Th, ^{235}U
3	Standard sample	
	First standard (U-Pb)	Plešovice [*1]
	Second standard (U-Pb)	OD-3 [*2, 3, 4] Nancy 91500[*5]

*1: Sláma et al. (2008), *2: Iwano et al. (2012), *3: Iwano et al. (2013), *4: Lukács et al. (2015), and *5: Wiedenbeck et al. (1995).

Clinopyroxene trace element compositions were measured using a laser ablation–inductively coupled plasma–mass spectrometry (LA–ICP–MS) system at the GSJ (Geological Survey of Japan) -Lab that consisted of an LA system (New Wave Research NWR213) coupled to a quadrupole ICP–MS (Agilent 7700x). Detailed information on the instrumentation and analytical methods are given by Yamasaki et al. (2016). The quality of the clinopyroxene LA–ICP–MS analyses was monitored using measurements of NIST615 geochemical reference materials.

The analytical instruments, methods and procedures of the whole-rock chemistry, mineral chemistry, and Sr–Nd isotope used in this chapter were reported in chapter 2 (section 2–4).

5–4–1 Zircon U–Pb dating

It is very important to determine the timing of the activity of the Kita-taku mafic complex because it is related to the large-scale igneous activity that formed the Northern Kyushu batholith. However, the Cumulate group, which occupies most of the Kita-taku mafic complex, do not contain zircon at all. In this study, Type 5 of the Gabbro group, which intrudes into the Cumulate group as a coeval dike (Figs. 5–5a and b) were provided for the zircon U–Pb dating. As a result, a zircon U-Pb weighted mean age of 105.8 ± 0.5 Ma was obtained from Type 5 (Fig. 5–9). The analyzed zircon grains show oscillatory zonation alike to the texture of igneous rocks (Fig. 5–10a). Furthermore, the Th/U ratios are greater than 0.1 (Th/U : 0.35–1.18, Appendix 5–3) at the measurement points of the zircon grains, suggesting that these zircons are of igneous origin. The Tdh dike that intrudes and forms part of the migmatite in this area was also measured for zircon U–Pb age. The zircon U-Pb weighted mean age of 105.9 ± 0.5 Ma was obtained from the Tdh dike (Fig. 5–9). The analyzed zircon grains show resorbed shapes (Fig. 5–10b). Moreover, the Th/U ratio at the measurement points of the zircon grains is more than 0.1 (Th/U : 0.31–1.17, Appendix 5–3), and the formation of a part of migmatite indicates that this age is the age of the

solidification of Tdh dike and the formation of migmatite. The Th/U ratios are often employed as a criterion to distinguish between zircon formation in magmatic, metamorphic, and hydrothermal environments. For example, a Th/U value of less than 0.1 is widely cited as a criterion for discriminating metamorphic zircons (Schaltegger et al., 1999; Hoskin and Black, 2000; Rubatto et al., 2001; Rubatto, 2002; Harley, 2007). Möller et al. (2003) showed that the Th/U ratios of recrystallized and newly grown metamorphic zircons were unchanged compared to their magmatic zircon precursors (and never less than 0.1). These ages imply that the magmatic activity of Kita-taku mafic complex and related igneous rocks, occurs at the coevally time. The age of ca.106 Ma corresponds to the early-stage magmatic activity of the Northern Kyushu batholith (Adachi et al., 2012; Tiepolo et al., 2012; Miyazaki et al., 2018; Yuhara et al., 2019a, b; Yuhara et al., 2020; Yuhara et al., 2021), which is consistent with the former study (e.g., Karakida, 1985; Owada and Kamei, 2010) that the mafic magma predates the granitoids. The Concordia plot, $^{206}Pb/^{238}U$ age probability density curve and histogram, and weighted average plot shown in Figure 5–9 were created using Isoplot R by Vermeesch (2018). The stereomicroscope and reflected microscope images of the measured zircon grains are shown in Appendix 5–2 and 5–3, and the measured data are listed in Appendix 5–4.

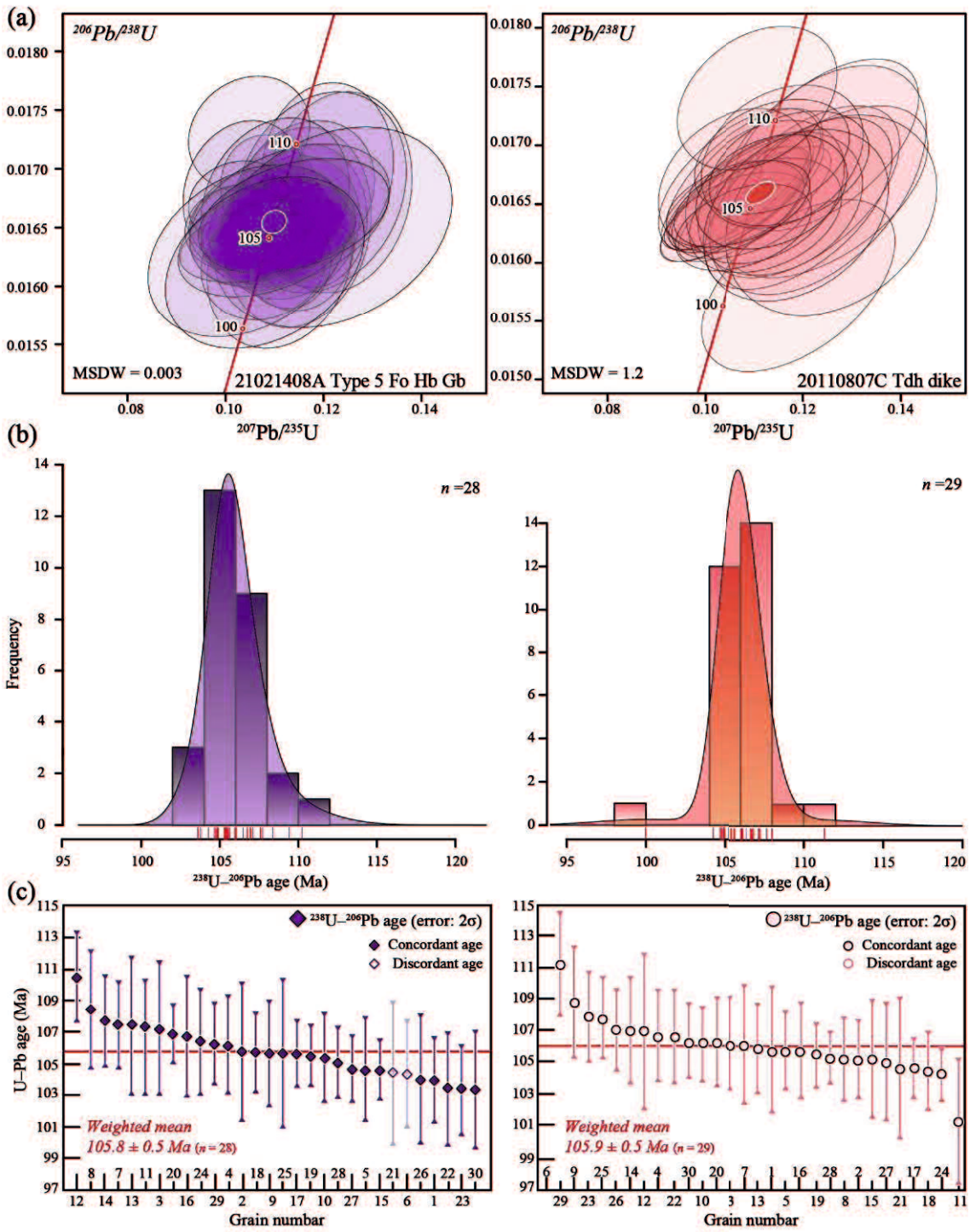

Figure 5–9. Zircon U–Pb dating. (a) Concordia plot. (b) $^{206}Pb/^{238}U$ grain age probability density curve and histogram. (c) Weighted mean plot. These diagrams were created using Isoplot R by Vermeesch (2018). The selected CL images, stereomicroscope whole images and reflected microscope whole images of the measured zircon grains are shown in Table 5–3, Appendix 5–2, 5–3, and the measured data are listed in Appendix 5–4.

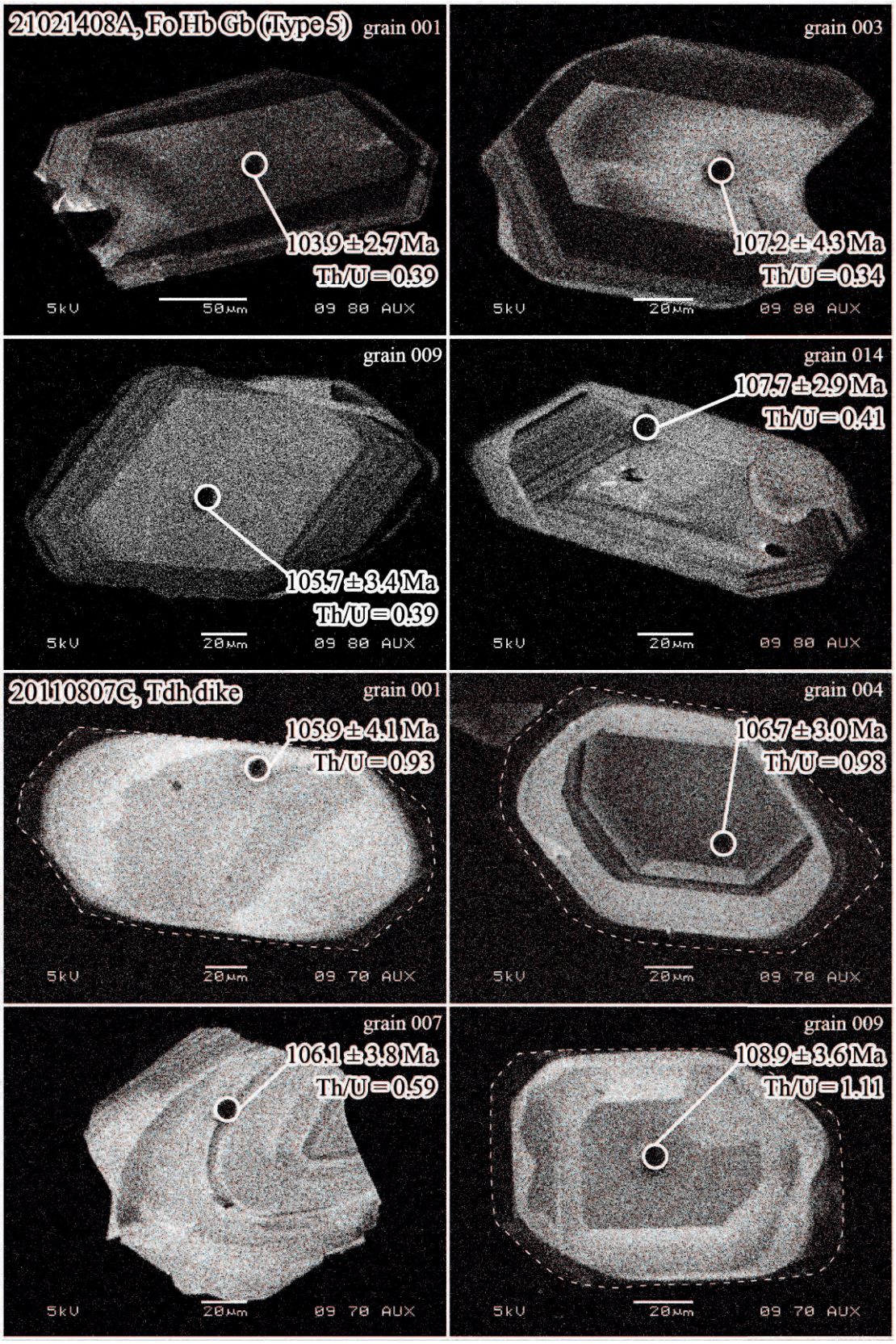

Figure 5–10. Cathodoluminescence images of selected zircon grains and ^{238}U–^{206}Pb ages. Blacky areas show positions of analyses. (a) Fo Hb Gb. (b) Tdh dike.

5–4–2 Major and trace elements of whole-rock

The variation diagrams of FeO^*/MgO vs. major and trace elements for the Kita-taku mafic complex (Type 1 to 7) are shown in Figure 5–11. Because the Kita-taku mafic complex show ultramafic to mafic lithofacies, the ratios of FeO and MgO (FeO^*/MgO), which are indicators of cooling or differentiation in mafic rocks, are set on the horizontal axis in Figure 5–11 to examine the whole-rock chemical characteristics of the Kita-taku mafic complex.

The FeO^*/MgO ratios of Type 1 range from 0.51 to 0.82, and SiO_2, Al_2O_3, TiO_2, Sr and V increase with increasing FeO^*/MgO ratio (Fig. 5–11). Type 1 possesses very high MgO (~ 25.6 wt%), Cr (~ 1677 ppm) and Ni (~ 455 ppm) contents and these elements decreases with increasing FeO^*/MgO ratios. The FeO^*/MgO ratios of Type 2 range from 0.60 to 0.68, and SiO_2, Al_2O_3, TiO_2 and Sr increase with increasing FeO^*/MgO ratio (Fig. 5–11). The FeO^*/MgO ratio of Type 2 is narrower than that of Type 1, and no significant compositional change can be observed. This is consequent upon the fact that it shows an adcumulate texture. The FeO^*/MgO ratios of Type 3 range from 0.56 to 2.02, and TiO_2, Sr and V increase with increasing FeO^*/MgO ratio (Fig. 5–11). The SiO_2 content of Type 3 increases until FeO^*/MgO ratio becomes 1.20, and then decreases. The Al_2O_3 content of Type 3 increases until FeO^*/MgO ratio becoming 1.20, and then it shows almost constant (Fig. 5–11). The FeO^*/MgO ratios of Types 4 and 5 range from 1.11 to 1.95, 1.50 to 2.32, respectively (Fig. 5–11). Type 4 possess very high TiO_2 (~ 2.2 wt%) and V (~ 823 ppm) contents and SiO_2 content decreases with increasing FeO^*/MgO ratio. The FeO^*/MgO ratios of Types 6 and 7 range from 0.92 to 1.27, 0.66 to 0.96, respectively (Fig. 5–11). The compositions of Type 6 are often intermediate between the Cumulate group and the Gabbro group, and Type 7 is low in FeO^*/MgO ratios (0.66 to 0.96), suggesting the possibility of pegmatite originating from the Cumulate group. The results of major and trace element analyses and ICP-MS analyses are listed in Appendix 5–5 and Appendix 5–6. Primitive mantle-normalized multi-element patterns and C1

chondrite-normalized rare earth element (REE) patterns are shown in Appendix 5–7.

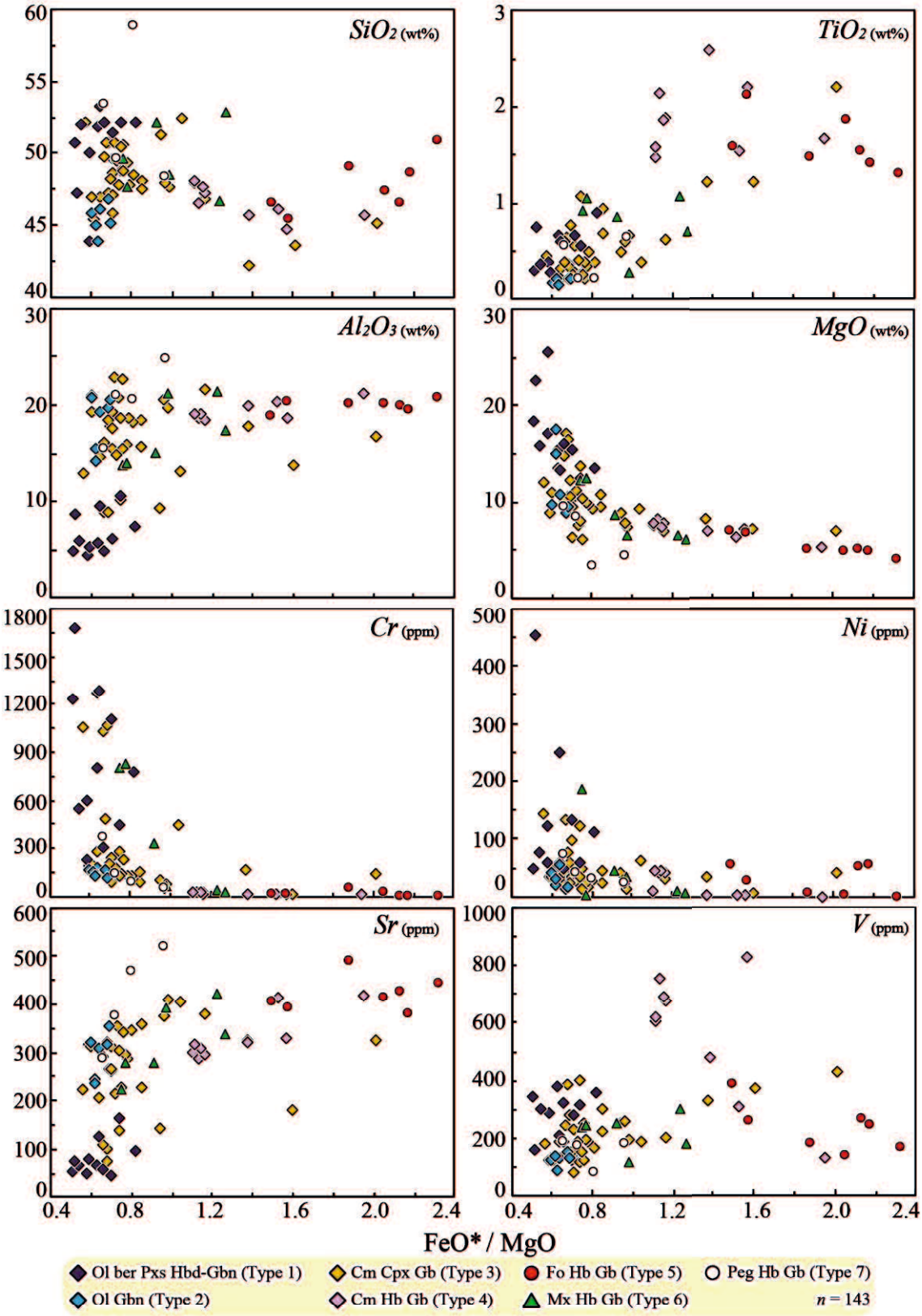

Figure 5–11. Major and trace element variation diagrams relative to FeO*/MgO for the

Kita-taku mafic complex. Abbreviations are shown in the text. The results of major and trace element analyses are listed in Appendix 5–5.

5–4–3 Mineral chemistry

The chemical compositions of plagioclase, olivine, clinopyroxene, orthopyroxene, amphibole, and chromian spinel of the Kita-taku mafic complex were analyzed (Figs. 5–12, 5–13, 5–14, 5–15, 5–16, 5–17, and 5–18). The results of the representative analyses are shown in Appendix 5–8. The chemical compositions of each mineral were examined by variation diagrams, comparing to specific elements against anorthite component [$An = 100 \times \{Ca/(Ca + Na)\}$] for plagioclase core, and against *Mg*# [$Mg\# = 100\times\{MgO/(FeO^*+MgO)\}$:mole] for olivine core, clinopyroxene core, orthopyroxene core and amphibole core (Figs. 5–12, 5–13, 5–14, 5–15, 5–16, and 5–17).

The *An* content of Type 1 ranges from 70.35 to 90.53, and SiO_2 and K_2O decrease with increasing *An* content (Fig. 5–12). On the other hand, CaO increases with increasing *An* content and FeO shows a scattered plot. The *An* content of Types 2, 3 and 4 range from 80.51 to 91.69, 66.65 to 90.56, and 81.86 to 89.27, respectively. The compositional trends of the Types 2, 3 and 4 shows similar to those of Type 1. Thus, these chemical features of the cumulate group show continuous trend (Fig. 5–12). The *An* content of Types 5 and 6 range from 44.79 to 76.70 and 27.32 to 63.03, respectively. FeO and K_2O trends of Types 5 and 6 are scattered and different from those of the Cumulate group (Type 1 to 4) (Fig. 5–12). In addition, the compositional trends of Type 6 shows between the Cumulus group and Type 5. The *An* content of Type 7 ranges from 70.35 to 90.53, and SiO_2 and K_2O decreases with increasing *An* content (Fig. 5–12). The *An* content of Type 7 ranges from 73.18 to 85.09 and 32.38 to 59.51, and SiO_2 and K_2O decrease with increasing *An* content (Fig. 5–12).

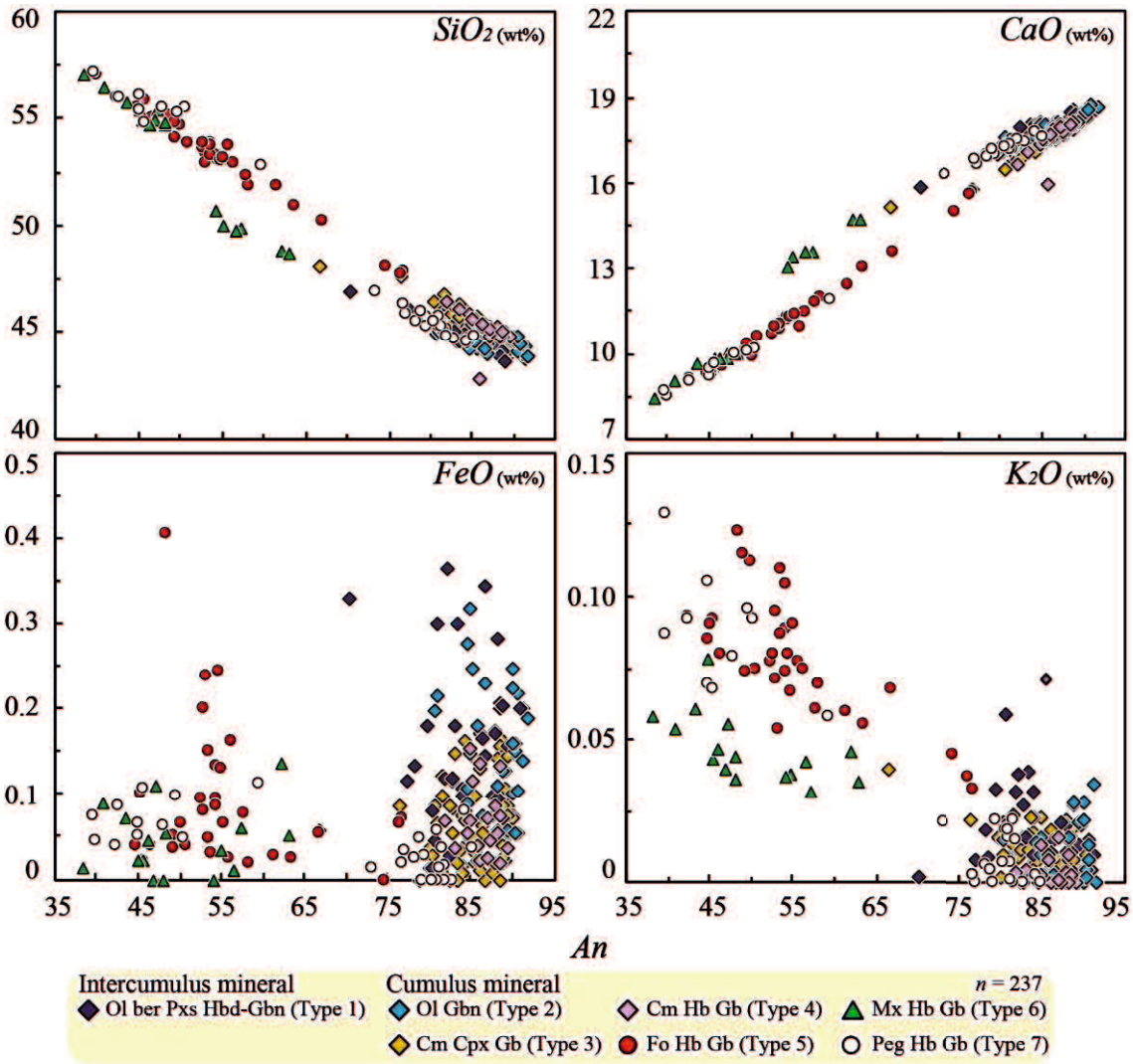

Figure 5–12. Major and trace element variation diagrams relative to *An* content of plagioclase for the Kita-taku mafic complex.

The olivine *Mg*# of Types 1 and 2 range from 70.01 to 74.99 and 68.46 to 72.37, respectively. SiO_2 and NiO contents of Types 1 and 2 roughly increase with increasing olivine *Mg*# (Fig. 5–13).

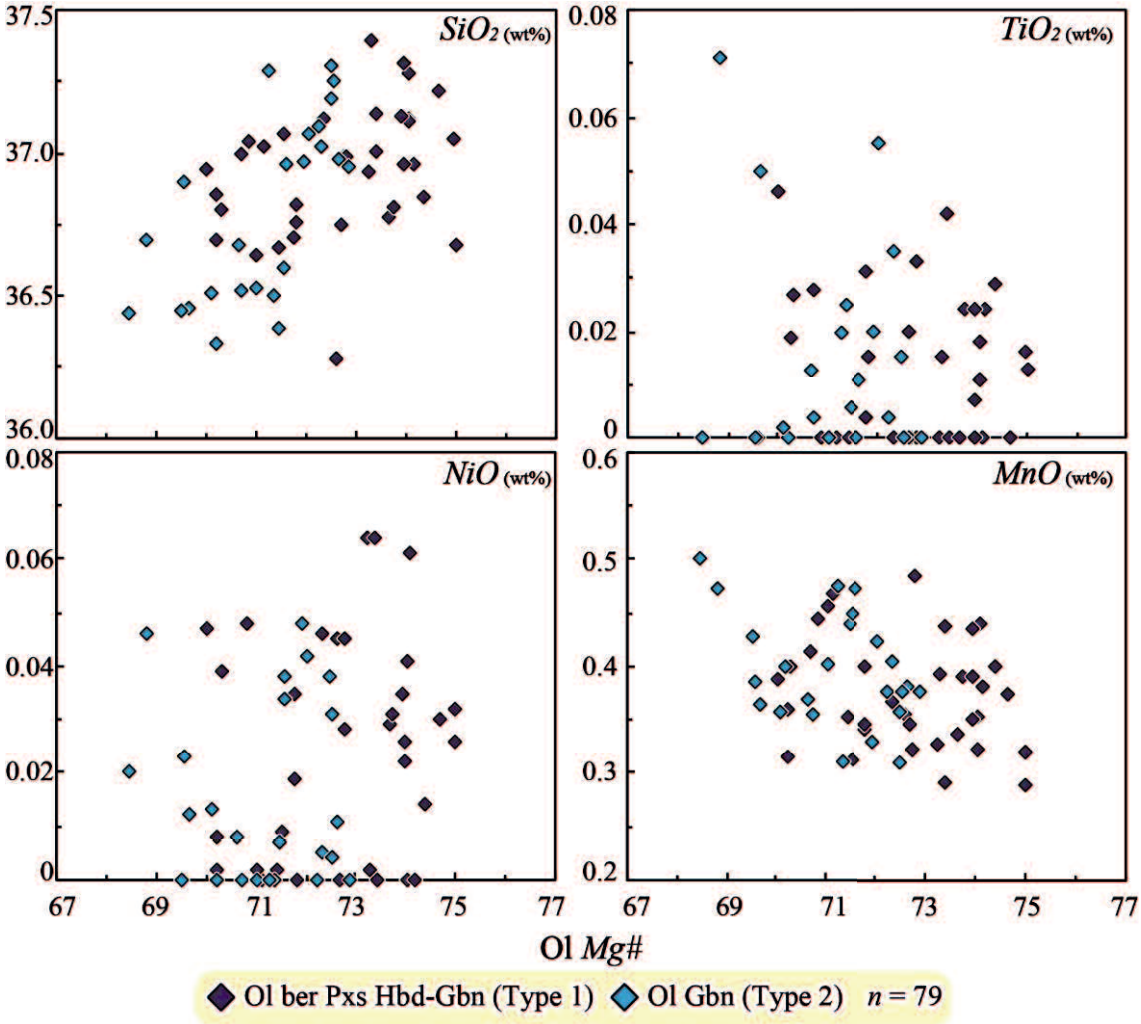

Figure 5–13. Major and trace element variation diagrams relative to *Mg#* content of olivine for the Kita-taku mafic complex.

The clinopyroxene *Mg#* of Types 1, 2, 3 and 7 range from 74.27 to 86.40, 75.68 to 82.28, 67.19 to 81.57, and 75.68 to 81.17, respectively. These diagrams show a continuous trend for the cumulate group (Type 1 to 3) (Fig. 5–14). The *Mg#* of Type 7 is overlapped with Types 1 and 2 (Fig. 5–14). In the pyroxene trapezoid (Fig. 5–16), all types are plotted in the augite to diopside composition field.

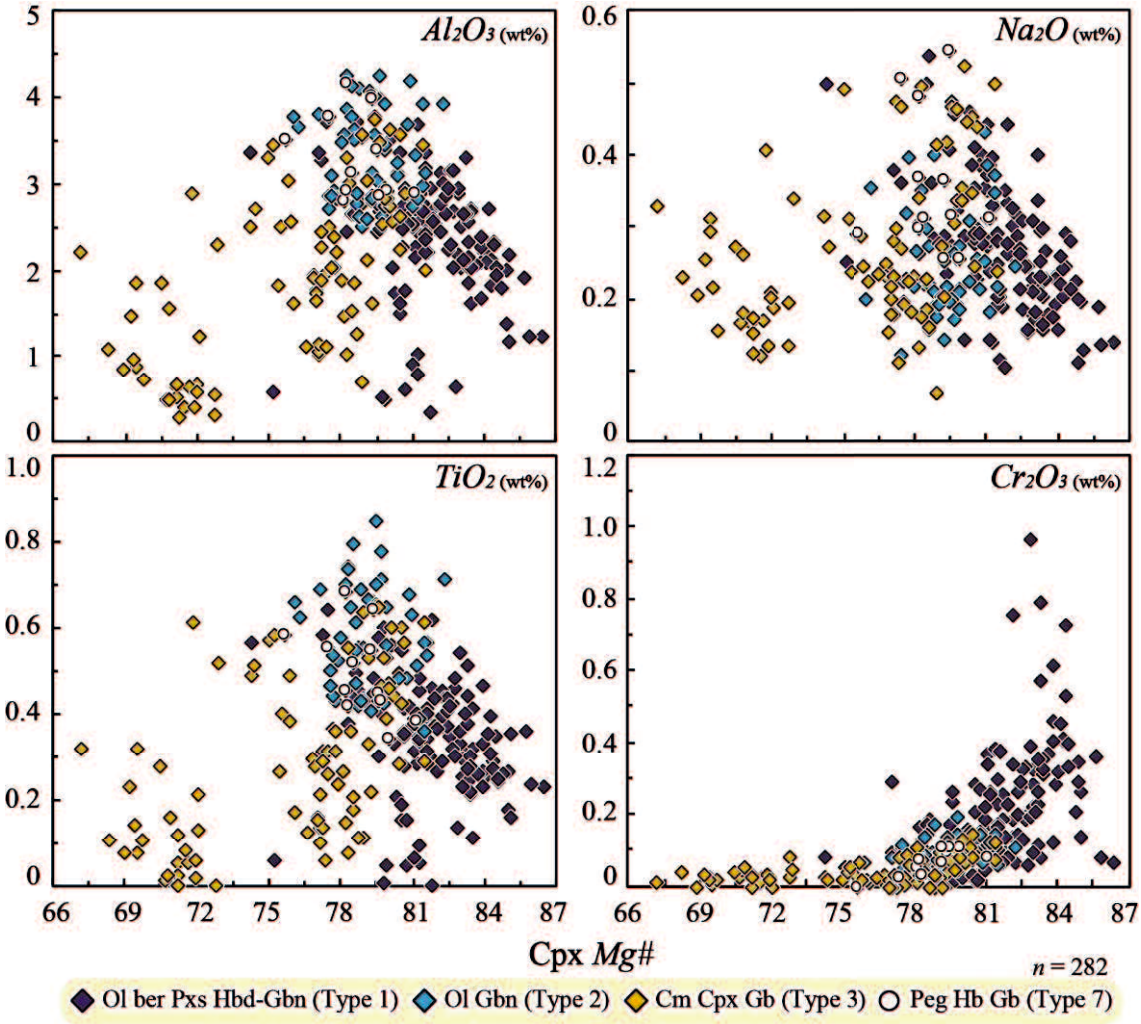

Figure 5–14. Major and trace element variation diagrams relative to *Mg#* content of clinopyroxene for the Kita-taku mafic complex.

The orthopyroxene *Mg#* of Types 1, 2 and 7 range from 71.36 to 77.86, 73.36 to 75.58, and 62.83 to 67.95 , respectively. Types 1 and 2 roughly make trends. The *Mg#* of Type 7 is deviated from that of Types 1 and 2 indicating their compositional gap (Fig. 5–15). In the pyroxene trapezoid (Fig. 5–16), all types are plotted in the enstatite to hypersthene compositional field.

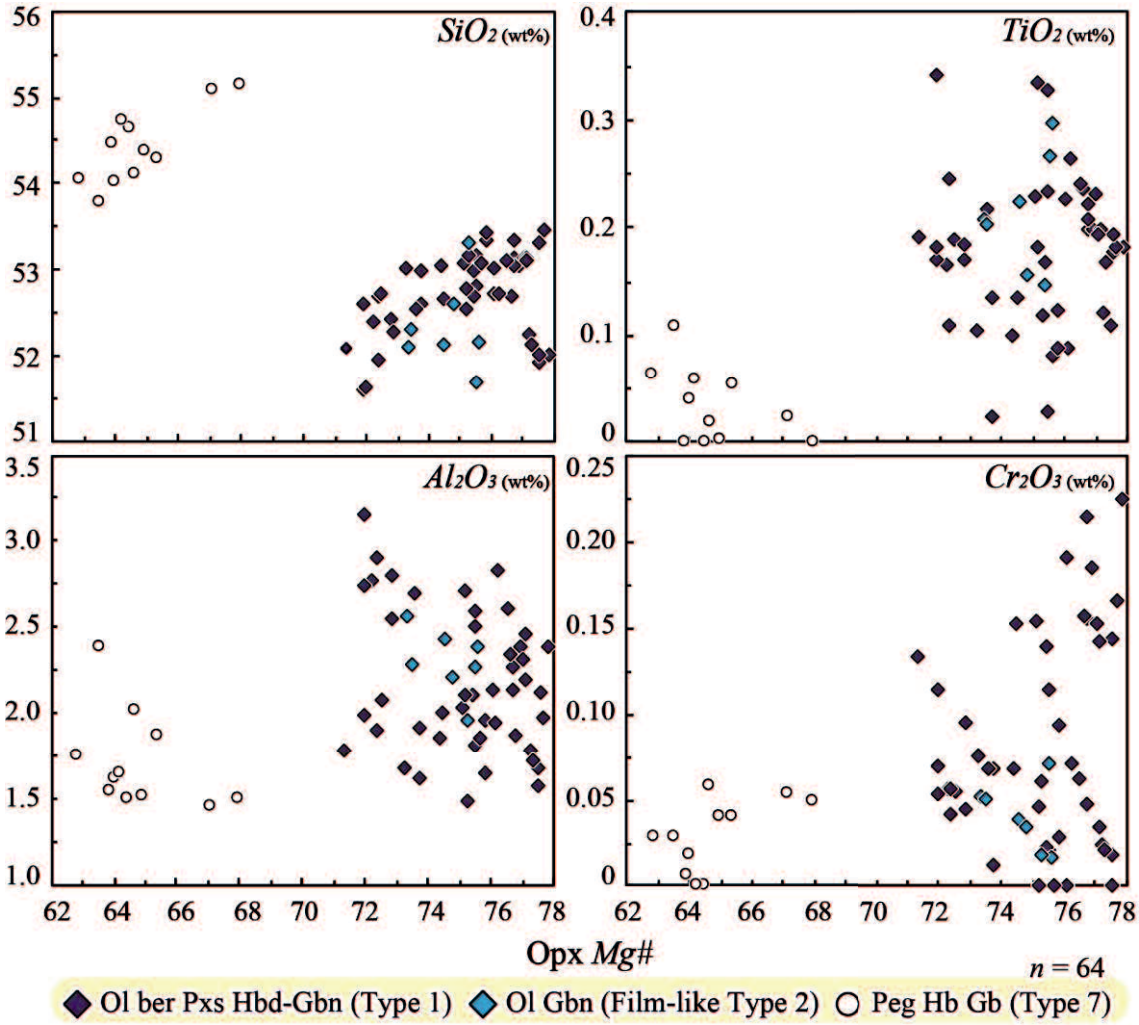

Figure 5–15. Major and trace element variation diagrams relative to *Mg#* content of orthopyroxene for the Kita-taku mafic complex.

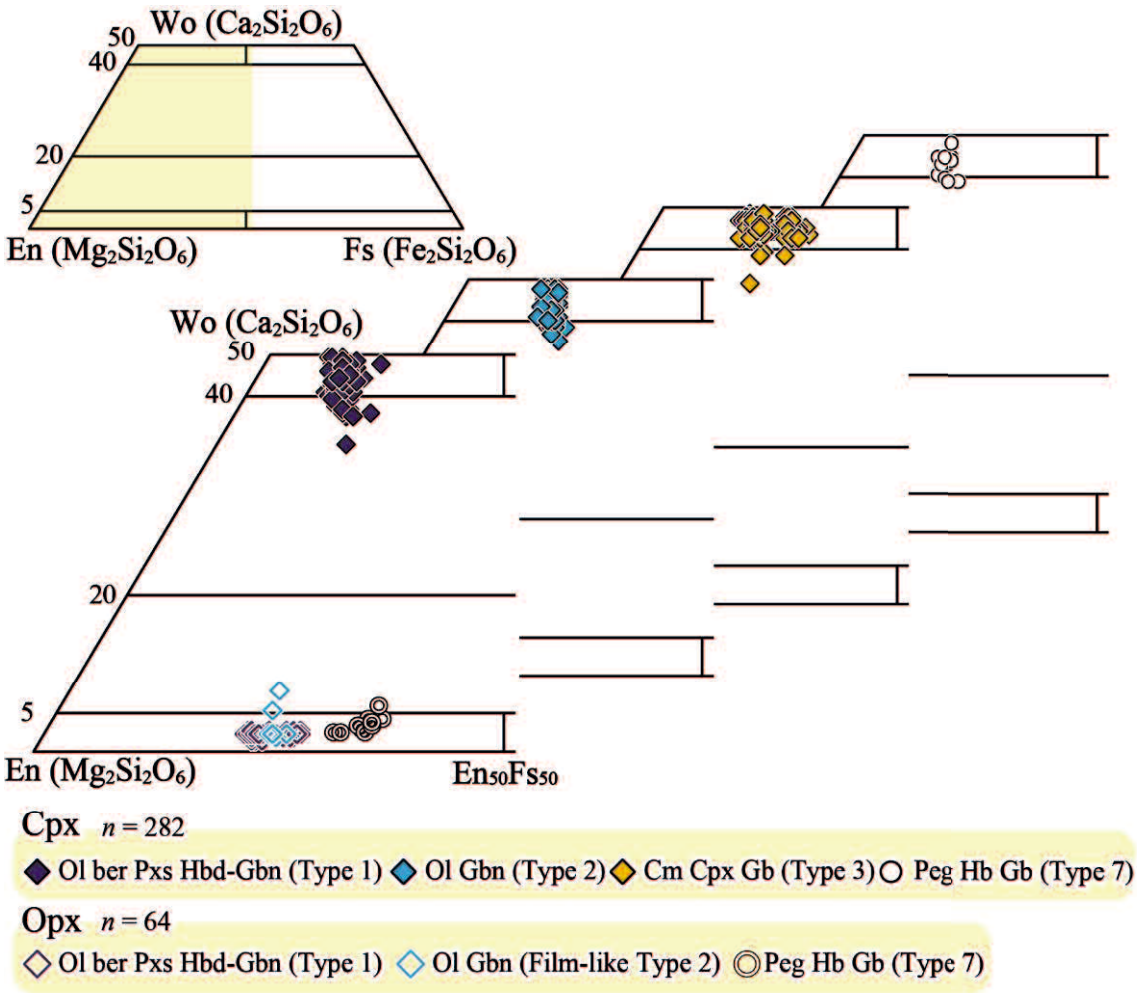

Figure 5–16. Pyroxene trapezoid plot (Morimoto et al., 1988; Deer et al., 2013) of the Kita-taku mafic complex.

The amphibole was separately analyzed for intercumulus mineral (Type 1 to 3) and cumulus ones (Type 4 to 7). The intercumulus amphibole Mg# of Types 1, 2, and 3 range from 67.58 to 80.58, 69.84 to 72.20, and 53.40 to 73.88, respectively (Fig. 5–17). In contrast, the cumulus amphibole *Mg#* of Types 4, 5, 6, and 7 range from 51.44 to 63.93, 42.05 to 45.64, 59.72 to 67.87 and 62.12 to 75.22, respectively (Fig. 5–17). The compositional trend of Type 6 shows between that of Types 3 and 5. On the other hand, Type 7 is overlapped with that of Types 1, 2, and 3 (Fig. 5–17).

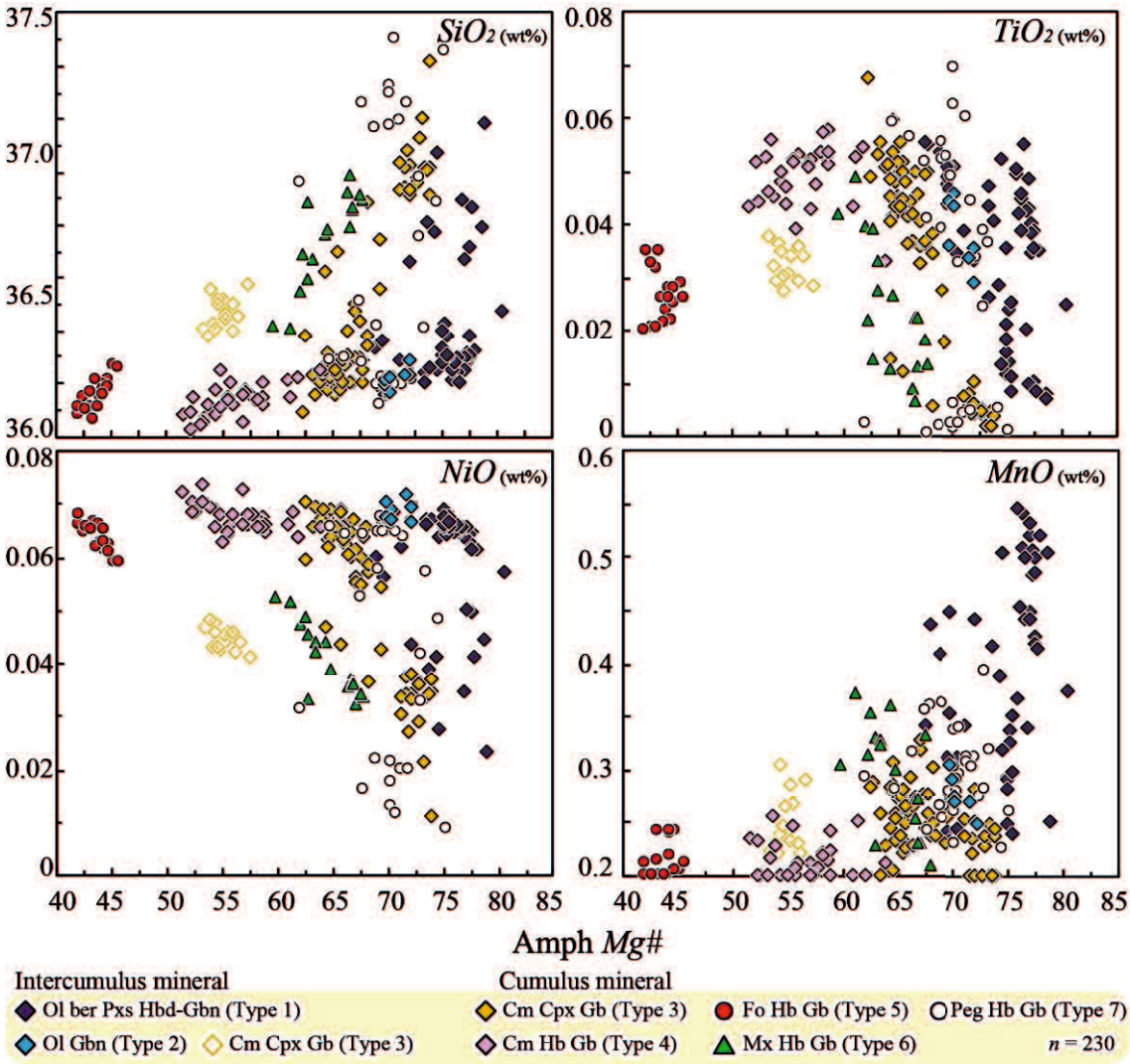

Figure 5–17. Major and trace element variation diagrams relative to *Mg#* content of amphibole for the Kita-taku mafic complex.

Overall, the mineral compositions of the Cumulate group roughly make compositional trends (Figs. 5–12, 5–13, 5–14, 5–15, and 5–17). On the other hand, the chemical compositions of plagioclase from the Cumulate group are different from those of the Gabbro group (Fig. 5–12: e.g., FeO and K_2O).

On the basis of the spinel prism (Fig. 5–18) for the solid-solution spinel–hercynite–chromite–magnesiochromite–magnesioferrite–magnetite, two chemical variation diagrams (Figs. 5–18b and c) were constructed with the projections on the triangular face “b” of the spinel prism (Figs. 5–18a and b) and the compositions on

the bottom-lateral face "c" of the prism (Figs. 5–18a and c). These two diagrams have been used to classify the spinel group minerals. Names of middle-member compositions were taken from Haggerty (1991) and Deer et al. (2013). The triangular diagram Cr^{3+}–Fe^{3+}–Al^{3+} (Figs. 5–18b) was after Gargiulo et al. (2013). In the triangular diagram Cr^{3+}–Fe^{3+}–Al^{3+} (Figs. 5–18b), spinel crystals of the Type 1 are plotted in the Al-chromite to picotite compositional field. In contrast, spinel crystals of the Type 1 for the compositions on the bottom-lateral face "c" of the prism (Figs. 5–18a and c) shows an intermediate composition between hercynite and chromite.

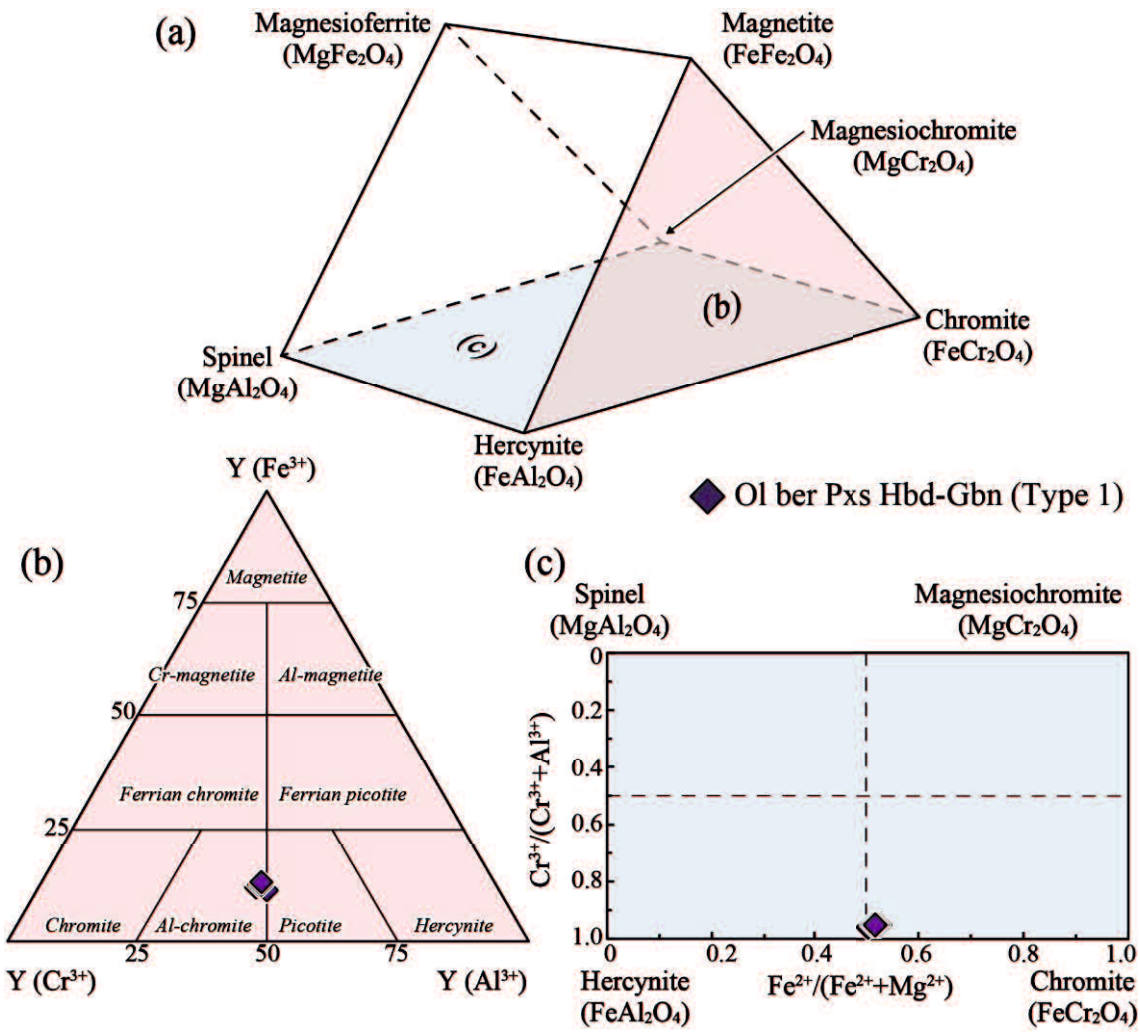

Figure 5–18. Chemical classification diagrams for the spinel group minerals of the Type 1 from Kita-taku mafic complex. (a) Spinel prism for the multi-component system: spinel–

hercynite–chromite–magnesiochromite–magnesioferrite–magnetite (after Deer et al., 2013). The letter "(b)" indicated in the triangle-front face and the letter "(c)" in the lateral-bottom face of the prism, represent the diagrams in the (b) and (c) respectively. (b) Triangular classification diagram (Cr^{3+}–Fe^{3+}–Al^{3+}: after Gargiulo et al., 2013): $Y(Cr^{3+}) = Cr/(Cr+Fe^{3+}+Al)$; $Y(Fe^{3+}) = Fe^{3+}/(Cr+Fe^{3+}+Al)$; $Y(Al^{3+}) = Al/(Cr+Fe^{3+}+Al)$. (c) Binary classification diagram considering the Mg^{2+}–Fe^{2+} exchange in the structural site "X". Field-contours in both diagrams are considering Stevens (1944), Haggerty (1991), and Deer et al. (2013).

5–4–4 Trace element composition of clinopyroxene

The trace element compositions of clinopyroxene grains are listed in Appendix 5–9. The constant ratios of Zr/Nb, Zr/Y, Zr/Ba and Zr/La in the Cumulate group (Types 1 to 3) means that the high field strength elements (HFSEs) behaved as incompatible elements within the crystallizing magma (Fig. 5–19). However, the Nb and Y contents of Type 3 are scattered rather than the other types, suggesting change of the partition coefficient between clinopyroxene and melt during magmatic differentiation.

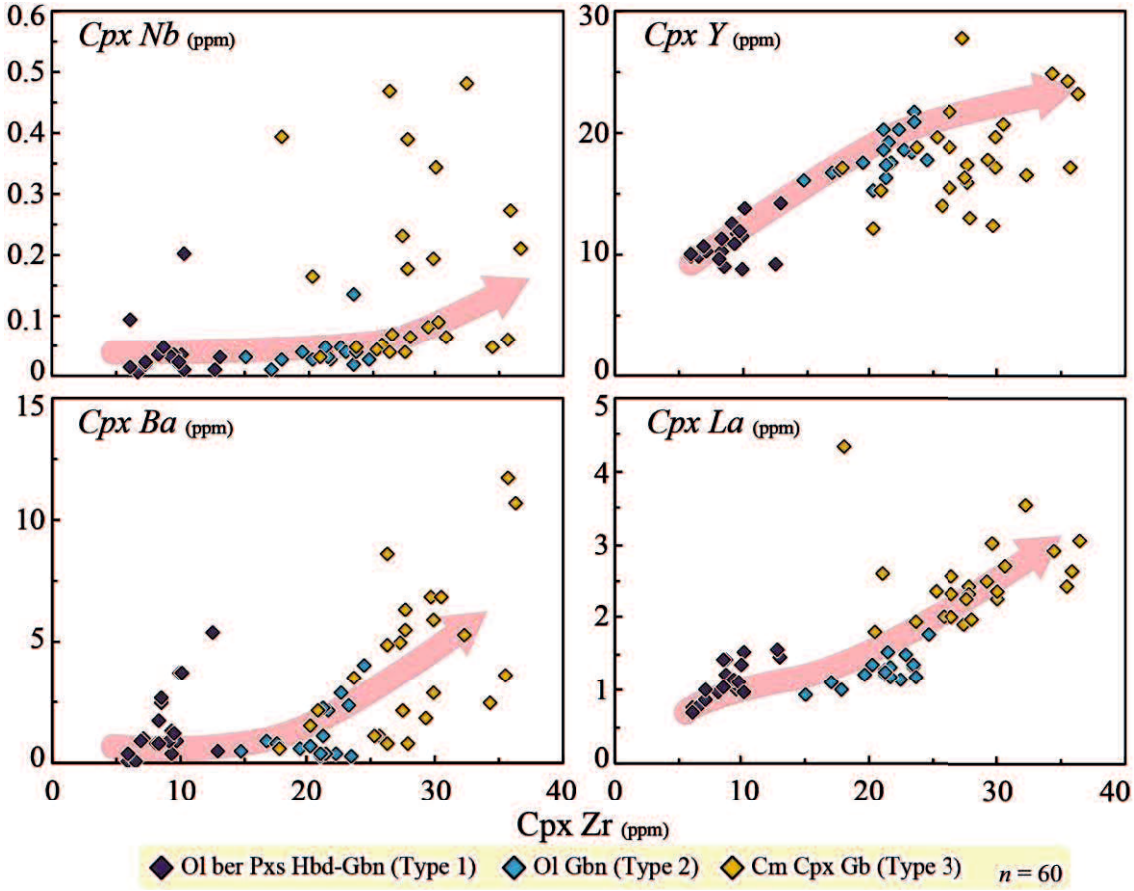

Figure 5–19. Trace element composition of clinopyroxene in the Kita-taku mafic complex plotting against Zr.

Primitive mantle-normalized multi-element patterns and C1 chondrite-normalized rare earth element (REE) patterns are shown in Figure 5–20. For the multi element patterns, Types 1, 2, and 3 show similar and/or parallel patterns, although the incompatible elements (Cs–Ta) are strongly scattered. These samples commonly show negative anomalies in Pb, Sr, and Zr, whereas show positive anomalies in Y. Since the Total REE contents (Σ REE) increase in this order (i.e., Type 1→Type 2→ Type 3), this difference in Sr content presumably reflects the onset of plagioclase crystallization (Fig. 5–20).

For C1 chondrite-normalized patterns, all samples (Types 1 to 3) commonly show gentle slopes upward in the left from Sm to Lu and opposite slopes from La to Sm (Fig. 5–20).

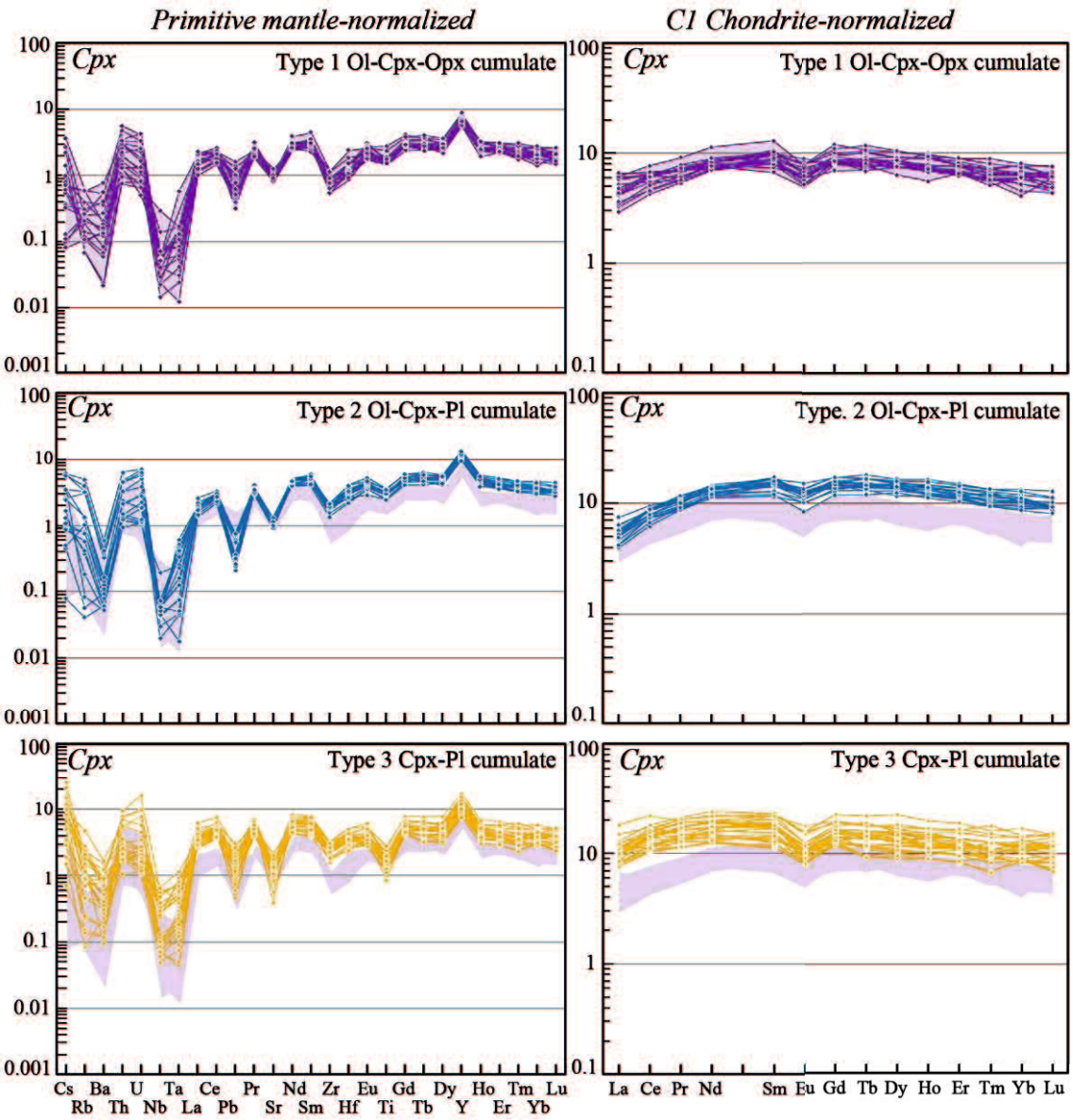

Figure 5–20. Primitive mantle- and C1 chondrite-normalized trace element diagrams for clinopyroxene from Kita-taku mafic complex. The normalizing values are from Sun and McDonough (1989).

5–4–5 Sr and Nd isotopes

The Sr and Nd isotopic ratios were corrected to 106 Ma because the average zircon U–Pb age is 106 Ma (section 5–4–1) The results of Sr and Nd isotopic analyses are listed in Appendix 5–10.

The initial Sr and Nd isotopic ratios are referred as SrI and NdI, respectively. Figure 5–21 shows the εSrI–εNdI diagram for the studied samples. The Cumulate group (Types 1, 2, 3, and 4) is plotted within the wide area in the epsilon diagram (εSrI = +7.3 –+12.60 and εNdI = +0.22 –+3.33), whereas the Gabbro group (Types 5, 6, and 7) has the limited values (εSrI = +11.3 –+17.0 and εNdI = -0.66 –+0.62) (Fig. 5–21). The amphibolite as host rock of the mafic complex possesses the high εNdI and relatively enriched εSrI values in the epsilon diagram (εSrI = +10.0 –+14.5 and εNdI = +1.54 –+6.28). The dikes including Tdh dike, PFD dike, and Ms-Bt granite show low εNdI and high εSrI values in the epsilon diagram (εSrI = +12.8 –+23.2 and εNdI = -0.87 –+0.27) (Fig. 5–21).

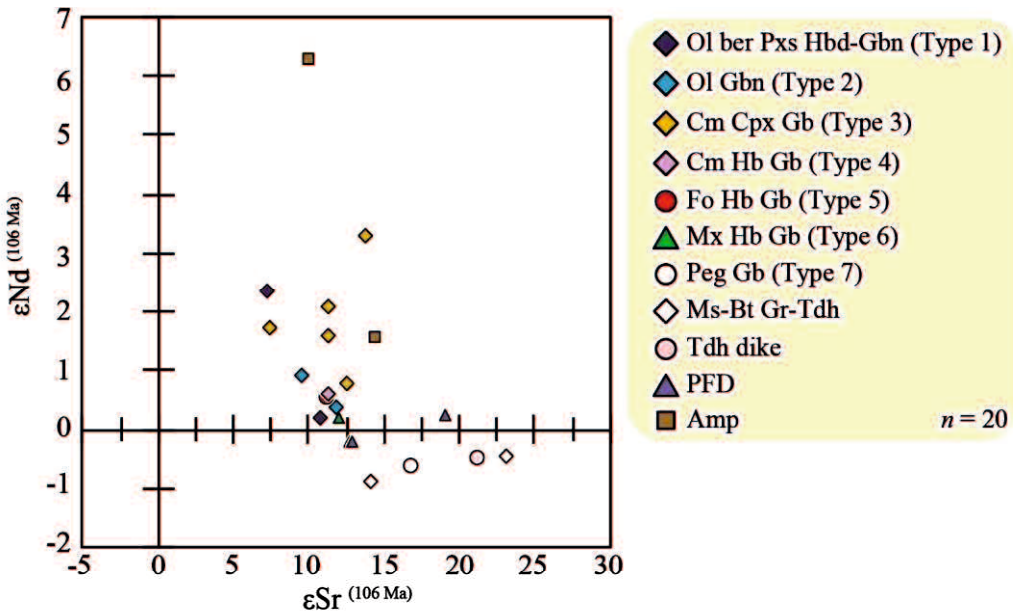

Figure 5–21. Sr and Nd isotopic compositions of the Kita-taku mafic complex and related rocks. εSrI (106 Ma)–εNdI (106 Ma) diagram. The results of Sr and Nd isotopic analyses are listed in Appendix 5–10.

5–5 Discussions

5–5–1 Activity period of the Kita-taku mafic complex and related igneous rocks

In the Kita-taku area, the Kita-taku mafic complex consists of the Cumulate group and the Gabbro group, and is intruded by granite (Fukae granite), Tdh and PFD dike (Fig. 5–2). The Kita-taku mafic complex is composed mainly of four types of cumulates (ultramafic to mafic), which are considered to have been active in the coevally time because of their inclusion relationships in each other (Figs. 5–4b, c, d, e, and f). However, the Cumulate is inadequate sample for zircon U–Pb dating because it rarely contains zircon grains (Figs. 5–6a, b, c, and d).

The Fo Hb Gb (Type 5) belonging to the Gabbro group, intrudes into the Cumulate group as a coeval dike (Figs. 5–5a and b). In this study, I used the Fo Hb Gb (Type 5) as a zircon U–Pb dating sample to determine the age of the Kita-taku mafic complex. As a result, the zircon U–Pb weighted average age of 105.8 ± 0.5 Ma was obtained from the zircon in the Fo Hb Gb (Type 5) (Figs. 5–9, 5–10a, Appendices 5–2, 5–3, and 5–4).

As for the age of the related igneous rocks, the granite intrudes into the Kita-taku mafic complex in the western part of the body shows mingling texture and ocellar quartz at the boundaries (Figs. 5–5f and g), suggesting that it was active simultaneously as the Kita-taku mafic complex. The Tdh and PFD dikes intrude into the Kita-taku mafic complex and form a composite dike (Fig. 5–5e), suggesting that they were active at the coevally time. In other words, if the age of either Tdh or PFD can be determined, the relationship with the activity of the Kita-taku mafic complex can be confirmed. In this study, I measured the zircon U–Pb age of the Tdh dike that runs through the sample. A zircon U–Pb weighted average age of 105.9 ± 0.5 Ma was obtained(Figs. 5–9, 5–10b, Appendices 5–2, 5–3, and 5–4). This age is consistent with the age of the Fo Hb Gb (Type 5) (i.e., the Kita-taku mafic complex) within the analytical error. Therefore, it can be concluded that the Kita-taku mafic complex and the intrusive rocks, granite, Tdh, migmatite, and PFD dikes in the Kita-taku area are

inferred to have been active around 106 Ma simultaneously.

5–5–2 Crystallization of the Kita-taku mafic complex

The chemical compositions of the cumulus minerals in the Cumulate group of the Kita-taku mafic complex show a series of magmatic trends and are considered to be derived from a common parent magma (Figs 5–12, 5–13, 5–14, 5–15, 5–16, 5–17, and Table 5–1). Based on the chemical compositions of the cumulus minerals (olivine, clinopyroxene, orthopyroxene, and hornblende) of the Cumulate group from Kita-taku mafic complex, the *Mg*# of the mafic cumulus minerals decreases in the order of Ol Gbn–Ol ber Pxs Hbd (Type 1), Ol Gbn (Type 2), Cm Cpx Gb (Type 3), and Cm Hb Gb (Type 4) (Fig. 5–22). This suggests that the crystallization occurred in the order of olivine (Ol)–clinopyroxene (Cpx)–orthopyroxene (Opx) cumulate (Type 1), olivine (Ol)–clinopyroxene (Cpx)–plagioclase (Pl) cumulate (Type 2), clinopyroxene (Cpx)–plagioclase (Pl)–hornblende (Hb) cumulate (Type 3), and plagioclase (Pl)–hornblende (Hb) cumulate (Type 4) and they were crystallized due to differentiation of the same parent magma (Fig. 5–22 and Table 5–1).

Ol Gbn–Ol ber Pxs Hbd (Type 1) and Cm Cpx Gb (Type 3) belonging to the Cumulate group has orthocumulus texture with a large amount of trapped melt between the grains of cumulus minerals, as described in section 5–3 (Figs 5–6a, c, and Table 5–1). From such trapped liquid (melt), the Ol–Cpx–Opx cumulate (Type 1) and Cpx–Pl–Hb cumulate (Type 3) have variably lithofacies, modal compositions, and whole-rock chemical compositions as a result of the occurrence of hornblende and plagioclase in the post-cumulus stage. The formation of film-like orthopyroxene and hornblende around the cumulus olivine (Fig. 5–6b) in the Ol–Cpx–Pl cumulate (Type 2) suggests that these minerals were produced by the reaction of magma (or trapped liquid) with olivine. Therefore, the start of orthopyroxene crystallization coeval with the stop of olivine crystallization and the disappearance of olivine. This suggests that the interstitial liquid (trapped liquid) drainage started at this time, and

that Ol–Cpx–Pl cumulate (Type 2) with adcumulus texture was formed (Fig. 5–6b). However, the interstitial liquid (trapped liquid) was restored by some influence, and Cpx–Pl–Hb cumulate (Type 3) and Pl–Hb cumulate (Type 4) were formed through the same process as mentioned above (Fig. 5–6c and d).

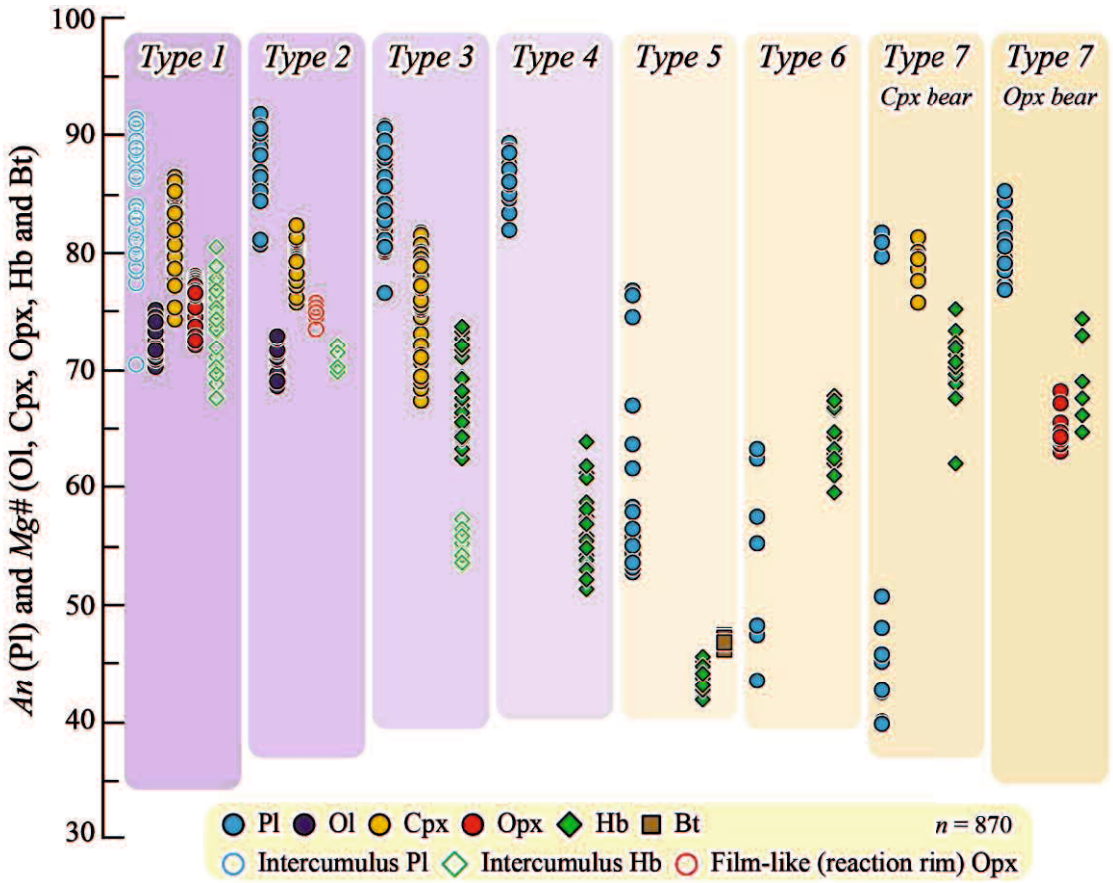

Figure 5–22. *An* content of plagioclase and *Mg#* of mafic minerals for the Kita-taku mafic complex. Type 7 is divided into 2 types, which bearing Cpx and Opx.

The Gabbro group of the Kita-taku mafic complex is divided into Fo Hb Gb (Type 5), Mx Hb Gb (Type 6) and Peg Hb Gb (Type 7), which are generally composed of plagioclase and hornblende (Figs. 5–6e, f, g, and Table 5–1). Fo Hb Gb (Type 5) is the most fine-grained mafic rock among the Kita-taku mafic complex, and it intrudes into the Cumulate group as a coeval dike (Figs, 5–5a, b, and 5–6e). The whole-rock and mineral compositions of Fo Hb Gb (Type 5) are not consistent with

the trend of the Cumulate group (Figs. 5–11 and 5–17), suggesting that it is either different from the parent magma of the Cumulate group or is a highly differentiated magma. Mx Hb Gb (Type 6) has the mixing texture with the Cumulate group in the field and shows intermediate compositions between Fo Hb Gb (Type 5) and the Cumulate group in whole-rock and mineral composition (Figs. 5–5c, 5–11, and 5–17). Peg Hb Gb (Type 7) is the most coarse-grained rock in this area, containing hornblende megacrysts attaining up to 30 mm in long (Figs. 5–4b and 5–6g). The composition of the hornblende is similar to that of intercumulus hornblende in the Cumulate group, and the compositions of the clinopyroxene and orthopyroxene in the hornblende megacrysts overlap with those in the Cumulate group (Figs. 5–14, 5–15, 5–17, and 5–22). These facts suggest that Mx Hb Gb (Type 6) is formed by the intrudes and mixing of Fo Hb Gb (Type 5) into the Cumulate group, and Peg Hb Gb (Type 7) is formed by the differentiated melt extruded from the of the interstitial liquid of the Cumulate group.

The relationship between *Mg#* of mafic minerals and *An* content of plagioclase was investigated from olivine, orthopyroxene and plagioclase in the Ol Gbn (Type 2) and Peg Hb Gb (Type 7) of the Kita-taku mafic complex (Fig. 5–23). The *Mg#* of orthopyroxene was converted to *Mg#* of olivine using Fe/Mg exchange coefficient (Beattie, 1993). As a result, the Cumulate group of the Kita-taku mafic complex shows a tendency of decreasing *Mg#* of mafic minerals, while the *An* content of plagioclase remains remarkably high (Fig. 5–23). The Cumulate group of the Kita-taku mafic complex is crystallized of olivine followed by clinopyroxene rather than plagioclase, suggesting two possibilities in terms of phase petrology: (1) crystallization under anhydrous and high-pressure conditions, or (2) crystallization under hydrous (low-pressure) conditions.

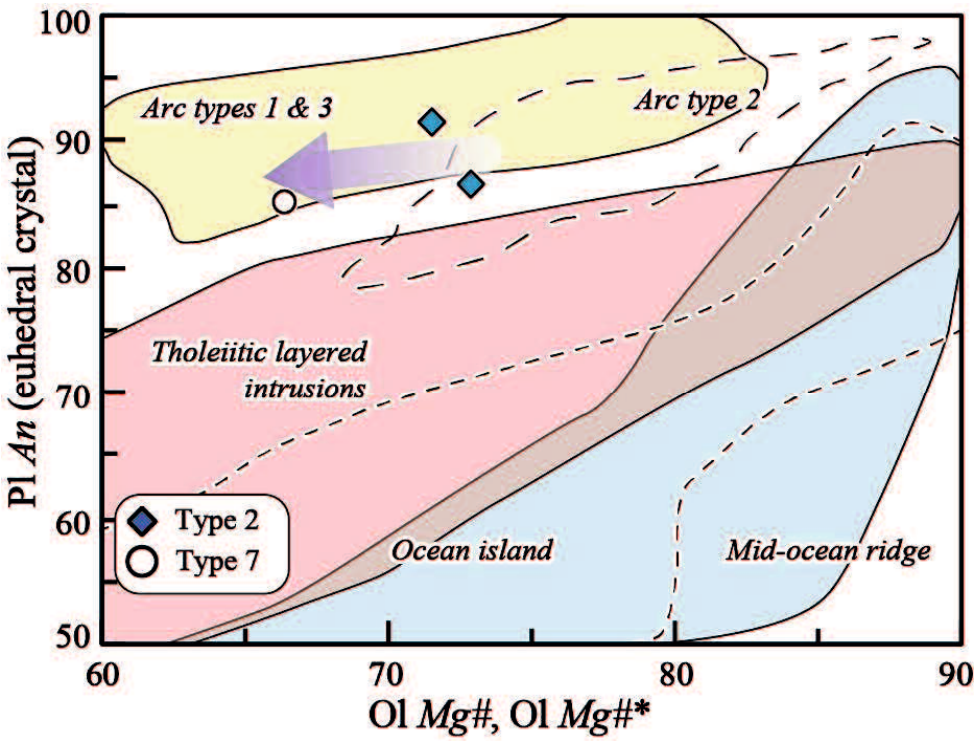

Figure 5–23. Plagioclase *An* vs. olivine *Mg#* and olivine *Mg# plot of the Kita-taku mafic complex. The *Mg#* of orthopyroxene was converted to *Mg#* of olivine (Ol *Mg#**) using Fe/Mg exchange coefficient (Beattie, 1993). Fields of various gabbro are from Barnes (1986).**

In basaltic systems under anhydrous conditions, the olivine-plagioclase and co-melt relationship disappears at about 7 kbar (Kushiro and Yoder, 1966; Presnall et al., 1978). Melting experiments on anhydrous peridotite with tholeiitic melt compositions show that olivine is followed by clinopyroxene, but not plagioclase, above 5 kbar (Green and Ringwood, 1967). The equilibrium temperature and crystallization pressure of the pyroxene in Ol Gbn–Ol ber Pxs Hbd (Type 1) were estimated using equations 37 and 39 of Putirka (2008) (Appendix 5–11). As a result, the temperature and pressure conditions were estimated to be 835 to 980 °C and 3.74 to 5.87 kbar. These results suggest that under anhydrous conditions, the co-melting relationship between olivine and plagioclase may disappear in this pressure range. However, this result is not consistent with the petrological features as described

previously, because a large amount of hornblende cannot be expected to be crystallized from magma under near-anhydrous conditions.

On the other hand, under hydrous conditions, the liquidus temperature of plagioclase is significantly lower than that of mafic minerals, resulting in early plagioclase desegregation as in high-pressure conditions (Yoder and Tilley, 1962; Yoder, 1965; Danyushevsky, 2001). Under hydrous conditions, the partition coefficient of Ca-Na between melt and plagioclase changes with decreasing plagioclase liquidus temperature, resulting in the crystallization of calcic plagioclase compared to anhydrous conditions and the continued crystallization of plagioclase with calcic composition even with decreasing temperature (Fig. 5–24: Yoder et al., 1957; Johannes, 1978). In other words. The relationship between *Mg#* and *An* content shown in Figures 5–22 and 5–23 can also be explained.

The crystallization of anhydrous minerals such as olivine, pyroxene and plagioclase from hydrous magmas is also in agreement with the large amount of hornblende in the Kita-taku mafic complex. In hydrous magmas, the water content in the magma is expected to increase relatively as the progress of its fractionation with anhydrous minerals. The increase of water content occurred not only in the residual magma, but also in the trapped liquid between the grains of cumulus minerals, resulting in the formation of the Kita-taku mafic complex characterized by oikocrystic hornblende.

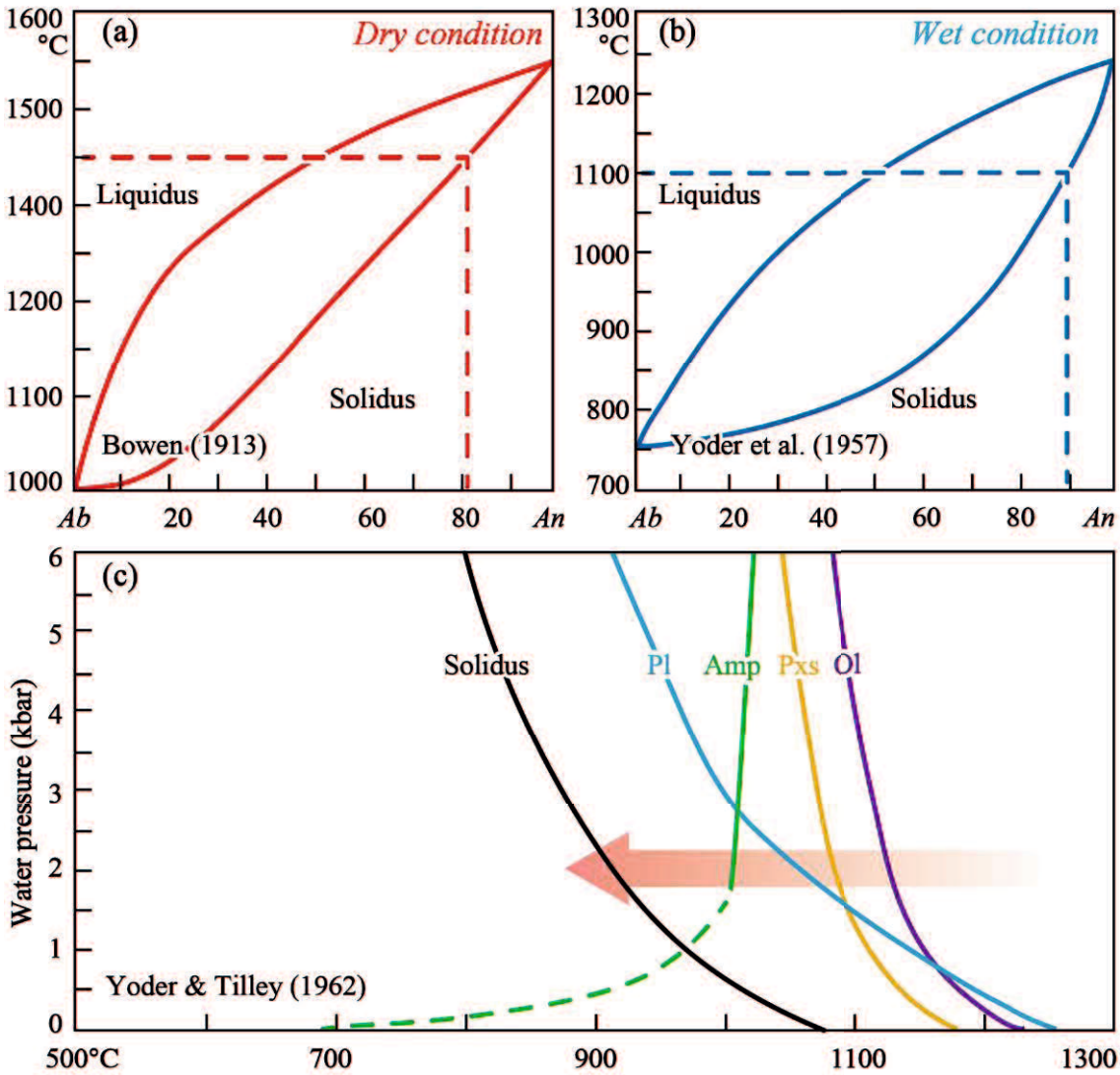

Figure 5–24. Phase diagram of plagioclase. (a) Dry (anhydrous) condition (Bowen, 1913), (b) Wet (hydrous) condition (Yoder et al., 1957). (c) Crystallized temperature vs. Water pressure diagram from Yoder and Tilley. (1962).

5–5–3 Characteristics of the parent magma for Kita-taku mafic complex

Based on the compositional relationship between coexisting spinel and olivine in Ol Gbn–Ol ber Pxs Hbd (Type 1) belonging to the Cumulate group of the Kita-taku mafic complex, the composition of mantle peridotite coexisting with primary magma in the Cumulate group can be estimated. The *Mg#* of olivine and *Cr#* of spinel from Type 1 rocks can estimate the compositions of source mantle in Figure 5–25.

According to Figure 5–25, the estimated source mantle possesses a spinel with *Cr#* =0.5. Such a source mantle is sufficiently depleted to be considered as mantle material under the Japanese Islands. However, it cannot be distinguished from the mantle under the Mid-ocean ridge (e.g., Arai et al., 2000; Arai and Ishimaru, 2008). In any case, mantle peridotites with *Cr#* (spinel)= 0.5 are expected to be depleted to about the boundary between harzburgite and lherzolite (Arai, 1987).

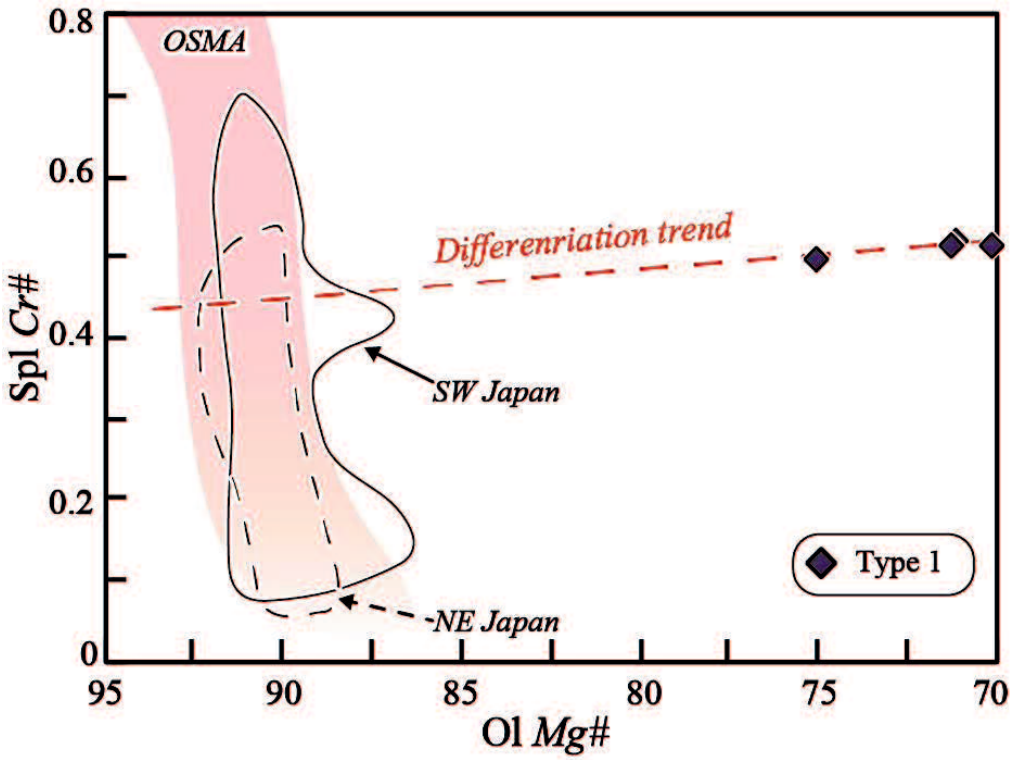

Figure 5–25. spinel *Cr#*–olivine *Mg#* relationships in Ol Gbn–Ol ber Pxs Hbd (Type 1) from the Kita-taku mafic complex. Fields of peridotites from SW Japan, NE Japan and abyssal peridotites are drawn from the data of Arai and Ishimaru (2008), Olivine–Spinel Mantle Array (OSMA) are from Arai (1987). Dashed red line is differentiation trend of the Kita-taku mafic complex.

In this study, I estimated the melt composition deduced from the compositions of clinopyroxene with high *Mg*# in Ol Gbn–Ol ber Pxs Hbd (Type 1) using the melt-clinopyroxene partition coefficient. The *Mg*# of the clinopyroxene used in this study ranged from 83.18 to 86.40, whose compositions are closed to coexistence of primitive magma. The multi-element patterns and rare earth element (REE) patterns normalized to N-MORB and C1 Chondrite are shown in Figure 5–26. The multi-element patterns and REE patterns are similar to those of high-Mg andesite (HMA). The most similar composition is Sanukitic HMA, which is not an impossible source magma composition because it is reported to coexist with mantle peridotite from experimental data such as melting experiments (e.g., Tatsumi, 1981, 1982). Since the Sanukitic HMA is a magma with relatively high-water content, the crystallization of the Kita-taku mafic complex is feasible. However, I could not examine the source magma for the Gabbro group Fo Hb Gb (Type 5) due to lack of data. The remaining liquid of the Cumulate group magma (i.e., Sanukitic HMA) or some kinds of hydrous magma are possible candidates for the parental magmas of the Gabbro group, which will be the subject of further study.

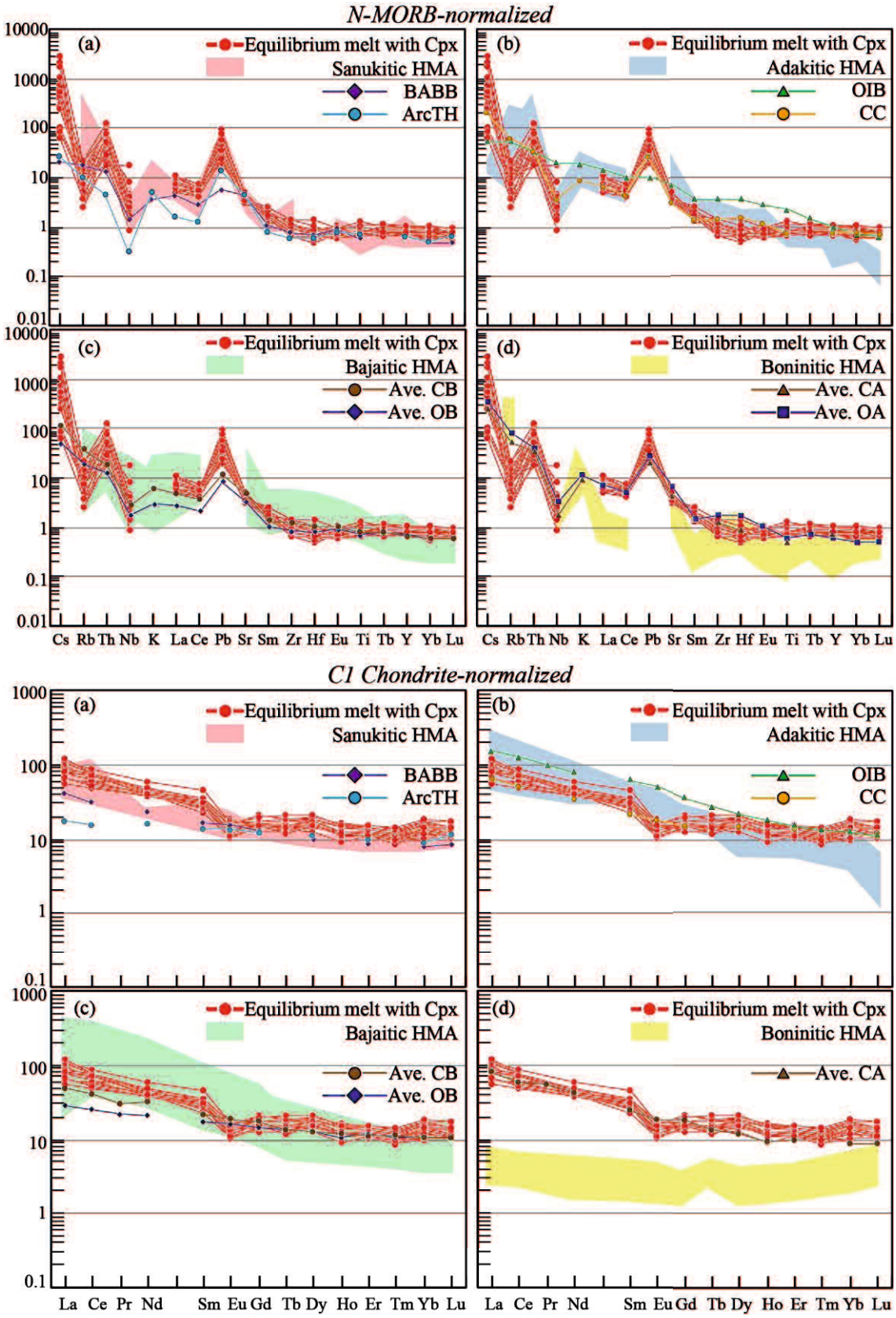

Figure 5–26. N-MORB- and C1 chondrite-normalized trace element diagrams for

equilibrium clinopyroxene from Kita-taku mafic complex. The normalizing values are from Sun and McDonough (1989). Cpx/melt partition coefficients and compared data sources listed in Appendix 5–12. HMA: high-Mg andesite, BABB: back arc basin basalt, OIB: ocean island basalt; ArcTH: arc tholeiite, CC: continental crust, Ave. OB: average oceanic basalt, Ave. CB: average continental basalt, Ave. OA: average oceanic andesite, and Ave. CA: average continental andesite.

5–5–4 Growth and formation processes of the Kita-taku mafic complex

In the Kita-taku mafic complex, the Cumulate group is often found to be inclusion–inclusion relationship with each other (Fig 5–4). Peg Hb Gb (Type 7) intrudes into the Cumulate and Gabbro group along the fractures (Figs. 5–4b, 5–27g, and h). In addition, Fo Hb Gb (Type 5) occurring in the central part of the body intrudes into the Cumulate group, where cumulus hornblende is rolled up (Fig. 5–27f).

On the other hand, Cm Hb Gb (Type 4) belonging to the Cumulate group has a layered structure and is characteristically distributed around Fo Hb Gb (Type 5), at which Mx Hb Gb (Type 6) tends to crop out close to the Cumulate group (Figs. 5–27a, b, c, d, and e). As a result of the above discussion, the Cumulate group is derived from the same parent magma (Fig. 5–22). The growth (formation) process of the Kita-taku mafic complex is shown in Fig. 5–28 inferred from the field survey and petrological investigations.

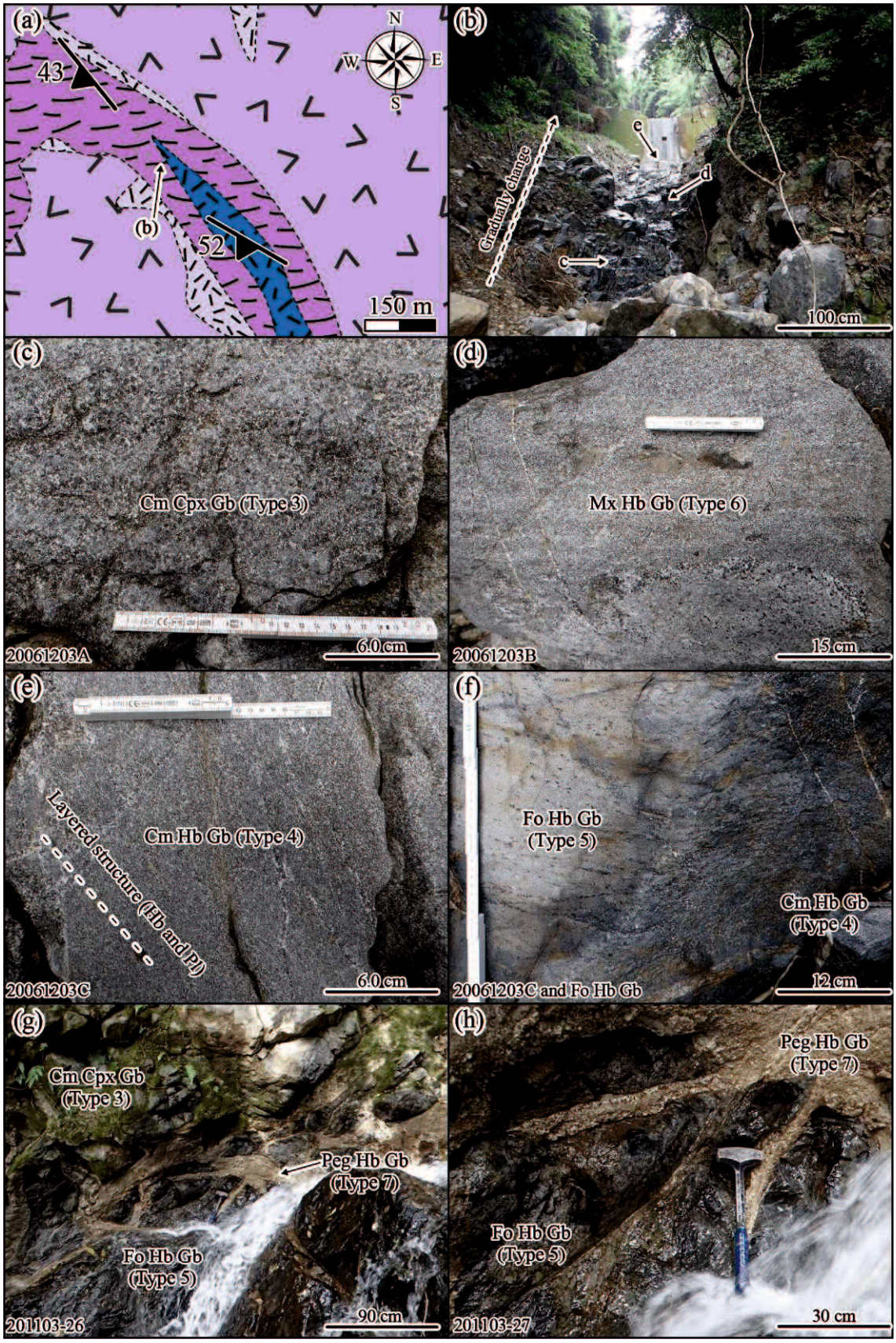

Figure 5–27. Characteristics occurrences of the Kita-taku mafic complex. (a) Close up to

geological map shows occurrence point of the Figures. 5–27b, c, d, and e. (b) The lithofacies are continuously changing (c→d→e). (c) Cm Hb Gb (Type 3). (d) Mx Hb Gb (Type 6). (e) Cm Hb Gb (Type 4). (f) Fo Hb Gb (Type 5) injects into the accumulating magma and rolls up each cumulate. (g and h) The Peg Hb Gb (Type 7) intrudes into the Fo Hb Gb (Type 5) along the fractures.

Firstly, olivine, clinopyroxene, plagioclase, orthopyroxene and hornblende begin to accumulate from the parent magma. When Ol Gbn–Ol ber Pxs Hbd (Type 1), Ol Gbn (Type 2), and Cm Cpx Gb (Type 3) are formed by accumulation, Fo Hb Gb (Type 5) injects into the accumulating magma and rolls up Types 1, 2, and 3 into the upper portion of the magma chamber (melt richer part). This injection increases the re-activation of the melts (or interstitial liquid). In addition, when Fo Hb Gb (Type 5) intrudes into the magma chamber, shear stress and flow differentiation (Best and Christiansen, 2001) act between the dike and the wall (crystal mush) to form Cm Hb Gb (Type 4) with a layered structure. During this intrusive phenomenon, Fo Hb Gb (Type 5) and Cumulate group mixing to form Mx Hb Gb (Type 6). It is inferred that the Kita-taku mafic complex was grown or formed by the above processes (Fig. 5–28).

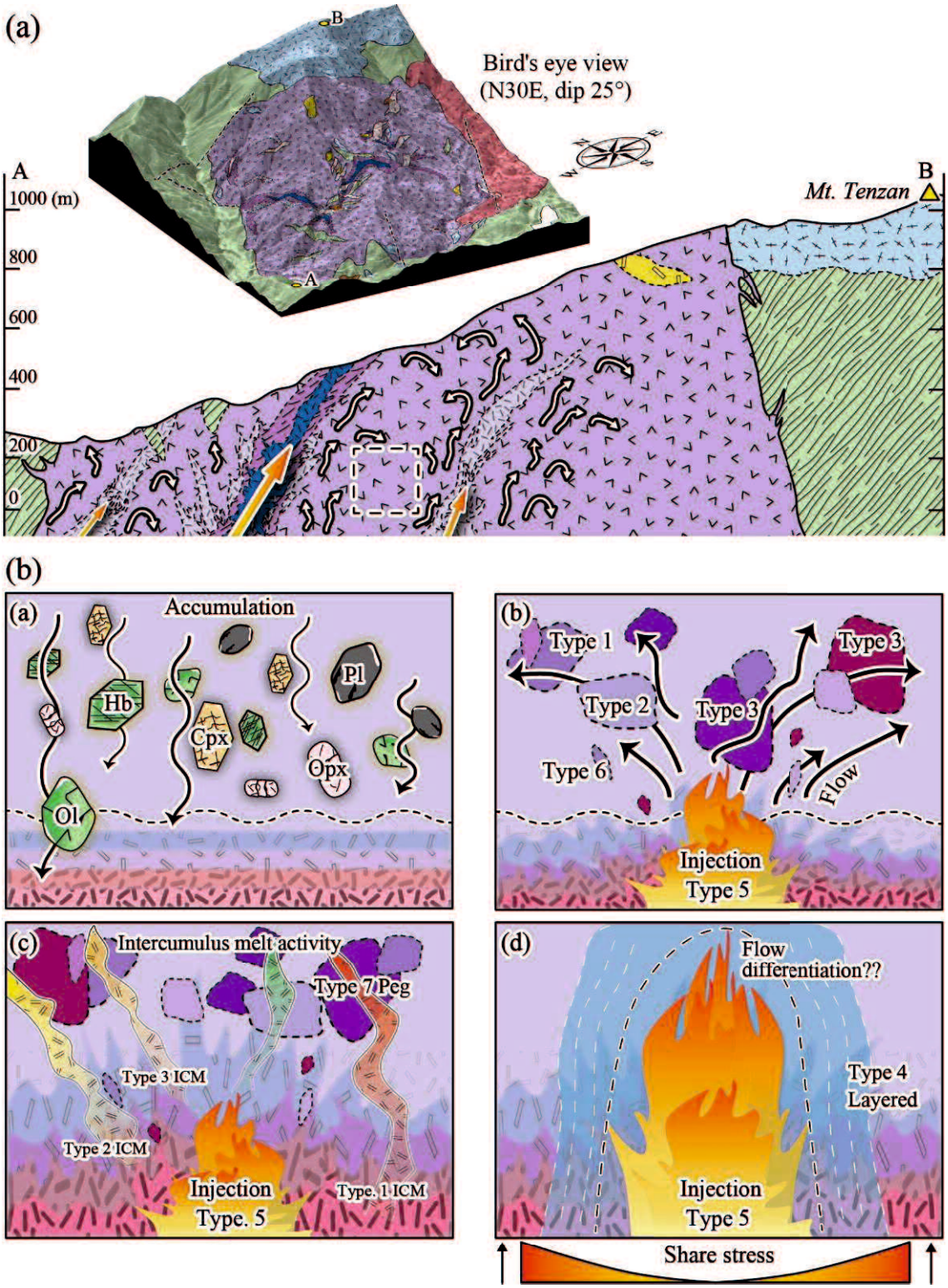

Figure 5–28. Growth and formation processes of the Kita-taku mafic complex. ICM: intercumulus melt.

6 Northern Kyushu batholith

6–1 Heat source of the large-scale Cretaceous igneous activity in northern Kyushu

The migmatite associated with the trondhjemite (Tdh) dike occurs in the Kita-taku mafic complex (detailed description in chapter 5). The presence of migmatite with Tdh dike in this area may be useful to determine the origin and genesis of the granitic magma in the Northern Kyushu batholith. In this study, I hypothesize that the Tdh was formed by partial melting of the amphibolite as a host rock of the Kita-taku mafic complex. The first evidence of partial melting is the occurrence of migmatite (Fig. 6–1). This occurrence is often observed at the contact between Kita-taku mafic complex and amphibolite. The migmatite outcrop consists of amphibolite (melanosome), felsic gabbro (leucosome) and Tdh that intrudes into the former two lithofacies as the dike (Fig. 6–1). The Tdh is not only a dike but also a member of migmatite as part of the migmatite leucosome (Fig. 6–1b), which means that the Tdh simultaneously formed with the migmatite, and the Tdh is considered to have formed by partial melting of the amphibolite (section 5–4–1). In addition, the zircon grains in the Tdh in the Kita-taku mafic complex is accompanied by an inherited zircon grain that shows a core-rim texture, and it gives a $^{206}U/^{238}Pb$ age of 261.3 ± 8.5 Ma (Fig. 6–2). This $^{206}U/^{238}Pb$ is similar to the young component in $^{206}U/^{238}Pb$ age of inherited zircon grains from Suo metamorphic complex.

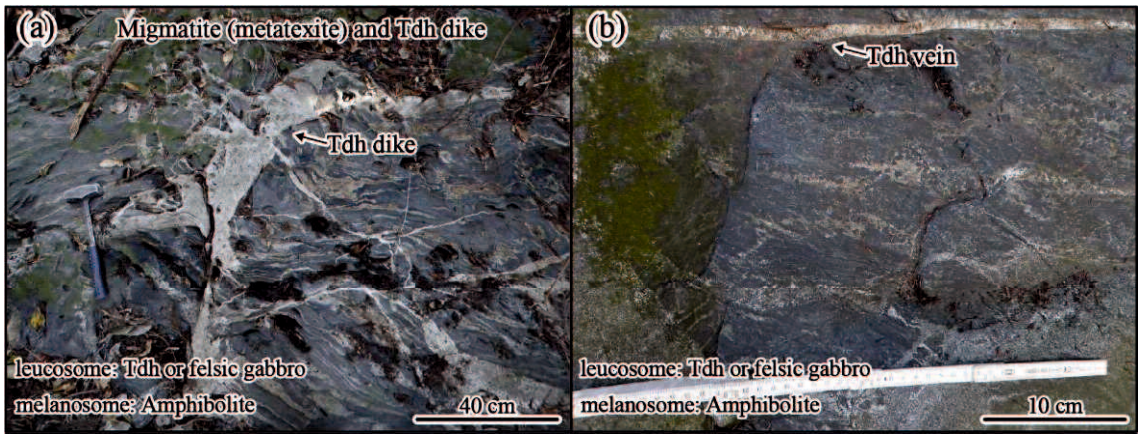

Figure 6–1. Field occurrences of the migmatite. (a) Trondhjemite (Tdh) dike intrudes into migmatite. (b) Close-up to (a). Abbreviations are show in the text.

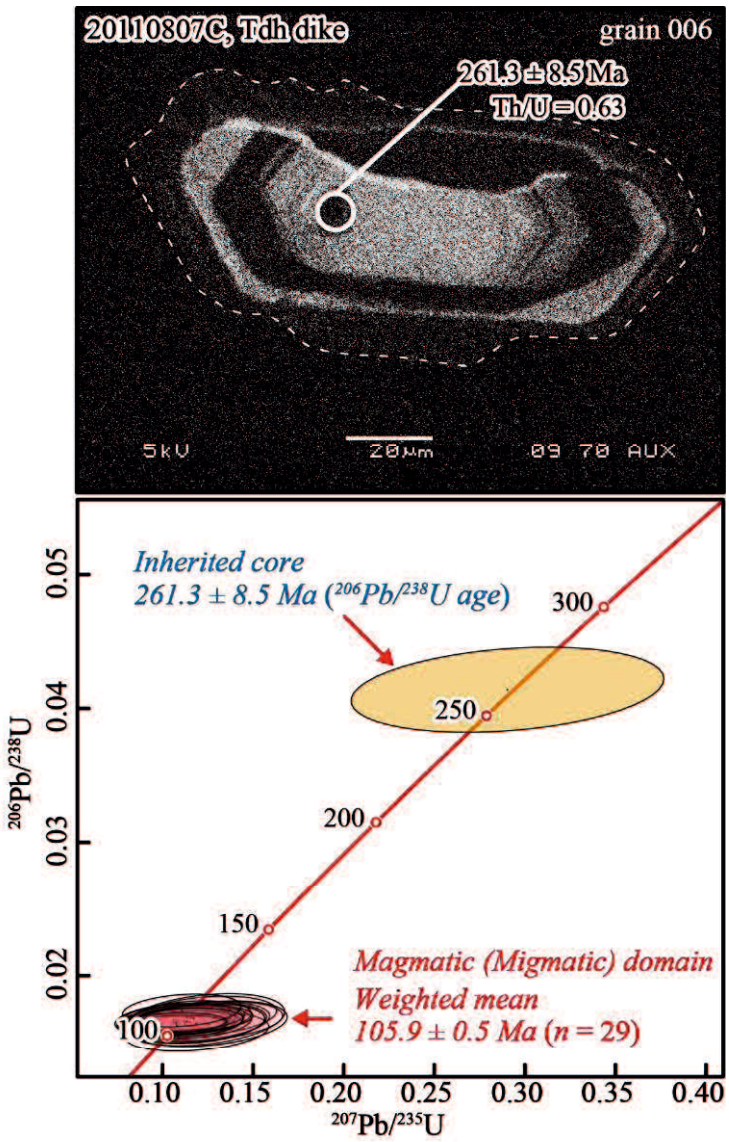

Figure 6–2. Cathodoluminescence (CL) image and concordia diagram of the zircon grain

006 in the Tdh.

The heat source for the partial melting of the amphibolite deems to be the parent magma of the Kita-taku mafic complex corresponding to the Sanukitic HMA magma as previously mentioned. The temperature of parent magma is of >835–980 °C based on the temperature conditions of the Cumulate group of the Kita-taku mafic complex. The amphibolite has undergone the partial melting under such temperature conditions, probably up to 40% degree of melting (Fig. 6–3).

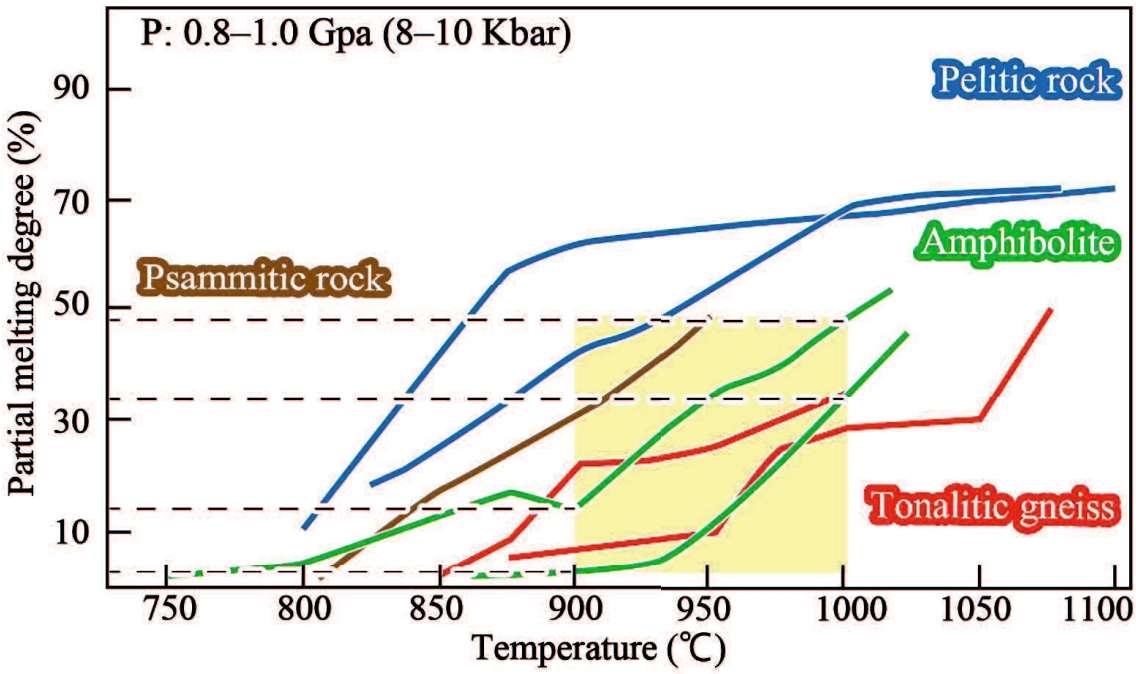

Figure 6–3. Partial melting degree vs. temperature diagram. These line of change in partial melting degree are from published experimental results. Data sources: Vielzeuf and Holloway (1988); Rutter and Wyllie (1988); Patiño Douce and Johnston (1991); Skjerlie and Johnston (1993); Wolf and Wyllie (1994); Montel and Vielzeuf (1997); Lopez and Castro (2001).

To verify above hypothesis, the geochemical modeling was performed for the amphibolite utilizing the equation of batch melting (Shaw, 1970). The results are shown in the multiple-element diagram (Fig. 6–4). The calculated liquid patterns almost resemble the pattern of the Tdh, enrichment of LIL and a negative Nb anomaly but the compositions of Zr–Lu except of Ti are slightly different. The lower partial melting degree (5%) is more similar to the composition of trondhjemite (Fig. 6–4). The different compositions are thought to be caused by assimilation of other crustal components such as a pelitic to psammitic rocks because the Tdh shows the negative εNdI values (Figure 5–21). Consequently, the field occurrence of migmatite suggests that the heat source should be of a Sanukitic HMA-like magma.

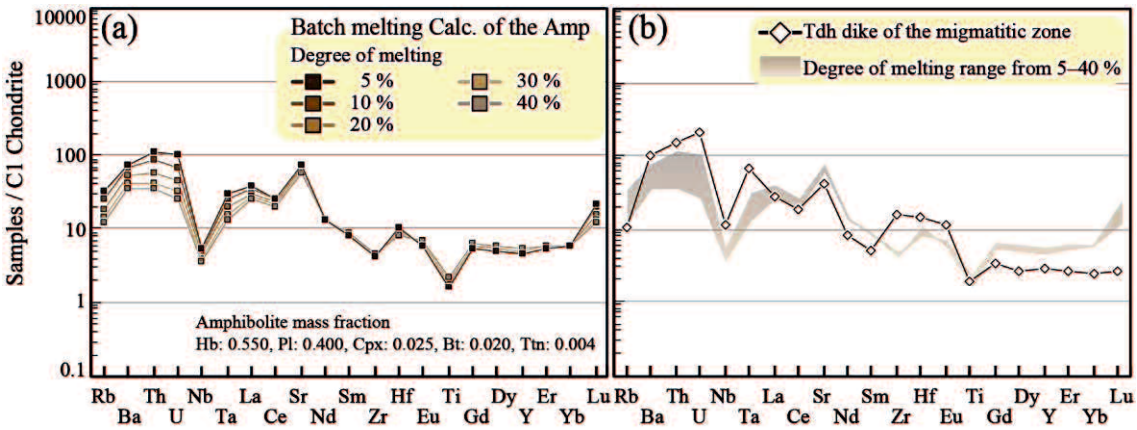

Figure 6–4. (a) Multiple-element diagram for the result of batch melting calculation. (b) Added the composition of trondhjemite. The partition coefficients used in batch melting calculation listed in Appendix 6–1.

6–2 Evidence of partial melting and formation of felsic magma in Northern Kyushu batholith at Cretaceous period

According to recent zircon U–Pb age studies of metamorphic rocks and migmatites from northern Kyushu, partial melting of crustal materials has been reported to have occurred during the Early Cretaceous (Miyazaki et al., 2013; Miyazaki et al., 2017; Mori et al., 2021). Figure 6–5 shows the geology of northern Kyushu and its zircon U–Pb dating, using the concordant zircon U–Pb ages (n = 409) obtained from nine plutonic rocks and two volcanic rocks, and inherited zircon U–Pb age (n = 342) obtained from 10 metamorphic rocks was used to produce the age spectrum of igneous rocks and young component of metamorphic rocks from northern Kyushu (Figs. 6–6 and 6–7). Zircon U-Pb ages have closure temperatures as high as 1000°C (Cherniak and Watson, 2000). At temperatures above 830–850°C, zircon ages are modified by diffusion after dissolution (Bea and Montero, 2013). Therefore, the zircon age of igneous rocks is the age of magma crystallization, and the inherited zircon age of metamorphic rocks is the age of the source igneous rock. Figure 6–6 shows the age spectrum of igneous rocks adopting the Kernel density estimation (KDE) plot (Varmeesh, 2012). The igneous activity in northern Kyushu took place from 135 Ma to 85 Ma (Fig. 6–6). Such long-term igneous activity means that a large amount of energy was continuously inputted from the mantle to the lower crust, and the heat energy caused anatexis at the lower crust and contributed to the formation of high-temperature metamorphic rocks accompanied by migmatite. The U–Pb age of zircons from migmatites and zircons with metamorphic rims in metamorphic rocks from northern Kyushu overlap with the age spectrum of igneous rocks (Figs. 6–5 and 6–6). In addition, based on the recent study of topological plate motion model (e.g., Seton et al., 2012; Liu et al., 2017), the U–Pb age of zircons from migmatite and metamorphic rims in metamorphic rocks become younger from the continentalward to the trenchward (Fig. 6–5). Therefore, the igneous activity in northern Kyushu during the Cretaceous is likely to have been caused by partial

melting of the crust. Moreover, the Tdh dike coexisting with migmatite in the Kita-taku area contains inherited zircons with an age of 261.3 ± 8.5 Ma. The age of 260 Ma is closed to the inherited zircon age (250 Ma) of metamorphic rocks in the Suo metamorphic complex widely distributed in northern Kyushu (Figs. 6–5 and 6–7).

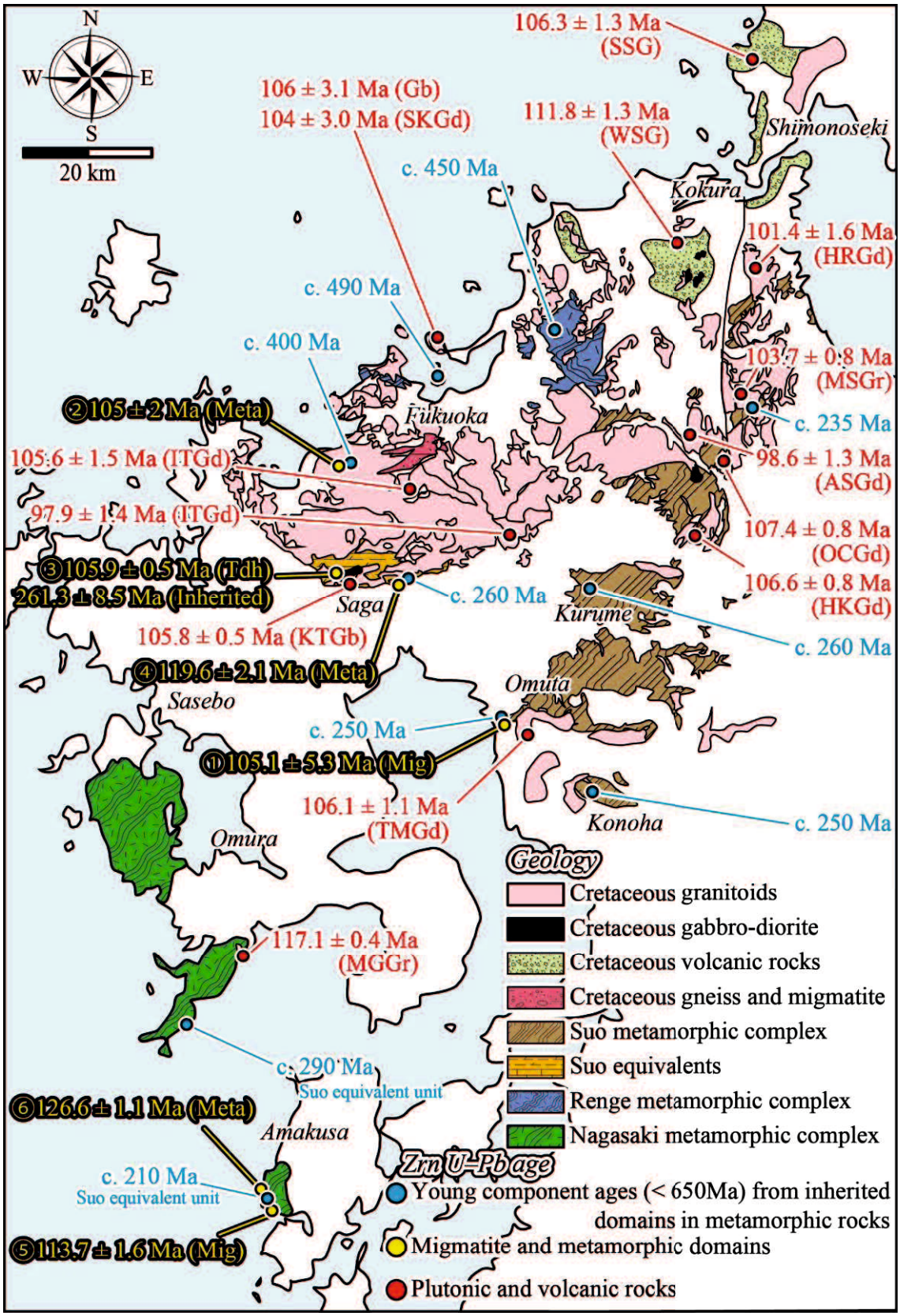

Figure 6–5. Geological map of Cretaceous volcanic, plutonic, metamorphic rocks and related rocks in northern Kyushu. Geological map and sample localities of the igneous,

metamorphic, and migmatitic rocks used for zircon U–Pb dating. Data sources: Tsutsumi et al., 2003, Tsutsumi et al., 2011, Adachi et al., 2012, Tiepolo et al., 2012, Miyazaki et al., 2013, Miyazaki et al., 2017, Miyazaki et al., 2018, Tsutsumi and Horie, 2019, Yuhara et al., 2019a, 2019b, 2020, 2021, and Mori et al., 2021. SSG: Shimonoseki sub-group, WSG: Wakino sub-group, HRGd: Hirao granodiorite, MSGr: Masaki granite, ASGd: Asakura granodiorite, OCGd: Ochiai granodiorite, HKGd: Haki granodiorite, TMGd: Tamana granodiorite, KTGb: Kita-taku mafic complex, ITGd: Itoshima granodiorite, MGGr: Mogi granite, and SKGd: Shikanoshima granodiorite.

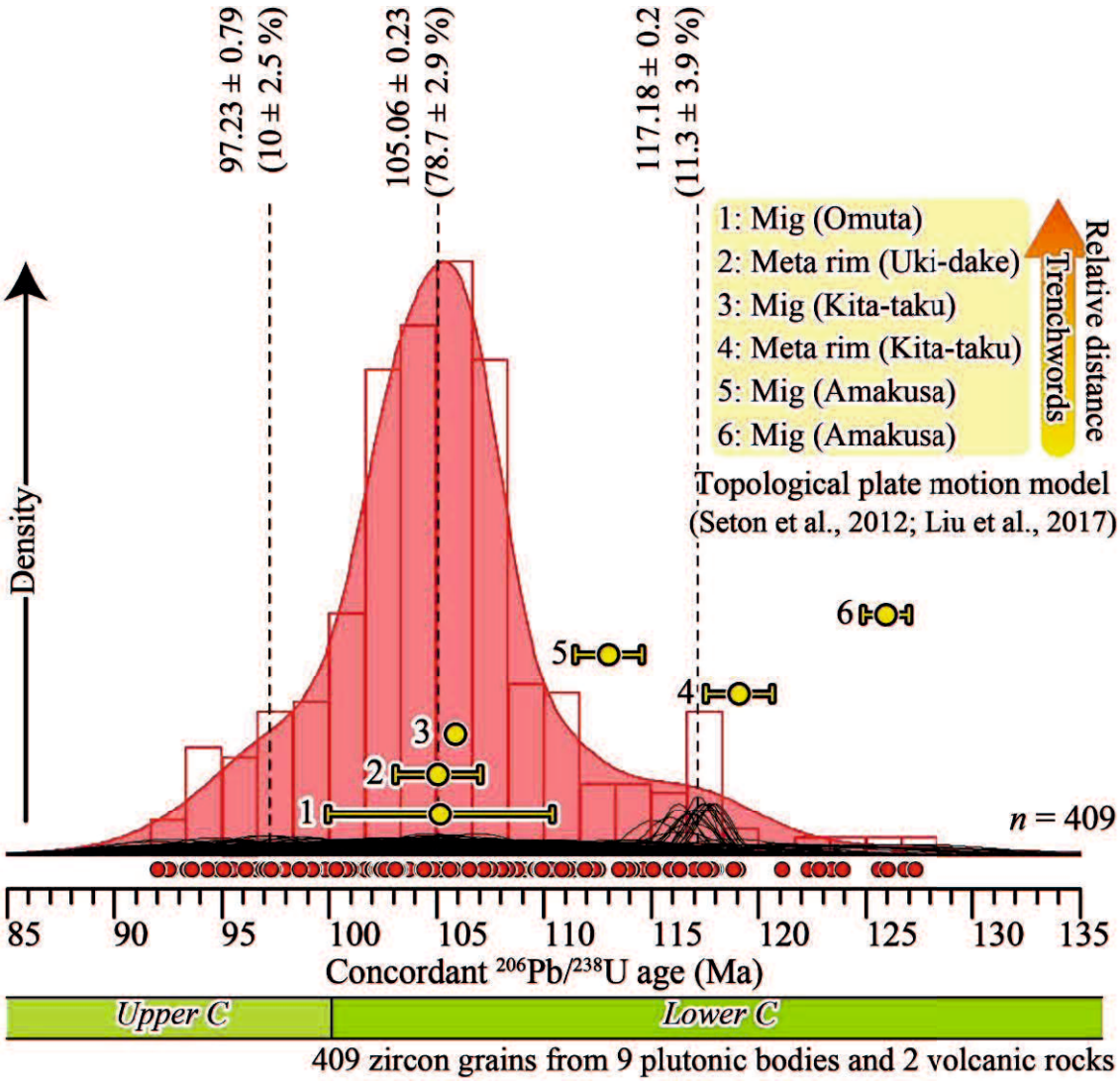

Figure 6–6. Age spectrum (KDE plot: Varmeesh, 2012) of zircon grains from nine plutonic bodies and two volcanic rocks from northern Kyushu with metamorphic zircon and

migmatitic zircon ages of 105.1 ± 5.3 Ma (1: Miyazaki et al., 2017), 105 ± 2 Ma (2: Adachi et al., 2012), 105.9 ± 0.5 Ma (3: This study), 119.6 ± 2.1 Ma (4: Tanaka, unpublish data), 113.7 ± 1.6 Ma (5: Miyazaki et al., 2013), and 126.6 ± 1.1 Ma (6: Mori et al., 2021) . Age component calculated using *Mixture Models (auto)* of *DensityPlotter* (Varmeesh, 2012) are also shown. Upper C: upper Cretaceous and Lower C: lower Cretaceous.

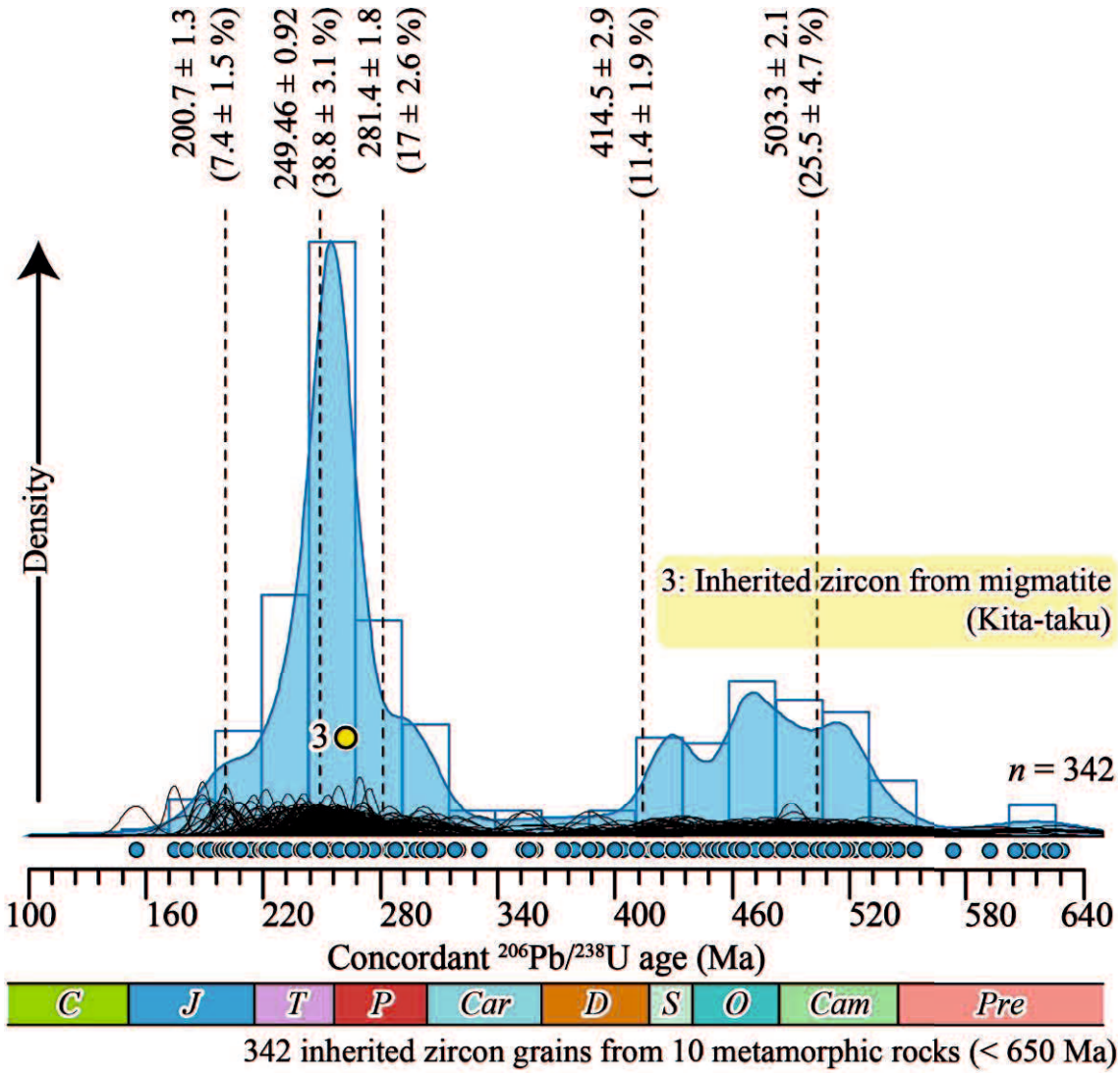

Figure 6–7. Age spectrum (KDE plot: Varmeesh, 2012) of zircon grains from 10 metamorphic rocks from northern Kyushu with inherited zircon ages of 261.3 ± 8.5 Ma from Tdh in Kita-taku mafic complex. Age component calculated using *Mixture Models (auto)* of *DensityPlotter* (Varmeesh, 2012) are also shown. C: Cretaceous, J: Jurassic, T: Triassic, P: Permian, Car: Carboniferous, D: Devonian, S: Silurian, O: Ordovician, Cam:

Cambrian, and Pre: Precambrian.

6–3 Anatomy of the Cretaceous igneous activity in northern Kyushu

As described in the previous chapters, the granitoids from the Northern Kyushu batholith have a high probability of coexisting with HMD (and/or HMA). The HMDs are distributed sporadically from Kunisaki Peninsula, Oita Prefecture to Taku City, Saga Prefecture (Fig. 6–8) , and is expected to the whole area of the Northern Kyushu batholith.

To reveal the characteristics of the HMDs, I try to address the petrological features of the HMDs distributed in northern Kyushu (Fig. 6–8). Figure 6–9 shows the N-MORB normalized trace elements pattern (Fig. 6–9a–d) and chondrite-normalized REE patterns (Fig. 6–9d–h) for the HMDs from the Northern Kyushu batholith comparing to the equilibrium melt with Cpx in the Kita-taku mafic complex and representative HMA magmas. The chemical compositions of northern Kyushu HMDs is similar to those of the parent magma of the Kita-taku mafic complex that would be derived from the Sanukitic HMA magma (Fig. 6–9). It means that the Sanukitic HMA magma was essentially activated over a whole area in northern Kyushu during the Cretaceous period.

The anatectic melt introduced in the previous section were generated by heat energy supplied from the Kita-taku mafic complex. In the case of the Kita-taku mafic complex, it is possible that the Sanukitic HMA magma mixed with the anatectic melt such as the Tdh. Such mechanism may expand to the formation of granitoid magmas in the Northern Kyushu batholith.

I calculated the mixing model between the parental Sanukitic HMA magma and the Tdh magma that was produced by partial melting of the amphibolite as previously described. The results are shown in Figure 6–10. The chemical compositions of the granodiorite and diorite distributed in the Mt. Ushikiri-yama, Mt. Shaku-dake, and northern part of Mt. Shaku-dake areas are compared to the

calculated magma (Fig. 6–10). The chemical compositions of the granodiorite and diorite are almost identical with those of calculated results (Fig. 6–10). Considering the distribution of HMD from the Northern Kyushu batholith, the Sanukitic HMA magma is a reasonable candidate for the magma that provided the thermal source for the large-scale igneous activity in northern Kyushu during the Cretaceous period.

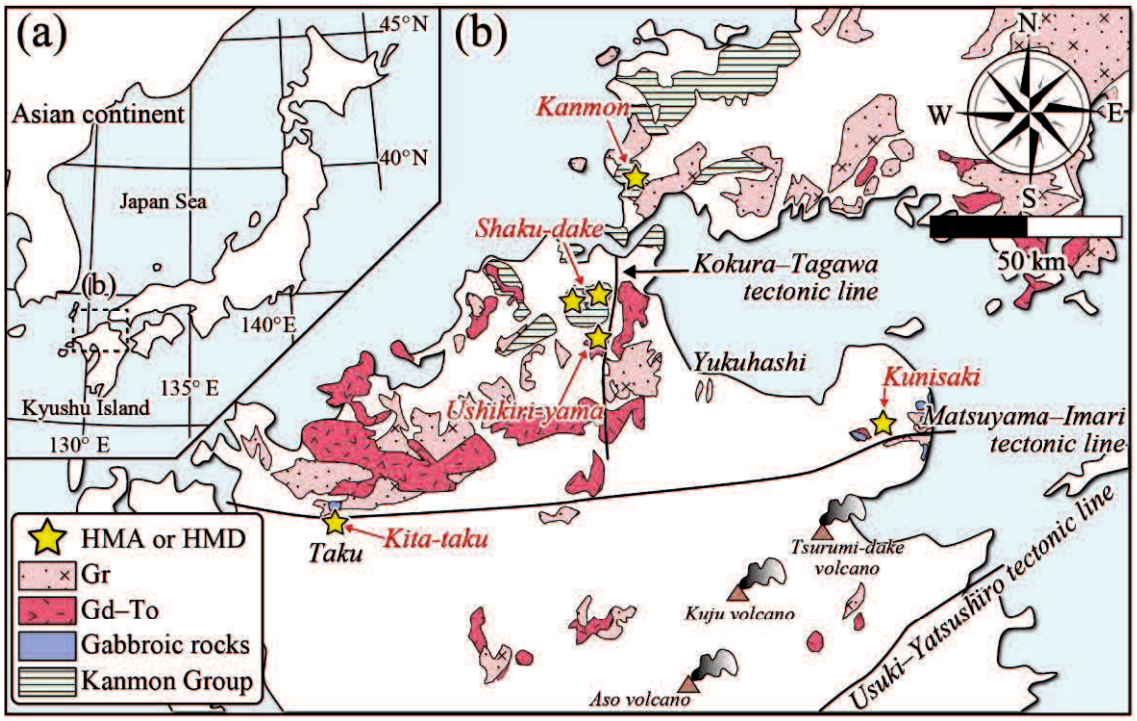

Figure 6–8. Simplified geological map of the Northern Kyushu batholith and related high-Mg diorites (Imaoka and Murakami, 1979; Karakida, 1985; Imaoka et al., 1993; Murakami, 1994; Kamei et al., 2004; Eshima et al., 2019; Eshima et al., 2020; Eshima, 2021a, b). HMA: high-Mg andesite, HMD: high-Mg diorite, Gr: granite, and To: tonalite.

Based on the important results in this study, the Mt. Ushikiri-yama, Mt. Shaku-dake, northern part of Mt. Shaku-dake, and Kita-taku areas, the following processes are considered as a scenario of the large-scale igneous activity in northern Kyushu. The cartoon of this scenario is depicted in Figure 6–11. At the initial stage, the Sanukitic HMA magma was generated and intruded into the lower crust at the

Early Cretaceous at c. 106 Ma. The injecting Sanukitic HMA magma gave energy for the partial melting of the lower crustal materials such as amphibolite to form trondhjemitic melts, then immediately mixing with the Sanukitic HMA magma. On the other hand, Sanukitic HMA magma itself would undergo the magmatic processes with fractional crystallization and assimilation to form dioritic to granodioritic magmas (chapters 2 and 3: Eshima et al., 2019, 2020). The granitoid magmas prior to the large flare-up event sporadically intruded into the upper crust as a small pulse and piled up. In the next culminated stage during 105–100 Ma, a large-scale batholith was formed by an assembly of many small-scaled plutonic bodies (Eshima, 2021a, 2021b). In this scenario, the heat source for the crustal melting would be of the underplated mafic magmas derived from the wedge mantle mainly the Sanukitic HMA magma but tinny basaltic magma (Eshima et al., 2020). The Cretaceous magma activities in the northern Kyushu were led by the highly thermal structure of the wedge mantle at that time. It is consistent with the ideas proposed by Iwamori (2000), Imaoka et al. (2014a), Iida et al. (2015), and Kim et al. (2016), where the highly thermal structure of the wedge mantle was the major heat source of the voluminous igneous activities during the Cretaceous in Southwest Japan and the Korean Peninsula.

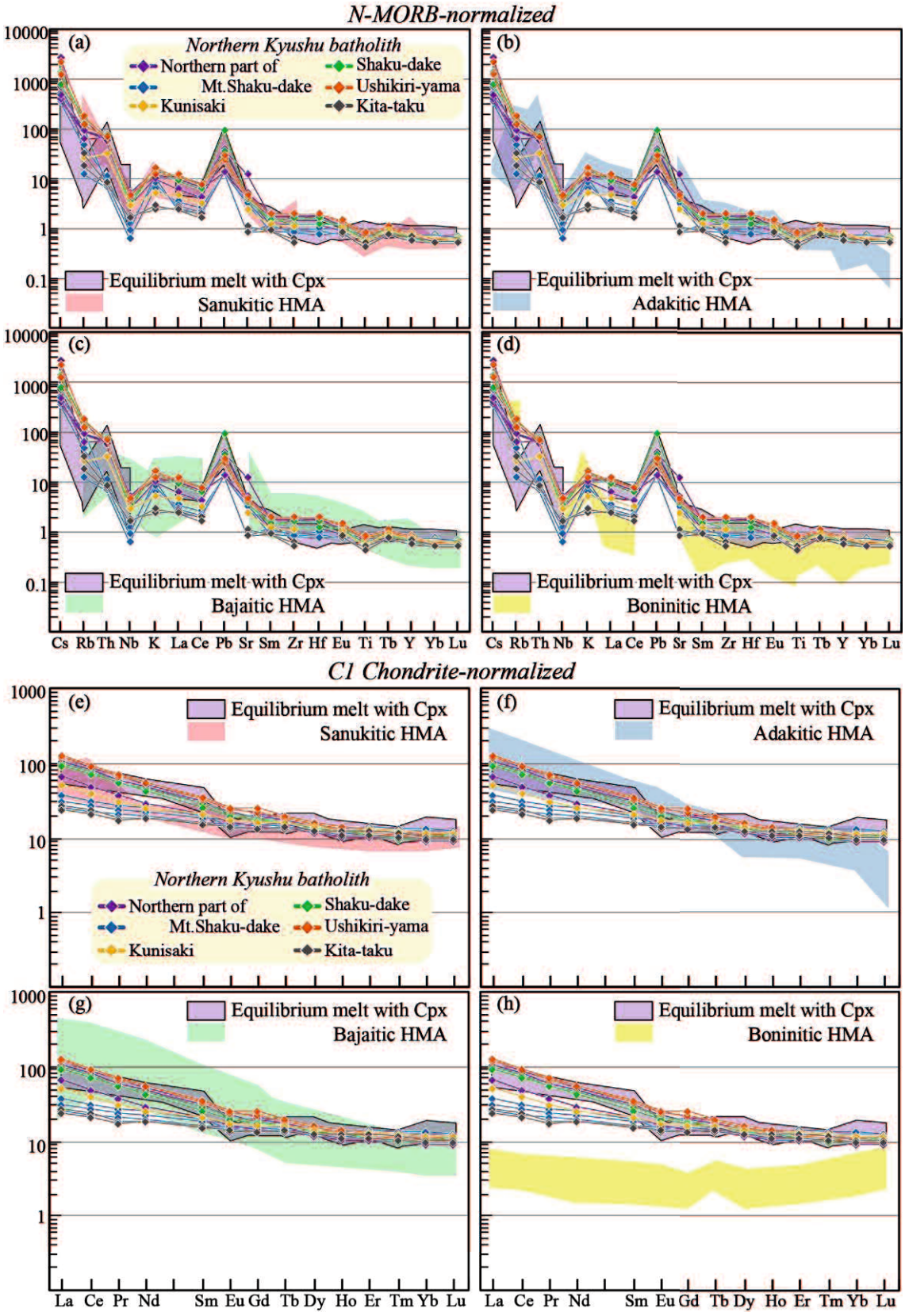

Figure 6–9. N-MORB- and C1 chondrite-normalized multi-element and rare earth element (REE) diagrams for high-Mg diorite from Northern Kyushu batholith. The normalizing

values are from Sun and McDonough (1989).

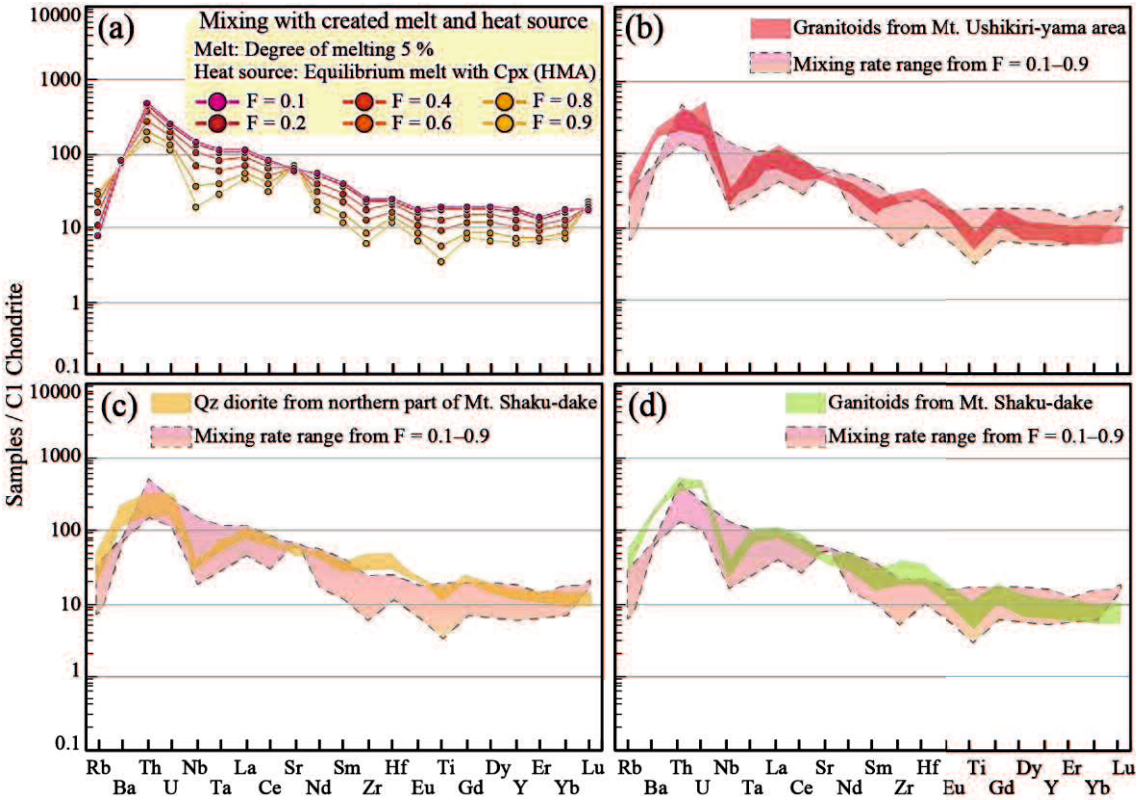

Figure 6–10. (a) Multiple-element diagram for the result of geochemical modeling, the parent magma (HMA) mixing with the trondhjemite magma (batch melting of the amphibolite) in the Kita-taku area. (b)–(d) Multiple-element diagram comparing (a) and related rocks from Mt, Ushikiri-yama, Mt. Shaku-dake, and northern part of Mt. Shaku-dake.

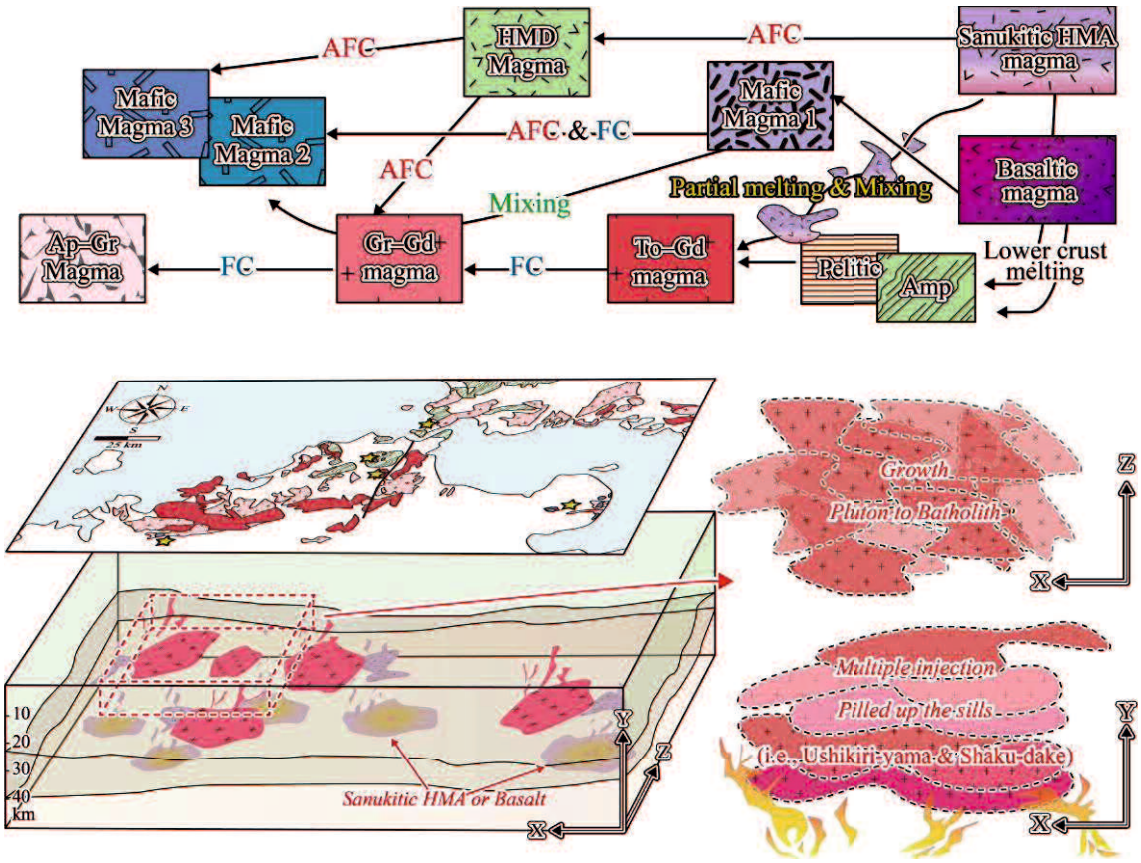

Figure 6–11. Schematic magmatic processes and growth model in Northern Kyushu batholith.

6–4 Geological development of northern Kyushu to the eastern edge of Eurasia –felsic magma generation and tectonic model–

Recent reconstructions of the world's continental and oceanic basins show that the Izanagi Plate subducted beneath Eurasia with a large orthogonal component for at least 200 Ma to 55 Ma (Seton et al., 2012, 2015; Müller et al., 2016; Liu et al., 2017). The formation of accretionary complexes during the Late Jurassic and Early Cretaceous suggests that subduction continued during these periods (e.g., Isozaki et al., 2010; Wakita et al., 2018). Despite the continuation of subduction, igneous activity during the Late Jurassic and Early Cretaceous only occurred in the interior of China, 400–1000 km away from the contemporaneous trenches, as mentioned earlier (Zhou and Li, 2000; Tang et al., 2018; Yang et al., 2018; Kang et al, 2019; Liu

et al, 2019; Zhao et al, 2020; Yu et al, 2021). A tectonic erosion model has been proposed to explain the absence of igneous rocks of a certain age, which was based on study of detrital (inherited) zircon ages (e.g., Hasegawa et al., 2020; Pastor-Galán et al., 2021). However, this erosion model does not take into account the isostatic heating of the lower crust (Miyazaki et al., 2017; Mori et al., 2021) and other features proposed in previous studies (including the trenchwards-younging trend of magmatic reactivation after the hiatus). These U–Pb ages become younger from the continentalward to the trenchward (Figs. 6–5, 6–6, and 6–7). This is consistent with the trend of younger ages of igneous rocks toward the trenchward, and supports the slab rollback model (e.g., Zhou and Li, 2000; Kiminami and Imaoka, 2013; Zhao et al., 2020; Yu et al., 2021).

In this section, I consider the rollback model of the Izanagi plate proposed by many authors (Zhou and Li, 2000; Kiminami and Imaoka, 2013; Tang et al., 2018; Liu et al., 2019; Yu et al., 2021) and propose tectonic evolution based on the timing of magmatic activity.

The location of the volcanic front is generally fixed at the depth of the top of subducting slab, and at each volcanic front the depth from the surface to the top of subducting slab is c. 100 km (Syracuse and Abers, 2006). Mori et al. (2021) implies that the flat subduction of the Izanagi plate at about 145 Ma caused the hiatus in magmatic activity around southwest Japan (Fig. 6–12a). The protoliths of the upper unit of the Nagasaki Metamorphic Complex correspond to the oceanic plate stratigraphy (OPS) member with trench-filled mudstones and sandstones during 145–135 Ma (Fig. 6–12b: Miyazaki et al., 2013; Mori et al., 2021). At this stage, the slab rollback started (Liu et al., 2019). Asthenosphere upwelling may occur to compensate for the open space caused by the slab rollback (Kiminami and Imaoka, 2013; Yang et al., 2018; Liu et al., 2019; Zhao et al., 2020), and the volcanic front are thought to have shifted to the trenchward (Fig. 12b). The accretionary complex continued to grow, and occurred in the crustal thinning due to extensional setting during the early

Cretaceous (135–130 Ma) (Fig. 6–12b). The contraction of the continental lithosphere implies a rise in mantle asthenosphere and warms the lower crust (e.g., Hyndman, 2019). The slab rollback and trench retreat continued to the early to middle Cretaceous at 130–90 Ma (Fig. 6–12c). This thermal effect and the underplating of magma beneath the shifted volcanic arc favored the formation of the High-*T* metamorphic belt and the generation of plutonic and volcanic rocks around southwest Japan (Fig. 6–12c). As mentioned above, the growth of metamorphic zircons surrounding inherited grains is possibly attributed to the intrusion of small gabbroic bodies (e.g., Kita-taku mafic complex) during high-*T* metamorphism. These results suggest that the onset of high-*T* metamorphism and large-scale igneous activity around southwestern Japan was at about 130 Ma (Miyazaki et al., 2018; Mori et al., 2021).

Wedge mantle flow due to slab rollback associated with trench retreat viscously drags the overriding plate toward the trenchward (Nakakuki and Mura, 2013). This drag force, combined with the drag of the wedge mantle corner flow due to the subducting plate, is thought to strengthen the wedge mantle corner flow and enhance mass transport from the deep part of the arc lower crust to the trenchward. The felsic magma around southwest Japan was 120 Ma to 60 Ma (Iida et al., 2015; Sato et al., 2016; Skrzypek et al., 2016; Takatsuka et al., 2017, 2018; Miyazaki et al., 2018), and high-*T* metamorphism around southwest Japan also continued from 120 Ma to 80 Ma (Kawakami et al., 2013; Maki et al., 2014; Miyazaki et al., 2017; Takatsuka et al., 2018; Vuong et al., 2019). Therefore, the partial melting event in the Kita-taku area may represent the initiation of voluminous felsic igneous activity during the same period.

In the crustal scale, the Sanukitic HMA and basaltic magma generated by the model described above ascends the lithosphere and underplates at the lower crust. Partial melting of the crustal material creates leucocratic granitic melts and these crustal melts are mixed with the mantle derived HMA and basaltic magmas. This

region acts not only as a partial melting zone but also as a storage zone of magmas, which is homogenized to some extent at each depth and forms a new crustal composition. Such a model is called the MASH (**M**elting, **A**ssimilation, **S**torage, and **H**omogenization) model (e.g., Hildreth, 1981; Hildreth and Moorbath, 1986). It then intrudes into the upper crust from the lower crust, forming a batholith. During the upwelling, the batholith underwent various plutonic processes, which are thought to have created the current variations. In this study, I am able to understand the magmatic activity from the lower crust to the upper crust from each body (Fig. 6–13).

6–5 Summary

1) The lithology of Northern Kyushu batholith can be reconstructed from the examination of small-scale bodies by the mixing and assimilation of various end-component magmas with crustal materials and their concomitant to differentiation and accumulation processes. The essential granitic magma of Northern Kyushu batholith can be formed by the partial melting of the lower crust and mixing to the mantle derived Sanukitic HMA, which is as an acted heat source and a parental magma for the crustal growth.

2) Based on the characterized Zrn U–Pb ages of igneous and metamorphic rocks and their spatial variations, the slab rollback could play an important role as a trigger of the Cretaceous large-scale igneous activity.

3) Important petrological constraints for the Cretaceous igneous activity along the eastern margin of Eurasia are as follows; 1) presence of the Sanukitic HMA as a heat source and as a parental magma, 2) MASH processes for magma generation and maturation mechanism during the growth of continental crust.

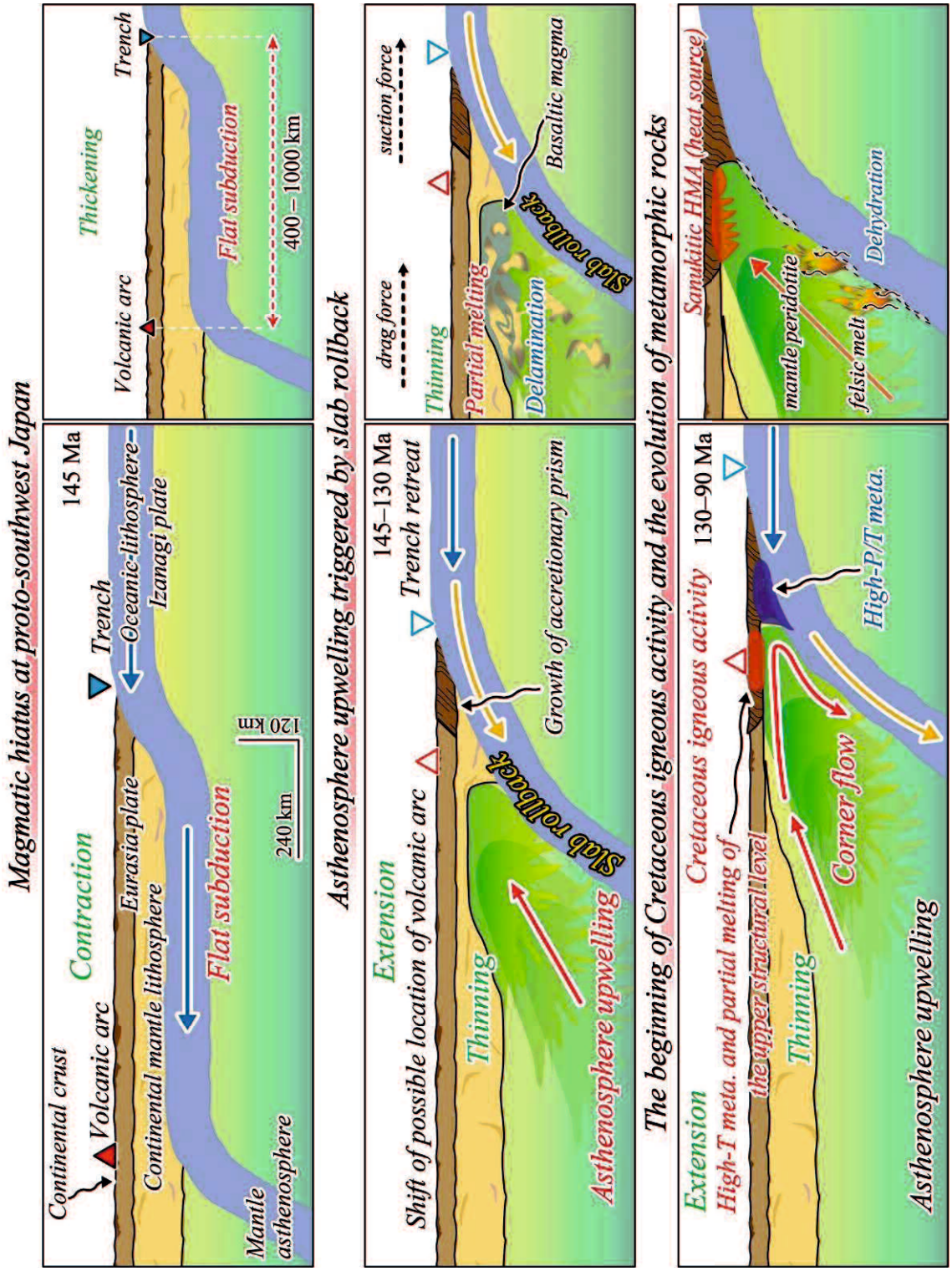

Figure 6–12. Schematic model of slab rollback modified from Mori et al. (2021).

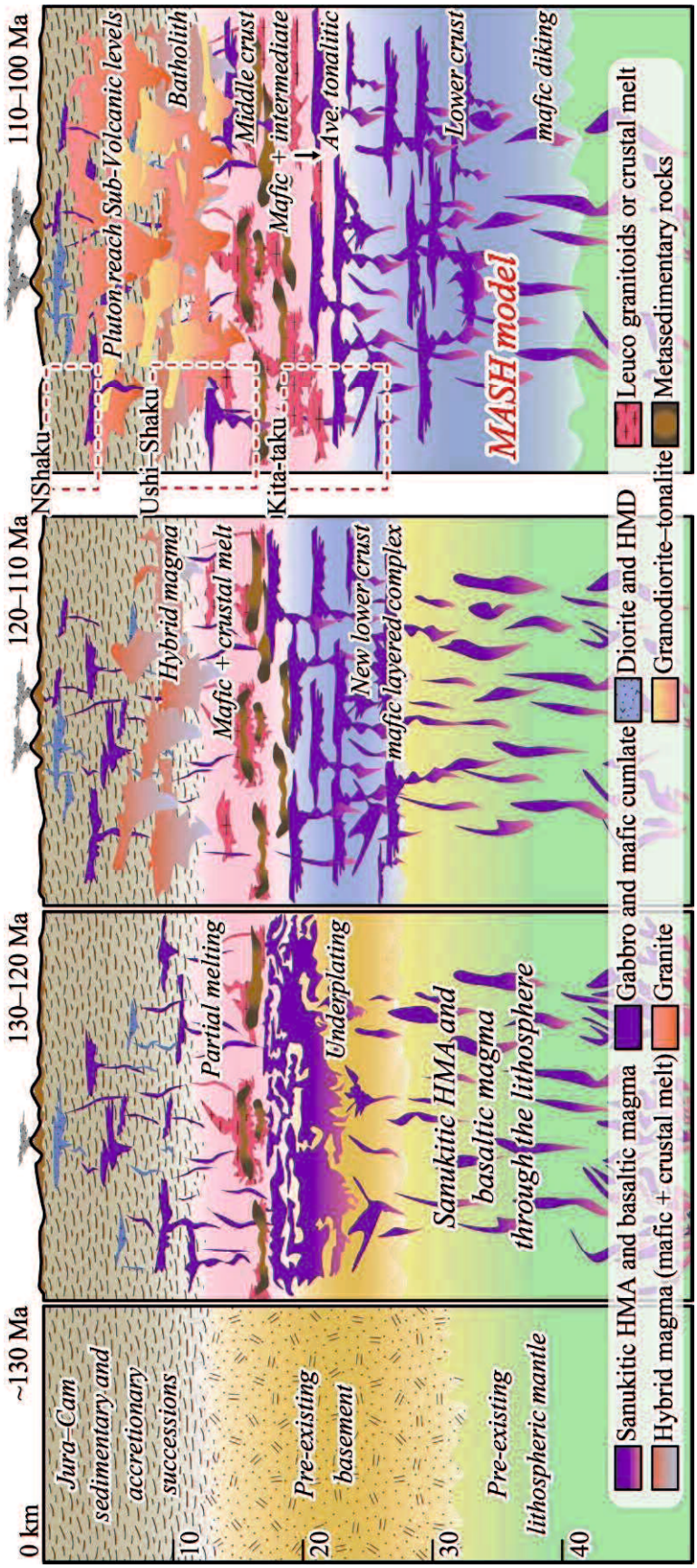

Figure 6–13. Crustal evolution model of Northern Kyushu batholith at cretaceous period.

References

Adachi, T., Osanai, Y., Nakano, N. and Owada, M. (2012) LA-ICP-MS U–Pb zircon and FE-EPMA U–Th–Pb monazite dating of pelitic granulites from the Mt. Ukidake area, Sefuri Mountains, northern Kyushu. Journal of the Geological Society of Japan, **118**, 39–52.

Adam, J. and Green, T. H. (1994) The effects of pressure and temperature on the partitioning of Ti, Sr and REE between amphibole, clinopyroxene and basanitic melts. Chemical Geology, **117**, 219–233.

Adam, J. and Green, T. (2006) Trace element partitioning between mica- and amphibole-bearing garnet lherzolite and hydrous basanitic melt: 1. Experimental results and the investigation of controls on partitioning behavior. Contributions to Mineralogy and Petrology, **152**, 1–17.

Akagi, K. (1935) Geological map of Japan 1:75,000. Ogi. Geological Survey of Japan, pp. 43 (in Japanese with English abstract).

Annen, C. (2011) Implications of incremental emplacement of magma bodies for magma differentiation, thermal aureole dimensions and plutonism–volcanism relationships. Tectonophysics, **500**, 3–10.

Annen, C. and Sparks, R. S. J. (2002) Effects of repetitive emplacement of basaltic intrusions on thermal evolution and melt generation in the deep crust. Earth and Planetary Science Letters, **203**, 937–955.

Arai, S. (1987) An estimation of the least depleted spinel peridotite on the basis of olivine-spinel mantle array. Neues Jahrbuch für Mineralogie-Monatshefte, **8**, 347–354.

Arai, S. and Ishimaru, S. (2008) Insights into petrological characteristics of the lithosphere of mantle wedge beneath arcs through peridotite xenolith: a review. Journal of Petrology, **49**, 665–695.

Arai, S., Hirai, H. and Uto, K. (2000) Mantle peridotite xenoliths from the Southwest Japan arc: a model for the sub-arc upper mantle structure and composition

of the Western Pacific rim. Journal of Mineralogical and Petrological Science, **95**, 9–23.

Arth, J. G. (1976) Behavior of trace elements during magmatic processes a summary of theoretical models and their applications. Journal of Research of the US Geological Survey, **4**, 41–47.

Bachl, C. A., Miller, C. F., Miller, J. S. and Faulds, J. E. (2001) Construction of a pluton: evidence from an exposed cross section of the Searchlight pluton, Eldorado Mountains, Nevada. Geological Society of America Bulletin, **113**, 1213–1228.

Bachmann, O. and Bergantz, G. W. (2004) On the origin of crystal-poor rhyolites: extracted from batholithic crystal mushes. Journal of Petrology, **45**, 1565–1582.

Bacon, C. R. and Druitt, T. H. (1988) Compositional Evolution of the Zoned Calc alkaline Magma Chamber of Mount-Mazama, Crater Lake, Oregon. Contributions to Mineralogy and Petrology, **98**, 224–256.

Barnes, S.-J. (1986) The effect of trapped liquid crystallization on cumulus mineral compositions in layered intrusions. Contributions to Mineralogy and Petrology, **93**, 524–531.

Barth, A. P. (1990) Mid-crustal emplacement of Mesozoic plutons, San Gabriel Mountains, California, and implications for the geologic history of the San Gabriel terrane. *In* Anderson, J. L. Eds., The Nature and Origin of Cordilleran Magmatism. Memoirs of Geological Society of America, **174**, 33–45.

Bea, F. and Montero, P. (2013) Diffusion-induced disturbances of the U–Pb isotope system in pre-magmatic zircon and their influence on SIMS dating. Chemical Geology, **349–350**, 1–17.

Beattie, P. (1993) Olivine-melt and orthopyroxene-melt equilibria. Contributions to Mineralogy and Petrology, **109**, 103–111.

Bédard, J. H. (2006a) A catalytic delamination-driven model for coupled genesis of Archaean crust and sub-continental lithospheric mantle. Geochimica et Cosmochimica Acta, **70**, 1188–1214.

Bédard, J. H. (2006b) Trace element partitioning in plagioclase feldspar. Geochimica et Cosmochimica Acta, **70**, 3717–3742.

Best, M. G. and Christiansen, E. H. (2001) Igneous Petrology. Oxford: Blackwell Science, pp. 458.

Brandon, A. D., Creaser, R. A. and Chacko, T. (1996) Constraints on rates of granitic magma transport from epidote dissolution kinetics. Science, **271**, 1845–1848.

Bowen, N. L. (1913) The melting phenomena of the plagioclase feldspars. American Journal of Science, **210**, 577–599.

Cabanis, B. and Leocolle, M. (1989) Le diagramme La/10-Y/15-Nb/8: un outil pour la discrimination des series volcaniques et la mise evidence des proccessus de mélange et/ou de contamination crustale. Comptes rendus de l'Academie des sciences. Serie 2, **309**, 2023–2029 (in French).

Chapman, J. B., Shields, J. E., Ducea, M. N., Peterson, S. R., et al. (2021) The causes of continental arc flare ups and drivers of episodic magmatic activity in Cordilleran orogenic systems. Lithos, **398–399**, 1–23.

Cherniak, D. J. and Watson, E. B. (2000) Pb diffusion in zircon. Chemical Geology, **172**, 5–24.

Crawford, A. J., Falloon, T. J. and Green, D. H. (1989) Classification, petrogenesis and tectonic setting of boninites. *In* Boninites and Related Rocks Crawford, A. J. Eds., Unwin Hyman, London, 1–49.

Danyushevsky, L. V. (2001) The effect of small amounts of H_2O on crystallization of mid-ocean ridge and back arc basin magmas. Journal of Volcanology and Geothermal Research, **110**, 265–280.

DeCelles, P. G., Ducea, M. N., Kapp, P. and Zandt, G. (2009) Cyclicity in Cordilleran orogenic systems. Nature Geoscience, **2**, 251–257.

Deer, W. A., Howie, R. A. and Zussman, J. (2013) An introduction to the rock-forming minerals (3rd editions). The Mineralogical Society of Great Britain and Ireland, pp. 498.

DePaolo, D. J. (1981) Trace element and isotopic effects of combined wallrock assimilation and fractional crystallization. Earth and Planetary Science Letters, **53**, 189–202.

DePaolo, D. J. and Wasserburg, G. J. (1976a) Nd isotopic variations and petrogenetic models. Geophysical Research Letters, **3**, 249–252.

DePaolo, D. J. and Wasserburg, G. J. (1976b) Inferences about magma sources and mantle structure from variations of $^{143}Nd/^{144}Nd$. Geophysical Research Letters, **3**, 743–746.

de Silva, S. L., Riggs, N. R. and Barth, A. P. (2015) Quickening the Pulse: Fractal Tempos in Continental Arc Magmatism. Elements, **11**, 113–118.

de Saint-Blanquat, M., Habert, G., Horsman, E., Morgan, S. S., et al. (2006) Mechanism and duration of non-tectonically assisted magma emplacement in the upper crust: the Black Mesa pluton, Henry Mountains, Utah. Tectonophysics, **428**, 1–31.

Dodson, M. H. and McClelland–Brown, E. (1985) Isotopic and paleomagnetic evidence for rates of cooling, uplift and erosion. *In* Snelling, N. L., Eds., The Chronology of the Geological Record. Geological Society of London Memoirs, Blackwell, Oxford., **10**, 315–325.

Ducea, M. N. (2001) The California arc: Thick granitic batholiths, eclogitic residues, lithospheric-scale thrusting, and magmatic flare-ups. GSA Today, **11**, 4–10.

Eshima, K. and Owada, M. (2018) Whole-rock geochemistry of diorite and dikes from Mt. Shaku-dake area, Fukuoka, Kyushu. Journal of the Geological Society of Japan, **124**, 857–862 (in Japanese with English abstract).

Eshima, K., Owada, M., Imaoka, T. and Kamei, A. (2019) Magma processes and genesis of the Cretaceous Kawara granodiorite ushikiri-yama body (Ushikiri-yama granodiorite), North Kyushu, SW Japan. Journal of the Geological Society of Japan, **125**, 237–253 (in Japanese with English abstract).

Eshima, K., Owada, M. and Kamei, A. (2020) Assimilation and fractional crystallization of Sanukitic high-Mg andesite-derived magmas, Kyushu Island, southwest Japan: An example of the Cretaceous Shaku-dake diorite body. Journal of Mineralogical and Petrological Science, **115**, 332–347.

Eshima, K. (2021a) Anatomy of Shaku-dake high-Mg diorite, southwest Japan: Lithofacies variations and growth process of high-Mg diorite stock. Journal of Mineralogical and Petrological Science, **116**, 83–95.

Eshima, K. (2021b) Compositional changes due to hydrothermal alteration and mixing combined with differentiation and accumulation of igneous rocks from northern part of Mt. Shaku-dake, northern Kyushu, southwest Japan. Journal of the Geological Society of Japan, **127**, 605–619 (in Japanese with English abstract).

Ewart, A. and Griffin, W. L. (1994) Application of proton-microprobe data to trace-element partitioning in volcanic rocks. Chemical Geology, **117**, 251–284.

Foley, S. (2008) A trace element perspective on Archean crust formation and on the presence or absence of Archean subduction. Geological Society of America Special Papers, **440**, 31–50.

Foley, S., Tiepolo, M. and Vannucci, R. (2002) Growth of early continental crust controlled by melting of amphibolite in subduction zones. Nature, **417**, 837–840.

Fujimaki, H., Tatsumoto, M. and Aoki, K. (1984) partition coefficients of Hf, Zr, and REE between phenocrysts and groundmass. Journal of Geophysical Research, **89**, 662–672.

Fukami, J. and Owada, M. (2017) Whole-rock geochemistry of metamorphosed mafic rocks from Mt. Sangun area, Fukuoka, Kyushu. Journal of the Geological Society of Japan, **123**, 1055–1060 (in Japanese with English abstract).

Gargiulo, M. F., Bjerg, E. A. and Mogessie, A. (2013) Spinel group minerals in metamorphosed ultramafic rocks from Rio de Las Tunas belt, Central Andes, Argentina. Geologica Acta, **11**, 133–148.

Gill, J. B. (1981) Orogenic Andesites and Plate Tectonics. Springer Verlag, Berlin Heidelberg, pp. 390.

Glazner, A. F., Bartley, J. M., Coleman, D. S., Gray, W., et al. (2004) Are plutons assembled over millions of years by amalgamation from small magma chambers? GSA Today, **14**, 4–11.

Green, D. H. and Ringwood, A. E. (1967) The genesis of basaltic magmas. Contributions to Mineralogy and Petrology, **15**, 103–190.

Green, T. H. and Pearson, N. J. (1987) An experimental study of Nb and Ta partitioning between Ti-rich minerals and silicate liquids at high pressure and temperature. Geochimica et Cosmochimica Acta, **51**, 55–62.

Green, T., Blundy, J., Adam, J. and Yaxley, G. (2000) SIMS determination of trace element partition coefficients between garnet, clinopyroxene and hydrous basaltic liquids at 2–7.5 Gpa and 1080–1200 ℃. Lithos, **53**, 165–187.

Gresens, R. L. (1967) Composition-volume relationships of metasomatism. Chemical Geology, **2**, 47–55.

Gudmundsson, A. (1990) Emplacement of dikes, sills and crustal magma chambers at divergent plate boundaries. Tectonophysics, **176**, 257–275.

Gudmundsson, A. (2011) Deflection of dykes into sills at discontinuities and magma-chamber formation. Tectonophysics, **500**, 50–64.

Haggerty, S. E. (1991) Oxide mineralogy of the upper mantle. *In* Lindsley, D. H. Eds., Oxide Minerals: Petrologic and Magnetic Significance. Reviews in Mineralogy. Mineralogical Society of America, **25**, 355–416.

Harley, S. L., Kelly, N. M. and Möller, A. (2007) Zircon behavior and the thermal histories of mountain chains. Elements, **3**, 25–30.

Harris, C., Marsh, J. S. and Milner, S. C. (1999) Petrology of the alkaline core of the Messum igneous complex, Namibia: Evidence for the progressively decreasing effect of crustal contamination. Journal of Petrology, **40**, 1377–1397.

Hart, S. R. and Dunn, T. (1993) Experimental Cpx/melt partitioning of 24 trace elements. Contributions to Mineralogy and Petrology, **113**, 1–8.

Hasegawa, R., Isozaki, Y., Yamamoto, A., and Tsutsumi, Y. (2020) Secular changes in fore-arc sandstones and their provenance in Cretaceous Southwest Japan: U–Pb Dating of Detrital Zircons. Journal of Geography (Chigaku Zasshi), **129**, 397–421 (in Japanese with English abstract).

Hauri, E. H., Wagner, T. P. and Grove, T. L. (1994) Experimental and natural partitioning of Th, U, Pb and other trace elements between garnet, clinopyroxene and basaltic melts. Chemical Geology, **117**, 149–166.

Hibbard, M. J. (1995) Petrography to Petrogenesis. Prentice Hall, New Jersey, pp. 587.

Hickey, R. L. and Frey, F. A. (1982) Geochemical characteristics of boninite series volcanics; implications for their source. Geochimica et Cosmochimica Acta, **46**, 2099–2116.

Hida, T., Ishiyama, D., Mizuta, T. and Ishikawa, Y. (1996) Geological characteristics and formation environments of the Yano–Shokozan pyrophyllite deposit, Hiroshima prefecture, Japan: Volcanic succession and hydrothermal alterations processes. Journal of the Clay Science Society of Japan, **36**, 62–72 (in Japanese with English abstract).

Hildreth, W. (1981) Gradients in silicic magma chambers: implications for lithospheric magmatism. Journal of Geophysical Research, **86**, 10153–10192.

Hildreth, W. (2004) Volcanological perspectives on Long Valley, Mammoth Mountain, and Mono Craters: several contiguous but discrete systems. Journal of Volcanology and Geothermal Research, **136**, 169–198.

Hildreth, W. and Moorbath, S. (1988) Crustal contributions to arc magmatism in the Andes of central Chile. Contributions to Mineralogy and Petrology, **98**, 455–489.

Hirose, K. (1997) Melting experiments on lherzolite KLB-1 under hydrous conditions and generation of high-magnesian andesite melts. Geology, **25**, 42–44.

Holland, T. and Blundy, J. (1994) Non-ideal interactions in calcic amphiboles and their bearing on amphibole-plagioclase thermometry. Contributions to Mineralogy and Petrology, **116**, 433–47.

Horsman, E., Morgan, S., de Saint-Blanquat, M., Habert, G., et al. (2010) Emplacement and assembly of shallow intrusions from multiple magma pulses, Henry Mountains, Utah. Earth and Environmental Sciences, Transaction of the Royal Society of Edinburgh, **100**, 117–132.

Hoskin, P. W. O. and Black, L. P. (2000) Metamorphic zircon formation by solid state recrystallization of protolith igneous zircon. Journal of Metamorphic Geology, **18**, 423–439.

Humphris, S. E. and Thompson, G. (1978a) Hydrothermal alteration of oceanic basalts by seawater. Geochimica et Cosmochimica Acta, **42**, 107–125.

Humphris, S. E. and Thompson, G. (1978b) Trace element mobility during hydrothermal alteration of oceanic basalts. Geochimica et Cosmochimica Acta, **42**, 127–136.

Hutchinson, J. W. (1996) Stresses and failure modes in thin films and multilayers. Notes for a Dcamm Course. Technical University of Denmark, Lyngby, pp. 1–45.

Hyndman, R. D. (2019) Origin of regional Burrovian metamorphism in hot backarcs prior to orogeny deformation. Geochemistry, Geophysics, Geosystems, **20**, 460–469.

Iida, K., Iwamori, H., Orihashi, Y., Park, T., et al. (2015) Tectonic reconstruction of batholith formation based on the spatiotemporal distribution of Cretaceous–Paleogene granitic rocks in southwestern Japan. Island Arc, **24**, 205–220.

Iizumi, S. (1996) Sr and Nd isotopic analyses, using a thermal ionization mass spectrometer MAT 262. Geoscience Report Shimane University, **15**, 153–159 (in Japanese with English abstract).

Imaoka, T. and Murakami, N. (1979) Petrochemistry of late Mesozoic to early Tertiary volcanic rocks in West Chugoku, Southwest Japan. The memoirs of the Geological Society of Japan, **17**, 259–271 (in Japanese with English abstract).

Imaoka, T., Nakashima, K. and Itaya, T. (1993) K–Ar ages of hornblendes in andesite and dacite from the Cretaceous kanmon Group, southwest Japan. Journal of Mineralogy, Petrology and Economic Geology, **88**, 265–271 (in Japanese with English abstract).

Imaoka, T., Nishimura, Y., Goto, Y., Nakashima, K., et al. (1997) Modes of Occurrence and K–Ar ages of Yamashima volcanic rocks in western San-in district, Southwest Japan. Journal of Mineralogy, Petrology and Economic Geology, **92**, 302–315 (in Japanese with English abstract).

Imaoka, T., Nakashima, K., Kamei, A., Itaya, T., et al. (2014a) Episodic magmatism at 105 Ma in the Kinki district, SW Japan: Petrogenesis of Nb–rich lamprophyres and adakites, and geodynamic implications. Lithos, **184–187**, 105–131.

Imaoka, T., Nakashima, K., Kamei, A., Hayasaka, Y., et al. (2014b) Anatomy of the Cretaceous Hobenzan pluton, SW Japan: Internal structure of a small zoned pluton, and its genesis. Lithos, **208–209**, 81–103.

Inoue, A. (1995) Formation of clay minerals in hydrothermal environments. *In* Velde, B. Eds., Origin and Mineralogy of Clays: Clays and the Environment, Springer, Heidelberg, Germany, 268–329.

Irving, A. J. and Frey, F. A. (1984) Trace-Element Abundances in Megacrysts and Their Host Basalts - Constraints on Partition-Coefficients and Megacryst Genesis. Geochimica et Cosmochimica Acta, **48**, 1201–1221.

Ishihara, S., Karakida, Y. and Sato, K. (1979) Distribution of the magnetic series and ilmenite-series granitoids in the northern Kyushu–western Chugoku district: With emphasis in re-evaluation of the Kokura–Tagawa fault zone. Journal of the Geological Society of Japan, **85**, 47–50 (in Japanese with English abstract).

Ishikawa. Y., Sawaguchi. T., Iwaya. S. and Horiuchi. M. (1976) Delineation of prospecting targets for Kuroko deposits based on modes of volcanism of underlying dacite and alteration haloes. Mining Geology, **26**, 105–117 (in Japanese with English abstract).

Isozaki, Y., Aoki, K., Nakama, T., and Yanai, S. (2010) New insight into a subduction-related orogen: A reappraisal of the geotectonic framework and evolution of the Japanese Islands. Gondwana Research, **18**, 82–105.

Iwamori, H. (2000) Thermal effects of ridge subduction and its implications for the origin of granitic batholiths and paired metamorphic belts. Earth and Planetary Science Letters, **181**, 131–44.

Iwano, H., Orihashi, Y., Danhara, T., Hirata, T., et al. (2012) Evaluation of fission-track and U-Pb double dating method for identical zircon grains; Using homogeneous zircon grains in Kawamoto Granodiorite in Shimane Prefecture, Japan. Journal of the Geological Society of Japan, **118**, 365–375 (in Japanese with English abstract).

Iwano, H., Orihashi, Y., Hirata, T., Ogasawara, M., et al. (2013) An inter-laboratory evaluation of OD-3 zircon for use as a secondary U–Pb dating standard. Island Arc, **22**, 382–394.

Izawa, E., Karakida, Y., Shimada, N. and Takahashi, M. (1990) Is the high-Sr granitoid indicative for the thick continental crust? Chikyu Monthly, **12**, 435–439 (in Japanese with English abstract).

Izawa, E., Karakida, Y., Shimada, N. and Takahashi, M. (1994) Geochemical characteristics of the Northern Kyushu granitoids. Study of Childhood Education. Seinan Gakuin university, **20**, 21–54 (in Japanese with English abstract).

Jenner, G. A. (1981) Geochemistry of high-Mg andesites from Cape Vogel, Papa New Guinea. Chemical Geology, **33**, 307–332.

Johannes, W. (1978) Melting of plagioclase in system Ab–An–H_2O and Qz–Ab–An–H_2O at P_{H_2O} = 5 kbars, an equilibrium problem. Contributions to Mineralogy and Petrology, **66**, 295–303.

Kagami, H., Iwata, M., Sano, S. and Honma, H. (1987) Sr and Nd isotopic compositions and Rb, Sr, Sm and Nd concentrations of standard samples. Technical Report, Institute for Study of the Earth's Interior, Okayama University, Ser **4**, 1–16.

Kagami, H., Yokose, H. and Honma, H. (1989) $^{87}Sr/^{86}Sr$ and $^{143}Nd/^{144}Nd$ rations of GSJ rock reference samples; JB-1a, JA-1 and JG-1a. Geochemical Journal, **23**, 209–214.

Kagami, H., Iizumi, S., Tainosho, Y. and Owada, M. (1992) Spatial variations of Sr and Nd isotope ratios of Cretaceous-Paleogene granitoid rocks, Southwest Japan Arc. Contributions to Mineralogy and Petrology, **112**, 165–177.

Kagami, H., Kawano, Y., Akiyama, M., Ikawa, T., et al. (2006) Provenance of Paleozoic–Mesozoic sedimentary rocks in the Inner Zone of Southwest

Japan: An evaluation based on Nd model ages. Gondwana Research, **9**, 142–151.

Kakubuchi, S., Kido, M. and Hikosan Collaborative Research Group. (1995) High-magnesian andesites from the northwestern margin of the Pliocene Kuju-Beppu Tectonic Basin, northern Kyushu, Japan. The memoirs of the Geological Society of Japan, **44**, 125–138 (in Japanese with English abstract).

Kamei, A., Owada, M., Nagao, T. and Shiraki, K. (2004) High-Mg diorite derived from sanukitic HMA magmas, Kyushu Island, southwest Japan arc: evidence from clinopyroxene and whole rock compositions. Lithos, **75**, 359–371.

Kang, Y., Shi, Y., and Anderson, J. L. (2019) Tectonic mechanism and evolution of eastern China during the Early Cretaceous: A view from magmatism in the middle to Southern Tan-Lu fault zone. International Geology Review, doi: 10.1080/00206814.2019.1700400.

Karakida, Y. (1985) Geological classification of granitic rocks in northern Kyushu Island. Proc. Nishinihon Branch Journal of the Japan Society of Engineering Geology, **6**, 2–12 (in Japanese with English abstract).

Katayama, R (1906) Contact metamorphism of limestone by granite at Sanno-take. Journal of the Geological Society of Japan, **13**, 345–353 (in Japanese with English abstract).

Kavanagh, J. L., Menand, T. and Sparks, R. S. J. (2006) An experimental investigation of sill formation and propagation in layered elastic media. Earth and Planetary Science Letters, **245**, 799–813.

Kawakami, T., Yamaguchi, I., Miyake, A., Shibata, T., et al. (2013) Behavior of zircon in the upper-amphibolite to granulite facies schist/migmatite transition, Ryoke metamorphic belt, SW Japan: Constraints from the melt inclusions in zircon. Contributions to Mineralogy and Petrology, **165**, 575–591.

Kawano, Y. and Ueda, Y. (1966) K–A dating on the igneous rocks in Japan (V) - Granitic rocks in southwestern Japan-. The Journal of the Japanese Association of Mineralogists, Petrologists and Economic Geologists, **56**, 191–211 (in Japanese with English abstract).

Kawano, Y., Akiyama, Y., Ikawa, T., Roser, B. P., et al. (2006) Whole rock geochemistry and Sr isotopic compositions of Phanerozoic sedimentary rocks in the Inner Zone of the Southwest Japan Arc. Gondwana Research, **9**, 126–141.

Kay, R. W. (1978) Aleutian magnesian andesites: melts from subducted Pacific Ocean crust. Journal of Volcanology and Geothermal Research, **4**, 117–132.

Kelemen, P. B., Hanghøj, K. and Greene, A. R. (2014) 4.21 - One view of the geochemistry of subduction-related magmatic arcs, with an emphasis on primitive andesite and lower Crust. *In* Rudnick, R. L. Eds., The Crust, 2nd edition. *In* Treatise on Geochemistry, vol. 4 Elsevier-permagon, Oxford, 749–805.

Klein, M., Stosch, H. G. and Seck, H. A. (1997) Partitioning of high field-strength and rare-earth elements between amphibole and quartz-dioritic to tonalitic melts: An experimental study. Chemical Geology, **138**, 257–271.

Kim, S. W., Kwon, S., Park, S.-I., Lee, C., et al. (2016) SHRIMP U–Pb dating and geochemistry of the Cretaceous plutonic rocks in the Korean Peninsula: a new tectonic model of the Cretaceous Korean Peninsula. Lithos, **262**, 88–106.

Kiminami, K. and Imaoka, T. (2013) Spatiotemporal variations of Jurassic-Cretaceous magmatism in eastern Asia (Tan-Lu Fault to SW Japan): Evidence for flat-slab subduction and slab rollback. Terra Nova, **25**, 414–422.

Kirsch, M., Paterson Scott, R., Wobbe, F., Martinez-Ardila, A. M., et al. (2016) Temporal histories of Cordilleran continental arcs: testing models for magmatic episodicity. American Mineralogist, **101**, 2133.

Kita-hata village History codification committee (2008) Kita-hata Village History "Natural Settlement Journal - Ethnicity" I. Geography and Geology of Kita-hata Village, 33–160 (in Japanese).

Kochibe, T. (1903) Geological map of Japan 1:200,000. Tsunoshima. Geological Survey of Japan, pp. 49 (in Japanese).

Kubo, K., Matsuura, H., Ozaki, M., Makimoto, H., et al. (1993) Geological Sheet Map at 1:200,000 of the Fukuoka District. Geological Survey of Japan (in Japanese with English abstract)..

Kushiro, I. and Yoder, H. S. Jr. (1966) Anorthite-forsterite and anorthite-enstatite reactions and their bearing on the basalt-eclogite transformation. Journal of Petrology, **7**, 337–362.

Large, R. R., Gemmell, J. B., Paulick, H. and Huston, D. L. (2001) The alteration box plot: A simple approach to understanding the relationship between alteration mineralogy and lithogeochemistry associated with volcanic hosted massive sulfide deposits. Economic Geology, **96**, 957–971.

Le Bel, L., Cocherie, A., Baubron, J. C., Fouillac, A. M. and Hawkesworth, C. J. (1985) A high-K, mantle derived plutonic suite from 'Linga', near Arequipa (Peru). Journal of Petrology, **26**, 124–148.

Liu, S., Gurnis, M., Ma, P., and Zhang, B. (2017) Reconstruction of northeast Asian deformation integrated with western Pacific plate subduction since 200 Ma. Earth-Science Reviews, **175**, 14–142.

Liu, J., Cai, R., Pearson, G., and Scott, J. M. (2019) Thinning and destruction of the lithospheric mantle root beneath the North China Craton. A Review: Earth-Science Reviews, 196, doi: 10.1016/j.earscirev.2019.05.017.

Lipman, P. W. (2007) Incremental assembly and prolonged consolidation of Cordilleran magma chambers: evidence from the Southern Rocky Mountain volcanic field. Geosphere, **3**, 42–70.

López, S. and Castro, A. (2001) Determination of the fluid–absent solidus and supersolidus phase relationships of MORB-derived amphibolites in the range 4–14 kbar. American Mineralogist, **86**, 1396–1403.

Lugmair, G. W. and Marti, K. (1978) Lunar initial $^{143}Nd/^{144}Nd$: Differential evolution of the lunar crust and mantle. Earth and Planetary Science Letters, **39**, 349–357.

Luhr, J. F. and Carmichael, I. S. E. (1980) The Colima volcanic complex, Mexico. I: post-caldera andesites from Volcano Colima. Contributions to Mineralogy and Petrology, **71**, 343–372.

Lukács, R., Harangi, S., Bachmann, O., Guillong, M., et al. (2015) Zircon geochronology and geochemistry to constrain the youngest eruption events and magma evolution of the Mid-Miocene ignimbrite flare-up in the Pannonian Basin, eastern central Europe. Contributions to Mineralogy and Petrology, **170**, 52, doi: 10.1007/s00410-015-1206-8.

MacDonald, R., Bagiński, B. and Upton, B. G. J. (2014) The volcano-pluton interface; the Longonot (Kenya) and Kûngnât (Greenland) peralkaline complexes. Lithos, **196–197**, 232–241.

MacLennan, S. M. and Taylor, S. R. (1996) Heat flow and the chemical composition of continental crust. The Journal of Geology, **104**, 369–377.

Maclennan, J., Hulme, T. and Singh, S. C. (2004) Thermal models of oceanic crustal accretion: Linking geophysical, geological and petrological observations. Geochemistry, Geophysics, Geosystems , **5**, Q02F25, doi: 10.1029/2003GC000605.

Maki, K., Yui, T.-F., Miyazaki, K., Fukuyama, M., et al. (2014) Petrogenesis of metatexite and diatexite migmatites determined using zircon U-Pb age, trace

element and Hf isotope data, Higo metamorphic terrane, central Kyushu, Japan. Journal of Metamorphic Geology, **32**, 301–323.

Matsui, Y., Onuma, N., Nagasawa, H., Higuchi, H., et al. (1977) Crystal structure control in trace element partition between crystal and magma. Tectonics, **100**, 315–324.

Matsushita, H. (1940) Geology and ore deposits in the Sanno-take area, Fukuoka Prefecture. Kyushu Branch Journal of Mining industrial, **11**, 175–182 (in Japanese).

Menand, T. (2008) The mechanics and dynamics of sills in elastic layered media and their implications for the growth of laccoliths. Earth and Planetary Science Letters, **267**, 93–99.

Menand, T., de Saint-Blanquat, M. and Annen, C. (2011) Emplacement of magma pulses and growth of magma bodies Preface. Tectonophysics, **500**, 1–2.

Michaud, C. and Jaupart, C. (2006) Ultra-rapid formation of large volumes of evolved magma. Earth and Planetary Science Letters, **250**, 38–52.

Miller, C. F., Furbish, D. J., Walker, B. A., Claiborne, L. L., et al. (2011) Growth of plutons by incremental emplacement of sheets in crystal-rich host: evidence from Miocene intrusions of the Colorado River regions, Nevada, USA. Tectonophysics, **500**, 65–77.

Miyahisa, M. and Mouri, M. (1959) Pyrometasomatic copper-iron sulphide ore deposits of the Yoshiwara mine, with special reference to the structural control of ore localization. Mining Geology, **9**, 276–286 (in Japanese with English abstract).

Miyashiro, A. (1974) Volcanic rock series in Island arcs and active continental margins. American Journal of Science, **274**, 321–355.

Miyazaki, T. and Shuto, K. (1998) Sr and Nd isotope ratios of twelve GSJ rock reference samples. Geochemical Journal, **32**, 345–350.

Miyazaki, K., Ikeda, T., Arima, K., Fukuyama, M., et al. (2013) Pressure–temperature structure of a mylonitized metamorphic pile, and the role of

advection of the lower crust, Nagasaki Metamorphic Complex, Kyushu, Japan. Lithos, **162–163**, 14–26.

Miyazaki, K., Ikeda, T., Matsuura, H., Danhara, T., et al. (2017) A high-T metamorphic complex derived from the high-P Suo metamorphic complex in the Omuta district, northern Kyushu, southwest Japan. Island Arc, **26**, e12208, doi: 10.1111/iar.12208.

Miyazaki, K., Ikeda, T., Matsuura, H., Danhara, T., et al. (2018) Ascent of migmatites of a high-temperature metamorphic complex due to buoyancy beneath a volcanic arc: A mid-Cretaceous example from the eastern margin of Eurasia. International Geology Review, doi: 10.1080/ 00206814.2018.1443403

Mizuta, T. and Ishiyama, D. (2009) Alteration of host rocks and ore deposition. Resource Geology, **59**, 165–180 (in Japanese with English abstract).

Möller, A., O'Brien, P. J., Kennedy, A. and Kröner, A. (2003) Linking growth episodes of zircon and metamorphic textures to zircon chemistry: an example from the ultrahigh-temperature granulites of Rogaland (SW Norway). *In*: Vance, D., Müller, W. and Villa, I. M. Eds., Geochronology: Linking the Isotopic Record with Petrology and Textures. Geological Society of London Special Publication, **220**, 65–81.

Montel, J. M. and Vielzeuf, D. (1997) Partial melting of metagreywackes, Part II. Compositions of minerals and melts. Contributions to Mineralogy and Petrology, **128**, 176–196.

Morgan, S. S., Stanik, A., Horsman, E., Tikoff, B., et al. (2008) Emplacement of multiple magma sheets and wall rock deformation: Trachyte Mesa intrusion, Henry Mountains, Utah. Journal of Structural Geology, **30**, 491–512.

Mori, Y., Miyazaki, K., Ikeda, T., Miyamoto, T., et al. (2021) Early Cretaceous partial melting recorded by pelitic gneiss from the Nagasaki Metamorphic Complex, western Kyushu, Japan: initiation of Cretaceous high-*T*

metamorphism at eastern margin of Eurasia, International Geology Review, doi: 10.1080/00206814.2021.1961104.

Morimoto, N., Fabries, J., Ferguson, A. K., Ginzburg, I. V., et al. (1988) Nomenclature of pyroxenes. American Mineralogist, **73**, 1123–1133.

Mullen, E. D. (1983) $MnO/TiO_2/P_2O_5$: a minor element discriminant for basaltic rocks of oceanic environments and its implications for petrogenesis. Earth and Planetary Science Letters, **62**, 53–62.

Müller, R. D., Seton, M., Zahirovic, S., Williams, S. E., et al. (2016) Ocean basin evolution and global-scale plate reorganization events since Pangea breakup. Annual Review of Earth and Planetary Sciences, **44**, 107–138.

Muraoka, Y., Owada, M., Kamei, A. and Miyazaki, K. (2020) Genesis of the low-Sr Granitoid from the Cretaceous Granitic rocks in Northern Kyushu. Journal of the Geological Society of Japan, **126**, 679–695 (in Japanese with English abstract)

Murakami, N. (1985) Late Mesozoic to Paleogene igneous activity in West Chugoku, Southwest Japan. Journal of the Geological Society of Japan, **91**, 723–742 (in Japanese with English abstract).

Murakami, N. (1994) Sporadically distributed granitoids and related gneissose metamorphic rocks in the southeastern area of Fukuoka Prefecture and Kunisaki Peninsula, Southwest Japan. Journal of Mineralogy, Petrology and Economic Geology, **89**, 335–347 (in Japanese with English abstract).

Nagao, T., Sawai, O., Itaya, T. and Kakubuchi, S. (1992) K–Ar ages and petrological characteristics of the tholeiitic basalts and high-magnesian andesite from Amakusa-Shimoshima, Kumamoto Prefecture, SW Japan. Journal of Mineralogy, Petrology and Economic Geology, **87**, 283–290 (in Japanese with English abstract).

Nagasawa, H. and Schnetzler, C. C. (1971) Partitioning of rare Earth, alkali, and alkaline Earth elements between phenocrysts and acidic igneous magmas. Geochimica et Cosmochimica Acta, **35**, 953–968.

Nakae, S., Ozaki, M., Ota, M., Yabumoto, Y., et al. (1998) Geology of the Kokura district. With geological sheet map at 1:50,000. Geological Survey of Japan, pp. 126 (in Japanese with English abstract).

Nakakuki, T., and Mura, E. (2013) Dynamics of slab rollback and induced back-arc basin formation. Earth and Planetary Science Letters, **361**, 287–297.

Nakajima, T., Kamiyama, H., Williams, I. S. and Tani, K. (2004) Mafic rocks from the Ryoke Belt, southwest Japan: implications for Cretaceous Ryoke/San-yo granitic magma genesis. Transactions of the Royal Society of Edinburgh: Earth Sciences, **95**, 249–263.

Nakajima, T., Kamiyama, H. and Williams, I. S. (2021) Formation of syn-plutonic dike in the Cretaceous Ryoke granitic rocks, SW Japan: A geochronological approach to magma chamber process. Journal of the Geological Society of Japan, **127**, 69–78 (in Japanese with English abstract).

Nash, W. P. and Crecraft, H. R. (1985) Partition coefficients for trace elements in silicic magmas. Geochimica et Cosmochimica Acta, **49**, 2309–2322.

Nielsen, R. L. and Beard, J. S. (2000) Magnetite-melt HFSE partitioning. Chemical Geology, **164**, 21–34.

Nishida, K., Imaoka, T. and Iizumi, S. (2005) Cretaceous–Paleogene magmatism in the central San-in district, Southwest Japan: an examination based on Rb-Sr isochron ages. Journal of the Geological Society of Japan, **111**, 123–140 (in Japanese with English abstract).

Nishioka, S., Arakawa, Y. and Kobayashi, Y. (1991) Strontium isotope profile of Carboniferous-Permian Akiyoshi Limestone in southwest Japan. Geochemical Journal, **25**, 137–146.

Oshima, T. (1961) Kita-taku gabbroic rocks, Taku city, Saga prefecture. Memoirs of the Faculty of Education, Saga university, **10**, 87–100 (in Japanese with English abstract).

Ota, Y. (1959) On the *"Nippononaia"* from the Lower Cretaceous Wakino sub-group, North Kyushu, Japan. (Studies on the molluscan fauna of the Cretaceous inkstone series, Part 3). Transactions and Proceedings of Paleontological Society of Japan. New Series, **34**, 105–110.

Owada, M. and Kamei, A. (2010) Mesozoic northern area. *In* Kyushu and Okinawa (Editorial Committee of Kyushu and Okinawa, Geological Society of Japan Eds.). Regional Geology of Japan, 8. Asakura Publishing Company, 304–311 (in Japanese).

Owada, M., Kamei, A., Yamamoto, K., Osanai, Y. and Kagami, H. (1999) Spatial-temporal variations and origin of granitic rocks from central to northern part of Kyushu, Southwest Japan. The memoirs of the Geological Society of Japan, **53**, 349–363 (in Japanese with English abstract).

Pasquarè, F. and Tibaldi, A. (2007) Structure of a sheet-laccolith system revealing the interplay between tectonic and magma stresses at Stardalur Volcano, Iceland. Journal of Volcanology and Geothermal Research, **161**, 131–150.

Pastor-Galán, D., Spencer, C. J., Furukawa, T., and Tsujimori, T. (2021) Evidence for crustal removal, tectonic erosion and flare-ups from the Japanese evolving forearc sediment provenance. Earth and Planetary Science Letters, **564**, 116893, doi: 10.1016/j.epsl.2021.116893.

Paterson, S.R. and Ducea, M.N. (2015) Arc magmatic tempos: gathering the evidence. Elements, **11**, 91–98.

Patiño Douce, A. E. and Johnston, A. D. (1991) Phase equilibria and melt productivity in the pelitic system: implications for the origin of peraluminous granitoids and aluminous granulites. Contributions to Mineralogy and Petrology, **107**, 202–218.

Peccerillo, A. and Taylor, S. R. (1976) Geochemistry of Eocene calc-alkaline volcanic rocks from the Kastamonu area, northern Turkey. Contributions to Mineralogy and Petrology, **58**, 63–81.

Peate, D. W., Pearce, J. A., Hawkesworth, C. J., Colley, H., et al. (1997) Geochemical variations in Vanuatu arc lavas: the role of subducted material and a variable mantle wedge composition. Journal of Petrology, **38**, 1331–1358.

Philpotts, J. A. and Schnetzler, C. C. (1970) Phenocryst-matrix partition coefficients for K, Rb, Sr and Ba, with applications to anorthosite and basalt genesis. Geochimica et Cosmochimica Acta, **34**, 307–322.

Presnall, D. C., Dixon, S. A., Dixon, J. R., O'Donnell. T. H., et al. (1978) Liquidus phase relations on the join diopside-forsterite-anorthite from 1 atm to 20 kbar: their bearing on the generation and crystallization of basaltic magma. Contributions to Mineralogy and Petrology, **66**, 203–220.

Putirka, K. D. (2008) Thermometers and Barometers for Volcanic Systems. Reviews in Mineralogy and Geochemistry, **69**, 61–120.

Reid, Jr. J. B., Evans, O. C. and Fates, D. G. (1983) Magma mixing in granitic rocks of the central Sierra Nevada, California. Earth and Planetary Science Letters, **66**, 243–261.

Rogers, G., Saunders, A. D., Terrell, D. J., Verma, S. P., et al. (1985) Geochemistry of Holocene volcanic rocks associated with ridge subduction in Baja California, Mexico. Nature, **315**, 389–392.

Rollinson, H. (1993) Using Geochemical Data: evaluation, presentation, interpretation. Longman Scientific & Technical, Essex, UK. pp. 352.

Rubatto, D. (2002) Zircon trace element geochemistry: partitioning with garnet and the link between U–Pb ages and metamorphism. Chemical Geology, **184**, 123–138.

Rubatto, D., Williams, I. S. and Buick, I. S. (2001) Zircon and monazite response to prograde metamorphism in the Reynolds Range, central Australia. Contributions to Mineralogy and Petrology, **140**, 458–468.

Rutter, M. J. and Wyllie, P. J. (1988) Experimental calibration of hornblende as a proposed empirical geobarometer. Transactions of the AGU, **69**, 86–87.

Sasaki, H. and Murakami, N. (1986) Mt. Ushikiri-yama area. *In* Murakami, N. and Imaoka, T., Eds, Acid to Intermediate Igneous Activity in West Chugoku and its Adjacent Area, Southwest Japan, Journal of Faculty of Liberal Arts, Yamaguchi University. Professor Nobuhide MURAKAMI Memorial Volume. 133–152 (in Japanese with English abstract).

Sato, D., Matsuura, H., and Yamamoto, T. (2016) Timing of the Late Cretaceous ignimbrite flare-up at the eastern margin of the Eurasian Plate: New zircon U–Pb ages from the Aioi–Arima–Koto region of SW Japan. Journal of Volcanology and Geothermal Research, **310**, 89–97.

Saunders, A. D., Rogers, G., Marriner, G. F., Terrell, D. J., et al. (1987) Geochemistry of Cenozoic volcanic rocks, Baja California, Mexico: implications for the petrogenesis of post-subduction magmas. Journal of Volcanology and Geothermal Research, **32**, 223–245.

Schaltegger, U., Fanning, C. M., Günther, D., Maurin, J. C., et al. (1999) Growth, annealing and recrystallization of zircon and preservation of monazite in high-grade metamorphism: conventional and in-situ U-Pb isotope, cathodoluminescence and microchemical evidence. Contributions to Mineralogy and Petrology, **134**, 186–201.

Schmidt, M. W. (1992) Amphibole composition in tonalite as a function of pressure: an experimental calibration of the Al-in-hornblende barometer. Contributions to Mineralogy and Petrology, **110**, 304–310.

Schmidt, M. W. and Poli, S. (2004) Magmatic epidote. *In* Schmidt, M. W. and Poli, S., Eds, Reviews in Mineralogy and Geochemistry, **56**, 399–430.

Schnetzler, C. C. and Philpotts, J. A. (1970) Partition coefficients of rare-earth elements between igneous matrix material and rock-forming mineral phenocrysts; II. Geochimica et Cosmochimica Acta, **34**, 331–340.

Seton, M., Müller, R. D., Zahirovic, S., Gaina, C., et al. (2012) Global continental and ocean basin reconstructions since 200 Ma. Earth-Science Reviews, **113**, 212–270.

Seton, M., Flament, N., Whittaker, J., Müller, R. D., et al. (2015) Ridge subduction sparked reorganization of the Pacific plate-mantle system 60–50 million years ago. Geophysical Research Letters, **42**, 1732–1740.

Shaw, D. M. (1970) Trace element fractionation during anatexis. Geochimica et Cosmochimica Acta, **34**, 237–243.

Shimura, T. and Kojima, M. (2015) Point count application by MS-Excel VBA). Geoinformatics, **26**, 15–20 (in Japanese with English abstract).

Shimoda, G., Tatsumi, Y., Nohda, S., Ishizaka, K. and Jahn, B. M. (1998) Setouchi high-Mg andesites revisited: geochemical evidence for melting of subducting sediments. Earth and Planetary Science Letters, **160**, 479–492.

Shiraki, K., Kuroda, N., Urano, H. and Maruyama, S. (1980) Clinoenstatite in boninites from the Bonin Island, Japan. Nature, **285**, 31–32.

Shiraki, K., Nagao, K., Nagao, T., Kakubuchi, S. and Matsumoto, Y. (1991) Trace element characteristics of the Setouchi volcanic rocks from western Setonaikai. Journal of Mineralogy, Petrology and Economic Geology, **86**, 459–472 (in Japanese with English abstract).

Shiraki, K., Yoshida, K. and Matsumoto, Y. (1995) Magnesian andesites in the Oono volcanic rocks, central Kyushu: westward continuation of the Setouchi volcanic belt. Journal Geological Society of Japan, **101**, 387–392 (in Japanese with English abstract).

Sial, A. N., Toselli, A. J., Saavedra, J., Parada, M. A., et al. (1999) Emplacement, petrological and magnetic susceptibility characteristics of diverse magmatic

epidote-bearing granitoid rocks in Brazil, Argentina and Chile. Lithos, **46**, 367–392.

Sial, A. N., Vasconcelos, P. M., Ferreira, B. P., Pessoa, R. R., et al. (2008) Geochronological and mineralogical constraints on depth of emplacement and ascension rates of epidote-bearing mamas from northeastern Brazil. Lithos, **105**, 225–238.

Sisson, T. W. (1994) Hornblende-melt trace-element partitioning measured by ion microprobe. Chemical Geology, **117**, 331–344.

Skjerlie, K. P. and Johnston, A. D. (1993) Fluid-absent melting behavior of a F-rich tonalitic gneiss at mid-crustal pressures: Implications for the generation of anorogenic granites. Journal of Petrology, **34**, 785–815.

Skrzypek, E., Kawakami, T., Hirajima, T., Sakata, S., et al. (2016) Revisiting the high temperature metamorphic field gradient of the Ryoke Belt (SW Japan): New constraints from the Iwakuni-Yanai area. Lithos, **260**, 9–27.

Sláma, J., Košler, J., Condon, D.J., Crowley, J.L., et al. (2008) Plešovice zircon− A new natural reference material for U–Pb and Hf isotopic microanalysis. Chemical Geology. **249**, 1–35.

Steiger, R. and Jäger, E. (1977) Subcommision on geochronology: convention on the use of decay constants in geo- and cosmo-chronology. Earth and Planetary Science Letters, **36**, 359–362.

Stern, R. J. (2002) Subduction zones. Reviews of Geophysics, **40**, 1012, doi:10.1029/2001RG000108.

Stern, R. A. and Hanson, G. N. (1991) Archean high-Mg granodiorite: a derivative of light rare earth element-enriched monzodiorite of mantle origin. Journal Petrology, **32**, 201–238.

Stern, C. R. and Kilian, R. (1996) Role of the subducted slab, mantle wedge and continental crust in the generation of adakites from the Andean Austral Volcanic Zone. Contributions to Mineralogy and Petrology, **123**, 263–281.

Streckeisen, A. (1976) To each plutonic rock its proper name. Earth-Science Reviews, **12**, 1–33.

Stevens, R. E. (1944) Composition of some chromites of the western hemisphere. American Mineralogist, **29**, 1–34.

Sun, S.-S. and McDonough, W. F. (1989) Chemical and isotopic systematics of oceanic basalts: implications for mantle composition and processes. *In* Magmatism in the Ocean Basins (Saunders, A. D. and Norry, M. J. Eds.). Geological Society, London, Special Publications, **42**, 313–345.

Syracuse, E. M., and Abers, G. A. (2006) Global compilation of variations in slab depth beneath arc volcanoes and implications. Geochemistry, Geophysics, Geosystems, **7**, doi: 10.1029/2005GC001045.

Tainosho, Y., Wadatsumi, K., Masaoka, K. and Collaborative Research Group for the Granites around Lake Biwa. (1985) Late Cretaceous to Paleogene igneous activities in the Kinki district, Japan. Earth Science (Chikyu kagaku), **39**, 358–371(in Japanese with English abstract).

Takagi, T. (2004) Origin of magnetite- and ilmenite-series granitic rocks in the Japan arc. American Journal of Science, **304**, 169–202.

Takahashi, T., Hirahara, Y., Miyazaki, T., Vaglarov, B. S., et al. (2009) Precise determination of Sr isotope ratios in igneous rock samples and application to micro-analysis of plagioclase phenocrysts. JAMSTEC-R IFREE Special issue, volume **2009**, 59–64.

Takatsuka, K., Kawakami, T., Skrzypek, E., Sakata, S., et al. (2017) Age gap between the intrusion of gneissose granitoids and regional high-temperature metamorphism in the Ryoke belt (Mikawa area), central Japan. Island Arc, **27**, 10.1111/iar.12224.

Takatsuka, K., Kawakami, T., Skrzypek, E., Sakata, S., et al. (2018) Spatiotemporal evolution of magmatic pulses and regional metamorphism during a

Cretaceous flare-up event: constraints from the Ryoke belt (Mikawa area, central Japan). Lithos, **308–309**, 428–445.

Tanaka, T., Togashi, S., Kamioka, H., Amakawa, H., et al. (2000) JNdi-1: a neodymium isotopic reference in consistency with LaJolla neodymium. Chemical Geology, **168**, 279–281.

Tang, J., Xu, W., Wang, F., and Ge, W. (2018) Subduction history of the Paleo-Pacific slab beneath Eurasian continent: Mesozoic-Paleogene magmatic records in Northeast Asia. Science China Earth Sciences, **61**, 527–559.

Tatsumi, Y. (1981) Melting experiments on a high-magnesian andesite. Earth and Planetary Science Letters, **54**, 357–365.

Tatsumi, Y. (1982). Origin of high-magnesian andesites in the Setouchi volcanic belt, southwest Japan: II. Melting phase relations at high pressures. Earth and Planetary Science Letters, **60**, 305–317.

Tatsumi, Y. and Ishizaka, K. (1982a) Origin of high-magnesian andesites in the Setouchi volcanic belt, southwest Japan: I. Petrographical and chemical characteristics. Earth and Planetary Science Letters, **60**, 293–304.

Tatsumi, Y. and Ishizaka, K. (1982b). Magnesian andesite and basalt from Shodo–Shima island, southwest Japan, and their bearing on the genesis of calc-alkaline andesites. Lithos, **15**, 161–172.

Tatsumi, Y. and Hanyu, T. (2003) Geochemical modeling of dehydration and partial melting of subducting lithosphere: Towards a comprehensive understanding of high-Mg andesite formation in the Setouchi volcanic belt, SW Japan. Geochemistry, Geophysics, Geosystems, **4**, 1081, doi: 10.1029/2003GC000530.

Tatsumi, Y., Shukuno, H., Sato, K., Shibata, Y., et al. (2003) The petrology and geochemistry of high-magnesium andesites at the western tip of the Setouchi Volcanic Belt, SW Japan. Journal of Petrology, **44**, 1561–1578.

Taylor, R. N., Nesbit, R., Vidal, P., Harmon, R. S., et al. (1994) Mineralogy, chemistry, and genesis of the boninite series volcanics, Chichijima, Bonin Islands, Japan. Journal of Petrology, **35**, 577–617.

Taylor, S. R., and McLennan, S. M. (1985) The Continental Crust: Its Composition and Evolution. Blackwell, Oxford, pp. 312.

Tepper, J. H., Nelson, B. K., Bergantz, G. W. and Irving, A. J. (1993) Petrology of the Chilliwack batholith, north Cascades, Washington: generation of calc-alkaline granitoids by melting of mafic lower crust with variable water fugacity. Contributions to Mineralogy and Petrology, **113**, 333–351.

Tiepolo, M., Langone, A., Morishita, T. and Yuhara, M. (2012) On the recycling of amphibole-rich ultramafic intrusive rocks in the arc crust: Evidence from Shikanoshima Island (Kyushu, Japan). Journal of Petrology, **53**, 1255–1285.

Tsuchiyama, A. (1985) Dissolution kinetics of plagioclase in the melt of the system diopside-albite-anorthite, and origin of dusty plagioclase in andesites. Contributions to Mineralogy and Petrology, **89**, 1–16.

Tsune, A. (2005) Mass balance calculator coded in Java. Geoinformatics, **16**, 235–241 (in Japanese with English abstract).

Tsutsumi, Y., Yokoyama, K., Terada, K. and Sano, Y. (2003) SHRIMP U–Pb dating of detrital zircons in metamorphic rocks from the northern Kyushu, western Japan. Journal of Mineralogical and Petrological Sciences, **98**, 181–193.

Tsutsumi, Y., Yokoyama, K., Terada, K. and Hidaka, H. (2011) SHRIMP Dating of Detrital Zircons from the Sangun-Renge Belt of Sangun Metamorphic Rocks, Northern Kyushu, Southwest Japan. Bulletin of the National Museum of Nature and Science, Series C, **37**, 5–16.

Tsutsumi, Y. and Horie, K. (2019) Zircon U–Pb age of the granitic tectonic block between the Suo metamorphic belt and Nagasaki metamorphic complex, Nagasaki Peninsula, southwest Japan. Bulletin of the National Museum of Nature and Science, Series C, **45**, 7–12.

Vermeesch, P. (2012) On the visualisation of detrital age distributions. Chemical Geology, **312–313**, 190–194.

Vermeesch, P. (2018) IsoplotR: A free and open toolbox for geochronology. Geoscience Frontiers, **9**, 1479–1493.

Vielzeuf, D. and Holloway, J. R. (1988) Experimental determination of the fluid-absent melting relations in the pelitic system. Contributions to Mineralogy and Petrology, **98**, 257–276.

Villemant, B., Jaffrezic, H., Joron, J.L. and Treuil, M. (1981). Distribution coefficients of major and trace elements; fractional crystallization in the alkali basalt series of Chaîne des Puys (Massif Central, France). Geochimica et Cosmochimica Acta, **45**, 1997–2016.

Vuong, B. T. S., Osanai, Y., Nakano, N., Adachi, T., Kitano, I. (2019) Geochronology and REE geochemistry of zircon and garnet in pelitic gneisses from the Higo metamorphic terrane, Kyushu, Japan: Constraints on the timing of high-temperature metamorphism. Journal of Mineralogical and Petrological Sciences, **114**, 47–59.

Wakita, K., Nakagawa, T., Sakata, M., Tanaka, N., et al. (2018) Phanerozoic accretionary history of Japan and western Pacific margin: Geological Magazine. doi: 10.1017/S0016756818000742.

Wells, P. R. A. (1977) Pyroxene thermometry in simple and complex systems. Contributions to Mineralogy and Petrology. **62**, 129–139.

Wiebe, R. A. (1994) Silicic magma chambers as traps for basaltic magmas: the Cadillac Mountain intrusive complex, Mount Desert Island, Maine. Journal of Geology, **102**, 423–437.

Wiebe, R. A. and Collins, W. J. (1998). Depositional features and stratigraphic sections in granitic plutons: implications for the emplacement and crystallization of granitic magma. Journal of Structural Geology, **20**, 1273–1289.

Wiedenbeck, M., Alle, P., Corfu, F., Griffin, W. L., et al. (1995) Three natural zircon standards for U-Th-Pb, Lu-Hf, trace element and REE analyses. Geostandards Newsletter, **19**, 1–23.

Wolf, M. B. and Wyllie, P. J. (1994) Dehydration-melting of amphibolite at 10 kbar: the effects of temperature and time. Contributions to Mineralogy and Petrology, **115**, 369–383.

Wood, B. J. and Banno, S. (1973) Garnet-Orthopyroxene and Orthopyroxene-Clinopyroxene in simple and complex system. Contributions to Mineralogy and Petrology, **42**, 109–124.

Yada, J. and Owada, M. (2003) Genetic relationship between the Cretaceous high-Sr tonalite (Itoshima mass) and trondhjemite (Fukae mass) in the central part of Saga Prefecture, northwest Kyushu: Implications for magmatic differentiation. Journal of the Geological Society of Japan, **109**, 518–532 (in Japanese with English abstract).

Yamasaki, T., Yamashita, K., Ogasawara, M. and Saito, G. (2016) Multiple trace element analyses for silicate minerals and glasses by laser ablation-inductively coupled plasma-mass spectrometry (LA-ICP-MS). Bulletin of the Geological Survey of Japan, **66**, 179–197.

Yang, F., Santosh, M., and Tang, L. (2018) Extensive crustal melting during craton destruction: evidence from the Mesozoic magmatic suite of Junan, eastern North China Craton. Journal of Asian Earth Sciences, **157**, 119–140.

Yoder, H. S. Jr. (1965) Diopside-anorthite-water at five and ten kilobars and its bearing on explosive volcanism. Carnegie Institution Yearbook Washington, **64**, 82–89.

Yoder, H. S. Jr. and Tilley, C. E. (1962) Origin of basalt magmas: An experimental study of natural and synthetic rock systems. Journal of Petrology, **3**, 342–532.

Yoder, H. S. Jr., Stewart, D. B. and Smith, J. R. (1957) Ternary feldspars. Carnegie Institution Yearbook Washington, **56**, 206–214.

Yogodzinski, G. M., Kay, R. W., Volynets, O. N., Koloskov, A. V., et al. (1995) Magnesian andesite in the western Aleutian Komandorsky region: implications for slab melting and processes in the mantle wedge. Bulletin of the Geological Society of America, **107**, 505–519.

Yokoyama, K., Shigeoka, M., Otomo, Y., Tokuno, K., et al. (2016) Uraninite and Thorite ages of around 400 granitoids in the Japanese Islands. Memoirs of the National Museum of Nature and Science, **51**, 1–24.

Yoshikura, S. and Atsuta, S. (2000) Magma mingling and mixing recorded in the granitic body. Chikyu Monthly, Extra edition, **30**, 140–145 (in Japanese with English abstract).

Yu, X., Chen, Z., Hu, J., Liu, M., He, Y., et al. (2021) Early Cretaceous extension in South China: Constraints from east–west-trending A-type granite belts and growth strata in terrigenous basins. International Geology Review, doi: 10.1080/ 00206814.2021.1881920.

Yuhara, M. and Uto, C. (2007) Relationship between the Shikanoshima Granodiorite and Shikanoshima basic rocks at the Shikanoshima Island, northern Kyushu, Southwest Japan: coexistence of high Mg dioritic magma and granodioritic magma. Journal of the Geological Society of Japan, **113**, 519–531 (in Japanese with English abstract).

Yuhara, M. and Masaki, K. (2013) Field occurrence and chemical composition of synplutonic intrusive rocks on the Soeda Granodiorite, northern Kyushu, Southwest Japan. Earth Science (Chikyu Kagaku), **67**, 21–36 (in Japanese with English abstract).

Yuhara, M., Kamei, A., Kawano, Y., Okano, O., et al. (2019a) U–Pb zircon ages and Sr and Nd isotope compositions of the Soeda Granodiorite, northern Kyushu,

Southwest Japan. Journal of the Geological Society of Japan, **125**, 405–420 (in Japanese with English abstract).

Yuhara, M., Mizuta, F., Nishi, E., Kiyoura, K., et al. (2019b) Chemical compositions and timing of activity of the Masaki Granite, northern Kyushu, Southwest Japan. Earth Science (Chikyu Kagaku) **73**, 163–178 (in Japanese with English abstract).

Yuhara, M., Kamei, A., Kawano, Y., Okano, O., et al. (2020) U-Pb zircon age and Sr and Nd isotope compositions of the Haki body of the Ochiai Granodiorite (Haki Granodiorite), northern Kyushu, Southwest Japan. Earth Science (Chikyu Kagaku) **74**, 83–98 (in Japanese with English abstract).

Yuhara, M., Kiyoura, K., Hidaka, M., Hokada, T., et al. (2021) The metamorphism of the Tagawa metamorphic rocks, eastern North Kyushu. Journal of the Geological Society of Japan, **127**, 447–459 (in Japanese with English abstract).

Zack, T. and Brumm, R. (1998) Ilmenite/liquid partition coefficients of 26 trace elements determined through ilmenite/clinopyroxene partitioning in garnet pyroxene. *In* 7th International Kimberlite Conference (Gurney, J.J., Gurney, J.L., Pascoe, M.D. and Richardson, S.H. Eds). Red Roof Design, Cape Town, 986–988.

Zen, E.-A. and Hammarstrom, J. M. (1984) Magmatic epidote and its petrologic significance. Geology, **12**, 515–518.

Zhao, Z., Liang, S., Santosh, M., and Wei, J. (2020) Lithospheric extension associated with slab rollback: insights from early Cretaceous magmatism in the southern segment of Tan-Lu fault zone, central-eastern China. Lithos, 362–263, doi: 10.1016/j. lithos.2020.105487.

Zhou, X. M. and Li, W. X. (2000) Origin of Late Mesozoic igneous rocks in Southeastern China: Implications for lithosphere subduction and underplating of mafic magmas. Tectonophysics, **326**, 269–287.

Appendix

Appendix 2–1. Modal value of the Ushikiri-yama granodiorite and Pr Fine Gr.

Type	Ushi Gd	Ushi Gd	Ushi Gd	Ushi Gd	Ushi Gd	Ushi Gd	Ushi Gd	Ushi Gd	Ushi Gd	Ushi Gd
No	14031502	14032702	14040302	14040303	14040305	14041002	14041006	14041007	14041009	14041012
Count (point)										
Qz	490	514	458	530	482	511	555	508	564	489
Pl	659	697	817	695	803	751	826	825	833	842
Kfs	354	313	300	411	335	317	237	204	163	274
Hb	229	210	275	183	189	192	200	195	228	148
Bt	223	216	124	155	156	186	131	220	154	185
Ep	2	3	2	2	1	4	4	2	1	5
Cal	0	0	1	0	1	6	8	1	1	0
Ttn	14	25	8	9	20	14	19	16	14	19
Aln	0	0	0	0	0	3	1	2	0	3
Chl	12	10	4	7	5	8	6	9	10	14
Zrn	1	2	0	1	2	0	1	0	1	0
Opq	16	10	11	7	6	8	12	18	31	21
Total	2000	2000	2000	2000	2000	2000	2000	2000	2000	2000
Modal value (%)										
Qz	24.5	25.7	22.9	26.5	24.1	25.6	27.8	25.4	28.2	24.5
Pl	33.0	34.9	40.9	34.8	40.2	37.6	41.3	41.3	41.7	42.1
Kfs	17.7	15.7	15.0	20.6	16.8	15.9	11.9	10.2	8.2	13.7
Hb	11.5	10.5	13.8	9.2	9.5	9.6	10.0	9.8	11.4	7.4
Bt	11.2	10.8	6.2	7.8	7.8	9.3	6.6	11.0	7.7	9.3
Ep	0.1	0.2	0.1	0.1	0.1	0.2	0.2	0.1	0.1	0.3
Cal	0.0	0.0	0.1	0.0	0.1	0.3	0.4	0.1	0.1	0.0
Ttn	0.7	1.3	0.4	0.5	1.0	0.7	1.0	0.8	0.7	1.0
Aln	0.0	0.0	0.0	0.0	0.0	0.2	0.1	0.1	0.0	0.2
Chl	0.6	0.5	0.2	0.4	0.3	0.4	0.3	0.5	0.5	0.7
Zrn	0.1	0.1	0.0	0.1	0.1	0.0	0.1	0.0	0.1	0.0
Opq	0.8	0.5	0.6	0.4	0.3	0.4	0.6	0.9	1.6	1.1
Total	100	100	100	100	100	100	100	100	100	100

Type	Ushi Gd	Ushi Gd	Ushi Gd	Ushi Gd	Ushi Gd	Ushi Gd	Ushi Gd	Ushi Gd	Ushi Gd	Ushi Gd
No	14041103	14041105	14041202	14041204	14042307	14042308	14042309	14042313	14051402	14051406
Count (point)										
Qz	579	496	479	490	500	471	486	597	503	503
Pl	794	820	846	828	771	848	741	818	767	803
Kfs	274	203	224	159	269	252	341	224	322	173
Hb	180	236	186	258	230	223	284	203	224	230
Bt	130	185	211	195	197	151	84	140	162	249
Ep	4	2	5	4	1	8	3	1	3	2
Cal	1	1	1	11	3	2	5	0	1	1
Ttn	12	12	16	12	10	19	34	4	8	11
Aln	1	2	1	1	2	2	2	1	1	2
Chl	6	8	14	13	4	5	5	6	4	12
Zrn	1	1	1	2	1	0	1	0	0	0
Opq	18	34	16	27	12	19	14	6	5	14
Total	2000	2000	2000	2000	2000	2000	2000	2000	2000	2000
Modal value (%)										
Qz	29.0	24.8	24.0	24.5	25.0	23.6	24.3	29.9	25.2	25.2
Pl	39.7	41.0	42.3	41.4	38.6	42.4	37.1	40.9	38.4	40.2
Kfs	13.7	10.2	11.2	8.0	13.5	12.6	17.1	11.2	16.1	8.7
Hb	9.0	11.8	9.3	12.9	11.5	11.2	14.2	10.2	11.2	11.5
Bt	6.5	9.3	10.6	9.8	9.9	7.6	4.2	7.0	8.1	12.5
Ep	0.2	0.1	0.3	0.2	0.1	0.4	0.2	0.1	0.2	0.1
Cal	0.1	0.1	0.1	0.6	0.2	0.1	0.3	0.0	0.1	0.1
Ttn	0.6	0.6	0.8	0.6	0.5	1.0	1.7	0.2	0.4	0.6
Aln	0.1	0.1	0.1	0.1	0.1	0.1	0.1	0.1	0.1	0.1
Chl	0.3	0.4	0.7	0.7	0.2	0.3	0.3	0.3	0.2	0.6
Zrn	0.1	0.1	0.1	0.1	0.1	0.0	0.1	0.0	0.0	0.0
Opq	0.9	1.7	0.8	1.4	0.6	1.0	0.7	0.3	0.3	0.7
Total	100	100	100	100	100	100	100	100	100	100

Type	Ushi Gd	Ushi Gd	Ushi Gd	Ushi Gd	Ushi Gd	Ushi Gd	Ushi Gd	Ushi Gd	Ushi Gd	Ushi Gd
No	14051409	14052102	14052104	14052105	14052107	14052108	14052109	14052111	14052114	14060101
Count (point)										
Qz	575	507	494	530	532	532	559	435	515	502
Pl	830	755	829	795	819	825	792	759	730	877
Kfs	152	404	293	292	131	82	154	346	340	243
Hb	223	197	184	154	217	231	208	276	261	190
Bt	180	87	161	203	260	290	263	158	122	136
Ep	3	3	1	1	2	4	4	1	2	1
Cal	0	1	1	0	0	1	1	0	0	2
Ttn	6	32	9	3	3	0	0	1	5	15
Aln	0	2	2	1	3	2	3	2	4	1
Chl	18	10	7	8	13	13	8	10	8	8
Zrn	0	1	1	0	1	0	0	0	0	1
Opq	13	1	18	13	19	20	8	12	13	24
Total	2000	2000	2000	2000	2000	2000	2000	2000	2000	2000
Modal value (%)										
Qz	28.8	25.4	24.7	26.5	26.6	26.6	28.0	21.8	25.8	25.1
Pl	41.5	37.8	41.5	39.8	41.0	41.3	39.6	38.0	36.5	43.9
Kfs	7.6	20.2	14.7	14.6	6.6	4.1	7.7	17.3	17.0	12.2
Hb	11.2	9.9	9.2	7.7	10.9	11.6	10.4	13.8	13.1	9.5
Bt	9.0	4.4	8.1	10.2	13.0	14.5	13.2	7.9	6.1	6.8
Ep	0.2	0.2	0.1	0.1	0.1	0.2	0.2	0.1	0.1	0.1
Cal	0.0	0.1	0.1	0.0	0.0	0.1	0.1	0.0	0.0	0.1
Ttn	0.3	1.6	0.5	0.2	0.2	0.0	0.0	0.1	0.3	0.8
Aln	0.0	0.1	0.1	0.1	0.2	0.1	0.2	0.1	0.2	0.1
Chl	0.9	0.5	0.4	0.4	0.7	0.7	0.4	0.5	0.4	0.4
Zrn	0.0	0.1	0.1	0.0	0.1	0.0	0.0	0.0	0.0	0.1
Opq	0.7	0.1	0.9	0.7	1.0	1.0	0.4	0.6	0.7	1.2
Total	100	100	100	100	100	100	100	100	100	100

Type	Ushi Gd	Ushi Gd	Ushi Gd	Ushi Gd	Ushi Gd	Ushi Gd	Ushi Gd	Ushi Gd	Ushi Gd	Ushi Gd
No	14060102	14060103	14060105	14060107	14060110	14060114	14060117	14060205	14060206	14060503
Count (point)										
Qz	485	712	577	516	655	664	619	771	666	608
Pl	850	942	815	861	800	748	824	805	858	840
Kfs	332	102	311	259	274	184	196	327	121	232
Hb	159	105	152	146	142	259	200	14	286	160
Bt	137	125	102	184	118	130	137	62	2	124
Ep	3	2	4	2	1	0	3	0	13	0
Cal	1	0	0	0	0	0	0	0	0	0
Ttn	8	1	2	10	3	2	6	0	37	7
Aln	1	1	1	0	1	0	4	3	1	1
Chl	1	1	4	5	5	5	4	4	8	4
Zrn	0	0	1	0	0	0	0	1	1	1
Opq	23	9	31	17	1	8	7	13	7	23
Total	2000	2000	2000	2000	2000	2000	2000	2000	2000	2000
Modal value (%)										
Qz	24.3	35.6	28.9	25.8	32.8	33.2	31.0	38.6	33.3	30.4
Pl	42.5	47.1	40.8	43.1	40.0	37.4	41.2	40.3	42.9	42.0
Kfs	16.6	5.1	15.6	13.0	13.7	9.2	9.8	16.4	6.1	11.6
Hb	8.0	5.3	7.6	7.3	7.1	13.0	10.0	0.7	14.3	8.0
Bt	6.9	6.3	5.1	9.2	5.9	6.5	6.9	3.1	0.1	6.2
Ep	0.2	0.1	0.2	0.1	0.1	0.0	0.2	0.0	0.7	0.0
Cal	0.1	0.0	0.0	0.0	0.0	0.0	0.0	0.0	0.0	0.0
Ttn	0.4	0.1	0.1	0.5	0.2	0.1	0.3	0.0	1.9	0.4
Aln	0.1	0.1	0.1	0.0	0.1	0.0	0.2	0.2	0.1	0.1
Chl	0.1	0.1	0.2	0.3	0.3	0.3	0.2	0.2	0.4	0.2
Zrn	0.0	0.0	0.1	0.0	0.0	0.0	0.0	0.1	0.1	0.1
Opq	1.2	0.5	1.6	0.9	0.1	0.4	0.4	0.7	0.4	1.2
Total	100	100	100	100	100	100	100	100	100	100

Type	Ushi Gd	Ushi Gd	Ushi Gd	Ushi Gd	Ushi Gd	Ushi Gd	Ushi Gd	Ushi Gd	Ushi Gd	Ushi Gd
No	14060504	14060506c	14060507a	14060509b	14060510b	14060512	14030505b	14030507	14050301	14050303
Count (point)										
Qz	513	548	489	544	534	452	508	487	492	475
Pl	799	820	896	851	783	887	837	852	733	785
Kfs	264	202	83	219	224	216	261	242	399	325
Hb	182	256	234	178	176	194	205	197	162	191
Bt	186	133	265	175	252	203	152	187	171	169
Ep	2	4	6	1	1	1	1	0	1	3
Cal	0	0	0	0	1	3	0	0	0	0
Ttn	21	9	7	5	7	6	6	8	15	16
Aln	2	4	1	1	0	3	2	1	2	3
Chl	4	7	4	10	6	7	9	3	6	11
Zrn	1	1	1	0	1	1	0	0	0	0
Opq	26	16	14	16	15	27	19	23	19	22
Total	2000	2000	2000	2000	2000	2000	2000	2000	2000	2000
Modal value (%)										
Qz	25.7	27.4	24.5	27.2	26.7	22.6	25.4	24.4	24.6	23.8
Pl	40.0	41.0	44.8	42.6	39.2	44.4	41.9	42.6	36.7	39.3
Kfs	13.2	10.1	4.2	11.0	11.2	10.8	13.1	12.1	20.0	16.3
Hb	9.1	12.8	11.7	8.9	8.8	9.7	10.3	9.9	8.1	9.6
Bt	9.3	6.7	13.3	8.8	12.6	10.2	7.6	9.4	8.6	8.5
Ep	0.1	0.2	0.3	0.1	0.1	0.1	0.1	0.0	0.1	0.2
Cal	0.0	0.0	0.0	0.0	0.1	0.2	0.0	0.0	0.0	0.0
Ttn	1.1	0.5	0.4	0.3	0.4	0.3	0.3	0.4	0.8	0.8
Aln	0.1	0.2	0.1	0.1	0.0	0.2	0.1	0.1	0.1	0.2
Chl	0.2	0.4	0.2	0.5	0.3	0.4	0.5	0.2	0.3	0.6
Zrn	0.1	0.1	0.1	0.0	0.1	0.1	0.0	0.0	0.0	0.0
Opq	1.3	0.8	0.7	0.8	0.8	1.4	1.0	1.2	1.0	1.1
Total	100	100	100	100	100	100	100	100	100	100

Type	Ushi Gd	Ushi Gd	Ushi Gd	Ushi Gd	Ushi Gd	Ushi Gd	Ushi Gd	Ushi Gd	Ushi Gd	Ushi Gd
No	14050304	14050306	14050310	14050311	14050313a	14050401	15050404	14050405	14050408	14031602
Count (point)										
Qz	530	441	542	525	574	485	530	578	480	486
Pl	867	844	884	877	793	800	804	890	750	826
Kfs	193	254	212	212	237	236	326	104	369	304
Hb	185	254	172	117	150	200	146	167	182	165
Bt	178	152	125	206	189	246	167	205	162	186
Ep	2	1	4	2	0	1	0	4	18	0
Cal	0	0	0	0	0	0	0	0	0	1
Ttn	8	22	26	18	14	9	6	10	15	16
Aln	1	0	2	2	0	1	1	0	0	0
Chl	8	3	7	10	16	4	2	11	11	4
Zrn	0	1	1	1	1	0	0	0	0	1
Opq	28	28	25	30	26	18	18	30	13	11
Total	2000	2000	2000	2000	2000	2000	2000	2000	2000	2000
Modal value (%)										
Qz	26.5	22.1	27.1	26.3	28.7	24.3	26.5	28.9	24.0	24.3
Pl	43.4	42.2	44.2	43.9	39.7	40.0	40.2	44.5	37.5	41.3
Kfs	9.7	12.7	10.6	10.6	11.9	11.8	16.3	5.2	18.5	15.2
Hb	9.3	12.7	8.6	5.9	7.5	10.0	7.3	8.4	9.1	8.3
Bt	8.9	7.6	6.3	10.3	9.5	12.3	8.4	10.3	8.1	9.3
Ep	0.1	0.1	0.2	0.1	0.0	0.1	0.0	0.2	0.9	0.0
Cal	0.0	0.0	0.0	0.0	0.0	0.0	0.0	0.0	0.0	0.1
Ttn	0.4	1.1	1.3	0.9	0.7	0.5	0.3	0.5	0.8	0.8
Aln	0.1	0.0	0.1	0.1	0.0	0.1	0.1	0.0	0.0	0.0
Chl	0.4	0.2	0.4	0.5	0.8	0.2	0.1	0.6	0.6	0.2
Zrn	0.0	0.1	0.1	0.1	0.1	0.0	0.0	0.0	0.0	0.1
Opq	1.4	1.4	1.3	1.5	1.3	0.9	0.9	1.5	0.7	0.6
Total	100	100	100	100	100	100	100	100	100	100

Type	Ushi Gd	Ushi Gd	Ushi Gd	Ushi Gd	Ushi Gd	Ushi Gd	Ushi Gd	Ushi Gd	Ushi Gd	Ushi Gd
No	14031608	14051407	14050417	14051309	14051302	14050416	14050420	14051307	14051306	14051304
Count (point)										
Qz	538	428	608	454	388	507	526	510	485	520
Pl	854	808	822	903	860	848	920	850	873	834
Kfs	227	298	228	367	352	357	416	334	310	310
Hb	172	211	131	111	186	109	54	144	146	122
Bt	169	179	158	142	173	158	77	131	165	192
Ep	14	25	2	0	0	3	1	0	5	0
Cal	0	0	0	0	2	0	0	0	0	0
Ttn	6	9	12	8	8	6	1	9	1	5
Aln	0	2	0	0	0	0	0	0	0	0
Chl	5	22	2	0	1	0	0	1	0	0
Zrn	0	1	3	0	2	2	1	2	1	0
Opq	15	17	34	15	28	10	4	19	14	17
Total	2000	2000	2000	2000	2000	2000	2000	2000	2000	2000
Modal value (%)										
Qz	26.9	21.4	30.4	22.7	19.4	25.4	26.3	25.5	24.3	26.0
Pl	42.7	40.4	41.1	45.2	43.0	42.4	46.0	42.5	43.7	41.7
Kfs	11.4	14.9	11.4	18.4	17.6	17.9	20.8	16.7	15.5	15.5
Hb	8.6	10.6	6.6	5.6	9.3	5.5	2.7	7.2	7.3	6.1
Bt	8.5	9.0	7.9	7.1	8.7	7.9	3.9	6.6	8.3	9.6
Ep	0.7	1.3	0.1	0.0	0.0	0.2	0.1	0.0	0.3	0.0
Cal	0.0	0.0	0.0	0.0	0.1	0.0	0.0	0.0	0.0	0.0
Ttn	0.3	0.5	0.6	0.4	0.4	0.3	0.1	0.5	0.1	0.3
Aln	0.0	0.1	0.0	0.0	0.0	0.0	0.0	0.0	0.0	0.0
Chl	0.3	1.1	0.1	0.0	0.1	0.0	0.0	0.1	0.0	0.0
Zrn	0.0	0.1	0.2	0.0	0.1	0.1	0.1	0.1	0.1	0.0
Opq	0.8	0.9	1.7	0.8	1.4	0.5	0.2	1.0	0.7	0.9
Total	100	100	100	100	100	100	100	100	100	100

Type	Ushi Gd	Ushi Gd	Ushi Gd	Ushi Gd	Ushi Gd	Ushi Gd	Ushi Gd	Ushi Gd	Ushi Gd	Ushi Gd
No	14050421	14050415	14051311	14051313	14051310	14051317	14071702	14071703	14071704	14071705
Count (point)										
Qz	476	670	507	446	515	434	538	536	530	448
Pl	849	836	841	804	894	755	839	816	880	805
Kfs	321	348	267	369	294	442	206	202	188	337
Hb	177	16	180	242	102	178	187	205	182	221
Bt	152	118	175	110	165	165	176	215	181	131
Ep	5	3	7	2	3	1	12	2	19	11
Cal	1	0	1	0	0	0	0	0	0	1
Ttn	14	3	9	14	6	9	10	4	4	14
Aln	0	1	0	0	0	1	0	1	4	1
Chl	0	0	0	3	3	10	25	12	9	21
Zrn	0	2	1	1	2	1	0	1	0	0
Opq	5	3	12	9	16	4	7	6	3	10
Total	2000	2000	2000	2000	2000	2000	2000	2000	2000	2000
Modal value (%)										
Qz	23.8	33.5	25.4	22.3	25.8	21.7	26.9	26.8	26.5	22.4
Pl	42.5	41.8	42.1	40.2	44.7	37.8	42.0	40.8	44.0	40.3
Kfs	16.1	17.4	13.4	18.5	14.7	22.1	10.3	10.1	9.4	16.9
Hb	8.9	0.8	9.0	12.1	5.1	8.9	9.4	10.3	9.1	11.1
Bt	7.6	5.9	8.8	5.5	8.3	8.3	8.8	10.8	9.1	6.6
Ep	0.3	0.2	0.4	0.1	0.2	0.1	0.6	0.1	1.0	0.6
Cal	0.1	0.0	0.1	0.0	0.0	0.0	0.0	0.0	0.0	0.1
Ttn	0.7	0.2	0.5	0.7	0.3	0.5	0.5	0.2	0.2	0.7
Aln	0.0	0.1	0.0	0.0	0.0	0.1	0.0	0.1	0.2	0.1
Chl	0.0	0.0	0.0	0.2	0.2	0.5	1.3	0.6	0.5	1.1
Zrn	0.0	0.1	0.1	0.1	0.1	0.1	0.0	0.1	0.0	0.0
Opq	0.3	0.2	0.6	0.5	0.8	0.2	0.4	0.3	0.2	0.5
Total	100	100	100	100	100	100	100	100	100	100

Type	Ushi Gd	Ushi Gd	Ushi Gd	Ushi Gd	Ushi Gd	Ushi Gd	Ushi Gd	Ushi Gd	Ushi Gd	Ushi Gd
No	14071706	14071801	14071802	14071803	14071805	14071806	14071808	14071809	14071810	14071811
Count (point)										
Qz	450	489	549	503	608	619	464	623	484	588
Pl	840	830	900	844	835	870	921	815	878	849
Kfs	379	269	205	303	183	144	165	156	224	202
Hb	183	212	212	177	63	165	196	124	176	123
Bt	113	169	99	150	283	159	188	250	205	195
Ep	5	4	8	2	1	4	10	2	0	8
Cal	1	2	8	2	0	0	0	0	0	0
Ttn	7	10	10	9	7	11	13	5	8	4
Aln	0	0	1	1	2	1	2	1	2	0
Chl	14	5	5	0	3	4	14	0	1	2
Zrn	0	0	0	0	0	0	0	2	0	0
Opq	8	10	3	9	15	23	27	22	22	29
Total	2000	2000	2000	2000	2000	2000	2000	2000	2000	2000
Modal value (%)										
Qz	22.5	24.5	27.5	25.2	30.4	31.0	23.2	31.2	24.2	29.4
Pl	42.0	41.5	45.0	42.2	41.8	43.5	46.1	40.8	43.9	42.5
Kfs	19.0	13.5	10.3	15.2	9.2	7.2	8.3	7.8	11.2	10.1
Hb	9.2	10.6	10.6	8.9	3.2	8.3	9.8	6.2	8.8	6.2
Bt	5.7	8.5	5.0	7.5	14.2	8.0	9.4	12.5	10.3	9.8
Ep	0.3	0.2	0.4	0.1	0.1	0.2	0.5	0.1	0.0	0.4
Cal	0.1	0.1	0.4	0.1	0.0	0.0	0.0	0.0	0.0	0.0
Ttn	0.4	0.5	0.5	0.5	0.4	0.6	0.7	0.3	0.4	0.2
Aln	0.0	0.0	0.1	0.1	0.1	0.1	0.1	0.1	0.1	0.0
Chl	0.7	0.3	0.3	0.0	0.2	0.2	0.7	0.0	0.1	0.1
Zrn	0.0	0.0	0.0	0.0	0.0	0.0	0.0	0.1	0.0	0.0
Opq	0.4	0.5	0.2	0.5	0.8	1.2	1.4	1.1	1.1	1.5
Total	100	100	100	100	100	100	100	100	100	100

Type	Ushi Gd	Ushi Gd	Ushi Gd	Ushi Gd	Ushi Gd	Ushi Gd	Ushi Gd	Ushi Gd	Ushi Gd	Ushi Gd
No	14031402	14031405	14031409	14031415	14060120	14060121	14060123	14042318	14051322	14051323
Count (point)										
Qz	480	482	500	505	688	689	600	532	429	492
Pl	646	820	854	677	782	778	826	802	760	760
Kfs	357	300	227	293	304	222	188	220	352	302
Hb	239	175	192	232	112	172	220	243	238	244
Bt	233	190	189	228	102	124	142	185	195	182
Ep	2	0	12	3	1	1	3	1	1	4
Cal	0	1	0	0	0	0	0	0	0	1
Ttn	14	17	5	33	4	3	6	3	7	6
Aln	0	0	0	0	0	0	4	2	3	1
Chl	16	3	9	12	4	4	4	5	8	3
Zrn	1	2	0	4	0	0	0	1	2	0
Opq	12	10	12	13	3	7	7	6	5	5
Total	2000	2000	2000	2000	2000	2000	2000	2000	2000	2000
Modal value (%)										
Qz	24.0	24.1	25.0	25.3	34.4	34.5	30.0	26.6	21.5	24.6
Pl	32.3	41.0	42.7	33.9	39.1	38.9	41.3	40.1	38.0	38.0
Kfs	17.9	15.0	11.4	14.7	15.2	11.1	9.4	11.0	17.6	15.1
Hb	12.0	8.8	9.6	11.6	5.6	8.6	11.0	12.2	11.9	12.2
Bt	11.7	9.5	9.5	11.4	5.1	6.2	7.1	9.3	9.8	9.1
Ep	0.1	0.0	0.6	0.2	0.1	0.1	0.2	0.1	0.1	0.2
Cal	0.0	0.1	0.0	0.0	0.0	0.0	0.0	0.0	0.0	0.1
Ttn	0.7	0.9	0.3	1.7	0.2	0.2	0.3	0.2	0.4	0.3
Aln	0.0	0.0	0.0	0.0	0.0	0.0	0.2	0.1	0.2	0.1
Chl	0.8	0.2	0.5	0.6	0.2	0.2	0.2	0.3	0.4	0.2
Zrn	0.1	0.1	0.0	0.2	0.0	0.0	0.0	0.1	0.1	0.0
Opq	0.6	0.5	0.6	0.7	0.2	0.4	0.4	0.3	0.3	0.3
Total	100	100	100	100	100	100	100	100	100	100

Type	Pr Fine Gr	Pr Fine Gr	Qz Mz	Fine Di
No	140605T01	14030508a	140327T01	14041205M
Count (point)				
Qz	876	732	69	62
Pl	404	498	941	803
Kfs	641	600	309	25
Hb	0	67	520	720
Bt	63	76	66	297
Ep	0	0	10	11
Cal	1	0	0	2
Ttn	0	10	80	17
Aln	3	4	0	0
Chl	2	1	3	16
Zrn	0	0	1	1
Opq	10	12	1	32
Total	2000	2000	2000	2000
Modal value (%)				
Qz	43.8	36.6	3.5	3.1
Pl	20.2	24.9	47.1	40.2
Kfs	32.1	30.0	15.5	1.3
Hb	0.0	3.4	26.0	36.0
Bt	3.2	3.8	3.3	14.9
Ep	0.0	0.0	0.5	0.6
Cal	0.1	0.0	0.0	0.1
Ttn	0.0	0.5	4.0	0.9
Aln	0.2	0.2	0.0	0.0
Chl	0.1	0.1	0.2	0.8
Zrn	0.0	0.0	0.1	0.1
Opq	0.5	0.6	0.1	1.6
Total	100	100	100	100

Appendix 2–2. Major (wt%) and trace element (ppm) concentrations of the Ushikiri-yama body

Type	Pr Fine Gr	Pr Fine Gr	Ushi Gd S	Ushi Gd S	Ushi Gd S	Ushi Gd S	Ushi Gd S	Ushi Gd S	Ushi Gd S	Ushi Gd S
No	14050415	14041011	14050411	14050416	14052102	14071809	14041002	14041012	14050405	14032702
(wt%)										
SiO_2	69.37	68.57	65.42	64.39	63.64	63.62	62.70	62.65	62.52	62.40
TiO_2	0.29	0.36	0.49	0.53	0.61	0.59	0.63	0.64	0.65	0.63
Al_2O_3	14.88	15.27	15.50	15.68	15.81	15.47	15.89	15.89	16.04	15.81
Fe_2O_3	2.36	2.88	4.27	4.56	3.64	4.95	5.44	5.39	5.48	5.40
MnO	0.03	0.06	0.07	0.07	0.07	0.08	0.10	0.10	0.09	0.08
MgO	1.02	0.97	1.78	1.94	2.41	2.21	2.44	2.50	2.48	2.49
CaO	2.95	2.65	3.83	3.85	4.72	4.10	5.13	5.25	5.01	5.02
Na_2O	3.36	3.99	3.11	3.07	3.00	3.14	3.32	3.31	3.35	3.13
K_2O	3.78	2.94	3.38	3.01	4.03	3.47	2.72	2.66	2.79	3.02
P_2O_5	0.07	0.11	0.13	0.14	0.15	0.15	0.16	0.17	0.17	0.16
LOI	0.48	0.75	0.58	1.27	0.85	0.65	0.52	0.43	0.54	0.61
Total	98.60	98.55	98.58	98.52	98.93	98.42	99.05	99.00	99.12	98.76
(ppm)										
Ba	307	546	403	415	448	401	416	424	380	377
Cr	12	12	20	21	29	30	32	31	31	36
Nb	4	8	6	5	6	9	9	10	12	9
Ni	6	7	7	6	8	7	7	7	7	8
Rb	*ICP-MS*	*ICP-MS*	123	*ICP-MS*	*ICP-MS*	*ICP-MS*	88	*ICP-MS*	101	95
Sr	*ICP-MS*	*ICP-MS*	362	*ICP-MS*	*ICP-MS*	*ICP-MS*	393	*ICP-MS*	398	402
V	49	38	83	86	106	103	119	121	120	117
Y	10	12	16	19	17	18	18	18	20	20
Zn	14	35	33	29	26	40	50	54	34	34
Zr	79	133	121	127	141	134	148	155	143	143
ICP-MS (ppm)										
Rb	120	88.0	–	100.0	111.0	120.0	–	87.0	–	–
Sr	283	320.0	–	338.0	351.0	335.0	–	375.0	–	–
La	15.1	22.5	–	17.3	26.1	20.7	–	21.3	–	–
Ce	26.8	43.1	–	35.2	46.8	37.8	–	40.6	–	–
Pr	2.7	4.4	–	4.1	4.7	4.3	–	4.5	–	–
Nd	9.6	15.8	–	15.5	18.1	15.7	–	16.9	–	–
Sm	1.7	3.0	–	3.5	3.5	3.3	–	3.5	–	–
Eu	0.5	0.7	–	1.0	1.0	0.9	–	1.0	–	–
Gd	1.7	2.3	–	3.1	3.3	3.1	–	3.3	–	–
Tb	0.2	0.3	–	0.5	0.5	0.5	–	0.5	–	–
Dy	1.4	1.8	–	2.9	2.9	2.7	–	2.7	–	–
Ho	0.3	0.3	–	0.5	0.6	0.6	–	0.6	–	–
Er	0.9	0.9	–	1.6	1.6	1.6	–	1.6	–	–
Yb	1.1	1.0	–	1.6	1.7	1.6	–	1.6	–	–
Lu	0.2	0.2	–	0.3	0.2	0.3	–	0.3	–	–
Ta	0.8	0.9	–	0.9	0.6	0.9	–	0.7	–	–
Hf	2.9	3.0	–	3.0	3.6	2.9	–	3.1	–	–
Th	8.9	9.0	–	7.8	6.5	8.3	–	9.5	–	–
Pb	11.0	12.0	–	8.0	8.0	7.0	–	9.0	–	–

Pr Fine Gr: Porphyritic fine-grained granite, Ushi Gd S: Ushikiri-yama granodiorite south body, Ushi Gd N: Ushikiri-yama granodiorite north body, Ushi Gd SF: Ushikiri-yama granodiorite south body fine-grained facies, Pr Fine To:Porohyritic fine-grained tonalite, and Pr Fine Di: Porphyrirtic fine-grained diorite. Total Fe reported as Fe^{3+}

Type No	Ushi Gd S 14041205	Ushi Gd S 14030507	Ushi Gd S 14031608	Ushi Gd S 14040303	Ushi Gd S 14071810	Ushi Gd S 14041009	Ushi Gd S 14031502	Ushi Gd S 14041104B	Ushi Gd S 14052104	Ushi Gd S 16112001
(wt%)										
SiO_2	62.40	62.24	62.22	62.21	62.11	62.03	61.85	61.73	61.35	–
TiO_2	0.65	0.65	0.66	0.64	0.66	0.66	0.64	0.62	0.67	–
Al_2O_3	16.06	16.08	16.02	16.01	16.12	16.05	16.22	16.17	15.79	–
Fe_2O_3	5.39	5.48	5.73	5.56	5.89	5.37	5.37	5.24	5.54	–
MnO	0.09	0.11	0.11	0.10	0.10	0.11	0.10	0.07	0.10	–
MgO	2.50	2.51	2.62	2.48	2.59	2.53	2.52	2.61	2.52	–
CaO	5.22	5.29	5.25	5.19	5.04	5.35	5.29	4.91	5.13	–
Na_2O	3.35	3.27	3.22	3.36	3.33	3.31	3.23	3.31	3.52	–
K_2O	2.85	2.89	2.63	2.77	2.74	3.03	2.90	2.88	2.89	–
P_2O_5	0.17	0.17	0.17	0.17	0.17	0.17	0.16	0.18	0.17	–
LOI	0.44	0.50	0.62	0.45	0.48	0.44	0.73	1.04	0.45	–
Total	99.11	99.17	99.25	98.93	99.24	99.04	99.03	98.75	98.12	–
(ppm)										
Ba	441	448	404	407	434	428	468	320	431	–
Cr	33	35	43	33	34	32	31	41	32	–
Nb	8	7	11	11	9	9	8	9	9	–
Ni	8	7	9	7	7	8	7	8	8	–
Rb	95	91	90	91	*ICP-MS*	*ICP-MS*	94	110	96	*ICP-MS*
Sr	410	409	408	410	*ICP-MS*	*ICP-MS*	418	448	385	*ICP-MS*
V	120	120	130	123	130	122	120	112	122	–
Y	18	19	20	19	19	19	19	18	20	–
Zn	41	60	54	41	46	50	51	28	36	–
Zr	140	142	155	144	143	157	145	122	149	–
ICP-MS (ppm)										
Rb	–	–	–	–	81.0	87.0	–	–	96.0	94.0
Sr	–	–	–	–	400.0	378.0	–	–	385.0	365.0
La	–	–	–	–	27.0	22.5	–	–	28.3	20.2
Ce	–	–	–	–	50.3	43.2	–	–	51.7	41.8
Pr	–	–	–	–	5.2	4.7	–	–	5.5	4.7
Nd	–	–	–	–	19.8	17.6	–	–	20.3	17.7
Sm	–	–	–	–	4.0	3.6	–	–	4.2	3.7
Eu	–	–	–	–	1.0	1.1	–	–	1.1	1.0
Gd	–	–	–	–	3.6	3.4	–	–	3.7	3.5
Tb	–	–	–	–	0.6	0.5	–	–	0.6	0.5
Dy	–	–	–	–	3.2	3.0	–	–	3.2	3.0
Ho	–	–	–	–	0.6	0.6	–	–	0.6	0.6
Er	–	–	–	–	1.8	1.6	–	–	1.8	1.8
Yb	–	–	–	–	1.8	1.7	–	–	1.8	1.8
Lu	–	–	–	–	0.3	0.3	–	–	0.3	0.3
Ta	–	–	–	–	1.0	0.8	–	–	1.0	1.5
Hf	–	–	–	–	3.9	3.3	–	–	3.4	3.4
Th	–	–	–	–	12.2	8.0	–	–	8.2	6.6
Pb	–	–	–	–	8.0	11.0	–	–	7.0	16.0

Pr Fine Gr: Porphyritic fine-grained granite, Ushi Gd S: Ushikiri-yama granodiorite south body, Ushi Gd N: Ushikiri-yama granodiorite north body, Ushi Gd SF: Ushikiri-yama granodiorite south body fine-grained facies, Pr Fine To:Porohyritic fine-grained tonalite, and Pr Fine Di: Porphyrirtic fine-grained diorite. Total Fe reported as Fe^{3+}

Type	Ushi Gd N	Ushi Gd N	Ushi Gd N	Ushi Gd N	Ushi Gd N	Ushi Gd N	Ushi Gd SF	Pr Fine To	Pr Fine To	Pr Fine To
No	14060114	14042313	14071706	14060117	14071707	16112003	14052107	14031604	14040304	140316T01
(wt%)										
SiO_2	65.66	65.63	64.77	64.46	64.17	–	60.91	59.77	59.44	58.90
TiO_2	0.45	0.45	0.45	0.49	0.50	–	0.73	0.66	0.71	0.75
Al_2O_3	14.95	14.69	14.94	15.15	15.17	–	16.36	14.63	15.84	15.58
Fe_2O_3	4.07	3.99	3.95	4.27	4.49	–	6.14	6.36	6.28	6.13
MnO	0.06	0.07	0.06	0.07	0.08	–	0.11	0.07	0.09	0.08
MgO	2.36	2.36	2.43	2.61	2.67	–	2.78	4.34	3.95	4.57
CaO	3.70	3.82	4.14	4.10	4.27	–	4.65	5.28	5.97	5.69
Na_2O	3.30	3.17	3.39	3.50	3.36	–	2.96	2.85	2.96	3.49
K_2O	3.66	3.88	3.61	3.13	3.35	–	2.60	2.90	2.53	2.74
P_2O_5	0.12	0.13	0.13	0.13	0.15	–	0.21	0.20	0.21	0.23
LOI	0.68	0.49	0.87	0.90	0.62	–	1.67	1.47	0.93	0.85
Total	99.00	98.67	98.75	98.80	98.84	–	99.12	98.52	98.92	99.01
(ppm)										
Ba	384	363	392	398	430	–	422	223	276	303
Cr	75	80	75	88	87	–	34	151	104	197
Nb	8	6	8	8	8	–	4	5	8	14
Ni	16	15	16	17	17	–	7	16	14	58
Rb	*ICP-MS*	*ICP-MS*	*ICP-MS*	122	*ICP-MS*	*ICP-MS*	*ICP-MS*	145	*ICP-MS*	129
Sr	*ICP-MS*	*ICP-MS*	*ICP-MS*	410	*ICP-MS*	*ICP-MS*	*ICP-MS*	468	*ICP-MS*	506
V	82	81	81	86	92	–	142	133	130	117
Y	13	14	13	14	14	–	21	17	19	16
Zn	26	30	21	25	35	–	56	39	35	34
Zr	120	111	101	122	117	–	148	100	121	118
ICP-MS (ppm)										
Rb	137	131.0	121.0	–	121.0	116.0	79.0	–	110.0	–
Sr	366	350.0	393.0	–	403.0	382.0	334.0	–	459.0	–
La	21.3	22.5	20.9	–	17.1	34.1	22.8	–	19.1	–
Ce	38.9	38.5	38.9	–	31.3	56.1	46.7	–	40.5	–
Pr	4.0	4.2	4.1	–	3.7	5.4	4.9	–	4.6	–
Nd	14.4	14.9	15.7	–	14.3	18.2	18.9	–	18.1	–
Sm	2.9	2.9	3.0	–	2.8	3.1	3.9	–	4.0	–
Eu	0.8	0.8	0.9	–	0.9	0.9	1.2	–	1.1	–
Gd	2.5	2.6	2.7	–	2.6	2.7	4.0	–	3.5	–
Tb	0.4	0.4	0.4	–	0.4	0.4	0.6	–	0.5	–
Dy	2.0	2.2	2.2	–	2.2	2.1	3.5	–	3.1	–
Ho	0.4	0.4	0.4	–	0.4	0.4	0.7	–	0.6	–
Er	1.1	1.2	1.1	–	1.2	1.2	1.8	–	1.6	–
Yb	1.1	1.3	1.2	–	1.2	1.2	1.9	–	1.6	–
Lu	0.2	0.2	0.2	–	0.2	0.2	0.3	–	0.3	–
Ta	0.8	1.0	0.9	–	0.9	1.3	0.8	–	0.7	–
Hf	2.8	2.8	3.1	–	2.7	2.8	3.8	–	2.7	–
Th	10.8	12.9	9.9	–	8.3	9.9	6.7	–	6.0	–
Pb	13.0	12.0	11.0	–	10.0	7.0	< 5	–	8.0	–

Pr Fine Gr: Porphyritic fine-grained granite, Ushi Gd S: Ushikiri-yama granodiorite south body, Ushi Gd N: Ushikiri-yama granodiorite north body, Ushi Gd SF: Ushikiri-yama granodiorite south body fine-grained facies, Pr Fine To:Porohyritic fine-grained tonalite, and Pr Fine Di: Porphyrirtic fine-grained diorite. Total Fe reported as Fe^{3+}

Type	Pr Fine To	Pr Fine To	Pr Fine Di	Pr Fine Di
No	14031607	14031606	14050412	14060109
(wt%)				
SiO_2	58.89	58.75	53.94	53.65
TiO_2	0.73	0.74	1.03	1.00
Al_2O_3	15.50	15.35	14.73	14.41
Fe_2O_3	6.03	6.01	7.81	7.84
MnO	0.08	0.08	0.13	0.13
MgO	4.55	4.59	7.85	8.05
CaO	5.39	5.44	7.07	7.09
Na_2O	3.53	3.52	3.24	2.42
K_2O	2.84	2.86	1.67	2.41
P_2O_5	0.22	0.22	0.37	0.35
LOI	1.12	1.12	1.72	1.91
Total	98.88	98.67	99.55	99.24
(ppm)				
Ba	310	319	317	296
Cr	207	200	399	425
Nb	9	12	22	15
Ni	58	57	193	199
Rb	*ICP-MS*	*ICP-MS*	*ICP-MS*	*ICP-MS*
Sr	*ICP-MS*	*ICP-MS*	*ICP-MS*	*ICP-MS*
V	118	115	174	173
Y	16	17	25	22
Zn	33	33	79	80
Zr	124	124	178	176
ICP-MS (ppm)				
Rb	114	124.0	70.0	103.0
Sr	493	465.0	405.0	377.0
La	17.1	22.5	30.0	28.2
Ce	33.9	45.3	54.9	55.0
Pr	3.9	5.2	6.7	6.2
Nd	15.7	19.8	25.5	25.1
Sm	3.5	3.9	5.2	5.1
Eu	1.2	1.1	1.5	1.4
Gd	3.6	3.5	5.1	4.7
Tb	0.5	0.5	0.7	0.7
Dy	2.9	2.9	4.2	4.0
Ho	0.6	0.6	0.8	0.8
Er	1.5	1.5	2.2	2.0
Yb	1.4	1.4	1.8	1.7
Lu	0.2	0.2	0.3	0.3
Ta	0.8	0.9	0.9	0.9
Hf	3.3	2.7	4.1	4.0
Th	4.4	6.0	8.1	8.1
Pb	8.0	9.0	7.0	9.0

Pr Fine Gr: Porphyritic fine-grained granite, Ushi Gd S: Ushikiri-yama granodiorite south body, Ushi Gd N: Ushikiri-yama granodiorite north body, Ushi Gd SF: Ushikiri-yama granodiorite south body fine-grained facies, Pr Fine To:Porohyritic fine-grained tonalite, and Pr Fine Di: Porphyrirtic fine-grained diorite. Total Fe reported as Fe^{3+}

Appendix 2–3. Rayleigh fractionation model using partition coefficients.

Stage-1 Low SiO_2 Gd → High SiO_2 Gd (south body)

Partition coefficent

element	Pl	ref	Hb	ref	Bt	ref	Mag	ref
Rb	0.016	e	0.0077	b	0.936	a	0.01	c
Ba	1.05	e	0.92	e	6.36	a	0.01	c
Th	0.03	d	0.45	e	0.27	d	0.09	d
Ta	0.05	d	1.3	c	1.9	d	4.5	d
Nb	0.26	e	0.12	e	4.6	e	0.0489	g
La	0.45	d	0.37	f	8.2	d	1.9	d
Ce	0.347	b	1.77	b	11	d	2.7	d
Sr	1.45	b	0.0224	b	0.31	e	0.01	c
Nd	0.29	d	4.49	d	5.7	d	3.5	d
Sm	0.23	d	8.2	b	4.3	d	1.9	d
Eu	1.25	b	5.9	b	0.59	d	1.5	d
Dy	0.452	b	14	b	0.76	d	1.6	d
Y	0.21	d	11.3	e	2.3	e	0.95	e
Yb	0.302	b	9	b	3	d	2.2	d
Lu	0.29	b	6.3	b	3.4	d	1.5	d

Stage-2 High SiO_2 Gd (south body)→ Pr Fine Gr

Partition coefficent

element	Pl	ref	Hb	ref	Bt	ref	Mag	ref
Rb	0.016	e	0.0077	b	0.936	a	0.01	c
Ba	1.05	e	0.92	e	6.36	a	0.01	c
Th	0.03	d	0.45	e	0.27	d	0.09	d
Ta	0.05	d	1.3	c	1.9	d	4.5	d
Nb	0.26	e	0.12	e	4.6	e	0.0489	g
La	0.45	d	0.37	f	8.2	d	1.9	d
Ce	0.347	b	1.77	b	7.2	d	2.7	d
Sr	4.4	b	0.094	b	0.25	e	0.01	c
Nd	0.29	d	4.49	d	5.7	d	3.5	d
Sm	0.23	d	6.3	b	4.3	d	1.9	d
Eu	2.8	b	5.9	b	0.59	d	1.5	d
Dy	0.1	b	6.2	b	0.76	d	1.6	d
Y	0.04	d	7.5	e	1	d	0.12	e
Yb	0.1	b	5	b	1	d	1	d
Lu	0.1	b	2.8	b	3	d	0.91	d

references

a Philpotts and Schnetzler, 1970
b Nagasawa and Schnetzler, 1971
c Gill, 1981
d Nash and Crecraft, 1985
e Ewart and Griffin, 1994
f Klein et al., 1997
g Nielsen and Beard, 2000

Appendix 3–1. Clinopyroxene compositions of TPD and Do.

Rock type	TPD	TPD	TPD	TPD	TPD	TPD	TPD	TPD	TPD	TPD	TPD
Mineral	Cpx	Cpx	Cpx	Cpx	Cpx	Cpx	Cpx	Cpx	Cpx	Cpx	Cpx
SiO_2	52.08	52.23	51.12	51.67	50.77	51.44	52.83	52.74	52.42	52.08	51.52
TiO_2	0.33	0.30	0.46	0.53	0.56	0.56	0.08	0.10	0.11	0.23	0.39
Al_2O_3	1.44	1.09	2.03	2.23	2.53	1.82	0.55	0.63	0.69	2.68	1.95
Cr_2O_3	0.10	0.10	0.20	0.15	0.24	0.05	0.06	0.05	0.10	0.79	0.30
FeO	8.22	8.37	8.07	7.14	7.47	8.03	7.96	8.11	8.13	4.77	7.96
MnO	0.21	0.27	0.18	0.22	0.23	0.26	0.20	0.20	0.22	0.15	0.31
MgO	14.63	14.44	13.95	14.62	14.18	14.16	14.82	14.76	14.74	17.35	14.92
CaO	21.55	21.89	22.01	22.37	22.15	21.88	22.21	22.05	21.74	20.32	21.10
Na_2O	0.38	0.31	0.40	0.32	0.36	0.31	0.23	0.28	0.26	0.26	0.35
K_2O	0.01	0.00	0.00	0.01	0.01	0.01	0.00	0.00	0.00	0.00	0.00
Total	98.96	99.00	98.41	99.25	98.50	98.52	98.93	98.93	98.43	98.63	98.81
O	6	6	6	6	6	6	6	6	6	6	6
Si	1.957	1.965	1.936	1.932	1.918	1.944	1.984	1.982	1.980	1.927	1.937
Ti	0.009	0.009	0.013	0.015	0.016	0.016	0.002	0.003	0.003	0.006	0.011
Al	0.064	0.048	0.091	0.098	0.113	0.081	0.024	0.028	0.031	0.117	0.087
Cr	0.003	0.003	0.006	0.005	0.007	0.002	0.002	0.002	0.003	0.023	0.009
Fe	0.258	0.263	0.256	0.223	0.236	0.254	0.250	0.255	0.257	0.148	0.250
Mn	0.007	0.009	0.006	0.007	0.007	0.008	0.006	0.006	0.007	0.005	0.010
Mg	0.819	0.810	0.787	0.815	0.798	0.798	0.829	0.827	0.830	0.956	0.836
Ca	0.868	0.882	0.893	0.896	0.897	0.886	0.894	0.888	0.880	0.806	0.850
Na	0.028	0.022	0.029	0.023	0.026	0.023	0.017	0.021	0.019	0.019	0.025
K	0.001	0.000	0.000	0.000	0.001	0.000	0.000	0.000	0.000	0.000	0.000
Total cation	4.014	4.012	4.017	4.014	4.019	4.011	4.009	4.011	4.010	4.006	4.017
Wo	44.60	45.12	46.14	46.33	46.43	45.73	45.30	45.09	44.74	42.19	43.90
En	42.11	41.41	40.67	42.13	41.34	41.18	42.03	41.97	42.20	50.09	43.18
Fs	13.29	13.47	13.19	11.54	12.22	13.09	12.67	12.95	13.06	7.73	12.92
Total	100	100	100	100	100	100	100	100	100	100	100
Al(IV)	0.04	0.03	0.06	0.07	0.08	0.06	0.02	0.02	0.02	0.07	0.06
Al(VI)	0.02	0.01	0.03	0.03	0.03	0.02	0.01	0.01	0.01	0.04	0.02
Mg#	76.02	75.45	75.50	78.50	77.18	75.88	76.84	76.43	76.36	86.63	76.97

Appendix 3–2. Major (wt%) and trace element (ppm) concentrations of the Shaku-dake body.

Type	*FBG	*FBG	HBG	HBG	HBG	HBG	*CG	*CG	*CG	*CG
No	16101503	16102108A	16101901	17022601	16101403	16101401A	16110611	16103007	16102411	16103008
(wt%)										
SiO_2	74.93	72.36	67.74	67.05	66.88	66.45	65.18	64.45	63.48	62.51
TiO_2	0.23	0.25	0.45	0.45	0.48	0.47	0.64	0.66	0.73	0.87
Al_2O_3	13.12	14.23	15.69	15.36	15.51	15.33	15.42	15.58	15.21	15.43
Fe_2O_3	0.98	1.43	3.25	3.19	3.44	3.46	4.30	4.53	4.96	5.62
MnO	0.02	0.03	0.06	0.06	0.07	0.06	0.08	0.08	0.08	0.10
MgO	0.79	0.72	2.01	1.98	2.14	2.32	2.36	2.62	2.78	2.96
CaO	0.63	1.05	3.50	3.37	3.55	3.68	3.84	4.00	4.32	4.45
Na_2O	3.22	4.08	3.73	3.79	3.88	3.74	3.52	3.38	3.08	3.34
K_2O	5.09	4.52	3.27	3.19	2.94	3.11	3.73	3.64	3.53	3.61
P_2O_5	0.06	0.09	0.13	0.13	0.14	0.14	0.21	0.20	0.23	0.29
LOI	0.98	1.03	0.70	0.80	0.56	0.94	0.67	1.37	1.48	0.71
Total	100.06	99.81	100.54	99.37	99.58	99.70	99.95	100.52	99.87	99.88
(ppm)										
Ba	516	346	552	536	423	464	516	488	548	507
Cr	29	21	70	62	66	81	69	82	78	75
Nb	8	18	11	12	13	12	17	16	16	20
Ni	24	19	37	40	44	47	35	36	33	36
Rb	151	190	129	122	127	118	160	157	147	164
Sr	195	199	358	369	369	355	352	353	371	346
V	35	33	74	71	77	79	100	111	122	137
Y	26	39	26	25	26	24	32	32	31	34
Zn	23	38	50	48	53	49	86	65	62	65
Zr	88	116	157	166	166	157	239	233	222	268
ICP-MS (ppm)										
Rb	141	–	128.0	–	122.0	–	164.0	–	–	–
Sr	161	–	310.0	–	326.0	–	319.0	–	–	–
La	17.9	–	22.9	–	26.5	–	31.6	–	–	–
Ce	29.5	–	40.4	–	47.0	–	60.7	–	–	–
Pr	2.7	–	4.5	–	4.9	–	6.5	–	–	–
Nd	8.3	–	15.9	–	16.8	–	23.6	–	–	–
Sm	1.3	–	3.0	–	3.3	–	4.1	–	–	–
Eu	0.4	–	0.8	–	0.8	–	1.0	–	–	–
Gd	1.2	–	2.5	–	2.5	–	3.3	–	–	–
Tb	0.2	–	0.4	–	0.4	–	0.5	–	–	–
Dy	1.0	–	2.2	–	2.2	–	2.9	–	–	–
Ho	0.2	–	0.4	–	0.4	–	0.6	–	–	–
Er	0.6	–	1.2	–	1.2	–	1.7	–	–	–
Yb	0.7	–	1.1	–	1.2	–	1.6	–	–	–
Lu	0.1	–	0.2	–	0.2	–	0.2	–	–	–
Ta	1.7	–	2.4	–	2.8	–	4.4	–	–	–
Hf	1.4	–	1.1	–	1.2	–	1.7	–	–	–
Th	18.5	–	11.5	–	14.0	–	17.9	–	–	–
Pb	9.0	–	18.0	–	18.0	–	30.0	–	–	–

Total Fe reported as Fe^{3+}. TPD: two-pyroxene diorite, Do: dolerite, PFT: Porphyritic fine-grained tonalite, CG: clinopyroxene granodiorite, HBG: hornblende - biotite granodiorite, and FBG: fine-grained biotite granite. *The (*) data are quote from Eshima and Owada (2018).

Type	*CG	CG	*CG	*PFT	*PFT	*PFT	*PFT	*PFT	*PFT	*PFT
No	16102101	16101506	16101508	17031103	17031001	17031009	17031010	17031102	17030904B	17031101
(wt%)										
SiO_2	62.44	60.80	60.49	63.64	63.41	63.33	62.87	62.62	62.59	61.87
TiO_2	0.85	0.84	0.93	0.63	0.61	0.62	0.64	0.65	0.63	0.63
Al_2O_3	15.46	15.74	15.21	16.10	16.23	16.17	16.02	15.93	16.08	15.69
Fe_2O_3	5.34	5.75	6.27	5.32	5.32	5.36	5.70	5.69	4.77	6.92
MnO	0.08	0.11	0.10	0.11	0.11	0.11	0.09	0.12	0.08	0.12
MgO	2.84	3.43	4.03	2.15	2.31	2.33	2.94	2.56	2.21	2.23
CaO	4.44	4.97	5.21	4.96	4.55	4.51	4.19	4.28	4.95	5.67
Na_2O	3.23	3.70	3.19	3.08	3.55	3.61	3.72	3.75	3.62	3.11
K_2O	3.72	2.58	3.21	2.97	2.55	2.85	2.87	2.83	3.39	2.73
P_2O_5	0.28	0.29	0.31	0.18	0.18	0.18	0.19	0.19	0.19	0.17
LOI	0.95	1.50	0.97	0.76	1.05	0.63	0.79	1.31	1.14	0.96
Total	99.64	99.71	99.92	99.90	99.88	99.70	100.01	99.93	99.66	100.11
(ppm)										
Ba	510	535	548	580	564	565	531	538	835	478
Cr	78	99	125	37	36	40	44	34	34	37
Nb	20	18	19	12	12	11	12	12	12	12
Ni	35	42	53	13	11	13	13	15	10	14
Rb	154	91	124	95	66	86	113	85	85	78
Sr	334	422	397	553	520	472	446	475	475	405
V	133	141	152	115	112	113	123	123	119	125
Y	33	25	29	22	19	22	24	22	22	22
Zn	63	73	69	65	77	74	73	87	43	80
Zr	267	257	236	185	174	169	168	176	177	161
ICP-MS (ppm)										
Rb	–	–	131.0	95.0	–	84.0	–	–	–	–
Sr	–	–	377.0	511.0	–	431.0	–	–	–	–
La	–	–	32.3	23.3	–	22.6	–	–	–	–
Ce	–	–	64.9	45.8	–	44.7	–	–	–	–
Pr	–	–	7.4	5.0	–	4.9	–	–	–	–
Nd	–	–	27.0	19.1	–	19.2	–	–	–	–
Sm	–	–	5.4	3.8	–	3.8	–	–	–	–
Eu	–	–	1.3	1.1	–	1.0	–	–	–	–
Gd	–	–	4.4	3.4	–	3.1	–	–	–	–
Tb	–	–	0.7	0.5	–	0.5	–	–	–	–
Dy	–	–	4.0	2.8	–	2.7	–	–	–	–
Ho	–	–	0.8	0.6	–	0.5	–	–	–	–
Er	–	–	2.2	1.6	–	1.6	–	–	–	–
Yb	–	–	2.0	1.5	–	1.4	–	–	–	–
Lu	–	–	0.3	0.3	–	0.2	–	–	–	–
Ta	–	–	4.1	2.9	–	2.7	–	–	–	–
Hf	–	–	1.7	1.0	–	1.1	–	–	–	–
Th	–	–	13.1	7.7	–	7.5	–	–	–	–
Pb	–	–	14.0	9.0	–	15.0	–	–	–	–

Total Fe reported as Fe^{3+}. TPD: two-pyroxene diorite, Do: dolerite, PFT: Porphyritic fine-grained tonalite, CG: clinopyroxene granodiorite, HBG: hornblende - biotite granodiorite, FBG: fine-grained biotite granite. *The (*) data are quote from Eshima and Owada (2018).

Type	TPD	TPD	TPD	*TPD	TPD	TPD	TPD	*TPD	TPD	TPD
No	16102103	16102401	16102105	16110609	16101905	16101810	16110608	16101811	16101801B	16100303
(wt%)										
SiO_2	63.50	63.25	63.21	60.92	60.29	60.18	59.98	59.90	59.81	59.70
TiO_2	0.83	0.83	0.83	0.93	0.83	0.90	0.99	0.91	0.91	0.83
Al_2O_3	15.41	15.17	15.43	15.30	15.70	15.42	15.75	15.21	15.18	17.11
Fe_2O_3	5.20	5.26	5.11	5.82	5.80	6.05	6.17	6.47	6.30	6.60
MnO	0.08	0.09	0.08	0.09	0.11	0.09	0.09	0.10	0.10	0.12
MgO	2.81	2.75	2.63	3.65	3.43	3.98	3.35	4.56	4.35	3.24
CaO	4.52	4.29	4.41	5.26	5.18	5.46	5.18	5.68	5.53	5.78
Na_2O	3.15	3.24	3.29	3.26	3.58	3.40	3.43	3.36	3.25	3.49
K_2O	3.81	3.71	3.77	3.46	2.43	3.13	3.33	3.03	3.08	2.63
P_2O_5	0.27	0.27	0.28	0.30	0.25	0.31	0.36	0.32	0.31	0.30
LOI	1.06	0.74	0.44	0.90	1.89	0.78	0.75	0.39	0.86	0.64
Total	100.64	99.60	99.47	99.90	99.49	99.61	99.38	99.94	99.69	100.43
(ppm)										
Ba	449	458	462	445	553	482	546	472	489	451
Cr	93	66	63	123	95	159	87	177	169	60
Nb	20	20	19	19	18	18	20	17	17	14
Ni	39	35	33	52	39	69	40	75	72	26
Rb	176	169	168	142	67	128	127	119	124	94
Sr	304	315	310	344	375	377	376	371	379	403
V	131	130	128	150	140	151	152	156	153	142
Y	37	35	35	31	22	30	29	28	29	25
Zn	64	64	61	67	73	73	74	73	72	75
Zr	264	268	261	248	234	239	213	220	222	193
ICP-MS (ppm)										
Rb	189.0	–	–	–	–	–	–	–	–	–
Sr	286.0	–	–	–	–	–	–	–	–	–
La	34.2	–	–	–	–	–	–	–	–	–
Ce	69.1	–	–	–	–	–	–	–	–	–
Pr	7.5	–	–	–	–	–	–	–	–	–
Nd	27.7	–	–	–	–	–	–	–	–	–
Sm	5.4	–	–	–	–	–	–	–	–	–
Eu	1.1	–	–	–	–	–	–	–	–	–
Gd	4.4	–	–	–	–	–	–	–	–	–
Tb	0.7	–	–	–	–	–	–	–	–	–
Dy	4.1	–	–	–	–	–	–	–	–	–
Ho	0.8	–	–	–	–	–	–	–	–	–
Er	2.2	–	–	–	–	–	–	–	–	–
Yb	2.1	–	–	–	–	–	–	–	–	–
Lu	0.3	–	–	–	–	–	–	–	–	–
Ta	4.7	–	–	–	–	–	–	–	–	–
Hf	1.5	–	–	–	–	–	–	–	–	–
Th	19.1	–	–	–	–	–	–	–	–	–
Pb	18.0	–	–	–	–	–	–	–	–	–

Total Fe reported as Fe^{3+}. TPD: two-pyroxene diorite, Do: dolerite, PFT: Porphyritic fine-grained tonalite, CG: clinopyroxene granodiorite, HBG: hornblende - biotite granodiorite, and FBG: fine-grained biotite granite. *The (*) data are quote from Eshima and Owada (2018).

Type	TPD	TPD	TPD	TPD	TPD	TPD	TPD	TPD	TPD	TPD
No	16101510	16101812	16101215	16101807	16101806	16101814	16102106A	16100210	16101216	16110606
(wt%)										
SiO_2	59.38	59.23	59.21	58.99	58.75	58.60	58.59	58.53	58.53	58.39
TiO_2	0.87	0.98	0.85	0.95	0.96	0.82	0.91	0.85	0.80	0.92
Al_2O_3	15.58	15.06	14.67	15.44	15.36	15.23	15.73	15.48	14.59	15.48
Fe_2O_3	6.09	7.10	6.43	6.56	6.68	6.61	6.66	6.81	6.45	6.60
MnO	0.09	0.12	0.10	0.12	0.11	0.11	0.10	0.11	0.11	0.11
MgO	4.46	4.57	5.53	4.11	4.37	5.43	4.03	5.21	5.74	4.46
CaO	5.77	5.91	5.96	5.53	5.66	6.20	6.22	6.51	5.89	6.05
Na_2O	3.47	3.17	3.26	3.39	3.08	3.36	3.36	3.28	3.49	3.39
K_2O	2.75	3.10	2.73	3.07	2.95	2.58	2.42	2.51	2.31	2.81
P_2O_5	0.28	0.34	0.29	0.31	0.33	0.27	0.32	0.27	0.27	0.33
LOI	0.94	0.56	0.45	1.05	1.29	0.71	1.30	0.43	0.87	1.05
Total	99.68	100.05	99.49	99.52	99.54	99.78	99.65	99.99	99.04	99.58
(ppm)										
Ba	444	450	427	490	460	441	354	399	427	478
Cr	177	148	260	120	135	205	123	184	291	135
Nb	15	17	13	18	17	13	16	13	13	15
Ni	60	60	121	47	59	102	51	77	129	54
Rb	102	123	112	98	111	103	116	89	91	94
Sr	399	349	383	360	369	384	376	392	411	431
V	152	168	156	159	164	154	159	161	149	155
Y	25	28	25	26	28	26	27	24	22	24
Zn	72	76	66	66	70	67	75	68	72	77
Zr	207	216	186	219	211	188	184	183	166	206
ICP-MS (ppm)										
Rb	–	–	–	–	–	–	–	–	–	–
Sr	–	–	–	–	–	–	–	–	–	–
La	–	–	–	–	–	–	–	–	–	–
Ce	–	–	–	–	–	–	–	–	–	–
Pr	–	–	–	–	–	–	–	–	–	–
Nd	–	–	–	–	–	–	–	–	–	–
Sm	–	–	–	–	–	–	–	–	–	–
Eu	–	–	–	–	–	–	–	–	–	–
Gd	–	–	–	–	–	–	–	–	–	–
Tb	–	–	–	–	–	–	–	–	–	–
Dy	–	–	–	–	–	–	–	–	–	–
Ho	–	–	–	–	–	–	–	–	–	–
Er	–	–	–	–	–	–	–	–	–	–
Yb	–	–	–	–	–	–	–	–	–	–
Lu	–	–	–	–	–	–	–	–	–	–
Ta	–	–	–	–	–	–	–	–	–	–
Hf	–	–	–	–	–	–	–	–	–	–
Th	–	–	–	–	–	–	–	–	–	–
Pb	–	–	–	–	–	–	–	–	–	–

Total Fe reported as Fe^{3+}. TPD: two-pyroxene diorite, Do: dolerite, PFT: Porphyritic fine-grained tonalite, CG: clinopyroxene granodiorite, HBG: hornblende - biotite granodiorite, and FBG: fine-grained biotite granite. *The (*) data are quote from Eshima and Owada (2018).

Type	TPD	TPD	TPD	TPD	TPD	TPD	TPD	TPD	TPD	TPD
No	16101009	16100307	16101813	16101008	16101201	17031408	16100304	16101808	16101010	16101809
(wt%)										
SiO_2	58.16	58.13	58.13	58.08	58.04	57.87	57.85	57.81	57.51	57.25
TiO_2	0.97	0.80	0.91	0.92	0.81	0.87	0.80	0.87	0.80	0.92
Al_2O_3	15.78	15.92	14.99	16.09	14.83	15.46	14.80	14.91	14.93	14.92
Fe_2O_3	7.24	6.27	6.83	7.04	6.86	7.04	6.91	6.64	6.84	6.96
MnO	0.12	0.10	0.10	0.11	0.12	0.13	0.12	0.10	0.11	0.11
MgO	4.46	4.66	5.37	4.37	6.30	4.83	5.97	5.77	5.89	5.78
CaO	6.37	6.86	6.39	6.40	6.55	6.57	6.39	6.19	6.45	6.79
Na_2O	3.29	3.40	3.10	3.40	3.23	2.93	3.26	3.15	3.26	3.10
K_2O	2.73	2.08	2.57	2.67	2.32	2.73	2.31	2.72	2.33	2.71
P_2O_5	0.30	0.26	0.34	0.30	0.26	0.27	0.24	0.31	0.24	0.32
LOI	0.23	0.83	0.86	0.30	0.50	0.91	1.21	0.70	0.62	0.49
Total	99.64	99.32	99.52	99.70	99.83	99.60	99.87	99.34	98.99	99.56
(ppm)										
Ba	410	429	393	468	374	408	395	422	417	413
Cr	117	127	255	100	288	154	254	279	255	265
Nb	15	12	14	14	13	12	12	16	12	14
Ni	44	54	114	45	119	44	114	122	113	107
Rb	104	78	99	98	84	102	82	110	82	100
Sr	363	401	372	374	371	356	358	381	365	361
V	169	160	161	164	156	162	156	156	157	172
Y	25	22	25	25	21	26	23	27	21	25
Zn	71	56	75	70	77	72	69	71	66	72
Zr	194	170	193	187	173	164	167	214	165	149
ICP-MS (ppm)										
Rb	–	–	–	–	91.0	–	–	121.0	–	–
Sr	–	–	–	–	362.0	–	–	362.0	–	–
La	–	–	–	–	22.4	–	–	30.0	–	–
Ce	–	–	–	–	44.8	–	–	60.0	–	–
Pr	–	–	–	–	5.2	–	–	6.7	–	–
Nd	–	–	–	–	20.0	–	–	25.5	–	–
Sm	–	–	–	–	3.9	–	–	4.8	–	–
Eu	–	–	–	–	1.1	–	–	1.2	–	–
Gd	–	–	–	–	3.6	–	–	4.0	–	–
Tb	–	–	–	–	0.6	–	–	0.6	–	–
Dy	–	–	–	–	3.3	–	–	3.8	–	–
Ho	–	–	–	–	0.7	–	–	0.7	–	–
Er	–	–	–	–	1.8	–	–	2.0	–	–
Yb	–	–	–	–	1.7	–	–	1.8	–	–
Lu	–	–	–	–	0.3	–	–	0.3	–	–
Ta	–	–	–	–	3.2	–	–	3.5	–	–
Hf	–	–	–	–	1.0	–	–	1.3	–	–
Th	–	–	–	–	9.0	–	–	13.3	–	–
Pb	–	–	–	–	27.0	–	–	13.0	–	–

Total Fe reported as Fe^{3+}. TPD: two-pyroxene diorite, Do: dolerite, PFT: Porphyritic fine-grained tonalite, CG: clinopyroxene granodiorite, HBG: hornblende - biotite granodiorite, and FBG: fine-grained biotite granite. *The (*) data are quote from Eshima and Owada (2018).

Type	TPD	TPD	TPD	TPD	TPD	*TPD	TPD	TPD	*TPD	TPD
No	16100713	16100309	17022605	16100707	16101820	16100203	17032503	16100306	17030907	16100204
(wt%)										
SiO_2	57.18	57.04	56.94	56.80	56.78	56.65	56.53	56.51	56.18	56.02
TiO_2	0.97	0.83	0.79	1.01	0.97	1.02	0.84	1.01	0.91	0.82
Al_2O_3	15.30	15.58	15.02	15.07	16.51	15.04	14.72	15.83	15.45	14.65
Fe_2O_3	7.22	7.41	7.08	7.44	7.51	7.53	7.22	7.30	8.06	7.55
MnO	0.13	0.13	0.12	0.13	0.12	0.13	0.12	0.12	0.13	0.15
MgO	5.19	5.79	5.93	5.70	4.60	5.59	6.13	5.26	6.14	6.28
CaO	6.64	7.08	6.64	7.09	6.88	7.25	6.67	6.72	7.48	7.65
Na_2O	3.36	3.21	3.06	3.25	3.48	3.24	2.92	3.22	3.11	2.85
K_2O	2.19	2.26	2.58	2.23	2.26	2.30	2.33	2.34	2.26	2.05
P_2O_5	0.35	0.26	0.25	0.33	0.33	0.40	0.30	0.32	0.29	0.26
LOI	0.87	0.35	1.04	0.59	0.39	0.80	1.67	1.04	0.40	1.29
Total	99.39	99.94	99.43	99.63	99.84	99.96	99.43	99.68	100.42	99.56
(ppm)										
Ba	457	398	339	415	486	459	311	493	415	398
Cr	164	209	251	205	116	183	272	157	240	259
Nb	14	12	12	14	13	17	12	16	11	12
Ni	52	89	96	76	59	63	120	68	91	44
Rb	71	83	114	74	71	72	99	83	76	73
Sr	456	392	355	459	408	476	408	413	405	391
V	175	172	163	189	182	192	171	182	196	179
Y	21	22	25	21	20	21	25	22	22	21
Zn	83	71	68	73	73	78	73	70	74	75
Zr	181	160	168	194	153	193	167	202	157	169
ICP-MS (ppm)										
Rb	–	–	–	–	–	–	–	–	–	–
Sr	–	–	–	–	–	–	–	–	–	–
La	–	–	–	–	–	–	–	–	–	–
Ce	–	–	–	–	–	–	–	–	–	–
Pr	–	–	–	–	–	–	–	–	–	–
Nd	–	–	–	–	–	–	–	–	–	–
Sm	–	–	–	–	–	–	–	–	–	–
Eu	–	–	–	–	–	–	–	–	–	–
Gd	–	–	–	–	–	–	–	–	–	–
Tb	–	–	–	–	–	–	–	–	–	–
Dy	–	–	–	–	–	–	–	–	–	–
Ho	–	–	–	–	–	–	–	–	–	–
Er	–	–	–	–	–	–	–	–	–	–
Yb	–	–	–	–	–	–	–	–	–	–
Lu	–	–	–	–	–	–	–	–	–	–
Ta	–	–	–	–	–	–	–	–	–	–
Hf	–	–	–	–	–	–	–	–	–	–
Th	–	–	–	–	–	–	–	–	–	–
Pb	–	–	–	–	–	–	–	–	–	–

Total Fe reported as Fe^{3+}. TPD: two-pyroxene diorite, Do: dolerite, PFT: Porphyritic fine-grained tonalite, CG: clinopyroxene granodiorite, HBG: hornblende - biotite granodiorite, and FBG: fine-grained biotite granite. *The (*) data are quote from Eshima and Owada (2018).

Type	TPD	*TPD	TPD	TPD	*TPD	TPD	TPD	TPD	TPD	TPD
No	16100706	16101501	16100705	16101406	17031409	17031405	16100209	17031407B	16103004	16102406
(wt%)										
SiO_2	55.93	55.81	55.77	55.74	55.46	55.35	55.04	55.04	54.50	54.46
TiO_2	1.00	0.92	0.91	0.93	1.09	0.98	0.90	1.00	0.95	0.82
Al_2O_3	15.81	14.71	15.41	14.82	15.31	15.20	14.49	14.81	14.49	14.84
Fe_2O_3	7.58	7.99	7.15	7.69	8.49	8.12	7.81	8.39	8.40	7.79
MnO	0.13	0.14	0.13	0.13	0.14	0.13	0.14	0.14	0.15	0.20
MgO	5.50	7.36	5.65	6.84	6.18	5.93	7.20	6.48	7.23	7.01
CaO	7.32	7.25	7.12	7.18	7.53	7.32	6.95	7.47	8.13	6.43
Na_2O	3.40	2.97	3.10	3.10	3.16	3.18	2.99	3.04	2.74	3.09
K_2O	2.06	2.40	2.22	2.45	2.31	2.34	1.91	2.27	2.17	1.80
P_2O_5	0.31	0.29	0.27	0.32	0.33	0.31	0.29	0.33	0.32	0.30
LOI	0.44	0.39	1.64	0.52	0.27	0.86	1.66	0.71	0.59	2.52
Total	99.47	100.24	99.37	99.70	100.26	99.74	99.37	99.68	99.66	99.25
(ppm)										
Ba	375	420	365	386	423	354	393	384	352	462
Cr	160	369	221	333	214	225	369	265	325	362
Nb	12	13	13	14	16	14	12	15	12	12
Ni	62	148	76	131	77	90	138	109	57	146
Rb	63	76	80	84	71	78	71	67	80	65
Sr	494	368	389	361	385	383	410	398	375	437
V	181	181	181	181	198	194	183	191	196	168
Y	20	21	23	24	21	23	20	21	22	19
Zn	78	69	76	70	79	76	76	75	75	281
Zr	154	146	176	160	180	184	197	183	148	165
ICP-MS (ppm)										
Rb	–	87.0	–	–	–	89.0	–	–	88.0	–
Sr	–	362.0	–	–	–	377.0	–	–	369.0	–
La	–	23.0	–	–	–	25.8	–	–	20.9	–
Ce	–	46.9	–	–	–	52.6	–	–	43.1	–
Pr	–	5.3	–	–	–	6.2	–	–	5.3	–
Nd	–	21.0	–	–	–	23.3	–	–	20.8	–
Sm	–	4.3	–	–	–	5.0	–	–	4.2	–
Eu	–	1.3	–	–	–	1.4	–	–	1.2	–
Gd	–	3.8	–	–	–	4.3	–	–	4.3	–
Tb	–	0.6	–	–	–	0.7	–	–	0.6	–
Dy	–	3.5	–	–	–	4.0	–	–	3.5	–
Ho	–	0.7	–	–	–	0.8	–	–	0.7	–
Er	–	1.9	–	–	–	2.2	–	–	2.0	–
Yb	–	1.9	–	–	–	2.1	–	–	2.0	–
Lu	–	0.3	–	–	–	0.3	–	–	0.3	–
Ta	–	2.4	–	–	–	3.4	–	–	2.5	–
Hf	–	1.0	–	–	–	1.0	–	–	0.6	–
Th	–	8.2	–	–	–	9.2	–	–	5.8	–
Pb	–	10.0	–	–	–	10.0	–	–	8.0	–

Total Fe reported as Fe^{3+}. TPD: two-pyroxene diorite, Do: dolerite, PFT: Porphyritic fine-grained tonalite, CG: clinopyroxene granodiorite, HBG: hornblende - biotite granodiorite, and FBG: fine-grained biotite granite. *The (*) data are quote from Eshima and Owada (2018).

Type	TPD	*Do	*Do	*Do	*Do	*Do	Do	*Do	Waki	Waki
No	16103002	16101006	16101410A	16102402	17031008	17031006	16101803	16110610	17022506	16101205
(wt%)										
SiO_2	51.97	62.20	56.78	55.19	54.82	53.66	52.68	49.81	–	–
TiO_2	0.99	0.61	0.85	0.91	0.89	1.03	0.72	0.75	–	–
Al_2O_3	15.18	14.86	15.81	14.31	15.28	14.34	13.57	13.89	–	–
Fe_2O_3	8.84	5.33	6.79	8.52	8.32	8.42	8.78	9.62	–	–
MnO	0.21	0.09	0.11	0.16	0.14	0.13	0.17	0.17	–	–
MgO	7.41	4.33	5.01	7.13	6.68	8.03	8.81	10.80	–	–
CaO	7.38	3.51	5.90	8.16	7.83	7.78	8.92	9.47	–	–
Na_2O	2.45	4.09	3.23	2.83	2.69	2.85	2.84	1.61	–	–
K_2O	1.60	3.01	2.12	1.84	1.32	1.41	1.70	1.25	–	–
P_2O_5	0.32	0.18	0.30	0.30	0.31	0.37	0.17	0.11	–	–
LOI	3.25	1.55	2.89	0.67	1.90	1.87	1.09	2.40	–	–
Total	99.60	99.76	99.79	100.03	100.18	99.90	99.44	99.88	–	–
(ppm)									–	–
Ba	313	505	454	347	316	279	358	193	–	–
Cr	343	212	284	303	256	410	767	825	–	–
Nb	11	11	13	11	11	15	6	5	–	–
Ni	61	103	120	54	108	178	147	191	–	–
Rb	73	143	86	67	48	48	55	45	–	–
Sr	350	363	395	374	415	456	556	249	–	–
V	215	112	176	193	193	193	199	222	–	–
Y	22	27	22	20	17	18	17	16	–	–
Zn	103	69	84	82	89	92	82	90	–	–
Zr	142	159	173	149	156	183	124	66	–	–
ICP-MS (ppm)										
Rb	79.0	–	–	–	–	51.0	61.0	50.0	69.0	16.0
Sr	346.0	–	–	–	–	454.0	562.0	253.0	480.0	288.0
La	20.8	–	–	–	–	27.4	10.7	6.8	29.2	15.5
Ce	43.6	–	–	–	–	55.8	23.5	15.9	59.3	31.0
Pr	5.3	–	–	–	–	6.6	2.9	2.1	6.6	3.8
Nd	20.7	–	–	–	–	26.2	11.7	8.5	23.9	15.2
Sm	4.4	–	–	–	–	5.2	3.1	2.2	4.7	3.5
Eu	1.2	–	–	–	–	1.4	1.0	0.8	1.0	1.0
Gd	4.3	–	–	–	–	4.4	2.9	2.8	4.1	3.1
Tb	0.7	–	–	–	–	0.6	0.5	0.5	0.6	0.5
Dy	3.9	–	–	–	–	3.5	3.2	3.0	3.8	3.1
Ho	0.7	–	–	–	–	0.7	0.6	0.6	0.8	0.6
Er	2.0	–	–	–	–	1.8	1.8	1.7	2.2	1.8
Yb	1.8	–	–	–	–	1.7	1.6	1.6	2.1	1.7
Lu	0.3	–	–	–	–	0.3	0.3	0.3	0.3	0.3
Ta	2.7	–	–	–	–	3.3	1.7	1.5	3.4	1.9
Hf	0.6	–	–	–	–	1.0	0.3	0.2	0.8	0.5
Th	5.6	–	–	–	–	7.8	2.4	1.7	9.4	3.9
Pb	7.0	–	–	–	–	8.0	8.0	7.0	11.0	7.0

Total Fe reported as Fe^{3+}. TPD: two-pyroxene diorite, Do: dolerite, PFT: Porphyritic fine-grained tonalite, CG: clinopyroxene granodiorite, HBG: hornblende - biotite granodiorite, and FBG: fine-grained biotite granite. *The (*) data are quote from Eshima and Owada (2018).

Type	GSJ STD	GSJ STD	GSJ STD
No	JH-1	JGb-2	JB-3
(wt%)			
SiO_2	50.22	48.31	–
TiO_2	0.62	0.53	–
Al_2O_3	5.80	23.44	–
Fe_2O_3	10.00	6.55	–
MnO	0.18	0.12	–
MgO	16.76	6.22	–
CaO	15.16	14.26	–
Na_2O	0.70	0.99	–
K_2O	0.54	0.04	–
P_2O_5	0.12	0.03	–
LOI	–	–	–
Total	100.08	100.49	–
(ppm)			
Ba	108	38	–
Cr	537	114	–
Nb	3	1	–
Ni	46	15	–
Rb	14	5	–
Sr	145	442	–
V	198	153	–
Y	7	3	–
Zn	57	48	–
Zr	37	49	–
ICP-MS (ppm)			
Rb	–	–	14.0
Sr	–	–	400.0
La	–	–	8.4
Ce	–	–	20.9
Pr	–	–	3.1
Nd	–	–	15.0
Sm	–	–	4.1
Eu	–	–	1.2
Gd	–	–	4.5
Tb	–	–	0.7
Dy	–	–	4.4
Ho	–	–	0.9
Er	–	–	2.5
Yb	–	–	2.4
Lu	–	–	0.4
Ta	–	–	0.1
Hf	–	–	2.4
Th	–	–	1.3
Pb	–	–	6.0

Total Fe reported as Fe^{3+}. TPD: two-pyroxene diorite, Do: dolerite, PFT: Porphyritic fine-grained tonalite, CG: clinopyroxene granodiorite, HBG: hornblende - biotite granodiorite, and FBG: fine-grained biotite granite. *The (*) data are quote from Eshima and Owada (2018).

Appendix 3–3. Representative chemical analyses for each mineral of the TPD.

Mineral	Plagioclase					
WR SiO_2wt%	54.5 (Sp-1)	55.4 (Sp-2)	55.8 (Sp-3)	57.8 (Sp-4)	58.0 (Sp-5)	63.5 (Sp-6)
SiO_2	50.53	52.65	53.70	54.77	55.66	56.63
TiO_2	0	0.04	0.06	0.07	0.09	0.01
Al_2O_3	31.27	29.38	28.70	28.18	27.53	26.70
FeO	0.16	0.26	0.19	0.13	0.25	0.21
MnO	0.05	0.03	0	0	0	0.01
MgO	0	0	0	0.03	0	0
CaO	13.89	11.88	11.11	10.34	9.52	9.18
Na_2O	3.43	4.66	5.04	5.69	6.10	6.41
K_2O	0.14	0.20	0.37	0.20	0.28	0.34
Total	99.45	99.11	99.18	99.40	99.44	99.51
O	8	8	8	8	8	8
Si	2.313	2.408	2.449	2.485	2.521	2.560
Ti	0	0.001	0.002	0.002	0.003	0.000
Al	1.687	1.584	1.543	1.507	1.470	1.423
Fe	0.006	0.010	0.007	0.005	0.010	0.008
Mn	0.002	0.001	0	0	0	0.001
Mg	0	0	0	0.002	0	0
Ca	0.681	0.582	0.543	0.503	0.462	0.445
Na	0.304	0.413	0.446	0.500	0.536	0.562
K	0.008	0.012	0.022	0.012	0.016	0.020
Total	5.000	5.011	5.011	5.015	5.017	5.019
Or	0.82	1.18	2.13	1.14	1.59	1.91
Ab	30.62	41.04	44.14	49.30	52.84	54.77
An	68.56	57.78	53.73	49.56	45.58	43.32

Mineral	Clinopyroxene					
WR SiO_2wt%	54.5 (Sp-1)	55.4 (Sp-2)	55.8 (Sp-3)	57.8 (Sp-4)	58.0 (Sp-5)	63.5 (Sp-6)
SiO_2	51.67	51.17	52.76	52.86	50.78	52.07
TiO_2	0.53	0.70	0.24	0.29	0.83	0.39
Al_2O_3	2.23	2.17	1.61	2.68	2.04	1.24
Cr_2O_3	0.15	0.13	0.27	0.77	0.25	0.13
FeO	7.14	8.83	6.63	4.63	11.06	11.93
MnO	0.22	0.21	0.23	0.21	0.30	0.23
MgO	14.62	14.42	16.53	18.00	16.20	16.25
CaO	22.37	20.96	20.64	19.30	17.04	17.04
Na_2O	0.32	0.39	0.32	0.41	0.26	0.27
K_2O	0.01	0	0	0.01	0	0
Total	99.25	98.97	99.24	99.15	98.77	99.56
O	6	6	6	6	6	6
Si	1.932	1.928	1.956	1.937	1.918	1.953
Ti	0.015	0.020	0.007	0.008	0.024	0.011
Al	0.098	0.096	0.071	0.116	0.091	0.055
Cr	0.005	0.004	0.008	0.022	0.008	0.004
Fe	0.223	0.278	0.205	0.142	0.349	0.374
Mn	0.007	0.007	0.007	0.006	0.010	0.007
Mg	0.815	0.810	0.913	0.983	0.912	0.908
Ca	0.896	0.846	0.820	0.758	0.690	0.685
Na	0.023	0.028	0.023	0.029	0.019	0.020
K	0	0	0	0.001	0	0
Total	4.014	4.017	4.010	4.001	4.019	4.017
Wo	46.33	43.75	42.29	40.25	35.35	34.81
En	42.13	41.87	47.12	52.22	46.74	46.16
Fs	11.54	14.38	10.60	7.53	17.91	19.03

The Cpx composition (Sp-1) is taken from the data reported in Eshima et al. (2020).

TPD: two-pyroxene diorite, Pl: plagioclase, Cpx: clinopyroxene, Opx: orthopyroxene, and Ilm: ilmenite.

Mineral	Orthopyroxene					
WR SiO_2wt%	54.5 (Sp-1)	55.4 (Sp-2)	55.8 (Sp-3)	57.8 (Sp-4)	58.0 (Sp-5)	63.5 (Sp-6)
SiO_2	54.01	51.70	52.19	52.95	52.81	51.68
TiO_2	0.33	0.47	0.33	0.18	0.15	0.20
Al_2O_3	1.26	1.70	0.90	1.84	1.78	0.93
Cr_2O_3	0.28	0.05	0.08	0.31	0.44	0.07
FeO	14.66	19.84	21.31	15.17	15.69	23.43
MnO	0.29	0.48	0.45	0.32	0.34	0.59
MgO	26.75	22.83	22.54	25.94	25.69	20.58
CaO	1.82	1.44	1.26	1.79	1.83	0.86
Na_2O	0.02	0.01	0.04	0.02	0.04	0.03
K_2O	0	0.03	0.01	0.01	0.01	0
Total	99.42	98.57	99.11	98.52	98.79	98.36
O	6	6	6	6	6	6
Si	1.959	1.941	1.960	1.945	1.941	1.974
Ti	0.009	0.013	0.009	0.005	0.004	0.006
Al	0.054	0.075	0.040	0.080	0.077	0.042
Cr	0.008	0.001	0.002	0.009	0.013	0.002
Fe	0.445	0.623	0.669	0.466	0.482	0.749
Mn	0.009	0.015	0.014	0.010	0.011	0.019
Mg	1.446	1.278	1.261	1.420	1.407	1.171
Ca	0.071	0.058	0.051	0.070	0.072	0.035
Na	0.001	0.001	0.003	0.002	0.003	0.002
K	0	0.001	0	0	0.001	0
Total	4.002	4.008	4.011	4.007	4.012	4.000
Wo	3.61	2.97	2.55	3.59	3.67	1.79
En	73.71	65.23	63.66	72.58	71.74	59.91
Fs	22.68	31.81	33.79	23.82	24.59	38.29

Mineral	Ilmenite					
WR SiO_2wt%	54.5 (Sp-1)	55.4 (Sp-2)	55.8 (Sp-3)	57.8 (Sp-4)	58.0 (Sp-5)	63.5 (Sp-6)
SiO_2	0.02	0	0.03	0.02	0.01	0.06
TiO_2	51.71	50.04	48.00	50.28	51.28	50.75
Al_2O_3	0	0.01	0	0	0	0
Cr_2O_3	0.02	0.04	0.16	0.12	0.09	0.07
FeO	44.43	47.67	49.58	47.86	46.54	46.01
MnO	3.39	1.04	0.91	1.18	1.38	1.74
MgO	0.06	0.09	0.20	0.10	0.09	0.04
CaO	0	0	0	0	0	0
Na_2O	0.01	0.02	0	0.02	0	0
K_2O	0.02	0	0	0	0	0.04
Total	99.66	98.90	98.89	99.57	99.39	98.71
O	6	6	6	6	6	6
Si	0.001	0	0.002	0.001	0	0.003
Ti	1.978	1.943	1.883	1.939	1.970	1.965
Al	0	0.001	0	0	0	0
Cr	0.001	0.002	0.006	0.005	0.003	0.003
Fe	1.890	2.058	2.164	2.053	1.988	1.980
Mn	0.146	0.045	0.040	0.051	0.060	0.076
Mg	0.004	0.007	0.016	0.007	0.007	0.003
Ca	0	0	0	0	0	0
Na	0.001	0.002	0	0.002	0	0
K	0.001	0	0	0	0	0.002
Total	4.022	4.057	4.112	4.058	4.029	4.032
Geikielite	0.21	0.32	0.72	0.35	0.34	0.15
Pyrophanite	7.16	2.15	1.82	2.43	2.90	3.68
Ilmenite	92.63	97.53	97.46	97.22	96.76	96.17

TPD: two-pyroxene diorite, Pl: plagioclase, Cpx: clinopyroxene, Opx: orthopyroxene, and Ilm: ilmenite.

Appendix 3–4. Rayleigh fractionation model using partition coefficients.

TPD–CG Partition coefficent

	Pl	ref	Cpx	ref	Opx	ref	Ilm	ref
Rb	0.0705	a	0.0129	a	0.0038	n	-	-
Ba	0.197	a	0.0414	a	0.0036	n	-	-
Th	0.08	f	0.23	f	0.0005	n	7.5	f
Ta	0.05	f	0.0022	n	0.0008	n	1.7	j
Nb	0.13	h	1	h	0.0007	n	0.16	h
La	0.45	f	1.7	f	0.0006	n	7.1	f
Ce	0.347	c	2.9	f	0.0017	n	7.8	f
Sr	1.45	c	3.1	h	0.0019	n	0.66	h
Nd	0.29	e	5.2	f	0.004	n	7.6	f
Sm	0.23	f	8.3	f	0.011	n	6.9	f
Eu	1.25	c	5.8	f	0.03	l	2.5	f
Dy	0.293	b	12.3	f	0.077	l	4.9	f
Y	0.066	h	7.6	h	0.046	n	0.024	h
Yb	0.033	b	11.6	f	0.077	n	0.17	j
Lu	0.1	b	10.7	f	0.09	n	0.084	j

Do–PFT Partition coefficent

	Pl	ref	Cpx	ref	Opx	ref	Ilm	ref
Rb	0.039	a	0.00031	a	0.0038	n	-	-
Ba	0.137	a	0.00041	a	0.0036	n	-	-
Th	0.013	d	0.007	n	0.0005	n	0.00055	k
Ta	0.03	j	0.021	n	0.0008	n	1.7	k
Nb	1.3	h	0.005	n	0.0007	n	2	k
La	0.21	e	0.23	e	0.0006	n	0.000029	k
Ce	0.18	e	0.36	e	0.0017	n	0.000054	k
Sr	1.83	a	0.0648	a	0.0019	n	1.07	k
Nd	0.16	e	0.645	a	0.004	n	0.00048	k
Sm	0.1	e	1.3	e	0.011	n	0.00059	k
Eu	0.73	e	1.2	e	0.03	l	0.0011	k
Dy	0.293	b	1.9	e	0.077	l	0.01	k
Y	0.066	h	2.4	h	0.046	n	0.024	f
Yb	0.033	b	1.3	b	0.077	n	0.17	k
Lu	0.1	e	1.4	e	0.09	n	0.084	k

HBG–FBG Partition coefficent

	Pl	ref	Hb	ref	Mag	ref
Rb	0.06	f	0.028	h	0.01	j
Ba	1	f	0.16	h	0.1	j
Th	0.03	f	0.16	j	0.09	f
Ta	0.05	f	0.43	j	4.5	f
Nb	2.5	h	6.7	f	0.18	m
La	0.45	f	1.92	i	1.9	f
Ce	0.34	f	4.23	i	2.7	f
Sr	12	f	0.25	h	0.01	j
Nd	0.29	f	8.7	i	3.5	f
Sm	0.23	f	11.3	i	4.5	f
Eu	3.8	f	3.2	j	2.1	f
Dy	0.07	f	12.3	i	1.6	f
Y	0.04	f	6	h	0.95	h
Yb	0.06	f	5.5	i	2.2	f
Lu	0.13	f	2.1	h	1.5	f

Fc vector for Do–PFT and TPD–CG.

	Opx	ref	Cpx	ref	Pl	ref	Bt	ref
Y	0.18	g	0.9	g	0.03	g	0.03	d
Rb	0.022	g	0.031	g	0.071	g	3.26	d
Ni	5	g	5	g				
Cr	10	g	34	g				

Fc vector for HBG–FBG.

	Hbl	ref	Pl	ref	Bt	ref
Y	6	d	0.1	d	0.03	d
Sr	0.022	d	2.84	d	0.12	d
Rb	0.014	d	0.048	d	3.26	d

references

a Philpotts and Schnetzler, 1970
b Schnetzler and Philpotts, 1970
c Nagasawa and Schnetzler, 1971
d Arth, 1976
e Luhr and Carmichael, 1980
f Nash and Crecraft, 1985
g Rollinson, 1993
h Ewart and Griffin, 1994
i Sission, 1994
j Bacon and Druitt, 1988
k Zack and Brumm, 1998
l Green et al., 2000
m Nielsen and Beard, 2000
n Adam and Green, 2006

Appendix 3–5. Modal value of the TPD and CG.

Type	Diorite	Diorite	Diorite	Diorite	Diorite	Diorite	Diorite	Diorite	Diorite	Diorite
No	16100203	16100204	16100210	16100305	16100306	16100309	16100707	16101008	16101009	16101010
Count (point)										
Qz	32	130	9	49	63	41	49	102	44	111
Kfs	14	28	1	38	43	40	28	61	10	21
Pl	1026	1036	1128	1101	1062	1117	1112	1124	1155	981
Opx	160	89	412	424	247	362	366	312	407	374
Cpx	407	455	246	255	420	307	287	286	256	375
Amp	108	95	15	11	16	8	14	0	0	4
Ol	0	0	0	0	0	0	0	0	0	0
Bt	222	124	167	87	111	99	120	89	103	121
Ap	0	0	2	1	1	0	0	0	2	2
Zr	1	0	0	1	0	1	0	0	1	0
Ep	1	0	0	0	0	0	0	0	1	0
Cal	0	0	0	0	0	0	0	0	0	0
Chl	14	11	2	0	3	1	2	0	0	0
Opq	15	32	18	33	34	24	22	26	21	11
Total	2000	2000	2000	2000	2000	2000	2000	2000	2000	2000
Modal value (%)										
Qz	1.6	6.5	0.5	2.5	3.2	2.1	2.5	5.1	2.2	5.6
Kfs	0.7	1.4	0.1	1.9	2.2	2.0	1.4	3.1	0.5	1.1
Pl	51.3	51.8	56.4	55.1	53.1	55.9	55.6	56.2	57.8	49.1
Opx	8.0	4.5	20.6	21.2	12.4	18.1	18.3	15.6	20.4	18.7
Cpx	20.4	22.8	12.3	12.8	21.0	15.4	14.4	14.3	12.8	18.8
Amp	5.4	4.8	0.8	0.6	0.8	0.4	0.7	0	0	0.2
Ol	0	0	0	0	0	0	0	0	0	0
Bt	11.1	6.2	8.4	4.4	5.6	5.0	6.0	4.5	5.2	6.1
Ap	0	0	0.1	0.1	0.1	0	0	0	0.1	0.1
Zr	0.1	0	0	0.1	0	0.1	0	0	0.1	0
Ep	0.1	0	0	0	0	0	0	0	0.1	0
Cal	0	0	0	0	0	0	0	0	0	0
Chl	0.7	0.6	0.1	0.0	0.2	0.1	0.1	0	0	0
Opq	0.8	1.6	0.9	1.7	1.7	1.2	1.1	1.3	1.1	0.6
Total	100	100	100	100	100	100	100	100	100	100

Type	Diorite	Diorite	Diorite	Diorite	Diorite	Diorite	Diorite	Diorite	Diorite	Diorite
No	16101201	16101215	16101216	16101501	16101510	16101801A	16101801B	16101808	16101809	16101810
Count (point)										
Qz	67	44	69	84	167	222	209	156	157	157
Kfs	34	0	12	60	27	34	19	124	134	70
Pl	998	1120	1114	953	1017	1116	1041	1006	929	1033
Opx	365	343	345	421	213	127	153	200	291	115
Cpx	379	365	323	329	235	199	217	259	305	277
Amp	6	14	43	3	4	2	0	6	1	8
Ol	0	0	0	0	0	0	0	0	0	0
Bt	133	97	78	139	327	289	351	234	156	333
Ap	0	0	0	0	0	0	0	0	4	2
Zr	0	1	0	0	0	0	1	0	0	0
Ep	0	0	0	0	0	0	0	0	0	1
Cal	0	0	0	0	3	4	0	0	1	0
Chl	0	3	0	0	0	0	0	0	0	0
Opq	18	13	16	11	7	7	9	15	22	4
Total	2000	2000	2000	2000	2000	2000	2000	2000	2000	2000
Modal value (%)										
Qz	3.4	2.2	3.5	4.2	8.4	11.1	10.5	7.8	7.9	7.9
Kfs	1.7	0	0.6	3.0	1.4	1.7	1.0	6.2	6.7	3.5
Pl	49.9	56.0	55.7	47.7	50.9	55.8	52.1	50.3	46.5	51.7
Opx	18.3	17.2	17.3	21.1	10.7	6.4	7.7	10.0	14.6	5.8
Cpx	19.0	18.3	16.2	16.5	11.8	10.0	10.9	13.0	15.3	13.9
Amp	0.3	0.7	2.2	0.2	0.2	0.1	0	0.3	0.1	0.4
Ol	0	0	0	0	0	0	0	0	0	0
Bt	6.7	4.9	3.9	7.0	16.4	14.5	17.6	11.7	7.8	16.7
Ap	0	0	0	0	0	0	0	0	0.2	0.1
Zr	0	0.1	0	0	0	0	0.1	0	0	0
Ep	0	0	0	0	0	0	0	0	0	0.1
Cal	0	0	0	0	0.2	0.2	0	0	0.1	0
Chl	0	0.2	0	0	0	0	0	0	0	0
Opq	0.9	0.7	0.8	0.6	0.4	0.4	0.5	0.8	1.1	0.2
Total	100	100	100	100	100	100	100	100	100	100

Type	Diorite	Diorite	Diorite	Diorite	Diorite	Diorite	Diorite	Diorite	Diorite	Diorite
No	16101811	16101812	16101813	16101814	16101820	16102103	16102105	16102106A	16103004	16110606
Count (point)										
Qz	136	187	151	227	258	169	402	242	69	183
Kfs	41	70	76	302	277	117	45	99	8	28
Pl	1108	1031	1049	135	106	304	1096	960	934	1037
Opx	142	195	272	1063	1127	1171	84	96	128	128
Cpx	237	192	249	47	47	39	188	321	621	273
Amp	0	0	0	199	170	192	0	6	27	5
Ol	0	0	0	0	0	0	0	0	0	0
Bt	323	309	180	0	0	0	178	270	194	342
Ap	4	0	3	13	5	4	0	0	6	0
Zr	0	0	1	0	0	0	0	0	0	0
Ep	0	0	0	0	0	0	0	0	0	0
Cal	0	0	0	0	0	0	0	0	0	0
Chl	0	6	11	0	1	1	1	1	0	0
Opq	9	10	8	14	9	3	6	5	13	4
Total	2000	2000	2000	2000	2000	2000	2000	2000	2000	2000
Modal value (%)										
Qz	6.8	9.4	7.6	11.4	12.9	8.5	20.1	12.1	3.4	9.2
Kfs	2.1	3.5	3.8	15.1	13.9	5.9	2.3	5.0	0.4	1.4
Pl	55.4	51.6	52.5	6.8	5.3	15.2	54.8	48.0	46.7	51.9
Opx	7.1	9.8	13.6	53.2	56.4	58.6	4.2	4.8	6.4	6.4
Cpx	11.9	9.6	12.5	2.4	2.4	2.0	9.4	16.1	31.0	13.7
Amp	0	0	0	10.0	8.5	9.6	0	0.3	1.3	0.3
Ol	0	0	0	0	0	0	0	0	0	0
Bt	16.2	15.5	9.0	0.0	0.0	0.0	8.9	13.5	9.7	17.1
Ap	0.2	0	0.2	0.7	0.3	0.2	0	0	0.3	0
Zr	0	0	0.1	0	0	0	0	0	0	0
Ep	0	0	0	0	0	0	0	0	0	0
Cal	0	0	0	0	0	0	0	0	0	0
Chl	0	0.3	0.6	0	0.1	0.1	0.1	0.1	0	0
Opq	0.5	0.5	0.4	0.7	0.5	0.2	0.3	0.3	0.6	0.2
Total	100	100	100	100	100	100	100	100	100	100

Type	Diorite	Diorite	Diorite	Diorite	Diorite	Diorite	Diorite	Diorite	Diorite	Diorite
No	16110608	16110609	17022405D	17030907	17031403	17031407B	17031409	16100209	16100307	16100705
Count (point)										
Qz	308	295	26	11	33	6	7	45	12	30
Kfs	109	137	0	1	13	0	1	15	8	25
Pl	991	991	1105	1108	1158	1161	1167	1111	1186	1135
Opx	8	55	211	410	333	379	369	247	250	210
Cpx	215	253	347	340	263	285	323	391	417	403
Amp	0	0	74	26	43	35	17	0	0	0
Ol	0	0	0	0	0	0	0	0	0	0
Bt	356	264	223	75	142	123	95	160	82	162
Ap	0	0	0	2	2	0	0	0	9	0
Zr	0	0	0	0	0	0	0	0	0	0
Ep	0	0	0	0	0	0	0	0	0	0
Cal	0	0	0	3	0	0	1	0	1	2
Chl	0	0	0	0	1	1	0	18	27	19
Opq	13	5	14	24	12	10	20	13	8	14
Total	2000	2000	2000	2000	2000	2000	2000	2000	2000	2000
Modal value (%)										
Qz	15.4	14.8	1.3	0.6	1.7	0.3	0.4	2.3	0.6	1.5
Kfs	5.5	6.9	0	0.1	0.7	0	0.1	0.8	0.4	1.3
Pl	49.6	49.6	55.3	55.4	57.9	58.1	58.4	55.6	59.3	56.8
Opx	0.4	2.8	10.6	20.5	16.7	19.0	18.5	12.4	12.5	10.5
Cpx	10.8	12.7	17.4	17.0	13.2	14.3	16.2	19.6	20.9	20.2
Amp	0	0	3.7	1.3	2.2	1.8	0.9	0	0	0
Ol	0	0	0	0	0	0	0	0	0	0
Bt	17.8	13.2	11.2	3.8	7.1	6.2	4.8	8.0	4.1	8.1
Ap	0	0	0	0.1	0.1	0	0	0	0.5	0
Zr	0	0	0	0	0	0	0	0	0	0
Ep	0	0	0	0	0	0	0	0	0	0
Cal	0	0	0	0.2	0	0	0.1	0	0.1	0.1
Chl	0	0	0	0	0.1	0.1	0	0.9	1.4	1.0
Opq	0.7	0.3	0.7	1.2	0.6	0.5	1.0	0.7	0.4	0.7
Total	100	100	100	100	100	100	100	100	100	100

Type	Diorite	Diorite	Diorite	Diorite	Diorite	Diorite	Diorite	Diorite	Diorite	Diorite
No	16100706	16100713	16101806	16101807	16101905	16102401	16103002	17031408	17032503	16100303
Count (point)										
Qz	21	88	194	123	251	261	17	75	71	109
Kfs	12	118	136	144	75	107	5	8	50	97
Pl	1114	1051	1020	990	1099	1040	1023	1117	1028	1061
Opx	238	177	115	175	125	133	224	196	273	206
Cpx	400	384	297	377	262	310	537	376	322	263
Amp	0	0	0	0	0	0	0	0	0	0
Ol	0	0	0	0	0	0	0	0	0	0
Bt	194	156	213	172	164	124	134	201	242	252
Ap	0	11	8	0	0	0	3	8	0	3
Zr	0	0	0	0	0	0	0	0	0	0
Ep	0	0	0	0	0	0	0	0	0	0
Cal	2	0	0	0	0	6	2	2	0	0
Chl	3	0	8	13	12	13	39	6	0	0
Opq	16	15	9	6	12	6	16	11	14	9
Total	2000	2000	2000	2000	2000	2000	2000	2000	2000	2000
Modal value (%)										
Qz	1.0	4.4	9.7	6.2	12.6	13.1	0.9	3.8	3.5	5.5
Kfs	0.6	5.9	6.8	7.2	3.8	5.4	0.3	0.4	2.5	4.9
Pl	55.7	52.6	51.0	49.5	55.0	52.0	51.2	55.9	51.4	53.1
Opx	11.9	8.9	5.8	8.8	6.3	6.7	11.2	9.8	13.6	10.3
Cpx	20.0	19.2	14.9	18.9	13.1	15.5	26.9	18.8	16.1	13.2
Amp	0	0	0	0	0	0	0	0	0	0
Ol	0	0	0	0	0	0	0	0	0	0
Bt	9.7	7.8	10.7	8.6	8.2	6.2	6.7	10.1	12.1	12.6
Ap	0	0.6	0.4	0	0	0	0.2	0.4	0	0.2
Zr	0	0	0	0	0	0	0	0	0	0
Ep	0	0	0	0	0	0	0	0	0	0
Cal	0.1	0	0	0	0	0.3	0.1	0.1	0	0
Chl	0.1	0	0.4	0.7	0.6	0.7	2.0	0.3	0	0
Opq	0.8	0.8	0.5	0.3	0.6	0.3	0.8	0.6	0.7	0.5
Total	100	100	100	100	100	100	100	100	100	100

Type	Diorite	Diorite	Diorite	Cpx-Gd	Cpx-Gd	Cpx-Gd	Cpx-Gd	Cpx-Gd	Cpx-Gd	Cpx-Gd
No	16101406	16102406	17022605	16101508	16102101	16102411	16102412A	16103007	16103008	16110611
Count (point)										
Qz	44	37	105	297	370	407	459	384	374	423
Kfs	73	10	57	152	161	81	43	77	27	198
Pl	1007	1013	978	947	1021	1088	996	1090	1140	980
Opx	273	255	340	347	251	274	303	275	340	215
Cpx	416	441	271	1	0	0	0	5	3	0
Amp	0	0	0	255	182	149	197	160	108	181
Ol	0	0	0	0	0	0	1	0	0	3
Bt	165	233	235	0	0	0	0	0	0	0
Ap	3	0	5	0	0	0	0	0	0	0
Zr	0	0	0	0	1	0	0	0	0	0
Ep	0	0	0	0	0	0	0	0	0	0
Cal	0	1	0	0	0	1	0	0	2	0
Chl	0	0	0	1	13	0	0	6	0	0
Opq	19	10	9	0	1	0	1	3	6	1
Total	2000	2000	2000	2000	2000	2000	2000	2000	2000	2000
Modal value (%)										
Qz	2.2	1.9	5.3	14.9	18.5	20.4	23.0	19.2	18.7	21.1
Kfs	3.7	0.5	2.9	7.6	8.1	4.1	2.2	3.9	1.4	9.9
Pl	50.4	50.7	48.9	47.4	51.1	54.4	49.8	54.5	57.0	49.0
Opx	13.7	12.8	17.0	17.4	12.6	13.7	15.2	13.8	17.0	10.7
Cpx	20.8	22.1	13.6	0.1	0	0	0	0.3	0.2	0
Amp	0	0	0	12.8	9.1	7.5	9.9	8.0	5.4	9.0
Ol	0	0	0	0	0	0	0.1	0	0	0.1
Bt	8.3	11.7	11.8	0	0	0	0	0	0	0
Ap	0.2	0	0.3	0	0	0	0	0	0	0
Zr	0	0	0	0	0.1	0	0	0	0	0
Ep	0	0	0	0	0	0	0	0	0	0
Cal	0	0.1	0	0	0	0.1	0	0	0.1	0
Chl	0	0	0	0.1	0.7	0	0	0.3	0	0
Opq	1.0	0.5	0.5	0	0.1	0	0.1	0.2	0.3	0
Total	100	100	100	100	100	100	100	100	100	100

Type	Cpx-Gd
No	16110614
Count (point)	
Qz	400
Kfs	152
Pl	1103
Opx	163
Cpx	0
Amp	150
Ol	27
Bt	0
Ap	1
Zr	0
Ep	0
Cal	0
Chl	0
Opq	4
Total	2000
Modal value (%)	
Qz	20.0
Kfs	7.6
Pl	55.2
Opx	8.2
Cpx	0
Amp	7.5
Ol	1.4
Bt	0
Ap	0.1
Zr	0
Ep	0
Cal	0
Chl	0
Opq	0.2
Total	100

Appendix 4–1. Modal compositions of the porphyritic fine-grained tonalite and clinopyroxene quartz diorite.

Type	PFT	PFT	PFT	PFT	PFT	PFT	PFT	PFT	PFT	PFT	PFT
No	18050509	19062209	19070102	19070204	19070401	19070404	19070409	19070411B	19070413	19070415	20040301
LOI	1.270	1.263	1.333	1.223	1.399	1.077	1.394	1.250	1.326	1.453	1.076
Count (point)											
Qz	344	410	340	376	360	372	377	383	345	335	336
Pl	1257	1329	1258	1316	1309	1329	1317	1315	1305	1323	1291
Kfs	0	0	0	0	0	0	0	0	0	0	0
Cpx	0	21	0	0	0	0	0	0	0	0	13
Opx	0	0	0	0	0	0	0	0	0	0	0
Bt	178	100	129	107	100	137	86	103	146	124	190
Hb	212	130	249	171	223	151	208	188	193	188	149
Opq	9	10	24	30	8	11	12	11	11	14	21
Chl	0	0	0	0	0	0	0	0	0	0	0
Cal	0	0	0	0	0	0	0	0	0	16	0
Total	2000	2000	2000	2000	2000	2000	2000	2000	2000	2000	2000
Modal value (%)											
Qz	17.2	20.5	17.0	18.8	18.0	18.6	18.9	19.2	17.3	16.8	16.8
Pl	62.9	66.5	62.9	65.8	65.5	66.5	65.9	65.8	65.3	66.2	64.6
Kfs	0	0	0	0	0	0	0	0	0	0	0
Cpx	0	1.1	0	0	0	0	0	0	0	0	0.7
Opx	0	0	0	0	0	0	0	0	0	0	0
Bt	8.9	5.0	6.5	5.4	5.0	6.9	4.3	5.2	7.3	6.2	9.5
Hb	10.6	6.5	12.5	8.6	11.2	7.6	10.4	9.4	9.7	9.4	7.5
Opq	0.5	0.5	1.2	1.5	0.4	0.6	0.6	0.6	0.6	0.7	1.1
Chl	0	0	0	0	0	0	0	0	0	0	0
Cal	0	0	0	0	0	0	0	0	0	0.8	0
Total	100	100	100	100	100	100	100	100	100	100	100

Type	PFT	PFT	PFT	PFT	PFT	PFT	PFT	PFT	PFT	PFT	PFT
No	20040401	20040402	18050511	19062207	19070104	19070105	19062206	20040202	20040205	20040206	20040207
LOI	0.847	1.014	1.655	3.092	1.867	2.143	2.731	2.374	2.084	1.682	2.123
Count (point)											
Qz	360	343	400	389	363	336	414	373	363	384	421
Pl	1246	1246	1224	1333	1198	1242	1289	1255	1264	1272	1309
Kfs	0	0	0	0	0	0		0	0	0	0
Cpx	0	0	0	0	0	0	0	0	0	0	0
Opx	0	0	0	0	0	0	0	0	0	0	0
Bt	141	118	168	148	153	190	151	168	116	148	96
Hb	240	284	200	119	274	215	120	194	236	182	161
Opq	13	9	8	11	12	17	26	10	21	14	13
Chl	0	0	0	0	0	0	0	0	0	0	0
Cal	0	0	0	0	0	0	0	0	0	0	0
Total	2000	2000	2000	2000	2000	2000	2000	2000	2000	2000	2000
Modal value (%)											
Qz	18.0	17.2	20.0	19.5	18.2	16.8	20.7	18.7	18.2	19.2	21.1
Pl	62.3	62.3	61.2	66.7	59.9	62.1	64.45	62.8	63.2	63.6	65.5
Kfs	0	0	0	0	0	0		0	0	0	0
Cpx	0	0	0	0	0	0	0	0	0	0	0
Opx	0	0	0	0	0	0	0	0	0	0	0
Bt	7.1	5.9	8.4	7.4	7.7	9.5	7.55	8.4	5.8	7.4	4.8
Hb	12.0	14.2	10.0	6.0	13.7	10.8	6	9.7	11.8	9.1	8.1
Opq	0.7	0.5	0.4	0.6	0.6	0.9	1.3	0.5	1.1	0.7	0.7
Chl	0	0	0	0	0	0	0	0	0	0	0
Cal	0	0	0	0	0	0	0	0	0	0	0
Total	100	100	100	100	100	100	100	100	100	100	100

PFT: porphyritic fine-grained tonalite, CQD: clinopyroxene quartz diorite, Qz: quartz, Pl: plagioclase, Kfs: K-feldspar, Cpx: clinopyroxene, Opx: orthopyroxene; Bt: biotite, Hb: homblende, Opq: opaque, Chl: chlorite, Cal: calcite, and LOI: loss on ignition.

Type	CQD	CQD	CQD	CQD	CQD	CQD	CQD	CQD	CQD	CQD	CQD
No	18050512	18050513	18050514	20040302	20040303	20040305	20040306	20040307	20040310	20040403	20040404
Count (point)											
Qz	180	174	145	154	177	182	141	133	199	101	159
Pl	1238	1256	1251	1098	1129	987	1189	1271	1176	1081	1166
Kfs	0	0	0	0	3	5	0	0	0	0	0
Cpx	272	267	289	352	352	472	326	258	349	412	332
Opx	0	0	0	6	0	0	0	12	1	0	1
Bt	297	290	256	369	311	281	321	302	250	378	320
Hb	0	0	29	0	0	0	0	0	0	0	0
Opq	11	8	13	16	15	18	11	17	8	15	17
Chl	2	5	17	5	13	49	12	7	17	13	5
Cal	0	0	0	0	0	6	0	0	0	0	0
Total	2000	2000	2000	2000	2000	2000	2000	2000	2000	2000	2000
Modal value (%)											
Qz	9.0	8.7	7.3	7.7	8.9	9.1	7.1	6.7	10.0	5.1	8.0
Pl	61.9	62.8	62.6	54.9	56.5	49.4	59.5	63.6	58.8	54.1	58.3
Kfs	0	0	0	0	0.2	0.3	0	0	0	0	0
Cpx	13.6	13.4	14.5	17.6	17.6	23.6	16.3	12.9	17.5	20.6	16.6
Opx	0	0	0	0.3	0	0	0	0.6	0.1	0	0.1
Bt	14.9	14.5	12.8	18.5	15.6	14.1	16.1	15.1	12.5	18.9	16.0
Hb	0	0	1.5	0	0	0	0	0	0	0	0
Opq	0.6	0.4	0.7	0.8	0.8	0.9	0.6	0.9	0.4	0.8	0.9
Chl	0.1	0.3	0.9	0.3	0.7	2.5	0.6	0.4	0.9	0.7	0.3
Cal	0	0	0	0	0	0.3	0	0	0	0	0
Total	100	100	100	100	100	100	100	100	100	100	100
Pl–dusty zoned-Pl ratio (grain)											
Pl	938	822	946	950	971	957	845	908	899	996	863
dusty-Pl	62	178	54	50	29	43	155	92	101	4	137
(DPl/Pl)*100	6.61	21.65	5.71	5.26	2.99	4.49	18.34	10.13	11.23	0.40	15.87

Type	CQD	CQD	CQD	CQD	CQD
No	20040405	20040406	20040407	20040408	20040602
Count (point)					
Qz	60	143	191	92	61
Pl	1132	1083	1128	1115	1140
Kfs	0	0	0	0	0
Cpx	376	372	305	404	409
Opx	25	14	0	8	0
Bt	384	364	347	353	371
Hb	0	0	0	0	0
Opq	18	16	18	12	12
Chl	5	8	11	16	7
Cal	0	0	0	0	0
Total	2000	2000	2000	2000	2000
Modal value (%)					
Qz	3.0	7.2	9.6	4.6	3.1
Pl	56.6	54.2	56.4	55.8	57.0
Kfs	0	0	0	0	0
Cpx	18.8	18.6	15.3	20.2	20.5
Opx	1.3	0.7	0	0.4	0
Bt	19.2	18.2	17.4	17.7	18.6
Hb	0	0	0	0	0
Opq	0.9	0.8	0.9	0.6	0.6
Chl	0.3	0.4	0.6	0.8	0.4
Cal	0	0	0	0	0
Total	100	100	100	100	100
Pl–dusty zoned-Pl ratio (grain)					
Pl	990	967	880	975	941
dusty-Pl	10	33	120	25	59
(DPl/Pl)*100	1.01	3.41	13.04	2.56	6.27

PFT: porphyritic fine-grained tonalite, CQD: clinopyroxene quartz diorite, Qz: quartz, Pl: plagioclase, Kfs: K-feldspar, Cpx: clinopyroxene, Opx: orthopyroxene; Bt: biotite, Hb: hornblende, Opq: opaque, Chl: chlorite, Cal: calcite, and DPl: dusty-zoned plagioclase.

Appendix 4–2. Major (wt%) and trace element (ppm) concentrations of the porphyritic fine-grained tonalite and clinopyroxene quartz diorite.

Type	PFT	PFT	PFT	PFT	PFT	PFT	PFT	PFT	PFT	PFT
No	20040202	20040206	20040204	19070505	20040301	20040207	20040203	20040402	19062209	18050502
(wt%)										
SiO_2	63.17	63.40	63.41	63.41	63.45	63.71	63.76	63.80	63.80	63.88
TiO_2	0.65	0.67	0.68	0.68	0.68	0.64	0.65	0.64	0.66	0.67
Al_2O_3	15.92	16.01	16.03	15.94	15.69	15.96	15.84	15.78	16.17	16.41
Fe_2O_3	5.60	5.81	5.85	6.39	6.09	5.52	5.70	5.82	5.95	5.74
MnO	0.12	0.13	0.11	0.12	0.12	0.11	0.11	0.13	0.12	0.12
MgO	2.27	2.29	2.63	2.45	3.18	2.26	2.37	2.41	2.48	2.31
CaO	4.39	4.94	3.95	4.07	3.88	4.55	4.87	4.84	4.66	4.12
Na_2O	3.93	3.35	3.61	4.71	3.10	3.54	3.36	3.53	3.39	3.56
K_2O	2.76	2.52	2.61	2.15	2.84	2.76	2.33	2.40	2.85	3.17
P_2O_5	0.19	0.19	0.19	0.18	0.19	0.18	0.18	0.18	0.18	0.18
LOI	2.37	1.68	3.69	4.21	1.08	2.12	3.72	1.01	1.26	2.10
Total	98.98	99.30	99.07	100.09	99.21	99.22	99.17	99.52	100.27	100.17
(ppm)										
Ba	596	483	572	630	587	595	500	543	614	647
Cr	28	32	33	48	43	30	33	36	43	36
Nb	12	12	13	12	12	12	12	13	14	14
Ni	13	14	13	14	17	13	14	14	16	14
Rb	79	*ICP-MS*	*ICP-MS*	62	*ICP-MS*	80	70	*ICP-MS*	*ICP-MS*	95
Sr	501	*ICP-MS*	*ICP-MS*	536	*ICP-MS*	440	360	*ICP-MS*	*ICP-MS*	528
V	117	124	120	128	129	117	119	124	125	122
Y	21	21	22	21	22	21	19	22	22	24
Zn	74	81	86	75	77	72	74	75	76	84
Zr	174	169	160	179	169	170	153	170	183	176
ICP-MS (ppm)										
Rb	–	75.0	82.0	–	95.0	–	–	85.0	78.0	–
Sr	–	407.0	345.0	–	391.0	–	–	447.0	464.0	–
La	–	25.4	24.5	–	22.6	–	–	24.1	23.3	–
Ce	–	48.1	47.3	–	44.6	–	–	46.2	44.7	–
Pr	–	5.4	5.2	–	5.0	–	–	5.1	5.1	–
Nd	–	21.3	20.4	–	19.4	–	–	19.8	19.9	–
Sm	–	4.4	4.1	–	4.1	–	–	4.2	4.0	–
Eu	–	1.2	1.2	–	1.1	–	–	1.1	1.1	–
Gd	–	3.8	3.6	–	3.5	–	–	3.6	3.5	–
Tb	–	0.5	0.5	–	0.5	–	–	0.5	0.5	–
Dy	–	3.1	3.0	–	2.9	–	–	3.0	3.0	–
Ho	–	0.6	0.6	–	0.6	–	–	0.6	0.6	–
Er	–	1.7	1.7	–	1.6	–	–	1.6	1.6	–
Yb	–	1.7	1.7	–	1.6	–	–	1.6	1.5	–
Lu	–	0.3	0.3	–	0.3	–	–	0.3	0.2	–
Ta	–	1.1	1.1	–	1.0	–	–	1.1	1.1	–
Hf	–	3.5	3.3	–	3.1	–	–	3.1	3.3	–
Th	–	8.1	8.1	–	7.8	–	–	8.0	8.1	–
Pb	–	13.0	12.0	–	11.0	–	–	12.0	11.0	–

Total Fe reported as Fe^{3+}. PFT: porphyritic fine-grained tonalite, CQD: clinopyroxene quartz diorite, and LOI: loss on ignition.

Type	PFT	PFT	PFT	PFT	PFT	PFT	PFT	PFT	PFT	PFT
No	19070106	20040401	18050501	19070404	19070403	19070413	19070411B	19070204	19062208	19062211
(wt%)										
SiO_2	63.91	63.91	63.94	63.94	63.96	63.98	64.01	64.02	64.03	64.03
TiO_2	0.67	0.62	0.66	0.67	0.66	0.66	0.64	0.65	0.67	0.65
Al_2O_3	15.97	15.93	16.07	16.04	15.89	16.03	16.15	16.13	15.94	16.40
Fe_2O_3	6.04	5.53	5.69	5.71	5.86	5.90	5.54	5.63	5.97	5.67
MnO	0.12	0.12	0.10	0.17	0.11	0.13	0.11	0.13	0.12	0.12
MgO	2.53	2.34	2.25	2.31	2.35	2.43	2.27	2.37	2.46	2.54
CaO	4.41	4.50	4.54	4.79	4.36	4.23	4.76	4.32	4.35	4.23
Na_2O	3.53	3.33	3.37	3.32	3.75	3.83	3.47	3.50	3.32	3.51
K_2O	3.00	2.96	3.08	2.92	2.76	2.80	2.87	2.95	3.02	2.97
P_2O_5	0.18	0.18	0.18	0.18	0.19	0.19	0.18	0.18	0.19	0.18
LOI	1.73	0.85	1.60	1.08	2.90	1.33	1.25	1.22	1.96	4.33
Total	100.36	99.41	99.88	100.05	99.85	100.18	100.00	99.88	100.06	100.30
(ppm)										
Ba	576	652	640	581	655	559	579	610	616	641
Cr	43	35	36	31	33	36	32	37	35	35
Nb	14	11	13	13	13	13	12	12	13	14
Ni	15	15	14	12	15	15	13	14	13	15
Rb	83	93	93	83	74	77	89	*ICP-MS*	*ICP-MS*	92
Sr	560	478	509	484	508	560	470	*ICP-MS*	*ICP-MS*	465
V	126	116	122	119	124	121	116	121	129	118
Y	23	23	26	21	22	22	22	23	25	24
Zn	75	84	62	96	71	78	70	76	81	70
Zr	188	170	177	178	176	182	175	186	178	175
ICP-MS (ppm)										
Rb	–	–	–	–	–	–	–	89.0	101.0	–
Sr	–	–	–	–	–	–	–	552.0	515.0	–
La	–	–	–	–	–	–	–	23.7	25.5	–
Ce	–	–	–	–	–	–	–	45.6	49.3	–
Pr	–	–	–	–	–	–	–	5.2	5.6	–
Nd	–	–	–	–	–	–	–	19.8	21.8	–
Sm	–	–	–	–	–	–	–	4.2	4.4	–
Eu	–	–	–	–	–	–	–	1.2	1.2	–
Gd	–	–	–	–	–	–	–	3.6	3.9	–
Tb	–	–	–	–	–	–	–	0.5	0.6	–
Dy	–	–	–	–	–	–	–	3.1	3.3	–
Ho	–	–	–	–	–	–	–	0.6	0.6	–
Er	–	–	–	–	–	–	–	1.6	1.8	–
Yb	–	–	–	–	–	–	–	1.5	1.9	–
Lu	–	–	–	–	–	–	–	0.2	0.3	–
Ta	–	–	–	–	–	–	–	1.1	1.2	–
Hf	–	–	–	–	–	–	–	3.8	3.5	–
Th	–	–	–	–	–	–	–	8.2	8.4	–
Pb	–	–	–	–	–	–	–	10.0	16.0	–

Total Fe reported as Fe^{3+}. PFT: porphyritic fine-grained tonalite, CQD: clinopyroxene quartz diorite, and LOI: loss on ignition.

Type	PFT	PFT	PFT	PFT	PFT	PFT	PFT	PFT	PFT	PFT
No	19070405	19070109	19070502	19070104	18050508	19070401	20040205	18050503	18050511	19070504
(wt%)										
SiO_2	64.04	64.05	64.07	64.08	64.10	64.13	64.14	64.15	64.20	64.20
TiO_2	0.65	0.69	0.65	0.65	0.66	0.64	0.66	0.66	0.65	0.67
Al_2O_3	16.13	16.20	16.11	16.25	16.33	16.07	16.15	16.05	15.78	15.94
Fe_2O_3	5.88	6.11	5.86	5.79	5.75	5.60	5.69	5.78	5.80	5.99
MnO	0.12	0.15	0.11	0.12	0.13	0.12	0.13	0.12	0.11	0.12
MgO	2.37	2.67	2.27	2.44	2.34	2.34	2.41	2.33	2.35	2.42
CaO	4.71	4.24	4.05	3.92	4.66	4.28	3.79	4.62	5.09	4.89
Na_2O	3.77	3.61	4.58	3.76	3.48	3.55	3.78	4.03	2.92	2.71
K_2O	2.05	2.29	2.04	3.04	2.67	3.13	2.52	2.17	3.08	2.81
P_2O_5	0.18	0.19	0.18	0.18	0.19	0.18	0.18	0.18	0.19	0.19
LOI	4.13	3.86	4.31	1.87	1.17	1.40	2.08	4.73	1.66	5.75
Total	99.90	100.18	99.92	100.22	100.30	100.04	99.42	100.09	100.16	99.93
(ppm)										
Ba	472	685	462	636	500	630	682	398	705	667
Cr	35	41	37	45	36	32	39	33	45	33
Nb	12	13	12	13	14	12	11	13	13	13
Ni	14	12	12	14	15	15	15	12	14	14
Rb	71	*ICP-MS*	69	78	91	98	60	76	94	*ICP-MS*
Sr	565	*ICP-MS*	579	669	486	566	637	517	471	*ICP-MS*
V	117	126	124	125	123	119	122	121	122	119
Y	20	21	21	22	24	25	19	21	23	26
Zn	73	96	61	73	79	75	80	70	75	77
Zr	184	184	189	201	179	182	191	180	171	168
ICP-MS (ppm)										
Rb	–	70.0	–	–	–	–	–	–	–	85.0
Sr	–	465.0	–	–	–	–	–	–	–	387.0
La	–	23.1	–	–	–	–	–	–	–	29.2
Ce	–	45.7	–	–	–	–	–	–	–	45.0
Pr	–	5.1	–	–	–	–	–	–	–	6.1
Nd	–	19.8	–	–	–	–	–	–	–	23.8
Sm	–	4.0	–	–	–	–	–	–	–	4.8
Eu	–	1.1	–	–	–	–	–	–	–	1.4
Gd	–	3.5	–	–	–	–	–	–	–	4.5
Tb	–	0.5	–	–	–	–	–	–	–	0.6
Dy	–	3.0	–	–	–	–	–	–	–	3.4
Ho	–	0.6	–	–	–	–	–	–	–	0.7
Er	–	1.6	–	–	–	–	–	–	–	1.9
Yb	–	1.6	–	–	–	–	–	–	–	1.7
Lu	–	0.3	–	–	–	–	–	–	–	0.3
Ta	–	0.9	–	–	–	–	–	–	–	0.9
Hf	–	3.3	–	–	–	–	–	–	–	3.2
Th	–	7.8	–	–	–	–	–	–	–	7.8
Pb	–	16.0	–	–	–	–	–	–	–	11.0

Total Fe reported as Fe^{3+}. PFT: porphyritic fine-grained tonalite, CQD: clinopyroxene quartz diorite, and LOI: loss on ignition.

Type	PFT	PFT	PFT	PFT	PFT	PFT	PFT	PFT	PFT	PFT
No	19070506	19070414	19070110	19070415	19070107	18050509	19070102	19062207	19070201	19070202A
(wt%)										
SiO_2	64.22	64.23	64.24	64.27	64.28	64.35	64.40	64.41	64.46	64.50
TiO_2	0.66	0.68	0.66	0.64	0.66	0.64	0.62	0.65	0.63	0.68
Al_2O_3	16.01	16.10	16.19	16.07	16.08	16.13	16.24	16.25	16.02	16.41
Fe_2O_3	5.80	5.84	5.76	5.78	5.68	5.69	5.49	5.70	5.62	5.60
MnO	0.11	0.09	0.12	0.13	0.12	0.13	0.11	0.11	0.12	0.12
MgO	2.35	2.60	2.33	2.38	2.29	2.30	2.31	2.45	2.25	2.51
CaO	3.82	4.32	4.07	4.76	3.67	4.82	4.27	4.34	3.61	3.13
Na_2O	4.54	2.73	4.75	3.33	4.20	3.38	3.76	3.13	4.48	3.83
K_2O	2.33	3.31	1.85	2.58	2.94	2.54	3.00	2.99	2.42	3.04
P_2O_5	0.18	0.19	0.18	0.18	0.18	0.18	0.18	0.18	0.18	0.18
LOI	3.89	1.98	4.68	1.45	3.26	1.27	1.33	3.09	2.32	1.88
Total	100.04	100.08	100.15	100.12	100.09	100.17	100.38	100.21	99.78	99.99
(ppm)										
Ba	613	692	624	604	652	614	582	665	705	632
Cr	37	36	37	37	37	36	36	43	38	41
Nb	13	13	14	12	13	13	14	14	12	13
Ni	13	13	13	13	14	14	15	18	13	15
Rb	61	*ICP-MS*	67	64	73	77	95	93	53	101
Sr	559	*ICP-MS*	611	535	569	452	502	460	646	472
V	122	123	123	123	120	121	115	122	119	117
Y	21	24	21	20	27	21	24	25	21	26
Zn	76	76	75	94	73	82	70	76	76	83
Zr	189	181	190	185	185	166	176	168	198	176
ICP-MS (ppm)										
Rb	–	104.0	–	–	–	–	–	–	–	–
Sr	–	408.0	–	–	–	–	–	–	–	–
La	–	23.3	–	–	–	–	–	–	–	–
Ce	–	45.2	–	–	–	–	–	–	–	–
Pr	–	5.1	–	–	–	–	–	–	–	–
Nd	–	20.1	–	–	–	–	–	–	–	–
Sm	–	4.2	–	–	–	–	–	–	–	–
Eu	–	1.2	–	–	–	–	–	–	–	–
Gd	–	3.5	–	–	–	–	–	–	–	–
Tb	–	0.6	–	–	–	–	–	–	–	–
Dy	–	3.1	–	–	–	–	–	–	–	–
Ho	–	0.6	–	–	–	–	–	–	–	–
Er	–	1.6	–	–	–	–	–	–	–	–
Yb	–	1.5	–	–	–	–	–	–	–	–
Lu	–	0.2	–	–	–	–	–	–	–	–
Ta	–	1.1	–	–	–	–	–	–	–	–
Hf	–	3.5	–	–	–	–	–	–	–	–
Th	–	8.0	–	–	–	–	–	–	–	–
Pb	–	10.0	–	–	–	–	–	–	–	–

Total Fe reported as Fe^{3+}. PFT: porphyritic fine-grained tonalite, CQD: clinopyroxene quartz diorite, and LOI: loss on ignition.

Type No	PFT 18050507	PFT 19070103	PFT 19062210	PFT 19070409	PFT 19070503	PFT 19070108	PFT 19062206	PFT 18050505	CQD 20040403	CQD 20040405
(wt%)										
SiO_2	64.53	64.55	64.68	64.69	64.70	64.71	64.79	65.09	55.69	55.69
TiO_2	0.63	0.66	0.64	0.61	0.67	0.66	0.63	0.66	0.97	1.05
Al_2O_3	16.19	16.12	16.13	16.04	16.17	16.17	16.06	16.56	17.15	16.95
Fe_2O_3	5.54	5.87	5.62	5.31	5.85	5.73	5.63	5.87	8.75	9.15
MnO	0.11	0.12	0.11	0.11	0.10	0.11	0.10	0.09	0.15	0.15
MgO	2.45	2.51	2.24	2.17	2.43	2.52	2.32	2.26	4.52	4.19
CaO	4.00	4.16	3.37	4.38	3.26	3.86	4.61	4.22	7.05	7.26
Na_2O	3.53	3.70	4.71	3.47	3.90	4.09	3.03	1.95	3.13	3.10
K_2O	3.08	2.34	2.39	3.01	2.85	2.13	2.82	3.32	1.71	1.67
P_2O_5	0.18	0.18	0.18	0.18	0.19	0.18	0.18	0.19	0.19	0.21
LOI	2.76	2.51	3.38	1.39	3.99	4.81	2.73	5.68	1.43	0.39
Total	100.23	100.20	100.07	99.97	100.11	100.16	100.17	100.20	99.30	99.41
(ppm)										
Ba	639	593	709	572	608	449	599	573	367	289
Cr	63	40	44	32	33	39	36	33	86	64
Nb	12	13	13	12	13	14	13	13	8	9
Ni	33	16	15	13	13	15	15	13	46	40
Rb	95	*ICP-MS*	*ICP-MS*	*ICP-MS*	97	77	80	*ICP-MS*	*ICP-MS*	*ICP-MS*
Sr	534	*ICP-MS*	*ICP-MS*	*ICP-MS*	427	418	497	*ICP-MS*	*ICP-MS*	*ICP-MS*
V	118	124	117	111	124	122	118	120	188	198
Y	24	19	21	24	24	23	22	25	18	20
Zn	75	75	71	71	73	77	77	83	96	91
Zr	177	182	186	172	168	173	175	149	141	152
ICP-MS (ppm)										
Rb	–	63.0	67.0	97.0	–	–	–	108.0	66.0	60.0
Sr	–	545.0	516.0	465.0	–	–	–	247.0	434.0	368.0
La	–	25.4	23.9	23.1	–	–	–	22.4	18.5	19.0
Ce	–	49.6	45.4	44.2	–	–	–	43.5	39.0	40.4
Pr	–	5.5	5.0	5.0	–	–	–	4.8	4.7	4.9
Nd	–	21.7	19.3	19.1	–	–	–	18.9	19.7	20.4
Sm	–	4.4	3.9	3.9	–	–	–	3.9	4.4	4.6
Eu	–	1.2	1.1	1.1	–	–	–	1.0	1.3	1.3
Gd	–	3.9	3.4	3.4	–	–	–	3.4	4.3	4.6
Tb	–	0.6	0.5	0.5	–	–	–	0.5	0.6	0.7
Dy	–	3.2	2.8	2.9	–	–	–	2.8	3.7	4.3
Ho	–	0.6	0.5	0.5	–	–	–	0.5	0.7	0.8
Er	–	1.7	1.5	1.5	–	–	–	1.5	2.1	2.4
Yb	–	1.9	1.6	1.4	–	–	–	1.5	2.1	2.3
Lu	–	0.3	0.2	0.2	–	–	–	0.2	0.3	0.4
Ta	–	1.1	1.0	1.1	–	–	–	0.8	0.8	0.7
Hf	–	3.8	3.2	3.6	–	–	–	2.9	3.1	3.3
Th	–	8.6	8.0	8.2	–	–	–	7.7	5.3	6.3
Pb	–	15.0	12.0	12.0	–	–	–	6.0	10.0	10.0

Total Fe reported as Fe^{3+}. PFT: porphyritic fine-grained tonalite, CQD: clinopyroxene quartz diorite, and LOI: loss on ignition.

Type	CQD	CQD	CQD	CQD	CQD	CQD	CQD	CQD	CQD	CQD
No	20040408	20040303	20040302	20040305	20040406	20040602	18050514	18050513	20040306	20040404
(wt%)										
SiO_2	55.99	56.99	57.07	57.15	57.16	57.65	57.87	58.54	58.57	58.62
TiO_2	1.12	1.05	1.01	0.93	1.03	1.04	1.03	0.94	0.93	0.98
Al_2O_3	17.33	16.57	16.51	16.74	16.50	16.83	16.91	17.11	16.81	17.05
Fe_2O_3	9.01	8.44	8.14	8.43	8.31	7.88	8.57	7.79	7.49	7.70
MnO	0.14	0.14	0.12	0.14	0.13	0.12	0.14	0.13	0.12	0.10
MgO	3.78	3.87	4.12	3.96	3.80	3.54	4.04	3.62	3.40	3.26
CaO	7.14	6.58	6.84	6.28	6.68	6.71	6.62	6.49	6.25	6.11
Na_2O	3.32	2.77	3.20	3.00	3.23	3.29	2.99	3.42	3.45	3.27
K_2O	1.44	2.39	1.72	2.39	1.88	1.83	1.80	1.81	1.86	2.05
P_2O_5	0.23	0.20	0.19	0.20	0.23	0.21	0.21	0.21	0.21	0.20
LOI	0.70	1.22	0.72	1.55	0.49	0.26	1.19	1.14	0.42	0.97
Total	99.49	98.98	98.93	99.23	98.94	99.11	100.17	100.07	99.08	99.35
(ppm)										
Ba	273	468	325	395	351	326	403	400	342	372
Cr	57	62	136	74	80	65	79	55	51	44
Nb	12	10	9	9	11	11	12	11	10	11
Ni	28	30	42	24	32	24	34	28	27	25
Rb	*ICP-MS*	79	*ICP-MS*	82	*ICP-MS*	*ICP-MS*	*ICP-MS*	*ICP-MS*	56	*ICP-MS*
Sr	*ICP-MS*	380	*ICP-MS*	399	*ICP-MS*	*ICP-MS*	*ICP-MS*	*ICP-MS*	420	*ICP-MS*
V	180	184	172	172	177	162	179	162	160	170
Y	18	23	19	24	20	19	22	20	19	24
Zn	98	87	92	90	93	92	79	91	90	87
Zr	177	174	157	123	178	162	163	159	164	179
ICP-MS (ppm)										
Rb	47.0	–	55.0	–	58.0	61.0	60.0	61.0	–	70.0
Sr	390.0	–	348.0	–	358.0	369.0	363.0	403.0	–	352.0
La	20.1	–	21.0	–	21.6	21.2	20.1	20.0	–	22.0
Ce	42.3	–	44.0	–	45.2	44.7	41.7	41.4	–	46.6
Pr	5.1	–	5.2	–	5.4	5.2	5.0	5.1	–	5.4
Nd	21.0	–	21.4	–	22.5	20.9	20.4	20.2	–	21.5
Sm	4.6	–	4.7	–	4.8	4.8	4.7	4.5	–	4.8
Eu	1.3	–	1.3	–	1.3	1.2	1.3	1.2	–	1.3
Gd	4.6	–	4.6	–	4.7	4.5	4.5	4.1	–	4.6
Tb	0.7	–	0.7	–	0.7	0.6	0.7	0.7	–	0.7
Dy	4.0	–	3.9	–	4.0	3.6	4.1	3.7	–	4.1
Ho	0.8	–	0.7	–	0.8	0.7	0.8	0.7	–	0.8
Er	2.1	–	2.1	–	2.2	1.8	2.3	1.9	–	2.2
Yb	1.9	–	1.9	–	2.1	1.6	2.0	1.7	–	2.1
Lu	0.3	–	0.3	–	0.3	0.2	0.3	0.3	–	0.3
Ta	0.9	–	0.8	–	0.7	0.8	0.8	0.8	–	0.8
Hf	3.7	–	3.4	–	3.8	3.2	3.8	3.3	–	4.0
Th	4.6	–	6.9	–	6.3	7.2	6.2	5.7	–	7.9
Pb	10.0	–	10.0	–	10.0	10.0	8.0	9.0	–	12.0

Total Fe reported as Fe^{3+}. PFT: porphyritic fine-grained tonalite, CQD: clinopyroxene quartz diorite, and LOI: loss on ignition.

Type No	CQD 20040310	CQD 20040407	CQD 20040307	CQD 18050512
(wt%)				
SiO_2	58.63	59.14	60.03	60.89
TiO_2	1.08	1.05	0.86	0.87
Al_2O_3	16.41	16.45	16.48	16.79
Fe_2O_3	8.15	7.72	7.07	7.09
MnO	0.13	0.11	0.12	0.11
MgO	4.07	3.20	2.98	2.98
CaO	3.64	5.97	5.80	5.76
Na_2O	3.79	3.23	3.41	3.40
K_2O	2.88	2.12	2.18	2.13
P_2O_5	0.20	0.22	0.19	0.19
LOI	3.41	1.03	0.27	0.78
Total	98.98	99.21	99.10	100.20
(ppm)				
Ba	531	380	349	370
Cr	84	63	48	46
Nb	12	11	10	12
Ni	27	26	21	25
Rb	*ICP-MS*	*ICP-MS*	71	*ICP-MS*
Sr	*ICP-MS*	*ICP-MS*	362	*ICP-MS*
V	174	155	147	149
Y	28	20	23	24
Zn	92	91	85	90
Zr	217	184	173	187
ICP-MS (ppm)				
Rb	106.0	67.0	–	70.0
Sr	368.0	352.0	–	333.0
La	23.5	24.1	–	22.9
Ce	50.5	50.9	–	47.2
Pr	6.0	5.9	–	5.6
Nd	24.2	23.7	–	22.0
Sm	5.3	5.2	–	4.7
Eu	1.1	1.3	–	1.2
Gd	5.1	4.8	–	4.4
Tb	0.8	0.7	–	0.7
Dy	4.5	3.8	–	4.1
Ho	0.9	0.7	–	0.8
Er	2.4	1.9	–	2.2
Yb	2.3	1.7	–	2.0
Lu	0.3	0.3	–	0.3
Ta	0.8	0.9	–	1.0
Hf	4.8	4.3	–	4.1
Th	9.0	9.1	–	8.9
Pb	13.0	10.0	–	12.0

Total Fe reported as Fe^{3+}. PFT: porphyritic fine-grained tonalite, CQD: clinopyroxene quartz diorite, and LOI: loss on ignition.

Appendix 4–3. Partition coefficients used in the Rayleigh fractionation modeling.

CQD Fc Partition coefficent

	Pl	ref	Cpx	ref	Bt	ref	Ilm	ref
Rb	0.197	a	0.0414	a	5.367	f	0.00034	k
Ba	0.0705	a	0.0129	a	3.2	f	–	–
Th	0.004	d	0.007	l	0.997	f	0.00055	k
Ta	0.03	h	0.0022	l	1.567	f	1.7	k
Nb	1.3	j	0.0012	l	4	f	2	k
La	0.21	d	0.23	d	2	f	0.000029	k
Ce	0.18	d	0.36	d	2	f	0.000054	k
Sr	1.83	a	0.0648	a	0.447	f	–	–
Nd	0.16	d	0.645	a	2.56	f	0.00048	k
Sm	0.1	d	1.3	d	2.117	f	0.00059	k
Eu	0.73	d	1.2	d	2.02	f	0.0011	k
Dy	0.293	b	1.9	d	1.72	f	0.01	k
Y	0.066	j	2.4	j	1	f	–	–
Yb	0.033	b	1.3	b	1.4	f	0.17	k
Lu	0.1	d	1.4	d	1.617	f	0.084	k

Fc and Ac vector Partition coefficent

	Cpx	ref	Pl	ref	Bt	ref	Opx	ref
Cr	34	i	0.01	e	–	–	4	i
Ni	6	i	0.01	e	–	–	5	i
Sr	0.06	i	2.84	c	0.12	a	0.04	i
Y	0.9	i	0.1	c	0.03	a	0.18	i

CQD Ac Partition coefficent

	Pl	ref	Cpx	ref	Opx	ref	Bt	ref	Ilm	ref
Rb	0.197	a	0.0414	a	0.0036	l	5.6	f	0.00034	k
Ba	0.24	j	0.03	h	0.0042	l	4.1	f	–	–
Th	0.19	d	0.16	d	0.0007	l	2	f	0.00055	k
Ta	0.05	f	0.57	f	0.001	l	1.9	f	6.6	g
Nb	0.27	j	0.0012	l	0.0007	l	4.5	f	2	k
La	0.21	d	0.23	d	0.0006	l	7.2	f	0.000029	k
Ce	0.18	d	0.36	d	0.0017	l	7.5	f	0.000054	k
Sr	1.83	a	0.0648	a	0.0019	l	0.447	f	–	–
Nd	0.24	b	0.645	b	0.004	l	5.7	f	0.00048	k
Sm	0.1	d	1.3	d	0.011	l	4.3	f	0.00059	k
Eu	0.73	d	1.2	d	0.03	l	2.02	f	0.0011	k
Dy	0.293	b	1.9	d	0.077	l	3.4	f	0.01	k
Y	0.51	j	2.4	j	0.046	l	1.4	f	5.09	j
Yb	0.1	i	2	h	0.077	l	3	f	4.1	f
Lu	0.241	b	2	h	0.09	l	3.4	f	3.6	f

References

a: Philpotts and Schnetzler, 1970
b: Schnetzler and Philpotts, 1970
c: Arth, 1976
d: Luhr and Carmichael, 1980
e: Gill, 1981
f: Nash and Crecraft, 1985
g: Green and Pearson, 1987
h: Bacon and Druitt, 1988
i: Rollinson, 1993
j: Ewart and Griffin, 1994
k: Zack and Brumn, 1998
l: Adam and Green, 2006

PFT: porphyritic fine-grained tonalite, CQD: clinopyroxene quartz diorite, Fc: fractional crystallization, and Ac: accumulation.

Appendix 5–1. Modal compositions of the Kita-taku mafic complex and related rocks.

No	1		2		3		4		5		6		7		8		9		10	
Sp.No	20061201		20110203		21021406B		21021407A		20110702		200612T05		20110507		200612T02		20110307A		20110607A	
Litho.	Ol Gbn-Ol ber Hd		Ol Gbn-Ol ber Hd		Ol Gbn-Ol ber Hd		Ol Gbn-Ol ber Hd		Ol ber Gbn-Gb		Ol ber Gbn-Gb		Ol ber Gbn-Gb		Ol ber Gbn-Gb		Ol ber Gbn-Gb		Ol ber Gbn-Gb	
Type	1		1		1		1		1		1		1		1		1		1	
Texture	Orthocumulate		Orthocumulate		Orthocumulate		Orthocumulate		Orthocumulate		Orthocumulate		Orthocumulate		Orthocumulate		Orthocumulate		Orthocumulate	
mineral	count	%	count	%	count	%	count	%	count	%	count	%	count	%	count	%	count	%	count	%
Qz	0	0	0	0	0	0	0	0	0	0	0	0	0	0	0	0	0	0	0	0
Kfs	0	0	0	0	0	0	0	0	0	0	0	0	0	0	0	0	0	0	0	0
Pl	506	16.9	278	9.3	154	5.1	428	14.3	282	9.4	642	21.4	838	27.9	944	31.5	772	25.7	650	21.7
Hb	1180	39.3	1118	37.3	1386	46.2	1836	61.2	1894	63.1	2178	72.6	1304	43.5	1838	61.3	2018	67.3	1940	64.7
Bt	0	0	0	0	0	0	0	0	0	0	0	0	0	0	26	0.9	0	0	0	0
Cpx	814	27.1	382	12.7	622	20.7	490	16.3	742	24.7	174	5.7	669	22.1	94	3.1	127	4.2	231	7.6
Opx	374	12.5	376	12.5	290	9.7	84	2.8	0	0	0	0	0	0	0	0	0	0	0	0
Ol	8	0.3	694	23.1	406	13.5	10	0.3	7	0.3	6	0.3	5	0.3	8	0.3	7	0.3	5	0.3
Opq	20	0.7	68	2.3	56	1.9	60	2.0	23	0.4	0	0	18	0.6	34	1.1	28	0.9	32	1.1
Ap	0	0	0	0	4	0.1	6	0.2	0	0	0	0	0	0	8	0.3	2	0.1	0	0
Cal	46	1.5	10	0.3	28	0.9	34	1.1	24	0.8	0	0	86	2.9	20	0.7	20	0.7	72	2.4
Chl	44	1.5	66	2.2	42	1.4	36	1.2	26	0.9	0	0	68	2.3	24	0.8	22	0.7	70	2.3
Ep	0	0	0	0	0	0	0	0	0	0	0	0	0	0	0	0	0	0	0	0
Ttn	8	0.3	8	0.3	12	0.4	16	0.5	12	0.4	0	0	14	0.5	4	0.1	4	0.1	0	0
Total	3000	100	3000	100	3000	100	3000	100	3000	100	3000	100	3000	100	3000	100	3000	100	3000	100

No	11		12		13		14		15		16		17		18		19		20	
Sp.No	20110204		20110703-1		21020605		21020607		21020611		21021302		20110607B		20110302C		20110509A		21021308	
Litho.	Ol Gbn		Ol Gbn		Ol Gbn		Ol Gbn		Ol Gbn		Ol Gbn		Cpx Gbn-Cpx Gb		Cpx Gbn-Cpx Gb		Cpx Gb-Hb Gb		Cpx Gb-Hb Gb	
Type	2		2		2		2		2		2		3		3		3		3	
Texture	Adcumulate		Adcumulate		Adcumulate		Adcumulate		Adcumulate		Adcumulate		Orthocumulate		Orthocumulate		Orthocumulate		Orthocumulate	
mineral	count	%	count	%	count	%	count	%	count	%	count	%	count	%	count	%	count	%	count	%
Qz	0	0	0	0	0	0	0	0	0	0	0	0	134	4.5	0	0	0	0	0	0
Kfs	0	0	0	0	0	0	0	0	0	0	0	0	0	0	0	0	0	0	0	0
Pl	1688	56.3	1650	55.0	1480	49.3	1654	55.1	1260	42.0	1344	44.8	706	23.5	556	18.5	1336	44.5	1090	36.3
Hb	182	6.1	242	8.1	230	7.7	158	5.3	268	8.9	240	8.0	1884	62.8	2084	69.5	1508	50.3	1350	45.0
Bt	0	0	0	0	0	0	0	0	0	0	0	0	0	0	0	0	10	0.3	0	0
Cpx	486	16.2	552	18.4	1020	34.0	658	21.9	770	25.7	630	21.0	192	6.4	268	8.9	20	0.7	416	13.9
Opx	16	0.5	12	0.4	46	1.5	50	1.7	70	2.3	10	0.3	0	0	0	0	0	0	0	0
Ol	560	18.7	490	16.3	194	6.5	438	14.6	588	19.6	738	24.6	0	0	0	0	0	0	0	0
Opq	18	0.6	18	0.6	14	0.5	20	0.7	24	0.8	12	0.4	22	0.7	28	0.9	24	0.8	62	2.1
Ap	0	0	0	0	0	0	0	0	0	0	0	0	4	0.1	10	0.3	0	0	20	0.7
Cal	0	0	8	0.3	8	0.3	8	0.3	10	0.3	10	0.3	24	0.8	16	0.5	22	0.7	16	0.5
Chl	16	0.5	22	0.7	8	0.3	14	0.5	10	0.3	16	0.5	30	1.0	28	0.9	80	2.7	40	1.3
Ep	28	0.9	0	0	0	0	0	0	0	0	0	0	0	0	0	0	0	0	0	0
Ttn	6	0.2	6	0.2	0	0	0	0	0	0	0	0	4	0.1	10	0.3	0	0	6	0.2
Total	3000	100	3000	100	3000	100	3000	100	3000	100	3000	100	3000	100	3000	100	3000	100	3000	100

No	21		22		23		24		25		26		27		28		29		30	
Sp.No	20110402		20110403		20110505B		20110711		20110302A		21021311		21021305		20061203A		20110607C		21020606A	
Litho.	Cpx Gb-Hb Gb		Cpx Gb-Hb Gb		Cpx Gb-Hb Gb		Cpx Gb-Hb Gb		Cpx Gb-Hb Gb		Cpx Gb-Hb Gb		Cpx Gb-Hb Gb		Hb Gb-Cpx Gb		Hb Gb-Cpx Gb		Hb Gb-Cpx Gb	
Type	3		3		3		3		3		3		3		3		3		3	
Texture	Orthocumulate		Orthocumulate		Orthocumulate		Orthocumulate		Orthocumulate		Orthocumulate		Orthocumulate		Orthocumulate		Orthocumulate		Orthocumulate	
mineral	count	%	count	%	count	%	count	%	count	%	count	%	count	%	count	%	count	%	count	%
Qz	144	4.8	0	0	0	0	0	0	0	0	0	0	0	0	0	0	12	0.4	0	0
Kfs	0	0	0	0	0	0	0	0	0	0	0	0	0	0	0	0	0	0	0	0
Pl	1132	37.7	1110	37.0	986	32.9	732	24.4	878	29.3	718	23.9	1356	45.2	1430	47.7	1932	64.4	1574	52.5
Hb	1584	52.8	1590	53.0	262	8.7	1788	59.6	248	8.3	1962	65.4	1278	42.6	1374	45.8	916	30.5	1206	40.2
Bt	0	0	0	0	0	0	0	0	0	0	0	0	2	0.1	0	0	38	1.3	0	0
Cpx	40	1.3	114	3.8	1540	51.3	392	13.1	1750	58.3	176	5.9	240	8.0	170	5.7	12	0.4	128	4.3
Opx	0	0	0	0	0	0	0	0	0	0	0	0	0	0	0	0	0	0	0	0
Ol	0	0	100	3.3	120	4.0	0	0	0	0	0	0	0	0	0	0	0	0	0	0
Opq	12	0.4	14	0.5	28	0.9	8	0.3	46	1.5	28	0.9	26	0.9	14	0.5	24	0.8	14	0.5
Ap	16	0.5	4	0.1	8	0.3	6	0.2	0	0	10	0.3	6	0.2	0	0	0	0	0	0
Cal	24	0.8	30	1.0	16	0.5	22	0.7	28	0.9	40	1.3	30	1.0	0	0	0	0	30	1.0
Chl	20	0.7	30	1.0	34	1.1	44	1.5	44	1.5	44	1.5	48	1.6	12	0.4	66	2.2	38	1.3
Ep	0	0	0	0	0	0	0	0	0	0	0	0	0	0	0	0	0	0	0	0
Ttn	28	0.9	8	0.3	6	0.2	8	0.3	6	0.2	22	0.7	14	0.5	0	0	0	0	10	0.3
Total	3000	100	3000	100	3000	100	3000	100	3000	100	3000	100	3000	100	3000	100	3000	100	3000	100

Gbn: gabbronorite, Hd: hornblendite, Gb: gabbro, Tdh: trondhjemite, Gr: granite, and PFD: Porphyritic fine-grained diorite.

Continued…

No	31		32		33		34		35		36		37		38		39		40	
Sp.No	21020610		21020701		21020702A		21020703		21020704A		21021303A		21021309A		21021405A		20110205		20110506	
Litho.	Hb Gb-Cpx Gb		Hb Gb-Cpx Gb		Hb Gb-Cpx Gb		Hb Gb-Cpx Gb		Hb Gb-Cpx Gb		Hb Gb-Cpx Gb		Hb Gb-Cpx Gb		Hb Gb-Cpx Gb		Hb Gb-Cpx Gb		Hb Gb-Cpx Gb	
Type	3		3		3		3		3		3		3		3		3		3	
Texture	Orthocumulate		Orthocumulate		Orthocumulate		Orthocumulate		Orthocumulate		Orthocumulate		Orthocumulate		Orthocumulate		Orthocumulate		Orthocumulate	
mineral	count	%	count	%	count	%	count	%	count	%	count	%	count	%	count	%	count	%	count	%
Qz	0	0	4	0.1	0	0	0	0	0	0	0	0	0	0	0	0	0	0	0	0
Kfs	0	0	0	0	0	0	0	0	0	0	0	0	0	0	0	0	0	0	0	0
Pl	1364	45.5	882	29.4	1526	50.9	1352	45.1	1294	43.1	1460	48.7	1560	52.0	1282	42.7	1204	40.1	2004	66.8
Hb	1342	44.7	1856	61.9	1260	42.0	1058	35.3	1246	41.5	1318	43.9	1172	39.1	1150	38.3	1020	34.0	690	23.0
Bt	0	0	0	0	30	1.0	6	0.2	2	0.1	14	0.5	2	0.1	8	0.3	0	0	0	0
Cpx	110	3.7	68	2.3	72	2.4	404	13.5	330	11.0	108	3.6	154	5.1	466	15.5	606	20.2	174	5.8
Opx	0	0	0	0	0	0	0	0	0	0	0	0	0	0	0	0	0	0	0	0
Ol	0	0	0	0	0	0	2	0.1	0	0	0	0	0	0	0	0	0	0	0	0
Opq	30	1.0	44	1.5	14	0.5	28	0.9	30	1.0	26	0.9	30	1.0	6	0.2	22	0.7	26	0.9
Ap	0	0	0	0	16	0.5	22	0.7	2	0.1	8	0.3	10	0.3	14	0.5	34	1.1	6	0.2
Cal	64	2.1	48	1.6	24	0.8	48	1.6	38	1.3	20	0.7	38	1.3	26	0.9	40	1.3	40	1.3
Chl	78	2.6	70	2.3	36	1.2	68	2.3	46	1.5	36	1.2	26	0.9	32	1.1	66	2.2	46	1.5
Ep	0	0	0	0	0	0	0	0	0	0	0	0	0	0	0	0	0	0	0	0
Ttn	12	0.4	28	0.9	22	0.7	12	0.4	12	0.4	10	0.3	8	0.3	16	0.5	8	0.3	14	0.5
Total	3000	100	3000	100	3000	100	3000	100	3000	100	3000	100	3000	100	3000	100	3000	100	3000	100

No	41		42		43		44		45		46		47		48		49		50	
Sp.No	20110603		20110704		20110709A		200612T04		20110306		20110511		20110604		20110707		20110802		21021306	
Litho.	Hb Gb-Cpx Gb		Hb Gb-Cpx Gb		Hb Gb-Cpx Gb		Hb Gb-Cpx Gb		Hb Gb-Cpx Gb		Hb Gb-Cpx Gb		Hb Gb-Cpx Gb		Hb Gb-Cpx Gb		Hb Gb-Cpx Gb		Hb Gb-Cpx Gb	
Type	3		3		3		3		3		3		3		3		3		3	
Texture	Orthocumulate		Orthocumulate		Orthocumulate		Orthocumulate		Orthocumulate		Orthocumulate		Orthocumulate		Orthocumulate		Orthocumulate		Orthocumulate	
mineral	count	%	count	%	count	%	count	%	count	%	count	%	count	%	count	%	count	%	count	%
Qz	0	0	0	0	0	0	0	0	0	0	2	0.1	0	0	0	0	0	0	0	0
Kfs	0	0	0	0	0	0	0	0	0	0	0	0	0	0	0	0	0	0	0	0
Pl	1052	35.1	1150	38.3	1312	43.7	1428	47.6	1590	53.0	1450	48.3	1906	63.5	1362	45.4	1454	48.5	1458	48.6
Hb	1454	48.5	1614	53.8	1448	48.3	784	26.1	1200	40.0	1416	47.2	984	32.8	1278	42.6	972	32.4	1240	41.3
Bt	0	0	0	0	0	0	0	0	0	0	2	0.1	6	0.2	0	0	0	0	48	1.6
Cpx	360	12.0	136	4.5	156	5.2	664	22.1	60	2.0	16	0.5	62	2.1	220	7.3	456	15.2	108	3.6
Opx	0	0	0	0	0	0	0	0	0	0	0	0	0	0	0	0	0	0	0	0
Ol	0	0	0	0	0	0	0	0	0	0	0	0	0	0	0	0	0	0	0	0
Opq	32	1.1	18	0.6	22	0.7	16	0.5	30	1.0	8	0.3	12	0.4	30	1.0	12	0.4	54	1.8
Ap	30	1.0	20	0.7	12	0.4	24	0.8	30	1.0	8	0.3	10	0.3	16	0.5	8	0.3	8	0.3
Cal	28	0.9	26	0.9	22	0.7	40	1.3	38	1.3	0	0	0	0	36	1.2	38	1.3	28	0.9
Chl	34	1.1	26	0.9	20	0.7	38	1.3	42	1.4	98	3.3	20	0.7	44	1.5	52	1.7	40	1.3
Ep	0	0	0	0	0	0	0	0	0	0	0	0	0	0	0	0	0	0	0	0
Ttn	10	0.3	10	0.3	8	0.3	6	0.2	10	0.3	0	0	0	0	14	0.5	8	0.3	16	0.5
Total	3000	100	3000	100	3000	100	3000	100	3000	100	3000	100	3000	100	3000	100	3000	100	3000	100

No	51		52		53		54		55		56		57		58		59		60	
Sp.No	20061203C		20110510		20110605		20110804		20110805		21021401		21021402		21021403		21021404A		20110308	
Litho.	Hb Gb		Hb Gb		Hb Gb		Hb Gb		Hb Gb		Hb Gb		Hb Gb		Hb Gb		Hb Gb		Hb Gb	
Type	4		4		4		4		4		4		4		4		4		5	
Texture	Adcum, layered		Adcum, layered		Adcum, layered		Adcum, layered		Adcum, layered		Adcum, layered		Adcum, layered		Adcum, layered		Adcum, layered		Fine, Foliated	
mineral	count	%	count	%	count	%	count	%	count	%	count	%	count	%	count	%	count	%	count	%
Qz	0	0	0	0	0	0	0	0	4	0.1	0	0	0	0	0	0	0	0	12	0.4
Kfs	0	0	0	0	0	0	0	0	0	0	0	0	0	0	0	0	0	0	0	0
Pl	1082	36.1	1466	48.9	1562	52.1	1796	59.9	1432	47.7	1290	43.0	1300	43.3	1336	44.5	1388	46.3	1688	56.3
Hb	1864	62.1	1370	45.7	1316	43.9	1076	35.9	1474	49.1	1558	51.9	1500	50.0	1538	51.3	1462	48.7	1120	37.3
Bt	0	0	6	0.2	4	0.1	4	0.1	2	0.1	62	2.1	106	3.5	52	1.7	74	2.5	14	0.5
Cpx	20	0.7	26	0.9	28	0.9	10	0.3	14	0.5	30	1.0	24	0.8	22	0.7	24	0.8	4	0.1
Opx	0	0	0	0	0	0	0	0	0	0	0	0	0	0	0	0	0	0	0	0
Ol	0	0	0	0	0	0	0	0	0	0	0	0	0	0	0	0	0	0	0	0
Opq	22	0.7	102	3.4	36	1.2	76	2.5	40	1.3	56	1.9	32	1.1	30	1.0	38	1.3	108	3.6
Ap	0	0	14	0.5	0	0	0	0	4	0.1	0	0	0	0	0	0	0	0	10	0.3
Cal	0	0	0	0	0	0	0	0	0	0	0	0	12	0.4	8	0.3	4	0.1	8	0.3
Chl	12	0.4	16	0.5	54	1.8	38	1.3	30	1.0	0	0	20	0.7	6	0.2	4	0.1	36	1.2
Ep	0	0	0	0	0	0	0	0	0	0	0	0	0	0	0	0	0	0	0	0
Ttn	0	0	0	0	0	0	0	0	0	0	4	0.1	6	0.2	8	0.3	6	0.2	0	0
Total	3000	100	3000	100	3000	100	3000	100	3000	100	3000	100	3000	100	3000	100	3000	100	3000	100

Gbn: gabbronorite, Hd: hornblendite, Gb: gabbro, Tdh: trondhjemite, Gr: granite, and PFD: Porphyritic fine-grained diorite.

Continued…

No	61		62		63		64		65		66		67		68		69		70	
Sp.No	20110312		20110312		21020603A		21021301A		21021407B		21021408A		21021409		21021409		20061203B		20110303	
Litho.	Hb Gb		Hb Gb		Hb Gb		Hb Gb		Hb Gb		Hb Gb		Hb Gb		Hb Gb		Hb Gb		Hb Gb	
Type	5		5		5		5		5		5		5		5		6		6	
Texture	Fine, Foliated		Fine, Foliated		Fine, Foliated		Fine, Foliated		Fine, Foliated		Fine, Foliated		Fine, Foliated		Fine, Foliated		Mixing		Mixing	
mineral	count	%	count	%	count	%	count	%	count	%	count	%	count	%	count	%	count	%	count	%
Qz	10	0.3	0	0	0	0	0	0	0	0	0	0	0	0	0	0	2	0.1	6	0.2
Kfs	0	0	0	0	0	0	0	0	0	0	0	0	0	0	0	0	0	0	0	0
Pl	1472	49.1	1620	54.0	1686	56.2	1584	52.8	1284	42.8	1588	52.9	1284	42.8	1288	42.9	1666	55.5	1346	44.9
Hb	1424	47.5	1156	38.5	1122	37.4	1126	37.5	1014	33.8	1234	41.1	1530	51.0	1504	50.1	1180	39.3	1544	51.5
Bt	8	0.3	0	0	0	0	76	2.5	630	21.0	46	1.5	50	1.7	80	2.7	2	0.1	0	0
Cpx	10	0.3	12	0.4	20	0.7	16	0.5	12	0.4	20	0.7	26	0.9	18	0.6	104	3.5	54	1.8
Opx	0	0	0	0	0	0	0	0	0	0	0	0	0	0	0	0	0	0	0	0
Ol	2	0.1	0	0	0	0	0	0	0	0	0	0	0	0	0	0	0	0	0	0
Opq	36	1.2	102	3.4	90	3.0	122	4.1	50	1.7	56	1.9	66	2.2	72	2.4	12	0.4	14	0.5
Ap	14	0.5	46	1.5	0	0	8	0.3	2	0.1	6	0.2	6	0.2	4	0.1	0	0	14	0.5
Cal	10	0.3	28	0.9	34	1.1	22	0.7	4	0.1	16	0.5	14	0.5	10	0.3	2	0.1	0	0
Chl	14	0.5	28	0.9	34	1.1	36	1.2	2	0.1	28	0.9	16	0.5	12	0.4	26	0.9	12	0.4
Ep	0	0	0	0	0	0	0	0	0	0	0	0	0	0	0	0	0	0	0	0
Ttn	0	0	8	0.3	14	0.5	10	0.3	2	0.1	6	0.2	8	0.3	12	0.4	6	0.2	10	0.3
Total	3000	100	3000	100	3000	100	3000	100	3000	100	3000	100	3000	100	3000	100	3000	100	3000	100

No	71		72		73		74		75		76		77		78		79		80	
Sp.No	20110303		20110401A		20110806		21021307		20110509B		200612T03		20110606A		20110309		201103011-1		20110602B	
Litho.	Hb Gb		Hb Gb		Hb Gb		Hb Gb		Hb Gb		Hb Gb		Hb Gb		Ms-Bt Tdh		Ms-Bt Tdh		Ms-Bt Tdh	
Type	6		6		6		6		7		7		7		-		-		-	
Texture	Mixing		Mixing		Mixing		Mixing		Pegmatitic		Pegmatitic		Pegmatitic		dike		dike		dike	
mineral	count	%	count	%	count	%	count	%	count	%	count	%	count	%	count	%	count	%	count	%
Qz	12	0.4	4	0.1	0	0	0	0	6	0.2	0	0	0	0	617	41.1	550	36.7	568	37.9
Kfs	0	0	0	0	0	0	0	0	0	0	0	0	0	0	6	0.4	21	1.4	83	5.5
Pl	1396	46.5	1178	39.3	930	31.0	1670	55.7	2112	70.4	990	33.0	1894	63.1	739	49.3	726	48.4	645	43.0
Hb	1508	50.3	1701	56.7	1782	59.4	918	30.6	726	24.2	1846	61.5	1006	33.5	0	0	0	0	0	0
Bt	12	0.4	16	0.5	0	0	98	3.3	10	0.3	0	0	0	0	99	6.6	169	11.3	141	9.4
Cpx	8	0.3	5	0.2	142	4.7	146	4.9	82	2.7	164	5.5	50	1.7	5	0.3	1	0.1	44	2.9
Opx	0	0	0	0	0	0	0	0	0	0	0	0	0	0	0	0	0	0	0	0
Ol	0	0	0	0	0	0	0	0	0	0	0	0	0	0	0	0	0	0	0	0
Opq	20	0.7	28	0.9	52	1.7	60	2.0	12	0.4	0	0	10	0.3	18	1.2	6	0.4	5	0.3
Ap	14	0.5	16	0.5	4	0.1	10	0.3	0	0	0	0	0	0	5	0.3	9	0.6	3	0.2
Cal	8	0.3	16	0.5	34	1.1	30	1.0	0	0	0	0	0	0	0	0	0	0	0	0
Chl	22	0.7	36	1.2	50	1.7	58	1.9	52	1.7	0	0	40	1.3	8	0.5	9	0.6	6	0.4
Ep	0	0	0	0	0	0	0	0	0	0	0	0	0	0	0	0	0	0	0	0
Ttn	0	0	0	0	6	0.2	10	0.3	0	0	0	0	0	0	3	0.2	9	0.6	5	0.3
Total	3000	100	3000	100	3000	100	3000	100	3000	100	3000	100	3000	100	1500	100	1500	100	1500	100

No	81		82		83		84		85		86		87		88		89		90	
Sp.No	20110606B		20110709B		20110313		20110607D		20110807C		21020603B		21020602B-2		21020604B		21020606B		21020704B	
Litho.	Ms-Bt Tdh		Ms-Bt Tdh		Bt Tdh		Bt Tdh		Bt Tdh		Bt Tdh		Bt Gr		Bt Gr		Bt Gr		Bt Gr	
Type	-		-		-		-		-		-		-		-		-		-	
Texture	dike		dike		dike		dike		dike		dike		felsic rich		felsic rich		felsic rich		felsic rich	
mineral	count	%	count	%	count	%	count	%	count	%	count	%	count	%	count	%	count	%	count	%
Qz	622	41.5	483	32.2	420	28.0	570	38.0	428	28.5	468	31.2	474	31.6	386	25.7	463	30.9	435	29.0
Kfs	117	7.8	113	7.5	83	5.5	24	1.6	69	4.6	115	7.7	242	16.1	293	19.5	327	21.8	162	10.8
Pl	524	34.9	818	54.5	942	62.8	836	55.7	773	51.5	770	51.3	671	44.7	655	43.7	612	40.8	679	45.3
Hb	0	0	0	0	0	0	0	0	0	0	0	0	0	0	0	0	0	0	0	0
Bt	201	13.4	52	3.5	46	3.1	65	4.3	221	14.7	109	7.3	98	6.5	143	9.5	59	3.9	212	14.1
Cpx	14	0.9	22	1.5	2	0.1	0	0	3	0.2	4	0.3	6	0.4	3	0.2	3	0.2	5	0.3
Opx	0	0	0	0	0	0	0	0	0	0	0	0	0	0	0	0	0	0	0	0
Ol	0	0	0	0	0	0	0	0	0	0	0	0	0	0	0	0	0	0	0	0
Opq	2	0.1	0	0	1	0.1	2	0.1	2	0.1	0	0	1	0.1	0	0	0	0	0	0
Ap	4	0.3	0	0	0	0	0	0	0	0	2	0.1	0	0	1	0.1	5	0.3	0	0
Cal	4	0.3	4	0.3	5	0.3	0	0	0	0	9	0.6	3	0.2	4	0.3	9	0.6	0	0
Chl	7	0.5	8	0.5	1	0.1	0	0	4	0.3	23	1.5	4	0.3	12	0.8	18	1.2	5	0.3
Ep	0	0	0	0	0	0	0	0	0	0	0	0	0	0	0	0	0	0	0	0
Ttn	5	0.3	0	0	0	0	3	0.2	0	0	0	0	1	0.1	3	0.2	4	0.3	2	0.1
Total	1500	100	1500	100	1500	100	1500	100	1500	100	1500	100	1500	100	1500	100	1500	100	1500	100

Gbn: gabbronorite, Hd: hornblendite, Gb: gabbro, Tdh: trondhjemite, Gr: granite, and PFD: Porphyritic fine-grained diorite.

Continued…

No	91		92		93		94		95		96		97		98	
Sp.No	21021301B		21021404B		21021407C-1		21021408B-2		20110405		20110709C		201103011-2		20110404	
Litho.	Bt Gr		Bt Gr		Bt Gr		Bt Gr		PFD		PFD		PFD		Gb vein	
Type	-		-		-		-		-		-		-		-	
Texture	felsic rich		felsic rich vein		felsic rich		felsic rich		Composite dike		Composite dike		Composite dike		Pl rich	
mineral	count	%	count	%	count	%	count	%	count	%	count	%	count	%	count	%
Qz	520	34.7	520	34.7	505	33.7	570	38.0	7	0.5	116	7.7	0	0	36	2.4
Kfs	281	18.7	16	1.1	403	26.9	179	11.9	0	0	0	0	0	0	0	0
Pl	634	42.3	826	55.1	486	32.4	619	41.3	670	44.7	753	50.2	672	44.8	1084	72.3
Hb	0	0	0	0	0	0	0	0	523	34.9	240	16.0	549	36.6	216	14.4
Bt	45	3.0	109	7.3	75	5.0	94	6.3	269	17.9	378	25.2	257	17.1	59	3.9
Cpx	0	0	2	0.1	2	0.1	1	0.1	11	0.7	3	0.2	4	0.3	2	0.1
Opx	0	0	0	0	0	0	0	0	0	0	0	0	6	0.4	0	0
Ol	0	0	0	0	0	0	0	0	0	0	0	0	0	0	0	0
Opq	0	0	0	0	0	0	0	0	0	0	0	0	0	0	0	0
Ap	4	0.3	6	0.4	3	0.2	4	0.3	0	0	0	0	0	0	0	0
Cal	0	0	7	0.5	5	0.3	8	0.5	0	0	0	0	0	0	26	1.7
Chl	12	0.8	12	0.8	13	0.9	23	1.5	17	1.1	10	0.7	7	0.5	62	4.1
Ep	0	0	0	0	4	0.3	0	0	0	0	0	0	0	0	0	0
Ttn	4	0.3	2	0.1	4	0.3	2	0.1	3	0.2	0	0	5	0.3	15	1.0
Total	1500	100	1500	100	1500	100	1500	100	1500	100	1500	100	1500	100	1500	100

Gbn: gabbronorite, Hd: hornblendite, Gb: gabbro, Tdh: trondhjemite, Gr: granite, and PFD: Porphyritic fine-grained diorite.

Appendix 5–2. Stereomicroscope whole images of the measured zircon grains.

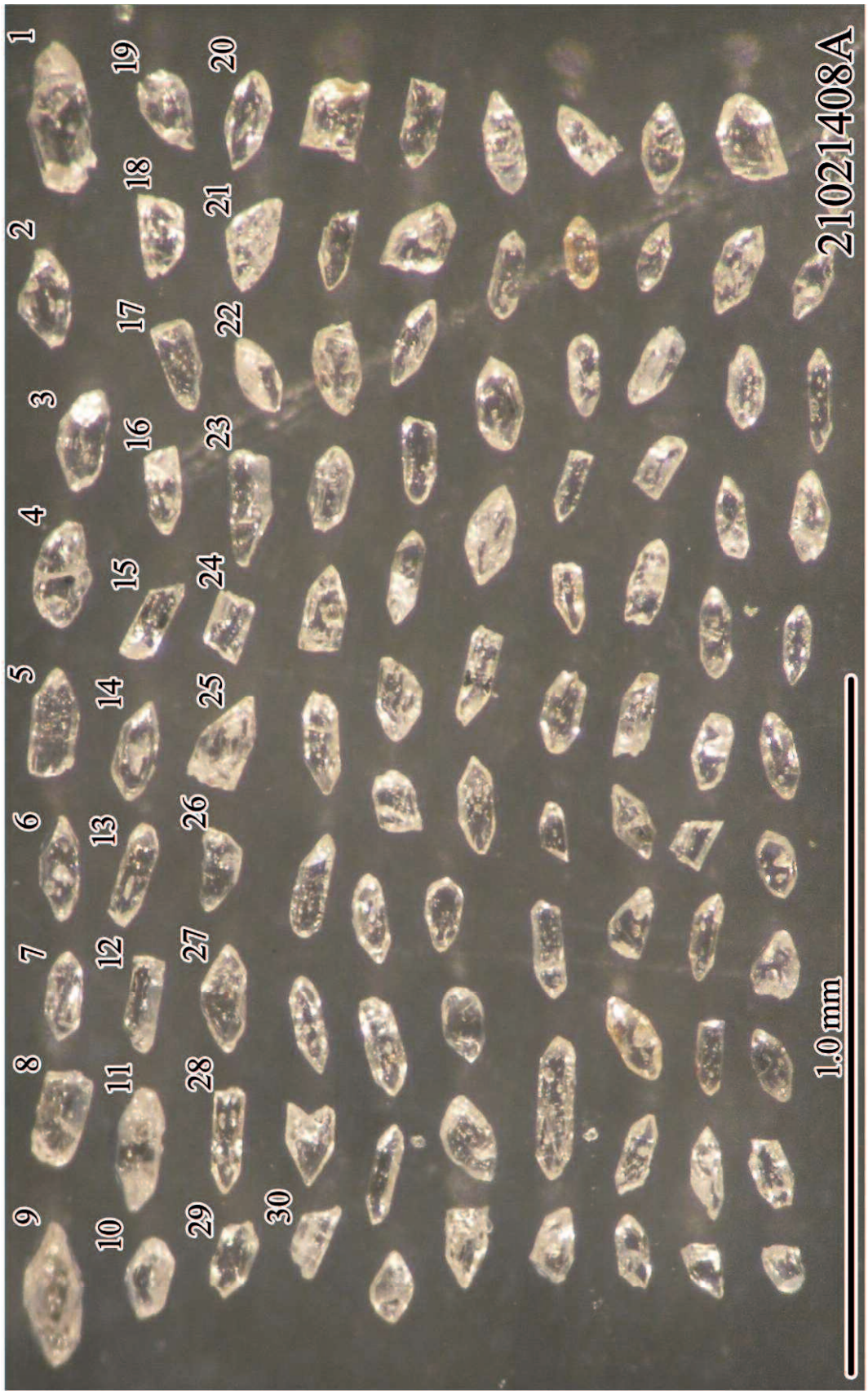

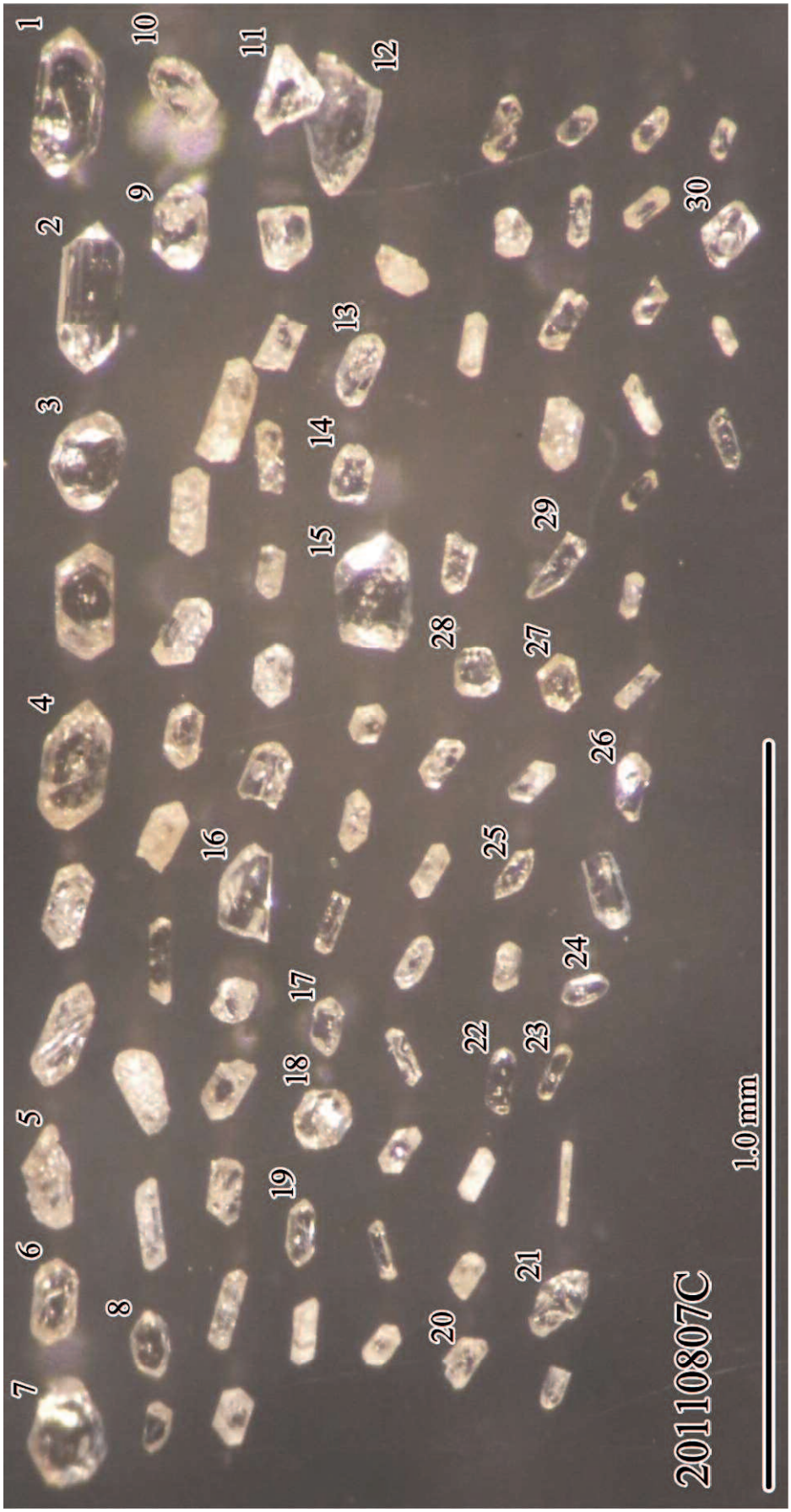
1
2
3
4
5
6
7
8
9
10
11
12
13
14
15
16
17
18
19
20
21
22
23
24
25
26
27
28
29
30
20110807C
1.0 mm

Appendix 5–3. Reflected microscope whole images of the measured zircon grains.

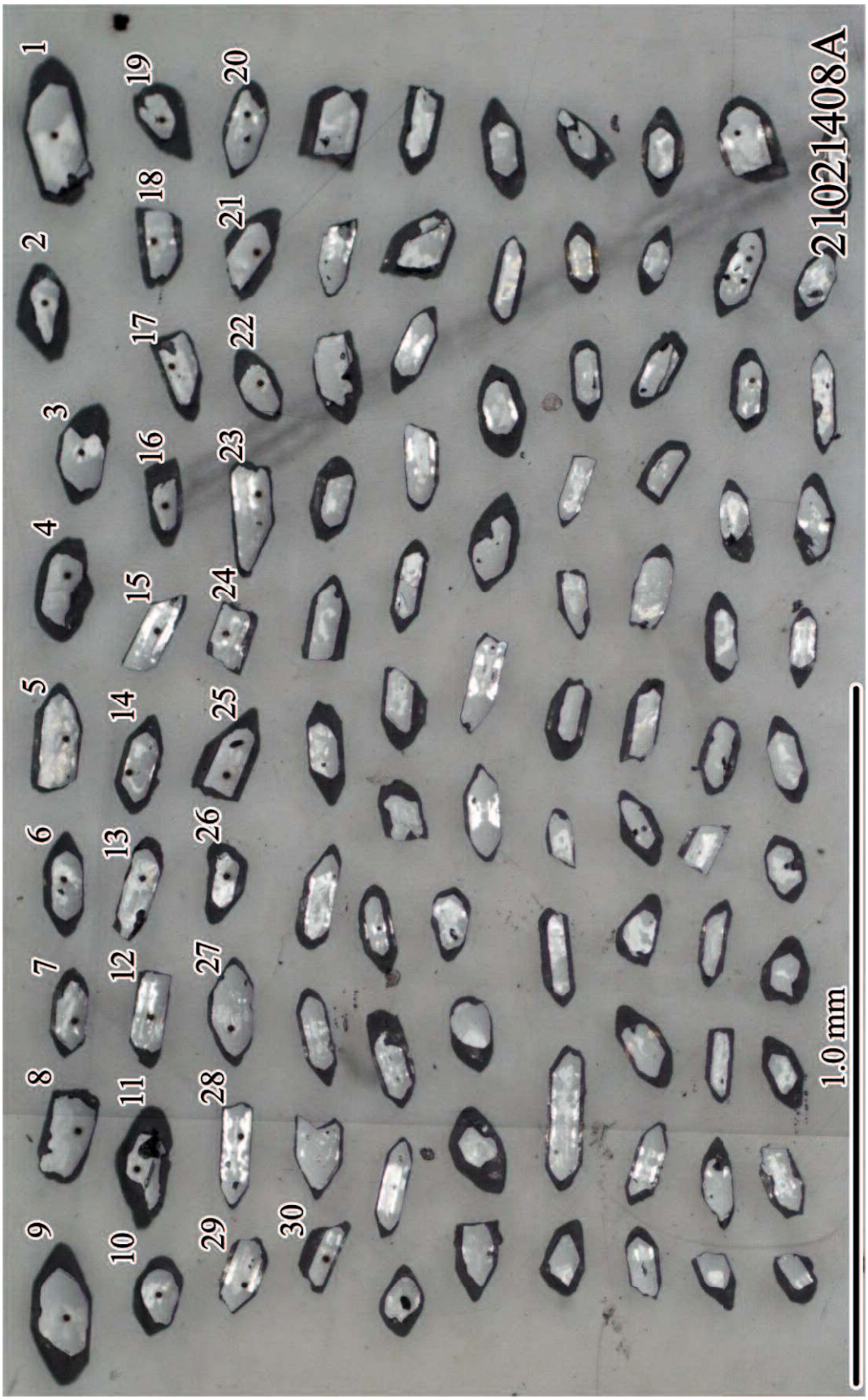

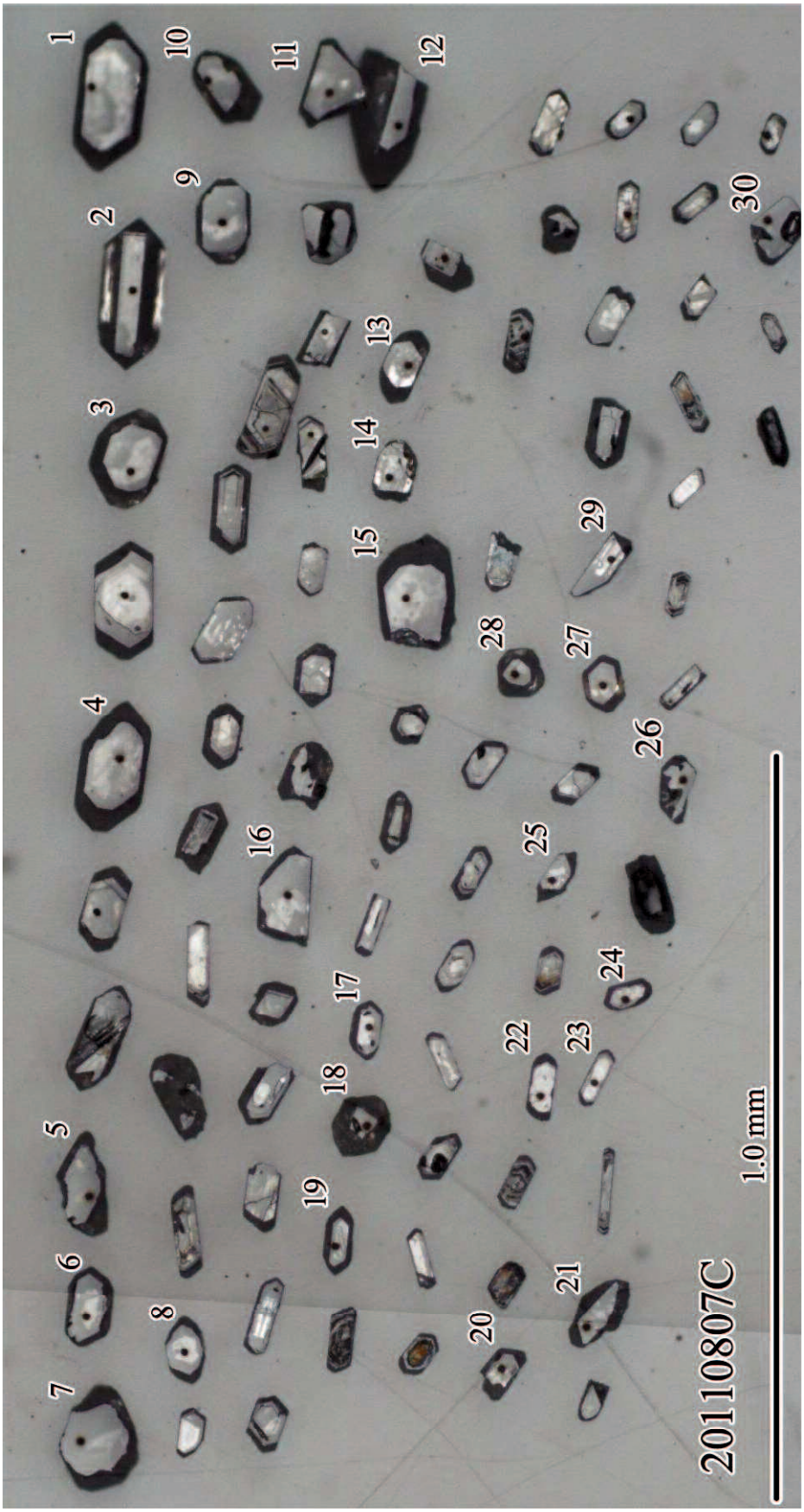
1
2
3
4
5
6
7
8
9
10
11
12
13
14
15
16
17
18
19
20
21
22
23
24
25
26
27
28
29
30
20110807C
1.0 mm

Appendix 5–4. U–Pb isotopic data of the zircon grains from 21021408A and 20110807C.

Sp. No. 21021407A Type.5 Foliated Hb gabbro

No	Grain No.	Total count ^{206}Pb	^{207}Pb	^{232}Th	^{235}U	^{238}U	Th/U	Isotopic ratios $^{207}Pb/^{206}Pb$	Error 2σ	$^{206}Pb/^{238}U$	Error 2σ	$^{207}Pb/^{235}U$	Error 2σ	Disc.*	Without correction U-Pb age (Ma) $^{206}Pb/^{238}U$	Error 2σ	$^{207}Pb/^{235}U$	Error 2σ	^{232}Th-^{208}Pb age (Ma) $^{208}Pb/^{232}Th$	Error 2σ	Pb-Pb age (Ma) $^{207}Pb/^{206}Pb$	Error 2σ	U(ppm)	Th(ppm)	rho
1	no.1	21119	1452	414313	12312	1697639	0.39	0.0497 ±	0.0040	0.0163 ±	0.0004	0.1115 ±	0.0082	concordant	103.9 ±	2.7	107.3 ±	8.3	98.9 ±	20.2	181.5 ±	185.6	237	92	0.35
2	no.2	7004	487	121958	4012	553213	0.35	0.0502 ±	0.0055	0.0165 ±	0.0007	0.1147 ±	0.0123	concordant	105.8 ±	4.4	110.3 ±	12.4	110.9 ±	23.8	206.4 ±	256.1	77	27	0.39
3	no.3	7837	576	131069	4428	610556	0.34	0.0531 ±	0.0055	0.0168 ±	0.0007	0.1229 ±	0.0124	concordant	107.2 ±	4.3	117.7 ±	12.5	109.7 ±	23.5	332.8 ±	236.3	85	29	0.39
4	no.4	15192	1076	402335	8667	1194947	0.53	0.0512 ±	0.0044	0.0166 ±	0.0005	0.1174 ±	0.0094	concordant	106.2 ±	3.2	112.7 ±	9.5	100.9 ±	20.7	250.4 ±	197.7	167	89	0.37
5	no.5	12509	876	338741	7245	998876	0.54	0.0506 ±	0.0046	0.0164 ±	0.0005	0.1143 ±	0.0098	concordant	104.6 ±	3.4	109.9 ±	9.9	98.8 ±	20.3	222.8 ±	210.5	139	75	0.37
6	no.6	11556	952	243663	6945	957553	0.40	0.0576 ±	0.0051	0.0163 ±	0.0005	0.1296 ±	0.0109	-5	104.3 ±	3.4	123.7 ±	11.0	111.7 ±	23.2	513.2 ±	195.7	133	54	0.39
7	no.7	20102	1307	579808	11334	1562731	0.59	0.0470 ±	0.0038	0.0168 ±	0.0004	0.1090 ±	0.0082	concordant	107.4 ±	2.9	105.0 ±	8.3	99.0 ±	20.1	48.3 ±	194.9	218	128	0.35
8	no.8	10424	744	255715	5824	802973	0.51	0.0516 ±	0.0049	0.0170 ±	0.0006	0.1208 ±	0.0110	concordant	108.4 ±	3.8	115.8 ±	11.1	100.5 ±	20.9	267.6 ±	219.5	112	57	0.38
9	no.9	11579	854	224355	6685	921747	0.39	0.0496 ±	0.0051	0.0165 ±	0.0005	0.1131 ±	0.0117	concordant	105.7 ±	3.4	108.8 ±	11.8	78.4 ±	24.0	177.2 ±	240.1	131	51	0.30
10	no.10	16584	1186	663351	9598	1323390	0.80	0.0481 ±	0.0046	0.0165 ±	0.0004	0.1094 ±	0.0105	concordant	105.4 ±	2.8	105.5 ±	10.6	73.6 ±	22.2	105.0 ±	226.4	188	150	0.28
11	no.11	14564	1088	369452	8279	1141513	0.52	0.0503 ±	0.0049	0.0168 ±	0.0005	0.1165 ±	0.0114	concordant	107.3 ±	3.1	111.9 ±	11.5	78.3 ±	23.8	208.5 ±	226.2	162	84	0.29
12	no.12	18254	1191	401819	10072	1388713	0.46	0.0439 ±	0.0042	0.0173 ±	0.0004	0.1048 ±	0.010[illegible]	concordant	110.5 ±	2.9	101.2 ±	10.2	74.6 ±	22.6	-115.1 ±	235.6	197	91	0.27
13	no.13	6722	514	145541	3817	526238	0.44	0.0515 ±	0.0061	0.0168 ±	0.0007	0.1194 ±	0.0143	concordant	107.4 ±	4.5	114.5 ±	14.4	76.7 ±	23.7	263.7 ±	271.0	75	33	0.34
14	no.14	16285	1080	326371	9222	1271528	0.41	0.0446 ±	0.0044	0.0168 ±	0.0005	0.1038 ±	0.0102	concordant	107.7 ±	2.9	100.2 ±	10.3	82.3 ±	25.0	-75.4 ±	238.6	181	74	0.28
15	no.15	39578	2760	1628275	23078	3181936	0.81	0.0469 ±	0.0040	0.0164 ±	0.0003	0.1059 ±	0.0089	concordant	104.6 ±	1.9	102.2 ±	9.0	73.3 ±	22.0	45.3 ±	201.6	452	368	0.21
16	no.16	8853	629	231046	5058	697440	0.53	0.0478 ±	0.0053	0.0167 ±	0.0006	0.1101 ±	0.0124	concordant	106.8 ±	3.9	106.1 ±	12.5	84.2 ±	25.7	88.8 ±	263.8	99	52	0.32
17	no.17	30865	2064	1211833	17826	2457799	0.78	0.0450 ±	0.0039	0.0165 ±	0.0003	0.1026 ±	0.0089	concordant	105.6 ±	2.1	99.2 ±	9.0	73.4 ±	22.1	-55.2 ±	212.8	349	274	0.23
18	no.18	20651	1406	600336	11916	1642984	0.58	0.0458 ±	0.0042	0.0165 ±	0.0004	0.1045 ±	0.0097	concordant	105.7 ±	2.6	100.9 ±	9.8	75.8 ±	22.9	-12.3 ±	224.1	233	136	0.26
19	no.19	38183	2574	1822954	22074	3043608	0.95	0.0454 ±	0.0039	0.0165 ±	0.0003	0.1033 ±	0.0088	concordant	105.5 ±	2.0	99.8 ±	8.8	74.5 ±	22.4	-36.0 ±	206.3	432	412	0.22
20	no.20	41689	2768	1913303	23782	3279087	0.93	0.0447 ±	0.0038	0.0167 ±	0.0003	0.1031 ±	0.0087	concordant	106.9 ±	1.9	99.6 ±	8.8	73.5 ±	22.1	-73.0 ±	206.1	466	433	0.21
21	no.21	6039	527	129119	3528	486438	0.42	0.0587 ±	0.0069	0.0163 ±	0.0007	0.1322 ±	0.0157	-1	104.4 ±	4.5	126.1 ±	15.9	82.6 ±	25.6	555.6 ±	256.5	69	29	0.36
22	no.22	9422	696	178824	5556	766070	0.37	0.0497 ±	0.0054	0.0162 ±	0.0006	0.1110 ±	0.012[illegible]	concordant	103.5 ±	3.6	106.9 ±	12.2	82.7 ±	25.4	181.9 ±	252.4	109	40	0.32
23	no.23	15227	1094	340274	8987	1239085	0.44	0.0483 ±	0.0047	0.0162 ±	0.0004	0.1078 ±	0.0105	concordant	103.4 ±	2.9	103.9 ±	10.6	75.0 ±	22.8	115.5 ±	229.7	176	77	0.28
24	no.24	13780	964	288305	7927	1092967	0.42	0.0493 ±	0.0069	0.0166 ±	0.0005	0.1131 ±	0.0167	concordant	106.3 ±	3.4	108.8 ±	16.8	93.7 ±	49.0	161.7 ±	328.7	157	66	0.22
25	no.25	6215	472	89129	3599	496256	0.29	0.0535 ±	0.0084	0.0165 ±	0.0007	0.1219 ±	0.0199	concordant	105.6 ±	4.7	116.8 ±	20.0	101.3 ±	53.4	350.0 ±	353.3	71	20	0.27
26	no.26	7590	529	135024	4700	647985	0.33	0.0466 ±	0.0071	0.0163 ±	0.0006	0.1046 ±	0.0167	concordant	104.0 ±	4.1	101.0 ±	16.8	101.5 ±	53.3	28.8 ±	366.6	93	31	0.25
27	no.27	56549	3860	3363963	33053	4557378	1.18	0.0481 ±	0.0062	0.0164 ±	0.0003	0.1086 ±	0.0147	concordant	104.7 ±	2.1	104.7 ±	14.8	84.6 ±	44.0	102.9 ±	302.9	653	770	0.15
28	no.28	43194	2933	2082991	25151	3467832	0.96	0.0478 ±	0.0062	0.0164 ±	0.0004	0.1084 ±	0.0148	concordant	105.1 ±	2.3	104.5 ±	14.9	83.9 ±	43.6	91.0 ±	306.8	497	477	0.16
29	no.29	27699	1954	774690	15951	2199330	0.56	0.0497 ±	0.0066	0.0166 ±	0.0004	0.1139 ±	0.0159	concordant	106.2 ±	2.6	109.5 ±	16.0	87.9 ±	45.8	179.9 ±	308.4	315	177	0.18
30	no.30	10008	688	273521	5925	816903	0.54	0.0485 ±	0.0071	0.0162 ±	0.0006	0.1080 ±	0.0166	concordant	103.4 ±	3.7	104.2 ±	16.7	87.1 ±	45.5	121.4 ±	345.6	117	63	0.23
Standards																									
	91500 10-3	65292	6943	113753	3367	464180	0.39	0.0749 ±	0.0095	0.1856 ±	0.00710	1.9174 ±	0.2635	concordant	1097.4 ±	45.6	1087.2 ±	237.6	896.2 ±	470.7	1065.7 ±	253.9	67	26	0.28
	91500 10-4	63694	6648	100652	3321	457837	0.35	0.0735 ±	0.0093	0.1835 ±	0.00707	1.8613 ±	0.2562	concordant	1086.3 ±	45.4	1067.4 ±	231.6	953.7 ±	501.3	1028.0 ±	255.6	66	23	0.28
	91500 10-5	65898	6963	114117	3393	467794	0.39	0.0744 ±	0.0094	0.1859 ±	0.00709	1.9081 ±	0.2622	concordant	1098.9 ±	45.5	1083.9 ±	236.5	895.0 ±	470.0	1052.9 ±	254.4	67	26	0.28
	91500 10-6	64601	6847	109016	3430	472951	0.37	0.0746 ±	0.0094	0.1802 ±	0.00685	1.8558 ±	0.2550	concordant	1068.1 ±	44.0	1065.5 ±	230.7	894.7 ±	469.9	1059.1 ±	254.3	68	25	0.28

Sp. No. 20110807C Tdh dike

No	Grain No.	Total count					Th/U	Isotopic ratios									Disc.*	Without correction U-Pb age (Ma)						^{232}Th-^{208}Pb age (Ma)			Pb-Pb age (Ma)			U(ppm)	Th(ppm)	rho
		^{206}Pb	^{207}Pb	^{232}Th	^{235}U	^{238}U		^{207}Pb/^{206}Pb	±	Error 2σ	^{206}Pb/^{238}U	±	Error 2σ	^{207}Pb/^{235}U	±	Error 2σ		^{206}Pb/^{238}U	±	Error 2σ	^{207}Pb/^{235}U	±	Error 2σ	^{208}Pb/^{232}Th	±	Error 2σ	^{207}Pb/^{206}Pb	±	Error 2σ			
1	no.1	10615	810	496067	6108	842113	0.93	0.0546	±	0.0066	0.0166	±	0.0006	0.1247	±	0.0170	concordant	105.9	±	4.1	119.3	±	17.1	96.0	±	29.3	396.5	±	270.9	120	112	0.29
2	no.2	171143	11146	3933127	99068	13659491	0.46	0.0466	±	0.0046	0.0165	±	0.0004	0.1058	±	0.0122	concordant	105.2	±	2.5	102.1	±	12.3	92.9	±	28.1	29.7	±	235.7	1941	885	0.20
3	no.3	43417	2822	1041994	24896	3432680	0.48	0.0465	±	0.0048	0.0166	±	0.0004	0.1066	±	0.0128	concordant	106.2	±	2.9	102.9	±	13.0	96.2	±	29.2	25.3	±	249.3	488	234	0.22
4	no.4	35939	2355	1743071	20507	2827516	0.98	0.0469	±	0.0049	0.0167	±	0.0005	0.1080	±	0.0131	concordant	106.7	±	3.0	104.2	±	13.3	92.7	±	28.0	44.7	±	251.8	402	392	0.23
5	no.5	119170	8034	2214031	68618	9461015	0.37	0.0483	±	0.0048	0.0165	±	0.0004	0.1101	±	0.0128	concordant	105.8	±	2.5	106.1	±	12.9	95.1	±	28.8	111.8	±	233.9	1345	498	0.21
6	no.6	39975	2842	503185	9206	1269264	0.63	0.0509	±	0.0053	0.0414	±	0.0013	0.2904	±	0.0353	concordant	261.3	±	8.5	258.9	±	35.2	232.6	±	70.6	236.1	±	239.7	180	113	0.26
7	no.7	13814	1015	408785	7932	1093707	0.59	0.0526	±	0.0061	0.0166	±	0.0006	0.1203	±	0.0159	concordant	106.1	±	3.8	115.4	±	16.0	96.6	±	29.5	311.2	±	264.7	155	92	0.27
8	no.8	70719	4612	1414179	40916	5641478	0.40	0.0467	±	0.0047	0.0165	±	0.0004	0.1060	±	0.0125	concordant	105.3	±	2.7	102.3	±	12.6	94.5	±	28.6	33.2	±	242.1	802	318	0.21
9	no.9	19248	1423	1036409	10767	1484538	1.11	0.0529	±	0.0059	0.0170	±	0.0006	0.1243	±	0.0158	concordant	108.9	±	3.6	118.9	±	15.9	94.6	±	28.7	324.7	±	251.9	211	233	0.26
10	no.10	285894	18550	4350782	163807	22585690	0.30	0.0464	±	0.0045	0.0166	±	0.0004	0.1065	±	0.0122	concordant	106.3	±	2.4	102.8	±	12.3	92.8	±	28.0	20.7	±	234.3	3210	979	0.20
11	no.11	10578	805	223366	6364	877419	0.40	0.0545	±	0.0066	0.0158	±	0.0006	0.1190	±	0.0162	concordant	101.3	±	3.9	114.1	±	16.3	102.9	±	31.7	390.4	±	271.5	125	50	0.28
12	no.12	6676	497	103503	3801	524142	0.31	0.0533	±	0.0071	0.0167	±	0.0008	0.1229	±	0.0182	concordant	107.0	±	5.0	117.7	±	18.4	104.2	±	32.8	340.6	±	303.3	74	23	0.31
13	no.13	45304	3003	880535	26048	3591480	0.39	0.0474	±	0.0049	0.0166	±	0.0004	0.1084	±	0.0130	concordant	105.9	±	2.9	104.5	±	13.1	94.8	±	28.7	71.8	±	246.1	510	198	0.22
14	no.14	20964	1358	904235	11933	1645314	0.87	0.0464	±	0.0052	0.0167	±	0.0005	0.1070	±	0.0136	concordant	107.0	±	3.4	103.2	±	13.7	92.6	±	28.1	16.4	±	267.9	234	203	0.25
15	no.15	13757	1008	697212	7965	1098230	1.00	0.0525	±	0.0061	0.0165	±	0.0006	0.1190	±	0.0157	concordant	105.2	±	3.8	114.2	±	15.8	95.1	±	28.9	305.3	±	265.2	156	157	0.27
16	no.16	17126	1208	1006162	9786	1349230	1.17	0.0505	±	0.0058	0.0165	±	0.0005	0.1153	±	0.0138	concordant	105.7	±	3.0	110.8	±	13.9	92.9	±	29.7	219.2	±	264.1	185	217	0.24
17	no.17	57816	3841	1095886	33389	4603680	0.37	0.0476	±	0.0049	0.0164	±	0.0003	0.1074	±	0.0117	concordant	104.6	±	2.0	103.6	±	11.8	95.1	±	30.4	78.7	±	244.4	633	236	0.18
18	no.18	26256	1825	465964	15173	2092005	0.35	0.0498	±	0.0054	0.0164	±	0.0004	0.1123	±	0.0128	concordant	104.6	±	2.6	108.1	±	13.0	95.5	±	30.7	185.4	±	253.2	287	100	0.21
19	no.19	54671	3555	1559106	31289	4314091	0.57	0.0466	±	0.0048	0.0165	±	0.0003	0.1061	±	0.0116	concordant	105.6	±	2.1	102.4	±	11.7	94.2	±	30.1	27.7	±	247.8	593	336	0.18
20	no.20	19387	1325	592079	11019	1519297	0.61	0.0489	±	0.0055	0.0166	±	0.0005	0.1122	±	0.0133	concordant	106.3	±	2.9	108.0	±	13.4	100.6	±	32.3	144.6	±	264.5	209	128	0.23
21	no.21	6494	505	179938	3749	516914	0.55	0.0557	±	0.0075	0.0164	±	0.0007	0.1258	±	0.0176	concordant	104.7	±	4.5	120.3	±	17.7	98.5	±	32.1	440.6	±	298.6	71	39	0.31
22	no.22	17114	1100	436207	9686	1335491	0.51	0.0460	±	0.0053	0.0167	±	0.0005	0.1060	±	0.0128	concordant	106.7	±	3.1	102.3	±	13.0	95.1	±	30.6	-0.2	±	278.5	183	94	0.24
23	no.23	19819	1374	194315	11089	1528983	0.20	0.0497	±	0.0056	0.0169	±	0.0005	0.1157	±	0.0136	concordant	108.0	±	3.0	111.2	±	13.7	112.9	±	36.7	179.1	±	261.6	210	42	0.23
24	no.24	103839	6949	963277	60177	8297188	0.18	0.0479	±	0.0048	0.0163	±	0.0003	0.1078	±	0.0114	concordant	104.3	±	1.8	104.0	±	11.5	96.3	±	30.8	95.9	±	237.9	1140	207	0.16
25	no.25	26455	1803	462623	14821	2043549	0.35	0.0488	±	0.0053	0.0169	±	0.0004	0.1136	±	0.0130	concordant	107.8	±	2.6	109.2	±	13.1	104.8	±	33.7	138.6	±	255.7	281	100	0.21
26	no.26	25406	1797	1161725	14331	1975944	0.92	0.0507	±	0.0055	0.0168	±	0.0004	0.1171	±	0.0134	concordant	107.1	±	2.7	112.4	±	13.5	98.4	±	31.5	225.4	±	251.8	271	250	0.22
27	no.27	9494	693	154734	5460	752825	0.32	0.0523	±	0.0065	0.0164	±	0.0006	0.1185	±	0.0155	concordant	105.1	±	3.9	113.7	±	15.6	106.4	±	34.8	298.0	±	285.6	103	33	0.28
28	no.28	120333	7950	3664123	69030	9517840	0.60	0.0473	±	0.0047	0.0165	±	0.0003	0.1075	±	0.0114	concordant	105.3	±	1.7	103.7	±	11.5	92.5	±	29.5	65.2	±	238.3	1308	789	0.15
29	no.29	16805	1081	266662	9121	1257618	0.33	0.0461	±	0.0053	0.0174	±	0.0005	0.1106	±	0.0134	concordant	111.3	±	3.3	106.5	±	13.5	102.8	±	33.2	0.3	±	279.2	173	57	0.24
30	no.30	34123	2356	742031	19378	2671844	0.44	0.0495	±	0.0053	0.0166	±	0.0004	0.1135	±	0.0127	concordant	106.4	±	2.4	109.2	±	12.8	96.4	±	30.9	169.5	±	248.2	367	160	0.20
Standards																																
91500	10-3	65292	6943	113753	3367	464180	0.39	0.0749	±	0.0095	0.1856	±	0.00710	1.9174	±	0.2636	concordant	1097.4	±	45.6	1087.2	±	237.6	896.2	±	470.7	1065.7	±	253.9	67	26	0.28
91500	10-4	63694	6648	100652	3321	457837	0.35	0.0735	±	0.0093	0.1835	±	0.00707	1.8613	±	0.2562	concordant	1086.3	±	45.4	1067.4	±	231.6	953.7	±	501.3	1028.0	±	255.6	66	23	0.28
91500	10-5	65898	6963	114117	3393	467794	0.39	0.0744	±	0.0094	0.1859	±	0.00709	1.9081	±	0.2622	concordant	1098.9	±	45.5	1083.9	±	236.5	895.0	±	470.0	1052.9	±	254.4	67	26	0.28
91500	10-6	64601	6847	109016	3430	472951	0.37	0.0746	±	0.0094	0.1802	±	0.00685	1.8558	±	0.2550	concordant	1068.1	±	44.0	1065.5	±	230.7	894.7	±	469.9	1059.1	±	254.3	68	25	0.28

Appendix 5–5. Major (wt%) and trace element (ppm) concentrations of the Kita-taku mafic complex and related rocks.

No	1	2	3	4	5	6	7	8	9	10
Sp.No	20061201	20110203	21021406B	21021407A	200612T05	20110302CGb	20110307A	20110507	20110607A	200612T02
Litho	Cm	Cm	Cm	Cm	Cm	Cm	Cm	Cm	Cm	Cm
Type	1	1	1	1	1	1	1	1	1	1
(wt%)										
SiO_2	50.13	43.92	50.78	51.93	52.13	51.54	52.22	52.05	47.30	52.19
TiO_2	0.38	0.28	0.31	0.67	0.61	0.68	0.91	0.37	0.75	0.56
Al_2O_3	4.49	5.32	4.95	5.87	5.05	6.22	7.55	5.93	8.78	10.70
Fe_2O_3	11.06	16.75	10.47	10.82	11.80	12.11	12.24	9.55	13.11	10.23
MnO	0.23	0.26	0.21	0.21	0.24	0.26	0.24	0.22	0.21	0.22
MgO	17.09	25.64	18.48	15.44	16.05	15.47	13.44	15.86	22.68	12.38
CaO	15.21	6.93	13.43	13.64	12.83	11.41	11.03	14.29	5.27	11.61
Na_2O	0.35	0.30	0.55	0.81	0.63	0.85	1.08	0.40	0.95	1.20
K_2O	0.12	0.14	0.23	0.24	0.23	0.52	0.40	0.59	0.13	0.40
P_2O_5	0.02	0.02	0.03	0.04	0.02	0.04	0.09	0.01	0.05	0.03
LOI	0.60	2.23	0.59	0.53	0.82	0.51	0.78	1.07	2.87	0.72
Total	99.08	99.57	99.44	99.66	99.58	99.10	99.20	99.27	99.24	99.52
(ppm)										
Ba	32	33	60	3	67	57	32	113	26	46
Cr	600	227	1231	794	307	1101	777	550	1677	440
Nb	1	0	1	3	3	7	6	2	4	2
Ni	60	123	50	51	48	135	113	75	455	59
Rb	3	3	5	5	6	12	10	26	3	16
Sr	48	77	51	67	58	44	95	66	74	162
V	284	120	337	376	320	273	357	296	152	312
Y	12	3	12	24	24	48	30	15	15	13
Zn	59	103	61	73	70	111	102	51	87	75
Zr	23	20	30	48	43	49	73	21	41	40

No	11	12	13	14	15	16	17	18	19	20
Sp.No	20110607B	20110607BR	20110204	20110703	21020605	21020607	21020611	21021302	20110302A	20110505B
Litho	Cm	Cm	Cm	Cm	Cm	Cm	Cm	Cm	Cm	Cm
Type	1	1	2	2	2	2	2	2	3	3
(wt%)										
SiO_2	53.34	53.32	45.85	46.10	46.86	45.13	44.95	43.83	51.27	43.59
TiO_2	0.61	0.61	0.18	0.21	0.22	0.21	0.23	0.16	0.51	1.22
Al_2O_3	9.56	9.54	20.94	19.38	19.86	20.64	15.66	14.37	9.36	13.95
Fe_2O_3	9.41	9.43	6.48	7.56	6.66	7.21	10.36	12.17	9.36	12.78
MnO	0.19	0.19	0.12	0.14	0.13	0.13	0.18	0.19	0.24	0.26
MgO	13.25	13.24	9.73	10.65	8.84	9.44	15.06	17.55	8.93	7.17
CaO	10.48	10.47	15.98	14.96	15.92	15.68	12.86	11.15	18.30	19.73
Na_2O	1.09	1.10	0.72	0.69	0.70	0.72	0.57	0.56	1.30	0.24
K_2O	0.93	0.93	0.05	0.21	0.06	0.04	0.09	0.08	0.34	0.59
P_2O_5	0.05	0.06	0.01	0.01	0.01	0.01	0.01	0.02	0.05	0.22
LOI	0.98	0.98	0.23	1.14	0.25	0.07	0.29	-0.06	0.35	2.88
Total	98.92	98.88	100.07	99.92	99.27	99.20	99.96	100.08	99.66	99.73
(ppm)										
Ba	129	103	15	26	40	13	19	45	20	124
Cr	1275	1278	165	170	160	113	149	124	99	14
Nb	4	4	2	1	1	2	1	1	3	1
Ni	249	60	42	55	12	15	19	30	42	5
Rb	35	33	1	8	1	1	0	3	15	24
Sr	125	125	318	307	314	354	243	234	142	181
V	205	204	120	123	150	126	134	88	251	371
Y	26	25	9	10	14	7	7	1	34	40
Zn	76	74	30	41	33	43	57	69	68	66
Zr	35	37	9	15	13	10	13	13	37	101

Total Fe reported as Fe^{3+}. LOI: loss on ignition, Cm: cumulate, Gb: gabbro, Tdh: trondhjemite, Gr: granite, PFD: porphyritic fine-grained diorite, Amp: amphibolite, and Serp: serpentinite.

Continued…

No	21	22	23	24	25	26	27	28	29	30
Sp.No	20110711	21021308	20110402	20110403	20110509A	21021311	21021305	21020702B	20061203A	20110205
Litho	Cm	Cm	Cm	Cm	Cm	Cm	Cm	Cm	Cm	Cm
Type	3	3	3	3	3	3	3	3	3	3
(wt%)										
SiO_2	48.87	46.92	52.52	52.11	50.75	50.75	48.69	48.26	48.06	45.85
TiO_2	1.08	0.34	0.38	0.45	0.36	0.65	0.57	0.77	0.69	0.25
Al_2O_3	10.18	14.68	13.17	13.10	9.03	9.09	15.66	8.95	18.62	17.85
Fe_2O_3	11.25	9.52	10.65	7.53	12.85	10.93	8.10	12.59	9.00	9.40
MnO	0.21	0.17	0.23	0.16	0.24	0.21	0.16	0.24	0.18	0.16
MgO	13.65	13.41	9.20	12.02	17.05	14.75	10.33	16.51	9.52	12.14
CaO	12.70	13.55	10.06	11.43	8.34	11.60	14.51	11.02	11.90	12.69
Na_2O	1.08	0.78	2.56	1.50	0.39	0.73	0.82	0.65	1.47	0.67
K_2O	0.39	0.34	0.50	1.07	0.28	0.62	0.37	0.25	0.55	0.41
P_2O_5	0.04	0.01	0.15	0.07	0.02	0.07	0.03	0.02	0.02	0.01
LOI	1.00	1.43	0.63	0.84	1.92	1.41	0.93	1.68	1.20	2.06
Total	99.44	99.74	99.42	99.43	99.32	99.39	99.23	99.26	99.99	99.44
(ppm)										
Ba	45	52	98	128	0	74	36	47	54	93
Cr	276	280	446	1055	482	1029	238	1064	90	142
Nb	3	1	2	4	1	2	2	2	2	1
Ni	123	37	61	145	134	41	34	23	25	59
Rb	9	14	17	40	13	24	11	7	20	18
Sr	138	207	404	224	99	107	258	76	356	263
V	395	182	183	178	380	242	226	279	222	121
Y	27	14	20	20	9	24	23	17	16	12
Zn	67	54	83	57	89	85	56	83	62	54
Zr	40	18	33	41	22	39	29	33	28	14

No	31	32	33	34	35	36	37	38	39	40
Sp.No	20110506	20110603	20110607C	20110704	20110709A	21020606A	21020610	21020701	21020702A	21020704A
Litho	Cm	Cm	Cm	Cm	Cm	Cm	Cm	Cm	Cm	Cm
Type	3	3	3	3	3	3	3	3	3	3
(wt%)										
SiO_2	49.61	47.26	50.77	47.48	48.47	47.72	47.80	49.85	47.97	49.42
TiO_2	0.28	0.35	0.28	0.95	0.39	0.66	0.49	0.39	0.61	0.36
Al_2O_3	19.36	18.42	23.03	15.81	18.35	19.84	18.67	16.28	20.69	15.92
Fe_2O_3	7.32	8.06	4.96	10.13	8.26	7.92	8.38	7.50	8.35	8.54
MnO	0.16	0.14	0.12	0.18	0.17	0.15	0.17	0.13	0.17	0.18
MgO	9.42	10.62	6.30	10.73	9.20	7.27	9.64	10.19	7.80	9.97
CaO	11.86	13.33	8.86	12.40	12.78	13.80	13.41	12.69	12.11	13.87
Na_2O	1.32	1.02	3.43	1.18	1.17	1.39	0.94	1.46	1.49	0.92
K_2O	0.54	0.40	1.61	0.57	0.59	0.35	0.24	0.68	0.41	0.36
P_2O_5	0.02	0.01	0.06	0.05	0.03	0.07	0.01	0.06	0.03	0.02
LOI	1.31	1.42	2.22	1.18	1.48	0.71	1.24	1.25	0.97	1.03
Total	99.89	99.61	99.44	99.47	99.41	99.17	99.74	99.23	99.61	99.55
(ppm)										
Ba	85	40	424	95	55	70	42	80	83	74
Cr	104	128	86	154	123	69	121	150	50	226
Nb	2	2	3	3	2	2	1	2	2	1
Ni	35	75	97	45	26	13	18	21	22	25
Rb	24	15	60	21	29	9	14	26	11	15
Sr	311	320	1203	227	343	409	284	289	376	296
V	137	136	77	301	160	192	183	181	258	194
Y	14	18	18	22	22	23	16	15	24	16
Zn	48	48	54	66	63	54	53	55	70	60
Zr	23	24	67	38	24	30	15	36	25	18

Total Fe reported as Fe^{3+}. LOI: loss on ignition, Cm: cumulate, Gb: gabbro, Tdh: trondhjemite, Gr: granite, PFD: porphyritic fine-grained diorite, Amp: amphibolite, and Serp: serpentinite.

Continued…

No	41	42	43	44	45	46	47	48	49	50
Sp.No	21021303A	21021309A	21021405A	200612T04	20110511	20110604	20110707	20110802	21020703	21021306
Litho	Cm	Cm	Cm	Cm	Cm	Cm	Cm	Cm	Cm	Cm
Type	3	3	3	3	3	3	3	3	3	3
(wt%)										
SiO_2	46.84	47.80	50.60	46.95	49.53	48.83	42.22	45.42	47.14	50.44
TiO_2	0.63	0.27	0.40	0.19	0.41	0.22	1.23	0.17	0.26	0.27
Al_2O_3	21.64	20.95	15.61	21.00	15.01	22.78	17.88	19.45	17.62	18.70
Fe_2O_3	8.97	6.24	8.62	5.89	8.96	5.19	12.61	7.40	8.16	6.68
MnO	0.18	0.13	0.19	0.11	0.19	0.11	0.23	0.14	0.15	0.15
MgO	6.94	7.63	10.27	8.88	11.11	6.16	8.26	11.02	10.52	8.08
CaO	12.29	14.92	12.02	15.60	12.98	14.92	15.12	14.88	14.83	13.55
Na_2O	1.49	1.04	1.20	0.64	0.76	1.46	1.32	0.76	0.67	1.26
K_2O	0.39	0.27	0.30	0.39	0.58	0.21	0.71	0.21	0.39	0.68
P_2O_5	0.12	0.02	0.02	0.01	0.04	0.06	0.13	0.01	0.02	0.01
LOI	1.63	0.62	0.45	1.20	0.94	0.62	0.39	2.12	1.16	0.98
Total	99.50	99.27	99.22	99.66	99.57	99.95	99.70	99.47	99.76	99.83
(ppm)										
Ba	48	44	56	94	82	32	196	37	20	107
Cr	30	124	132	188	170	144	164	203	197	120
Nb	3	1	3	2	2	3	1	1	2	2
Ni	31	38	47	33	28	15	33	34	24	35
Rb	12	10	10	17	27	6	12	8	19	30
Sr	378	352	225	313	211	341	322	311	262	302
V	201	113	246	129	184	121	327	120	147	145
Y	23	17	21	16	18	15	32	8	19	21
Zn	72	43	63	32	66	39	99	39	50	47
Zr	24	22	42	10	31	29	103	10	17	24

No	51	52	53	54	55	56	57	58	59	60
Sp.No	20110306-2	20061203C	20110510	20110605	20110804	20110805	21021401	21021402	21021403	21021404A
Litho	Cm	Cm	Cm	Cm	Cm	Cm	Cm	Cm	Cm	Cm
Type	3	4	4	4	4	4	4	4	4	4
(wt%)										
SiO_2	45.22	44.67	45.66	48.03	45.68	46.19	46.54	47.32	47.61	48.14
TiO_2	2.20	2.21	2.60	1.49	1.67	1.55	2.14	1.88	1.88	1.59
Al_2O_3	16.75	18.77	20.03	19.23	21.26	20.36	18.83	18.48	19.16	19.06
Fe_2O_3	15.73	12.58	10.71	9.27	11.35	10.59	10.19	10.04	9.51	9.57
MnO	0.22	0.15	0.16	0.14	0.21	0.18	0.14	0.15	0.14	0.14
MgO	7.03	7.22	6.98	7.52	5.24	6.25	8.10	7.78	7.46	7.75
CaO	11.50	12.15	12.00	11.80	10.99	11.73	12.39	11.82	12.07	11.09
Na_2O	1.32	1.69	1.68	1.97	2.18	2.04	1.73	1.89	2.01	2.03
K_2O	0.19	0.53	0.29	0.44	0.80	0.58	0.37	0.58	0.50	0.74
P_2O_5	0.19	0.04	0.03	0.04	0.37	0.07	0.03	0.04	0.04	0.03
LOI	0.28	0.61	0.37	0.97	1.14	1.02	0.60	0.98	0.83	1.11
Total	100.36	99.99	100.13	99.94	99.74	99.54	100.46	99.99	100.37	100.15
(ppm)										
Ba	63	107	48	72	97	96	52	84	101	122
Cr	139	9	9	23	15	13	21	16	19	22
Nb	3	3	6	5	12	6	4	5	5	4
Ni	41	3	1	8	0	1	42	43	44	45
Rb	6	11	7	7	28	12	5	15	11	22
Sr	322	328	317	298	417	413	287	294	304	313
V	427	823	476	602	130	304	751	673	692	616
Y	9	18	7	23	21	26	19	20	20	20
Zn	116	78	67	64	103	85	60	68	58	66
Zr	38	50	43	41	56	51	42	50	47	43

Total Fe reported as Fe^{3+}. LOI: loss on ignition, Cm: cumulate, Gb: gabbro, Tdh: trondhjemite, Gr: granite, PFD: porphyritic fine-grained diorite, Amp: amphibolite, and Serp: serpentinite.

Continued…

No	61	62	63	64	65	66	67	68	69	70
Sp.No	20110308	20110312	21020603A	21021301A	21021407B	21021408A	21021409	20061203B	20110303	20110306-1
Litho	Gb	Gb	Gb	Gb	Gb	Gb	Gb	Gb	Gb	Gb
Type	5	5	5	5	5	5	5	6	6	6
(wt%)										
SiO_2	50.86	47.40	49.07	45.42	46.51	48.71	46.53	46.64	52.20	52.87
TiO_2	1.31	1.86	1.49	2.13	1.54	1.43	1.60	1.09	0.87	0.72
Al_2O_3	20.87	20.32	20.28	20.41	19.95	19.65	18.91	21.52	15.19	17.55
Fe_2O_3	10.06	11.04	10.57	11.62	12.08	11.58	11.62	8.88	8.72	8.67
MnO	0.20	0.20	0.21	0.21	0.20	0.21	0.17	0.16	0.17	0.19
MgO	3.90	4.83	5.06	6.64	5.10	4.79	6.99	6.50	8.55	6.16
CaO	8.36	10.51	9.17	10.71	10.35	9.43	11.37	12.48	10.36	9.85
Na_2O	4.07	2.90	3.14	1.52	2.80	3.33	2.53	1.79	2.74	3.17
K_2O	0.41	0.34	0.60	0.73	1.31	0.53	0.43	0.59	0.82	0.56
P_2O_5	0.25	0.43	0.37	0.21	0.37	0.32	0.15	0.07	0.18	0.04
LOI	1.24	0.67	0.98	1.72	1.02	0.80	0.68	1.12	0.69	0.78
Total	100.28	99.83	99.94	99.60	100.21	99.97	100.30	99.72	99.80	99.77
(ppm)										
Ba	145	117	126	64	342	162	128	80	102	119
Cr	4	19	52	16	4	1	15	31	324	29
Nb	9	14	10	7	9	8	6	4	6	5
Ni	0	2	7	28	52	54	56	9	43	7
Rb	15	12	27	29	36	16	9	18	24	20
Sr	444	412	486	391	427	380	402	421	279	334
V	164	133	180	254	262	238	383	296	245	177
Y	13	20	22	8	37	29	32	27	24	18
Zn	84	106	104	87	117	104	93	70	82	86
Zr	120	65	229	43	116	127	63	37	78	43

No	71	72	73	74	75	76	77	78	79	80
Sp.No	21021307	20110401A	20110806	200612T03	20110302CPg	20110509B	20110606A	20110302B	20110401B	21020609
Litho	Gb	Gb	Gb	Gb	Gb	Gb	Gb	Gb	Gb	Gb
Type	6	6	6	7	7	7	7	Hetero	Hetero	Hetero
(wt%)										
SiO_2	48.53	49.66	47.66	53.39	58.91	49.66	48.37	51.70	48.79	45.33
TiO_2	0.28	0.93	1.05	0.55	0.22	0.21	0.65	0.94	1.27	1.97
Al_2O_3	21.33	13.94	14.03	15.58	20.62	21.16	24.98	16.21	11.79	18.53
Fe_2O_3	7.03	10.17	10.69	6.93	2.92	6.80	4.76	9.56	13.39	14.54
MnO	0.14	0.23	0.21	0.14	0.07	0.14	0.07	0.18	0.32	0.26
MgO	6.47	12.21	12.47	9.42	3.26	8.46	4.44	7.49	11.16	5.77
CaO	13.10	9.86	11.69	10.54	8.57	11.33	13.70	9.97	10.20	9.89
Na_2O	1.83	1.98	1.20	2.40	5.46	1.29	2.37	2.84	1.49	2.16
K_2O	0.52	0.83	0.37	1.14	0.31	0.65	0.60	1.01	0.73	0.86
P_2O_5	0.04	0.12	0.03	0.04	0.13	0.02	0.05	0.08	0.05	0.52
LOI	0.92	1.42	0.99	1.81	0.39	1.23	1.11	0.70	1.15	1.13
Total	99.27	99.93	99.39	100.13	100.46	99.73	99.98	99.97	99.19	99.82
(ppm)										
Ba	57	122	87	180	138	114	80	107	92	125
Cr	61	794	827	361	93	136	47	232	289	7
Nb	1	6	3	4	6	3	5	9	2	5
Ni	36	187	2	75	29	40	25	96	152	17
Rb	21	27	11	48	10	28	18	33	26	37
Sr	392	221	279	286	468	375	519	284	198	421
V	111	236	241	182	75	171	176	333	288	155
Y	18	28	21	20	32	12	28	53	19	12
Zn	48	97	68	57	31	52	31	81	122	116
Zr	16	60	35	43	15	21	28	44	42	25

Total Fe reported as Fe^{3+}. LOI: liss on ignition, Cm: cumulate, Gb: gabbro, Tdh: trondhjemite, Gr: granite, PFD: porphyritic fine-grained diorite, Amp: amphibolite, and Serp: serpentinite.

Continued…

No	81	82	83	84	85	86	87	88	89	90
Sp.No	21020705	20110309	20110311-1	20110313	20110313R	:0110602B	20110606B	20110709B	20110607D	20110807C
Litho	Gb	Ms-Bt Tdh	Ms-Bt Tdh	Ms-Bt Tdh	Ms-Bt Tdh	Ms-Bt Tdh	Ms-Bt Tdh	Ms-Bt Tdh	Bt Tdh	Bt Tdh
Type	Hetero	dike	dike	dike	dike	dike	dike	dike	dike	dike
(wt%)										
SiO_2	49.63	75.09	71.16	74.77	74.90	74.60	74.07	75.86	77.79	73.73
TiO_2	0.39	0.14	0.23	0.04	0.04	0.05	0.18	0.05	0.07	0.17
Al_2O_3	15.97	14.74	16.35	13.57	13.58	15.05	13.88	13.52	13.44	14.47
Fe_2O_3	7.26	1.22	1.61	0.43	0.43	0.62	2.70	0.57	0.42	1.62
MnO	0.17	0.02	0.02	0.01	0.01	0.04	0.02	0.02	0.00	0.03
MgO	9.02	0.36	0.45	0.08	0.08	0.06	0.37	0.05	0.25	0.46
CaO	15.97	3.21	4.57	0.24	0.24	1.27	2.21	0.68	2.59	2.23
Na_2O	0.98	4.41	4.36	1.88	1.92	3.97	3.92	3.28	5.12	3.37
K_2O	0.27	0.93	0.54	7.87	7.88	3.72	2.11	5.30	0.15	3.80
P_2O_5	0.03	0.06	0.07	0.03	0.03	0.03	0.04	0.02	0.01	0.08
LOI	0.71	0.54	0.60	0.20	0.20	0.68	0.29	0.37	0.28	0.35
Total	99.67	100.15	99.36	98.92	99.10	99.42	99.50	99.33	99.84	99.95
(ppm)										
Ba	35	280	203	1536	1575	627	593	65	203	1310
Cr	180	12	7	6	5	5	7	8	7	4
Nb	2	7	8	7	6	16	16	12	5	5
Ni	27	4	3	4	57	8	5	8	11	3
Rb	10	29	24	229	230	90	64	209	6	86
Sr	233	314	370	167	167	176	256	45	372	235
V	221	14	14	6	8	7	9	5	5	16
Y	23	9	12	11	11	6	16	22	11	14
Zn	48	12	20	3	4	7	34	11	14	20
Zr	27	64	108	28	28	55	150	50	41	190

No	91	92	93	94	95	96	97	98	99	100
Sp.No	21020603B	21021404B	21020602B	21020604B	21020606B	21020704B	21021301B	21021407C	21021408B	20110311-2
Litho	Bt Tdh	Bt Tdh	Bt Gr	Bt Gr	Bt Gr	Bt Gr	Bt Gr	Bt Gr	Bt Gr	PFD
Type	dike	dike	Fukae	Fukae	Fukae	Fukae	Fukae	Fukae	Fukae	dike
(wt%)										
SiO_2	72.18	77.11	74.95	73.38	76.92	72.42	77.05	75.59	75.41	45.01
TiO_2	0.29	0.11	0.15	0.27	0.07	0.31	0.02	0.05	0.21	1.59
Al_2O_3	15.07	13.78	13.66	14.44	12.80	14.99	13.36	14.45	13.35	20.23
Fe_2O_3	2.51	0.92	1.40	2.17	0.71	2.65	0.41	0.67	1.91	13.07
MnO	0.04	0.01	0.02	0.03	0.01	0.05	0.01	0.01	0.03	0.22
MgO	0.96	0.33	0.33	1.21	0.14	0.59	0.06	0.17	0.55	5.81
CaO	0.82	3.20	1.36	2.36	0.44	2.63	0.73	2.31	0.69	10.95
Na_2O	4.90	4.09	3.31	4.15	3.54	3.39	3.85	4.71	3.10	2.01
K_2O	2.91	0.49	4.53	1.69	5.27	3.04	4.38	2.14	4.76	1.08
P_2O_5	0.09	0.04	0.07	0.07	0.05	0.06	0.01	0.11	0.03	0.32
LOI	1.26	0.55	0.40	1.31	0.44	0.49	0.42	0.36	0.73	1.43
Total	99.76	100.07	99.76	99.76	99.95	100.12	99.88	100.22	100.04	100.29
(ppm)										
Ba	516	205	768	280	719	609	187	138	641	242
Cr	12	8	5	9	8	6	3	0	6	0
Nb	10	7	7	9	4	11	2	8	9	10
Ni	8	46	6	11	14	26	29	53	55	0
Rb	115	17	122	45	145	122	114	62	123	33
Sr	431	314	180	360	154	245	137	153	222	373
V	25	12	14	14	8	15	5	7	20	290
Y	6	11	12	8	8	12	13	8	4	42
Zn	27	10	13	20	7	48	3	11	24	122
Zr	124	101	128	155	129	121	54	27	83	89

Total Fe reported as Fe^{3+}. LOI: liss on ignition, Cm: cumulate, Gb: gabbro, Tdh: trondhjemite, Gr: granite, PFD: porphyritic fine-grained diorite, Amp: amphibolite, and Serp: serpentinite.

Continued…

No	101	102	103	104	105	106	107	108	109	110
Sp.No	20110405	20110406A	20110709C	20061202	200612T01	20110202C	20110301	20110304	20110305	20110407
Litho	PFD	PFD	PFD	Amp	Amp	Amp	Amp	Amp	Amp	Amp
Type	dike	dike	dike	-	-	-	-	-	-	-
(wt%)										
SiO_2	46.83	49.68	61.32	44.35	49.32	54.64	45.89	53.49	52.23	46.09
TiO_2	1.43	1.22	0.82	1.21	1.31	1.49	1.48	1.43	1.98	0.48
Al_2O_3	19.40	18.73	17.76	14.08	14.62	14.45	13.91	14.59	14.29	18.74
Fe_2O_3	11.87	8.80	7.04	11.35	14.17	11.48	13.83	13.50	13.00	11.36
MnO	0.19	0.14	0.13	0.22	0.24	0.20	0.26	0.22	0.22	0.14
MgO	5.59	6.31	2.85	7.07	5.62	4.12	8.82	4.44	4.37	9.05
CaO	10.04	9.57	5.02	21.05	11.42	7.61	13.67	7.32	8.59	10.63
Na_2O	2.27	2.20	2.96	0.28	3.10	5.75	1.15	4.71	4.50	2.38
K_2O	1.90	3.01	1.82	0.49	0.38	0.43	0.60	0.57	0.26	0.95
P_2O_5	0.30	0.27	0.14	0.06	0.13	0.15	0.14	0.15	0.22	0.02
LOI	2.42	3.26	1.62	0.93	0.29	0.33	0.97	0.68	0	1.53
Total	99.81	99.93	99.86	100.17	100.32	100.32	99.75	100.40	99.68	99.86
(ppm)										
Ba	321	491	260	15	66	74	110	77	36	160
Cr	30	30	18	37	26	23	166	16	16	28
Nb	12	10	11	0	1	3	3	2	3	0
Ni	1	14	9	16	1	14	55	1	2	35
Rb	79	113	116	18	5	3	23	16	0	41
Sr	319	268	241	189	196	130	192	316	104	616
V	176	173	110	379	467	371	313	406	440	431
Y	37	30	29	27	24	21	25	24	23	3
Zn	110	92	80	71	103	93	107	100	98	58
Zr	179	124	111	67	43	95	61	69	118	1

No	111	112	113	114	115	116	117	118	119	120
Sp.No	20110503	20110512	20110602A	20110705	20110801	21020601	21020602A	21020603C	21020604A	21021303B
Litho	Amp	Amp	Amp	Amp	Amp	Amp	Amp	Amp	Amp	Amp
Type	-	-	-	-	-	-	-	-	-	-
(wt%)										
SiO_2	44.36	52.72	54.20	48.79	48.46	50.18	50.81	44.78	49.90	48.02
TiO_2	1.39	1.52	1.16	0.34	1.56	1.38	1.32	1.56	1.54	0.68
Al_2O_3	16.57	15.03	14.73	18.08	16.37	15.10	15.33	16.40	16.09	12.94
Fe_2O_3	13.35	12.82	12.76	7.92	14.29	13.49	10.72	12.38	11.70	13.45
MnO	0.22	0.20	0.21	0.17	0.22	0.21	0.19	0.23	0.20	0.25
MgO	6.88	4.49	4.15	9.36	5.88	5.93	6.33	6.71	5.82	10.13
CaO	14.55	8.06	8.17	13.58	9.84	9.42	11.69	14.72	10.81	11.32
Na_2O	1.37	4.67	3.75	1.11	2.62	3.24	3.12	0.67	3.52	1.84
K_2O	0.82	0.34	0.41	0.36	0.42	0.57	0.36	1.96	0.49	0.26
P_2O_5	0.14	0.18	0.14	0.04	0.21	0.14	0.13	0.13	0.16	0.25
LOI	0.88	0.38	0.53	1.10	0.43	0.57	0.31	1.80	0.85	0.85
Total	99.66	100.02	99.68	99.75	99.85	99.68	100.00	99.53	100.22	99.14
(ppm)										
Ba	173	101	96	23	101	100	59	350	105	72
Cr	107	10	22	120	25	43	144	104	91	101
Nb	2	3	1	2	4	2	3	2	2	0
Ni	25	6	7	30	9	4	5	9	10	32
Rb	26	5	8	13	7	15	5	101	7	6
Sr	297	271	259	340	305	147	158	360	183	475
V	357	448	406	161	397	374	333	340	358	329
Y	34	25	22	22	27	22	24	38	22	14
Zn	113	99	152	55	102	89	77	90	86	106
Zr	107	105	75	29	83	64	68	107	79	14

Total Fe reported as Fe^{3+}. LOI: liss on ignition, Cm: cumulate, Gb: gabbro, Tdh: trondhjemite, Gr: granite, PFD: porphyritic fine-grained diorite, Amp: amphibolite, and Serp: serpentinite.

Continued…

No	121	122	123	124	125	126	127	128	129	130
Sp.No	21021304	21021310	20110201	20110202A	20110202B	20110406B	20110501	20110502	20110505A	20110508A
Litho	Amp	Amp	Serp	Serp	Serp	Serp	Serp	Serp	Serp	Serp
Type	-	-	-	-	-	-	-	-	-	-
(wt%)										
SiO_2	49.50	50.40	43.77	47.74	45.45	42.92	44.45	41.97	41.88	41.95
TiO_2	0.82	1.63	0.01	0.07	0.07	0.02	0.03	0.02	0.07	0.03
Al_2O_3	16.58	14.27	0.16	0.76	1.06	0.25	1.77	0.48	0.79	0.65
Fe_2O_3	9.02	12.76	7.22	10.21	13.98	11.51	12.07	12.51	16.62	13.33
MnO	0.17	0.20	0.08	0.19	0.32	0.09	0.17	0.17	0.20	0.11
MgO	6.24	4.84	47.47	38.65	34.03	41.39	36.26	40.78	35.97	41.63
CaO	14.96	10.93	0.03	0.09	2.11	0.30	1.42	0.06	0.77	0.06
Na_2O	1.92	4.13	0	0	0.01	0	0	0	0	0
K_2O	0.60	0.42	0	0	0.01	0.01	0.01	0	0	0.03
P_2O_5	0.10	0.23	0	0.01	0	0	0	0	0	0
LOI	0.52	0.43	14.17	8.82	5.48	10.83	7.68	0.22	6.75	11.60
Total	99.90	99.82	98.73	97.70	97.03	96.50	96.19	96.00	96.31	97.80
(ppm)										
Ba	92	68	11	29	26	3	0	10	27	0
Cr	111	48	3373	2534	2859	4633	3699	5120	3902	3938
Nb	3	2	4	3	1	2	2	2	0	2
Ni	33	40	2754	819	398	1728	1193	1384	1390	1317
Rb	20	1	3	3	5	4	4	5	3	4
Sr	230	141	4	4	10	6	15	5	7	6
V	243	386	15	33	65	17	53	34	96	37
Y	26	31	3	4	0	1	0	0	0	1
Zn	64	102	28	54	81	57	86	103	85	53
Zr	48	112	3	5	4	4	5	4	5	5

No	131	132	133	134	135	136	137	138	139	140
Sp.No	20110601	20110701	20110708	20110710	20110803	21020608	210206T01	21021309B	21021405B	20110404
Litho	Serp	Serp	Serp	Serp	Serp	Serp	Serp	Serp	Serp	Hb Gb vein
Type	-	-	-	-	-	-	-	-	-	Vein
(wt%)										
SiO_2	43.06	44.72	43.94	47.28	40.93	42.60	44.69	46.89	44.44	62.35
TiO_2	0.02	0.11	0.07	0.02	0.07	0.01	0.06	0.01	0.01	0.48
Al_2O_3	0.33	1.33	0.84	0.63	1.09	0.21	0.96	0.21	0.08	18.87
Fe_2O_3	12.93	14.01	13.78	7.50	16.79	11.46	11.52	7.10	11.47	3.63
MnO	0.14	0.22	0.21	0.11	0.23	0.13	0.19	0.07	0.12	0.06
MgO	40.14	32.81	39.82	37.45	37.81	42.19	37.37	44.76	41.20	2.11
CaO	0.14	4.39	0.08	0.91	0.20	0.07	2.45	0.04	0.05	4.32
Na_2O	0	0	0	0	0	0	0	0	0	6.98
K_2O	0	0.01	0.01	0.01	0.02	0	0.03	0	0	2.53
P_2O_5	0	0	0.01	0	0.01	0	0	0	0.01	0.17
LOI	9.23	6.48	7.01	8.49	5.91	11.68	9.69	12.41	11.04	1.66
Total	96.77	97.61	98.76	93.89	97.14	96.67	97.26	99.08	97.39	101.52
(ppm)										
Ba	0	20	0	18	0	28	16	21	34	226
Cr	4760	2293	1647	6919	3856	5229	3288	1710	3715	21
Nb	2	1	2	3	0	1	2	3	2	7
Ni	1159	879	1232	2407	1558	16	20	39	48	32
Rb	4	3	5	1	3	2	4	5	3	82
Sr	6	11	6	9	7	8	14	5	4	137
V	36	89	54	25	82	21	48	11	17	50
Y	0	1	2	5	0	2	1	2	1	14
Zn	71	77	61	65	97	64	74	22	67	34
Zr	4	7	9	7	5	4	7	3	3	353

Total Fe reported as Fe^{3+}. LOI: liss on ignition, Cm: cumulate, Gb: gabbro, Tdh: trondhjemite, Gr: granite, PFD: porphyritic fine-grained diorite, Amp: amphibolite, and Serp: serpentinite.

Continued…

No	141	142	143
Sp.No	20110404R	20110508B	21021406A
Litho	Hb Gb vein	Calc silicate	Migmatite
Type	Vein	-	-
(wt%)			
SiO_2	62.19	41.68	44.67
TiO_2	0.48	0.91	2.24
Al_2O_3	18.87	18.05	20.57
Fe_2O_3	3.63	10.15	14.61
MnO	0.06	0.18	0.19
MgO	2.12	4.47	2.92
CaO	4.33	23.52	11.23
Na_2O	6.97	0	2.71
K_2O	2.53	0	0.54
P_2O_5	0.18	0.13	0.12
LOI	1.66	1.94	0.51
Total	101.35	99.10	99.80
(ppm)			
Ba	214	0	92
Cr	13	36	244
Nb	6	1	0
Ni	58	3	49
Rb	83	0	11
Sr	137	67	392
V	52	327	416
Y	14	30	6
Zn	33	23	115
Zr	354	64	37

Total Fe reported as Fe^{3+}. LOI: liss on ignition, Cm: cumulate, Gb: gabbro, Tdh: trondhjemite, Gr: granite, PFD: porphyritic fine-grained diorite, Amp: amphibolite, and Serp: serpentinite.

Appendix 5–6. Trace element and rare earth element (REE) concentrations of the Kita-taku mafic complex and related rocks determined by LA-ICP-MS.

No	1	2	3	4	5	6	7	8	9	10
Sp.No	21021406B	20110607A	20110204	21021302	20110302A	21021311	21021405A	21020610	20110604	21021401
Litho	Cm	Cm	Cm	Cm	Cm	Cm	Cm	Cm	Cm	Cm
Type	1	1	2	2	3	3	3	3	3	4
(ppm)										
V	340	161	131	93	255	247	256	188	125	765
Cr	1230	1680	190	130	110	1030	140	130	160	<20
Co	73	84	61	110	54	57	51	57	36	57
Ni	110	420	60	110	60	170	40	40	30	30
Cu	50	20	70	70	120	150	70	40	20	40
Zn	60	90	40	70	70	80	70	50	40	60
Ga	5	9	13	10	11	10	12	15	15	16
Ge	1.6	1.2	1	1.1	1.8	1.7	1.4	1.3	1	1.2
As	<5	<5	<5	<5	<5	<5	<5	<5	<5	<5
Rb	5	1	1	2	18	22	8	12	5	4
Sr	48	67	335	238	144	102	230	298	339	289
Y	8.5	13.2	4.9	4.6	18.7	15.9	11.9	8.8	8.1	24.8
Zr	21	32	5	8	25	28	33	9	21	27
Nb	0.8	1.8	<0.2	<0.2	1.6	1.4	1.7	0.3	1	4.1
Mo	<2	<2	<2	<2	<2	<2	<2	<2	<2	<2
Ag	<0.5	<0.5	<0.5	<0.5	<0.5	<0.5	<0.5	<0.5	<0.5	<0.5
In	<0.1	<0.1	<0.1	<0.1	0.1	<0.1	<0.1	<0.1	<0.1	0.1
Sn	<1	1	<1	<1	1	1	<1	1	<1	<1
Sb	<0.2	<0.2	<0.2	<0.2	0.2	<0.2	<0.2	<0.2	<0.2	<0.2
Cs	0.4	0.2	0.3	0.3	6.5	1.7	1.2	2.9	0.3	0.4
Ba	28	20	19	26	32	88	50	23	49	58
La	3.49	5.42	1.17	1.46	7.08	5.76	4.52	1.31	3.85	4.25
Ce	7.72	11.6	2.72	3.22	17.5	12.3	10.7	3.22	8.37	12.4
Pr	0.99	1.56	0.4	0.43	2.34	1.79	1.47	0.56	1.08	2.04
Nd	4.4	7.02	2.11	2.12	10.5	8.62	6.93	3	4.74	11.7
Sm	1.21	1.92	0.67	0.64	2.89	2.44	1.85	1.09	1.24	3.89
Eu	0.368	0.598	0.381	0.319	0.678	0.763	0.647	0.573	0.656	1.16
Gd	1.42	2.22	0.83	0.71	3.09	2.67	2.04	1.53	1.35	4.55
Tb	0.25	0.38	0.16	0.14	0.57	0.45	0.35	0.28	0.23	0.8
Dy	1.6	2.35	0.97	0.9	3.58	2.78	2.11	1.73	1.48	5.03
Ho	0.33	0.48	0.19	0.18	0.74	0.56	0.43	0.36	0.3	1.01
Er	0.94	1.41	0.54	0.5	2.01	1.61	1.29	1.06	0.86	2.67
Tm	0.133	0.206	0.074	0.076	0.287	0.234	0.188	0.146	0.131	0.362
Yb	0.87	1.37	0.46	0.52	1.86	1.55	1.23	0.96	0.86	2.22
Lu	0.132	0.211	0.067	0.08	0.29	0.243	0.185	0.138	0.127	0.327
Hf	0.6	1	0.2	0.2	0.9	0.9	1	0.4	0.6	1.1
Ta	0.13	0.16	0.04	0.06	0.28	0.17	0.17	0.08	0.11	0.3
W	60	14.3	68.1	93.9	75.5	16.7	58.8	58	48.7	56.5
Tl	<0.05	<0.05	<0.05	<0.05	<0.05	0.07	<0.05	<0.05	<0.05	<0.05
Pb	<5	<5	<5	<5	<5	<5	<5	<5	<5	<5
Bi	<0.1	0.2	<0.1	<0.1	<0.1	<0.1	<0.1	<0.1	0.1	<0.1
Th	0.33	1.45	0.1	0.21	1.54	0.76	0.59	0.08	0.38	0.22
U	0.09	0.29	0.02	0.05	0.68	0.2	0.16	0.02	0.11	0.06

Cm: cumulate, Gb: gabbro, Tdh: trondhjemite, Gr: granite, PFD: porphyritic fine-grained diorite, and Amp: amphibolite.

Continued…

No	11	12	13	14	15	16	17	18	19	20
Sp.No	20110605	20110303	20110302CPg	20110309	21021404B	21020606B	20110405	20110709C	20110705	20061202
Litho	Cm	Gb	Gb	Ms-Bt Tdh	Bt Tdh	Bt Gr	PFD	PFD	Amp	Amp
Type	4	6	7	dike	dike	Fukae	dike	dike	-	-
(ppm)										
V	598	253	72	9	<5	5	189	104	164	376
Cr	30	340	90	<20	<20	<20	30	20	130	40
Co	57	44	48	89	123	142	38	39	50	71
Ni	20	50	30	<20	<20	<20	20	<20	40	30
Cu	30	20	10	<10	<10	<10	20	<10	60	90
Zn	60	90	30	<30	<30	<30	120	80	60	70
Ga	16	16	19	13	13	11	21	18	13	14
Ge	1.1	1.4	1	0.8	0.8	0.9	1.3	1.4	1.3	1.9
As	<5	<5	<5	<5	<5	<5	<5	<5	<5	<5
Rb	6	23	5	25	16	141	84	116	13	21
Sr	282	287	454	288	290	150	325	229	336	191
Y	20.5	20.8	18.5	4.5	5.3	10.1	36.1	24.5	10.7	18.5
Zr	27	63	8	60	96	122	147	93	23	49
Nb	3.2	5.5	2.3	2.8	1.8	3	10.8	8.9	0.6	0.7
Mo	<2	<2	<2	<2	<2	<2	<2	<2	<2	<2
Ag	<0.5	<0.5	<0.5	<0.5	<0.5	0.5	0.6	<0.5	<0.5	<0.5
In	0.1	0.1	<0.1	<0.1	<0.1	<0.1	0.1	0.1	<0.1	0.1
Sn	<1	2	1	<1	<1	1	3	4	<1	2
Sb	<0.2	<0.2	<0.2	<0.2	<0.2	<0.2	<0.2	<0.2	<0.2	<0.2
Cs	0.5	1.4	0.6	0.9	1.2	2.1	4.3	14.6	1.4	2.1
Ba	76	94	104	234	175	721	314	242	47	25
La	5.24	15	12.6	6.71	14.2	26.2	14.9	15.3	3.66	3.78
Ce	13.4	33.9	26.6	11.1	24.3	49	41.8	31.8	8.48	9.68
Pr	2	4.26	3.54	1.11	2.41	4.94	6.23	3.86	1.21	1.51
Nd	10.5	16.9	15.6	3.95	8.1	16.6	28.5	16.3	6.08	7.36
Sm	3.33	4.02	3.85	0.76	1.35	3	6.91	4.11	1.65	2.31
Eu	1.02	1.11	1.11	0.643	0.715	0.486	1.66	0.992	0.633	0.837
Gd	3.7	3.69	3.77	0.71	1.04	2.21	6.62	3.86	1.75	2.76
Tb	0.66	0.62	0.61	0.11	0.16	0.36	1.09	0.68	0.31	0.52
Dy	4.08	3.87	3.44	0.67	0.9	1.99	6.81	4.17	1.98	3.41
Ho	0.79	0.77	0.65	0.14	0.18	0.34	1.34	0.85	0.41	0.69
Er	2.18	2.21	1.78	0.44	0.52	0.98	3.87	2.45	1.19	2.07
Tm	0.298	0.318	0.249	0.067	0.08	0.155	0.56	0.354	0.167	0.298
Yb	1.84	2.08	1.51	0.43	0.56	1.13	3.58	2.3	1.06	1.98
Lu	0.273	0.322	0.222	0.065	0.09	0.173	0.53	0.353	0.167	0.303
Hf	1	1.8	0.4	1.6	2.4	3.7	3.5	2.6	0.6	1.3
Ta	0.24	0.42	0.35	0.95	0.98	1.03	0.56	1.33	0.1	0.19
W	83.1	49.8	148	439	598	688	47.8	125	61	156
Tl	<0.05	0.06	<0.05	0.08	<0.05	0.64	0.29	0.66	0.07	<0.05
Pb	<5	6	11	13	10	34	<5	8	<5	<5
Bi	<0.1	0.1	<0.1	<0.1	<0.1	<0.1	<0.1	0.1	<0.1	0.7
Th	0.48	2.8	1.45	4.48	6.49	31.2	0.58	6.72	0.45	0.45
U	0.12	0.97	0.69	1.69	1.81	4.75	0.32	3.82	0.09	0.17

Appendix 5–7. Primitive mantle- and C1 chondrite-normalized trace element diagrams of the Kita-taku mafic complex and related rocks. The normalizing values are from Sun and McDonough (1989).

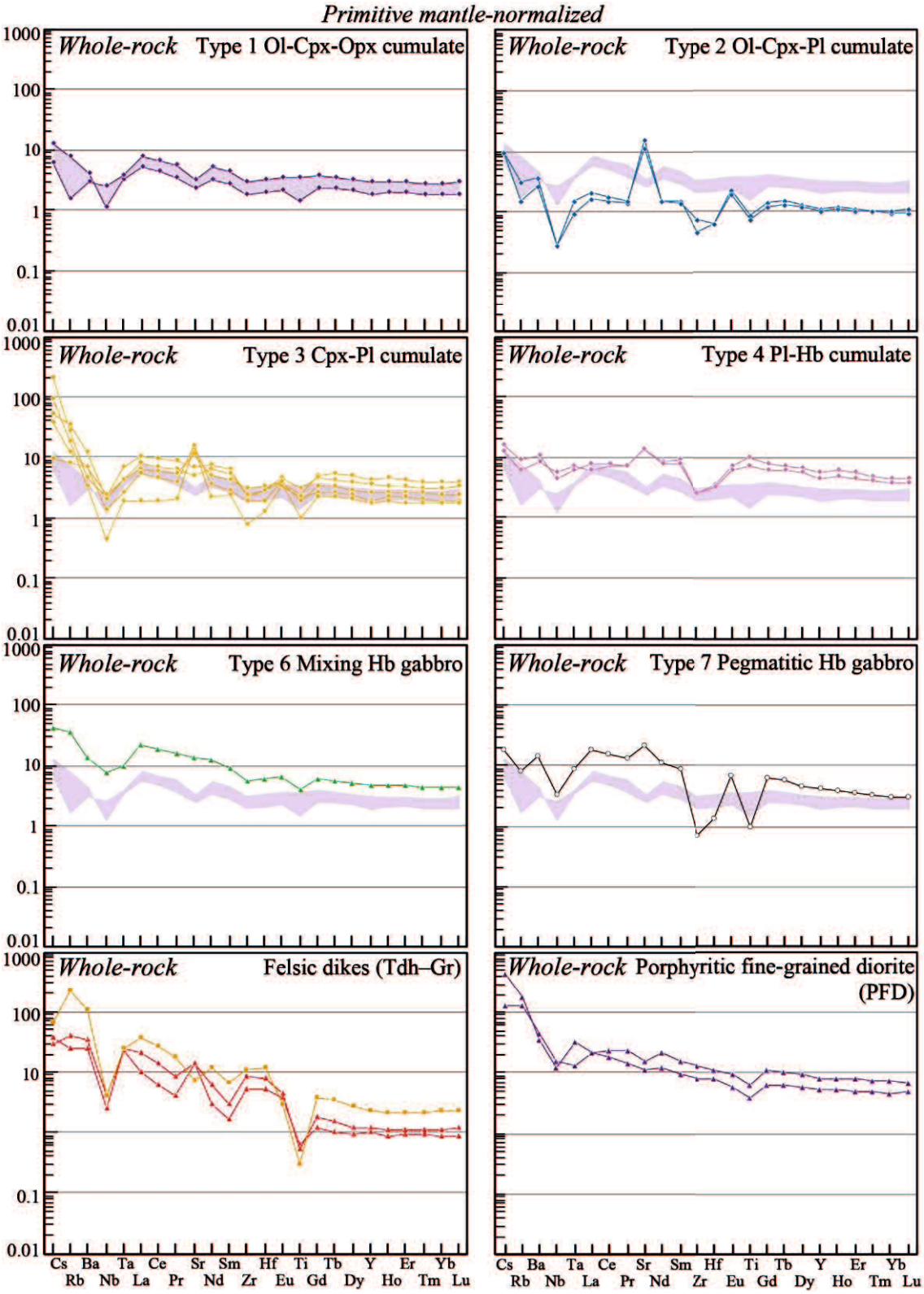

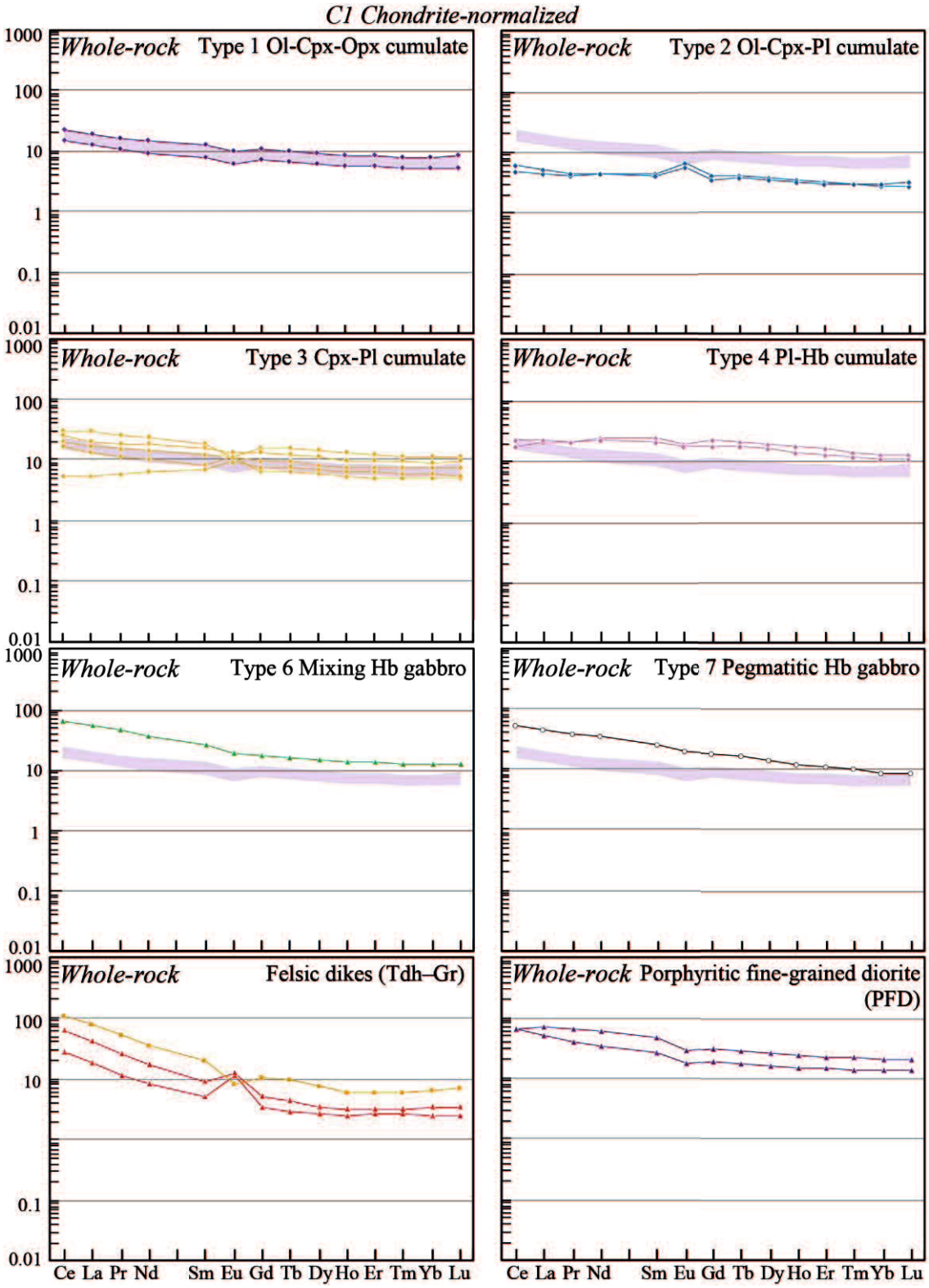
C1 Chondrite-normalized
Whole-rock Type 1 Ol-Cpx-Opx cumulate
Whole-rock Type 2 Ol-Cpx-Pl cumulate
Whole-rock Type 3 Cpx-Pl cumulate
Whole-rock Type 4 Pl-Hb cumulate
Whole-rock Type 6 Mixing Hb gabbro
Whole-rock Type 7 Pegmatitic Hb gabbro
Whole-rock Felsic dikes (Tdh–Gr)
Whole-rock Porphyritic fine-grained diorite (PFD)
1000
100
10
1
0.1
0.01
Ce La Pr Nd Sm Eu Gd Tb Dy Ho Er Tm Yb Lu

Appendix 5–8. Representative chemical analysis for the Kita-taku mafic complex.

Mineral	Plagioclase													
Type	1		2		3		4		5		6		7	
Position	core	core	core	core	core	core	core	core	core	core	core	core	core	core
SiO_2	44.17	44.51	44.49	44.84	44.56	46.30	45.07	45.42	48.08	53.65	48.84	57.07	45.71	59.96
TiO_2	0.02	0.03	0	0.01	0	0	0	0.026	0	0.03	0.03	0.02	0	0
Al_2O_3	35.73	35.22	36.27	35.55	35.78	33.68	35	34.89	33.25	29.95	31.70	26.69	33.86	25.60
Cr_2O_3	0	0	0.02	0	0.00	0	0	0	0.01	0.03	0.01	0.02	0	0
FeO	0.15	0.10	0.10	0.25	0.14	0.09	0.08	0.07	0	0.10	0.14	0.01	0.03	0.04
MnO	0	0.01	0	0.02	0.02	0.04	0	0.01	0.06	0.03	0	0.01	0.05	0
MgO	0	0.01	0.01	0.02	0.01	0	0	0	0.01	0	0	0.02	0.01	0.02
CaO	18.31	17.68	18.67	18.30	18.04	16.51	18.03	17.48	14.95	10.70	14.67	8.41	17.03	6.83
Na_2O	1.05	1.39	1.07	1.12	1.28	2.18	1.3	1.70	2.80	5.28	4.90	7.42	2.42	7.15
K_2O	0.02	0.02	0.01	0	0.00	0.01	0.01	0.01	0.05	0.08	0.05	0.06	0.02	0.40
NiO	0	0.01	0.02	0	0.02	0.05	0.05	0.03	0	0	0.04	0.01	0	0
ZnO	0	0	0	0	0.00	0.03	0	0	0	0.02	0.01	0.005	0	0
Total	99.44	98.97	100.64	100.10	99.86	98.86	99.53	99.63	99.21	99.85	100.38	99.73	99.12	100.02
O	8	8	8	8	8	8	8	8	8	8	8	8	8	8
Si	2.051	2.073	2.042	2.068	2.059	2.152	2.088	2.100	2.213	2.424	2.240	2.570	2.126	2.668
Ti	0.001	0.001	0	0	0	0	0	0.001	0	0.001	0.001	0.001	0	0
Al	1.955	1.934	1.962	1.932	1.949	1.845	1.911	1.901	1.804	1.595	1.714	1.417	1.857	1.343
Cr	0	0	0.001	0	0	0	0	0	0	0.001	0.001	0.001	0	0
Fe	0.006	0.004	0.004	0.010	0.005	0.003	0.003	0.003	0	0.004	0.005	0	0.001	0.002
Mn	0	0	0	0.001	0.001	0.001	0	0	0.002	0.001	0	0	0.002	0
Mg	0	0.001	0.001	0.001	0.001	0	0	0	0.001	0	0	0.001	0	0.002
Ca	0.911	0.882	0.918	0.904	0.893	0.822	0.895	0.866	0.738	0.518	0.721	0.406	0.849	0.326
Na	0.094	0.125	0.095	0.100	0.115	0.196	0.117	0.153	0.250	0.463	0.435	0.647	0.218	0.617
K	0.001	0.001	0	0	0	0.001	0.001	0.001	0.003	0.004	0.003	0.003	0.001	0.023
Ni	0	0	0.001	0	0.001	0.002	0.002	0.001	0	0	0.001	0	0	0
Zn	0	0	0	0	0	0.001	0	0	0	0.001	0	0	0	0
Total	5.018	5.022	5.024	5.016	5.024	5.024	5.016	5.025	5.011	5.011	5.121	5.046	5.055	4.980
An	90.53	87.45	90.58	90.01	88.60	80.68	88.40	84.94	74.50	52.59	62.21	38.39	79.46	33.74

Mineral	Hornblende													
Type	1		2		3		4		5		6		7	
Position	core	core	core	core	core	core	core	core	core	core	core	core	core	core
SiO_2	42.63	41.70	42.84	41.91	42.09	45.20	41.49	40.82	42.56	41.05	49.85	46.83	48.82	44.18
TiO_2	2.24	2.45	1.45	2.23	2.99	1.55	2.64	2.18	1.31	1.01	0.33	1.10	0.27	2.78
Al_2O_3	12.99	13.46	13.92	13.52	13.72	8.85	13.70	14.52	11.91	13.67	7.22	9.76	9.69	11.57
Cr_2O_3	0.31	0.04	0.05	0.09	0.11	0.03	0.05	0.03	0.01	0.01	0.07	0.15	0.03	0.16
FeO	8.72	11.10	9.82	10.92	12.14	16.55	13.55	16.83	18.72	19.53	12.87	13.85	9.43	10.73
MnO	0.12	0.14	0.17	0.11	0.16	0.26	0.18	0.19	0.36	0.36	0.23	0.27	0.16	0.14
MgO	15.84	14.25	14.23	14.23	12.44	11.42	12.04	10.00	8.82	7.96	14.50	12.93	15.48	13.51
CaO	11.35	11.13	11.41	11.23	11.31	11.52	11.18	10.54	11.52	11.13	11.43	11.31	11.55	11.19
Na_2O	2.31	1.47	0.75	0.90	1.54	1.07	2.01	2.00	1.40	1.84	1.13	1.64	1.38	1.54
K_2O	0.50	0.54	0.89	0.78	0.62	0.58	0.52	0.51	0.53	0.59	0.13	0.46	0.11	0.85
NiO	0	0	0.03	0.01	0.01	0.03	0	0	0	0.02	0	0.03	0	0
ZnO	0.08	0.01	0	0.01	0.04	0	0	0	0	0	0	0	0	0
Total	97.07	96.28	95.54	95.92	97.17	97.07	97.37	97.62	97.15	97.17	97.76	98.33	96.92	96.65
O	23	23	23	23	23	23	23	23	23	23	23	23	23	23
Si	6.216	6.177	6.331	6.218	6.208	6.782	6.160	6.123	6.469	6.278	7.209	6.824	7.014	6.495
Ti	0.245	0.273	0.162	0.249	0.331	0.175	0.294	0.246	0.150	0.116	0.036	0.120	0.029	0.308
Al	2.233	2.350	2.424	2.364	2.385	1.565	2.397	2.568	2.134	2.463	1.231	1.676	1.640	2.005
Cr	0.036	0.005	0.006	0.011	0.012	0.004	0.006	0.004	0.001	0.001	0.008	0.018	0.003	0.019
Fe	1.063	1.375	1.214	1.355	1.498	2.077	1.682	2.111	2.380	2.498	1.556	1.688	1.133	1.319
Mn	0.015	0.017	0.021	0.014	0.020	0.033	0.023	0.024	0.047	0.047	0.028	0.034	0.019	0.017
Mg	3.442	3.145	3.134	3.146	2.734	2.555	2.665	2.236	1.999	1.813	3.124	2.807	3.315	2.961
Ca	1.773	1.767	1.807	1.785	1.788	1.853	1.779	1.693	1.876	1.823	1.772	1.766	1.778	1.763
Na	0.654	0.421	0.214	0.258	0.441	0.312	0.579	0.581	0.413	0.546	0.317	0.462	0.384	0.439
K	0.093	0.102	0.167	0.148	0.117	0.111	0.099	0.098	0.102	0.115	0.024	0.085	0.021	0.159
Ni	0	0	0.003	0.002	0.001	0.004	0	0	0	0.003	0	0.004	0	0
Zn	0.008	0.002	0	0.001	0.004	0	0	0	0	0	0	0	0	0
Total	15.778	15.634	15.483	15.549	15.541	15.470	15.683	15.685	15.570	15.704	15.305	15.483	15.337	15.484
Mg#	76.40	69.58	72.08	69.90	64.60	55.15	61.31	51.44	45.64	42.05	66.75	62.45	74.52	69.18

Contiued…

Mineral	Olivine				Orthopyroxene						Spinel			
Type	1		2		1		2		7		1			
Position	core	core	core	core	core	core	core	core	core	core	core	core	core	core
SiO_2	37.05	37.07	37.31	36.44	51.99	52.37	51.66	52.08	55.13	54.62	0.06	0.05	0.03	0.05
TiO_2	0.02	0	0.02	0	0.18	0.17	0.27	0.21	0	0	1.23	1.14	1.52	1.14
Al_2O_3	0.00	0.01	0	0.03	2.39	2.77	2.28	2.57	1.50	1.50	21.23	22.22	21.33	22.22
Cr_2O_3	0	0.01	0.01	0	0.23	0.06	0.07	0.05	0.05	0	33.22	33.23	33.45	33.23
FeO	22.92	25.95	24.91	28.36	14.34	17.43	14.87	16.54	18.25	20.29	40.22	40.12	40.02	40.12
MnO	0.29	0.31	0.36	0.50	0.28	0.43	0.38	0.32	0.44	0.55	1.13	0.98	1.22	0.98
MgO	38.53	36.60	36.82	34.54	28.29	25.47	25.70	25.56	21.72	20.66	0.84	0.84	0.89	0.84
CaO	0	0	0.01	0	1.09	1.10	2.61	1.07	0.97	0.98	0.01	0.01	0	0.01
Na_2O	0	0	0	0	0.03	0.03	0.05	0.01	0.02	0.11	0.02	0	0.02	0
K_2O	0	0	0	0	0	0.00	0.01	0	0.02	0	0	0	0	0
NiO	0.03	0.01	0.04	0.02	0.01	0	0	0	0.03	0	0.15	0.09	0.12	0.09
ZnO	0	0	0.01	0	0	0	0	0	0	0	0.01	0	0.02	0
Total	98.84	99.96	99.48	99.90	98.83	99.83	97.89	98.41	98.12	98.69	98.12	98.68	98.62	98.68
O	4	4	4	4	6	6	6	6	6	6	32	32	32	32
Si	0.982	0.984	0.990	0.981	1.898	1.915	1.917	1.924	2.041	2.032	0.017	0.014	0.008	0.014
Ti	0	0	0	0	0.005	0.005	0.007	0.006	0	0	0.258	0.236	0.316	0.236
Al	0	0	0	0.001	0.103	0.119	0.100	0.112	0.065	0.066	6.969	7.211	6.955	7.211
Cr	0	0	0	0	0.007	0.002	0.002	0.002	0.001	0	7.314	7.233	7.315	7.233
Fe	0.508	0.576	0.553	0.639	0.438	0.533	0.461	0.511	0.565	0.631	9.368	9.238	9.258	9.238
Mn	0.006	0.007	0.008	0.011	0.009	0.013	0.012	0.010	0.014	0.017	0.267	0.229	0.286	0.229
Mg	1.521	1.448	1.457	1.386	1.539	1.388	1.421	1.407	1.198	1.146	0.349	0.345	0.367	0.345
Ca	0	0	0.000	0	0.043	0.043	0.104	0.043	0.038	0.039	0.003	0.003	0	0.003
Na	0	0	0	0	0.002	0.002	0.004	0.001	0.002	0.008	0.011	0	0.011	0
K	0	0	0	0	0	0	0	0	0.001	0	0	0	0	0
Ni	0.001	0	0.001	0	0	0	0	0	0.001	0	0.034	0.020	0.027	0.020
Zn	0	0	0	0	0	0	0	0	0	0	0.002	0	0.004	0
Total	3.018	3.016	3.009	3.018	4.043	4.021	4.027	4.014	3.927	3.939	24.590	24.528	24.546	24.528
Mg#	74.97	71.54	72.48	90.01	77.86	72.26	75.50	73.36	67.95	64.48	–	–	–	–
Cr#	–	–	–	–	–	–	–	–	–	–	0.51	0.50	0.51	0.50

Mineral	Clinopyroxene							
Type	1		2		3		7	
Position	core	core	core	core	core	core	core	core
SiO_2	51.54	51.29	50.24	50.19	51.83	51.23	51.39	51.85
TiO_2	0.25	0.41	0.57	0.58	0.21	0.07	0.38	0.34
Al_2O_3	2.19	2.48	3.92	3.51	1.02	0.85	2.87	2.92
Cr_2O_3	0.29	0.23	0.15	0	0.02	0.01	0.08	0.11
FeO	5.35	6.32	5.91	8.55	7.87	10.39	6.33	6.84
MnO	0.17	0.25	0.22	0.22	0.27	0.29	0.24	0.19
MgO	15.79	15.67	14.56	14.93	14.88	13.30	15.31	15.30
CaO	23.16	22.60	22.54	20.62	23.27	23.17	22.21	21.98
Na_2O	0.16	0.20	0.37	0.29	0.18	0.22	0.31	0.25
K_2O	0.01	0	0.00	0.00	0	0.00	0	0.01
NiO	0	0.02	0	0	0.01	0.01	0	0
ZnO	0.08	0	0	0	0	0	0.02	0.02
Total	98.98	99.48	98.47	98.88	99.57	99.53	99.14	99.80
O	6	6	6	6	6	6	6	6
Si	1.923	1.910	1.887	1.889	1.945	1.947	1.916	1.920
Ti	0.007	0.012	0.016	0.016	0.006	0.002	0.011	0.009
Al	0.096	0.109	0.174	0.156	0.045	0.038	0.126	0.127
Cr	0.008	0.007	0.004	0	0.001	0.000	0.002	0.003
Fe	0.167	0.197	0.186	0.269	0.247	0.330	0.197	0.212
Mn	0.005	0.008	0.007	0.007	0.009	0.009	0.008	0.006
Mg	0.878	0.869	0.815	0.837	0.832	0.753	0.850	0.844
Ca	0.926	0.902	0.907	0.832	0.936	0.943	0.887	0.872
Na	0.011	0.015	0.027	0.021	0.013	0.016	0.022	0.018
K	0.001	0	0	0	0	0	0	0
Ni	0	0.001	0	0	0	0	0	0
Zn	0.002	0	0	0	0	0	0.001	0
Total	4.024	4.028	4.022	4.027	4.033	4.040	4.020	4.014
Mg#	84.04	81.54	81.44	75.68	77.11	69.52	81.17	79.94

Appendix 5–9. Trace element and rare earth element (REE) concentrations of the clinopyroxene from Kita-taku mafic complex determined by LA-ICP-MS at GSJ-lab.

No.		1	2	3	4	5	6	7	8	9	10	11	12
Sample. No.		21021406B	21021406B	21021406B	21021406B	21021406B	21021406B	21021406B	21021406B	21021406B	21021406B	21021406B	21021406B
Beam Dia.		40 mm	100 mm	80 mm	100 mm	100 mm	100 mm	100 mm	80 mm	100 mm	100 mm	80 mm	80 mm
Sc	ppm	125.20	122.24	109.64	117.36	111.02	100.01	123.55	121.28	132.05	117.68	100.90	110.22
Ti	ppm	2171.98	1993.99	1887.33	2341.55	1917.32	1890.44	2376.53	2216.28	2403.20	2226.94	2113.83	2187.09
V	ppm	670.93	511.32	549.84	537.37	546.58	508.24	709.46	699.33	758.63	563.33	487.22	536.99
Cr	ppm	5201.87	1671.39	2660.98	1671.87	4005.16	3194.70	1587.12	4709.65	5477.01	3725.49	2422.35	2352.11
Mn	ppm	1682.53	1787.31	1576.25	1537.14	1728.87	1709.67	1653.87	1794.30	1766.04	1633.80	1633.52	1657.12
Co	ppm	33.65	34.72	34.32	31.35	35.16	39.28	32.89	37.85	37.31	32.42	33.39	33.78
Ni	ppm	47.05	38.93	45.64	41.69	57.14	54.23	38.27	59.77	63.15	41.92	42.21	47.15
Zn	ppm	46.91	47.09	47.17	43.21	54.77	53.45	48.92	56.42	55.37	46.08	49.81	49.20
Rb	ppm	0.07	0.04	0.25	0.20	0.16	0.38	0.06	0.25	0.15	0.36	0.15	0.04
Sr	ppm	18.52	16.41	21.46	20.68	19.38	23.79	18.17	20.18	19.39	20.24	19.15	18.58
Y	ppm	11.66	9.64	8.90	11.04	10.21	8.73	11.44	10.69	12.48	11.72	9.42	9.81
Z	ppm	9.55	6.08	8.65	8.69	8.53	10.13	9.95	9.47	9.31	9.76	8.18	6.64
Nb	ppm	0.03	0.10	0.05	0.05	0.05	0.02	0.04	0.04	0.04	0.03	0.04	0.01
Cs	ppm	<0.000	0.03	0.01	0.01	0.00	0.11	<0.000	0.02	0.09	0.02	0.01	0.04
Ba	ppm	0.47	0.16	2.51	2.76	1.85	3.76	1.01	1.40	1.01	1.27	0.88	0.15
La	ppm	1.00	0.78	1.40	1.23	1.44	1.51	1.36	1.06	1.14	1.12	0.97	0.81
Ce	ppm	3.28	2.86	3.93	3.36	3.78	4.10	3.89	3.86	3.81	3.91	3.78	3.13
Pr	ppm	0.62	0.55	0.67	0.54	0.57	0.66	0.72	0.69	0.68	0.66	0.68	0.58
Nd	ppm	4.22	3.56	3.51	3.38	3.57	3.35	3.79	4.03	4.05	4.12	3.81	3.61
Sm	ppm	1.50	1.31	1.02	1.47	1.13	1.25	1.23	1.44	1.49	1.32	1.61	1.36
Eu	ppm	0.51	0.34	0.28	0.37	0.37	0.34	0.33	0.48	0.45	0.40	0.37	0.33
Gd	ppm	1.63	1.73	1.61	1.75	1.62	1.42	1.94	1.73	2.03	1.87	1.64	1.80
Tb	ppm	0.33	0.29	0.29	0.33	0.28	0.26	0.37	0.27	0.38	0.32	0.31	0.32
Dy	ppm	2.34	2.02	1.60	2.04	1.92	1.86	2.31	2.10	2.28	2.14	2.04	1.89
Ho	ppm	0.51	0.42	0.31	0.44	0.40	0.40	0.50	0.56	0.50	0.42	0.39	0.39
Er	ppm	1.38	1.16	1.09	1.26	1.12	1.06	1.27	1.24	1.32	1.25	1.02	1.10
Tm	ppm	0.19	0.14	0.14	0.15	0.16	0.15	0.18	0.18	0.18	0.16	0.15	0.17
Yb	ppm	1.29	0.98	0.69	1.00	1.09	0.90	1.12	1.09	1.30	1.15	0.77	1.05
Lu	ppm	0.20	0.14	0.15	0.15	0.13	0.11	0.15	0.17	0.16	0.16	0.11	0.13
Hf	ppm	0.45	0.26	0.33	0.39	0.39	0.37	0.46	0.43	0.43	0.46	0.29	0.37
Ta	ppm	0.00	0.01	0.00	0.00	0.00	0.00	0.02	<0.000	0.01	0.01	0.00	0.00
Pb	ppm	0.10	0.08	0.17	0.26	0.20	0.30	0.15	0.09	0.14	0.09	0.07	0.09
Th	ppm	0.14	0.16	0.17	0.26	0.40	0.47	0.22	0.30	0.26	0.10	0.12	0.08
U	ppm	0.02	0.03	0.02	0.06	0.07	0.09	0.05	0.09	0.04	0.01	0.02	0.02
Ca (ISTD)	CPS	272608	1090627	826568	1296165	1248229	797154	1259153	737443	1202211	1262564	817952	812536
	CPS RSD	9.80	4.03	4.40	5.48	6.88	10.90	12.42	10.54	12.20	8.85	2.85	6.55

Continued…

No.		13	14	15	16	17	18	19	20	21	22	23	24
Sample. No.		21021406B	21021406B	21021406B	21021406B	21021406B	21021406B	21021406B	20110204	20110204	20110204	20110204	20110204
Beam Dia.		100 mm	100 mm	60 mm	80 mm	100 mm	100 mm	100 mm	100 mm	100 mm	100 mm	100 mm	100 mm
Sc	ppm	110.86	97.90	119.81	122.49	117.03	122.66	96.05	168.34	159.17	139.76	151.32	133.54
Ti	ppm	2225.51	2065.16	3608.66	3050.92	2426.30	2227.06	1982.06	4667.09	3636.99	3257.22	4157.56	3650.42
V	ppm	536.23	462.60	623.04	790.22	632.58	689.01	381.65	518.81	424.55	388.17	470.59	429.54
Cr	ppm	2735.84	1768.66	1936.07	2140.11	1979.26	1650.08	2627.06	597.60	651.88	292.32	529.78	766.24
Mn	ppm	1694.49	1446.26	1592.39	2025.68	1553.37	1533.59	1631.92	1819.92	1878.11	1741.72	1635.78	1700.47
Co	ppm	34.18	28.01	35.85	39.25	33.81	32.86	34.32	38.00	36.23	35.03	33.58	34.34
Ni	ppm	45.50	35.09	44.52	47.19	36.92	37.27	33.67	18.40	23.84	13.26	14.86	21.54
Zn	ppm	49.58	33.20	44.35	56.92	39.87	34.30	41.08	31.21	35.21	36.69	34.71	33.20
Rb	ppm	0.09	0.07	0.17	0.11	0.13	0.37	0.07	0.05	0.04	0.81	1.96	0.85
Sr	ppm	20.82	16.80	24.87	21.32	17.51	26.64	18.89	22.52	22.76	19.02	23.52	20.99
Y	ppm	11.13	9.89	13.68	14.08	10.05	9.01	10.58	21.56	17.48	16.69	18.18	16.19
Zr	ppm	8.52	6.02	10.17	13.00	7.17	12.70	7.11	23.48	19.47	17.00	23.43	21.26
Nb	ppm	0.05	0.02	0.21	0.04	0.02	0.02	0.03	0.14	0.04	0.01	0.02	0.04
Cs	ppm	0.02	0.07	0.00	0.02	0.00	0.02	0.00	0.11	0.01	0.11	0.08	0.08
Ba	ppm	0.85	0.40	3.82	0.57	1.12	5.42	0.92	0.36	0.65	0.99	2.43	1.14
La	ppm	1.03	0.69	0.98	1.44	0.85	1.55	1.02	1.33	1.22	1.10	1.37	1.30
Ce	ppm	3.68	2.58	3.67	4.67	2.78	4.08	3.69	5.31	4.45	4.50	5.40	4.74
Pr	ppm	0.66	0.51	0.74	0.86	0.54	0.65	0.69	1.05	0.82	0.85	1.05	0.90
Nd	ppm	3.85	3.24	4.17	5.27	3.31	3.51	3.56	6.88	5.59	5.45	6.35	5.82
Sm	ppm	1.46	1.21	1.55	1.97	1.31	1.30	1.37	2.54	2.28	1.99	2.20	1.95
Eu	ppm	0.39	0.29	0.46	0.44	0.30	0.36	0.42	0.88	0.68	0.58	0.69	0.63
Gd	ppm	1.77	1.73	2.44	2.23	1.67	1.71	1.73	3.50	3.10	2.75	2.93	3.01
Tb	ppm	0.32	0.29	0.40	0.44	0.30	0.25	0.30	0.68	0.58	0.54	0.56	0.49
Dy	ppm	2.17	1.93	2.56	2.66	1.89	1.91	1.91	4.22	3.53	3.45	3.71	3.30
Ho	ppm	0.44	0.39	0.54	0.53	0.42	0.38	0.40	0.93	0.74	0.67	0.75	0.70
Er	ppm	1.23	1.09	1.47	1.48	1.14	1.11	1.08	2.49	1.98	1.85	1.94	1.83
Tm	ppm	0.17	0.13	0.20	0.23	0.16	0.15	0.14	0.34	0.28	0.27	0.31	0.25
Yb	ppm	1.08	1.00	1.26	1.35	1.05	0.88	1.01	2.26	1.73	1.69	1.76	1.64
Lu	ppm	0.16	0.12	0.16	0.19	0.15	0.12	0.15	0.33	0.24	0.24	0.24	0.23
Hf	ppm	0.37	0.35	0.47	0.73	0.33	0.57	0.33	1.26	1.11	0.71	0.94	0.80
Ta	ppm	0.00	0.00	0.01	0.01	0.00	0.01	0.00	0.01	0.01	0.00	0.00	0.01
Pb	ppm	0.06	0.08	0.10	0.11	0.07	0.23	0.18	0.06	0.11	0.04	0.10	0.05
Th	ppm	0.11	0.07	0.06	0.25	0.11	0.28	0.19	0.10	0.20	0.17	0.27	0.27
U	ppm	0.01	0.02	0.01	0.03	0.03	0.07	0.05	0.02	0.04	0.06	0.11	0.08
Ca (ISTD)	CPS	1256518	1245923	743461	770797	1214639	1198714	1061232	1444446	1410378	1018399	1156780	1028278
	CPS RSD	7.17	7.66	7.90	6.12	8.47	8.94	6.79	9.89	9.80	7.23	4.40	5.48

Continued…

No.		25	26	27	28	29	30	31	32	33	34	35	36
Sample. No.		20110204	20110204	20110204	20110204	20110204	20110204	20110204	20110204	20110204	20110204	20110204	20110204
Beam Dia.		100 mm	100 mm	100 mm	100 mm	100 mm	100 mm	100 mm	100 mm	100 mm	100 mm	100 mm	100 mm
Sc	ppm	134.06	161.49	130.79	145.10	139.69	148.49	151.16	161.32	128.77	163.99	154.39	165.77
Ti	ppm	3233.63	4588.41	3961.93	3714.28	3719.77	3710.91	3773.56	3957.92	3160.24	4204.77	3903.93	4516.26
V	ppm	392.42	500.82	406.91	432.09	459.27	442.05	443.03	464.56	393.28	486.00	462.48	514.07
Cr	ppm	433.95	460.46	592.33	367.80	843.08	443.15	349.65	400.64	616.93	454.03	628.19	621.57
Mn	ppm	1795.61	1700.81	1521.59	1739.88	1835.61	1843.24	1896.80	1855.41	1741.07	1850.73	1820.73	1916.12
Co	ppm	37.12	33.43	35.19	34.68	39.47	34.93	37.31	36.79	34.65	36.40	36.34	38.76
Ni	ppm	18.08	12.62	21.00	11.40	93.42	16.66	18.09	13.51	20.90	16.93	21.00	20.82
Zn	ppm	40.69	33.96	34.55	37.30	39.22	36.38	38.88	48.76	36.15	40.75	38.72	42.95
Rb	ppm	0.51	0.23	0.64	2.07	2.02	3.16	2.50	0.26	0.48	0.37	0.03	0.12
Sr	ppm	19.28	20.37	20.51	22.28	24.85	27.41	24.11	20.63	20.14	19.30	20.71	20.63
Y	ppm	15.96	20.04	16.87	17.46	17.30	17.62	18.52	20.22	15.18	19.15	18.49	20.79
Zr	ppm	14.98	22.39	17.77	21.68	21.37	24.61	22.79	21.22	20.26	21.51	21.20	23.62
Nb	ppm	0.03	0.05	0.03	0.03	0.05	0.03	0.04	0.04	0.03	0.04	0.05	0.04
Cs	ppm	0.03	0.04	0.02	0.11	0.19	0.19	0.18	0.03	0.03	0.03	0.00	0.05
Ba	ppm	0.56	0.43	0.88	2.20	2.28	4.10	2.92	0.39	0.77	0.44	0.42	0.37
La	ppm	0.94	1.15	0.99	1.33	1.53	1.77	1.51	1.21	1.34	1.19	1.25	1.17
Ce	ppm	3.78	5.44	4.10	5.32	5.19	5.80	5.26	5.31	4.82	4.80	5.37	4.84
Pr	ppm	0.83	1.11	0.89	1.05	1.01	1.05	0.98	1.11	0.87	1.01	0.99	0.95
Nd	ppm	5.25	6.68	5.43	6.15	6.12	6.33	5.91	6.45	5.38	6.19	6.47	6.32
Sm	ppm	1.76	2.34	2.24	2.34	2.54	2.28	2.15	2.60	1.83	2.62	2.26	2.41
Eu	ppm	0.59	0.78	0.64	0.70	0.71	0.67	0.75	0.68	0.48	0.72	0.74	0.78
Gd	ppm	2.64	3.57	3.01	3.33	2.85	3.06	2.81	3.24	2.44	3.08	3.07	3.54
Tb	ppm	0.49	0.63	0.52	0.56	0.54	0.53	0.56	0.63	0.45	0.63	0.51	0.63
Dy	ppm	2.96	3.82	3.43	3.62	3.44	3.67	3.82	3.93	3.16	3.94	3.96	4.05
Ho	ppm	0.67	0.84	0.71	0.70	0.74	0.78	0.77	0.81	0.63	0.79	0.81	0.88
Er	ppm	1.79	2.28	1.89	1.93	2.01	1.92	2.13	2.24	1.72	2.14	2.00	2.39
Tm	ppm	0.24	0.32	0.25	0.27	0.26	0.27	0.29	0.32	0.24	0.29	0.30	0.34
Yb	ppm	1.51	2.02	1.58	1.79	1.79	1.80	1.87	1.93	1.47	1.90	1.78	2.17
Lu	ppm	0.23	0.28	0.23	0.23	0.23	0.23	0.22	0.24	0.21	0.24	0.26	0.29
Hf	ppm	0.68	1.06	0.94	0.90	0.89	1.09	0.98	0.96	0.81	1.11	1.02	1.23
Ta	ppm	0.00	0.02	0.00	0.02	0.01	0.00	0.00	0.02	0.02	0.01	0.02	0.01
Pb	ppm	0.05	0.06	0.04	0.12	0.11	0.13	0.14	0.07	0.10	0.06	0.05	0.05
Th	ppm	0.10	0.11	0.12	0.37	0.40	0.54	0.38	0.08	0.18	0.12	0.12	0.13
U	ppm	0.02	0.04	0.05	0.12	0.14	0.15	0.13	0.02	0.06	0.02	0.02	0.03
Ca (ISTD)	CPS	985638	1074439	1083383	1065051	913063	966640	969191	991871	982833	1139371	1095712	1111008
	CPS RSD	6.88	10.90	12.42	10.54	12.20	8.85	2.85	6.55	7.17	6.29	8.79	7.90

Continued…

No.		37	38	39	40	41	42	43	44	45	46	47	48
Sample. No.		20110302A	20110302A	20110302A	20061203A	20061203A	20061203A	20061203A	20061203A	20061203A	20061203A	20110707	20110707
Beam Dia.		100 mm	100 mm	100 mm	100 mm	100 mm	100 mm	100 mm	100 mm	100 mm	80 mm	100 mm	Cpx5-3 100mm
Sc	ppm	97.98	81.76	77.12	98.87	87.58	95.48	93.43	81.02	120.25	139.07	95.47	109.84
Ti	ppm	3606.75	2292.00	1577.63	2012.03	1866.44	1714.56	2223.37	1452.04	3142.25	3697.52	1839.07	1793.13
V	ppm	243.21	273.18	284.77	272.13	234.29	244.70	281.42	197.53	391.70	469.22	269.45	340.79
Cr	ppm	199.87	70.58	230.37	135.89	107.79	137.64	183.21	101.87	341.33	423.95	232.58	291.48
Mn	ppm	2681.90	2424.06	2470.38	2097.54	2254.46	2354.11	2118.56	2108.13	2168.22	2059.37	2451.52	2178.20
Co	ppm	28.40	36.17	30.00	41.17	37.30	36.44	34.85	39.48	39.09	39.01	34.84	35.99
Ni	ppm	21.96	22.86	16.83	24.39	21.68	22.71	21.99	24.69	24.57	22.98	42.14	24.91
Zn	ppm	92.15	121.91	102.10	68.48	54.54	57.03	60.60	66.60	58.66	57.65	53.05	52.91
Rb	ppm	1.50	1.77	1.02	1.17	0.05	0.10	0.15	0.95	0.45	0.56	0.78	0.62
Sr	ppm	24.14	12.07	8.37	26.26	26.82	32.69	30.53	45.95	34.48	37.20	43.04	23.11
Y	ppm	27.60	16.43	16.95	15.24	12.01	12.86	13.89	12.31	15.73	17.04	17.64	18.65
Zr	ppm	27.40	32.33	17.96	26.39	20.34	27.98	25.79	29.69	27.72	30.00	29.29	23.66
Nb	ppm	0.23	0.49	0.40	0.47	0.17	0.07	0.05	0.20	0.40	0.35	0.08	0.05
Cs	ppm	0.47	0.10	0.48	0.08	0.05	0.18	0.36	0.35	0.06	0.06	0.67	0.39
Ba	ppm	5.07	5.38	0.67	8.70	1.59	0.84	1.18	6.93	5.56	6.00	1.95	3.60
La	ppm	1.92	3.55	4.33	2.34	1.81	1.99	2.03	3.01	2.41	2.26	2.50	1.94
Ce	ppm	6.27	10.59	13.50	7.86	6.34	6.57	6.65	8.75	7.45	6.97	8.97	7.16
Pr	ppm	1.25	1.41	1.86	1.30	1.07	1.07	1.10	1.32	1.27	1.31	1.54	1.38
Nd	ppm	7.61	6.74	8.71	7.54	5.87	6.04	5.84	7.07	6.50	6.46	8.20	7.99
Sm	ppm	3.40	2.26	2.92	2.36	1.71	1.77	1.83	1.90	2.01	2.12	2.70	2.81
Eu	ppm	0.90	0.48	0.47	0.53	0.52	0.45	0.56	0.47	0.63	0.57	0.62	0.53
Gd	ppm	4.68	2.53	2.97	3.07	2.52	2.64	2.62	2.46	2.68	3.25	3.23	3.22
Tb	ppm	0.83	0.46	0.50	0.41	0.35	0.35	0.42	0.35	0.54	0.57	0.55	0.56
Dy	ppm	5.78	3.10	3.51	2.63	2.27	2.61	2.72	2.42	3.19	3.75	3.27	3.85
Ho	ppm	1.14	0.66	0.68	0.60	0.51	0.51	0.58	0.51	0.70	0.68	0.71	0.77
Er	ppm	3.15	1.99	2.01	1.66	1.35	1.40	1.60	1.42	1.80	1.97	2.08	1.92
Tm	ppm	0.41	0.26	0.28	0.23	0.18	0.24	0.21	0.17	0.24	0.29	0.29	0.28
Yb	ppm	2.89	1.83	2.05	1.46	1.44	1.40	1.50	1.58	1.43	1.71	1.72	1.85
Lu	ppm	0.38	0.29	0.33	0.22	0.19	0.24	0.18	0.18	0.21	0.23	0.30	0.26
Hf	ppm	1.23	1.28	0.83	1.10	0.89	1.13	1.03	0.93	1.22	1.39	1.22	1.01
Ta	ppm	0.02	0.02	0.03	0.05	0.04	0.01	0.01	0.02	0.03	0.03	0.01	0.01
Pb	ppm	0.40	0.56	0.49	0.27	0.24	0.24	0.17	0.31	0.17	0.11	0.42	0.39
Th	ppm	0.16	0.20	0.80	0.31	0.26	0.45	0.64	0.66	0.17	0.14	0.15	0.14
U	ppm	0.05	0.05	0.34	0.05	0.07	0.17	0.20	0.21	0.02	0.05	0.06	0.03
Ca (ISTD)	CPS	1183943	1135526	1337781	545512	713711	640531	685765	749440	691607	517989	1190518	1191294
	CPS RSD	7.23	4.40	6.88	9.80	4.03	7.23	4.40	4.40	10.90	12.42	9.89	7.23

Continued…

No.		49	50	51	52	53	54	55	56	57	58	59	60
Sample. No.		20110707	20110707	20110707	20110707	20110707	20110707	20110707	20110707	20110707	20110707	20110707	20110707
Beam Dia.		100 mm	100 mm	100 mm	100 mm	100 mm	100 mm	100 mm	100 mm	100 mm	100 mm	80 mm	80 mm
Sc	ppm	105.71	113.21	96.25	117.20	114.28	102.95	93.90	100.71	88.49	106.92	111.10	107.04
Ti	ppm	1729.48	2220.22	1842.18	1929.42	2426.27	2687.54	1725.04	1687.53	1126.89	2545.05	2161.64	2179.75
V	ppm	355.05	352.98	287.57	347.37	376.30	328.22	271.47	287.97	231.79	346.17	381.21	374.78
Cr	ppm	321.04	301.19	238.32	218.78	336.26	312.30	215.97	249.41	235.37	322.85	425.17	420.32
Mn	ppm	2117.14	2409.72	2376.65	2346.39	2533.62	2620.40	2383.33	2359.90	2706.79	2658.46	2467.24	2595.86
Co	ppm	37.92	46.66	38.90	39.73	44.07	49.34	39.46	40.26	41.73	40.58	40.51	39.26
Ni	ppm	26.42	33.05	25.91	20.40	29.77	30.31	23.75	24.20	25.60	28.79	29.64	28.09
Zn	ppm	63.49	74.28	58.03	66.60	76.70	80.31	63.20	67.94	69.73	59.70	62.06	68.04
Rb	ppm	0.16	0.73	0.09	0.29	0.60	1.50	1.34	3.09	0.58	0.57	1.34	0.29
Sr	ppm	21.70	26.07	20.10	20.92	26.37	31.93	30.77	27.11	17.57	31.10	28.47	22.58
Y	ppm	19.42	24.16	18.71	15.03	20.62	23.15	17.22	16.98	16.23	24.76	21.66	19.56
Zr	ppm	25.29	35.54	26.37	20.91	30.66	36.47	27.79	35.80	27.59	34.37	26.43	30.07
Nb	ppm	0.05	0.06	0.04	0.04	0.07	0.21	0.18	0.28	0.04	0.05	0.07	0.09
Cs	ppm	0.09	0.26	0.02	0.05	0.12	0.27	0.22	0.31	0.11	0.32	0.82	0.16
Ba	ppm	1.18	3.69	0.83	2.21	6.90	10.76	6.35	11.83	2.17	2.56	4.94	2.93
La	ppm	2.34	2.44	2.02	2.60	2.70	3.06	2.34	2.62	2.27	2.90	2.57	2.37
Ce	ppm	8.79	10.33	8.66	6.89	9.54	11.12	8.66	9.50	8.40	9.93	9.37	8.77
Pr	ppm	1.66	1.94	1.66	1.21	1.83	2.02	1.53	1.57	1.40	1.96	1.81	1.62
Nd	ppm	9.01	10.45	8.88	6.17	9.20	11.26	8.01	8.21	7.32	10.12	9.35	9.16
Sm	ppm	2.91	3.33	2.71	2.21	3.10	3.50	2.62	2.86	2.59	3.55	3.35	2.77
Eu	ppm	0.61	1.04	0.66	0.59	0.73	0.91	0.67	0.60	0.59	0.87	0.72	0.68
Gd	ppm	3.18	4.13	3.18	2.61	3.42	3.92	3.12	2.89	2.74	4.00	3.65	3.42
Tb	ppm	0.58	0.68	0.55	0.44	0.60	0.70	0.53	0.53	0.44	0.67	0.72	0.55
Dy	ppm	3.91	4.42	3.50	2.78	3.95	4.24	3.35	3.29	3.02	4.70	3.99	3.82
Ho	ppm	0.78	0.94	0.76	0.59	0.80	0.87	0.67	0.65	0.64	0.97	0.87	0.85
Er	ppm	2.30	2.73	2.13	1.78	2.31	2.57	1.83	1.91	1.89	2.76	2.26	2.21
Tm	ppm	0.32	0.46	0.27	0.24	0.33	0.36	0.32	0.25	0.21	0.39	0.32	0.27
Yb	ppm	2.05	2.50	2.14	1.54	2.16	2.47	1.94	2.02	2.14	2.39	1.89	2.27
Lu	ppm	0.28	0.38	0.30	0.24	0.36	0.37	0.31	0.28	0.29	0.39	0.29	0.30
Hf	ppm	1.04	1.55	1.09	0.74	1.23	1.58	1.10	1.18	1.09	1.35	1.01	1.11
Ta	ppm	0.00	0.01	0.01	0.00	0.01	0.03	0.02	0.02	0.01	0.00	0.00	0.01
Pb	ppm	0.17	0.20	0.09	0.35	0.28	0.35	0.25	0.32	0.15	0.31	0.22	0.14
Th	ppm	0.15	0.23	0.15	0.09	0.18	0.19	0.59	0.49	0.23	0.18	0.25	0.22
U	ppm	0.04	0.04	0.02	0.02	0.03	0.04	0.12	0.10	0.05	0.03	0.06	0.02
Ca (ISTD)	CPS	1043587	1027403	1079573	1138145	988853	1026579	931421	906762	898500	884061	635452	606367
	CPS RSD	4.40	4.40	5.48	6.88	10.90	12.42	10.54	12.20	8.85	2.85	6.55	7.17

Appendix 5–10. Results of Sr-Nd isotope analyses of the Kita-taku mafic complex and related rocks.

Sample. No	Type	Rb(ppm)	Sr(ppm)	$^{87}Rb/^{86}Sr$	$^{87}Sr/^{86}Sr$	$SrI^{(106Ma)}$	εSr	Sm(ppm)	Nd(ppm)	$^{147}Sm/^{144}Nd$	$^{143}Nd/^{144}Nd$	$NdI^{(106Ma)}$	εNd	2σ (Sr)	2σ (Nd)
21021406B	1	5	48	0.3013	0.705586	0.705132	10.7	1.21	4.40	0.1663	0.512628	0.512513	0.22	1	14
20110607A	1	1	67	0.0432	0.704954	0.704889	7.3	1.92	7.02	0.1654	0.512737	0.512622	2.35	1	13
20110204	2	1	335	0.0086	0.705220	0.705207	11.8	0.67	2.11	0.1920	0.512655	0.512522	0.40	1	14
21021302	2	2	238	0.0243	0.705093	0.705056	9.7	0.64	2.12	0.1825	0.512676	0.512550	0.94	1	14
20110302A	3	18	144	0.3616	0.705809	0.705264	12.6	2.89	10.5	0.1664	0.512659	0.512543	0.81	1	12
21021311	3	22	102	0.6239	0.705839	0.704899	7.4	2.44	8.62	0.1711	0.512710	0.512591	1.75	1	13
21021405A	3	8	230	0.1006	0.705329	0.705177	11.4	1.85	6.93	0.1614	0.512721	0.512609	2.09	1	14
21020610	3	12	298	0.1165	0.705354	0.705179	11.4	1.09	3.00	0.2197	0.512735	0.512583	1.58	1	14
20110604	3	5	339	0.0427	0.705414	0.705350	13.8	1.24	4.74	0.1582	0.512782	0.512672	3.33	1	14
20110303	6	23	287	0.2318	0.705574	0.705225	12.1	4.02	16.90	0.1438	0.512613	0.512513	0.22	1	13
21021401	4	4	289	0.0400	0.705240	0.705179	11.4	3.89	11.70	0.2010	0.512671	0.512531	0.58	1	14
20110605	4	6	282	0.0615	0.705267	0.705175	11.3	3.33	10.5	0.1917	0.512666	0.512533	0.62	1	12
20110302CPg	7	5	454	0.0319	0.705622	0.705574	17.0	3.85	15.6	0.1492	0.512571	0.512468	-0.66	1	13
20110309	Tdh	25	288	0.2511	0.706257	0.705878	21.3	0.76	3.95	0.1163	0.512555	0.512475	-0.52	1	14
21021404B	Tdh	16	290	0.1596	0.706250	0.706009	23.2	1.35	8.10	0.1008	0.512551	0.512481	-0.40	1	11
21020606B	Gr	141	150	2.7201	0.709467	0.705369	14.1	3.00	16.60	0.1093	0.512533	0.512457	-0.87	1	14
20110405	PFD	84	325	0.7477	0.706406	0.705280	12.8	6.91	28.50	0.1466	0.512594	0.512492	-0.18	1	14
20110405	PFD	84	325	0.7477	0.706413	0.705287	12.9	6.91	28.50	0.1466	0.512594	0.512492	-0.18	1	14
20110709C	PFD	116	229	1.4656	0.707933	0.705725	19.2	4.11	16.30	0.1524	0.512621	0.512516	0.27	1	13
20110705	Amp	13	336	0.1119	0.705562	0.705394	14.5	1.65	6.08	0.1641	0.512695	0.512581	1.54	1	14
20061202	Amp	21	191	0.3180	0.705562	0.705083	10.0	2.31	7.36	0.1898	0.512955	0.512823	6.28	1	12

Error values are 5 and 4 decimal places for Sr and Nd, respectively.

Appendix 5–11. Results of geothermometer and geobarometer of the Kita-taku mafic complex.

	Putirka (2008)		Wood & Banno (1973)	Wells (1977)
	Eqn 37	Eqn 39		
Sp. No	T (°C)	P (kbar)	T (°C)	T (°C)
1	939.14	4.87	992.53	973.95
2	943.55	5.32	986.08	972.08
3	965.70	5.04	999.54	993.13
4	913.04	4.01	975.30	946.52
5	957.38	4.58	1011.03	1006.23
6	883.28	4.53	936.67	907.54
7	980.50	3.80	1026.61	1031.73
8	978.45	5.27	989.81	1001.62
9	873.70	3.74	891.39	862.69
10	877.35	4.93	892.12	871.39
11	970.96	5.69	998.99	1014.66
12	933.90	4.91	972.36	958.91
13	856.66	4.36	900.36	859.78
14	926.20	5.87	963.20	945.80
15	946.32	4.98	988.84	973.10
16	907.07	4.74	957.35	925.58
17	934.31	3.98	975.32	950.15
18	937.63	3.97	968.59	958.72
19	884.58	4.87	919.49	890.01
20	915.90	4.37	969.63	947.51
21	921.55	4.86	967.33	950.83
22	960.22	5.63	993.08	986.54
23	872.69	4.89	925.35	896.22
24	857.07	3.81	918.07	879.14
25	842.23	4.31	913.17	868.05
26	835.47	4.06	898.08	849.35
27	912.48	4.14	962.95	934.28
Min.	835.47	3.74	891.39	849.35
Max.	980.50	5.87	1026.61	1031.73
Ave.	915.83	4.65	959.01	939.09

Appendix 5–12. Cpx/melt partition coefficients and compared data sources in the Figure 5–24.

Cpx/melt partition coefficients													
	Cs	Rb	Ba	Th	U	Nb	Ta	La	Ce	Pb	Sr	Nd	Sm
	0.0058	0.031	0.026	0.03	0.04	0.005	0.013	0.0536	0.0858	0.0102	0.06	0.1873	0.291
Ref.	e	d	d	d	d	d	d	c	c	e	d	c	c
	Zr	Hf	Eu	Ti	Gd	Tb	Dy	Y	Ho	Er	Tm	Yb	Lu
	0.1234	0.256	0.474	0.384	0.556	0.57	0.5	0.467	0.6	0.6	0.6	0.43	0.433
Ref.	c	c	b	c	b	b	a	c	a	a	a	c	c

References a: Irving & Frey, 1984, b: Fujimaki et al., 1984, Hart and Dunn, 1993, d: Rollinson, 1993, e: Hauri et al., 1994.

Data source of HMA fields and compile date in the Fugure 5–26.	
Snukitic HMA	Tatsumi and Ishizaka, 1982b; Shiraki et al., 1991; Nagao et al., 1992; Kakubuchi et al., 1995; Shiraki et al., 1995; Shimoda et al., 1998; Tatsumi et al., 2003; Kamei et al., 2004.
Adakitic HMA	Kay, 1978; Yogodozinski et al., 1995; Stern and Kilian, 1996.
Bajaitic HMA	Rogers et al., 1985; Saunders et al., 1987.
Boninitic HMA	Hickey and Frey, 1982; Taylor et al., 1994.
Back arc basin basalt (BABB) Stern, 2002.	
Arc tholeiite (ArcTH) Peate et al., 1997.	
Continental crust (CC) Taylor and McLenan, 1985; MacLenan and Taylor, 1996.	
Ocean island basalt (OIB) Sun and McDonough, 1989.	
Average oceanic basalt (Ave. OB) Kelemen et al., 2014.	
Average continental basalt (Ave. CB) Kelemen et al., 2014.	
Average oceanic andesite (Ave. OA) Kelemen et al., 2014.	
Average continental andesite (Ave. CA) Kelemen et al., 2014.	

Appendix 6–1. Partition coefficients used in the batch melting calculation.

	Amphibole		Plagioclase		Biotite		Clinopyroxene		Titanite	
Rb	0.055	i	0.068	i	3.2	e	0.01	i	0.5	i
Ba	0.046	i	0.2	k	5.367	e	0.006	i	1.5	i
Th	0.055	i	0.095	i	0.997	e	0.104	i	0.16	i
U	0.05	i	0.091	i	0.13	c	0.032	i	0.14	i
Nb	0.44	h	0.239	i	4	e	0.007	i	2.2	i
Ta	0.22	h	0.053	i	1.567	e	0.028	i	6.55	i
La	0.319	i	0.358	i	2	e	0.028	i	4.73	i
Ce	0.56	i	0.339	i	2	e	0.059	i	7.57	i
Sr	0.389	i	1	k	0.447	e	0.032	i	2.68	i
Nd	1.32	i	0.289	i	2.56	e	0.115	i	12.4	i
Sm	2.09	i	0.237	i	2.117	e	0.259	i	14	i
Zr	0.417	i	0.078	i	0.59	g	0.125	i	1.92	i
Hf	0.781	i	0.069	i	1.8	c	0.208	i	2.43	i
Eu	1.79	i	2.17	i	2.02	e	0.341	i	13.8	i
Ti	4.03	i	1	k	0	c	0.473	i	67	i
Gd	2.53	i	0.192	i	0.442	b	0.422	i	11.9	i
Dy	2.55	i	0.15	i	1.72	e	0.57	i	8.27	i
Y	2.47	i	0.138	i	1	e	0.603	i	5.42	i
Er	2.22	i	0.117	i	0.162	a	0.64	i	5.54	i
Yb	1.79	i	0.094	i	1.4	e	0.635	i	3.02	i
Lu	0.32	f	0.027	a	1.617	e	0.49	d	6	d

References

a: Schnetzler and Philpots (1970), b: Matsui et al. (1977), c: Villemant et al. (1981), d: Green and Pearson (1985), e: Rollinson (1993), f: Adam and Green (1994), g: Ewart and Griffin (1994), h: Foley et al. (2002), i: Bédard (2006a), j: Bédard (2006b), and k: Foley (2008).